Springer Series in Materials Science 220

Dusan Losic
Abel Santos *Editors*

Electrochemically Engineered Nanoporous Materials

Methods, Properties and Applications

Springer

Springer Series in Materials Science

Volume 220

The Springer Series in Materials Science covers the complete spectrum of materials physics, including fundamental principles, physical properties, materials theory and design. Recognizing the increasing importance of materials science in future device technologies, the book titles in this series reflect the state-of-the-art in understanding and controlling the structure and properties of all important classes of materials.

More information about this series at http://www.springer.com/series/856

Dusan Losic · Abel Santos
Editors

Electrochemically Engineered Nanoporous Materials

Methods, Properties and Applications

Springer

Editors
Dusan Losic
School of Chemical Engineering
The University of Adelaide
Adelaide
Australia

Abel Santos
School of Chemical Engineering
The University of Adelaide
Adelaide
Australia

ISSN 0933-033X ISSN 2196-2812 (electronic)
Springer Series in Materials Science
ISBN 978-3-319-20345-4 ISBN 978-3-319-20346-1 (eBook)
DOI 10.1007/978-3-319-20346-1

Library of Congress Control Number: 2015943364

Springer Cham Heidelberg New York Dordrecht London

Printed on acid-free paper

Springer International Publishing AG Switzerland is part of Springer Science+Business Media (www.springer.com)

Preface

The aim of this book is to present the recent progress in the three most popular *Electrochemically Engineered Nanoporous Materials*, including porous silicon, nanotubular titania, and nanoporous anodic alumina. Electrochemical engineering based on anodization and etching processes is recognized as one of the most cost-effective and simplest approaches to engineer nanoscale materials with controllable dimensions and properties. The book covers a selected range of topics presented throughout 11 chapters, which cover the most significant aspects involved in the understanding, properties, preparation methods, and emerging applications of these outstanding nanoporous materials. The chapters are written by a selected group of expert scientists in the field and we believe that this book represents valuable contribution to this emerging and fast developing field, with direct implications for a plethora of disciplines, including electronics, optics and photonics, medicine, engineering, physics, and chemistry.

The first chapter presents the fundamental aspects involved in the fabrication of porous silicon structures, with special focus on the different concepts and approaches used to produce nanostructures with precisely engineered geometric features. A more detailed insight into the properties and applications of porous silicon is presented in the second chapter. The third chapter is devoted to the synthesis of nanotubular titania produced by electrochemical anodization of titanium substrates, and its subsequent application as a template material. The fourth chapter compiles a fresh insight into the combination of porous silicon structures with emerging capture probes aimed to develop highly sensitive and selective sensing systems. Porous silicon has been extensively used in biomedical applications during the past decade. The fifth chapter highlights the most outstanding advances in this emerging and exciting field and the sixth chapter compiles fundamental aspects of porous silicon in drug delivery applications. The seventh chapter compiles a variety of examples of applicability of nanoporous anodic alumina as optical biosensing platform, which is recognized as one of the most promising applications for this nanomaterial. The eighth chapter is devoted to the different chemical and electrochemical approaches used to engineer the structure of nanoporous anodic alumina to develop optical systems and applications. The different fundamental aspects of

nanotubular titania as a new material for solar cell applications are presented in the ninth chapter. Finally, the tenth chapter shows a detailed review on the recent advances in nanotubular titania for drug delivery applications.

As a result of the highly interdisciplinary nature of this book, it should be of profound and immediate interest for a broad audience, including undergraduate students, academics, and industrial scientists and engineers across many disciplines, ranging from physics, chemistry, engineering, materials science, bioengineering, and medicine. We believe that this book will also be valuable to many entrepreneurial and business people, who are in the process of trying to better understand and valuate nanotechnology and new nanomaterials for future high-tech emerging applications and disrupting industries.

Adelaide, Australia

Dusan Losic
Abel Santos

Contents

Contributors

Gerald Atkins Discipline of Orthopaedics and Trauma, University of Adelaide, Adelaide, Australia

Anna Brudzisz Faculty of Chemistry, Department of Physical Chemistry and Electrochemistry, Jagiellonian University, Kraków, Poland

Agnieszka Brzózka Faculty of Chemistry, Department of Physical Chemistry and Electrochemistry, Jagiellonian University, Kraków, Poland

Polycarpos Falaras Institute of Nanoscience and Nanotechnology (INN), National Centre for Scientific Research Demokritos, Athens, Greece

Josep Ferré-Borrull Nanoelectronic and Photonic Systems (NePhoS), Departament d'Enginyeria Electrònica, Elèctrica i Automàtica, Universitat Rovira i Virgili, Tarragona, Spain

David Findlay Discipline of Orthopaedics and Trauma, University of Adelaide, Adelaide, Australia

Karan Gulati School of Chemical Engineering, University of Adelaide, Adelaide, Australia

Katarzyna Hnida AGH University of Science and Technology, Academic Centre for Materials and Nanotechnology, Kraków, Poland

Masakazu Kogawa Discipline of Orthopaedics and Trauma, University of Adelaide, Adelaide, Australia

Tushar Kumeria School of Chemical Engineering, The University of Adelaide, Adelaide, Australia

Vesa-Pekka Lehto Department of Applied Physics, University of Eastern Finland, Kuopio, Finland

Dusan Losic School of Chemical Engineering, University of Adelaide, Adelaide, Australia

Rachel D. Lowe Biological Micro- and Nanotechnology, Max Plank Institute for Biophysical Chemistry, Göttingen, Germany

Jan M. Macak Center of Materials and Nanotechnologies, Faculty of Chemical Technology, University of Pardubice, Pardubice, Czech Republic

Shaheer Maher School of Chemical Engineering, University of Adelaide, Adelaide, Australia; Faculty of Pharmacy, Assiut University, Assiut, Egypt

Lluís F. Marsal Nanoelectronic and Photonic Systems (NePhoS), Departament d'Enginyeria Electrònica, Elèctrica i Automàtica, Universitat Rovira i Virgili, Tarragona, Spain

Steven J.P. McInnes ARC Centre of Excellence in Convergent Bio-Nano Science and Technology, Mawson Institute, University of South Australia, Mawson Lakes, Australia

Josep Pallarés Nanoelectronic and Photonic Systems (NePhoS), Departament d'Enginyeria Electrònica, Elèctrica i Automàtica, Universitat Rovira i Virgili, Tarragona, Spain

Joakim Riikonen Department of Applied Physics, University of Eastern Finland, Kuopio, Finland

Abel Santos School of Chemical Engineering, The University of Adelaide, Adelaide, Australia

Ester Segal Department of Biotechnology and Food Engineering, Technion-Israel Institute of Technology, Haifa, Israel; Russell Berrie Nanotechnology Institute, Technion-Israel Institute of Technology, Haifa, Israel

Thomas Stergiopoulos Institute of Nanoscience and Nanotechnology (INN), National Centre for Scientific Research Demokritos, Athens, Greece

Grzegorz D. Sulka Department of Physical Chemistry and Electrochemistry, Faculty of Chemistry, Jagiellonian University, Kraków, Poland

Elena Tenenbaum Department of Biotechnology and Food Engineering, Technion-Israel Institute of Technology, Haifa, Israel

Katharina Urmann Institute of Technical Chemistry, Gottfried-Wilhelm Leibniz Universität Hannover, Hannover, Germany; Department of Biotechnology and Food Engineering, Technion-Israel Institute of Technology, Haifa, Israel

Naoum Vaenas Institute of Nanoscience and Nanotechnology (INN), National Centre for Scientific Research Demokritos, Athens, Greece

Johanna-Gabriela Walter Institute of Technical Chemistry, Gottfried-Wilhelm Leibniz Universität Hannover, Hannover, Germany

Elisabet Xifré-Pérez Nanoelectronic and Photonic Systems (NePhoS), Departament d'Enginyeria Electrònica, Elèctrica i Automàtica, Universitat Rovira i Virgili, Tarragona, Spain

Wujun Xu Department of Applied Physics, University of Eastern Finland, Kuopio, Finland

Chapter 1
Electrochemical Etching Methods for Producing Porous Silicon

Abel Santos and Tushar Kumeria

Abstract Porous silicon produced by electrochemical etching of silicon has become one of the most popular materials used in many scientific disciplines as a result of its outstanding and unique set of chemical and physical properties and cost-competitive fabrication processes. To understand the electrochemical mechanisms taking place in the course of the etching of silicon is a key factor to control and modify the structure of this versatile porous material. This makes it possible to produce a broad range of structures, which can range from a porous matrix to arrays of nanowires. These structures are unique and bring new opportunities for multiple research fields and applications such as biotechnology, medicine, optoelectronics, chemistry and so forth. This chapter is aimed at compiling and summarising the fundamental aspects behind the production of porous silicon structures by electrochemical and metal-assisted etching of silicon wafers. Our objective is to provide a simple but detailed overview about the fabrication process of porous silicon, with special emphasis on the different fabrication conditions and geometric and morphological features of the resulting silicon nanostructures.

1.1 Introduction

Regardless of the emergence of other materials with supreme electronic properties such as graphene, gallium nitride (GaN) or gallium arsenide (GaAs), silicon is and will most probably continue to be the material of choice in semiconductor technology for developing integrated circuits and other microdevices during the next decades. Silicon is the second most abundant element on earth and it is most widely distributed in dusts and sands as various forms of silica (silicon dioxide) or silicates. Typically, electronic grade silicon wafers (high purity silicon 99.9999999 %—9 N)

A. Santos (✉) · T. Kumeria
School of Chemical Engineering, The University of Adelaide,
North Engineering Building, Adelaide 5005, Australia
e-mail: abel.santos@adelaide.edu.au

D. Losic and A. Santos (eds.), *Electrochemically Engineered Nanoporous Materials*, Springer Series in Materials Science 220,
DOI 10.1007/978-3-319-20346-1_1

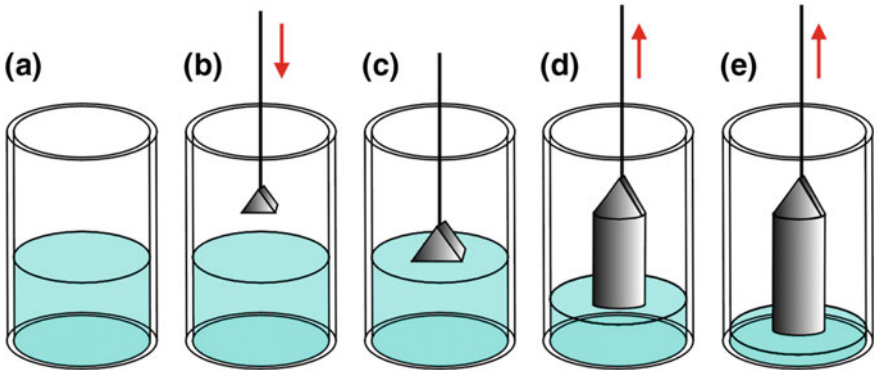

Fig. 1.1 Schematic diagram illustrating the Czochralski growth method for producing silicon wafers at industrial scale [1]. **a** Melting of polysilicon from raw silicon sources. **b** Introduction of the seed crystal. **c** Beginning of the silicon crystal growth. **d** Silicon crystal pulling (withdraw mode). **e** Resulting silicon crystal with residue of melted polysilicon

are produced by Czochralski growth method. In this process, a cylindrical ingot of high purity monocrystalline silicon is formed by pulling a seed crystal from a bath composed of polysilicon (Fig. 1.1) [1]. Silicon can be doped in the course of this process with donor impurity atoms (e.g. boron or phosphorus) by adding precisely controlled amounts of these elements to the batch. This process makes it possible to produce n-type (P doping) or p-type (B doping) silicon wafers with controlled doping and thus with different electronic properties. To avoid undesired contaminations, this process is normally performed under inert atmosphere (e.g. argon gas) in an inert crucible made of quartz. The width of the resulting cylindrical ingot is accurately controlled by the temperature and the speeds of rotation and withdrawn. After that, the crystal ingot, which can be up to 2 m in length, is sliced to produce silicon wafers. Note that commercial silicon wafers are available as single-crystalline wafers featuring diameters of 100, 125, 150, 200 and 300 mm, the thickness of which is usually within the range of 0.4–0.7 mm. Moreover, these wafers can be produced with different crystal orientations, which typically are (100), (111) and (110). These silicon wafers became the base of the silicon age, which started with the invention of the integrated circuitry by Jack Kilby and Robert Noyce [2].

Silicon wafers can be electrochemically etched through different approaches to produce a broad range of porous silicon (pSi) structures. The first report on pSi dates back to 1956, when the Uhlirs discovered coloured deposits on electrochemically etched silicon when they were working on electrochemical methods to machine silicon wafers for microelectronic applications at the Bell Laboratories. However, the obtained results differed from the expected polish finishing and the potential applications of the resulting material were almost ignored [3]. This work was followed by a flood of studies focused on different chemical/electrochemical approaches aimed to etch silicon wafers under different conditions [4–10]. The first

study on the porous nature of pSi was reported by Watanabe and Sakai in 1971 [11]. Throughout the following decades, many studies on pSi and its properties were published. In particular, interest in pSi nanostructures exploded when Ulrich Gösele identified quantum confinement effects in the absorption spectrum of pSi and Leigh Canham observed efficient, bright red-orange photoluminescence from pSi nanostructures [12, 13]. These studies were the origin of a series of works aimed at understanding the pore formation mechanism and controlling the properties of pSi such as surface chemistry and pore geometry. The objectives of these studies were to expand and explore the use of pSi in different applications such as optoelectronic devices and sensors. Several theories about the formation mechanisms of pSi were postulated, including crystallographic face selectivity, enhanced electric field, tunnelling, quantum confinement and space-charge limited [14–30].

This chapter is aimed at describing the fundamental aspects of electrochemical and metal-assisted etching methods used to produce porous silicon structures. First, the fundamental and basic concepts related with the production and fabrication of pSi will be summarised and described. Then, we will introduce the main aspects involved in the fabrication of pSi by electrochemical etching method. Subsequently, we will provide a detailed description of metal-assisted etching of silicon, which is considered as an outstanding alternative or complementary method to traditional electrochemical etching of silicon. Finally, we will conclude this chapter with a general overview and a prospective outlook on the future trends in this field.

1.2 Basic Concepts

Typically, porous silicon structures are produced by electrochemical etching of silicon wafers in organic solutions of acetonitrile (CH_3CN) or dimethylformamide (C_3H_7NO) containing hydrofluoric acid (HF) [31, 32]. Nevertheless, other approaches such as chemical etching in mixtures of HF and nitric acid (HNO_3) and metal-assisted etching have been intensively used to produce a variety of pSi structures. It is worth stressing that HF is highly corrosive towards living tissues and its inhalation, ingestion or skin contact are all extremely hazardous and can be lethal. Therefore, in addition to the standard laboratory protection, it is mandatory to first consider all the safety aspects related to HF handling. In general, during production of porous silicon by chemical or electrochemical etching methods, HF should be handled under a hood with proper ventilation, wearing personal HF gas monitor with audible alarm, safety sensor for liquids and proper personal protective equipment such as safety goggles, face shield, chemically resistant butyl rubber gloves and apron [31]. Note that prior to etching, the native oxide layer formed on commercial silicon wafers under ambient atmospheric conditions must be removed. There are several procedures to remove that oxide layer although the most widespread method is the so-called RCA cleaning process [33]. This process is divided into three steps: namely; (i) removal of organic contaminants, (ii) removal of the native oxide layer and (iii) removal of ionic contaminations. The first step is

performed in a mixture of deionised water, ammonium hydroxide (NH_4OH) and hydrogen peroxide (H_2O_2) at 80 °C for 10 min. This step removes organic residues and also particles from the surface of the silicon wafer. Furthermore, this treatment results in the formation of a layer of silicon dioxide with controlled thickness (i.e. 10 Å). The second step consists of a short immersion in a mixture of HF and water at 25 °C for about 15 s in order to remove the native oxide layer and some fraction of ionic contaminants. Finally, the third step is typically performed in order to effectively remove the remaining traces of metallic contaminants and create a thin passivating layer on the wafer surface. This step is carried out by dipping the silicon wafer in a mixture of water, hydrochloric acid (HCl) and H_2O_2 at 80 °C for 10 min. Finally, after these pre-treatments, silicon wafers are ready to be electrochemically or chemically etched to produce pSi structures.

Another important aspect to have into account in the fabrication of pSi structures is the design of the electrochemical cell. This is extremely important as an inappropriate design of the cell can lead to broken samples, leaky set-ups and corroded contacts. Note that aspects such as materials, contacts and sealants are critical in the design of the electrochemical cell used to produce pSi by electrochemical or chemical etching approaches. Traditionally, since most common acid electrolytes used to prepare pSi are HF-based solutions, the materials of choice used to fabricate the body of the etching cells are resistant to HF. The most representative examples of these are polyvinyl chloride (PVC) and polytetrafluoroethylene (PTFE). However, other alternatives such as polyvinylidene fluoride (PVDF) can be used as well. As far as the sealant is concerned, standard black O-rings made of acrylonitrile-butadiene copolymer (Perbunan) or vinylidene fluoride-hexafluoropropylene (Viton) are preferred as they are stable in HF at concentrations up to 50 %. Furthermore, a good ohmic contact must be implemented in these cells used to produce pSi by electrochemical etching. In that respect, it is critical to consider the resistance of the metal used as a contact towards corrosion since a continuous exposure to the etching electrolyte can degrade its integrity with use and thus its performance. Typically, noble metals such as platinum or gold are the best choice as they are inert. Other materials such as stainless steel, brass, tungsten or aluminium can be used if the electrochemical cell is designed to prevent the electrical contact from exposure to the etching electrolyte (i.e. etchant). Therefore, an optimal design of the electrochemical cell becomes essential in order to produce pSi structures with controlled features under optimised conditions. It is worth stressing that, in addition to the aforementioned fundamental aspects, etching cells can feature multiple characteristics such as circulation of etching electrolyte, temperature controller and cooling system, automated stirring for bubble removal and enhanced reaction rate, illumination and so forth. The most representative examples of etching cells are the immersion cell, the O-ring cell and the double cell. Figure 1.2 shows illustrations of these etching cells used in pSi technology.

As discussed above, after the cleaning step and immersion in HF solutions, the silicon wafer surface is terminated with hydrogen atoms (Si–H). Hydrogen-terminated silicon surfaces are hydrophobic, showing a large contact angle for a drop of water [34, 35]. Silicon surfaces dipped in HF or in ammonium fluoride (NH_4F) show equivalent hydrophobic character. However, the roughness of these

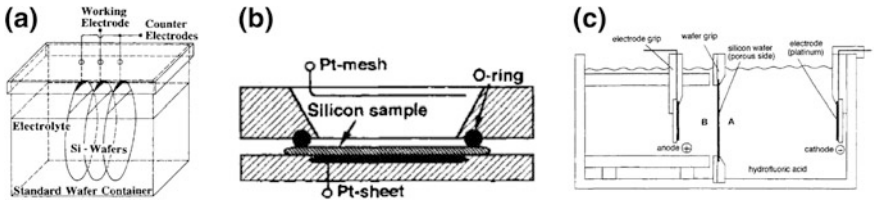

Fig. 1.2 Schemes depicting basic designs of electrochemical cells typically used to produce porous silicon by electrochemical etching (adapted from [31]). **a** Immersion cell. **b** O-ring cell. **c** Double cell

surfaces is highly dependent on the chemical treatment and type of etchant. While NH_4F provides atomically flat surfaces for (111) and (100) oriented silicon surfaces, a treatment with HF creates surfaces with nanometric roughness [36, 37].

As far as the chemical dissolution of hydrogen-terminated silicon is concerned, this process requires the replacement of superficial H atoms by fluoride ions (F^-), which are incorporated from the etching electrolyte solution. Under open circuit conditions, the silicon surface remains passivated. Therefore, an electronic hole (h^+) must be generated to create a neutralized Si–F bound. The Si–F bound can be created under certain anodic bias by the polarisation effect induced by the F atom over the Si atom. Following this mechanism, a new F^- atom bounds the Si atom at a different position and a gas hydrogen molecule (H_2) is generated. The progressive repetition of this process weakens the Si–Si bounds by the strong electronegativity of F atoms through nucleophilic attack (1.1).

$$\mathrm{Si} + 4\mathrm{HF}_2^- + \mathrm{h}^+ \rightarrow \mathrm{SiF}_6^{2-} + 2\mathrm{HF} + \mathrm{H}_2 + \mathrm{e}^- \tag{1.1}$$

Finally, Si atoms are etched away from the Si surface by reaction with HF and thus pores are generated into the Si wafer progressively [38, 39]. For this reason, the fabrication process of pSi is considered a top-bottom approach. So far, many different mechanisms have been proposed to explain the pore formation in pSi. Most of the theories deal only with certain aspects of the pore formation mechanism. Nonetheless, it is generally accepted that pore formation in pSi is a result of different mechanisms [32]. Therefore a complete model explaining the formation mechanism of pSi is yet to come.

Another important aspect in the fabrication of pSi structures is the use of wet chemical etching with alkaline etchants, which are mainly used for chemical polishing or anisotropic etching of silicon. These pre- and post-treatments make it possible to design and engineer a broad range of pSi structures. The most widespread alkaline etchants used to etch silicon are potassium hydroxide (KOH) and tetramethyl ammonium hydroxide (TMAH), although other inorganic and organic compounds such as lithium hydroxide (LiOH), sodium hydroxide (NaOH), rubidium hydroxide (RbOH), caesium hydroxide (CsOH), ammonium hydroxide (NH_4OH), cholin and ethylenediamine have been used as well [33, 40–53]. It is worthwhile mentioning that the etching rate of silicon in these etchants is highly dependent on

the crystal planes, the doping level of the silicon crystal and the etchant concentration and its temperature.

Porous silicon structures featuring a broad range of pore geometries, sizes and morphologies can be produced by electrochemical etching of silicon wafers. The resulting pore features of pSi rely not only on the etching conditions but also on such parameters as the doping level of the Si wafer, its crystallographic structure, pre- or post-treatments and so on [30, 54]. Following the International Union of Pure and Applied Chemistry (IUPAC) nomenclature used to classify porous materials as a function of their pore size (d_p), pSi structures can be divided into three categories: (i) microporous silicon (μpSi) with $d_p < 2$ nm, mesoporous silicon (mpSi) with 2 nm $< d_p <$ 50 nm and macroporous silicon (MpSi) with $d_p > 50$ nm. Although pSi can present a variety of morphological details, these can be divided into two main categories: (i) sponge-like pSi, which features densely and randomly distributed branched pores and (ii) pSi featuring cylindrical pores, which can have rough or smooth walls. While μpSi and mpSi structures feature sponge-like morphology, MpSi structures have cylindrical pores.

As far as the spatial distribution of pores, MpSi structures present a random distribution. However, these structures can be produced featuring a perfectly ordered spatial distribution of pores. To this end, the surface of the silicon wafer must be patterned by lithographic techniques before the electrochemical etching process is carried out. In contrast, the sponge-like morphology of μpSi and mpSi cannot be defined by a concrete spatial distribution because of the complex structure of their porous network.

As mentioned above, the resulting pore structure in pSi is intrinsically dependent on the doping level of the Si wafer. For example, MpSi is produced by electrochemical etching of n-type wafers. The etching of p- and n-type Si wafers with a high or moderate level of doping yields mpSi structures and μpSi structures. The reason why the pore characteristics of the resulting pSi structures depend upon the doping type and its level of the silicon wafer is that the pore formation mechanisms relies on these parameters. For instance, different formation mechanisms are involved in the formation of MpSi structures by electrochemical etching of n-type Si wafers (i.e. crystallographic face selectivity, enhanced electric field, tunnelling and quantum confinement). The enhanced electric field and tunnelling mechanisms are associated with the formation of mpSi structures when highly or moderately doped Si wafers are electrochemically etched in HF solutions. Finally, the space-charge limited mechanism is associated with the pore formation in μpSi structures, which results when n-type silicon wafers are electrochemically etched in HF solutions.

1.3 Electrochemical Etching of Silicon

The fabrication process of pSi structures by electrochemical etching is a cost-competitive and versatile method, by means of which a variety of porous structures with outstanding physical and chemical properties can be produced. This

Table 1.1 Summary of the most representative electrochemical etching conditions used to produce porous silicon structures and their geometric features (adapted from [31])

Type	J (mA cm^{-2})		Doping Density (cm^{-3})		
			1×10^{17}	1×10^{18}	1×10^{19}
p	300	Pore morphology and porosity	Sponge-like 80 %	Narrow long pores with dendritic branches 75 %	Wide long pores with high wall roughness 80 %
	30		Sponge-like 70 %	Sponge-Like 60 %	Medium long pores with dendritic branches 50 %
	3		Sponge-like 60 %	Sponge-Like 40 %	Narrow long pores with dendritic branches 40 %
n	300	Pore morphology and porosity	Wide long pores with low wall roughness 35 %	Wide long pores with medium wall roughness 40 %	Narrow long pores with dendritic branches 45 %
	30		Medium long pores with dendritic branches 10 %	Narrow long pores with dendritic branches 15 %	Narrow long pores with dendritic branches 20 %
	3		Sponge-like 10 %	Sponge-like 20 %	Sponge-like 30 %

has turned pSi into one of the most widespread materials, which is currently present in many research fields with multiple applications. This section deals with the different aspects involved in the production of MpSi, mpSi and μpSi structures by electrochemical etching of silicon wafers. Table 1.1 summarises the most representative etching conditions and geometric features of pSi structures produced by electrochemical etching of silicon wafers.

1.3.1 Macroporous Silicon

Macroporous silicon is typically produced by electrochemical etching of n-type silicon wafers. The porous structure of MpSi is very versatile and can be broadly modified by different electrochemical approaches. As far as the pore formation mechanism of MpSi is concerned, electronic holes initiate the dissolution process of silicon and these are minority charge carriers in n-type silicon. Therefore, the concentration of electronic holes in n-type silicon under equilibrium conditions is very low. However, electronic holes can be generated by illuminating the backside

of the silicon wafer. Under such circumstances, three types of charges are present in the bulk silicon: namely, electronic holes, electrons and ionized donors. The system is at neutral state when the concentration of electrons is equal to the concentration of electronic holes and ionized donors together. Therefore, for a given level of doping, the growth of MpSi in n-type silicon substrates can be led by the current density and the illumination applied in the course of the etching process. As-produced MpSi has a random pore distribution since pores nucleate uniformly on the Si wafer surface (Fig. 1.3a, c). Nonetheless, a pre-treatment by a lithographic patterning stage enables the production of MpSi structures with perfectly ordered pores featuring square or triangular arrangement (Fig. 1.3b, c).

The growth of well-defined cylindrical macropores from top to bottom in MpSi can be precisely controlled through the etching parameters (e.g. etching current density, HF concentration and its temperature, wafer doping, illumination intensity, etc.). In particular, among these parameters, the etching current density (J) is a critical factor to lead a homogeneous pore growth as the longer the pore the more effective the collection of photo-generated holes. Therefore, the etching current density must be increased as macropores grow in order to obtain straight and well-defined cylindrical pores from top to bottom. This can be achieved by adjusting the illumination intensity at the backside of the Si wafer during the etching process. Otherwise, according to the Lehmann's law, the increasing collection of photo-generated holes results in a progressive reduction of the pore diameter with depth, yielding cone-like pores with decreasing diameter from top to bottom [31].

This effect is shown in Fig. 1.4, which depicts the difference between macroporous silicon structures formed under constant (Fig. 1.4a) and progressively modified (Fig. 1.4b) illumination intensity. However, far from being a disadvantage, this approach can be readily used to develop some optical structures such as photonic crystals and optical waveguides in the visible and NIR range as the refractive index of MpSi can be engineered in depth along the pore yielding a waveguide structure embedded in the array of macropores [55, 56]. Furthermore, this technique can be combined with lithographic patterning to produce 2D infrared photonic crystals featuring perfectly ordered and straight macropores [57–64]. In this process, arrays of macropores are coated by a lithographic mask after electrochemical etching. Next, MpSi is selectively removed from the unmasked areas by a wet chemical etching. This results in a set of deep bars of macropore rows with well-defined pore geometry [61–63, 65].

Following a similar approach based on the Lehmann's model, the pore diameter in macroporous silicon can be periodically modulated (Fig. 1.5). This approach takes advantage from the fact that the porosity of the resulting MpSi structure is established by the ratio between the total current density and the critical current density (i.e. J_{PS}—current density limit between the formation of pSi and electropolishing of silicon). According to the Lehmann's model for the formation of MpSi, the current density at the pore bottom tips is equal to the critical current density.

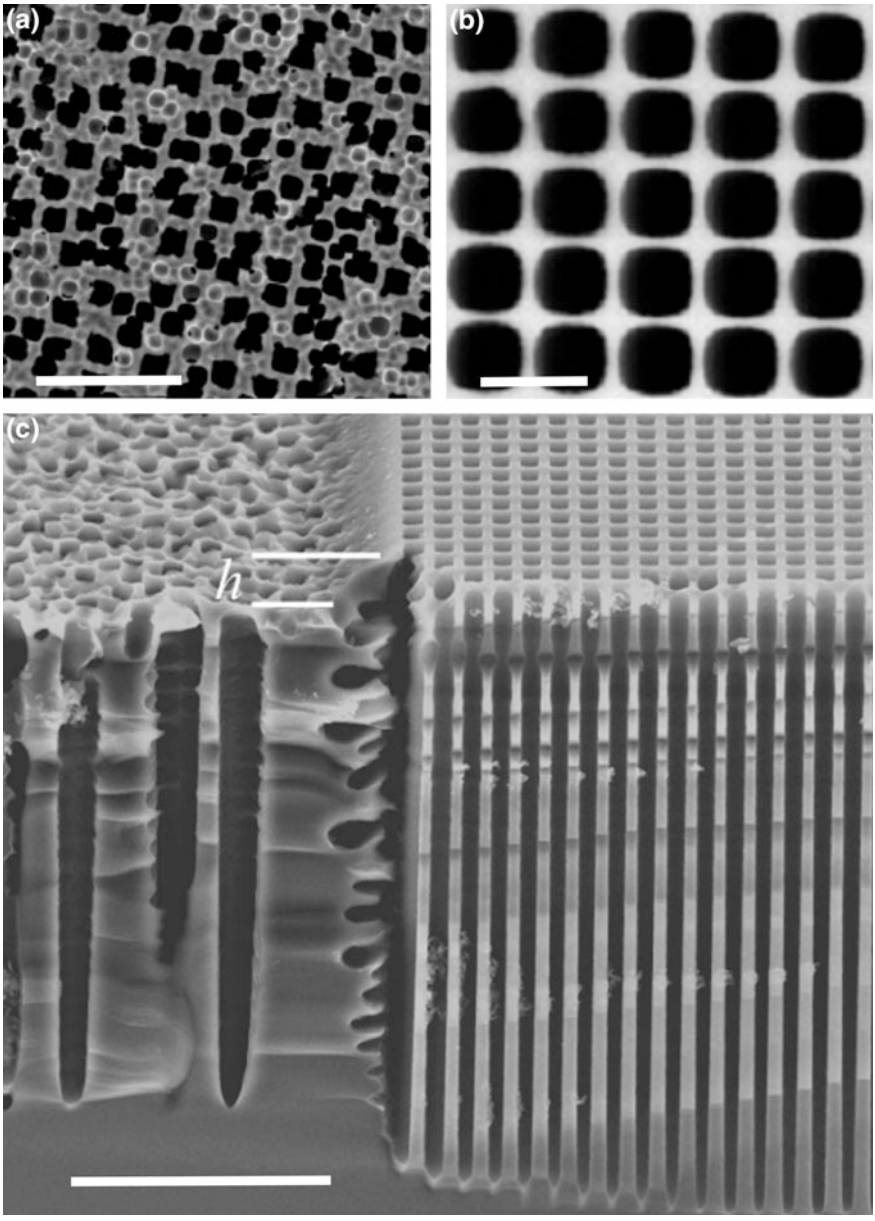

Fig. 1.3 Scanning electron microscopy images of macroporous silicon structures produced in n-type silicon substrates (adapted from [54]). **a** *Top-view* of as-produced MpSi (scale bar = 40 μm). **b** *Top-view* of MpSi patterned by photolithography (scale bar = 5 μm). **c** Cross-section depicting details of pores shown in structures (**a**) and (**b**) (scale bar = 40 μm)

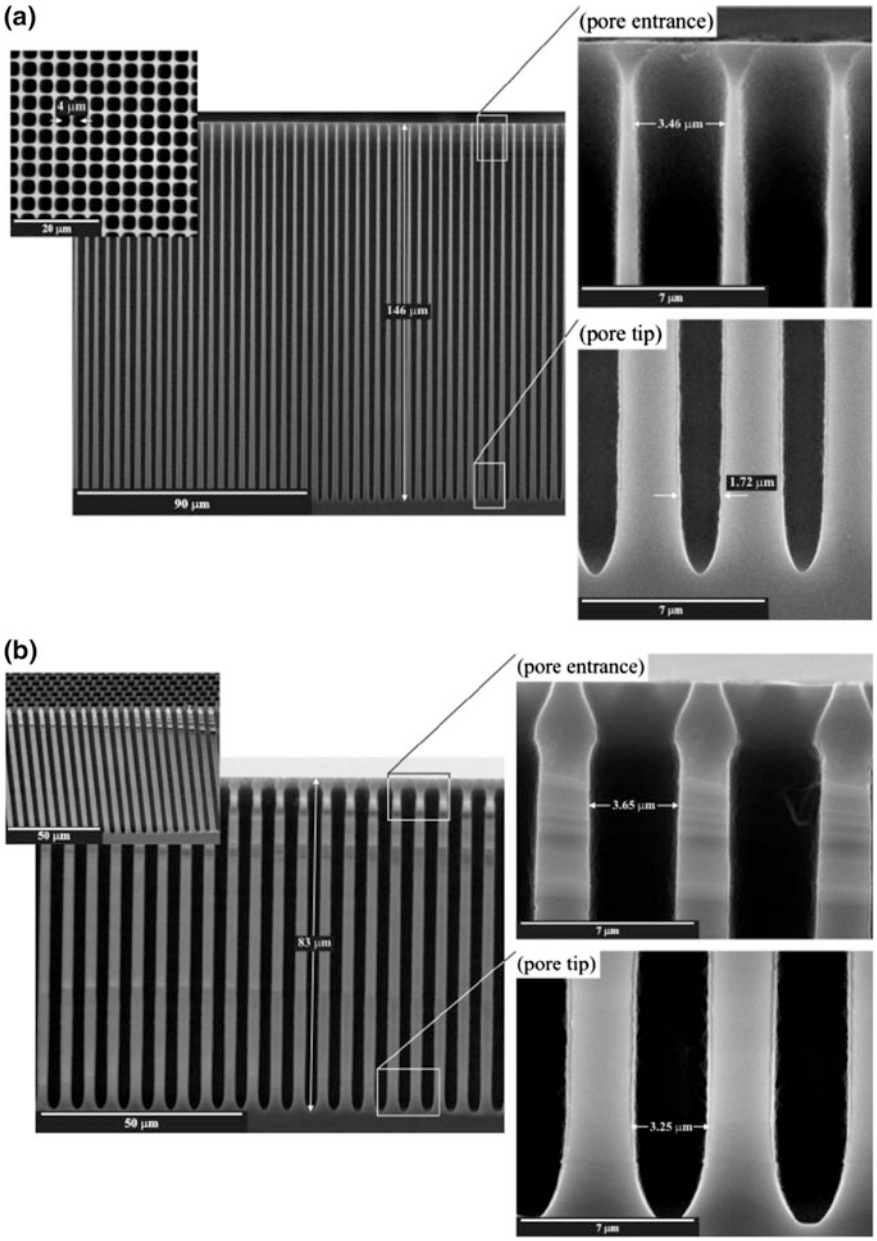

Fig. 1.4 Scanning electron microscopy images of macroporous silicon structures produced in n-type silicon substrates under **a** constant and **b** progressively adjusted illumination intensity (adapted from [54])

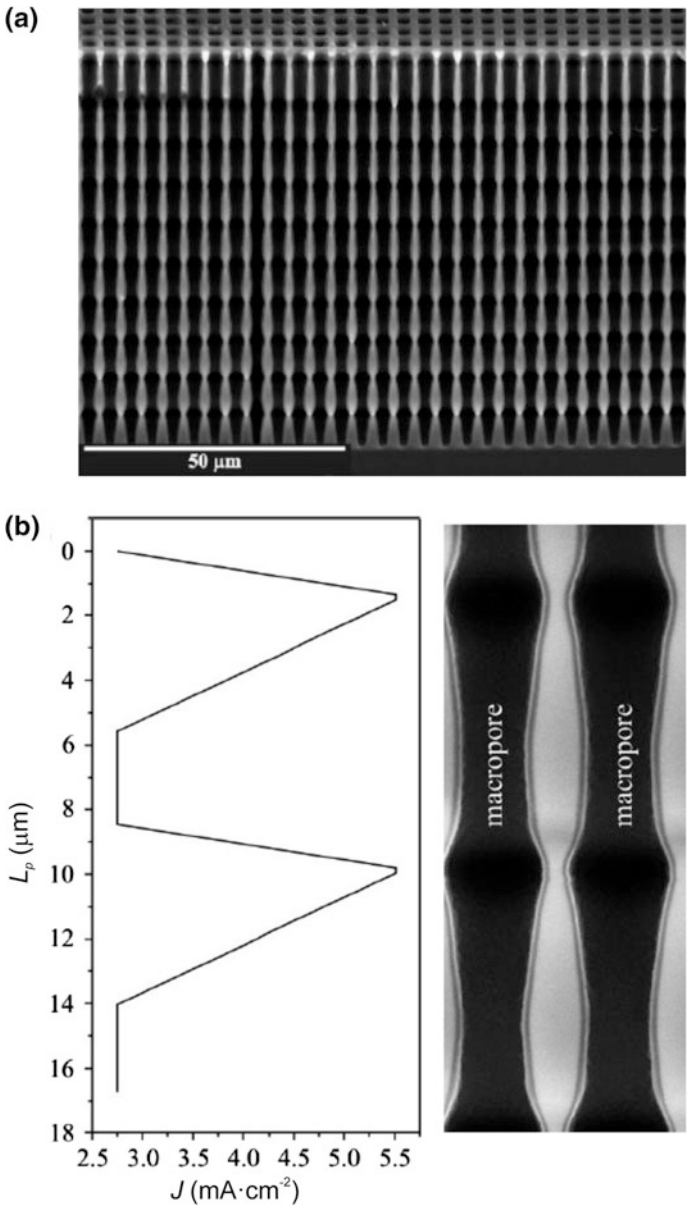

Fig. 1.5 Scanning electron microscopy images of macroporous silicon structures featuring pore diameter modulations with depth (adapted from [54]). **a** Slanted cross-section view of MpSi with pore diameter modulations. **b** Relationship between current density profile and pore length and magnified view of macropores featuring diameter modulations

Therefore, an increment of the illumination intensity at the backside of the silicon wafer during etching leads to the generation of electronic holes, which directly contribute to the total current density. Note that the critical current density is constant at the pore bottom tips and thus the increment of the total current density produced by the generation of electronic holes widens the pore diameter. Following this procedure, the pore structure of MpSi can be modulated to produce periodic ratchet-type (i.e. asymmetric) or circular (i.e. symmetric) pore modulations.

In summary, pore diameter in MpSi can be periodically modulated by a periodical change of the illumination intensity at the backside of the Si wafer during the etching process since the current density profile is translated into the pore structure [66]. It is worth stressing that, if the etching conditions are not controlled, the period length, which is defined as the distance between two consecutive pore modulations, decreases with the pore depth due to diffusion limitations (i.e. lower concentration of HF at the pore bottom tips). As a result, the critical current density decreases and the pore growth rate becomes slower. Finally, pore diameter modulations in MpSi can yield a 3D network of interconnected macropores, which can be achieved by a suitable post-treatment (Fig. 1.6).

Other interesting structures that can be obtained from MpSi are silicon dioxide micropillars, the geometry of which is directly related to the pore geometry of the macroporous silicon structure (Fig. 1.7). To this end, a post-treatment is required after the fabrication of MpSi. This post-treatment starts with a thermal treatment of the MpSi structure at 1100 °C for 100 min under oxygen atmosphere. This generates a silicon dioxide layer of 200 nm along the inner surface of the pores of MpSi. Note that the structure of MpSi can result broken by oxide-induced stress in the course of this stage. Thinner MpSi layers minimise this problem since the bending curvature of silicon wafers relies linearly on the specific area of the MpSi structure [67]. Next, the silicon oxide layer is selectively removed from the backside of the silicon wafer by a wet chemical etching in a buffer HF solution (BHF). Finally, the remaining silicon is etched away by a wet chemical etching in a solution of TMAH 25 % wt at 85 °C. After that, a new structure based on silicon dioxide micropillars rises from the backside of the wafer as the silicon dioxide layer covering the pore walls is not etched by TMAH. The length of the resulting silicon dioxide pillars can be established by the etching time and by the pore length in the MpSi structure [68]. Additionally, free-standing silicon dioxide pillars (i.e. micropods) can be obtained if the TMAH etching step is extended until the whole Si wafer is removed. Furthermore, the backside of the silicon wafer can be patterned by lithographic methods after the oxidation stage, enabling a selective etching on the wafer backside by TMAH. Given that the etching process in TMAH is selectively performed over these areas without protective mask in an anisotropic manner, this approach makes it possible to produce arrays of silicon dioxide pillars inside truncated pyramids. The features of these 3D structures can be precisely controlled by the etching parameters and the features of the lithographic patterning. Furthermore, arrays of cone-like silicon dioxide pillars can be produced when conical MpSi is used as the starting material.

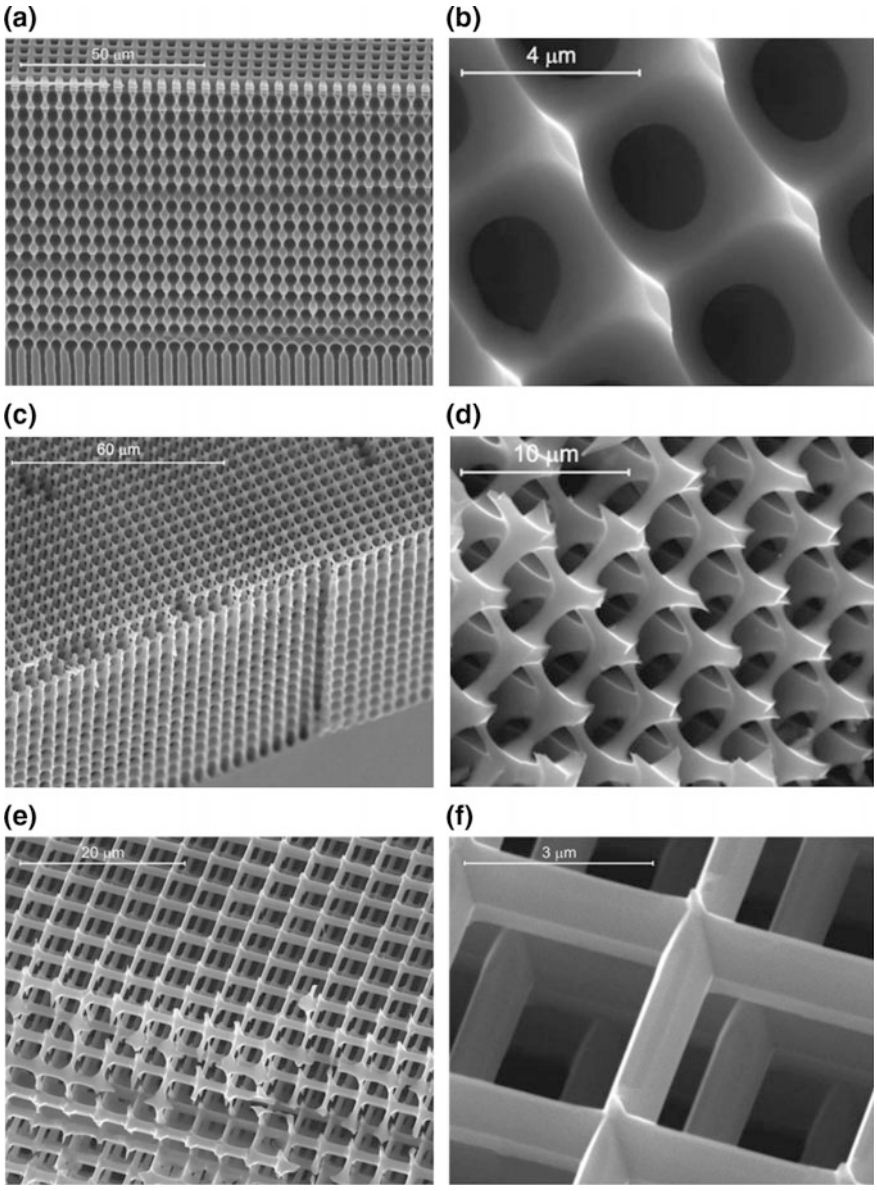

Fig. 1.6 Examples of 3D networks produced from MpSi structures with modulated pores in depth (adapted from [54])

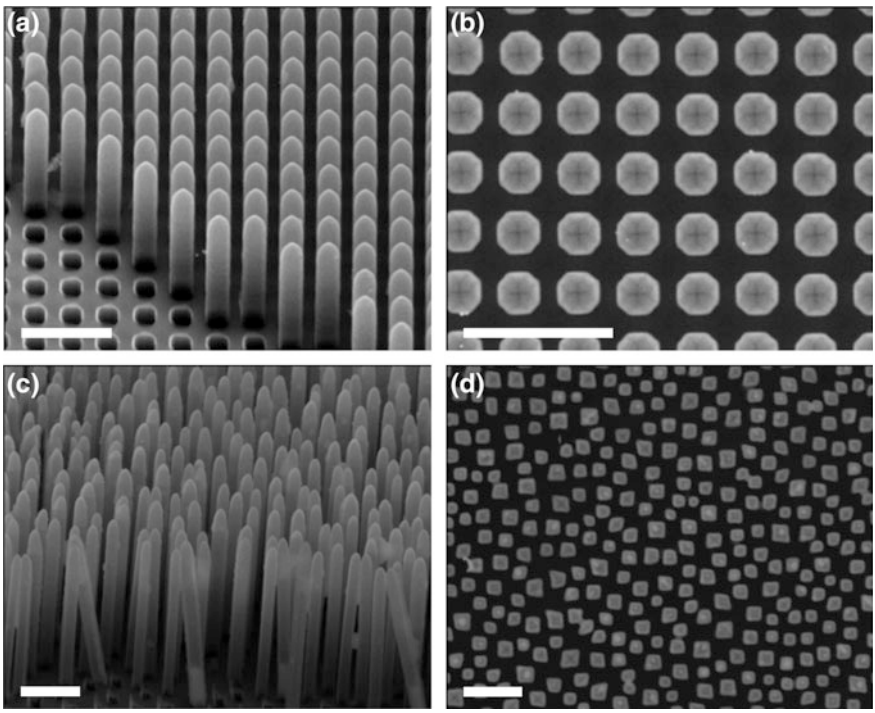

Fig. 1.7 Scanning electron microscopy images of silicon dioxide micropillars produced from macroporous silicon structures (scale bars = 10 μm) (adapted from [54]). **a**, **b** Slanted cross-section and *top views* of silicon dioxide micropillars produced from MpSi featuring perfectly organised pore arrays, respectively. **c**, **d** Slanted cross-section and *top views* of silicon dioxide micropillars produced from MpSi featuring randomly distributed pore arrays, respectively

1.3.2 Mesoporous and Microporous Silicon

As discussed above, pore formation in pSi takes place under anodic conditions in HF electrolytes for current densities lower than J_{PS}. When the doping density in the silicon wafer is increased, the electric field strength increases, decreasing the width of the depletion region and enabling charge carriers to pass through the space charge region (SCR) by tunnelling. Therefore, at high doping densities (i.e. $\geq 10^{18}$ cm^{-3}) tunneling mechanism dominates the charge transfer while avalanche breakdown is the dominant mechanism at low doping densities. Note that the electric field relies also on the pore geometry [20]. The electric field strength increases around the depressions and pits present on the silicon wafer surface. This results in a local reduction of the depletion region width, which increases the tunneling probability of charge carriers, incrementing the local current density. This effect becomes more significant when the size of the depression or pit is smaller than the SCR width [69]. In the course of the first seconds of the electrochemical

etching, some of these pits present on the surface of the silicon wafer develop into mesopores, the density of which across the surface is established by the doping level and the etching conditions. These mesopores are randomly distributed across the surface without organisation. Therefore, mpSi structures feature a sponge-like morphology with a distribution of pore diameters.

Microporous silicon structures can be obtained by electrochemical etching of p-type silicon wafers. Pore formation in μpSi is a complex phenomenon involving different mechanisms (i.e. quantum confinement, crystallographic face selectivity, tunnelling and enhanced electric field) [40]. μpSi structures have high porosity and feature a porous structure with silicon walls of a few nanometres thick separating adjacent micropores. The formation of μpSi structures can be explained by the quantum confinement model, in which the energy bandgap in the wall region increases as a result of quantum confinement effect, generating an energy barrier for electronic holes. If that energy barrier is bigger than that of the bias-dependent energy of electronic holes, the porous structure is depleted of holes and thus passivated from dissolution during the etching process. Under these conditions, electronic holes enter the electrolyte preferentially at the pore bottom tips rather than across the pore walls, yielding the formation of micropores in the silicon structure from top to bottom [13]. Note that other models considering tunnelling effect and crystallographic face selectivity have been proposed to explain the formation of μpSi [70]. Nevertheless, a complete model explaining all the aspects involved in the formation of μpSi structures is yet to come.

In contrast to MpSi, the geometric dimensions of mpSi and μpSi are too small to scatter light in the visible range. So, the interaction of light with mpSi and μpSi structures is explained by the effective medium concept, where the optical properties of the material are established by its bandgap. Therefore, the interaction between light and matter in these porous structures can be designed by engineering their effective refractive index [71]. In that respect, it is worth noting that the refractive index of mpSi and μpSi structures presents certain anisotropy along the specific crystallographic axes. This anisotropy, which can range from 1 to 10 %, is associated with the elongated pore shape along the growth direction [72]. Furthermore, the effective refractive index of mpSi and μpSi structures is inversely proportional to their porosity [73]. The porosity of mpSi and μpSi relies mainly on the current density applied during the etching process. For this reason, multilayered mpSi and μpSi structures, which consist of stacks of porous silicon layers featuring different levels of porosity, can be produced from top to bottom by modifying the current density in the course of the etching process [74]. As a result of their geometric and optoelectronic properties, these structures have been extensively used to produce a variety of optical structures such as microcavities, distributed Bragg reflectors, waveguides, omnidirectional mirrors and rugate filters. The effective refractive index of each layer is directly related with the porosity level. So, the effective refractive index of pSi can be engineered in depth by alternating the current density during the etching process. In addition, the thickness of each layer can be precisely controlled by the etching time as the former is directly proportional to the latter. Therefore, the interaction between incident light and matter in mpSi

and μpSi structures can be engineered to produce optical nanostructures for a broad range of applications.

For instance, multilayered mpSi and μpSi structures can be used to develop distributed Bragg reflectors (DBR). Basically, a pSi-based DBR structure consists of multiple layers of pSi with different porosity levels and thicknesses (Fig. 1.8a) [75]. The interfaces between two consecutive layers of dielectric material reflect incident light due to the effective refractive index contrast. Therefore, constructive light interference can be engineered by designing the structure of the mpSi- or μpSi-based DBR (i.e. by designing the porosity and thickness of each layer). These

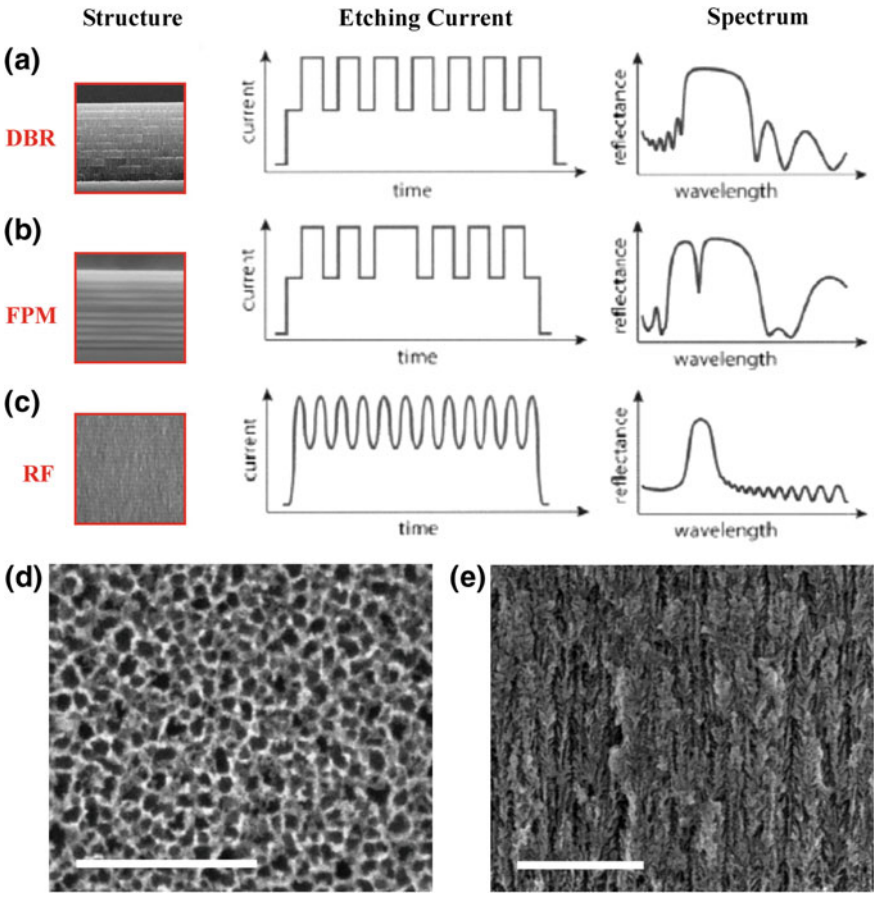

Fig. 1.8 Schematic diagram showing the most representative optical structures based on meso and microporous silicon, their fabrication conditions (i.e. etching current) and their optical spectra. **a** Distributed Bragg reflector (DBR). **b** Fabry–Pérot microcavity (FPM). **c** Rugate filter (RF). **d** Scanning electron microscopy *top view* image of microporous silicon (scale bar = 200 nm) (adapted from [75]). **d** Scanning electron microscopy cross-section view image of microporous silicon (scale bar = 500 nm) (adapted from [83])

structures have been extensively used to develop optical filters and sensors [74, 76–82]. Furthermore, DBR structures based on mpSi and μpSi can be implemented into Fabry–Pérot filters, also called optical microcavities, which are composed of two parallel DBRs with a space layer of different effective refractive index in between (Fig. 1.8b). Note that the effective optical thickness of the space layer (i.e. product between the physical thickness and the effective refractive index of the layer) is typically engineered as the wavelength of the incident light or half of it [83]. The reflectivity spectrum of microcavities based on mpSi and μpSi shows a narrow pass-band centred at the wavelength where the light is reflected with the highest intensity. Therefore, the structural design of microcavities based on mpSi and μpSi makes it possible to develop optical pass-band filters and sensors [84, 85]. If the current density profile is modified in a sinusoidal manner in the course of the electrochemical etching, the effective refractive index of mpSi and μpSi can be modulated to produce rugate filters, which are another type of optical structure used in optoelectronic and sensing applications (Fig. 1.8c) [86, 87].

Another important optical property of mpSi and μpSi structure is their photoluminescence (PL), which has been extensively studied during the last decades [88]. Bulk crystalline silicon presents a very weak PL peak at 1100 nm. This limits the use of silicon to develop optoelectronic devices, which are aimed at converting light into electricity (e.g. photodetectors, solar cells, etc.). However, the discovery of bright red-orange photoluminescence and the identification of confinement effects in the absorption spectrum of pSi by Canham and Gösele in 1990, respectively, were the starting point of a flood of studies focused on the development of optoelectronic devices based on mpSi and μpSi structures such as switches, displays and lasers [12, 13]. PL properties of mpSi and μpSi structures depend on the etching conditions. The different PL bands in pSi can be tuned from blue-green, red-orange to IR by adjusting the etching conditions. For instance, an increment of the current density, a decrease in the concentration of HF or an increase of the illumination intensity lead to blue shifts in the PL peak of mpSi and μpSi. In addition, it is worth stressing that PL in pSi is dependent on the porosity level as well as the doping density [89].

1.4 Metal-Assisted Etching of Silicon

Metal-assisted chemical etching of silicon is considered a simple and cost-competitive alternative to conventional electrochemical methods. This approach has been used to produce pSi structures with precisely defined geometric features and characteristics not achievable by other fabrication approaches [90, 91]. As discussed above, electrochemical etching of silicon occurs anisotropically along (100) directions. In contrast, the etching direction in metal-assisted etching can be controlled on (100) and non-(100) directions to produce pSi structures with slanted growth directions [92, 93]. Furthermore, metal-assisted etching enables the fabrication of pSi structures with high surface-to-volume ratio, high crystalline quality

and low level of defects [94–96]. In addition, metal-assisted etching makes it possible to produce pSi structures within a broad range of feature sizes, which can range from 5 nm to >1 μm [97, 98]. For these reasons, metal-assisted etching of silicon has become an alternative approach to conventional electrochemical etching methods. Porous silicon structures produced by this approach have demonstrated their applicability in a broad range of fields such as sensing, energy storage and conversion and so on [99–110]. Metal-assisted etching of silicon was pioneered by Dimova et al. in 1997 when they etched a silicon substrate covered by a thin film of aluminium in a solution composed of HF, HNO_3 and H_2O_2 [111]. After this, Li and Bohn found that thin films of noble metals such as gold (Au) and platinum (Pt) sputtered on the surface of silicon catalysed the formation of pSi in an ethanoic electrolyte composed of HF and H_2O_2 [112]. The resulting pSi structures featured wires and straight pores. These studies revealed that when a silicon substrate is partly covered by a noble metal and it is immersed in an etchant solution composed of an oxidative agent (e.g. hydrogen peroxide) and HF, the silicon beneath the noble metal is etched at a faster rate than that of the uncovered silicon. As a result, the noble metal sinks into the silicon substrate, producing pores or pillars depending on the etching conditions and the metal features. Basically, the geometric features of the resulting pSi structures are established by the noble metal mask. Furthermore, under some conditions and likewise in electrochemical etching, microporous silicon structures can be generated in the off-metal regions of the silicon wafer (i.e. areas without noble metal cover) as a result of chemical etching [112, 113].

1.4.1 Pore Formation Mechanism in Metal-Assisted Etching of Porous Silicon

As far as the mechanisms and reactions involved in the formation of pSi structures produced by metal-assisted etching is concerned, it is well-known that chemical and electrochemical reactions occur near the interface between the noble metal and the silicon substrate when the system is immersed in an etchant composed of HF and H_2O_2 [114–120]. So far, several reaction models have been proposed to describe the electrochemical reactions taking place during the formation of porous silicon by metal-assisted etching [112, 121]. In this system, the noble metal works as a cathode, where hydrogen peroxide is reduced at the metal surface following these electrochemical reactions (1.2 and 1.3) while the silicon works as the anode:

$$H_2O_2 + 2H^+ \rightarrow 2H_2O + 2H^+ \tag{1.2}$$

$$2H^+ \rightarrow H_2 \uparrow + 2H^+ \tag{1.3}$$

It is worth stressing that, although these electrochemical reactions are well-accepted, other studies have attributed the evolution of gas during the etching process to anodic reactions [118, 122]. As far the anode, the silicon substrate is

progressively oxidised and dissolved in the course of the metal-assisted etching. Several electrochemical models explaining the anodic reactions taking place in this process have been proposed. These can be divided into three groups:

Model I: In this model, silicon is first oxidised (1.4), yielding silicon dioxide, which is subsequently dissolved by HF (1.5) [118, 119, 123–127].

$$Si + 2H_2O \rightarrow SiO_2 + 4H^+ + 4e^- \tag{1.4}$$

$$SiO_2 + 6HF \rightarrow H_2SiF_6 + 2H_2O \tag{1.5}$$

Model II: Silicon is directly dissolved in divalent state (1.6) [115, 118].

$$Si + 4HF_2^- \rightarrow SiF_6^{-2} + 2HF + H_2 \uparrow + 2e^- \tag{1.6}$$

Model III: Silicon is directly dissolved in tetravalent state (1.7 and 1.8) [112, 114, 116, 117, 121, 128–130].

$$Si + 4HF_2^- + 4H^+ \rightarrow SiF_4 + 4H^+ \tag{1.7}$$

$$SiF_4 + 2HF \rightarrow H_2SiF_6 \tag{1.8}$$

Although these models explain partially the formation process of porous silicon by metal-assisted etching, a complete model explaining this electrochemical phenomenon as a whole is yet to come [90]. In analogy with chemical etching of silicon, it is accepted that charge transfer between noble metal and silicon occurs for the oxidation and dissolution of the latter by hole injection mechanism [112, 128, 131–135]. In that system, the noble metal plays the role of cathode, where the reduction of the oxidant takes place. Holes generated in the noble metal are then injected into the silicon substrate, oxidising silicon atoms, which subsequently are dissolved by reacting with HF. Note that electronic hole injection is verified by the dependence of the etching morphologies on the level of doping and the etchant solution. In summary, metal-assisted etching of porous silicon can be divided into five stages (Fig. 1.9):

Stage 1: The oxidant is reduced at the noble metal surface due to its catalytic activity.
Stage 2: The reduction of the oxidant generates electronic holes, which are subsequently injected into the silicon substrate through the noble metal interface.
Stage 3: Electronic holes oxidise silicon atoms at the interface noble metal-silicon, which are then etched away by HF molecules.
Stage 4: The concentration of electronic holes is maximum at the interface noble metal-silicon and thus its dissolution rate is much faster there.
Stage 5: The remaining electronic holes (i.e. those not consumed during the dissolution of silicon) diffuse from the interface noble metal-silicon to the bulk silicon.

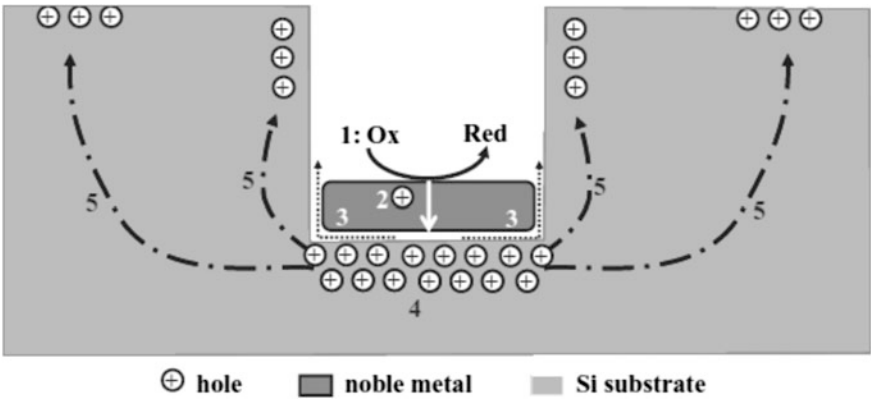

Fig. 1.9 Schematic diagram illustrating the formation mechanism of porous silicon by metal-assisted etching of silicon (adapted from [90]). Note that numbers 1, 2, 3, 4 and 5 denote the different stages involved in this electrochemical process

1.4.2 Influence of Fabrication Parameters in Metal-Assisted Etching of Porous Silicon

The resulting structural features of pSi produced by metal-assisted approach rely on different parameters such as the etchant composition and its temperature, the nature of the noble metal, the illumination and the intrinsic properties of the silicon substrate (e.g. doping type and level, crystallographic orientation, etc.). In this section, we will provide a brief but comprehensive description of the main parameters playing a role in the fabrication process of pSi by metal-assisted etching of silicon.

Regarding the type of oxidant, hydrogen peroxide is the most commonly used although other oxidants such as oxygen bubbles, oxygen dissolved in water, silver nitrate ($AgNO_3$), chloroauric acid ($HAuCl_4$), potassium gold(III) chloride ($KAuCl_4$), chloroplatinic acid (H_2PtCl_6), potassium hexachloroplatinate (K_2PtCl_6), iron nitrate ($Fe(NO_3)_3$), nickel nitrate ($Ni(NO_3)_2$), magnesium nitrate ($Mg(NO_3)_2$), potassium permanganate ($KMnO_4$), sodium persulphate ($Na_2S_2O_8$) and potassium dichromate ($K_2Cr_2O_7$) have been explored as well [93, 112, 115, 125, 129, 136–142]. Note that the resulting morphologies and structural features of metal-assisted etched pSi differ from one oxidant to another as they can change the morphology of the metal or produce different precipitates in the course of the etching process [90].

Another important parameter that directly affects the geometric features of the resulting pSi produced by metal-assisted etching is the concentration and composition of the etchant electrolyte. For instance, etching of silicon wafers coated with platinum particles in an etchant with low concentration of HF (HF(50 %): H_2O_2(30 %):H_2O = 2:1:8; *v*:*v*:*v*) yields pores with cone-like morphology from top to bottom. Nevertheless, this effect can be notoriously reduced by increasing the

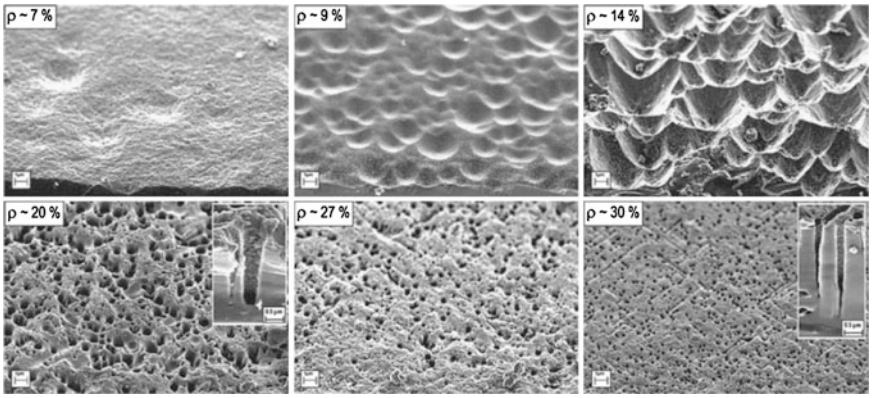

Fig. 1.10 Scanning electron microscopy images showing morphological details of porous silicon structures produced by metal-assisted etching of silicon with different ratio acid/etchant (ρ = [HF]/([HF] + [H_2O_2])) (adapted from [118])

concentration of HF fourfold (HF(50 %):H_2O_2(30 %) = 10:1; *v*:*v*) [113]. In that respect, Chartier et al. studied the effect of the ratio HF/H_2O_2 on the resulting morphology of pSi in a systematic manner (Fig. 1.10) [118]. In their study, p-type (100) silicon wafers were first coated with silver particles by electroless deposition. The obtained results revealed that for 100 % > [HF]/([HF] + [H_2O_2]) > 70 %, the resulting pores featured cylindrical and straight geometry, which almost matched the diameter of the silver nanoparticles at the bottom of the pores. Nevertheless, cone-line pores where obtained for 70 % > [HF]/([HF] + [H_2O_2]) > 20 %, with decreasing pore diameter from top to bottom. For 20 % > [HF]/([HF] + [H_2O_2]) > 9 %, crater-like pSi structures featuring micrometric opening diameters were obtained. Finally, a nanometric pitted surface was obtained when the silicon wafers were etched in an etchant with 9 % > [HF]/([HF] + [H_2O_2]) > 0 %. This change of pore morphology and geometric features with the ratio acid/oxidant was explained by the fact that at high concentrations of HF (i.e. 100 % > [HF]/([HF] + [H_2O_2]) > 70 %), the etching rate is determined by the oxidant concentration and the electronic holes generated at the interface noble metal-silicon are rapidly consumed as a result of the excess of HF available to dissolve silicon. However, when the ratio acid/oxidant is lower than 70 %, the etching rate starts to be determined by the HF concentration. In such a scenario, the generation of electronic holes is higher than their consumption rate and thus the excess of electronic holes diffuse away to the pore walls, where μpSi structures are generated. At high concentrations of oxidant (i.e. 20 % > [HF]/([HF] + [H_2O_2]) > 9 %) electronic holes diffuse massively towards the surface of silicon in contact with HF, resulting in an isotropic etching independent on the silver particles present on the wafer surface.

Apart from the ratio between acid and oxidant, the etching rate is also affected by other factors such as the etchant temperature and the diffusion of by-products (e.g. SiF_6^{2-}) and etchant through the pores [117]. In that respect, some studies have

demonstrated that bigger pores enable faster etching rates as a result of a more efficient diffusion of etchant and by-products through the pores and the interface noble metal-silicon. Furthermore, more efficient diffusion rates can be achieved by stirring the etchant during the etching process. Another important factor directly related with the etching rate is the temperature of the etchant. Cheng et al. demonstrated that the etching rate of silicon nanowires produced by metal-assisted etching of silicon in HF/H_2O_2 and $HF/AgNO_3$ increases with the temperature from 0 to 50 °C [143]. Moreover, it was established a linear relationship between the silicon nanowires length and the etching time within the aforementioned range of temperature.

As far as the different aspects associated with the noble metal is concerned, the most typical metals used to etch silicon by metal-assisted approach are silver, gold, platinum and palladium. These metals can be deposited by thermal evaporation, electroless deposition, electrodeposition, sputtering, electron beam evaporation, focused ion beam deposition, spin-coating and self-assembly of particles [93, 112, 121, 122, 124–127, 142, 144–146]. Furthermore, some of these deposition methods can be combined with lithography masks generated by micro and nanofabrication techniques. This enables the production of metal-assisted pSi structures with highly ordered geometric features. When isolated particles are used to produce metal-assisted pSi, the structure, geometric features and morphology of the resulting pSi are dependent on the noble metal. For instance, while Ag or Au particles yield pSi featuring straight pores (Fig. 1.11a, b), the pore geometry in pSi produced by etching through Pt particles can vary from well-defined straight pores,

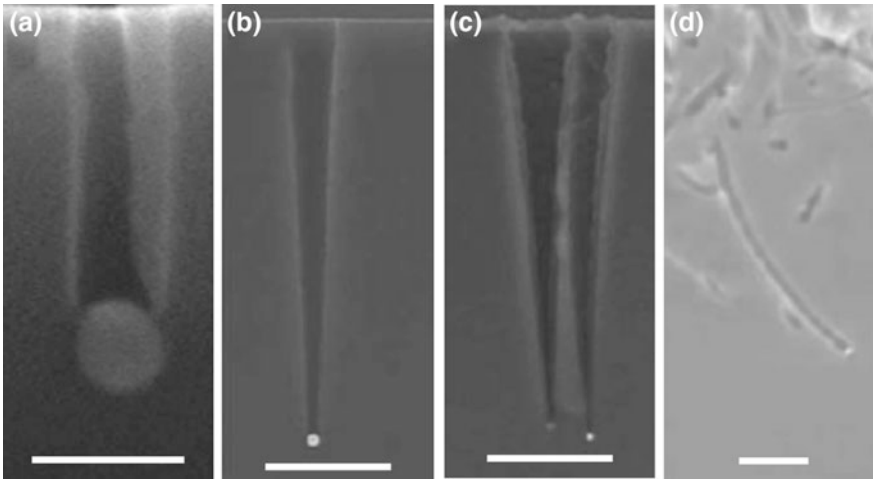

Fig. 1.11 Scanning electron microscopy images showing morphological details of pores produced by different noble metal nanoparticles through metal-assisted etching of silicon. **a** Silver nanoparticles (scale bar = 75 nm) (adapted from [130]). **b** Gold nanoparticles (scale bar = 10 μm) (adapted from [117]). **c** Platinum nanoparticles (scale bar = 15 μm) (adapted from [117]). **d** Platinum nanoparticles (scale bar = 1 μm) (adapted from [125])

helical-like pores or curvy-like pores (Fig. 1.11c). Under some conditions, Pt particles move randomly in the course of the etching process, producing complex pSi structures (Fig. 1.11d) [117, 130, 134, 135]. In addition, the etching rate varies from one noble metal to another. As an example, the etching rate achieved during the etching through Au particles is much slower than that obtained when Pt particles are used [112]. Another interesting phenomenon dependent on the noble metal is the formation of μpSi structures on the side walls of pores or wires during the etching process [113, 117, 135]. A detailed explanation of the origin of these effects is yet to come although some authors have pointed out towards the role of the noble metal type in the catalytic activity for the reduction of the oxidant. In that respect, Huang and Meyer et al. indicated that the more the injected electronic holes the faster the etching rate, resulting in a more efficient diffusion of electronic holes towards the side walls during the etching process and enabling the formation of μpSi structures on the side walls of pores or wires [147]. Apart from these effects, the geometric features and morphology of the resulting pSi structures are mainly established by the shape of the noble metal deposited on the surface of the silicon wafer as a result of its catalytic effect, which results in a much faster etching rate at the interface noble metal-silicon. Usually, well-defined and separated pores are produced from single particles distributed across the silicon surface. In contrast, when the distance between adjacent particles is reduced, wire-like or wall-like pSi structures are produced [148].

Typically, pores produced by metal assisted etching feature a cone-like structure with pore diameter decreasing with depth. This conical effect can be more or less pronounced, depending on the etching conditions, and the pore diameter at the pore mouth can be bigger or smaller than that of the initial noble metal particle [117]. This effect can be associated with the diffusion of electronic holes injected from the noble metal-silicon interface to the side walls, the partial dissolution of silicon by the etchant and the progressive dissolution and re-deposition of noble metal in the course of the etching process [31, 93, 113, 118, 120, 137]. In addition, silicon wires with well-defined geometry and shape are obtained when a homogeneous noble metal film featuring holes is deposited on the surface of a silicon substrate and subsequently etched in a suitable etchant solution. Note that the resulting silicon wires can be produced with highly ordered distribution and precisely controlled geometry if the surface of the silicon is patterned by lithographic approaches prior to the deposition of the noble metal film. Note that the thickness of the noble metal film has a direct effect on the morphology of the resulting pSi structures as well. For instance, 3 and 5 nm thick films of gold lead to pores or wires, respectively [134]. In the case of silver films, 5 nm thick films yield pores while films of 20–50 nm thickness result in silicon wires [144]. Furthermore, it is important to bear in mind that the morphology of the resulting noble metal films can vary with the deposition technique and the nature of the noble metal [93, 145].

Regarding the stability of the noble metal in the etchant, this is highly dependent on its nature and some noble metals can be oxidised and dissolved in the course of the etching process according to the existing relationship between the electrochemical potentials of the noble metal and the oxidant. Typically, Au and Pt

particles are stable at high concentrations of oxidants, maintaining their shapes during the etching. However, as mentioned above, Ag particles dissolve and re-deposit during the etching process as a result of the relatively low electrochemical potential of silver. Therefore, Ag particles can change their shape and morphology during this process, leading to pores or wires with heterogeneous geometric features and morphologies with depth [117, 135]. Usually, Au particles and films are preferably used to produce pSi structures with well-defined and precisely controlled geometric features and morphologies due to its stability in the etchant. For instance, Au meshes have been used to fabricate silicon wires of high aspect ratio (i.e. >200) [145].

As far as the effect of light illumination in metal-assisted etching of silicon, this has a direct effect on the etching rate. It has been reported that the etching rates for p-type and n-type (100) silicon substrates of resistivity 1–10 Ω cm differ whether the etching process is conducted with or without illumination. For instance, the etching rate of p- and n-type silicon wafers under room light illumination is about 0.05 times faster than under dark conditions. This difference becomes even higher (i.e. 150 times faster) when 20 W illumination is used. This effect can be explained by the fact that under illumination the number of photoexcited electronic holes can be higher than the number of electronic holes injected from the oxidant agent, thus enabling faster etching rates.

Another important parameter affecting the resulting pSi structures produced by metal-assisted etching are the different intrinsic properties of the silicon substrate, which have a direct effect on the geometric features and characteristics of the resulting pSi structures. Actually, metal assisted etching of silicon is anisotropic and dependent on the crystallographic orientation of silicon. As an example, slanted porous silicon structures can be produced by etching (111) and (110) silicon wafers (Fig. 1.12a, b) [104, 116, 117, 119, 149, 150]. In analogy with anisotropic electrochemical etching of silicon in HF and chemical etching in alkaline solutions, this phenomenon has been related to the back-bond breaking theory [97, 119, 151, 152]. In this theory, the number of the back-bonds of a silicon atom on the surface of the substrate is established by the crystallographic orientation of the substrate. The back-bonds of the silicon atoms located on the surface of the substrate must be broken during the oxidation and dissolution of silicon. Therefore, the etching of silicon atoms becomes more difficult for stronger back-bonds. In that respect, it is worth noting that silicon atoms have one, two and three back-bonds in (100), (110) and (111) substrates [153].

Regardless of this hypothesis, which explains some aspects of the dependence of the metal-assisted etching of silicon with the crystallographic orientation, a definitive and complete model entirely explaining this phenomenon is yet to come [90]. Furthermore, other aspects such as the influence of the doping type and its level on the etching rate of silicon by metal-assisted approach remain unclear [112, 134]. As far as the doping type is concerned, Zhan et al. reported that the etching rate in n-type silicon is faster than that of p-type silicon for (100) and (111) crystallographic orientations with the same resistivity (i.e. 7–13 Ω cm) [120]. Nevertheless, the etching rate is not the only parameter affected by the type of doping. It has been

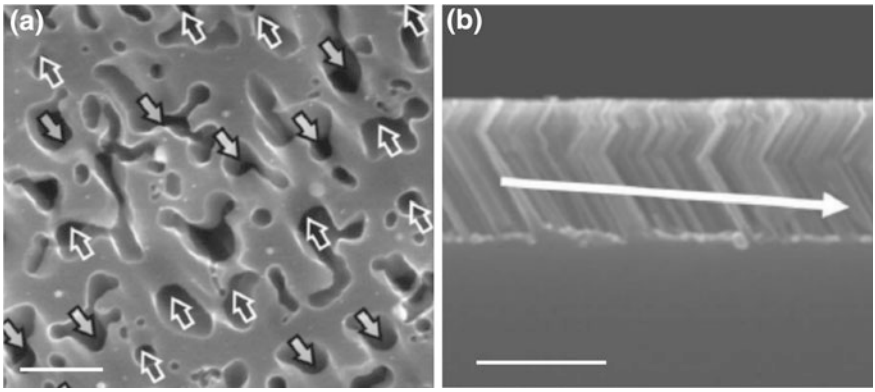

Fig. 1.12 Scanning electron microscopy images showing the effect of the crystallographic orientation of the silicon substrate on the resulting pores produced by metal-assisted etching of silicon. **a**, **b** *Top* and cross-section images of a (110) silicon substrate etched by silver nanoparticles (scale bars = 200 and 800 nm, respectively) (adapted from [93]). Note that the *white arrow* in (**b**) denotes the propagation direction of silver nanoparticles in the course of the etching process

reported that the morphology of silicon nanowires produced by metal-assisted etching of silicon changes with the doping level of the wafer as well and they can present rough surface or contain mpSi or μpSi structures on the side walls with increasing doping level [109, 120, 154, 155]. This result could be ascribed to the fact that in highly doped silicon wafers the diffusion of electronic holes occurs from the interface noble metal-silicon to the bulk silicon substrate, which would result in the etching of the side walls, producing mpSi or μpSi structures.

1.4.3 Metal-Assisted Etching of Porous Silicon Combined with Lithographic Methods

As mentioned above, pSi structures with precisely controlled and exquisitely defined morphology and geometric features can be produced when the surface of the silicon wafer is patterned by lithographic techniques prior to the etching step. In particular, some lithographic methods have demonstrated outstanding results when combined with metal-assisted etching. The most representative ones are interference lithography, nanoporous anodic alumina masks and nanospheres lithography.

Interference lithography (IL) is a top-down nanofabrication technique with high throughput and scalability for large surface areas used in the production of nanostructures. IL provides excellent definition of features at nanometric scale. Usually, an IL pattern is generated by two coherent laser beams and subsequently transferred to a film of photoresist covering the substrate [156]. Then, the resist film is developed and an array of parallel and orthogonal lines of photoresist is generated

on the silicon substrate surface. IL can be combined with metal-assisted etching to produce silicon nanowires. For instance, Choi et al. used this approach to produce silicon nanowires by metal-assisted etching [94]. In this study, first, silicon substrates were coated by a layer of photoresist, which was cured and exposed to IL. Unexposed photoresist areas were removed after immersion in the developer, revealing free areas for etching. Then, the size of the photoresist features was enlarged by oxygen plasma etching. After that, the patterned silicon substrate was coated with a layer of gold and metal-assisted etching was carried out. This process resulted in perfectly ordered arrays of silicon nanowires. Note that the geometric features and arrangement of these arrays of silicon wires can be accurately designed by modifying the IL patterns and the feature size and its shape [95]. Therefore, silicon wires with square, rectangular and circular cross-sections can be produced by this approach.

Another approach used to etch the surface of silicon wafers at specific positions by metal-assisted etching is the use of nanoporous anodic alumina (NAA) masks. Self-ordered NAA is basically a nanoporous matrix based on alumina (aluminium oxide–Al_2O_3) that features close-packed arrays of hexagonally arranged cells, at the centre of which a cylindrical nanopore grows perpendicularly to the underlying aluminium substrate [157–161]. NAA is produced by electrochemical anodization of aluminium, which is typically performed in acid electrolytes based on aqueous solutions of sulphuric (H_2SO_4), oxalic ($H_2C_2O_4$) or phosphoric acids (H_3PO_4). In this system and similar to electrochemical etching of silicon, the anode (i.e. aluminium foil) and cathode (e.g. platinum wire) are immersed in the acid electrolyte and the growth of nanopores is produced by the application of current or voltage. Note that the geometric features of pores in NAA can be precisely controlled by the anodization parameters. Typically, pore sizes in NAA can range from 20 to 400 nm, with a pore density from 5×10^8 to 3×10^{10} pores per cm^2 [161–163]. Huang et al. used ultrathin masks of NAA in order to deposit noble metal films on the surface of silicon wafers [137]. The noble metal films were patterned with holes, the size, geometry and arrangement of which were determined by the NAA mask. In this approach, a NAA mask 300 nm thick with pores of 20 nm of diameter was placed on the surface of a silicon substrate by solution-based transfer process. Then, RIE etching was carried out in order to transfer the NAA pattern on the silicon surface with high accuracy and fidelity. Subsequently, the NAA mask was dissolved by wet chemical etching and a thin layer of Au or Ag was deposited on the surface of the patterned silicon substrate. Next, the system was etched in a solution composed of HF and H_2O_2 in order to generate silicon nanowires. This lithographic approach makes it possible to produce silicon wires with controlled geometry, morphology and size with high crystalline quality and smooth surface. Furthermore, the geometric and morphological features of the resulting silicon nanowires are dependent on the thickness of the noble metal film. Nonetheless, the pores produced by RIE etching can have a thin defective region, which can prevent or hinder the metal-assisted etching process. To overcome this drawback, the same authors used a slight modification of the aforementioned approach in order to avoid the use of RIE (Fig. 1.13a, b) [93]. In this new approach, a film of Ag was deposited on the

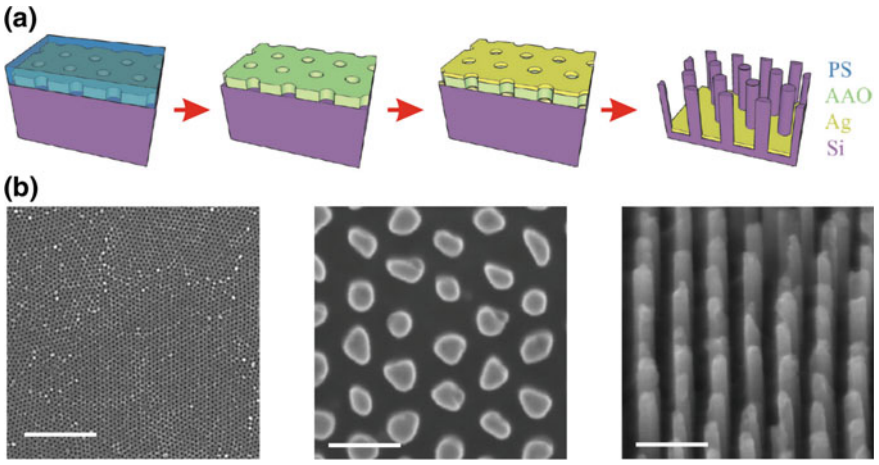

Fig. 1.13 Approach developed by Huang et al. to use nanoporous anodic alumina mask to produce porous silicon nanowires by metal-assisted etching of silicon (adapted from [93]). **a** Schematic diagram illustrating the fabrication process. **b** *Top view* of Ag-coated NAA mask, cross-section and slanted cross-section images of the resulting silicon nanowires (scale bars = 100 nm)

NAA mask and the whole system etched in the aforementioned etchant solution. In this way, the Ag film with holes was transferred from the top of the NAA mask to the surface of the silicon substrate as a result of the dissolution of the NAA mask. Then, the etching occurred on the surface of the silicon by metal-assisted etching catalysed by the Ag film.

The main advantage of the use of NAA masks to produce pSi structures by metal-assisted etching is that it can be carried out in a simple wet chemistry laboratory without expensive facilities. However, self-ordered NAA structures present defects and domains, which are inevitably transferred to the patterned structure on the silicon substrate and thus to the resulting arrays of silicon nanowires. This can be overcome by producing NAA mask with perfect pore organisation, which can be achieved by nanoimprint lithography [164, 165]. Another limitation of this approach is that only silicon nanowires featuring circular section can be obtained.

Nanosphere lithography method is another lithographic approach extensively used to produce pSi structures by metal-assisted etching. Huang et al. developed an approach where a monolayer of self-assembled polystyrene (PS) nanospheres was first deposited on the surface of a silicon substrate (Fig. 1.14a, b) [136]. After this, the size and distance between adjacent nanospheres were increased by RIE etching and a noble metal film was deposited on the silicon surface by thermal evaporation. Note that the feature size and geometric and morphological characteristics of the noble metal film were determined by the mask created by the nanospheres. Therefore, a noble metal film with ordered arrays of pores resulted after metal deposition. The resulting system was etched in a mixture of HF and H_2O_2 and silicon nanowires with well-defined morphology and geometry were produced by

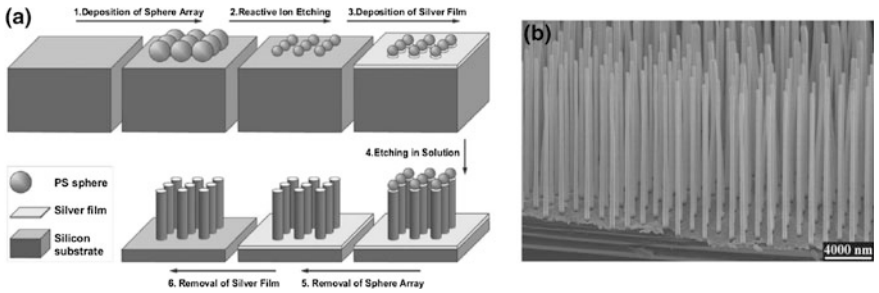

Fig. 1.14 Nanospheres lithography used to produce porous silicon by metal-assisted etching of silicon (adapted from [136]). **a** Schematic diagram depicting the fabrication process. **b** Cross-section scanning electron microscopy image of the resulting silicon nanowires

this approach. Silicon nanowires matched with high degree of fidelity the pattern determined by the nanospheres mask. This approach can be extended over large areas with a broad range of geometries given that these features are established by the size of the spheres, which can be produced with controlled geometry. Furthermore, a broad range of nanospheres composed of different materials can be used for this purpose [149]. Finally, it is worthwhile mentioning that silicon nanowires of high aspect ratio trend to form bundles or collapse as a result of surface tension forces during the drying process [166]. This drawback can be overcome by supercritical drying approach [145, 162].

1.5 Conclusions

Micro and nanostructures based on porous silicon have been used in research fields, which range from optoelectronics, sensing, energy generation and storage, medicine, chemistry and so forth. Traditionally, electrochemical and chemical etching methods have been used to produce a variety of porous silicon structures featuring multiple geometric and morphological details. These methods have become more and more popular in the last years, making porous silicon one of the most extensively used materials in science. In that respect, a good understanding of the different physical and chemical phenomena taking place during chemical and electrochemical etching of silicon is a key factor in the development of this technology. A better understanding of the different formation mechanisms playing a role in the formation of porous silicon has enabled the implementation of multiple strategies and approaches aimed at engineering the structure of this porous material. Note that this is a critical factor given that the physical and chemical properties of the resulting porous silicon are directly related to its porous structure. Particularly, in the recent years, special attention has been devoted to the development of optical sensing systems and drug delivery nanocarriers based on porous silicon. While its outstanding optical properties make porous silicon a unique material to develop

optical structures suitable for optical sensing, its biocompatibility and degradability properties have enabled the use of porous silicon structures as micro and nanocarriers for drug delivery.

In this chapter, we have compiled and described the fundamental and basic aspects of the fabrication of porous silicon by electrochemical and metal-assisted etching methods. While conventional electrochemical etching is the most widespread approach used to produce macro, meso and microporous silicon, metal-assisted etching has become a popular method to produce other type of structures based on porous silicon such as silicon nanowires. The different mechanisms involved in these processes have been properly described, although completed models explaining all the physical and chemical phenomena taking place during the formation of porous silicon are yet to come.

Acknowledgments Financial support from Australian Research Council (DE14010054) and the School of Chemical Engineering of The University of Adelaide are greatly acknowledged.

References

1. J. Czochralski, Ein neues verfahren zur messung der kristallisationsgeschwindigheit der metalle. Z. Phys. Chem. **92**, 219–221 (1918)
2. J. Kilby, Invention of the integrated circuit. IEEE Trans. Electron Devices **7**, 648–654 (1976)
3. A. Jr, Uhlir, Electrolytic shaping of germanium and silicon. The Bell Syst. Tech. J. **35**, 333–347 (1956)
4. C.S. Fuller, J.A. Ditzenberger, Diffusion of donor and acceptor elements in silicon. J. Appl. Phys. **27**, 544–553 (1956)
5. D.R. Turner, Electropolishing silicon in hydrofluoric acid solutions. J. Electrochem. Soc. **105**, 402–408 (1958)
6. P.F. Schmidt, D.A. Keiper, On the jet etching of n-type Si. J. Electrochem. Soc. **106**, 592–596 (1959)
7. R.J. Archer, Stain films on silicon. J. Phys. Chem. Solids **14**, 104–110 (1960)
8. D.R. Turner, in *The electrochemistry of semiconductors*, ed. by P.J. Holmes (Academic Press, London, 1962), pp. 155–204
9. H. Gerischer, *Surface Chemistry of Metals and Semiconductors*, ed. by H.C. Gatos (Wiley, New York, 1960)
10. K.H. Beckmann, Investigation of the chemical properties of stain films on silicon by means of infrared spectroscopy. Surf. Sci. **3**, 314–332 (1965)
11. Y. Watanabe, T. Sakai, Application of a thick anode film to semiconductor devices. Rev. Electr. Commun. Lab. **19**, 899–903 (1971)
12. L.T. Canham, Silicon quantum wire array fabrication by electrochemical and chemical dissolution. Appl. Phys. Lett. **57**, 1046–1048 (1990)
13. V. Lehmann, U. Gösele, Porous silicon formation: a quantum wire effect. Appl. Phys. Lett. **58**, 856–858 (1991)
14. M.I.J. Beale, J.D. Benjamin, M.J. Uren, N.G. Chew, A.G. Cullis, An experimental and theoretical study of the formation and microstructure of porous silicon. J. Cryst. Growth **73**, 622–636 (1985)
15. R.L. Smith, S.D. Collins, A theoretical model of the formation morphologies of porous silicon. J. Electron. Mater. **17**, 534–541 (1988)

16. R.L. Smith, S.D. Collins, Generalized model for the diffusion-limited aggregation and Eden models of cluster growth. Phys. Rev. A: At. Mol. Opt. Phys. **39**, 5409–5413 (1989)
17. R.L. Smith, S.D. Collins, Porous silicon formation mechanisms. J. Appl. Phys. **71**, R1–R22 (1992)
18. T. Unagami, Formation mechanism of porous silicon layer by anodization in HF solution. J. Electrochem. Soc. **127**, 476–483 (1980)
19. V.P. Parkhutik, L.K. Glinenko, V.A. Labunov, Kinetics and mechanism of porous layer growth during n-type silicon anodization in HF solution. Surf. Coat. Technol. **20**, 265–277 (1983)
20. X.G. Zhang, Mechanism of pore formation on n-type silicon. J. Electrochem. Soc. **138**, 3750–3756 (1991)
21. J. Carstensen, M. Christophersen, H. Föll, Pore formation mechanisms for the Si-HF system. J. Mater. Sci. Eng. B **69**, 23–28 (2000)
22. H. Föll, J. Carstensen, M. Christophersen, G. Hasse, A new view of silicon electrochemistry. Phys. Status Solidi A **182**, 7–16 (2000)
23. J. Carstensen, M. Christophersen, G. Hasse, H. Föll, Parameter dependence of pore formation in silicon within a model of local current bursts. Phys. Status Solidi A **182**, 63–69 (2000)
24. C. Levy-Clement, A. Lagoubi, M. Tomkiewicz, Morphology of porous n-type silicon obtained by photoelectrochemical etching: I. Correlations with material and etching parameters. J. Electrochem. Soc. **141**, 958–967 (1994)
25. C. Levy-Clement, A. Lagoubi, R. Tenne, M. Neumann-Spallart, Photoelectrochemical etching of silicon. Electrochim. Acta **37**, 877–888 (1992)
26. A. Albu-Yaron, S. Bastide, J.L. Maurice, C. Lévy-Clement, Morphology of porous n-type silicon obtained by photoelectrochemical etching II: study of the tangled Si wires in the nanoporous layer. J. Lumin. **57**, 67–71 (1993)
27. E.K. Propst, P.A. Kohl, The electrochemical oxidation of silicon and formation of porous silicon in acetonitrile. J. Electrochem. Soc. **141**, 1006–1013 (1994)
28. R.B. Wehrspohn, F. Ozanam, J.N. Chazalviel, Nano- and macropore formation in p-type silicon. J. Electrochem. Soc. **146**, 3309–3314 (1999)
29. V. Lehmann, S. Rönnebeck, The physics of macropore formation in low-doped p-type silicon. J. Electrochem. Soc. **146**, 2968–2975 (1999)
30. S. Lust, C. Lévy-Clément, Chemical limitations of macropore formation on medium-doped p-type silicon. J. Electrochem. Soc. **149**, C338–C344 (2002)
31. V. Lehmann, *Electrochemistry of silicon—instrumentation, science, materials and applications* (WILEY-VCH Verlag GmbH & Co. KGaA, Weinheim, 2002)
32. M.J. Sailor, *Porous silicon in practice: preparation, characterization and applications* (WILEY-VCH Verlag GmbH & Co. KGaA, Weinheim, 2012)
33. W. Kern, Purifying Si and SiO_2 surfaces with hydrogen peroxide. Semicond. Int. **7**, 94–99 (1984)
34. R.C. Henderson, Silicon cleaning with hydrogen peroxide solutions: a high energy electron diffraction and auger electron spectroscopy study. J. Electrochem. Soc. **119**, 772–775 (1972)
35. S.I. Raider, R. Flitsch, M.J. Palmer, Oxide growth on etched silicon in air at room temperature. J. Electrochem. Soc. **122**, 413–418 (1975)
36. G.S. Higashi, Y.J. Chabal, G.W. Trucks, K. Raghavachari, Ideal hydrogen termination of the Si (111) surface. Appl. Phys. Lett. **56**, 656–658 (1990)
37. V. Le Thanh, D. Bouchier, G. Hincelin, Low-temperature formation of Si(001). J. Appl. Phys. **87**, 3700–3706 (2000)
38. V.A. Burrows, Y.J. Chabal, G.S. Higashi, K. Raghavachari, S.B. Christman, Infrared spectroscopy of Si(111) surfaces after HF treatment: hydrogen termination and surface morphology. Appl. Phys. Lett. **53**, 998–1000 (1988)
39. Y. Kato, T. Ito, A. Hiraki, Initial oxidation process of anodized porous silicon with hydrogen atoms chemisorbed on the inner surface. Jpn. J. Appl. Phys. **27**, L1406–L1409 (1988)
40. H. Seidel, L. Csepregi, A. Heuberger, H. Baumgärtel, Anisotropic etching of crystalline silicon in alkaline solutions. J. Electrochem. Soc. **137**, 3612–3626 (1990)

41. Y.H. Seo, K.S. Nahm, K.B. Lee, Mechanistic study of silicon etching in HF-KBr O3–H2O solution. J. Electrochem. Soc. **140**, 1453–1458 (1993)
42. J.B. Price, Semiconductor silicon, in *Electrochemical Society Symposium Series, Electrochemical Society*, ed. by H.R. Huff, P.R. Burgess (Princeton, New Jersey, 1973)
43. X.H. Xia, J.J. Kelly, Electrochemistry of hypochlorite at silicon in alkaline etchantsm: Applications in device fabrication. J. Electrochem. Soc. **148**, C348–C352 (2001)
44. O. Tabata, R. Asahi, H. Funabashi, K. Shimaoka, S. Sugijama, Anisotropic etching of silicon in TMAH solutions. Sens. Actuators, A **34**, 51–57 (1992)
45. A. Merlos, M.C. Acero, M.H. Bao, J. Bausells, J. Esteve, TMAH/IPA anisotropic etching characteristics. Sens. Actuators, A **37–38**, 737–743 (1993)
46. T. Wang, S. Surve, P.J. Hesketh, Anisotropic etching of silicon in rubidium hydroxide. J. Electrochem. Soc. **141**, 2493–2497 (1994)
47. L.D. Clark, J.L. Lund, D.J. Edell, in *Proceedings of the IEEE Solid-State Sensor and Actuator Workshop* (Hilton Head Island, SC, USA, 1988)**,** pp. 5–8
48. J.D.I. Yam, J.J. Santiago-Aviles, J.N. Zemel, An investigation of the anisotropic etching of (100) silicon using cesium hydroxide. Sens. Actuators, A **29**, 121 (1991)
49. S. Yao, P.J. Hesketh, Etching high aspect ratio (110) silicon grooves in CsOH. J. Electrochem. Soc. **142**, L23–L25 (1995)
50. G. Gould, E.A. Irene, An in situ ellipsometric study of aqueous NH_4OH treatment of silicon. J. Electrochem. Soc. **136**, 1108–1112 (1989)
51. G. Schulze, M. Henzler, Adsorption of atomic hydrogen on clean cleaved silicon (111). Surf. Sci. **124**, 336–350 (1993)
52. M. Asano, T. Cho, H. Muraoka, Application of choline in semiconductor technology. Electrochem. Soc. Ext. Abstr. **354**, 911–913 (1976)
53. A. Reisman, M. Berkenbilt, S.A. Chan, F.B. Kaufmann, D.C. Green, The controlled etching of silicon in catalyzed ethylenediamine-pyrocatechol-water solutions. J. Electrochem. Soc. **126**, 1406–1415 (1979)
54. T.T. Trifonov, Photonic band gap analysis and fabrication of macroporous silicon by electrochemical etching. (Universitat Rovira i Virgili, Departament d'Electrònica, Elèctrica i Automàtica, Tarragona, 2004). http://www.tdx.cat/handle/10803/8477
55. C. Jamois, R.B. Wehrspohn, J. Schilling, F. Müller, R. Hillebrand, W. Hergert, Silicon-based photonic crystals slabs: two concepts. IEEE J. Quantum Electron. **38**, 805–810 (2002)
56. R. Hillebrand, C. Jamois, J. Schilling, R.B. Wehrspohn, W. Hergert, Computation of optical properties of Si-based photonic crystals with varying pore diameters. Phys. Status Solidi B **240**, 124–133 (2003)
57. U. Grüning, V. Lehmann, S. Ottow, K. Busch, Macroporous silicon with a complete two-dimensional photonic band gap centered at 5 μm. Appl. Phys. Lett. **68**, 747–749 (1996)
58. J. Schilling, A. Birner, F. Müller, R.B. Wehrspohn, R. Hillebrand, U. Gösele, K. Bursch, S. John, S.W. Leonard, H.M. Van Driel, Optical characterisation of 2D macroporous silicon photonic crystals with bandgaps around 3.5 and 1.3 μm. Opt. Mater. **17**, 7–10 (2001)
59. U. Grüning, V. Lehmann, C.M. Engelhardt, Two-dimensional infrared photonic band gap structure based on porous silicon. Appl. Phys. Lett. **66**, 3254–3256 (1995)
60. S. Rowson, A. Chelnokov, J.M. Lourtioz, Two-dimensional photonic crystals in macroporous silicon: from mid-infrared (10 μm) to telecommunication wavelengths (1.3 × 1.5 μm). J. Lightwave Technol. **17**, 1989–1995 (1999)
61. F. Müller, A. Birner, U. Gösele, V. Lehmann, S. Ottow, H. Föll, Structuring of macroporous silicon for applications as photonic crystals. J. Porous Mater. **7**, 201–204 (2000)
62. J. Schilling, R.B. Wehrspohn, A. Birner, F. Müller, R. Hillebrand, U. Gösele, S.W. Leonard, J.P. Mondia, F. Genereux, H.M. Van Driel, P. Kramper, V. Sandoghdar, K. Busch, A model system for two-dimensional and three-dimensional photonic crystals: macroporous silicon. J. Opt. A: Pure Appl. Opt. **3**, S121–S132 (2001)
63. A. Birner, R.B. Wehrspohn, U. Gösele, K. Bursch, Silicon-based photonic crystals. Adv. Mater. **13**, 377–388 (2001)

64. S. Ottow, V. Lehmann, H. Föll, Processing of three-dimensional microstructures using macroporous n-type silicon. J. Electrochem. Soc. **143**, 385–390 (1996)
65. G. von Freymann, W. Koch, D.C. Meisel, M. Wegener, M. Diem, A. García-Martín, S. Pereira, K. Busch, J. Schilling, R.B. Wehrspohn, U. Gösele, Diffraction properties of two-dimensional photonic crystals. Appl. Phys. Lett. **83**, 614–616 (2003)
66. S. Matthias, F. Müller, U. Gösele, Simple cubic three-dimensional photonic crystals based on macroporous silicon and anisotropic posttreatment. J. Appl. Phys. **98**, 023524 (2005)
67. E.V. Astrova, V.V. Ratnikov, A.D. Remenyuk, I.L. Shulpina, Strains in macroporous silicon introduced by cyclic oxidation. Phys. Status Solidi A **197**, 16–21 (2003)
68. M. Alba, E. Romano, P. Formentín, P.J. Eravuchira, J. Ferré-Borrull, J. Pallarès, L.F. Marsal, Selective dual-side functionalization of hollow SiO_2 micropillar arrays for biotechnological applications. RSC Adv. **4**, 11409–11416 (2014)
69. V. Lehmann, R. Stengl, A. Luigart, On the morphology and the electrochemical formation mechanism of mesoporous silicon. Mater. Sci. Eng., B **69–70**, 11–22 (2000)
70. S. Frohnhoff, M. Marsa, M.G. Berger, M. Thönissen, H. Lüth, H. Münder, An extended quantum model for porous silicon formation. J. Electrochem. Soc. **142**, 615–620 (1995)
71. W. Theiss, S. Henkel, M. Arntzen, Connecting microscopic and macroscopic properties of porous media: Choosing appropriate effective medium concepts. Thin Solid Films **255**, 177–180 (1995)
72. I. Mihalcescu, G. Lerondel, R. Rome-stain, Porous silicon anisotropy investigated by guided light. Thin Solid Films **297**, 245–249 (1997)
73. A. Loni, L.T. Canham, M.G. Berger, R. Arens-Fischer, H. Münder, H. Lüth, H.F. Arrand, T. M. Benson, Porous silicon multilayer optical waveguides. Thin Solid Films **276**, 143–146 (1996)
74. C. Mazzoleni, L. Pavesi, Application to optical components of dielectric porous silicon multilayers. Appl. Phys. Lett. **67**, 2983–2985 (1995)
75. H.J. Kim, Y.Y. Kim, K.W. Lee, S.H. Park, A distributed Bragg reflector porous silicon layer for optical interferometric sensing of organic vapour. Sens. Actuators, B **155**, 673–678 (2011)
76. V. Agarwal, J.A. del Río, Tailoring the photonic band gap of a porous silicon dielectric mirror. Appl. Phys. Lett. **82**, 1512–1514 (2003)
77. S. Setzu, P. Ferrand, R. Romestain, Optical properties of multilayered porous silicon. Mater. Sci. Eng., B **69**, 34–42 (2000)
78. M.G. Berger, C. Dieker, M. Thönissen, L. Vescan, H. Lüth, H. Münder, W. Tehiss, M. Wernke, P. Grosse, Porosity superlattices: a new class of Si heterostructures. J. Phys. D Appl. Phys. **27**, 1333–1336 (1994)
79. S. Chan, P.M. Fauchet, Tunable, narrow, and directional luminescence from porous silicon light emitting devices. Appl. Phys. Lett. **75**, 274–276 (1999)
80. J.E. Lugo, H.A. López, S. Chan, P.M. Fauchet, Porous silicon multilayer structures: a photonic band gap analysis. J. Appl. Phys. **91**, 4966–4972 (2002)
81. E.K. Squire, P.A. Snow, P.St.J. Russel, L.T. Canham, A.J. Simons, C.L. Reeves, D.J. Wallis, Light emission from highly reflective porous silicon multilayer structures. J. Porous Mater. **7**, 209–213 (2000)
82. S. Setzu, G. Lérondel, R. Romestain, Temperature effect on the roughness of the formation interface of p-type porous silicon. J. Appl. Phys. **84**, 3129–3133 (1998)
83. T.C. Do, H. Bui, T.V. Nguyen, T.A. Nguyen, T.H. Nguyen, V.H. Pham, A microcavity based on a porous silicon multilayer. Adv. Nat. Sci.: Nanosci. Nanotechnol. **2**, 035001 (2011)
84. J. Volk, J. Balázs, A.L. Tóth, I. Bársony, Porous silicon multilayers for sensing by tuneable IR-transmission filtering. Sens. Actuators, B **100**, 163–167 (2004)
85. M.A. Anderson, A. Tinsley-Bown, P. Allcock, E.A. Perkins, P. Snow, M. Hollings, R.G. Smith, C. Reeves, D.J. Squirrell, S. Nicklin, T.I. Cox, Sensitivity of the optical properties of porous silicon layers to the refractive index of liquid in the pores. Phys. Status Solidi A **2**, 528–533 (2003)

86. M.G. Berger, R. Arens-Fischer, M. Thönissen, M. Krüger, S. Billat, H. Lüth, S. Hilbrich, W. Theiss, P. Grosse, Dielectric filters made of PS: advanced performance by oxidation and new layer structures. Thin Solid Films **297**, 237–240 (1997)
87. F. Cunin, T.A. Schmedake, J.R. Link, Y.Y. Li, J. Koh, S.N. Bhatia, M.J. Sailor, Biomolecular screening with encoded porous-silicon photonic crystals. Nat. Mater. **1**, 39–41 (2002)
88. A.G. Cullis, L.T. Canham, P.D.J. Calcott, The structural and luminescence properties of porous silicon. J. Appl. Phys. **82**, 909–965 (1997)
89. J.V. Behren, P.M. Fauchet, E.H. Chimowitz, C.T. Lira, Optical properties of free-standing ultrahigh porosity silicon films prepared by supercritical drying. Mat. Res. Soc. Symp. Proc. **452**, 565–570 (1997)
90. Z. Huang, N. Geyer, P. Werner, J. de Boor, U. Gösele, Metal-assisted chemical etching of silicon: a review. Adv. Mater. **23**, 285–308 (2011)
91. V. Schmidt, S. Senz, U. Gösele, Diameter-dependent growth direction of epitaxial silicon nanowires. Nano Lett. **5**, 931–935 (2005)
92. Z. Huang, T. Shimizu, S. Senz, Z. Zhang, N. Geyer, U. Gösele, Oxidation rate effect on the direction of metal-assisted chemical and electrochemical etching of silicon. J. Phys. Chem. C **114**, 10683–10690 (2010)
93. Z.P. Huang, T. Shimizu, S. Senz, Z. Zhang, X.X. Zhang, W. Lee, N. Geyer, U. Gösele, Ordered arrays of vertically aligned [110] silicon nanowires by suppressing the crystallographically preferred <100> etching directions. Nano Lett. **9**, 2519–2525 (2009)
94. W.K. Choi, T.H. Liew, M.K. Dawood, Synthesis of silicon nanowires and nanofin arrays using interference lithography and catalytic etching. Nano Lett. **8**, 3799–3802 (2008)
95. J. de Boor, N. Geyer, J.V. Wittemann, U. Gösele, V. Schmidt, Sub-100 nm silicon nanowires by laser interference lithography and metal-assisted etching. Nanotechnology **21**, 095302 (2010)
96. S.G. Cloutier, C.H. Hsu, P.A. Kossyrev, J. Xu, Enhancement of radiative recombination in silicon via phonon localization and selection-rule breaking. Adv. Mater. **18**, 841 (2006)
97. V. Lehmann, The physics of macropore formation in low doped n-type silicon. J. Electrochem. Soc. **140**, 2836–2843 (1993)
98. P. Kleimann, X. Badel, J. Linnros, Toward the formation of three-dimensional nanostructures by electrochemical etching of silicon. Appl. Phys. Lett. **86**, 183108 (2005)
99. B.H. Zhang, H.S. Wang, L.H. Lu, K.L. Ai, G. Zhang, X.L. Cheng, Large-area silver-coated silicon nanowire arrays for molecular sensing using surface-enhanced Raman spectroscopy. Adv. Funct. Mater. **18**, 2348–2355 (2008)
100. M.L. Zhang, C.Q. Yi, X. Fan, K.Q. Peng, N.B. Wong, M.S. Yang, R.Q. Zhang, S.T. Lee, A surface-enhanced Raman spectroscopy substrate for highly sensitive label-free immunoassay. Appl. Phys. Lett. **92**, 043116 (2008)
101. J. Goldberger, A.I. Hochbaum, R. Fan, P. Yang, Silicon certically integrated nanowire field effect transistors. Nano Lett. **6**, 973–977 (2006)
102. B. Tian, X. Zheng, T.J. Kempa, Y. Fang, N. Yu, G. Yu, J. Huang, C.M. Lieber, Coaxial silicon nanowires as solar cells and nanoelectronic power sources. Nature **449**, 885 (2007)
103. K.Q. Peng, Y. Xu, Y. Wu, Y.J. Yan, S.T. Lee, J. Zhu, Aligned single-crystalline Si nanowire arrays for photovoltaic applications. Small **1**, 1062–1067 (2005)
104. H. Fang, X.D. Li, S. Song, Y. Xu, J. Zhu, Fabrication of slantingly-aligned silicon nanowire arrays for solar cell applications. Nanotechnology **19**, 255703 (2008)
105. E.C. Garnett, P.D. Yang, Silicon nanowire radial p-n junction solar cells. J. Am. Chem. Soc. **130**, 9224–9225 (2008)
106. K.Q. Peng, X. Wang, S.T. Lee, Silicon nanowire array photoelectrochemical solar cells. Appl. Phys. Lett. **92**, 163103 (2008)
107. Y.J. Hwang, A. Boukai, P.D. Yang, High density n-Si/n-TiO_2 core/shell nanowire arrays with enhanced photoactivity. Nano Lett. **9**, 410–415 (2009)

108. V. Sivakov, G. Andra, A. Gawlik, A. Berger, J. Plentz, F. Falk, S.H. Christiansen, Silicon nanowire-based solar cells on glass: synthesis, optical properties, and cell parameters. Nano Lett. **9**, 1549–1554 (2009)
109. A.I. Hochbaum, R.K. Chen, R.D. Delgado, W.J. Liang, E.C. Garnett, M. Najarian, A. Majumdar, P.D. Yang, Enhanced thermoelectric performance of rough silicon nanowires. Nature **451**, 163–167 (2008)
110. K. Peng, J. Jie, W. Zhang, S.T. Lee, Silicon nanowires for rechargeable lithium-ion battery anodes. Appl. Phys. Lett. **93**, 033105 (2008)
111. D. Dimova Malinovska, M. Sendova Vassileva, N. Tzenov, M. Kamenova, Preparation of thin porous silicon layers by stain etching. Thin Solid Films **297**, 9–12 (1997)
112. X. Li, P.W. Bohn, Metal-assisted chemical etching in HF/H_2O_2 produces porous silicon. Appl. Phys. Lett. **77**, 2572–2574 (2000)
113. K. Tsujino, M. Matsumura, Helical nanoholes bored in silicon by wet chemical etching using platinum nanoparticles as catalyst. Electrochem. Solid St. Lett. **8**, C193–C195 (2005)
114. S. Chattopadhyay, X.L. Li, P.W. Bohn, In-plane control of morphology and tunable photoluminescence in porous silicon produced by metal-assisted electroless chemical etching. J. App. Phys. **91**, 6134–6140 (2002)
115. K.Q. Peng, H. Fang, J.J. Hu, Y. Wu, J. Zhu, Y.J. Yan, S. Lee, Metal-particle-induced, highly localized site-specific etching of Si and formation of single-crystalline Si nanowires in aqueous fluoride solution. Chem. Eur. J. **12**, 7942–7947 (2006)
116. C.Y. Chen, C.S. Wu, C.J. Chou, T.J. Yen, Morphological control of single-crystalline silicon nanowire arrays near room temperature. Adv. Mater. **20**, 3811–3815 (2008)
117. C.L. Lee, K. Tsujino, Y. Kanda, S. Ikeda, M. Matsumura, Pore formation in silicon by wet etching using micrometre-sized metal particles as catalysts. J. Mater. Chem. **18**, 1015–1020 (2008)
118. C. Chartier, S. Bastide, C. Levy-Clement, Metal-assisted chemical etching of silicon in $HF–H_2O$. Electrochim. Acta **53**, 5509–5516 (2008)
119. K. Peng, A. Lu, R. Zhang, S.T. Lee, Motility of metal nanoparticles in silicon and induced anisotropic silicon etching. Adv. Funct. Mater. **18**, 3026–3035 (2008)
120. M.L. Zhang, K.Q. Peng, X. Fan, J.S. Jie, R.Q. Zhang, S.T. Lee, N.B. Wong, Preparation of large-area uniform silicon nanowires arrays through metal-assisted chemical etching. J. Phys. Chem. C **112**, 4444–4450 (2008)
121. Y. Harada, X.L. Li, P.W. Bohn, R.G. Nuzzo, Catalytic amplification of the soft lithographic patterning of Si. Nonelectrochemical orthogonal fabrication of photoluminescent porous Si pixel arrays. J. Am. Chem. Soc. **123**, 8709–8717 (2001)
122. S. Yae, Y. Kawamoto, H. Tanaka, N. Fukumuro, H. Matsuda, Formation of porous silicon by metal particle enhanced chemical etching in HF solution and its application for efficient solar cells. Electrochem. Commun. **5**, 632–636 (2003)
123. X.H. Xia, C.M.A. Ashruf, P.J. French, J.J. Kelly, Galvanic cell formation in silicon/metal contacts: the effect on silicon surface morphology. Chem. Mater. **12**, 1671–1678 (2000)
124. K.Q. Peng, Y. Wu, H. Fang, X.Y. Zhong, Y. Xu, J. Zhu, Uniform, axial-orientation alignment of one-dimensional single-crystal silicon nanostructure arrays. Angew. Chem. Int. Ed. **44**, 2737–2742 (2005)
125. K.Q. Peng, J.J. Hu, Y.J. Yan, Y. Wu, H. Fang, Y. Xu, S.T. Lee, J. Zhu, Fabrication of single-crystalline silicon nanowires by scratching a silicon surface with catalytic metal particles. Adv. Funct. Mater. **16**, 387–394 (2006)
126. H. Asoh, S. Sakamoto, S. Ono, Metal patterning on silicon surface by site-selective electroless deposition through colloidal crystal templating. J. Colloid Interface Sci. **316**, 547–552 (2007)
127. S. Ono, A. Oide, H. Asoh, Nanopatterning of silicon with use of self-organized porous alumina and colloidal crystals as mask. Electrochim. Acta **52**, 2898–2904 (2007)
128. K.Q. Peng, Y.J. Yan, S.P. Gao, J. Zhu, Dendrite-assisted growth of silicon nanowires in electroless metal deposition. Adv. Funct. Mater. **13**, 127–132 (2003)

129. T. Hadjersi, Oxidizing agent concentration effect on metal-assisted electroless etching mechanism in HF-oxidizing agent-H_2O solutions. Appl. Surf. Sci. **253**, 4156–4160 (2007)
130. K. Tsujino, M. Matsumura, Morphology of nanoholes formed in silicon by wet etching in solutions containing HF and H_2O_2 at different concentrations using silver nanoparticles as catalysts. Electrochim. Acta **53**, 28–34 (2007)
131. E.S. Kooij, K. Butter, J.J. Kelly, Silicon etching in HNO3/ HF solution: charge balance for the oxidation reaction. Electrochem. Solid St. Lett. **2**, 178–180 (1999)
132. D.R. Turner, On the mechanism of chemically etching germanium and silicon. J. Electrochem. Soc. **107**, 810–816 (1960)
133. T. Hadjersi, N. Gabouze, E.S. Kooij, A. Zinine, A. Ababou, W. Chergui, H. Cheraga, S. Belhousse, A. Djeghri, Metal-assisted chemical etching in HF/$Na_2S_2O_8$ OR HF/$KMnO_4$ produces porous silicon. Thin Solid Films **459**, 271–275 (2004)
134. S. Cruz, A. Honig-dOrville, J. Muller, Fabrication and optimization of porous silicon substrates for diffusion membrane applications. J. Electrochem. Soc. **152**, C418–C424 (2005)
135. K. Tsujino, M. Matsumura, Boring deep cylindrical nanoholes in silicon using silver nanoparticles as a catalyst. Adv. Mater. **17**, 1045–1047 (2005)
136. Z.P. Huang, H. Fang, J. Zhu, Fabrication of silicon nanowire arrays with controlled diameter, length, and density. Adv. Mater. **19**, 744–748 (2007)
137. Z.P. Huang, X.X. Zhang, M. Reiche, L.F. Liu, W. Lee, T. Shimizu, S. Senz, U. Gösele, Extended arrays of vertically aligned sub-10 nm diameter [100] Si nanowires by metal-assisted chemical etching. Nano Lett. **8**, 3046–3051 (2008)
138. K.Q. Peng, J. Zhu, Morphological selection of electroless metal deposits on silicon in aqueous fluoride solution. Electrochim. Acta **49**, 2563–2568 (2004)
139. K.Q. Peng, Z.P. Huang, J. Zhu, Fabrication of large-area silicon nanowire p-n junction diode arrays. Adv. Mater. **16**, 73–76 (2004)
140. K.Q. Peng, Y.J. Yan, S.P. Gao, J. Zhu, Synthesis of large-area silicon nanowire arrays via self-assembling nanoelectrochemistry. Adv. Mater. **14**, 1164–1167 (2002)
141. K.Q. Peng, J. Zhu, Simultaneous gold deposition and formation of silicon nanowire arrays. J. Electroanal. Chem. **558**, 35–39 (2003)
142. Z.P. Huang, Y. Wu, H. Fang, N. Deng, T.L. Ren, J. Zhu, Large-scale $Si_{1-x}Ge_x$ quantum dot arrays fabricated by templated catalytic etching. Nanotechnology **17**, 1476 (2006)
143. S.L. Cheng, C.H. Chung, H.C. Lee, A study of the synthesis, characterization, and kinetics of vertical silicon nanowire arrays on (001) Si substrates. J. Electrochem. Soc. **155**, D711–D714 (2008)
144. H. Fang, Y. Wu, J.H. Zhao, J. Zhu, Silver catalysis in the fabrication of silicon nanowire arrays. Nanotechnology **17**, 3768 (2006)
145. S.W. Chang, V.P. Chuang, S.T. Boles, C.A. Ross, C.V. Thompson, Densely packed arrays of ultra-high-aspect-ratio silicon nanowires fabricated using block-copolymer lithography and metal-assisted etching. Adv. Funct. Mater. **19**, 2495–2500 (2009)
146. S. Chattopadhyay, P.W. Bohn, Direct-write patterning of microstructured porous silicon arrays by focused-ion-beam Pt deposition and metal-assisted electroless etching. J. App. Phys. **96**, 6888–6894 (2004)
147. H. Han, Z. Huang, W. Lee, Metal-assisted chemical etching of silicon and nanotechnology applications. Nano Today **9**, 271–304 (2014)
148. R. Elnathan, M. Kwiat, F. Patolsky, N.H. Voelcker, Engineering vertically aligned semiconductor nanowire arrays for applications in the life sciences. Nano Today **9**, 172–196 (2014)
149. K.Q. Peng, M.L. Zhang, A.J. Lu, N.B. Wong, R.Q. Zhang, S.T. Lee, Ordered silicon nanowire arrays via nanosphere lithography and metal-induced etching. Appl. Phys. Lett. **90**, 163123 (2007)
150. Y.M. Yang, P.K. Chu, Z.W. Wu, S.H. Pu, T.F. Hung, K.F. Huo, G.X. Qian, W.J. Zhang, X. L. Wu, Catalysis of dispersed silver particles on directional etching of silicon. Appl. Surf. Sci. **254**, 3061–3066 (2008)

151. H. Morinaga, M. Suyama, T. Ohmi, Mechanism of metallic particle growth and metal-induced pitting on Si wafer surface in wet chemical processing. J. Electrochem. Soc. **141**, 2834–2841 (1994)
152. X.H. Xia, C.M.A. Ashruf, P.J. French, J. Rappich, J.J. Kelly, Etching and passivation of silicon in alkaline solution: a coupled chemical/electrochemical system. J. Phys. Chem. B **105**, 5722–5729 (2001)
153. X.G. Zhang, *Electrochemistry of silicon and its oxide* (Kluwer Academic/Plenum Publisher, New York, 2001)
154. M. Schade, N. Geyer, B. Fuhrmann, F. Heyroth, H.S. Leipner, High-resolution analytical electron microscopy of catalytically etched silicon nanowires. Appl. Phys. A Mater. Sci. Process. **95**, 325 (2009)
155. A.I. Hochbaum, D. Gargas, Y.J. Hwang, P. Yang, Single crystalline mesoporous silicon nanowires. Nano Lett. **9**, 3550–3554 (2009)
156. A. Santos, M.J. Deen, L.F. Marsal, Conventional and low-cost fabrication technologies for nanostructures: state-of-the-art and potential. Nanotechnology (2014) (in press)
157. H. Masuda, K. Fukuda, Ordered metal nanohole arrays made by a two-step replication of honeycomb structures of anodic alumina. Science **268**, 1466–1468 (1995)
158. H. Masuda, F. Hasegwa, Self-ordering of cell arrangement of anodic porous alumina formed in sulfuric acid solution. J. Electrochem. Soc. **144**, L127–L130 (1997)
159. H. Masuda, K. Yada, A. Osaka, Self-ordering of cell configuration of anodic porous alumina with large-size pores in phosphoric acid solution. Jpn. J. Appl. Phys. **37**, L1340–L1342 (1998)
160. K. Nielsch, J. Choi, K. Schwirn, R.B. Wehspohn, U. Gösele, Self-ordering regimes of porous alumina: the 10 % porosity rule. Nano Lett. **2**, 677–680 (2002)
161. W. Lee, R. Ji, U. Gösele, K. Nielsch, Fast fabrication of long-range ordered porous alumina membranes by hard anodization. Nat. Mater. **5**, 741–747 (2006)
162. A.P. Li, F. Müller, A. Birner, K. Nielsch, U. Gösele, Hexagonal pore arrays with a 50–420 nm interpore distance formed by self-organization in anodic alumina. J. Appl. Phys. **84**, 6023–6026 (1998)
163. W. Lee, R. Ji, C. A. Ross, U. Gösele, K. Nielsch, Wafer-scale Ni imprint stamps for porous alumina membranes based on interference lithography. Small **2**, 978–982 (2006)
164. H. Masuda, H. Yamada, M. Satoh, H. Asoh, M. Nakao, T. Tamamura, Highly ordered nanochannel-array architecture in anodic alumina. Appl. Phys. Lett. **71**, 2770–2772 (1997)
165. K. Zhu, T.B. Vinzant, N.R. Neale, A.J. Frank, Removing structural disorder from oriented TiO2 nanotube arrays: reducing the dimensionality of transport and recombination in dye-sensitized solar cells. Nano Lett. **7**, 3739–3746 (2007)
166. Y.Q. Liang, C.G. Zhen, D.C. Zou, D.S. Xu, Preparation of free-standing nanowire arrays on conductive substrates. J. Am. Chem. Soc. **126**, 16338–16339 (2004)

Chapter 2
Methods, Properties and Applications of Porous Silicon

Elisabet Xifré-Pérez, Josep Ferré-Borrull, Josep Pallarés and Lluís F. Marsal

Abstract Porous silicon is a very versatile material with an interestingly wide range of micro and nanostructures. Its large effective surface area, controllable morphology and high interaction with light makes of porous silicon an excellent platform for the development of optical and biosensing devices. This chapter is aimed at reviewing the fabrication process of porous silicon and describing its optical properties and most relevant applications.

2.1 Introduction

Porous silicon has been known for more than 50 years. Porous silicon was discovered in 1956 by the Uhlir [1] while performing electropolishing experiments on silicon wafers using an electrolyte containing hydrofluoric acid. They found that under the appropriate conditions of applied current and solution composition, silicon did not dissolve uniformly but instead fine holes were produced. As the aim of their research was not a porous material, their discovery remained unconsidered. In the seventies and eighties the interest on porous silicon increased: it was used as a precursor to generate thick oxide layers on silicon, as a dielectric layer in capacitance based chemical sensors [2] and its high surface area was found to be useful as a model of the crystalline silicon surface in spectroscopic studies [3, 4]. Since that time, the interest of researchers and technologists to porous silicon (and other porous semiconductors as well) is constantly growing and the number of publications dedicated to this class of materials increases every year. A renewed interest in porous silicon occurred in 1990 when its photoluminescence and electroluminescence properties were demonstrated [5, 6].

E. Xifré-Pérez · J. Ferré-Borrull · J. Pallarés · L.F. Marsal (✉)
Nanoelectronic and Photonic Systems (NePhoS), Departament d'Enginyeria Electrònica, Elèctrica i Automàtica, Universitat Rovira i Virgili, Avda, Països Catalans 26, 43007 Tarragona, Spain
e-mail: lluis.marsal@urv.cat

D. Losic and A. Santos (eds.), *Electrochemically Engineered Nanoporous Materials*, Springer Series in Materials Science 220,
DOI 10.1007/978-3-319-20346-1_2

The formation process of porous silicon consists of the electrochemical etching of silicon wafers in solutions based on hydrofluoric acid. Porous silicon is usually designed in a complex shape, using suitably doped silicon structures that are dissolved selectively [7]. Depending on the anodization conditions, this material presents a porous texture with pore diameters varying from 2 to 15 nm, density varying from 20 to 80 % and specific surface area varying from 100 to 600 m^2/cm^3 [8].

Porous silicon is a very interesting material due to its excellent mechanical, physical, optical and thermal properties, its low cost, and its obvious compatibility with silicon-based microelectronics [9]. Its large surface area within a small volume, controllable pore size, convenient surface chemistry, and the ability to modulate its refractive index as a function of depth [10] makes of porous silicon a suitable dielectric material for the formation of several complex structures.

This chapter is aimed at explaining the electrochemical method for porous silicon fabrication and describing its optical properties and most relevant applications. First, we introduce the electrochemical etching process for porous silicon formation and discuss the influence of the anodization parameters on the physical and optical properties of the material. Subsequently we describe the most relevant optical properties of porous silicon and finally we review outstanding applications of the material.

2.2 Fabrication Process and Morphological Structure of Porous Silicon

2.2.1 Porous Silicon Formation by Electrochemical Etching

One of the most important advantages of porous silicon is its simple and easy preparation [11]. Since the first studies of Uhlir [1] and Turner [12] in the fifties, porous silicon has been mainly obtained by electrochemical dissolution of silicon wafers in solutions based on hydrofluoric acid (HF) [5]. Other less extended methods have also been used for the preparation of porous silicon [13–18], though the discovery of visible photoluminescence in electrochemically-etched porous silicon by Canham [5] in the nineties strongly stimulated the production of material with visible light emission and relegated other formation methods.

The schematic of the basic system for the electrochemical etching of porous silicon is presented in Fig. 2.1, where its simplicity can be observed. A voltage is applied between the anode and the cathode. The anode is the silicon wafer, in contact with the electrolyte consisting of a solution of hydrofluoric acid (HF). The cathode, immersed in the electrolyte, is usually a platinum wire with a spiral or circular shape.

Pore growth by partial dissolution of the silicon wafer starts when applying the appropriate voltage between the wafer backside contact and the cathode in the HF solution. The interface between the porous silicon layer and the silicon substrate is

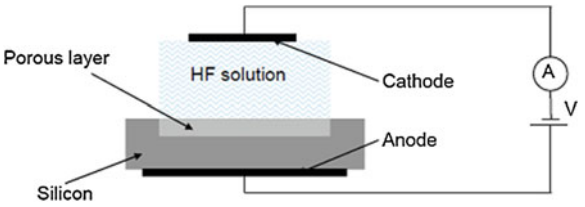

Fig. 2.1 Schematic diagram of the porous silicon anodization circuit

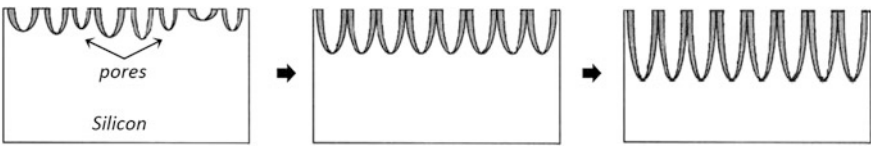

Fig. 2.2 Schematic of the macropore growth by partial dissolution of the silicon wafer. The initial random growth (*left*) becomes stable and highly directional when the depth of the pores increases (*right*)

essentially flat and the growth of the porous layer is always perpendicular to the surface of the substrate with back electrical contact [19]. Dissolution of silicon only occurs at the pore tips therefore when a porous silicon layer is formed no more electrochemical etching occurs but a slow chemical one starts, due to the permanence in HF [20]. An example of macropores growth by partial dissolution of silicon in HF solution is observed in Fig. 2.2. At the beginning of the dissolution process, pores appear randomly on the silicon surface and grow isotropically as the process proceeds until overlap. Then the pore growth becomes highly directional as the dissolution only occurs at the pore tips [21].

In spite of the simplicity and the easy assembly required for the silicon dissolution, porous silicon has extremely rich morphological features and its formation process is a very complex function of numerous factors [22]. Porous silicon microstructure is sensitive to many parameters which need to be controlled during etching, being the most important the current density and the applied potential. Besides, for achieving excellent reproducibility from run to run, other parameters such as electrolyte composition and silicon substrate must be considered [23]. The influence of all these parameters on the resulting porous structure is discussed in the following sections.

2.2.2 *Porous Silicon Formation Mechanisms*

Numerous theories explaining the mechanisms responsible for producing porous silicon have been reported since it was discovered. Theories from Smith and Collins

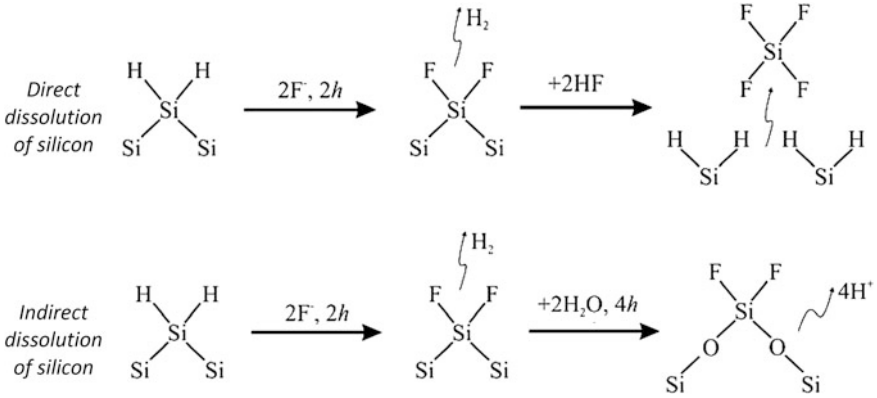

Fig. 2.3 Schematic of a proposed dissolution mechanism of silicon in HF solution (Adapted from [38])

[24, 25], Beale [26, 27], Zhang [28, 29], Unagami [30], Turner [31], Dubin [32], Lehman and Gosele [33] and others [34] are part of the literature about porous silicon. Although the exact chemistry of silicon anodic dissolution is not yet completely understood, almost all theories accept that for both electropolishing and pore formation the existence of holes is essential [35–37].

Figure 2.3 illustrates the reaction scheme generally accepted for the anodic dissolution of silicon, discussed in detail in [36, 38]. Briefly, it is widely acknowledged that the surface of silicon in HF solution with or without active dissolution is terminated by hydrogen [39, 40]. As shown in Fig. 2.3, dissolution of a surface silicon atom involves the replacement of a surface hydrogen atom with F^-, supplied by the HF solution. Although the exact chemistry of the silicon anodic dissolution is not yet completely understood, it is accepted that two hydrogen atoms are released for every silicon that reacted during the direct dissolution of silicon [41, 42]. During the indirect dissolution, four electrons are consumed for every silicon atom that reacted [27, 41]. Therefore, the existence of different regions during the anodization of silicon in HF solutions is associated with the two competing reactions: direct dissolution of silicon and indirect dissolution [20, 38].

2.2.3 *Current-Voltage Curves*

Current density flowing through the aqueous electrolyte is a determining parameter in silicon electrochemical etching process. When applying a voltage between the silicon substrate and the platinum cathode (Fig. 2.1), a current flows. The current-voltage curve provides important information for understanding porous silicon formation process [43]. In the literature, absolute current is commonly considered nevertheless current density at the silicon-electrolyte interface is the

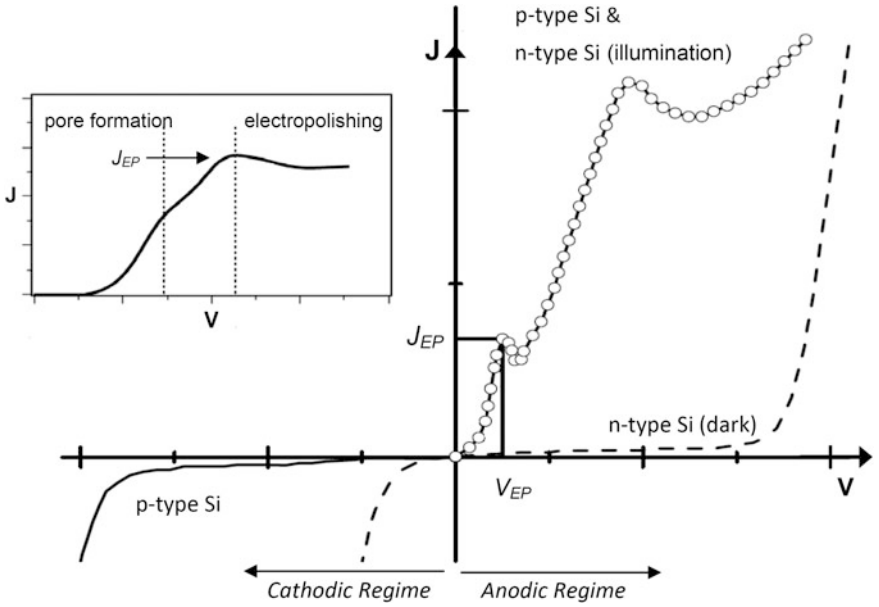

Fig. 2.4 Typical current-voltage curve of silicon dissolution in an aqueous solution for p- and n-type silicon substrates (Adapted from [44]). *Inset* Zoom of the curve for the low potential area near J_{EP} (Adapted from [45])

quantity with physical meaning. In fact, current density is the current flowing over the silicon sample area exposed to the electrolyte, being this area different for each fabrication setup.

The typical current-voltage curves for silicon dissolution in hydrofluoric aqueous solutions is similar to a Schottky diode [44], as observed in Fig. 2.4. For n-type substrates, this typical current-voltage behavior is observed only under illumination as the required holes must be externally generated.

Three differentiated regions are distinguished for the anodic regime (Fig. 2.4). Pore formation occurs at the initial part of the curve where current increases sharply with the potential. Within this region, surface morphology consists of a dense array of channels penetrating deeply into the silicon substrate. The etching of the substrate is anisotropic and porosity is strongly determined by current density: an increment of current density results in an increment of porosity when the rest of anodization parameters are fixed.

For potentials beyond the small sharp current density peak (J_{EP}), current density is relatively large. This is the electropolishing region, characterized by isotropic etching. Within this region, surface conserves a relatively smooth and planar morphology. J_{EP} is the so-called electropolishing or critical current peak and its value depends on the silicon substrate, especially on the dopant concentration, and the solution composition.

Between these two regions, a transition region exists where pore formation and electropolishing compete for control over the surface and features of both are observed [29]. The resulting structure is generally porous but the pore diameters increase rapidly as the electropolishing potential (V_{EP}) is approached.

The anodization can be performed either in potentiostatic (voltage-controlled) or in galvanostatic (current-controlled) mode although the anodization under galvanostatic conditions is widely preferred for attaining higher levels of homogeneity and reproducibility and a better control of the thickness and the porosity of the porous silicon layers.

2.2.4 Pore Size and Morphology

The average pore size of porous silicon structures covers four orders of magnitude, from nanometers to tens of micrometers. Pore size is defined as the distance between two opposite walls of the pore. The existing nomenclature, adopted by the International Union of Pure and Applied Chemistry (IUPAC), distinguishes three categories with regard to the pore dimensions [46]: mostly microporous ($d < 2$ nm), mostly mesoporous ($2 \text{ nm} < d < 50$ nm), and macroporous ($d > 50$ nm). The term 'nanoporous' is sometimes used to denote the microporous size pores. The smallest pores that can be electrochemically formed in silicon have a diameter of approximately 1 nm. Under certain conditions, two different pore distributions can coexist in the same structure. For example, walls of porous silicon macropores can be partially or fully covered with micropores [47].

Pore diameter generally increases with increasing potential and current density [48–50]. It is also sensitive to the electrolyte solution: wider pores are obtained by decreasing the HF concentration [28] and a wider range of pore diameters can be obtained in organic solvents than in aqueous solutions [51–53].

The diameter of the pores is not completely uniform in depth. The pores at the surface are smaller than near the bulk. This increase in pore diameter from surface to bulk is due to the transition from pore initiation to steady growth [30, 51] The uniformity of the pores in depth is favored by a low HF concentration, low temperature and low growth rate [28].

The categorization of the IUPAC previously mentioned is related only to the pore diameter, but does not consider pore morphology. The term pore morphology is used for properties like shape (smooth, branched, facetted, etc.), orientation, interconnection of pores, etc. The morphology is the least quantifiable aspect of porous silicon. It is very difficult to systematically characterize the morphology of porous silicon, which has extremely rich details with respect to variations in pore size, shape and spatial distribution.

In terms of pore morphology, it can be summarized that microporous and mesoporous silicon generally present a sponge-like structure where the direction of individual pores is totally random. For certain cases, these pores are prone to branch. This tendency increases with decreasing pore diameter. In contrast,

macroporous silicon is formed of discrete pores with smooth walls, with short branches or with dendritic branches and tend to have less anisotropic effect. Macropores grow more dominantly towards the source of holes, that is perpendicular to the surface [54, 55]. Figure 2.5 shows morphologies of different pore size porous silicon ranging from micro to macroporous. In this figure, we can observe that the dimensions of the microporous silicon skeleton are so small that can only observed with a very high magnification microscopic technique like TEM (Transmission Electron Microscopy). However, for investigating mesoporous and macroporous silicon, where pore diameters are considerably higher, SEM (Scanning Electron Microscopy) is preferred due to the simplest sample preparation procedure.

2.2.4.1 Porosity

Closely related to pore size, porosity is the ratio of the empty pore volume to the total volume. For porous silicon, high pore diameters generally imply high porosity values whereas small pore diameters indicate a small porosity of the material. Prosity values for porous silicon range from 5 % [47] to 95 % [58].

2.2.5 Anodization Parameters

As mentioned in the previous sections, the formation process of porous silicon is sensitive to several anodization conditions. In Sect. 2.2.3 the decisive influence of current density has been already discussed. Besides current density, other important anodization parameters are electrolyte composition, silicon substrate type, anodization time and illumination, essential for n-type substrates.

2.2.5.1 Electrolyte

Electrolyte composition is an important anodization parameter as it determines the porosity and the quality of the porous silicon layer (homogeneity and uniformity). Electrolytes of aqueous or ethanoic HF solutions are used for the formation process of porous silicon. Generally, the commercially available HF is a 48–49 % aqueous solution, that is diluted until the desired concentration with water or ethanol. For the silicon dissolution process HFconcentrations of 15–30 % are generally used [47].

When water is used for adjusting the HF concentration, the hydrogen bubbles generated during the porous silicon formation process stick to the substrate surface and induce lateral and in-depth inhomogeneity. For reducing this problem a surfactant agent is added to the HF solution. The surfactant generally used for the porous silicon formation is absolute ethanol. Since porous silicon is organophilic and hydrophobic, the use of ethanol guarantees a higher homogeneity and promotes

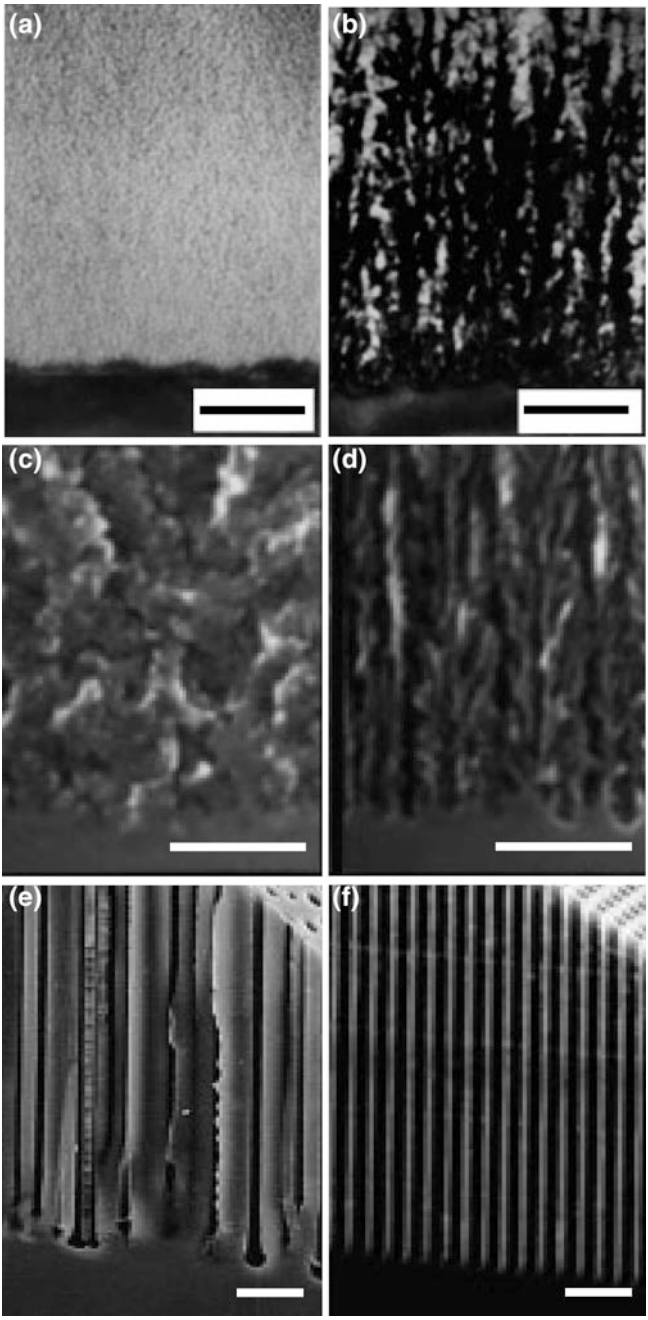

Fig. 2.5 Different morphologies of porous silicon. Microporous (**a**) and mesoporous silicon (**b**) images obtained with TEM (scale bar 100 nm) (Adapted from [56]). Random (**c**) and ordered (**d**) mesoporous silicon images obtained with SEM (scale bar 100 nm) (Adapted from [50]). Macroporous silicon with a random pattern of macropores (**e**) and ordered macropores induced by standard lithography, images obtained with SEM (scale bar 20 μm) (Adapted from [57])

a better wettability of the surface than deionized water. Ethanol supports the penetration of the fluid inside the nanometric pores, minimizing the formation of hydrogen bubbles during the anodization [59] and therefore improving the layer uniformity.

The HF concentration of the electrolyte also determines the value of the electropolishing density current (J_{EP}), that is the upper limit current density value for pore formation (Sect. 2.2.3). When HF concentration is low the range over which the current density can be varied is short, becoming wider by increasing the HF concentration [20]. However, Canham [60] establishes that the optimum HF concentration for a wider current density and porosity range is 10 %. The HF concentration also determines the pore size and the porosity: an increase of HF concentration results in a decrease of the pore size and of the porosity.

2.2.5.2 Silicon Substrate

Since the availability of holes controls the silicon dissolution process, the doping level of the silicon wafer is an important parameter for the porous silicon production. Porous silicon formation is selective with respect to the doping of the substrate.

Silicon is produced in a highly pure form. Its low concentration of impurities can be increased by the intentional addition of dopants which, in turn increase the semiconductor conductivity. Dopants for producing p-type silicon are usually Group III elements being boron the most generally used and less frequently aluminum, gallium and indium. For producing n-type silicon, phosphorous is generally used but also other Group V elements like antimony and arsenic [45].

Pore morphology is closely dependent on the dopant concentration of the silicon wafer. Some general trends on the layer morphology can be derived for different types of starting silicon substrates [61]. For p-type and p^+-type doped silicon both size and interpore spacing are in the nanometric range, between 1 and 5 nm, and the pore network looks very homogeneous and interconnected (Fig. 2.6a). For n-type doped silicon, pores are generally much larger than for p-type doped silicon, and pore size and interpore spacing decreases with increasing dopant concentrations. Lightly doped n-type substrates anodized in the dark have low porosity (1–10 %), with pores in the micrometer range. Under illumination higher values of porosity can be achieved, and mesopores are formed together with macropores (Fig. 2.6b). The final structure depends strongly on anodization conditions, especially on light intensity and current density.

Conductivity—Resistivity

Conductivity measures the ability of a material to carry electrical current. The conductivity of the silicon substrate is directly dependent on the doping level as the impurities intentionally introduced to silicon modify its electrical properties. Highly

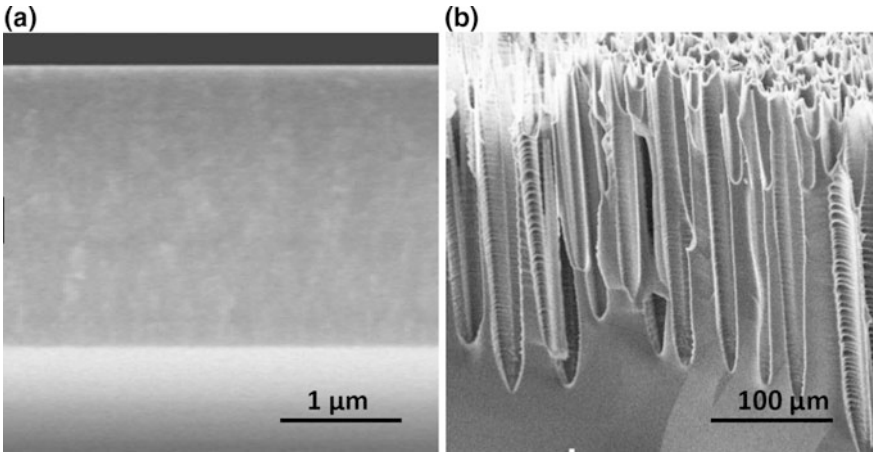

Fig. 2.6 Cross sectional SEM images of porous silicon obtained with different doped silicon wafers: **a** p^+-type silicon and **b** n-type silicon. The effect of the dopant on the pore morphology is clearly observed

doped silicon, both p-type and n-type, have very high conductivity. The conductivity of silicon substrates decreases when the dopant concentration decreases, until the conductivity of pure silicon for no doped substrates.

Very often, the resistivity values are used to indicate the characteristics of silicon substrates. Resistivity is the inverse of conductivity, measuring the propensity of the material to impede charge transport. Low resistivity substrates enable good contact between wafer and the back-side metallic connection whereas high resistivity wafers require a high dose implantation on the back surface of the wafer.

2.2.5.3 Anodization Time

As explained in the previous sections, the anodization preferentially occurs at the pore tips. This implies that once a porous silicon layer is formed no more electrochemical etching occurs. For this reason, the time current density is applied—anodization time—determines the thickness of the porous silicon layer.

Longer anodization times lead to thicker layers, but for long times in-depth anisotropy is introduced due to the chemical action of the electrolyte [20].

2.2.5.4 Illumination

Illumination during anodization is essential to generate porous silicon when using n-type substrates [62]. For n-type silicon, where the holes are the minority carriers, the electrochemical dissolution of silicon depends on the generation of

hole-electron pairs by illumination. In other words, the substrate needs the light to generate the current required for the dissolution process.

N-type silicon substrates under illumination generally produce macropores. Back-side or front-side illumination can be used for the silicon dissolution, however back-side illumination results in a more uniform diameter macropores and the shadowing effects of the electrode or the bubbles are avoided. Silicon dissolution with back-side illumination can be performed in potentiostatic or galvanostatic regime. Potentiostatic regime allows a further control on the hole injection and the etch rate and the porosity are controlled by the light source. Performing back-side potentiostatic regime the growth of the pore is very regular and the diameter of the pores can be modulated in the direction of the pore propagation.

2.2.6 *Experimental Aspects of Silicon Electrochemical Etching*

The theoretical background of the porous silicon formation and the different aspects of the electrochemical etching process have been discussed in the previous sections. However, some experimental aspects should be considered for the formation of good quality porous silicon.

2.2.6.1 Electrochemical Etching Assembly

The electrochemical etching cell is where the electrochemical reaction takes place and the main part of the experimental set-up. The design of the cell for the fabrication of homogeneous and reproducible porous silicon layers requires some details to consider. Several cell structures are proposed in the literature [44, 45, 60], being the cell showed in Fig. 2.7a one of the most generally used. Cells for n-type silicon substrates dissolution include wafer illumination for hole supply (Fig. 2.7b) [63].

The most extended material used for the cell body is Teflon due to its high resistance to the HF solution corrosion. Any other material resistant to HF and organic solvents is also suitable for the cell body. For low concentration HF solutions, PVC has been used [63] due to its resistance and price, lower than Teflon.

The cathode of the system is usually a platinum wire. This material is generally used because of its cleanness to the reaction, free of impurities. Any shape—spiral, circular, bow tie or mesh—can be appropriate for the cathode but a size similar or bigger than the surface to be etched is recommended. For increasing the homogeneity of the porous silicon layer, the cathode is recommended to be as parallel as possible to the surface of the substrate.

During the electrochemical anodization process, HF-molecules are consumed and hydrogen is produced generating bubbles. These hydrogen bubbles tend to stick to the surface of the silicon substrate decreasing the local concentration of HF and

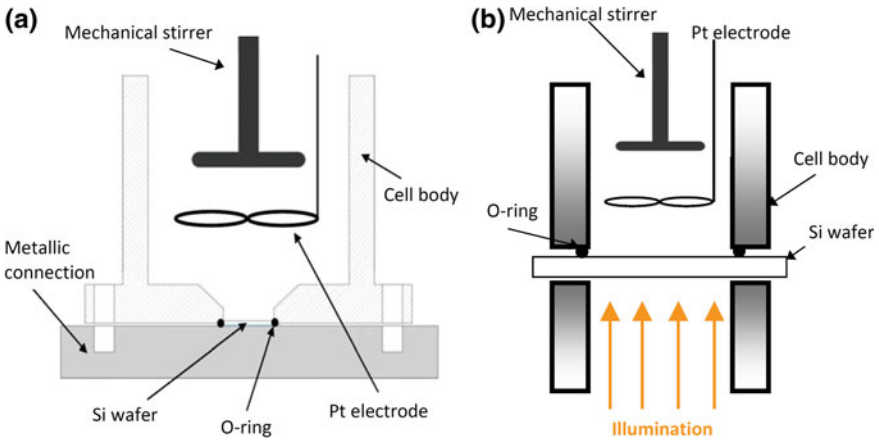

Fig. 2.7 **a** Schematic of an electrochemical cell. **b** Cell designed for n-type silicon substrates under illumination

harming the homogeneity of the porous silicon layer. Although the addition of a surfactant to the electrolyte helps the removal of these bubbles, the use of a stirrer or a pump for controllably shaking the electrolyte during the pore etching also promotes bubble removal.

2.2.6.2 Pre-etching Substrate Preparation

Surface Cleaning and Smoothing

Although commercial silicon substrates show a clean and mirror-like surface in fact this surface shows microscopic roughness, impurities and a very thin oxide layer due to atmospheric agents.

Several methods can be used for a thorough cleaning of the surface like the RCA clean consisting of a set of cleaning steps for removing organic and ionic contamination from the substrate surface [64] or using a strong base (NaOH or KOH) [45]. For general applications not requiring so deep cleaning, only the thin oxide layer on the substrate surface needs to be removed. For these cases, the oxide layer can be easily removed by dipping the substrate for a few seconds in the HF solution used as electrolyte, subsequently cleaning with ethanol and drying with nitrogen gas.

Lithography

Lithography is used to pattern the silicon substrate specially for the formation of macroporous silicon. The growth of macropores in silicon is not a self-ordering

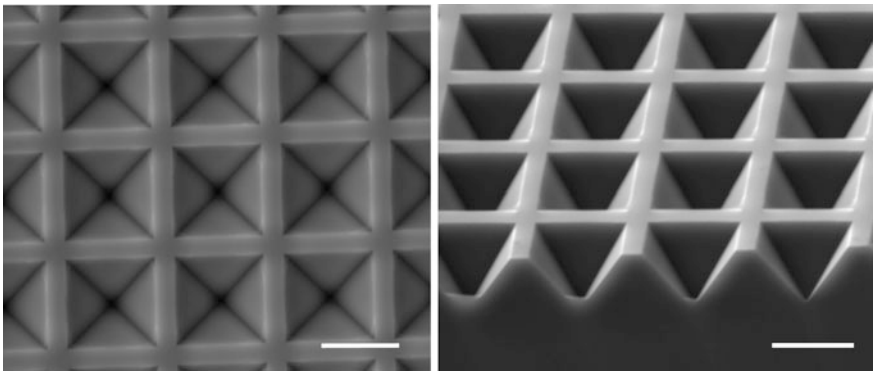

Fig. 2.8 *Top view* (*left*) and cross section (*right*) SEM images of pyramidal notches lithographically formed. They are the nucleation centers for the macropore growth. Scale bar 10 μm

process, the pores would not form a periodic arrangement naturally. However, porous silicon with ordered pores can be obtained by marking the positions were the pores should grow by a lithographic step before the anodization [57]. Figure 2.8 shows controlled etch pits marked by lithography on the surface of the silicon wafer. Lithographic resolution lowest limits are in the range of a hundred of nm, therefore only macrometric arranges of pores can be obtained in porous silicon [44].

2.2.7 Porous Silicon Structures

2.2.7.1 Microporous Multilayers

The electrochemical dissolution of silicon only occurs at the pore tips, at the interface between the silicon substrate and the electrolyte. When a porous layer is formed it is not affected by the subsequent variations of the etching parameters. Therefore, the modulation in time of an etching parameter shall result in the controlled modulation of the porosity in the pore growth direction [65]. Current density is generally the etching parameter modulated for producing these varied porosity structures called multilayers.

Figure 2.9 shows schematically the current profile and growth of a porous silicon multilayer formed by the periodic repetition of two layers with different porosity. The transversal cut of the porous silicon multilayer obtained with this current density profile is observed in Fig. 2.10. This image, performed with a Scanning Electron Microscope (SEM) clearly shows the different porosities and thicknesses of the layers.

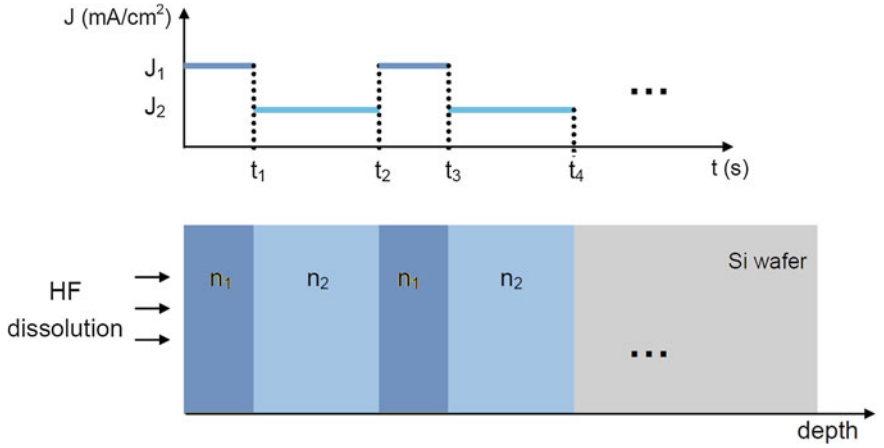

Fig. 2.9 Schematic structure and current density profile of a porous silicon multilayer

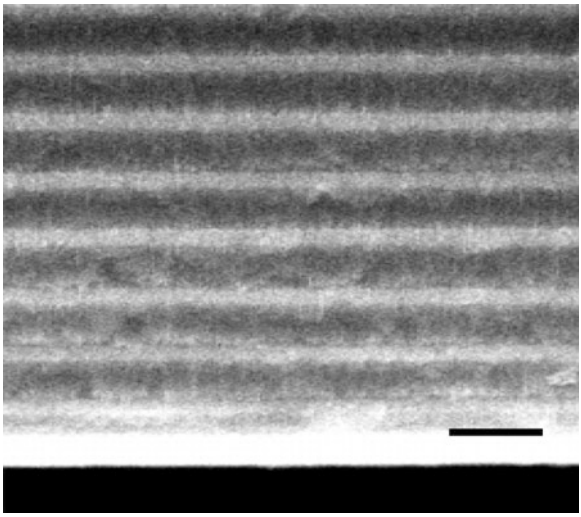

Fig. 2.10 SEM image of a porous silicon multilayer consisting of two different porosity layers repeated periodically. *Scale bar* 1 μm

Some advantages of porous silicon multilayers are the almost free combination of layers with different porosity and thickness, the fast and simple process for its formation, and the dielectric nature of the material. All these characteristics make of porous silicon a very suitable material for the formation of multilayers [66, 67].

Porous silicon multilayers have been widely used for the fabrication of optical devices like sensors [68, 69], filters [70, 71], mirror structures [66, 72] or waveguides [73].

Although the formation of multilayers with the modulation of etching parameters is used by almost all the authors working with porous silicon multilayers [70, 74–76], another formation method of porous silicon multilayers consists on using periodically doped substrates and maintaining constant the etching parameters [74, 77, 78]. This alternative method has been little used because requires of special silicon substrates and allows less freedom to select the thicknesses and porosities of the different layers.

2.2.7.2 Macroporous Structures

Perfect periodic macropore arrays with different arrangements can be easily obtained with porous silicon. These interesting macroporous structures, with applications in micromachining, gas sensing or biotechnology, can attain extremely large aspect ratios and are fully compatible with the silicon microtechnology.

Silicon dioxide pillars are attracting structures based on macroporous silicon. The key technique for their fabrication is the post etching process that the macropores were subjected to after their formation [79, 80]. A thin silicon dioxide layer can be easily grown on the surface by thermal oxidation. This characteristic allows inverted structures—hollow SiO_2 micropillars—to be released by dissolving the silicon bulk from the sample backside using selective anisotropic etchants [81] (Fig. 2.11a). The length of the pillars depends on the backside silicon etching and on the total length of the macropores. The pillar arrangement is determined by the pre-etching pattern. By adjusting such etching conditions as wafer resistivity and photogenerated current, a wide variety of pore and therefore pillar arrangements can be achieved.

Opening a hole at the pillar tip makes possible to convert the hollow silicon dioxide pillars into arrays of microneedles or microsyringes [82] (Fig. 2.11b). These microneedles can be potentially useful as microchannels for fluid delivery or for precisely located chemical-reaction stimulation [83]. The diameter of the microtubes is mainly determined by the electrochemically etched pores. Downscaling the pore diameter will enable narrower tubes to be fabricated.

A unique feature of the electrochemical etching technique is that it makes it possible to periodically and asymmetrically modulate the pore diameter in the growing direction by controlling the backside illumination intensity. The variations in the backside illumination intensity are reflected in the pore diameter [84], efficiently providing 3D-like photonic structures [85]. Macropores with periodic but asymmetric variations in the pore diameter with depth (Fig. 2.11c) have been used to fabricate ratchet-type particle separation devices [84, 86, 87].

The post-processing of the modulated macropores arrays leads to structures like Fig. 2.11. It is a fully 3D network of interconnected voids separated by thin silicon walls. This was achieved by a few oxidation/oxide-removal steps of the asymmetric macropores to dissolve the thin silicon walls only at the positions of diameter maxima [88].

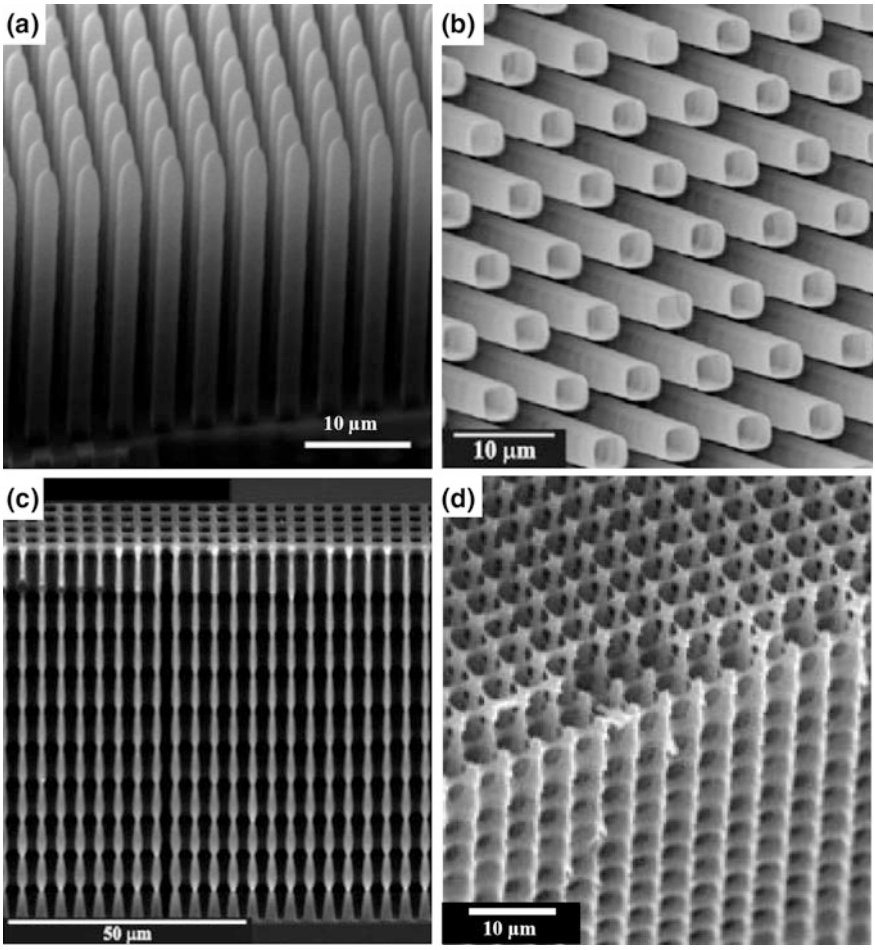

Fig. 2.11 Composition of structures based on macroporous silicon: **a** silicon dioxide pillars (Adapted from [80]); **b** silicon oxide microneedles (Adapted from [82]); **c**, **d** macroporous silicon 3D structures (Adapted from [88])

2.2.7.3 Porous Silicon Membranes

Porous silicon structures fabricated by electrochemical etching of silicon can be detached from the silicon substrate for obtaining free standing membranes. The detaching process is very simple and is performed at the end of the structure fabrication. After the formation of a single layer or multilayer the application of a short pulse of high current density causes the electropolishing of silicon and consequently the detachment of the porous silicon structure from the substrate. The magnitude of this current is very important, it must excess the electropolishing threshold (J_{EP}).

2.3 Optical Properties of Porous Silicon

2.3.1 Photoluminescence

The bright luminescence of porous silicon is one of the most important properties of the material. The strong visible luminescence from anodically etched p-doped silicon discovered by Canham in the nineties [5, 89] opened up a wide range of attractive applications of the material in the fields of electronics and optoelectronics.

The photoluminescence reported to porous silicon based structures covers a wide range that extends from the long wave UV band, through the visible and to the near infrared region. The photoluminescence of porous silicon offers a considerable technological interest because it may allow the convenient incorporation of optical elements into silicon integrated circuits [90].

The photoluminescent band that has attracted more technological attention is the visible red-to-yellow band, called S-band [91–94]. Its interest lies in three aspects: this band can be efficiently electrically excited [92, 95]; has a very wide range of spectral tunability as the phololuminescence peak can be tuned from the near infrared, through the visible range to the violet [5, 96–99]; and this band is observed from high porosity silicon regardless of the time elapsed since its fabrication [100]. The photoluminescence efficiency of red to yellow output is high under blue-UV photoexcitation [96] whereas blue emission is quite weak [97]. The origin of this emission band is still unclear although the quantum confinement based models [96, 101, 102] are considered more consistent with the experimental data [103] above models based on nanocrystal surface states [104, 105], specific defects or molecules [106, 107], and structurally disordered phases [42, 100].

The visible green-to-blue photoluminescence emission (the so-called F-band due to its fast nanosecond decay time) was first reported in [108] and has attracted a lower level interest than the S-band. The photoluminescence at this band is present in aged [109, 110] and oxidised [111, 112] porous silicon. Although still not clear, the most accepted theory for the origin of this photoluminescence band is the contaminated or defective oxide [113, 114].

Infrared emission at room temperature was firstly reported for porous silicon annealed under ultrahigh vacuum (UHV) [115]. The peak energy of the IR band shifts as a function of the material porosity, for this reason this band is called tunable IR band. This band becomes much stronger at cryogenic temperatures, and may be even more intense than the S-band [116]. The origin of this radiation could be dangling bond related [117], although no direct correlation has yet been demonstrated. The model proposed by Koch [117] relying on quantum size-effect and surface states is accepted for explaining the phololuminescence of this band.

Ultraviolet emission was first reported from oxidized material under soft x-ray excitation [118]. Stronger room temperature output was subsequently reported [119–123]. As with the F-band, the UV bands are only observed from oxidized layers and are also likely to arise from the defective oxide phase [120].

2.3.2 Refractive Index

The refractive index provides a direct measure of the optical density of a material [124]. It is usually denoted as a complex value $n + ik$ where the real part n is generally called refractive index and the imaginary part k is the extinction coefficient. For any application of a material in optics or optoelectronics it is essential to know its refractive index.

The refractive index of porous silicon is closely dependent of the porosity. In fact, porous silicon can be conveniently described as a mixture of silicon and air and its refractive index is evaluated as a suitable combination of the refractive indices of these two materials. Therefore, the refractive index of porous silicon is expected to be lower than that of silicon substrate and decreases with increasing porosity.

Porosity tunability of porous silicon optically results in refractive index tunability. However, determining the refractive index of a porous silicon layer is not trivial as it depends on the microtopology of the material. Several non-destructive techniques have been used to determine the refractive index of porous silicon like spectroscopic ellipsometry [125, 126] or the measurement of interference fringes [76, 127–129].

2.4 Applications of Porous Silicon

2.4.1 Optical Applications

Porous silicon is a very suitable material for developing optical devices based on multilayer structures. When a light beam is reflected by various dielectric interfaces, an effect of multiple interferences occurs. Different optical devices based on this simple principle can be found in the literature.

Distributed Bragg Reflectors (DBR) are multilayer structures formed by the periodic repetition of two layers with different refractive index and thicknesses. DBRs reflectivity spectrum consists of a high reflectivity spectral region centered at wavelength λ. The optical response of DBRs has been widely studied [128, 130], and also their photo-emission [131] and the roughness between their layers [132]. The most common application of porous silicon DBRs is filtering [74, 133], but they are also used as sensors of light polarization [134], waveguides [135] and part of lasers [136].

Microcavities or Fabry-Perot filters consist of two parallel DBR separated by a spacer layer, whose refractive index can be the same or different to the ones used for the DBRs [137]. The reflectivity spectrum of microcavities is characterized by a very narrow pass-band centered in a high reflectivity wavelength range. Microcavities can be used as band-pass filters with a tuned peak position [128, 138], tunable mirrors

[139] and detectors of substances like ethanol, methanol, acetone, chlorobenzene and nitrogen dioxide [68, 140–143].

Omnidirectional mirrors are multilayers that reflect light for any incidence angle and for any polarization in a wavelength range. One-dimensional mirrors consisting of the periodic repetition of two dielectric layers with different refractive index [144] are the most common structures, although other structures have been reported. [66, 67, 72, 145]. Dielectric mirrors have many advantages over metallic mirrors such as low optical loss, no light absorption, high mechanical strength, and high reflectivity within a wide range of wavelengths [146, 147].

Finally, porous silicon has also been used for the development of waveguides. Waveguides based on multilayers have attracted great interest because their guiding mechanism is completely different to the conventional waveguides based on total internal reflection [148]. Studies about the basic properties of porous silicon waveguides like modes, losses, etc. [73, 149, 150] can be found in the literature. Porous silicon waveguides have been specially used for sensing, where the infiltration of liquids in the pores results in induced phase shifts and/or variation of the guided light intensity. For example, the introduction of solvents (acetone, methanol, and propan-2-ol) into the pores is shown to dramatically reduce the loss of the waveguides in a reversible manner [151]. Waveguides based on porous silicon multilayers allow the micromachining of photonic integrated circuits that are used to confine, manipulate, and guide the photons [152].

2.4.2 Biological Applications

Among all the areas in which porous silicon is a relevant material, biology is the most prominent field. Over the last few years, the number of publications referring biological applications of porous silicon has increased dramatically. There are several reasons for this interest: porous silicon is inorganic and can be sterilized, the pore formation process is precisely controllable with pores sizes ranging from nanometers to micrometers [153], it has very high surface area (200–800 m^2/g), can be loaded with drugs or bioactive species [154] and is biocompatible [155, 156] and biodegradable [157]. Morevover, porous silicon has the ability to completely degrade into non-toxic orthosilicic acid in biological solutions [157], the major form of silicon in the human body [158] that is excreted through the urine [159].

Porous silicon was firstly used as an active biomaterial with the growth of hydroxyapatite on a microporous film of silicon [157]. From that moment, porous silicon has been considered for developing numerous biological applications: drug delivery, biosensing, biomolecular screening, tissue engineering, etc. Some of these extensive areas are explained in the next subsections.

2.4.2.1 Cell Culture

Porous silicon has revealed to be convenient cell culture platforms for the growth of mammalian cells [155, 160–162], neuronal cells [163], lens cells [156], human aortic endothelial cell [164] mesenchymal stem cells [165, 166]. Nerve fibers have also been regenerated on porous silicon surfaces [167, 168].

Substrate topography affects cell functions such as adhesion, proliferation, migration, and differentiation [169, 170]. The controllable and tunable pore size and structure of porous silicon during its formation process facilitates the development of suitable substrates for the proliferation and adhesion of cells [171, 172].

Cell adhesion and growth is improved by surface modification introducing chemical functional groups. Porous silicon surface has been successfully modified with functional groups such as amines, imines, esters, or carboxylic acids [173, 174]. Oxidation is the most common and simple surface treatment. It can be performed by ozone, aging, thermal, or chemical treatments. Amine-terminated modifications such as silanization are the most widely used for porous silicon functionalization [80, 163, 175] because they improve porous silicon stability and enhance cell adhesion [176].

2.4.2.2 Drug Delivery

Porous silicon is a very suitable material for drug delivery due to its high porosity and high surface area associated (up to 800 m^2/gr). Different therapeutic and diagnostic agents have been successfully loaded into porous silicon pores: small drug molecules such as dexamethasone [177], ibuprofen [178, 179], anticancer drugs like cisplatin [180], doxorubicin [181], and camptothecin [182].

For drug delivery applications, several aspects have to be considered: the pore size, since the molecule must be smaller than the pore diameter to penetrate into the pores; the porosity, as the quantity of drug loaded into the pores is closely associated to capacity of the pores; and finally the moment the drug starts to be released, that can be controlled by nanoscopic molecular movable gate-like functional hybrid systems [183].

2.4.3 Nanoparticles

When we talk about drug delivery and localized treatments, we have to specially talk about nanoparticles, the porous silicon element most widely used for biological applications. As its name suggests, the particles size is nanometric although micrometric particles are also used for some other applications [184].

Porous silicon nanoparticles have the same interesting properties for biological applications as the material they are made of (biocompatibility, tunable porous structure, ease surface modification with organic compounds, great chemical

stability, etc.). But also the advantages of their nanometric size, particularly interesting for localized treatments: they can freely circulate in the bloodstream and be phagocytosed by the cells [185]. In cancer therapy, porous silicon particles are suitable for developing tools minimally invasive and respectful with the healthy cells surrounding the tumor.

High selectivity for localized treatments is obtained with the surface modification of the particles. Moreover, their inherent photoluminescence emission in the visible makes of porous silicon particles outstanding materials for novel label-free biomarkers [186].

Extensive studies have been have been carried out using porous silicon nanoparticles for biological applications [187, 188]. Nowadays the use of porous silicon particles as carriers for drugs is by far the most intense research area [189–191], specially for the development of cancer treatments [192–194].

2.4.4 Sensors

The optical and/or electrical properties of porous silicon are key sensing parameters used in many chemical and biological sensing applications. Most porous silicon based sensors are interferometric sensors where the optical response of the porous silicon structure is altered with the introduction of the element to be detected in the pores. Porous silicon structures can be simple layers that display well-resolved Fabry Perot fringes or multilayered structures like Bragg reflectors of rugate filters. With the introduction of the molecule to be detected inside the pores, the effective refractive index of the porous layers changes leading to a shift of the reflectance peaks. Interferometric sensors based on porous silicon have been developed for the detection of organic vapours [184, 195], glucose [196], enzymes [197], bacterial growth [198, 199], rabitt IgG [200], and organic molecules [201].

2.4.5 Templates

Devices made of materials with interesting electrical, mechanical or chemical characteristics face very frequently the material limitations in the assembly of pores and formation of high surface area layers. The use of porous silicon as a template solves these problems providing the means for construction of complex structures. Porous silicon is an appropriate template because it can be fabricated with high precision and uniformity in a large scale and porosity, average pore size and pore depth can be tuned by adjusting the electrochemical preparation techniques.

Many nanocomposites have been reported in the literature such as nickel nanowires in mesoporous silicon templates [202], porous silicon-carbon composite for optical biosensors [200], discotic columnar liquid crystals [203], and porous silicon coated with graphene carbon for developing a ultracapacitor device [204].

Fibers, tubes or porous layers of several materials are fabricated by replicating the porous silicon structure. In these cases the porous silicon matrix is removed. This template-assisted technique has the advantage of readily create large-area and ordered arrays of micro and nanostructures with control over structural parameters. This is the fabrication method used for silica needles [82], colloidal crystal wires with tubular packing [205], silica colloids [206], porous polymer substrates [207, 208], or polymer nanotubes with a monodisperse size distribution and uniform orientation [209].

References

1. A. Ulhir, Bell Syst. Technol. J. **35**, 333 (1956)
2. R.C. Anderson, R.S. Muller, C.W. Tobias, Sens. Actuators, A **21**, 835 (1990)
3. P. Gupta, A.C. Dillon, A.S. Bracker, S.M. George, Surf. Sci. **245**, 360 (1991)
4. A.C. Dillon, M.B. Robinson, M.Y. Han, S.M. George, J. Electrochem. Soc. **139**, 537 (1992)
5. L.T. Canham, Appl. Phys. Lett. **57**, 1046 (1990)
6. D.E. Aspnes, J. Theeten, R. Hottier, Phys. Rev. B **20**, 3292 (1979)
7. P.C. Searson, Appl. Phys. Letters. **59**, 832 (1991)
8. S.G. Johnson, J.D. Joannopoulos, *Photonic Crystals the Road from Theory to Practice* (Kluwer, Boston, 2002)
9. K.D. Hirschman, L. Tsybeskov, S.P. Duttagupta, P.M. Fauchet, Nature **384**, 338 (1996)
10. C.C. Striemer, P.M. Fauchet, Appl. Phys. Lett. **81**, 2980 (2002)
11. P.C. Searson, *Advances in Electrochemical Sciences and Engineering* (VCH, Mannheim, 1994)
12. D.R. Turner, J. Electrochem. Soc. **138**, 807 (1991)
13. R.W. Fathauer, T. George, A. Ksendzov, R.P. Vasquez, Appl. Phys. Lett. **60**, 995 (1992)
14. S. Liu, C. Palsule, S. Yi, S. Gangopadhyay, Phys. Rev. **49**, 10318 (1994)
15. R.R. Chandler-Henderson, J.L. Coffer, L.A. Filessesler, J. Electrochem. Soc. **141**, L166 (1994)
16. J. Sarathy, S. Shih, K. Jung, C. Tsai, K.-H. Li, D.-L. Kwong, J.C. Campbell, S.L. Yau, A. J. Bard, Appl. Phys. Lett. **60**, 1532 (1992)
17. A.J. Steckl, J. Xu, H.C. Mogul, S.M. Prokes, J. Electrochem. Soc. **142**, L69 (1995)
18. H. Liu, Z.L. Wang, Appl. Phys. Lett. **87**, 261913 (2005)
19. C.G. Vayenas, R.E. White, M.E. Gamboa-Adelco (eds.), *Modern Aspects of Electrochemistry*, vol. 39. (Springer, New York, 2006)
20. C. Vinegoni, M. Cazzanelli, L Pavesi, Porous silicon microcavities, in Silicon-Based Materials and Devices, Properties and Devices, vol. 2, ed. by N. Hari Singh (Academic Press, London, 2001)
21. O. Bisi, S. Ossicini, L. Pavesi, Surf. Sci. Rep. **38**, 1 (2000)
22. X.G. Zhang, *Electrochemistry of Silicon and Its Oxide* (Kluwer Academic, New York, 2001)
23. V. Lehmann, U. Grüning, Thin Solid Films **297**, 13 (1997)
24. R.L. Smith, S.D. Collins, J. Appl. Phys. **71**, R1 (1992)
25. R.L. Smith, S.-F. Chuang, S.D. Collins, J. Electron. Mater. **17**, 533 (1988)
26. M.I.J. Beale, N.G. Chew, M.J. Uren, A.G. Cullis, J.D. Benjamin, Appl. Phys. Lett. **46**, 86 (1985)
27. M.I.J. Beale, J.D. Benjamin, M.J. Uren, N.G. Chew, A.G. Cullis, J. Cryst. Growth **73**, 622 (1985)
28. X.G. Zhang, J. Electrochem. Soc. **138**, 3750 (1991)
29. X.G. Zhang, S.D. Collins, R.L. Smith, J. Electrochem. Soc. **136**, 1561 (1989)

30. T. Unagami, J. Electrochem. Soc. **127**, 476 (1980)
31. D.R. Turner, in *The Electrochemistry of Semiconductors*, ed. by P.J. Holmes (Academic, London, 1962)
32. V.M. Dubin, Surf. Sci. **274**, 82 (1992)
33. V. Lehmann, U. Gosele, Appl. Phys. Lett. **58**, 856 (1991)
34. V. Labunov, V. Bondarenko, L. Glinenko, A. Dorofeev, L. Tabuulina, Thin Solid Films **137**, 123 (1986)
35. D.R. Turner, J. Electrochem. Soc. **105**, 402 (1958)
36. R. Memming, G. Schwandt, Surf. Sci. **4**, 109 (1966)
37. A. K. Vijh, in *Encyclopedia of Electrochemistry of the Elements*, vol. V, ed. by A.J. Bard (Dekker, New York, 1986)
38. X.G. Zhang, J. Electrochem. Soc. **151**, C69 (2004)
39. V.A. Burrows, Y.J. Chabal, G.S. Higashi, K. Raghavachari, S.B. Christman, Appl. Phys. Lett. **53**, 998 (1988)
40. C.M. Gronet, N.S. Lewis, G. Cogan, J. Gibbons, Proc. Natl. Acad. Sci. U.S.A. **80**, 1152 (1983)
41. M.J. Eddowes, J. Electroanal. Chem. **280**, 297 (1990)
42. C. Pickering, M.I.J. Beale, D.J. Robbins, P.J. Pearson, R. Greef, Phys. C **17**, 6535 (1984)
43. H. Foll, Appl. Phys. A **53**, 8 (1991)
44. Z. Gaburro, N. Daldosso, L. Pavesi, *Encyclopedia of Condensed Matter Physics, Chapter Porous Silicon* (Elsevier Ltd., Amsterdam, 2005)
45. M.J. Sailor, *Porous Silicon in Practice: Preparation, Characterization and Applications* (Wiley-VCH Verlag & Co Germany, Weinheim, 2011)
46. IUPAC, Manual of symbols and terminology, Appendix 2, Part 1. Pure Appl. Chem. **31**, 578 (1972)
47. V. Lehmann, *Electrochemistry of Silicon* (Wiley-VCH Verlag, Weinheim, 2002)
48. G. Bomchil, R. Herino, K. Barla, J.C. Pfister, J. Electrochem. Soc. **130**, 1611 (1983)
49. R. Herino, G. Romchil, K. Boala, C. Bertrand, J. Electrochem. Soc. **134**, 1994 (1987)
50. V. Lehmann, R. Stengl, A. Luigart, Mater. Sci. Eng., B **69**, 11 (2000)
51. Y. Watanabe, Y. Arita, T. Yokoyama, Y. Lgarashi, J. Electrochem. Soc. **122**, 1315 (1975)
52. G. Hasse, M. Christophersen, J. Carstensen, H. Foil, Phys. Status Solidi A **182**, 23 (2000)
53. J.-N. Chazalviel, R.B. Wehrspohn, F. Ozanam, Mater. Sci. Eng., B **69**, 1 (2000)
54. E.A. Ponomarev, C. Levy-Clement, Electrochem. Solid-State Lett. **1**, 42 (1998)
55. V. Lehmann, S. Ronnebeck, J. Electrichem. Soc. **146**, 2968 (1999)
56. V. Lehmann, H. Cerva, U. Gösele, Mater. Res. Soc. Symp. Proc. **256**, 3 (1992)
57. V. Lehmann, J. Electrochem. Soc. **140**, 2836 (1993)
58. L.T. Canham, A.G. Cullis, C. Pickering, O.D. Dosser, T.I. Cox, T.P. Lynch, Nature **368**, 133 (1994)
59. K. Barla, G. Bomchil, R. Herino, J.C. Pfister, J. Baruchel, J. Cryst. Growth **68**, 721 (1984)
60. A. Halimaoui, *Porous Silicon Formation by Anodization (in Properties of Porous Silicon)*, ed. by L. Canham (Short Run Press Ltd., London, 1997)
61. W. Theiss, Surf. Sci. Rep. **29**, 91 (1997)
62. N. Koshida, H. Koyama, Jpn. J. Appl. Phys. **1**(30), L1221 (1991)
63. A. Langner, F. Müller, U. Gösele, Macroporous silicon, in *Molecular- and Nano-Tubes*, ed. by O. Hayden, K. Nielsch (Springer, New York, 2011)
64. K.A. Reinhardt, W. Kern, *Handbook of Semiconductor Wafer Cleaning Technology* (William Andrew Inc, New York, 2008)
65. S. Frohnhoff, M. Berger, Adv. Mater. **12**, 963 (1994)
66. E. Xifré-Pérez, L.F. Marsal J. Ferré-Borrull J. Pallarès, Appl Phys B **95**, 169 (2009)
67. A. Bruyant, G. Lérondel, P.J. Reece, M. Gal, Appl. Phys. Lett. **82**, 3227 (2003)
68. E. Xifre-Perez, L.F. Marsal, J. Ferre-Borrull, T. Trifonov, J. Pallares, Low-dimensional systems and nanostructures. Physica E **38**, 172 (2007)
69. G. Palestino, R. Legros, V. Agarwal, E. Pérez, C. Gergely, Sens. Actuators, B: Chem. **135**, 27 (2008)

70. T.L. Kelly, T. Gao, M.J. Sailor, Adv. Mater. **23**, 1776 (2011)
71. M.S. Salem, M.J. Sailor, T. Sakka, Y.H. Ogata, J. Appl. Phys. **101**, 063503 (2007)
72. E. Xifré-Pérez, L.F. Marsal, J. Pallarès, J. Ferré-Borrull, J. Appl. Phys. **97**, 064503 (2005)
73. E. Xifré-Pérez, L.F. Marsal, J. Ferré-Borrull, J. Pallarès, J. Appl. Phys. **102**, 063111 (2007)
74. M.G. Berger, C. Dieker, M. Thönissen, L. Vescan, H. Lüth, H. Munder, W. Theiss, M. Wernke, P. Grosse, J. Phys. D **27**, 1333 (1994)
75. J. Volk, M. Fried, O. Polgár, I. Bársony, Phys. Stat. Sol. (a) **197**, 208 (2003)
76. E. Xifré-Pérez, J. Pallarès, J. Ferré-Borrull, T. Trifonov, L.F. Marsal, Phys. Stat. Sol. (c) **4**, 2034 (2007)
77. L. Pavesi, G. Giebel, F. Ziglio, G. Mariotto, F. Priolo, S.U. Campisano, C. Spinella, Appl. Phys. Lett. **65**, 2182 (1994)
78. S.T. Frohnhoff, M.G. Berger, M. Thonissen, C. Dieker, L. Vescan, H. Munder, H. Luth, Thin Sol. Films **255**, 59 (1995)
79. S. Izuo, H. Ohji, P.J. French, K. Tsutsumi, M. Kimata, Sens. Mater. **14**, 239 (2002)
80. M. Alba, E. Romano, P. Formentin, P.J. Eravuchira, J. Ferre-Borrull, J. Pallares, L.F. Marsal, RSC Adv. **4**, 11409 (2014)
81. T. Trifonov, A. Rodriguez, F. Servera, L.F. Marsal, J. Pallares, R. Alcubilla, Phys. Status Solidi A **202**, 1634 (2005)
82. A. Rodríguez, D. Molinero, E. Valera, T. Trifonov, L.F. Marsal, J. Pallarès, R. Alcubilla, Sens. Actuators, B **109**, 135 (2005)
83. K. Chun, G. Hashiguchi, H. Toshiyoshi, H. Fujita, Jpn. J. Appl. Phys. **38**, L279 (1999)
84. F. Müller, A. Birner, J. Schilling, U. Gösele, C. Kettner, P. Hänggi, Phys. Stat. Sol. A **182**, 585 (2000)
85. J. Schilling, F. Müller, S. Matthias, R.B. Wehrspohn, U. Gösele, K. Busch, Appl. Phys. Lett. **78**, 1180 (2001)
86. S. Matthias, F. Müller, Nature **424**, 53 (2003)
87. C. Kettner, P. Reimann, P. Hänggi, F. Müller, Phys. Rev. E **61**, 312 (2000)
88. T. Trifonov, A. Rodríguez, L.F. Marsal, J. Pallarès, R. Alcubilla, Sens. Actuators, A **141**, 662 (2008)
89. L.T. Canham, Adv. Mater. **7**, 1033 (1995)
90. T. Wadayama, S. Yamamoto, A. Hatta, Appl. Phys. Lett. **65**, 1653 (1994)
91. A. Richter, P. Steiner, F. Kozlowski, W. Lang, IEEE Electron Device Lett. **12**, 691 (1991)
92. N. Koshida, H. Koyama, Appl. Phys. Lett. **60**, 347 (1992)
93. W. Lang, P. Steiner, F. Kozlowski, J. Luminescence **57**, 341 (1993)
94. H. Mimura, T. Matsumoto, T. Futagi, Y. Kanemitsu, J. Phys. Soc. Jpn. **63**, 203 (1994)
95. A. Halimaoui, C. Oules, G. Bomchil, A. Bsiesy, F. Gaspard, R. Herino, M. Ligeon, F. Muller, Appl. Phys. Lett. **59**, 304 (1991)
96. J.C. Vial, A. Bsiesy, F. Gaspard, R. Hérino, M. Ligeon, F. Muller, R. Romestain, R.M. Macfarlane, Phys. Rev. B **45**, 14171 (1992)
97. H. Mizuno, H. Koyama, N. Koshida, Appl. Phys. Lett. **69**, 3779 (1996)
98. A. Nakajina, T. Itakura, S. Wanatake, N. Nakayama, Appl. Phys. Lett. **61**, 46 (1992)
99. F. Muller, R. Herino, M. Ligeon. F. Gaspard, R. Romestain, J.C. Vial, A. Bsiesy, J. Luminescence **57**, 283 (1993)
100. V. Petrov-Koch, T. Muschik, A. Kux, B.K. Meyer, F. Koch, V. Lehman, Appl. Phys. Lett. **61**, 943 (1992)
101. A.G. Cullis, L. Canham, Nature **353**, 331 (1991)
102. P. Williams, C. Lévy-Clément, J.-E. Péou, N. Brun, C. Colliex, R. Wehrspohn, J.-N. Chazalviel, A. Albu-Yaron, Thin Solid Films **298**, 66 (1997)
103. A.G. Cullis, L.T. Canham, P.D.J. Calcott, Appl. Phys. Lett. **82**, 909 (1997)
104. F. Koch, Microelectron. Eng. **28**, 237 (1995)
105. G. Allan, C. Delerve, M. Lannoo, Phys. Rev. Lett. **76**, 296 (1996)
106. S.M. Prokes, O.J. Glembocki, V.M. Bermudez, R. Kaplan, L.E. Friedersdorf, P.C. Searson, Phys. Rev. B **45**, 13788 (1992)

107. M.S. Brandt, H.D. Fuchs, M. Stutzmann, J. Weber, M. Cardona, Solid State Commun. **81**, 307 (1992)
108. J.F. Harvey, M. Shen, R.A. Lux, M. Dutta, J. Pamulapti, R. Tsu, Mater. Res. Soc. Symp. Proc. **256**, 175 (1992)
109. T. Ito, T. Ohta, A. Hiraki, Jpn. J. Appl. Phys. **31**, L1 (1992)
110. P.D.J. Calcott, K.J. Nash, L.T. Canham, M.J. Kane, D. Brumhead, J. Lumin. **57**, 257 (1993)
111. D.I. Kovalev, I.D. Yaroshetzkii, T. Muschik, V. Petrova-Koch, F. Koch, Appl. Phys. Lett. **64**, 214 (1994)
112. X.Y. Hou, G. Shi, W. Wang, F.L. Zhang, P.H. Hao, D.M. Huang, X. Wang, Appl. Phys. Lett. **62**, 1097 (1993)
113. L.T. Canham, A. Loni, P.D.J. Calcott, A.J. Simons, C. Reeves, M.R. Houlton, J.P. Newey, K.J. Nash, T.I. Cox, Thin Solid Films **276**, 112 (1996)
114. H. Tamura, M. Rückschloss, T. Wirschem, S. Vepřek, Appl. Phys. Lett. **65**, 1537 (1994)
115. P.M. Fauchet, E. Ettedgui, A. Raisanen, L.J. Brillson, F. Seiferth, S.K. Kurinec, Y. Gao, C. Peng, L. Tsybeskov, Mater. Res. Soc. Symp. Proc. **298**, 271 (1993)
116. L.T. Canham, M.R. Houlton, W.Y. Leong, C. Pickering, J.M. Keen, J. Appl. Phys. **70**, 422 (1991)
117. F. Koch, Mater. Res. Soc. Symp. Proc. **298**, 319 (1993)
118. D.T. Jiang, I. Coulthard, T.K. Sham, J.W. Lorimer, S.P. Frigo, X.H. Feng, R.A. Rosenberg, J. Appl. Phys. **74**, 6335 (1993)
119. J. Zuk, R. Kuduk, M. Kulik, J. Liskiewicz, D. Maczka, P.V. Zhukovski, V.F. Stelmakh, V.I. Bondarenko, A.M. Dorofeev, J. Luminescence **57**, 57 (1993)
120. J. Lin, G.Q. Yao, J.Q. Duan, G.G. Qin, Solid State Commun. **97**, 221 (1996)
121. I. Coulthard, D.T. Jiang, T.K. Sham, J. Electr. Spectrosc. Relat. Phenom. **79**, 233 (1996)
122. G. Qin, J. Lin, J.Q. Duan, G.Q. Yao, Appl. Phys. Lett. **69**, 1689 (1996)
123. Q. Chen, G. Zhou, J. Zhu, C. Fan, X.G. Li, Y. Zhang, Phys. Lett. A **224**, 133 (1996)
124. J.D. Jackson, *Classical Electrodynamics* (Wiley, New York, 1975)
125. E. Xifre-Perez, E. Garcia-Caurel, J. Pallares, J. Ferre-Borrull, L.F. Marsal, Mater. Sci. Eng., B **147**, 205 (2008)
126. G.E. Jellison, V.I. Merkulov, A.A. Puretzky, D.B. Geohegan, G. Eres, D.H. Lowndes, Thin Solid Films **377**, 68 (2000)
127. L. Pavesi, Riv. del Nuovo Cimento **10**, 1 (1997)
128. C. Mazzoleni, L. Pavesi, Appl. Phys. Lett. **67**, 2983 (1995)
129. M. Born, E. Wolf, *Principle of Optics* (Pergamon, Oxford, 1980)
130. S. Setzu, P. Ferrand, R. Romestain, Mat. Sci. Eng. B **69**, 34 (2000)
131. E.K. Squire, P.A. Snow, P. St, Russell. J. Porous Mater. **7**, 209 (2000)
132. S. Setzu, G. Lérondel, R. Romestain, J. Appl. Phys. **84**, 3129 (1998)
133. G. Vincent, Appl. Phys. Lett. **64**, 2367 (1994)
134. J. Diener, N. Künzner, D. Kovalev, E. Gross, V.Y. Timoshenko, G. Polisski, F. Koch, Appl. Phys. Lett. **78**, 3887 (2001)
135. C.P. Hussell, R.V. Ramaswamy, IEEE Photonics Technol. Lett. **9**, 636 (1997)
136. A. Szerling, D. Wawer, K. Hejduk, T. Piwonski, A. Wojcik, B. Mroziewicz, M. Bugajski, Optica Applicata **32**, 523 (2002)
137. L. Pavesi, C. Mazzoleni, A. Tredicucci, V. Pellegri, Appl. Phys. Lett. **67**, 3280 (1995)
138. A. Loni, L.T. Canham, M.G. Berger, R. Arens-Fischer, H. Munder, H. Luth, H.F. Arrand, T. M. Benson, Thin Solid Films **276**, 143 (1996)
139. S.M. Weiss, P.M. Fauchet, Phys. Stat. Sol (a) **2**, 556 (2003)
140. T. Gao, J. Gao, M.J. Sailor, Langmuir **18**, 9953 (2002)
141. L. De Stefano, I. Rendina, L. Moretti, A.M. Rossi, Mater. Sci. Eng. B. **100**, 271 (2003)
142. J. Volk, J. Balazs, A.L. Tóth, I. Bársony, Sens. Actuators, B **100**, 163 (2004)
143. M.A. Anderson, A. Tinsley-Bown, P. Allcock, E.A. Perkins, P. Snow, M. Hollings, R.G. Smith, C. Reeves, D.J. Squirrell, S. Nicklin, T.I. Cox, Phys. Stat. Sol. (a) **197**, 528 (2003)
144. D. Bria, B. Djafari-Rouhani, E.H. El Boudouti, A. Mir, A. Akjouj, A. Nougaoui, J. Appl. Phys. **91**, 2569 (2002)

145. E. Yablonovitch, Opt. Lett. **23**, 1648 (1998)
146. S.M. Weiss, P.M. Fauchet, Phys. Stat. Sol (a) **197**, 556 (2003)
147. Y. Fink, J.N. Winn, S. Fan, C. Chen, J. Michel, J.D. Joannopoulos, E.L. Thomas, Science **282**, 1679 (1998)
148. P. Ferrand, D. Loi, R. Romestain, Appl. Phys. Lett. **79**, 3017 (2001)
149. P. Ferrand, R. Romestain, Appl. Phys. Lett. **77**, 3535 (2000)
150. A.M. Rossi, G. Amato, V. Camarchia, L. Boarino, S. Borini, Appl. Phys. Lett. **78**, 3003 (2001)
151. H.F. Arrand, T.M. Benson, A. Loni, R. Arens-Fischer, M.G. Krueger, M. Thönissen, H. Lüth, S. Kershaw, N.N. Vorozov, J. Luminescence **80**, 119 (1999)
152. H. Taniyama, J. Appl. Phys. **91**, 3511 (2002)
153. H. Foell, M. Christophersen, J. Carstensen, G. Hasse, Mater. Sci. Eng. R Rep. **39**, 93 (2002)
154. J. Salonen, A.M. Kaukonen, J. Hirvonen, V.P. Lehto, J. Pharm. Sci. **97**, 632 (2008)
155. S.C. Bayliss, R. Heald, D.I. Fletcher, L.D. Buckberry, Adv. Mater. **11**, 318 (1999)
156. S.P. Low, N.H. Voelcker, L. Canham, K.A. Williams, Biomaterials **30**, 2873 (2009)
157. L.T. Canham, Adv. Mater. **7**, 1033 (1995)
158. D.M. Reffit, R. Jugdaohsingh, R.P. Thompson, J.J. Powell. J. Inorg. Biochem. **76**, 141 (1999)
159. J.F. Popplewell, S.J. King, J.P. Day, P. Ackrill, L.K. Fifield, R.G. Cresswell, M.L. di Tada, K. Liu, J. Inorg. Biochem. **69**, 177 (1998)
160. M.J. Sweetman, M. Ronci, S.R. Ghaemi, J.E. Craig, N.H. Voelcker, Adv. Funct. Mater. **22**, 1158 (2012)
161. A.V. Sapelkin, S.C. Bayliss, B. Unal, A. Charalambou, Biomaterials **27**, 842 (2006)
162. Y. Irani, S.J.P. Mcinnes, H.M. Brereton, K.A. Williams, N.H. Voelcker, Eur. Cells Mater. **26**, 54 (2013)
163. M. Sweetman, C. Shearer, J.G. Shapter, N.H. Voelcker, Langmuir **27**, 9497 (2011)
164. P. Formentín, M. Alba, U. Catalán, S. Fernández-Castillejo, J. Pallarès, R. Solà, L.F Marsal. Nanoscale Res. Lett. **9**, 421 (2014)
165. L.R. Clements, P.Y. Wang, F. Harding, W.B. Tsai, H. Thissen, N.H. Voelcker, Physica Status Solidi **208**, 1440 (2011)
166. P.-Y. Wang, L.R. Clements, H. Thissen, A. Jane, W.-B. Tsai, N.H. Voelcker, Adv. Funct. Mater. **22**, 3414 (2012)
167. F. Johansson, L. Wallman, N. Danielsen, J. Schouenborg, M. Kanje. Acta Biomater. **5**, 2230 (2009)
168. J. Persson, N. Danielsen, L. Wallman, J. Biomater. Sci. Polym. Ed. **18**, 1301 (2007)
169. W. Sun, J.E. Puzas, T.J. Sheu, X. Liu, P.M. Fauchet, Adv. Mater. **19**, 921 (2007)
170. M.J. Dalby, N. Gadegaard, R. Tare, A. Andar, M.O. Riehle, P. Herzyk, C.D.W. Wilkinson, R.O.C. Oreffo, Nat. Mater. **6**, 997 (2007)
171. Y.L. Khung, G. Barritt, N.H. Voelcker, Exp. Cell Res. **314**, 789 (2008)
172. P.Y. Collart-Dutilleu, E. Secret, I. Panayootov, D. Deville de Périère, R. Martín-Palma, V. Torres-Costa, M. Martin, C. Gergely, J.O. Durand, F. Cunin, F.J. Cuisinier, ACS Appl. Mater. Interfaces **6**, 1719 (2014)
173. T. Gumpenberger, J. Heitz, D. Bäuerle, H. Kahr, I. Graz, C. Romanin, V. Svorcik, F. Leisch, Bimaterials **24**, 5139 (2003)
174. S. Lakard, G. Herlem, A. Proper, A. Kastner, G. Michel, N. Vallès-Villarreal, T. Gharbi, B. Fahys, Bioelectrochemistry **62**, 19 (2004)
175. M. Hiraoui, M. Guendouz, N. Lorrain, A. Moadhen, L. Haji, M. Oueslati, Mater. Chem. Phys. **128**, 151 (2011)
176. S.P. Low, K.A. Williams, L.T. Canham, N.H. Voelcker, Biomaterials **27**, 4538 (2006)
177. E.J. Anglin, M.P. Schwartz, V.P. Ng, L.A. Perelman, M.J. Sailor, Langmuir **20**, 11264 (2004)
178. C. Charnay, S. Begu, C. Tourne-Peteilh, L. Nicole, D.A. Lerner, J.M. Devoisselle, Eur. J. Pharm. Biopharm. **57**, 533 (2004)
179. J. Salonen, L. Laitinen, A.M. Kaukonen, J. Tuura, M. Bjorkqvist, T. Heikkila, K. Vähä-Heikkilä, J. Hirvonen, V.-P. Lehto, J. Control. Release **108**, 362 (2005)

180. J.S. Park, J.M. Kinsella, D.D. Jandial, S.B. Howell, M.J. Sailor, Small **7**, 2061 (2011)
181. O. Tabasi, C. Falamaki, Z. Khalaj, Colloids Surf., B **98**, 1 (2012)
182. S.J.P. McInnes, Y. Irani, K.A. Williams, N.H. Voelcker, Nanomedicine **7**, 995 (2012)
183. E. Aznar, M.D. Marcos, R. Martínez-Máñez, F. Sancenón, J. Soto, P. Amorós, C.J. Guillem, Am. Chem. Soc. **131**, 6833 (2009)
184. F. Cunin, T.A. Schmedake, J.R. Link, Y.Y. Li, J. Koh, S.N. Bhatia, M.J. Sailor, Nat. Mater. **1**, 39 (2002)
185. J.A. Kim, C. Åberg, A. Salvati, K.A. Dawson, Nat. Nanotechnol. **7**, 62 (2011)
186. M.J. Sailor, E.C. Wu, Adv. Funct. Mater. **19**, 3195 (2009)
187. S. Low, K. Williams, L. Canham, N.H. Voelcker, J. Biomed. Mater. Res.: Part A **93**, 1124 (2010)
188. L. Xiao, L. Gu, S.B. Howell, M.J. Sailor, ACS Nano **5**, 3651 (2011)
189. L.M. Bimbo, O.V. Denisova, E. Mäkilä, M. Kaasalainen, J.K. De Brabander, J. Hirvonen, J. Salonen, L. Kakkola, D. Kainov, H.A. Santos, ACS Nano **7**, 6884 (2013)
190. L. Gu, J.-H. Park, K.H. Duong, E. Ruoslahti, M.J. Sailor, Small **6**, 2546 (2010)
191. B. Xia, B.W. Zhang, J. Shi, S.-J. Xiao, ACS Mate. Interfaces **5**, 11718 (2013)
192. M.J. Sailor, J.H. Park, Adv. Mater. **24**, 3779 (2012)
193. K. Yokoi, B. Godin, C.J. Oborn, J.F. Alexander, X. Liu, I.J. Fidler, M. Ferrari, M. Cancer Lett. **334**, 319 (2013)
194. B. Godin, C. Chiappini, S. Srinivasan, J.F. Alexander, K. Yokoi, M. Ferrari, P. Decuzzi, X. Liu, x. Adv. Funct. Mater. **22**, 4224 (2012)
195. M. Sweetman, N.H. Voelcker, RSC Adv. **2**, 4620 (2012)
196. F.S.H. Krismastuti, W.L.A. Brooks, M.J. Sweetman, B.S. Sumerlin, N.H. Voelcker J. Mater. Chem. B **2**, 3972 (2014)
197. E.J. Szili, A. Jane, S.P. Low, M. Sweetman, P. Macardle, S. Kumar, R.St.C. Smart, N.H. Voelcker, Sens. Actuators B **160**, 341 (2011)
198. Y. Tang, L. Zhen, J. Liu, J. Wu, Anal. Chem. **85**, 2787 (2013)
199. Y. Mirsky, A. Nahor, E. Edrei, N. Massad-Ivanir, L.M. Bonanno, E. Segal, A. Sa'Ar, Appl. Phys. Lett. **103**, 033702 (2013)
200. C.K. Tsang, T.L. Kelly, M.J. Sailor, Y.Y. Li, ACS Nano **6**, 10546 (2012)
201. V.S.-Y. Lin, K. Motesharei, K.-P.S. Dancil, M.J. Sailor, M.R. Ghadiri, Science **278**, 840 (1997)
202. A.L. Dolgiy, S.V. Redko, I. Komissarov, V.P. Bondarenko, K.I. Yanushkevich, S.L. Prischepa, Thin Solid Films **543**, 133 (2013)
203. C.V. Cerclier, M. Ndao, R. Busselez, R. Lefort, E. Grelet, P. Huber, A.V. Kityk, L. Noirez, A. Schonhals, D. Morineau, J. Phys. Chem. C **116**, 18990 (2012)
204. L. Oakes, A. Westover, J.W. Mares, S. Chatterjee, W.R. Erwin, R. Bardhan, S.M. Weiss, C. L. Pint, Sci. Rep. **3**, 3020 (2013)
205. F. Li, X. Badel, J. Linnros, J.B. Wiley, J. Am. Chem. Soc. **127**, 3268 (2005)
206. M. Tymczenko, L.F. Marsal, T. Trifonov, I. Rodriguez, F. Ramiro-Manzano, J. Pallares, A. Rodriguez, R. Alcubilla, F. Meseguer, Adv. Mater. **20**, 2315 (2008)
207. R. Palacios, P. Formentín, T. Trifonov, M. Estrada, R. Alcubilla, J. Pallarés, L.F. Marsal, Phys. Stat. Sol- RRL **2**, 206 (2008)
208. Y.Y. Li, F. Cunin, J.R. Link, T. Gao, R.E. Betts, S.H. Reiver, V. Chin, S.N. Bhatia, M. J. Sailor, Science, **299**, 2045 (2003)
209. M. Steinhart, J.H. Wendorff, A. Greiner, R.B. Wehrspohn, K. Nielsch, J. Schilling, J. Choi, U. Gösele, Science **296**, 1997 (2002)

Chapter 3
Self-organized Anodic TiO_2 Nanotubes: Functionalities and Applications Due to a Secondary Material

Jan M. Macak

Abstract Among various nanostructures, either electrochemically prepared or electrochemically applicable, vertically oriented, highly ordered TiO_2 nanotubular layers have attracted great scientific and technological interest in recent years. They posses a wide range of application opportunities across many fields due to the combination of their unique structure, mechanical and chemical stability, dimensions tunability, intrinsinc properties of TiO_2, and the relatively simple and low-cost production. While many recent reviews focus on the synthesis of nanotubes, their properties and applications, there is no comprehensive report summarizing existing results on modifications of TiO_2 nanotube layers by a secondary material. Therefore, this chapter gives the state of the art and comprehensive overview on the routes for deposition of secondary materials inside and on tops of TiO_2 nanotubes by various means. Such depositions in all known cases exclusively lead either to new tube functionalities that are interesting from the fundamental point of view, or eventually to new advanced applications, most likely not plausible for tubes and deposited materials alone. Most frequently, the deposition proceeds on the very top surface of nanotube layers. However, there are techniques and tricks that allow deposition, decoration, coating or complete filling of nanotube interiors by a secondary material. The whole range of deposition techniques used until now for TiO_2 nanotube layers will be introduced and discussed. Selected results achieved for nanotube with secondary materials will be discussed in details. Finally, outlook towards future opportunities of the deposition methods for nanotube functionalizations will be given.

List of Symbols

AR	Aspect ratio
PAA	Porous anodic alumina
ALD	Atomic layer deposition
QDs	Quantum dots

J.M. Macak (✉)
Center of Materials and Nanotechnologies, Faculty of Chemical Technology, University of Pardubice, Pardubice, Czech Republic
e-mail: jan.macak@upce.cz

D. Losic and A. Santos (eds.), *Electrochemically Engineered Nanoporous Materials*, Springer Series in Materials Science 220,
DOI 10.1007/978-3-319-20346-1_3

IPCE Incident photon-to-electron conversion efficiency
SEM Scanning electron microscope
TEM Transmission electron microscope
VIS Visible

3.1 Introduction

In the past three decades, nanostructured TiO_2 has attracted huge scientific and technological interest motivated by its possible use in many functional applications, including photocatalysis [1], water splitting [2], self-cleaning windows [3], solar cells [4] and others. Many various TiO_2 nanomaterials with distinct morphologies, such as nanoparticles, nanotubes, or nanofibers have been prepared and reported (see e.g. [5–7]). For their fabrication a range of various techniques including hydrothermal [8, 9], template synthesis [10], anodization [11, 12], electrospinning [13], etc. can be used.

However, not all nanostructures of TiO_2 are suitable for all TiO_2 applications. Nanoparticles are the most traditional and most widely used form of TiO_2. For applications in catalysis, food industries, nanoparticles are materials of choice. In case of the other applications, such as in photoelectrochemistry, TiO_2 nanoparticles have in recent years received serious competitors represented by one dimensional TiO_2 nanostructures—nanotubes and nanofibers. Examples of these nanostructures are given in Fig. 3.1. Distinct features and differences among these structures are clearly apparent, however, they all are consisting of TiO_2.

These nanotube and nanofiber shapes possess intriguing properties, such as improved charge separation that stems from the possibility of vectorial charge transport along one direction of the tube or fiber body. This structural feature has been recently invoked as responsible for enhanced performance in photoelectrochemical devices [14, 15]. Furthermore, one-directional diffusion path for the organic reactants in nanotubes (as compared to less defined diffusion geometry in traditional porous or nanoparticle aggregates) has been suggested to facilitate enhanced photocatalytic conversions [16, 17]. This is particularly true for nanotubes that show a degree of ordering and alignment. Moreover, there are other

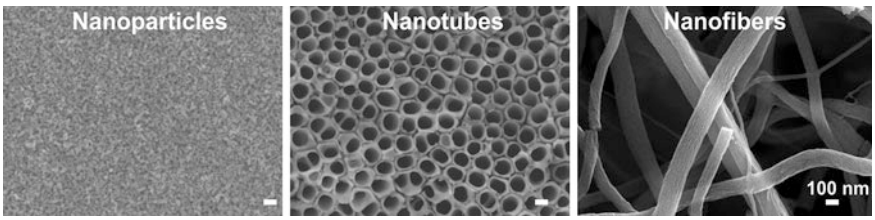

Fig. 3.1 Nanostructures of TiO_2 with specific shape, properties and applications

reasons why TiO_2 nanotubes are extraordinary interesting apart of other non-particulate TiO_2 materials. Their handling is easier, there are (yet) no safety constrains, they can be used as photocatalytic filtration membranes [18], templates for deposition of other materials to create functional structures or to structure materials that cannot be otherwise created in such ordered shape [19, 20].

In the last decade various techniques for synthesis of TiO_2 nanotubes have become available. Apart from hydrothermal methods [8, 9], one of the simplest and cheapest approaches that lead to ordered nanostructures are anodization techniques [6]. Before they were developed and optimized for the synthesis of self-organized TiO_2 nanotubes, anodization techniques have been known for the exclusive ability to create extremely highly organized nanoporous structures of silicon and alumina [21, 22]. Alumina nanopores became popular as templates used for a deposition of secondary materials [23]. More information about templating are provided in Sect. 3.3.

Synthesis of ordered alumina and silicon has stimulated around year 2003 tremendous research efforts in electrochemical materials sciences, and has given rise to many other materials to be processed in a similar fashion by anodization [6]. The most outstanding and successful example represents highly ordered TiO_2 nanotube layers (or arrays), followed by other valve metal oxide nanotubes and nanopores.

Upon anodization in suitable electrolytes, starting Ti substrates convert into highly ordered nanotubular layers [6]. These layers exhibit a certain aspect ratio (further noted as AR, AR = tube length/tube diameter), which spans from 5 (for shortest nanotubes) to several thousands (for nanotubes with length on the scale of hundreds of μm).

TiO_2 nanotube layers can be prepared into several distinct nanotube morphologies and aspect ratios using well established protocols. The most representative generations of tubes prepared in various electrolytes are shown in Fig. 3.2. Some electrolytes have been extremely successful and significant for the whole field, such as viscous ethylene glycol electrolytes that the all research groups worldwide adopted as "THE GOLDEN STANDARD" up to know. However, some other electrolyte may not have been so widely used by the nanotube TiO_2 scientific community, yet they were important for the evolution of the whole field, such as aqueous sulphate electrolytes [12].

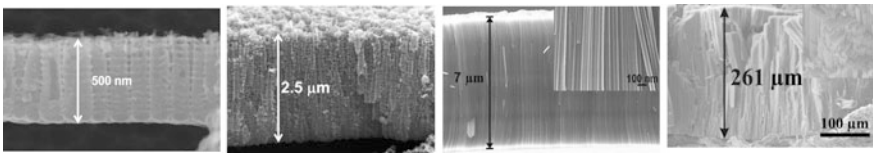

Fig. 3.2 Scanning electron microscope (SEM) images of four different generations of TiO_2 nanotube layers (in the cross-sectional view) produced throughout the years 1999–2008 in various electrolytes. Latter two images include *insets* that show magnified views on tube walls. Redrawn from [6]

TiO_2 nanotubes were in past years prepared not only from the bulky Ti substrates, but also on the magnetron sputtered Ti thin films on Silicon [24] or Kapton [25]. A pioneering work on anodization of thermally evaporated and annealed Ti has been recently reported [26]. Moreover, efforts have been carried out to improve the ordering of the nanotubes by using advanced anodization treatments [27, 28].

Throughout the past years, many researchers have tried to evaluate the influence of various parameters that were thought to play a certain role on the thickness, the diameter, the shape and the regularity of the resulting nanotubular structures. To give several examples of typically investigated parameters: anodization potential, electrolyte composition, time, temperature, strirring, titanium surface roughness and composition, sweep rate (how fast the potential is swept from 0 V or open-circuit potential to the final potential), shape and distance of electrodes (working vs. counter electrode), sample to electrode surface ratio, electrochemical cell design and so one.

Recently, several excellent and comprehensive reviews on anodic TiO_2 nanotubes have been published [29–33] that address all possible aspect about these nanotubes. They focus mainly on their synthesis by controlled electrochemical anodization of various substrates, in particular on mechanistic descriptions aided by a whole range of experimental techniques and theoretical calculations. Currently, the dissemination of the know-how about the tube growth has worldwide reached the highest level ever. As a results, many research groups adopt existing recipes to produce nanotubes with the aim to use them for a certain purpose, instead of developing own new protocols for nanotube preparation.

To a lesser extent, reviews on nanotube applications have become available recently as well, mainly focusing on biomedical applications of nanotubes [34, 35].

As demonstrated in the review by the Schmuki's group [29], until now the most comprehensive and monumental review on TiO_2 nanotubes ever published, the number of publications having "anodic", or "self-organized" in combination of "nanotubes" is substantially increasing every year.

3.2 TiO_2 Nanotubes as Functional Supports

The interesting nanotube shape, in combination with intriguing properties of TiO_2, provoke researchers to use nanotubes as functional supports. It is the porous anodic alumina (further noted as PAA), that has been a role model for TiO_2 nanotubes to be considered for these applications. PAA membranes that are prepared by anodic oxidation of aluminium under suitable electrochemical conditions, have been widely used as template materials of the first choice [23, 36], apart from polycarbonate membranes with typically much lower degree of ordering. It is the flexibility of the pore diameter/length and the relative ease of the alumina dissolution that make this material so attracting for the deposition of secondary materials. Nowadays, perfectly ordered porous alumina templates are available [23] and,

mainly by a choice of the electrolyte and the applied potential, the pore diameters can be tuned between some nanometers and several 100 nm [37–40].

The typical approach of the alumina template filling is shown in Fig. 3.3. In principle, the resulting structure after the material filling can be used as such (with an advantage of having rigid oxide as the mechanical support, see e.g. [41]), or it can be selectively dissolved leaving the deposited material in the corresponding nanostructured form. For the deposition of a metal, such as Pt or Pd, one side of the membrane has to be dissolved and coated with a conductive material, where later on the electrodeposition will start and in the course of time the whole pore is filled subsequently from that place.

In contrast to alumina (which is essentially an insulator), TiO_2 is much more fascinating material, owing to its semiconducting nature (n-type semiconductor with band gap energy E_g for anatase = 3.2 eV, biocompatibility (most biocompatible from all metal oxides), optical properties (high refractive index 2.4 vs. 1.7 of alumina at $\lambda = 1.55$ μm), photoelectrochemical stability (it does not undergo corrosion), all responsible for its versatility in a range of applications.

However, there are two aspects that are not favorable for TiO_2 nanotubes to be used as templates. At first, semiconducting properties of TiO_2 preclude an easy electrodeposition of a secondary material inside TiO_2 nanotubes as in the case of alumina. Alumina is comparably less conducting and the deposition of a secondary material within PAA starts always at the conductive material, additionally brought to one side of the PAA layer. Secondly, TiO_2 is so chemically stable that it can be dissolved quantitatively in fact by HF only. However, this naturally means that any other material deposited inside nanotubes will be chemically attacked (and likely dissolved out) as well.

All in all, TiO_2 nanotubes cannot be used specifically as a template for a synthesis of replicated structures, but only as a support for a secondary material (or more materials). It may seem disadvantageous. However, in fact this is the key advantage of TiO_2 nanotubes over PAA, because they offer, apart of a highly defined and tunable geometry, also great TiO_2 intrinsic properties. This

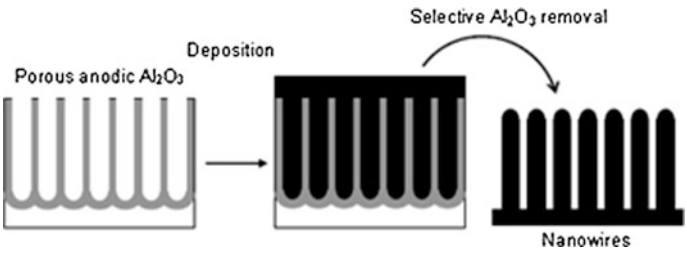

Fig. 3.3 Regular pore array of porous alumina as a template for micro- or nano-fabrication: a thick porous oxide is grown by anodization, then the secondary material is deposited into the pores, finally the alumina template can be dissolved leaving nanowires of the deposited material behind

combination is extremely promising for a vaste range of applications, including solar cells, biomedical devices, sensors, catalyst, and many others.

3.3 TiO_2 Nanotube Modifications by a Secondary Material

The potential of TiO_2 nanotubes for various functional and advanced devices, in particular when considering all possible tube shapes and geometries, has not at all been exploited. One of the major obstacles to extend the functional range of nanotubes is to coat homogeneously tube interiors by a secondary material, potentially until the complete tube filling. Somewhat unsurprisingly, shortly after the development of first generations of nanotubes, researchers carried out efforts in the direction of using TiO_2 nanotubes as a supporting material for a secondary material. As a result, TiO_2 nanotubes have also been successfully decorated, coated or filled by various host materials that added range of functionalities to resulting layers. The deposited materials were shown to influence strongly optical, electrical and mechanical properties of nanotubes.

Up to now, various materials have been deposited inside the tube openings and tube interiors ranging from various metals, quantum dot materials, semiconducting oxides, conducting polymers, dyes and chalcogenides. Nowadays, several distinct groups of deposition techniques that are of reasonable use for the deposition of a secondary material into self-organized TiO_2 nanotubes exist. Wet chemical routes including soaking, dipping, dropping, spin-coating and in situ syntheses represent techniques that have been employed most frequently until now. There are also electrochemical deposition routes available. Two physico-chemical deposition techniques—atomic layer deposition and sputtering—have also been already considered as viable tools for this purpose.

The presentation in this section will therefore develop detailed introduction of these techniques and will summarize corresponding results for the deposition of secondary materials in TiO_2 nanotubes and resulting functionalities.

In this chapter, however, no story on a dye anchorage on TiO_2 is developed, as it is fundamentally different activity than those depositions of the scope of this chapter. The anchorage represents only one step in the construction of a dye-sensitized solar cells.

3.3.1 Electrodeposition

As already mentioned in Sect. 3.3, filling of nanotubes by electrodeposition is not so straight-forward, due to the semiconductive nature of TiO_2. Due to different electronic conductivities it matters, whether the electrodeposited TiO_2 nanotubes are amorphous (as formed), or whether a they are crystalline (anatase or rutile form). Several filling-by-electrodeposition approaches have been reported.

Macak and coworkers showed filling of amorphous (as formed) TiO_2 nanotubes by two-step approach [19]. In the first step, the nanotube bottoms were selectively reduced from Ti^{4+} to Ti^{3+}. The goal was to obtain more conducting bottom regions from where the nanotube filling would start preferentially. If optimized, the main electrodeposition experiment carried out in the second step led to a successful filling of nanotubes by a metal.

Figure 3.4 shows results of the Cu-filling inside amorphous nanotubes by the tailored reduction of tube bottom and subsequent electrodeposition of Cu from $CuSO_4$ electrolyte [19], as depicted in Fig. 3.4a. During the reduction at negative voltage held for few seconds, the conductivity of bottoms increased significantly, while nanotube walls remained comparably more resistant. Once the Cu was electrodeposited inside the tubes, it filled homogeneously the entire volume of tube interiors. Even though no functional device was produced in this rather fundamental work, and relatively low aspect ratio (AR up to ≈50) were picked-up, it gave inspiration to many other researchers, who followed this work and tried to deposit a secondary material in their tubes, potentially until their complete filling.

The previously introduced tube-bottom reaction concept was also introduced for the deposition fo Pb inside TiO_2 nanotubes (AR ≈ 5), as shown in Fig. 3.5. The as-deposited Pb nanotubes were thermally converted into Ferroelectric Lead Titanate Nanocellular Structure with interesting piezoelectric response [42]. A complete conversion of TiO_2 to $PbTiO_3$ was achieved by tailored thermal

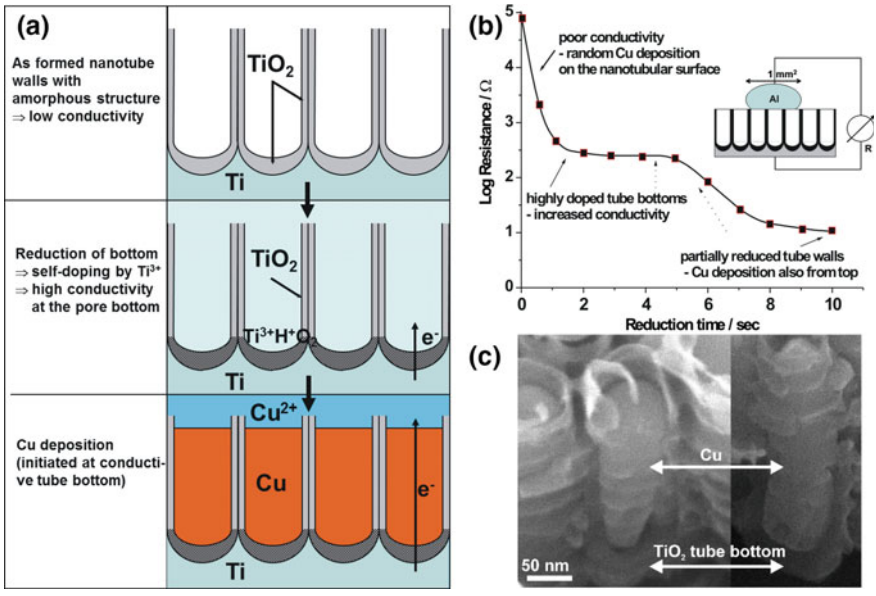

Fig. 3.4 **a** Scheme of selective reduction of tube bottoms followed by Cu deposition inside nanotubes, **b** resistance of the tubes as a function of reduction time, **c** SEM images of Cu-filled TiO_2 nanotubes. Modified from [19]

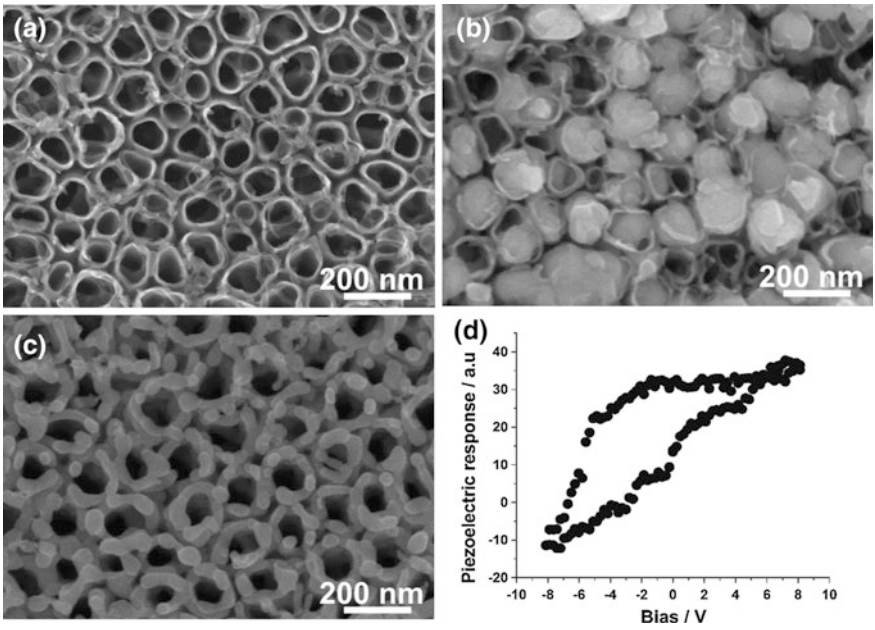

Fig. 3.5 SEM images of **a** empty TiO_2 nanotubes with a diameter of 100 nm and length ≈ 450 nm, **b** same nanotubes filled with metallic Pb, **c** same nanotubes after thermal conversion to $PbTiO_3$, **d** typical piezoelectric hysteresis loop of the $PbTiO_3$ nanotube layer shown in (**c**). Modified from [42]

treatment at 550 °C in air. Moreover, the original tube architecture was entirely resembled by the newly produced $PbTiO_3$.

In these two reports [19, 42], the goal was to initiate the deposition of nuclei at the bottom of the tube and then to continuously fill up the tubes from this point, which is in particular comparably easy if the tube walls are insulating and a conductive bottoms can be established.

It should be also mentioned, that if this particular tube reduction treatment is not carried out, the electrodeposition can proceed, but it proceeds in a random fashion —the deposits are created on the tube surface, wherever the electrons find a pathway to flow. Such deposition can be, however, practical for-, as shown by Assaud and coworkers [43] who deposited p-type Cu_2O clusters on the tube n-type TiO_2 nanotube surface.

Another electrodeposition treatment was performed in analogy to a treatment most typically used for porous alumina. The tube layers (with a very high degree of ordering) were lifted off from the metal substrate and opened at the bottom [44, 45]. Fang and coworkers have afterwards deposited an Ag sol on one side of the nanotube membrane and subsequently electrodeposited Cu nanotubes, as shown in Fig. 3.6a, using constant current and $CuSO_4$ electrolytes [45]. Their nanotube layers

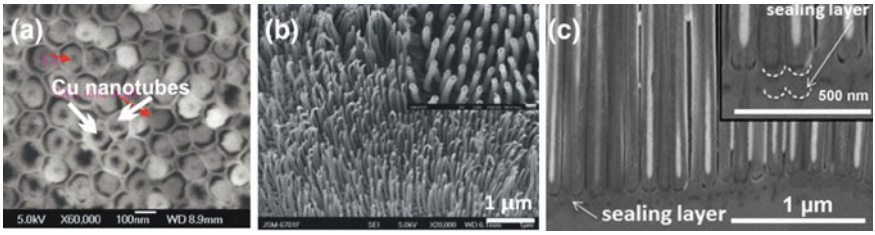

Fig. 3.6 SEM images of **a** Cu nanotube arrays electrodeposited inside TiO_2 nanotubes, modified from [45], **b** Pt nanotube arrays electrodeposited inside TiO_2 nanotubes, modified from [44], **c** Ag-filled TiO_2 nanotubes with additional bottom sealing layer, modified from [46]. In all cases, optimized electrodeposition protocols were used

had thickness of approximately 116 μm and tube diameter of approximately 120 nm, thus quite impressively high aspect ratio nanotubes (AR ≈ 967) were filled.

In another work, Wang and coworkers filled tubes by Pt using using constant current electrodeposition from H_2PtCl_6 electrolyte, supported by an evaporated-noble-metal contact, resulting in very uniform arrays of Pt nanotubes [44], as shown in Fig. 3.6b. Dimensions of their TiO_2 nanotube layers and resulting electrodeposited Pt nanotube layers were not specified, however.

In order to achieve complete filling of the tubes during electrodeposition, recently another interesting, yet very simple strategy was introduced by Liu and coworkers [46] of for deposition of several metals, including Cu, Ag, Au and Pt. Their strategy is based on initiation of the formation of nuclei by pulsed electrodeposition over the entire tube wall and continuous of grow of these nuclei until complete filling. What is more, they have shown the importance of another synergic and key step carried out with nanotubes: defect-sealing of the bottom layer by anodization in ethylene glycol and H_3PO_4 electrolytes [46] that led to short-circuit-free nanotube layers. Indeed, the use of an adequate initial pulse and sealed nanotubes led to homogeneous formation of nuclei all over the tube walls, inside as well as outside, as shown in Fig. 3.6c. Their nanotube layers had thickness of approximately 4 μm and tube diameter of approximately 150 nm (AR ≈ 27).

Another electrodeposition technique of nanotubes was recently introduced for RuO_2 doping of TiO_2 nanotubes by Gim and coworkers [47]. It is based on applying a high potential sep (200 V, so-called potential shock) on nanotubes in electrolytes in the presence of $KRuO_4$ species. The resulting structure consist of TiO_2 with incorporated RuO_2 species along tube interiors and exteriors. In it an interesting approach, however, due to the potential step applied on the nanotubes for only few seconds, the barrier oxide layer at the tube bottoms significantly thickness, which might be an issue.

Except metals (Cu, Pb, Pt, Ag, etc.) and oxides (Cu_2O, RuO_2), electrodeposition has been used also to deposit in the nanotube layers other compounds: sulfides and selenides.

Electrodeposition of sulfides (CdS, ZnS) into nanotubes has been developed already in comparably higher number of papers, compared to oxides [43, 47]. The

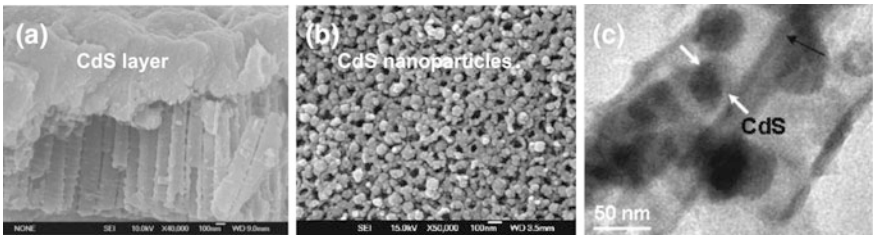

Fig. 3.7 SEM images of CdS modified nanotube layers showing: **a** CdS overlayer, modified from [48], **b** CdS nanoparticles decorating tube openings, modified from [49], **c** CdS crystals inside tubes, modified from [50]

main goal of the deposition of sulfides (most typically resulting to particles or eventually complete tube filling by the material) is to improve photoelectrochemical and photocatalytical properties of the nanotube layers.

As shown in Fig. 3.7a, for example, Chen and coauthors have have deposited CdS nanoparticles on the surface of 450 nm thick tube layers with a tube diameter of 76 nm (AR ≈ 6), from $CdCl_2$ containing dimethylsulfoxide solution [48] by cathodic constant current electrodeposition. Yin and coworkers have used similar approach for surface decoration of 1.5 μm thick tube layers with a tube diameter of 150 nm (AR ≈ 10) by CdS layer [49], as shown in Fig. 3.7b. As shown in Fig. 3.7c, the paper by Banerjee and coworkers [50] showed for the first time the deposition of CdS also inside the tubes, decorating the entire tube interiors. It has to be noted that their tubes very also of very low aspect ratio (AR ≈ 7).

Due to the fact that various types of tubes were used for CdS electrodeposition and the results are hardly comparable, it remains still unresolved, which of the options for CdS to be present in the tube (either as particles decorating tubes, or a complete filling of tube interiors) is essentially most suitable for the highest degree of desired photoelectrochemical response.

Electrodeposition of nanocrystals of selenides (ZnCdSe) on openings of anodic TiO_2 nanotubes was demonstrated by Kang and coworkers [51]. They showed that the electrodeposition is plausible technique for deposition of selenides onto nanotube arrays, as shown in Fig. 3.8a. Their composite $Zn_xCd_{1-x}Se/TiO_2$ nanotube arrays exhibited a high absorption in the VIS light region due to the narrow band gap of $Zn_xCd_{1-x}Se$ and demonstrated a sensitive photoelectrochemical response under VIS light illumination with an optimal response achieved for $Zn_{0.8}Cd_{0.2}Se/TiO_2$ electrodes. Their paper does not contain any information about tube dimensions. Moreover, there is no evidence about any successful deposition of selenides in interiors of nanotubes, including bottom tube parts.

An additional improvement of photoelecrochemical properties could be expected, if the electrodeposition would lead to deposition of a sensitizer inside nanotubes, instead of their top surface only. Efforts to achieve that were carried out.

Somewhat intermediate deposition resulting into CdSe cluster deposited inside nanotubes as well on the tube surface was demonstrated by Zhang and coworkers

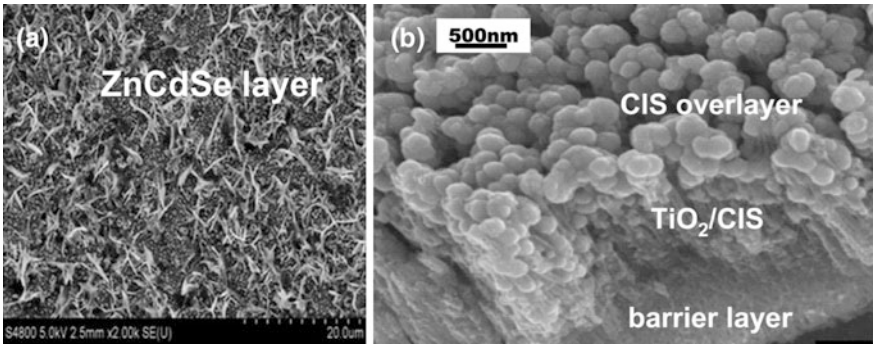

Fig. 3.8 **a** ZnCdSe layers coating TiO_2 nanotubes, modified from [52], **b** $CuInSe_2$ filling interiors of TiO_2 nanotubes and leaving an overlayer on the tube surface, modified from [53]

[52]. They have demonstrated that their resulting $CdSe/TiO_2$ composite structure had better photoelectrochemical performance than TiO_2 nanotubes alone.

Wang and coworkers showed the complete filling of TiO_2 interiors by p-type $CuInSe_2$ [53] using electrodeposition from ethanolic electrolytes consisting of 1 mM $CuCl_2$, 5 mM H_2SeO_3, and 30 mM $InCl_3$ with small additions of water or 0.1 M $TBAClO_4$. As shown in Fig. 3.8b, their approximately 2 μm thick tube layers with a tube diameter of approximately 80 nm,where indeed entirely filled and to a certain extent also overgrown. However, no evidence on any photoelectrochemical improvement was provided in their work.

3.3.2 Deposition from a Chemical Bath

In situ or ex situ synthesis of secondary materials inside nanotubes from suitable precursor solution is another approach for deposition of various functional nanoparticles (most typically) or nanolayers inside nanotubes.

If soaking of nanotube layers in a chemical bath is employed, frequently the deposits can be found inside the tubes, not only on their surface. However, this is naturally also function of the polarity of the solvent, aspect-ratio of nanotubes (only layers with nanotubes up to few microns long and with comparably large diameter can be filled like that), and wettability of the layer (given mainly by its hydroxilation).

Efforts to deposit suflides (such as CdS, ZnS) into nanotubes by chemical soaking in solutions of halide precursors were carried out with the same motivation, as for the electrodeposition—improve photelectrochemical response of TiO_2 nanotubes, in particular to achieve and efficient carrier injection from an in situ formed sensitizer into nanotubular titania.

For example, Sun and coworkers deposited CdS QDs into the pores of the nanotube arrays by a sequential chemical bath deposition [54]. They showed that

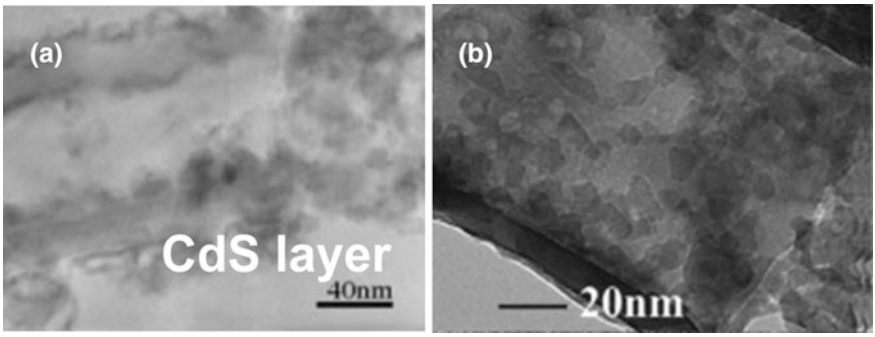

Fig. 3.9 TEM images of the TiO_2 nanotubes with CdS QDs deposited **a** inside and outside nanotubes, modified from [54]; **b** inside nanotubes, modified from [55]

CdS QDs deposited in interiors of TiO_2 nanotube arrays (20 mm thick with a tube diameter of 120 nm, AR ≈ 167) may significantly increase the liquid junction PEC short circuit photocurrent (from 0.22 to 7.82 mA/cm^2) and cell efficiency (up to 4.15 %). However, eventhough they provided a detailed TEM evidence on the presence of QDs inside and outside nanotubes, example of which is shown in Fig. 3.9a, it is not obvious that QDs were present over the entire tube layer (including bottom parts). Their nanotube layers had thickness of approximately 12 μm and tube diameter of approximately 120 nm, resulting in AR ≈ 100.

More recently, Baker and Kamat have compared CdS decorated TiO_2 nanotubes and nanoparticles in order to evaluate, which of the two structures will be able to achieve better pohotoelectrochemical parameters [55]. Upon repetition of the deposition cycles using solution consisting of $CdSO_4$, Na_2S and water, they were able to coat nanoparticulate layers and nanotube layers (preferentially tube interiors) by CdS QD's, as shown on TEM image in Fig. 3.10b. As a result, they demonstrated nearly double IPCE values for decorated TiO_2 nanotubes over decorated nanoparticles and attributed this interesting difference to the increased efficiency of charge separation and transport of electrons in nanotube walls. Their nanotube layers had thickness of approximately 10 μm and tube diameter of approximately 100 nm, resulting in AR ≈ 100.

These results clearly demonstrate that the unique nanotube structure can facilitate the propagation and kinetic separation of photogenerated charges, suggesting potentially important applications of the inorganic QDs sensitized TiO_2 nanotube-array films in solar cell applications.

Macak and coworkers have the shown decoration of entire nanotube layers (interiors as well as exteriors) by Au nanoparticles [56], as shown in Fig. 3.10a. They soaked 500 nm thick nanotube layers (with a tube diameter of ≈100 nm, thus AR ≈ 5) in the presence of $HAuCl_3$, sodium citrate and tannic acid as reducing agents. Their decorated Au-nanotubes showed interesting results for the electroreduction of oxygen [56], compared to flat Au-loaded TiO_2 layers.

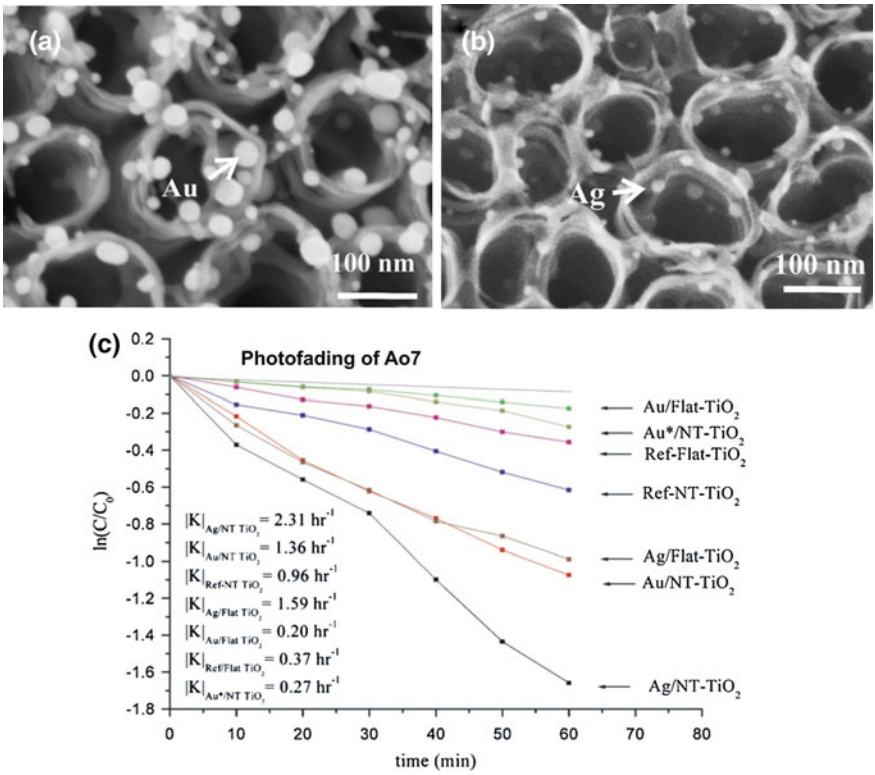

Fig. 3.10 SEM images of TiO_2 nanotubes decorated by **a** Au nanoparticles and **b** Ag nanoparticles, **c** comparison of photocatalytic decomposition of (AO7) azo-dye for different photocatalytic systems (Ref-NT-TiO_2: Reference Nanotube TiO_2; Ag/-TiO_2: Ag-loaded Nanotube TiO_2; Au/NT-TiO_2; Au-loaded on anatase TiO_2 with post annealing; Au*/NT-TiO_2: Au-loaded on anatase TiO_2 without post annealing). Kinetic rate constant 'k' values are shown as an inset. Modified from [57]

Paramasivam and coworkers have shown also a complete decoration of nanotube layers but with Ag nanoparticles. They soaked 2 μm thick nanotube layers (with a tube diameter of ≈100 nm, thus AR ≈ 15) in 1 M $AgNO_3$ solution and subsequently irradiated the samples by the UV-light generated using the He-Cd laser. This irradiation led to photocatalytic reduction of Ag^+ to metallic Ag on the form of nanoparticles [57], as shown in Fig. 3.10b. They utilized both Au-decorated nanotubes as well as Ag-decorated nanotubes (and flat TiO_2 reference layers) for the investigation of photocatalytic activities to decompose a model organic dye. As shown in Fig. 3.10c, they achieved distinctly higher photocatalytic decomposition rates for decorated nanotube layers.

Similarly prepared and decorated Ag-nanotubes have also shown to have interesting photochromic properties [58].

Except noble metals, efforts to decorate nanotubes by semiconducting oxides, such as WO_3, were carried out. The main motivation has been to improve the VIS light absorption properties, or in particular to enhance the photochromic behavior of the nanotube layers.

Benoit and coworkers were first who showed decoration of WO_3 nanoparticles by chemical deposition of WCl_6 solutions [59]. These solutions were described to age upon prolonged soaking time and ethanol additions. Upon a thermal treatment at 450 °C, finally WO_3 crystalline nanoparticles decorating TiO_2 nanotubes were obtained. Their nanotube layers had thickness of approximately 1.5 μm and tube diameter of approximately 100 nm, resulting in AR ≈ 15. According to the description of the experiment, the WO_3 nanocrystals of size of approximately 5 nm decorated predominantly the tube surface.

In the follow up work by Song and coworkers, sodium tungstate was employed to decorate nanotubes with WO_3 nanoparticles of different size, depending on the number of repeated chemical batch deposition and annealing cycles [60]. They achieved complete decoration of comparably higher aspect ratio nanotubes, as shown in Fig. 3.11a, b. Their nanotube layers had thickness of approximately 5.3 μm and tube diameter of approximately 90 nm, resulting in AR ≈ 59. Compared

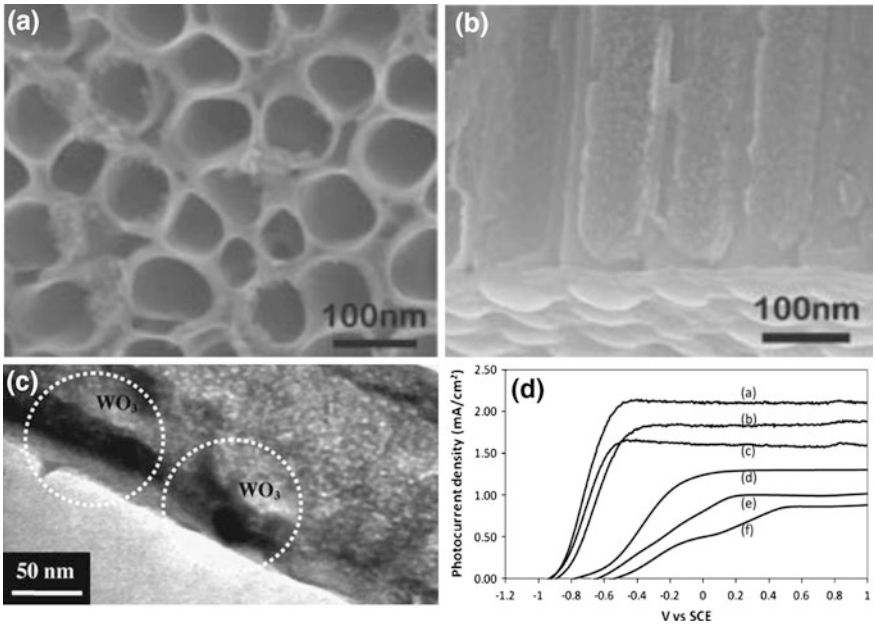

Fig. 3.11 SEM images of WO_3-decorated TiO_2 nanotubes (after loading by 6 cycles) showing: **a** the top view and **b** the tube near-bottom view, modified from [60]; **c** TEM image of WO_3-decorated TiO_2 nanotube exteriors, **d** photocurrent density versus applied potential for the TiO_2 and WO_3-decorated TiO_2 nanotubes prepared by soaking at different molarities of ammonium paratugnstate aqueous solution: **a** 0.3 mM, **b** 0.1 mM, **c** 0.5 mM, **d** pure TiO_2 nanotubes, **e** 1 mM, and **f** 5 mM, modified from [61]

to non-decorated nanotube arrays, their nanotube arrays showed enhanced electrochromic properties of longer lifetime, higher contrast ratio (bleaching time/coloration time), and improved tailored electrochromic behavior compared to plane nanotubes.

Finally, Lai and Sreekantan showed decoration by WO_3 nanoparticle using soaking in ammonium paratungstate and subsequent annealing at 400 °C in argon [61]. Their nanotube layer had thickness of approximately 12 μm and tube diameter of approximately 120 nm, resulting in already quite high AR of ≈100. Eventhough a detailed TEM evidence of decoration of the tube walls by WO_3 nanocrystals was provided, as shown in Fig. 3.11c, it was not obvious that the deposits had reached also the lowest tube layer parts-tube bottoms. Nevertheless, they showed an enhancement of photocurrent densities for WO_3-decorated nanotubes, prepared from low to moderately concentrated tungstate solutions, as shown in Fig. 3.11d. High tungstate concentrations evidently led to the clogging of the nanotubes resulting in the blockage of the tube surface and lower photocurrent than for plane nanotubes.

Shrestha and coworkers have shown also decoration of nanotubes by NiO nanoparticles using soaking in $NiCl_2$ ethanolic solution followed by a reduction to NiO using NH_4OH solutions [62]. They utilized the as-decorated nanotubes for photocatalytical degradation of an organic dye with strongly enhanced performance compared to plane nanotubes.

3.3.3 Nanoparticle Deposition from a Colloidal Suspension

Infilling of nanoparticles of a secondary materials form a colloidal suspension is one of the seemingly easiest approaches, but suprizingly not that straight-forward in reality.

As shown by Macak and coworkers, when for example suspensions of Pt/Ru nanoparticles have been dropped on the tube layers from the top by a micropippete, hardly any nanoparticles went inside the nanotubes [63]. Instead, the surfaces were blocked due to a local clogging of nanotube openings by large clusters of agglomerated nanoparticles. Nevertheless, even as-decorated nanotube layers displayed enhanced catalytic activity for the electrocatalytic oxidation of methanol.

Considerably larger success in decorating interiors of the nanotubes, apart of tube openings, was achieved when superparamagnetic nanoparticles were dropped by a micropippete from a commercial Ferrofluid solution, followed by a suction inside driven by a strong magnetic force coming from a permanent magnet placed underneath the nanotube layer. As shown in the work of Shrestha and coworkers [64], it was possible to achieve decorated nanotube interiors as well as exteriors quantitatively by these magnetic nanoparticles using this approach. This very fancy functionality was employed for a local photocatalytic removal of an organic day in an agar solution, followed by movement of the magnetic nanotube photocatalyst to another place by magnetic forces form a permanent magnet. Their nanotube layers

had thickness of approximately 28 μm and tube diameter of approximately 100 nm, resulting in nanotubes with a high aspect ratio (AR ≈ 280).

In general, if short aspect ratio nanotubes and small amounts of Ferrofluid are employed the tube are significantly loaded or eventually completely filled by nanoparticles, as shown in Fig. 3.12a, b. When an optimized amount of the Ferrofluid solution was dropped on the plane TiO_2 nanotube layer in an optimized way, as shown in Fig. 3.12c, extremely uniform layers of nanoparticles on the tube walls were be achieved [65], as shown in Fig. 3.12d.

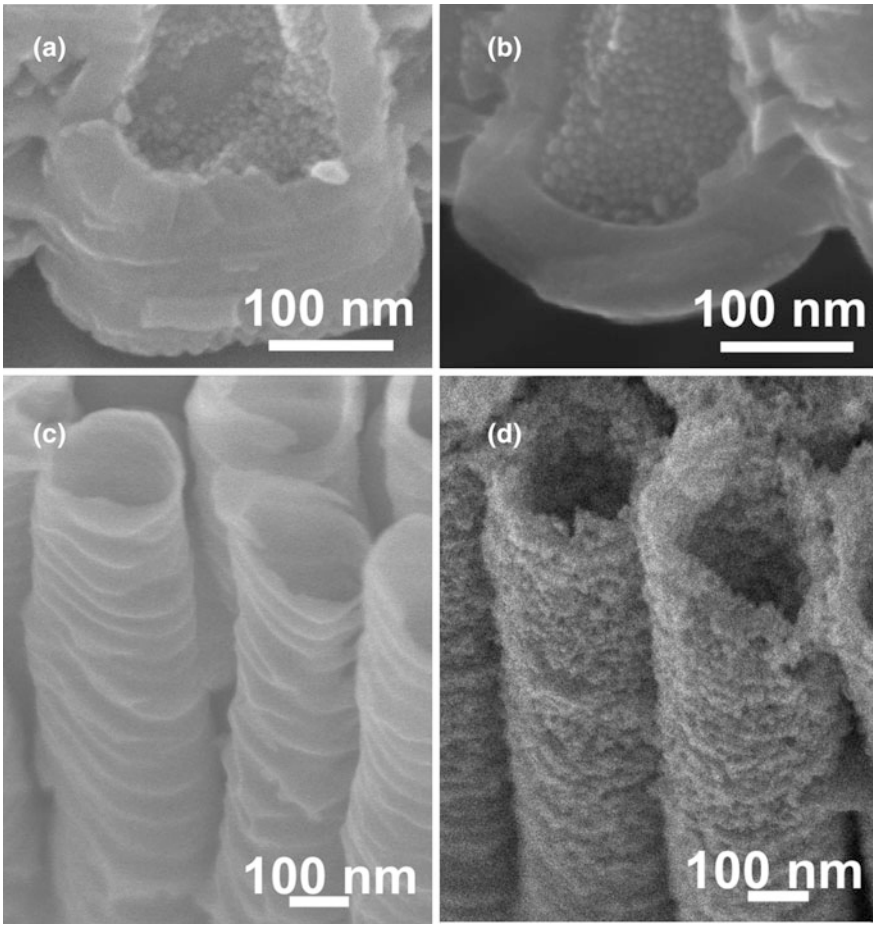

Fig. 3.12 SEM images of short aspect ratio (AR ≈ 10) nanotubes with a partial (**a**) and complete filling by superparamagnetic nanoparticles. SEM images of (**a**) a high aspect ratio (AR = 77) nanotubes without (**c**) and with (**d**) homogeneous coating of nanotube walls by the same nanoparticles. All nanotubes were decorated via pippeting of magnetic nanoparticles from the commercial Ferrofluid solution

3.3.4 Spincoating

Deposition of a secondary material inside (or onto) nanotubes by spincoating has been used very seldom until now, somewhat surprizingly. In fact, there are only 2 reports employing spincoating to coat/fill TiO_2 nanotubes [20, 66].

Typically, spincoating of solutions containing either dissolved species or dispersed nanoparticles leads to a lower concentration of deposits (for example nanoflakes, or nanoparticles) on the tube surface and in the tube interiors compared to the dip-coating or a simple soaking of nanotubes in the corresponding solution. The main reason is that when the spinning solution is spread (e.g. by dropping) on the nanotube layer being rotated at a certain speed (easily ranging from 1 to 3k rpm), the solution is forced by centrifugal forces to firstly spread out over the tube surface, immediately after it comes in contact, and subsequently to leave the surface quantitatively. As a result, the solution retention time on the tube surface is comparably shorter, on the order of seconds, whereas soaking is performed at comparably longer times (typically on the scale of minutes or even hours).

Validity of these statements was recently demonstrated by Ju and coworkers [66], who explored several routes for copper phthalocyanine deposition onto and into nanotubes. The difference is obvious from Fig. 3.13 that demonstrates the difference in the concentration of phthalocyanin deposits when either the spincoating (Fig. 3.13a), or the soaking (Fig. 3.13b) of phthalocyanin aqueous solution is carried out. In addition, if the soaking solution consist of a polar solvent with dissolved phthalocyanine and, the phthalocyanine could be deposited partly inside the tubes, as apparent in Fig. 3.13c.

Use of solutions based on polar organic solvents is not really desired for spincoating, as the solutions dry extremely quickly and the solution deposition on the surface is inhomogeneous or too low concentration of deposits is achieved. Typically, as a result, some surface regions are overloaded by deposits (i.e. islands of nanoparticles), whereas other remaining regions are more or less without

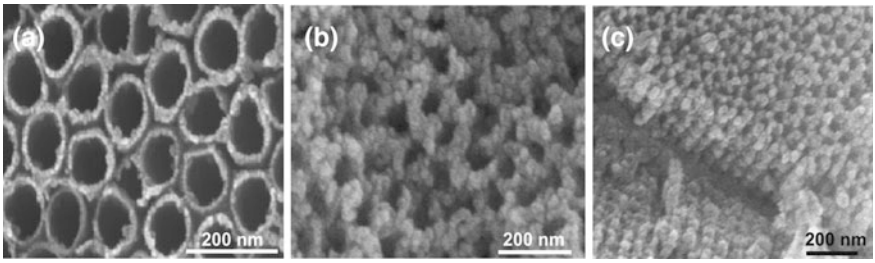

Fig. 3.13 Comparison of the two approaches used for deposition of phthalocyanine nanoparticles on the nanotubes: **a** spincoating and **b** soaking of aqueous phthalocyanine solution. Soaking leads to significantly higher concentration of deposits on the surface. Soaking of tubes in polar solvent (**c**) results in the deposition of phthalocyanine nanoparticles also inside nanotubes. Modified from [66]

deposits. This difference can be usually easily observed by a naked eye. On the tube surface, islands have different colour than the blank surface. All in al, for high polar solutions, soaking is the preferred solution.

However, if an appropriate tunning of rheological properties of the solution is carried out (i.e. solutions are more dense), the retention time of the solution (and particles in that particular solution) on the tube surface is comparably longer. The deposited material has not only chance be deposited at a higher concentration on the surface, but also to enter tube interiors and get deposited there.

This is shown in a recent report by Macak and coworkers [20], who demonstrated a robust infiltration of a chalcogenide glass sensitizer into nanotubes by spin-coating of viscous propylamine based solutions with different amounts of dissolved As_3S_7 glass. By tunning the glass:solvent ratio, the chalcogenide material content inside the tubes could influenced, as depicted in Fig. 3.14a. The solutions had in general moderately high viscosities, similar to absolute ethylene glycol. More importantly, owing to its viscosity, the as-prepared solutions had a chance to

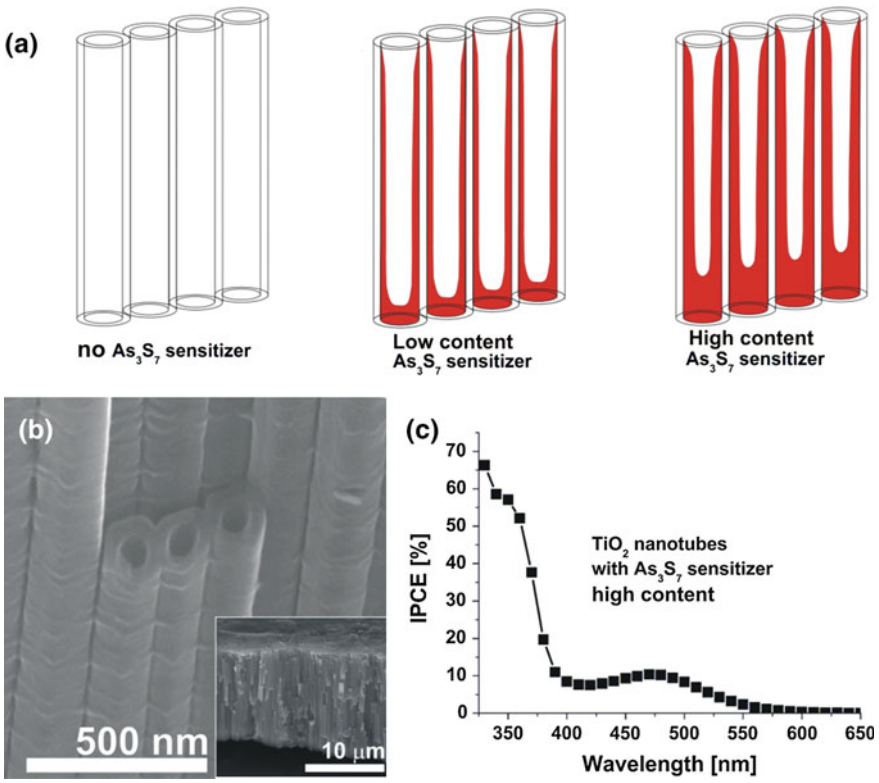

Fig. 3.14 **a** drawing of TiO_2 nanotubes with different contents of As_3S_7 sensitizer, **b** SEM image of tubes with a low sensitizer content, **c** incident-photon-to-electron conversion efficiency spectra for nanotubes sensitized with a high sensitizer content. Modified from [20]

infiltrate inside the nanotubes, being enhanced by the directionality of the resulting forces (between centrifugal and gravity forces). Upon vacuum drying, a few nm thick and homogeneous coating of the tube walls was achieved, as shown in Fig. 3.14b. The as-coated nanotubes have shown an increased VIS light absorption, as shown in Fig. 3.14c, due to a sensitization by the glass. However, the magnitude of the VIS light response is rather low due to an amorphous nature of the glass sensitizer.

3.3.5 Atomic Layer Deposition

Atomic layer deposition represent one of the most modern techniques for deposition of a high-quality thin films with uniform composition and thicknesses [67]. In the same time, it is the most efficient techniques for creation of uniform layers of a wide compositional range on virtually any material with any shape. The ALD thin film deposition is based on periodic cycling of 4 steps: chemisorption of a precursor on the deposited surface, purging of the precursor's residues, decomposition of the precursor, purging. Each cycle results in creation of 1 atomic layer. Naturally, the more cycles, the thicker layers.

In various modification, ALD has been used to prepare titania or other valve metal nanotubes, most typically by using porous alumina or polycarbonate templates and their post-ALD selective etching or removal. Figure 3.15a, b shows selected examples of resulting nanotubular structures that were published in several reports [67–71]. Another approach—etch-back technique—was used recently to prepare low-aspect ratio titania nanotubes, but with extremely high degree of ordering [72].

In the early reports (before 2010), however, the aspect ratio of resulting nanotubes was rather moderate, up to approximately 80 [68, 69]. However, recent report by Gao and coworkers shows synthesis of TiO_2 nanotubes with AR $\approx$ 200 nm, shown in Fig. 3.15c, using templating of PAA by ALD [71]. Moreover, they have shown, that an additional coating of Al_2O_3 (shown in Fig. 3.15d, approximately 5 nm thick) has a beneficial effect on the photoelectrochemical performance of the nanotubes, in particular on the electron lifetime for dye-sensitized solar cells.

Although ALD appears to be probably most suitable technique for coating of (not only TiO_2) nanotube walls by a secondary material, it has not been considered for this purpose and for TiO_2 self-organized nanotubes by many researchers. There are only 2 reports demonstrating the use of ALD for deposition of a secondary material inside TiO_2 nanotubes.

The first paper by Tupala and coworkers [73] reports on conformal ALD deposition of 5 nm thin coating of amorphous tantala, alumina and titania by ALD in anodic TiO_2 nanotubes grown on Ti thin films evaporated on the ITO glass. Example of the tantala-coated TiO_2 nanotubes is given in Fig. 3.16a, b. They compared optical and electrical properties of all their as-prepared structures and

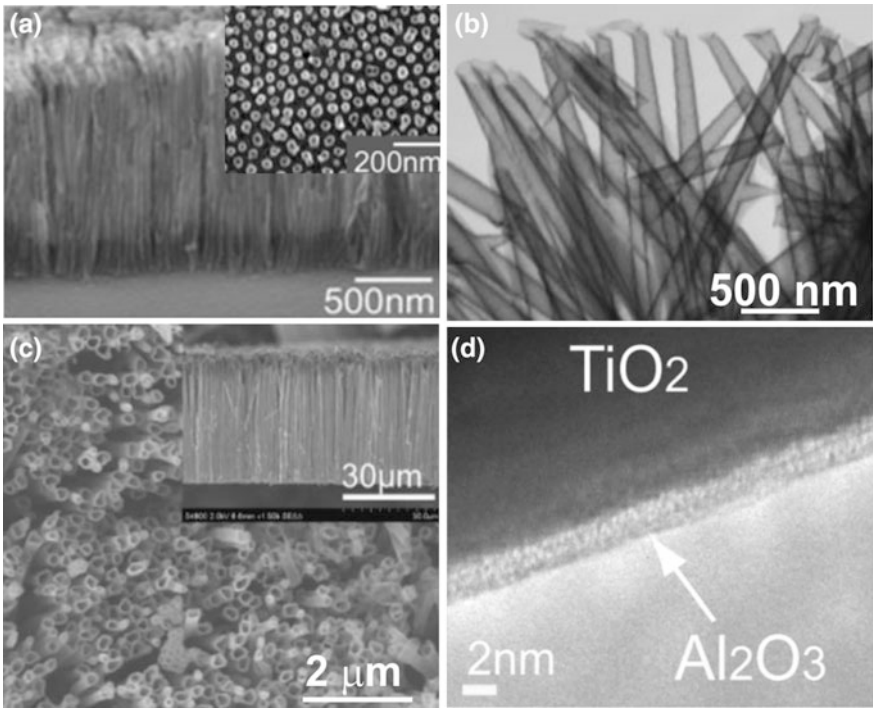

Fig. 3.15 SEM images of nanotubes prepared by ALD using porous AAO showing **a** 1.5 μm long TiO_2 nanotubes with average outer diameter of 40 nm, modified from [68], **b** 12 μm long ZrO_2 nanotubes with average outer diameter of 200 nm, modified from [70], **c** 40 μm long TiO_2 nanotubes with average outer diameter of 200 nm, modified from [71], **d** HRTEM image of 5 nm thick Al_2O_3 coating by ALD on TiO_2 nanotubes shown in (**c**), modified from [71]

showed that even a very thin (5 nm) coating on the tube walls can quite dramatically alter the TiO_2 nanotube properties.

The second paper by Turkevych and coauthors [74] has recently reported on the synergic effect between TiO_2 nanotubes and ubiquitous metal oxides on the photocatalytic activity of composite nanostructures, as depicted in Fig. 3.16c. Their work is based on a pioneering work of Nolan [75] that altering the TiO_2 surface with nanoclusters of non-stoichometric oxides can induce an upward shift of the valence band to the conduction band. Nolan's calculations predicted that upward shift of the valence band near TiO_2 surface on 0.3, 0.4 and 0.6 eV by low valence FeO_x, CrO_2 and MoO_2 cluster. It is commonly accepted now that sensitization of TiO_2 towards VIS light is realized by the utilization of low valence state of the metal ions, utilizing unusual electronic states.

To achieve that by ALD in TiO_2 nanotubes, Turkevych and coauthors (7) in the first turn deposited various oxide clusters (e.g. ZnO, SnO_2, WO_3) by using conventional ALD cycles (typically 5–6) using appropriate precursors into nanotubes with a tube diameter of 95 nm and the layer thickness of 7.5 μm (AR ≈ 80). In the

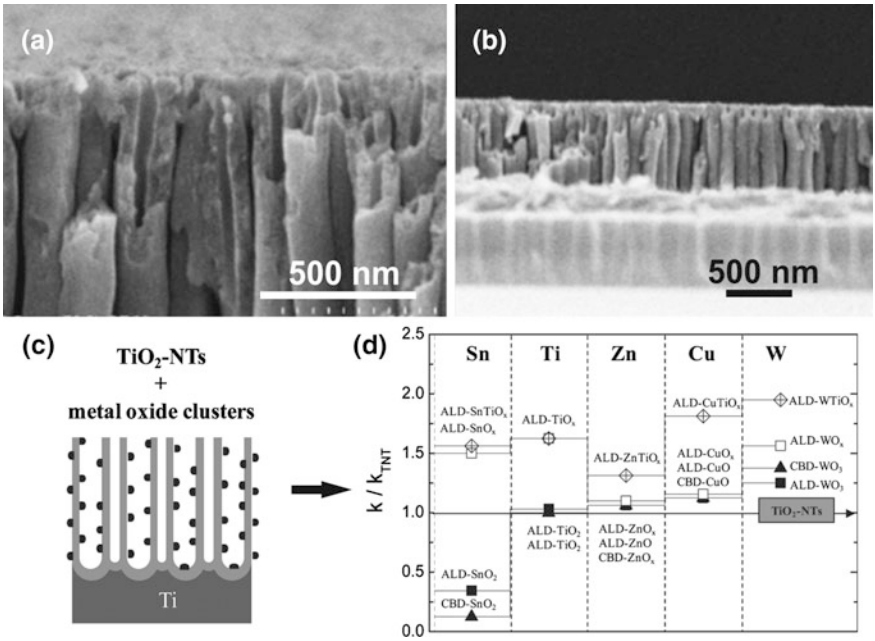

Fig. 3.16 **a** SEM top-view and **b** cross-sectional image of 350 nm thick TiO_2 nanotube layer after ALD deposition of 5 nm thick coating of Ta_2O_5 inside nanotubes, modified from [73], **b** schematic drawing of nanoparticle synthesis inside nanotubes by ALD deposition of metalorganic precursors and subsequent reduction, modified from [74], **c** methylene blue decomposition rates k for TiO_2 nanotubes decorated as in (**b**) with various suboxides relative to the kTNT for plane TiO_2 nanotubes, modified from [74]

next turn, they have used a tailored reduction by using atomic hydrogen flow through the as-deposited nanotubes. Using this approach, they managed to obtain non-stoichometric suboxides strongly attached to tube walls. Eventhough in their paper, SEM details are not shared, the photocatalytic activity of as-prepared composites is significantly higher compared to plane TiO_2 nanotubes [74], as shown in Fig. 3.16.

The 2 published reports on the deposition of a secondary material in nanotubes by ALD deal with nanotubes of an AR of ≈15 [73] and ≈80 [74]. However, the recent results of the author (J. Macak) show that it is possible to achieve conformal coating of nanotubes with AR ratio well over 200 [76], as shown in Fig. 3.17. It can be expected that further optimization of ALD process will allow its increasing utilization for modifications of TiO_2 nanotubes (and other high-aspect ratio nanotubular and nanoporous structure) with aspect ratios well over 1000.

All in all, it is evident that ALD provides great tool for coating or deposition of a whole range of materials into complex geometrical structures, like the presented TiO_2 nanotube layers. Currently, there is no better technique available that would

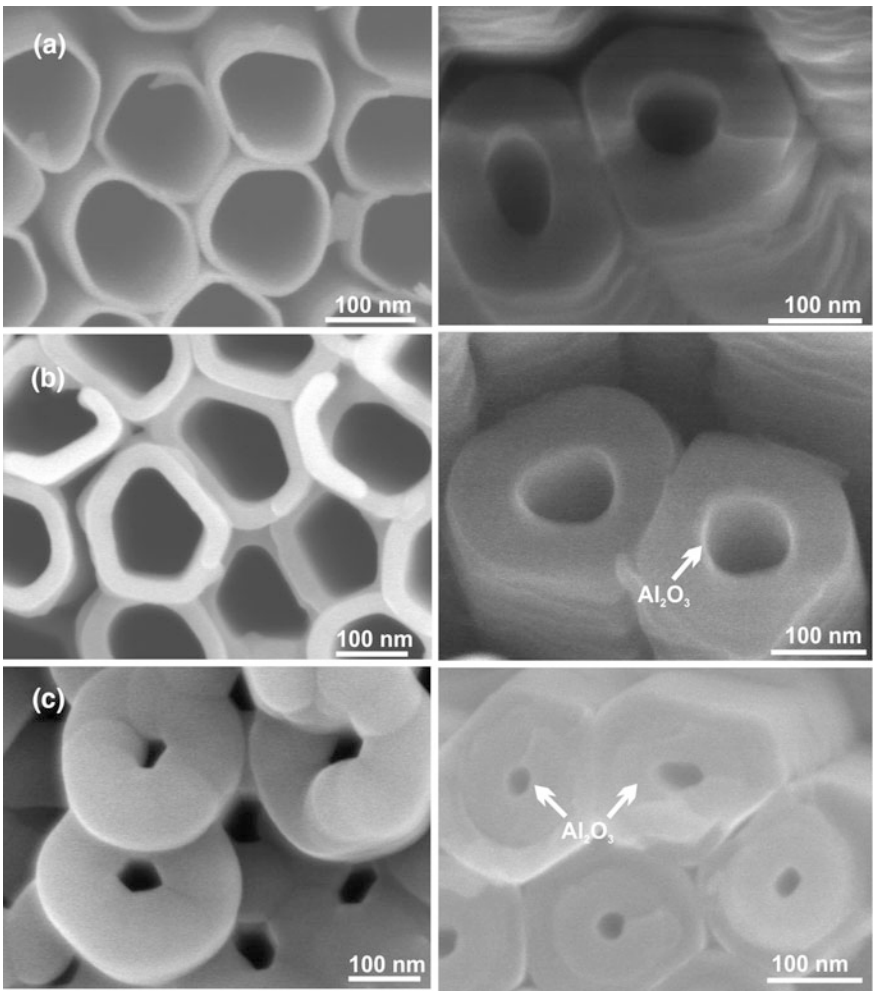

Fig. 3.17 SEM top-view images (*left column*) and cross-sectional view images (*right column*) of self-organized TiO_2 nanotube layers: **a** as-prepared; homogeneously coated by Al_2O_3 layer with thickness of 10 nm (**b**) and 50 nm (**c**) using ALD. Modified from [76]

enable such conformal and uniform coating of nanopores and nanotubes in the deep level of pores and tubes until their very bottoms.

3.3.6 Sputtering

Other deposition techniques, such as magnetron sputtering, or thermal evaporation, have not been able to deposit a homogeneous coating inside the nanotubes or to

uniformly fill their interiors. This seems to be in particular difficult, if not impossible for a high aspect ratio nanotubes. In fact, sputtering efforts have always led to the tube surface coverage and blockage, which is somewhat in the line with expectations. Until recently, these techniques were in fact only useful for contacting the tubes for solid-state electrical measurement (such as for an impedance measurement or Van der Pauw measurements).

Very recently, Schmuki and coworkers developed a novel type of nanoporous TiO_2 structures by anodization of Ti in hot H_3PO_4/HF electrolytes [28]. On the first look, as shown in Fig. 3.18, this structure exhibits an extremely high ordering of pores, similar to PAA [27]. Indeed, they have proven by fast Fourier transformation of the structures that they are indeed very regularly ordered. As the pores are only approximately 200 nm deep and have diameter of approximately 100 nm, thus the resulting AR is ≈2, it is relatively straight-forward to coat these porous layers by a secondary material using sputtering. In their first paper [28], they have shown that by self-ordered dewetting of the metal sputtered film, as shown in Fig. 3.18c, Au nanoparticles in the pore cavities can be formed homogeneously. They employed

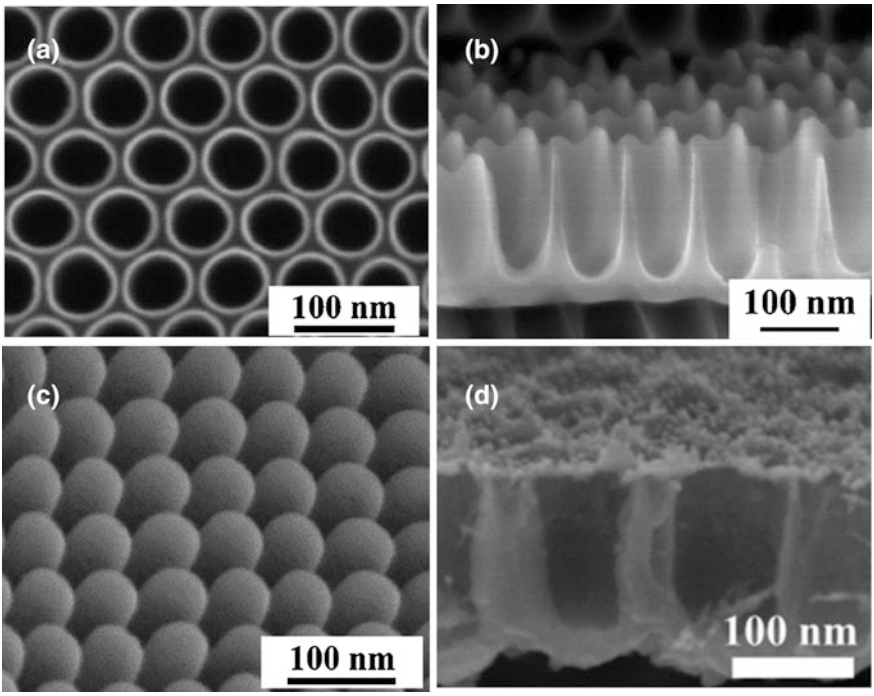

Fig. 3.18 SEM **a** top view and cross-sectional (**b**) images of extremely ordered TiO_2 porous structure by tailored anodization in hot H_3PO_4/HF electrolytes, **c** Au metal replica by sputtering the ideal filling of the TiO_2 pores, modified from [28]; **d** SEM image of the same structure as in (**b**) but with TiO_2 nanofibrils with decorated Pt nanoparticles by dewetting of previously sputtered thin Pt film, modified from [77]

this system as photocatalyst to produce hydrogen from aqueous ethanolic solutions. In their follow up paper [77], they first modified the as-prepared pores by NaOH to create TiO_2 nanofibrils onto which they subsequently deposited very thin Pt layer (1 nm), as shown in Fig. 3.18d. By the subsequent dewetting they finally achieved decoration of the fibrils by Pt nanoparticles, used similarly as in the first report for the H_2 production [77]. In their next follow up paper [78], they demonstrated use of the porous structure for templating of a range of metals, including Au, Pt, AuPd, Pd and polystyrene. All in all, their work is a true templating work that utilizes TiO_2 nanotubes for creating of replicas resembling nanotube dimensions.

It has to be noted that eventhough these porous layers have a short aspect ratio (AR ≈ 2), they clearly show that if perfectly ordered nanotubular or nanoporous TiO_2 structures would be synthesized, in particular with a wide tube or pore diameter (say d ≥ 100 nm), same sputtering procedures with a range of targets and dewetting steps could be applied to these layers with potentially very interesting results.

3.3.7 *Special Cases of Functionalizations of TiO_2 Nanotube Layers*

In this section, special techniques for nanotube functionalization, not introduced in previous sections, will be tackled. These techniques are somewhat specific to be easily put into a category. Eventually, the functionalization is performed using several closely related and dependent techniques. However, they have in common that they lead to interesting properties or applications of nanotube layers.

Kowalski and coworkers have shown that nanotube layers (approximately 3 μm thick, tube diameter ≈150 nm, AR ≈ 20) can be wetted by pyrrole solutions with the presence of surfactant [79]. In turn, by using electropolymerization, the were able to obtain polypyrole filling in the tubes (in fact replica structures of the tube interiors). As polypyrrole is resistant against HF, they dissolved by HF soaking selectively TiO_2 nanotubes, leaving nicely ordered polypyrrole nanotube or nanoporous arrays [80]. In fact, this is also the true templating approach. The polypyrrole ifself would hardly be prepared into this interesting architecture with a suitable template.

An interesting approach, biomedically highly relevant and actual, was reported by Gulati and coworkers [81]. They have demonstrated use of the drug-loaded nanotube layers for osteoblast adhesion. They used sequence shown in Fig. 3.19. In the first step, they loaded nanotube layers well attached on a Ti implant by a drug—indomethacin—dissolved in ethanol using dropping of a certain amount of the solution by micropippete, wiping out the excess drug from the surface and repeating the loading procedure up to 20 times. In the next step, they soaked the as-loaded nanotube layers in polymeric solution of either chitosan or poly(lactit-co-glycolic) acid. These polymers were tested for their ability to extend the drug release time of TNTs and produce favourable bone cell adhesion properties. Excellent osteoblast adhesion and cell proliferation on polymer-coated TNTs compared with uncoated TNTs were also

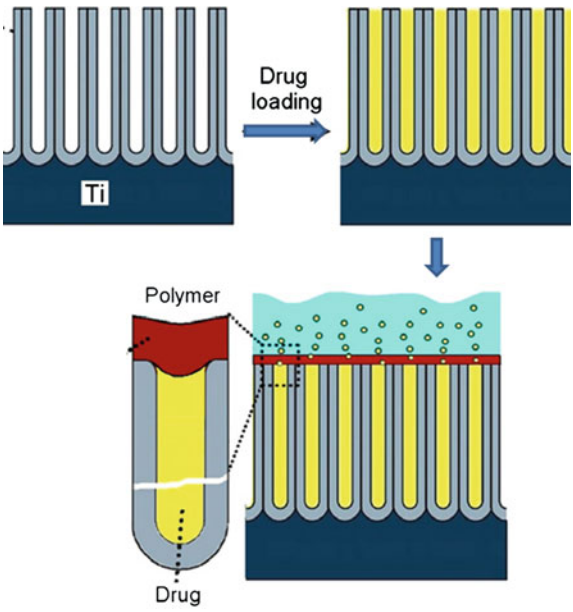

Fig. 3.19 Sequence showing modification steps of the nanotube layers to be ready for a drug delivery. Loading of a model drug (indomethacin) into nanotube layers is followed by closing the tube opening by a suitable biopolymer. Modified from [81]

observed. These results suggest that polymer-modified implants with a TNT layer are capable of delivering a drug to a bone site over an extended period and with predictable kinetics. Their nanotube layers had thickness of approximately 50 μm and the tube diameter of approximately 120 nm, resulting in nanotubes with a high aspect ratio (AR ≈ 417). However, authors did not specify, whether the model drug coated the tube walls, or decorated the walls and at what depth.

In another paper of the same group, Vasilev and coworkers published report about a new type of surface functionalization of nanotubes to tailor interfacial properties relevant for many biomedical applications of TiO_2 nanotubes [82]. They modified nanotube surface by plasma-assisted deposition of allylamine plasma polymer from allylamine precursor. This as-deposited polymer film rich in amine functional groups was further used to functionalize tube surfaces for the attachment of desired biomolecules. Their nanotube layers had thickness of approximately 20 μm and tube diameter of approximately 140 nm, resulting in nanotubes with a high aspect ratio (AR ≈ 143). However, this report is indeed about the tube surface modification, no filling was achieved (and necessary) for the desired application.

3.4 Summary and Outlook

Some of the papers presented in this chapter that are reporting functionalization of nanotube layers using the same material, as for example CdS, using various techniques, show results that are not easily comparable. The main reason is that various

tube generations and with a range of aspect ratios have been used. Therefore, it was the author's intention to provide a certain connecting point between the papers reporting various aspect ratios of the nanotubes and to show in particular using SEM or TEM images differences in the achieved magnitude of tube decoration, tube filling or last but not least, the tube coating.

It is probably too early to judge on which deposition route of what material is the most valuable for TiO_2 nanotubes and for the future success stories. Some more efforts will have to be carried out and some more time will have to pass before a better picture can be provided.

It is clear, however, that numerous deposition approaches presented here provide an added value for the properties and application range (already very broad) of TiO_2 nanotubes. As any process used in the research and the industry, presented routes for depositions of secondary materials inside nanotubes have advantages (simplicity, speed, low-cost) and disadvantages (stress generation, chemical attack of tubes, potential delamination, etc.). Nevertheless, there are techniques that one can expect to play a major role for exploitation of currently existing applications as well as for future nanotube applications. Among these, likely the electrodeposition and ALD will be two of the most developing techniques for future TiO_2 nanotube functionalizations and applications.

References

1. N. Serpone, E. Pelizzetti (eds.), *Photocatalysis—fundamentals and applications* (Wiley, Toronto, 1989)
2. A. Fujishima, K. Honda, Nature **238**, 37 (1972)
3. R. Wang et al., Nature **388**, 431 (1997)
4. B. O'Regan, M. Grätzel, Nature **353**, 737 (1991)
5. B. Ohtani, O.O.P. Mahaney, F. Amano, N. Murakami, R. Abe, J. Adv. Oxid. Technol. **13**, 247 (2010)
6. J.M. Macak, H. Tsuchiya, A. Ghicov, K. Yasuda, R. Hahn, S. Bauer, Curr. Opin. Solid State Mater. Sci. **1–2**, 3 (2007)
7. J.M.Macak, J. Pytel, J.R. Ruiz, R. Beranek, Mater. Res. Soc. Symp. Proc. **1211,** 1211-R08-34 (2010)
8. T. Kasuga, M. Hiramatsu, A. Hoson, T. Sekino, K. Niihara, Langmuir **14**, 3160 (1998)
9. Poudel et al., Nanotechnology **16**, 1935 (2005)
10. P. Hoyer, Langmuir **12**, 1411 (1996)
11. V. Zwilling, M. Aucouturier, E. Darque-Ceretti, Electrochim. Acta **35**, 921 (1999)
12. J.M. Macak, H. Tsuchiya, P. Schmuki, Angew. Chem. Int. Ed. **44**, 2100 (2005)
13. D. Li, Y. Xia, Nano Lett. **3**, 555 (2003)
14. X. Chen, S.S. Mao, Chem. Rev. **107**, 2891 (2007)
15. V. Thavasi, V. Renugopalakrishnan, R. Jose, S. Ramakrishna, Mater.Sci. Eng. R. **63**, 81 (2009)
16. J.M. Macak, M. Zlamal, J. Krysa, P. Schmuki, Small **3**, 300 (2007)
17. S. Sreekantan, L.-Ch. Wei, J. Alloys Comp. **490**, 436 (2010)
18. S.P. Albu, A. Ghicov, J.M. Macak, P. Schmuki, Nano Lett. **7**, 1286 (2007)
19. J.M. Macak, B.G. Gong, M. Hueppe, P. Schmuki, Adv. Mater. **19**, 3027 (2007)
20. J.M. Macak, T. Kohoutek, L. Wang, R. Beranek, Nanoscale **5**, 9541 (2013)

21. L.T. Canham, App. Phys. Lett. **57**, 1046 (1990)
22. G.E. Thompson, G.C. Wood, Nature **290**, 230 (1981)
23. H. Masuda, K. Fukuda, Science **268**, 1466 (1995)
24. J.M. Macak et al., Chem. Phys. Lett. **428**, 421 (2006)
25. S. Farsinezhad et al., J. Nanosci. Nanotechnol. **13**, 2885 (2013)
26. J. Tupala, M. Kemell, E. Harkonen, M. Ritala, M. Leskela, Nanotechnology **23**, 125707 (7 pp) (2012)
27. J.M. Macak, S.P. Albu, P. Schmuki, Physica Status Solidi (RRL) **1**, 187 (2007)
28. J.E. Yoo, K. Lee, M. Altomare, E. Selli, P. Schmuki, Angew. Chem. Int. Ed. **52**, 7514 (2013)
29. K. Lee, A. Mazare, P. Schmuki, Chem. Rev. **114**, 9385 (2014)
30. X. Zhou, N.T. Nguyen, S. Özkan, P. Schmuki, P. Electrochem. Commun. **46**, 157 (2014)
31. A. Ghicov, P. Schmuki, Chem. Commun. **28**, 2791 (2009)
32. P. Roy, S. Berger, P. Schmuki, Angew. Chem. Int. Ed. **50**, 2904 (2011)
33. D. Kowalski, D. Kim, P. Schmuki, Nano Today **8**, 235 (2013)
34. A.F. Cipriano, Ch. Miller, H. Liu, J. Biotech. Nanotech. **10**, 2997 (2014)
35. M. Kulkarni, A. Mazare, E. Gongadze, Š. Perutkova, V. Kralj-Iglic, I. Milošev, P. Schmuki, A. Iglic, M. Mozetic, Nanotechnology **26**, 062002 (2015)
36. R.B. Wehrspoon (Ed.), *Ordered Porous Structures and Applications* (Springer, Berlin, 2005)
37. S.Z. Chu, K. Wada, S. Inoue, M. Isogai, A. Yasumori, Adv. Mater. **17**, 2115 (2005)
38. W. Lee, R. Ji, U. Gösele, K. Nielsch, Nat. Mater. **5**, 741 (2006)
39. H. Masuda, H. Yamada, M. Satoh, H. Asoh, M. Nakao, T. Tamamura, Appl. Phys. Lett. **71**, 2770 (1997)
40. H. Asoh, K. Nishio, M. Nakao, T. Tamamura, H. Masuda, J. Electrochem. Soc. **148**, B152 (2001)
41. J. Kolar, J.M. Macak, K. Terabe, T. Wagner, J. Mat. Chem. C **2**, 349 (2014)
42. J.M. Macak, C. Zollfrank, B.J. Rodriguez, H. Tsuchiya, M. Alexe, P. Greil, P. Schmuki, Adv. Mater. **21**, 3121 (2009)
43. L. Assaud, V. Heresanu, M. Hanbücken, L. Santinacci, C.R. Chimie 16 (2013) 89
44. D. Wang, B. Yu, C. Wang, F. Zhou, W. Liu, Adv. Mater. **21**, 1964 (2009)
45. D. Fang, K. Huang, S. Liu, D. Qin, Electrochem. Commun. **11**, 901 (2009)
46. N. Liu, K. Lee, P. Schmuki, Angew. Chem. Int. Ed. **52**, 12381 (2013)
47. Y. Gim, M. Seong, Y.-W. Choi, J. Choi, Electrochem. Commun. **52**, 37 (2015)
48. S. Chen, M. Paulose, Ch. Ruan, G.K. Mor, O.K. Varghese, D. Kouzoudis, C.A. Grimes, J. Photochem. Photobiol. A: Chem **177**, 177 (2006)
49. Y. Yin, Z. Jin, F. Hou, Nanotechnology **18**, 495608 (2007)
50. S. Banerjee, S.K. Mohapatra, P.P. Das, M. Misra, Chem. Mater. **20**, 6784 (2008)
51. Q. Kang, Q. Cai, S.Z. Yao, C.A. Grimes, J. Ye, J. Phys. Chem. C **116**, 16885 (2012)
52. H. Zhang, X. Quan, S. Chen, H. Yu, N. Ma, Chem. Mater. **21**, 3090 (2009)
53. Q. Wang, K. Zhu, N.R. Neale, A.J. Frank, Nano Lett. **9**, 806 (2009)
54. W.-T. Sun, Y. Yum, H.-Y. Pan, X.-F. Gao, Q. Chen, L.-M. Peng, J. Am. Chem. Soc. **130**, 1124 (2008)
55. D.R. Baker, P. Kamat, Adv. Func. Mater. **19**, 805 (2009)
56. J.M. Macak, F. Schmidt-Stein, P. Schmuki, Electrochem. Commun. **9**, 1783 (2007)
57. I. Paramasivam, J.M. Macak, P. Schmuki, Electrochem. Commun. **10**, 71 (2008)
58. I. Paramasivam, J.M. Macak, A. Ghicov, P. Schmuki, Chem. Phys. Lett. **445**, 233 (2007)
59. A. Benoit, I. Paramasivam, Y.-C. Nah, P. Roy, P. Schmuki, Electrochem. Commun. **11**, 728 (2009)
60. Y.-Y.Son, Z.-D. Gao, J.-H. Wang, X.-H. Xia, R. Lynch, Adv. Funct. Mater. **21**, 1941 (2011)
61. C.W. Lai, S. Sreekantan, Electrochim. Acta **87**, 294 (2013)
62. N.K. Shrestha, M. Yang, Y.-C. Nah, I. Paramasivam, P. Schmuki, Electrochem. Commun. **12**, 254 (2010)
63. J.M. Macak, P.J. Barczuk, H. Tsuchiya, M.Z. Nowakowska, A. Ghicov, M. Chojak, S. Bauer, P.J. Kulesza, P. Schmuki, Electrochem. Commun. **7** 1417 (2005)

64. N.K. Shrestha, J.M. Macak, F. Schmidt-Stein, C. Mierke, B. Fabry, P. Schmuki, Angew. Chem. Int. Ed. **48**, 969 (2009)
65. J.M. Macak, R. Kupcik, P. Rehulka, Z. Bilkova, Adv. Funct. Mater, (in preparation)
66. S.H. Ju, S. Han, J.S. Kim, J. Ind. Eng. Chem. **19**, 272 (2013)
67. M. Leskelä, M. Ritala, Angew. Chem. Int. Ed. **42**, 5548 (2003)
68. M.S. Sander, M.J. Cote, W. Gu, B. Kile, C.P. Tripp, Adv. Mater. **16**, 2052 (2004)
69. M. Kemell, V. Pore, J. Tupala, M. Ritala, M. Leskelä, Chem. Mater. **19**, 1816 (2007)
70. H. Shin, D.-K. Jeong, J. Lee, M. Sung, J. Kim, Adv. Mater. **16**, 1197 (2004)
71. X. Gao, D. Guan, J. Huo, J. Chen, C. Yuan, Nanoscale **5**, 10438 (2013)
72. Y. Huang, G. Pandraud, P.M. Sarro, Nanotechnology **23**, 485306 (2012)
73. J. Tupala, M. Kemell, E. Härkönen, M. Ritala, M. Leskelä, Nanotechnology **23**, 125707 (2012)
74. I. Turkevych, S. Kosar, Y. Pihosh, K. Mawatari, T. Kitamori, J. Ye, K. Shimamura, J. Ceram. Soc. Jap. **122**, 393 (2014)
75. M. Nolan, Phys. Chem. Chem. Phys. **13**, 18194 (2011)
76. J.M. Macak, J. Prikryl, Ms in Preparation
77. N.T. Nguyen, J.E. Yoo, M. Altomare, P. Schmuki, Chem. Commun. **50** 9653 (2014)
78. J.E. Yoo, K. Lee, P. Schmuki, ChemElectroChem **1**, 64 (2014)
79. D. Kowalski, P. Schmuki, Chem. Commun. **46**, 8585 (2010)
80. D. Kowalski, A. Tighineanu, P. Schmuki, J. Mater. Chem. **21**, 17909 (2011)
81. K. Gulati, S. Ramakrishnan, M.S. Aw, G.J. Atkins, D.M. Findlay, D. Losic, Acta Biomater. **8**, 449 (2012)
82. K. Vasilev, Z. Poh, K. Kant, J. Chan, A. Michelmore, D. Losic, Biomaterials **31**, 532 (2010)

Chapter 4
Porous Silicon Biosensors Employing Emerging Capture Probes

Katharina Urmann, Elena Tenenbaum, Johanna-Gabriela Walter and Ester Segal

Abstract The application of porous silicon (PSi) for biosensing was first described by Thust et al. in 1996, demonstrating a potentiometric biosensor for the detection of penicillin. However, only in the past decade PSi has established as a promising nanomaterial for label-free biosensing applications. This chapter focuses on the integration of new emerging capture probes with PSi-based biosensing schemes. An overview of natural and synthetic receptors and their advantageous characteristics for the potential application in PSi biosensors technology is presented. We also review and discuss several examples, which successfully combine these new bio-receptors with PSi optical and electrochemical transducers, for label-free biosensing.

4.1 Introduction

Although porous silicon (PSi) was already discovered in the 1950s, it only gained scientific attention in the 1990s when Leigh Canham reported bright photoluminescence of the material [1]. While the interest in PSi for optoelectronic switches, displays and lasers quickly faded due to its poor chemical and mechanical stability, it became a material of choice for sensors design. PSi unique combination of properties i.e., high surface area and volume, tunable nanostructure, versatile surface chemistry and compatibility with other silicon microfabrication technologies,

K. Urmann · J.-G. Walter
Institute of Technical Chemistry, Gottfried-Wilhelm Leibniz Universität Hannover, Hannover, Germany

K. Urmann · E. Tenenbaum · E. Segal (✉)
Department of Biotechnology and Food Engineering, Technion-Israel Institute of Technology, Haifa, Israel
e-mail: esegal@tx.technion.ac.il

E. Segal
Russell Berrie Nanotechnology Institute, Technion-Israel Institute of Technology, Haifa, Israel

D. Losic and A. Santos (eds.), *Electrochemically Engineered Nanoporous Materials*, Springer Series in Materials Science 220,
DOI 10.1007/978-3-319-20346-1_4

allow for the design of sophisticated biosensing platforms [1, 2]. Indeed, a growing number of biosensing schemes employing PSi as a transducer are reported in recent years. By 2013, the yearly number of new publications already reached 40. Included here are not only electrochemical biosensors taking advantage of the semiconductor electrical properties, but also many optical biosensing schemes, which utilize the unique optical properties of this nanostructured material. The most common fabrication method of PSi is electrochemical etching in the presence of hydrofluoric acid (HF). This method allows to easily define the properties of the formed porous layer in terms of pore dimensions, morphology and porosity, by adjustment of the etching parameters (e.g., current density, anodization time, HF concentration) [3, 4]. By controlling the current density during the etching process, different porous structures can be fabricated such as single porous layers, double layers, photonic crystals and microcavities [2].

The freshly-etched PSi is unstable in ambient environment and in aqueous medium as the Si hydride-terminated surface is prone to nucleophilic attack by water molecules. A simple method to stabilize PSi is to grow an oxide layer on the surface to slow spontaneous oxidation ($PSiO_2$ formation). The resulting $PSiO_2$ layer provides a convenient means for subsequent surface modification, as it enables the simple reaction with different alkyl silanes [2, 5, 6]. Reactive groups at the distal end of the silane molecules, such as amines and thiols, provide attachment points for biorecognition elements. Silanization of oxidized PSi has been used to create biorecognition interfaces composed of DNA [5], antibodies [7–9] and small molecules [10].

Porous silicon has proven to be a suitable transducer, showing excellent sensitivity, and allowing for label-free detection of many analytes of interest [11, 12]. PSi optical biosensors are based on changes in the photoluminescence or the reflectivity spectra upon exposure to the target analyte, which replace the media in the pores. A change in the refractive index (RI) of the liquid in the pores affects the average RI of the porous film, and is commonly observed as quenching of the PSi photoluminescence or as a wavelength shift in the reflectivity spectrum. For analytes that are size excluded from penetrating into the porous nanostructure, changes in the reflected light intensity are observed as a result from a change in the RI contrast at the PSi-medium (air or other) interface [13].

Optical transducers received significant attention in the field of PSi-based biosensors since the pioneering work of Sailor and co-workers [14–16], and there are already few commercially-available optical sensing systems (Silicon Kinetics, Inc.). Nevertheless, PSi is also studied as an electrochemical transducer for biosensing applications [17]. The two main electrochemical transduction types are potentiometry and amperometry. Potentiometric biosensors measure the potential difference occurring as a result of an acidic/alkaline substance formation. These substances are usually a product of an enzymatic reaction, where the catalyzing enzyme is immobilized onto the PSi surface. Amperometric biosensors measure current density resulting from redox reactions, catalyzed by immobilized enzymes. Amperometric PSi-based biosensors are less applicable due to the relatively poor conductivity of PSi and therefore, coupling of metal electrodes to the PSi may increase their sensitivity [17, 18].

Apart from the transducer quality, the properties of the biorecognition elements to be used for analyte binding have a critical effect on the performance of any biosensor system. The use of novel capture probes is emerging for new assay designs and for targeting a wide variety of analytes. These capture probes: aptamers, peptide nucleic acid (PNA), synthetic antibodies, antimicrobial peptides (AMPs) or enzymes, hold in store many advantages over the common bioreceptors. These include improved conformational stability, higher affinity towards the target analyte, and reduced production costs. We believe that the integration of these novel biorecognition elements with the advantageous properties of PSi will improve the performance of PSi-based biosensors dramatically, especially in terms of sensitivity. Low limits of detection will allow these biosensors to meet the requirements in the fields of food safety, medical diagnostics or homeland security.

4.2 Emerging Bioreceptors

All biosensors rely on an element facilitating molecular recognition—the so-called bioreceptor, which specifically binds the target analyte. Binding between the bioreceptor and the analyte occurs due to biomolecular recognition which is based on the complementarities of the surfaces of the two binding partners [19]. Different molecular interactions can contribute to binding: Hydrogen bonding, van der Waals forces, electrostatic interactions, π-π interactions, and combination of thereof are working in concert to enable high specific and high affinity binding. Moreover, during the binding event, successive replacement of water from the binding sites of the bioreceptor and the analyte takes place, resulting in an increase of enthalpy, making binding favorable. In aqueous solutions—which are most often the media to be analyzed by biosensors—this so-called hydrophobic effect has a profound role and may even dominate the bioreceptor-analyte complex formation [20].

In this section a brief overview on bioreceptors will be given with an emphasis on emerging new types of recognition elements. This section makes no claim to be complete, more comprehensive reviews can be found elsewhere (e.g. [21, 22]). The main features of the bioreceptors described in this chapter are summarized in Table 4.1.

4.2.1 Natural Bioreceptors

The first biosensor systems utilized bioreceptors provided by living organisms. Examples for such biological recognition elements are antibodies and enzymes. These naturally occurring receptors have been developed by nature via evolutional processes. Today, biotechnology allows not only the construction of completely new bioreceptors, which will be discussed in Sect. 4.2.2, but also facilitates rational modification of naturally occurring bioreceptors e.g. manipulation of their binding

Table 4.1 Main features of the bioreceptors

Bioreceptor	Classification	Targets/Analytes	Advantages	Disadvantages
Antibody	Natural/engineered	Proteins, small molecules	High affinity, well established production and application	Low stability, not readily available for all analytes
Enzyme	Natural/engineered	Small molecules	High affinity	Not available for all analytes of interest
AMP (antimicrobial peptides)	Natural/engineered	Bacteria	High affinity, chemical stability when compared to antibodies, broad antimicrobial spectrum	Not specific towards certain strain
DNA	Synthetic	DNA/RNA	Ease of production, well established technologies	Prone to nucleases, negative charge
PNA (peptide nucleic acid)	Artificial	DNA/RNA	Higher affinity when compared to DNA, resistant to nucleases	Poor solubility (depending on the length and sequence)
Aptamer	Artificial	Proteins, small molecules, cells (including pathogens)	High affinity and specificity, in vitro selection and production	Less established selection and application techniques, negative charge
MIP	Artificial	Proteins, DNA	High stability	High amount of target required

site to permit new specificities. Therefore, a precise discrimination between natural and synthetic bioreceptors is difficult and the line between them is blurred. In this subsection we are summarizing some naturally occurring bioreceptors as well as engineered variants derived from these molecules.

4.2.1.1 Antibodies

The most prominent example for bioreceptors may be antibodies. In nature, antibodies are produced by the immune system in an evolutional process resulting in high affinity and specificity. The human immune system is estimated to possess a repertoire of 10^{15} distinct antibody structures from which appropriate antibodies are chosen by recombinant selection [23]. This allows the production of antibodies directed against numberless potential antigens. This diversity in combination with the well-established techniques of antibody development and production are responsible for the broad use of antibodies in biosensing systems. The dominance of antibodies was especially boosted by the development of monoclonal antibody technology, facilitating the production of large amounts of antibodies directed against one single epitope of the antigen in cell culture. Instead of using the complete, intact antibody, Fab fragments or even smaller fragments can be used as bioreceptors [24–26].

Based on their generation in living organisms—cells or animals—antibodies possess some limitations. For instance, antibodies directed against small molecules in general, and especially against toxic or non-immunogenic molecules, are difficult to generate. Here the analyte has to be coupled to a protein before immunization [27] and the obtained antibodies have to be purified in order to isolate the fraction binding to the target of interest. The development of antibodies against small molecules is thus laborious, time-consuming and expensive.

Detailed understanding of the genetic background of antibodies has resulted in the possibility to manipulate antibodies structure [25]. Recombinant expression of antibodies allows the design of chimeric antibodies; the binding sites of antibodies can be selected by phage display techniques using genetic engineered phage libraries. In antibody phage display, the minimized antibodies are fused to a coat protein of the virus, resulting in phages presenting the antibody on the phage surface. The phages are then used for the selection of antibody fragments with the desired binding properties, they not only display the antibody fragment on their surface, but also carry the corresponding genetic information and can thus be used for the amplification of these features [28].

Although these modern selection techniques have overcome the limitations associated with the development of antibodies in living organisms, other problems remain unsolved. These include poor antibody stability and their limitation to near-physiological conditions.

4.2.1.2 Enzymes

Enzymes do not only bind a substance—the so-called substrate—they also convert it to a product. The binding of the substrate to the active binding pocket of the enzyme is driven by the forces described above and results in high specificity. Moreover, the catalytic process results in detectable reaction products like protons and electrons, which can be exploited for signal amplification. Enzymes were the first recognition elements used in biosensors. The pioneering work of Clark and Lyons [29], immobilizing glucose oxidase on an electrode to allow for the determination of glucose concentration, has boosted the development of numerous enzymatic biosensor platforms, exploiting the outstanding specificity of enzymes [30].

Drawbacks of naturally occurring enzymes are their rather low stability with regard to environmental conditions (temperature and pH) [31], and the lack of specific enzymes for all analytes of interest. Here, genetic engineering can broaden up the diversity of possible substrates and fine-tune the characteristics of the bioreceptor [32]. An interesting approach to develop enzymes, which can be tailored to allow the detection of specific analytes of interest, was described by Ostermeier (2005) [33]. Target binding sites were engineered and inserted into the regulatory subunit of an allosteric enzyme. Binding of the target to the regulatory subunit resulted in a structural switch affecting the activity of the catalytic site [33, 34].

4.2.1.3 Antimicrobial Peptides

Antimicrobial peptides (AMPs) are positively charged short (10–50 amino acids) oligopeptides occurring as natural antibiotics and immunomodulating substances which have been evolved as a part of the innate immune system [35]. Various types of AMPs have already been identified including defensins, cecropins, magainins and cathelicidins [36]. AMPs are stable molecules, which can survive under flow or heat conditions, as well as different salt concentrations and pH variations. They can also bind to a broad spectrum of microorganisms. As such, they have already been successfully used for the detection of pathogens in various formats of diagnostic assays [37]. Although their affinity towards many bacteria strains might also be a drawback for biosensing applications, it is interesting to mention that it has been shown that the natural AMP Magainin I exhibits preferential binding towards some pathogenic species [38].

Besides naturally occurring peptides, synthetic peptides which mimic the biophysical characteristics of naturally occurring AMPs can be generated by combinational synthesis. For a synthetic peptide, consisting of 10 of the 20 essential amino acids, 20^{10} (2×10^{11}) distinct peptides are possible, but the diversity can be further expanded by the use of non-essential and unnatural amino acids [39]. These huge libraries have to be screened for peptides with the desired binding properties by high throughput screening. Molecular modeling is expected to improve and simplify the identification of peptides derived by combinational synthesis. Peptides with desired affinity against a given target can also be selected by phage display technology. These synthetic peptides have the advantages of simple cost-effective synthesis procedure, stability in the presence of proteases and the ability to design their binding properties [40].

4.2.2 Synthetic Receptors

As already mentioned, natural bioreceptors are limited by their low stability, poor performance in organic solvents, and/or their availability against a specific analyte. Therefore, technologies have been developed to advance naturally occurring bioreceptors or to even completely substitute them by novel types of bioreceptors. Using modern DNA technology, naturally occurring bioreceptors can be further evolved to result in engineered receptors with improved properties. In addition, completely synthetic bioreceptors are developed by rational design, computational chemistry, combinatorial chemistry, molecular imprinting, self assembly or combinations of these techniques [41].

4.2.2.1 DNA and PNA

DNA oligonucleotides can be used as bioreceptors for the detection of complementary DNA sequences. Here, the hybridization between the DNA and the oligonucleotide is exploited for the detection of the DNA—or more specifically—the source of the DNA. Thus, oligonucleotides are most valuable for a variety of targets ranging from pathogens in infectious diseases [42] and food-borne contaminations [43], cancer biomarkers [44], to the diagnosis of genetic diseases by microarray-based multiplexed detection of genes and gene alterations [45–47].

One drawback associated with DNA oligonucleotides as bioreceptors is their susceptibility to degradation by nucleases. In this context, the use of phosphorothioates can improve DNA stability [48] and locked nucleic acids (LNAs) have been developed, which contain at least one bicyclic furanose unit that nucleases do not accept as a substrate [49]. Other disadvantages associated with DNA are the limited sensitivity and rapidity of the sensing. Conventionally, the DNA originating from the sample to be analyzed needs to be amplified via PCR prior to sensing, resulting in a lengthy procedure. Moreover, the negatively charged phosphate backbone of the oligonucleotides is also the source of some concerns. The negative charge results in electrostatic repulsion, which further increases upon duplex-formation and causes Coulomb blockage of the hybridization [50, 51]. To circumvent these problems, a new type of nucleic acid oligomers has been developed. In peptide nucleic acids (PNAs) [52], the negatively charged phosphate backbone of natural oligonucleotides is replaced by a neutral peptide-like backbone composed of repeated N-(2-aminoethyl)glycine units linked by amide bonds. The number of bonds between the bases in the obtained PNA is similar to that in DNA, resulting in a proper inter-base spacing, which allows for hybridization of DNA and PNA. The use of PNA in DNA biosensors offers some major advantages. PNA is not recognized by nucleases and proteases and is thus stable in biological fluids. Due to the lack of electrostatic repulsion, existing between two DNA oligonucleotides, the binding between PNA and DNA is even stronger and more specific than the formation of DNA duplexes. Thus, PNA is considered to offer extraordinary specific detection of DNA to facilitate the identification of single-nucleotide mismatches [53].

Despite their improved properties, PNAs are limited to the detection of DNA sequences. Another type of oligonucleotide—termed aptamer—broadens up the specificity of oligonucleotide-based detection to virtually all types of analytes.

4.2.2.2 Aptamers

Aptamers are single-stranded oligonucleotides composed of RNA or DNA generated by in vitro selection techniques like SELEX (systematic evolution of ligands by exponential enrichment) [54–56], modified SELEX procedures [57, 58] or MonoLEX [59]. During the selection, aptamers are isolated from combinational oligonucleotide libraries containing up to 10^{15} individual sequences based on their

affinity and specificity towards the desired target molecules. Once an aptamer sequence has been identified, the aptamer can be produced by chemical synthesis.

In contrast to conventional DNA, which binds complementary DNA based on Watson-Crick base-pairing and is usually thought of as a rather linear molecule, aptamers fold into unique three-dimensional (3D) structures that enable the molecular recognition of their corresponding targets [60, 61]. Thus, they are often described as nucleic acid-based alternatives to antibodies. While the development of antibodies depends on the immunization of animals and their production via cell culture techniques, aptamers are selected by in vitro techniques and can be produced via chemical synthesis. Consequently, aptamers can be selected against virtually all types of targets, including those with low immunogenicity or high toxicity. Moreover, aptamers can be selected under non-physiological conditions in order to generate aptamers that are functional under desired conditions. Thus, in case of aptamers, a tailor-made bioreceptor can be designed and optimized to meet the requirements of specific applications [62, 63].

In the special context of biosensing, the major advantages of aptamers over their amino acid-based counterparts include their superior stability, ease of regeneration (to allow subsequent usage in multiple sensing cycles), and highly reproducible production by chemical synthesis. During this synthesis, the aptamer can be modified at defined positions; for instance linker molecules can be incorporated to facilitate highly controlled immobilization of the aptamer on the transducers surface. Moreover, due to their oligonucleotide nature, aptamers offer completely new biosensing schemes, as we reviewed recently [64, 65]. For instance, oligonucleotides complementary to the target-binding site of the aptamer can be designed and hybridized to the aptamer. Thus, in the presence of the target, the target will replace the complementary oligonucleotide, while the release of the oligonucleotide can be detected and quantified via different labeling techniques. This strategy has been already successfully applied for the detection of ethanolamine, which is the smallest analyte against which an aptamer has been selected [66]. In more sophisticated sensing schemes, the aptamer can simultaneously act as both the bioreceptor and the transducer. In these so called aptamer beacons, the aptamer can be modified with a quencher and a fluorophore positioned in close proximity, resulting in low fluorescence in the absence of the target. Binding to the target results in conformational changes; fluorophore and quencher depart from each other to yield an increase in the fluorescence intensity [67].

One concern associated with aptamers is their sensitivity to degradation by nucleases. Today, this problem can be easily overcome by different modifications [68] and even non-modified aptamers are already successfully applied in complex biological samples [69, 70]. In addition, the high negative charge presented by the aptamer molecule may result in failure to select aptamers, which are directed against negatively charged species, and may also induce non-specific binding to aptamer-modified surfaces. To overcome these issues, PNA aptamers have been developed in recent years. Lee et al. have synthesized a PNA aptamer using the same base sequence known from a DNA aptamer directed against thrombin [71]. However, it remains uncertain whether this simple transition from DNA to PNA

may be applicable for other aptamers, in which the folding of the aptamer may be influenced strongly by the negatively charged phosphate backbone. In this context, the direct selection of aptamers from a PNA library, which has already been used to develop PNA aptamers directed against dihydrofolate reductase [72], may prove to be a more versatile tool.

4.2.2.3 Molecularly Imprinted Polymers

Molecularly imprinted polymers (MIPs) are synthesized by contacting the target of interest with a complementary mixture of functional monomers to allow complex formation. Subsequently, the monomers are polymerized to form a matrix, which entraps the target. Removal of the target leaves behind a cavity with a surface complementary to the target.

Depending on the used monomers, the MIP offers some advantages over natural and other artificial bioreceptors, including their inherent stability with regard to temperature, pH, and organic solvents, low cost, and ease of preparation [41, 73]. The affinity and specificity of MIPs are generally inferior in comparison to that of antibodies and aptamers; e.g. apparent dissociation constants within the micro molar range have been determined for MIPs [74]. Moreover, MIPs produced by available techniques are polyclonal binders [75, 76], also restricting their specificity. The major disadvantage of MIPs is the large amount of target that is required for MIP production. In the case of antibodies, small amounts of the antigen (corresponding to the target) are needed for the immunization of the animal, after which large quantities of the antibody can be expressed with no need for additional target. The same applies for the production of aptamers; the target is only required during the SELEX process. Accordingly, the obtained DNA sequence can be used for the reproduction of the bioreceptor. In contrast, each cavity within the MIP requires one target molecule.

4.2.3 Today's Use of Bioreceptors and Future Perspectives

Today biosensors employ a broad diversity of different bioreceptors, as discussed in previous sections. Nevertheless, most biosensors still rely on conventional bioreceptors based on nature's well-known binding mechanisms. These include DNA detection, which is based on Watson-Crick base pairing, proteins are most frequently detected using antibodies, and small molecules are mostly detected by enzymes. Figure 4.1 summarizes the number of academic publications (between 1980–2013) dealing with biosensors, categorized in accordance to the type of employed bioreceptor. Clearly, enzymes, DNA and antibodies are dominating the field, but new capture probes are emerging and gaining significant momentum. Among these novel types of bioreceptors, AMPs and especially aptamers have

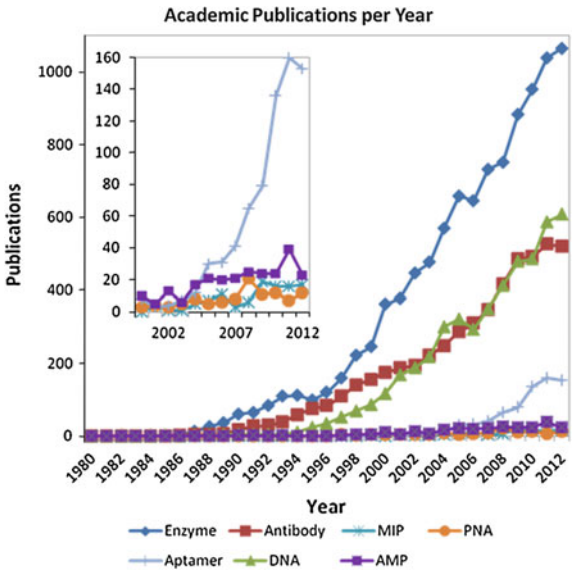

Fig. 4.1 Publications dealing with biosensors utilizing different natural and artificial bioreceptors. Search for publications was performed using the term "biosensor" in combination with the terms "enzyme", "antibody", "MIP", "PNA", "aptamer", "DNA", or "AMP". Data was created using MEDSUM: an online MEDLINE summary tool by Galsworthy, MJ. Hosted by the Institute of Biomedical Informatics (IBMI), Faculty of Medicine, University of Ljubljana, Slovenia. URL: www.medsum.info

attracted much attention (insert in Fig. 4.1). Our perspective is that aptamers have the potential to dominate the field in the future due to the fact that they can be developed to target almost all classes of analytes and produced at relatively low cost.

4.3 Porous Silicon-Based Biosensors

Over the past decade, a great number of PSi-based biosensors were reported in the literature [2, 12, 77]. With its most attractive property, the large surface area of up to 500 m^2/cm^3, PSi allows dense immobilization of different capture probes: enzymes [78], DNA fragments [79], antibodies [7], or any of the aforementioned emerging bioreceptors. Optical biosensors make up for the largest share in PSi-based assays and can be further categorized to two subgroups, based on the optical transduction mechanism, to include biosensors based on changes in photoluminescence [10, 80] and those based on changes in reflectivity [5, 81]. Upon infiltration of the target analyte molecules into the porous layer and their subsequent binding to the respective bioreceptors, which are immobilized onto the pore walls, a

Table 4.2 Examples of PSi-based biosensor schemes categorized in terms of the type of bioreceptor employed

Capture probe	Analyte	Detection method	Porous architecture	Working range	Reference
Antibody	*E. coli* Streptavidin Opiates	Optical-reflectivity	Single mesoporous layer	10^4–10^5 cells/ml	[9]
		Optical-fluorescence	Single nanoporous layer	n/a	[87]
		Optical-reflectivity	Single mesoporous layer	0.018–10.8 μM	[88]
Enzyme	Specifically cleaved peptide fragments Proteins (e.g. cholesterol)	Optical-reflectivity	Single mesoporous layer	n/a	[89]
		Electrical-amperometry	Single mesoporous layer	1–50 mM	[84]
Peptide	Enzyme	Optical-reflectivity	1D Photonic crystal	0.037–37 μM	[90]
DNA	DNA	Electrical-impedance	Single macroporous layer	0.1–5 μM	[5]
PNA	DNA	Optical-reflectivity	Single mesoporous layer	n/a	[91]
Aptamers	ATP	Optical-fluorescence	Single macroporous layer	0.1–100 μM	[92]
	Tetracycline	Electrical-impedance	Single mesoporous layer	2–100 nM	[86]
	His-tag proteins	Optical-reflectivity	Single mesoporous layer	11–56 μM	[93]

change in the RI of the thin film can be observed, as a modulation in the photoluminescence or as a wavelength shift in the reflectivity spectra, respectively. Other biosensors based on PSi are mainly electrochemical, relying on PSi semiconductor characteristics [82]. Examples include voltammetric approaches [83] as well as amperometric [84], potentiometric characterization [85] and impedance-based sensors [86].

Another appealing characteristic of PSi transducers is the ability to easily tailor their nanostructure [1]: pore sizes to accommodate the interacting species, pore architecture, as well as surface chemistry, can be varied and tuned to meet the needs of any specific application.

Table 4.2 provides an overview of existing PSi-based biosensor schemes and the type of bioreceptor employed. Without the claim of being complete, it shows that a wide diversity of bioreceptors in concert with different transduction approaches is used for the development of PSi-based biosensors.

4.3.1 Optical Biosensors

While the discovery of photoluminescence in PSi kick-started scientists' attention on the material, this emission of secondary photons upon light induced excitation has not established itself as a prevalent transduction methodology for biosensors development. This is in spite of the promising early studies by Starodub et al. [94], in which specific protein binding to the corresponding antibody was demonstrated by a decrease in the PSi photoluminescence. The complex photoluminescence mechanisms, associated with electron transfer and interfacial charging [1, 95, 96], pose a major challenge in the development of reliable biosensors [97]. Yet, a recent study demonstrated the quenching of a reporter-label inside the porous structure in a very interesting manner [92], this work will be discussed in more detail in the next section.

Fluorescent labels have also been used in assays to combine both, a fluorescent signal and reflectivity spectra [98] or electrical impedance [87], respectively. Nonetheless, label-free methods are often preferred. The necessity of additional steps for labeling the capture probes or target, add cost and complexity to the assay and may interfere with target recognition. Other disadvantages of labeled approaches include the rapid photobleaching of fluorescent organic dyes conjugated to the biomolecules of interest, as well as challenges associated with quantitative analysis due to the fluorescence signal bias, as the number of fluorophores on each molecule cannot be precisely controlled [99].

For label-free PSi biosensors based on reflectance, two different signals can be monitored: the shift in the wavelength due to RI variation [16] and a change in the intensity of the reflected light due to scattering effects [9]. Different PSi architectures e.g., single and double layers [88, 100], microcavities [78, 101], and photonic crystals [90, 102], have been used for the construction of reflectivity-based optical biosensors. The tunable architecture of PSi allows incorporating additional functionalities within the optical transducer, such as internal reference channels, and size exclusion features. Pacholski et al. [103] demonstrated a double layer biosensor, where a layer with smaller pore size serves for separation of biomolecules by size exclusion and also as an internal signal reference channel. This nanostructure allowed for simultaneous detection of a macromolecule (*bovine* serum albumin) and a small molecule (sucrose). This concept was later exploited by Bonanno and DeLouise [101] using a microcavity structure for filtering, enabling a label-free detection of rabbit IgG in complex media (such as whole blood samples).

We believe that a combination of the advantageous properties of the novel capture probes, described in the previous section, with PSi can bring forth a new generation of high performance biosensing concepts. While there are certainly many more publications to be expected within the next years, in this review, we focus on few recent studies, which have demonstrated promising results. The first example of a fluorescence-based optical biosensor employing PSi in combination with novel capture probes, is a one-step assay presented by Yoo et al. [92]. In this assay, a macroporous PSi is modified with streptavidin through physical adsorption followed

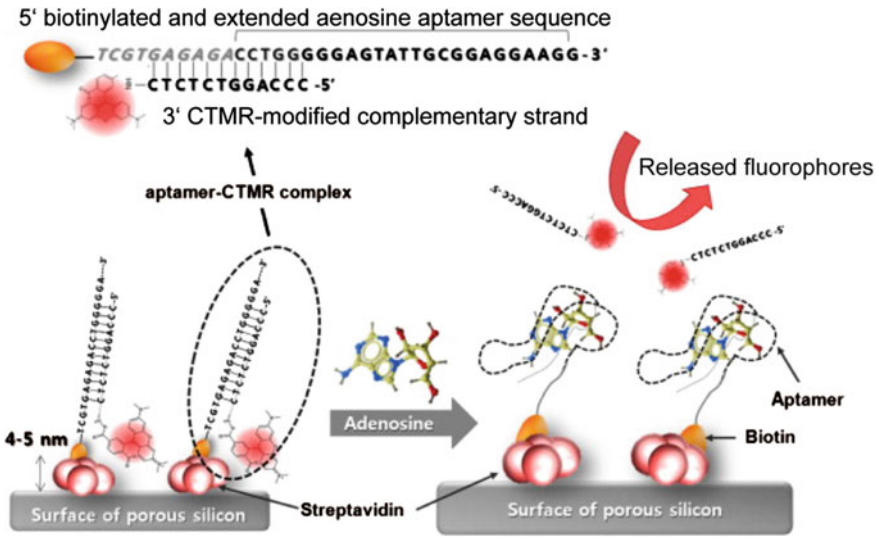

Fig. 4.2 Schematic illustration of the assay for adenosine detection based on fluorescence-quenching in an aptamer-based macroporous silicon structure. Adapted with permission [92]

by the introduction of biotin-conjugated DNA aptamer, directed against the target adenosine. The biosensor is geared up by hybridization of a complementary strand modified with the fluorescent reporter probe, carboxytetramethylrhodamine (CTMR), to the aptamer. A detailed scheme of the assay is presented in Fig. 4.2. Close proximity of the CTMR to the PSi surface effectively quenches the fluorescence, while a target-induced dissociation of the complementary strand in the presence of adenosine target, restores the fluorescence by releasing the fluorophore. The macroporous silicon structure is produced by electrochemical etch with a characteristic pore size distribution between 0.8 and 1.6 μm, and its protein adsorption capacity is determined to be 93.75 μg/cm^2. The high hydrophilicity and high surface area of the scaffold allows for simple and dense immobilization of the protein probes [104] building further up to the attachment of the aptamer receptor. The quenching of organic dyes on the scaffold was found to be most efficient when close proximity of the molecules to the silicon matrix is kept, as this ensures efficient energy transfer [105, 106], whereas oxide layers or other spacers can hinder this phenomenon in distances >30 nm from the scaffold [105–107]. Additional quenching effects are not only achieved by the suitable transducer here, but also by the guanines abundantly contained in the aptamer sequence due to electron transfer from aromatic compounds [108]. This combination of fluorescence quenching renders the biosensor highly effective to sensitive target detection and indeed, the proposed platform showed reliable detection in sub-micromolar concentrations. While basal adenosine blood-levels range from 20 to 200 nM [109], hypoxic tissue

or inflammatory response easily boost the concentrations to the 10–100 fold [110, 111]. Therefore, the presented assay has the potential to differentiate between normal blood-level and increased adenosine concentrations. In comparison to conventional analytical methods for the detection of adenosine, e.g. HPLC or enzyme-based electrochemical sensors, which are not suitable for fast and high throughput analysis [112, 113], usage of aptamers as receptor molecules profits from easy labeling procedures, high affinity and specificity of this novel capture probe [114]. However, previously developed aptasensors either lack in sufficient sensitivity [115] or require implementation of other nanomaterials such as graphene [116] or single-walled carbon nanotubes [117], involving laborious and time intensive production processes, whereas the use of PSi as transducer provides a simple platform and invites this proof-of-concept study to be extended with other aptamer-target pairs. Nevertheless, the assay should be studied with real samples, as components in complex biological fluids may impede with the quenching and de-quenching effects and nonspecific adsorption onto the biosensor surface should be assessed. Moreover, assay time dependency should to be carefully studied, especially when application in the field might necessitate washing steps prior to analysis.

Our own research efforts are aimed at the development of a generic biosensor scheme that utilizes aptamers as capture probes. Herein, we exploit the aptamers' superior properties in terms of stability and reversible folding. Our work [93, 118] describes, for the first time, the design and characterization of a label-free optical PSi-based aptasensor. An oxidized porous silicon nanostructure (Fabry-Pérot thin film), serving as the optical transducer, is conjugated with a well-characterized his-tag binding aptamer (6H7) [119, 120]. This aptamer system has been previously used in protein downstream processing and was thoroughly studied in microarray applications as described by Walter et al. [121]. In a first step, we confirmed successful immobilization of the aptamer throughout the oxidized PSi ($PSiO_2$) scaffold. Aptamer-protein binding events, occurring within the nano-scale pores, are monitored in real time, confirming affinity of the aptamer-immobilized $PSiO_2$ towards the target proteins in μM range (as anticipated by this specific aptamer binding characteristics) [69]. The assay scheme is outlined in Fig. 4.3, showing a typical biosensing experiment in which the reflectivity spectra of the porous film are monitored in real time and corresponding effective optical thickness (EOT) values are computed. The figure presents the change in the relative EOT values ($EOT/EOT_{t=0}$) upon exposure of the 6H7-functionalized $PSiO_2$ to lipase (T6 from *Geobacillus stearothermophilus*, molecular weight 44 kDa), which is used as a model his-tagged protein. After baseline establishment with an appropriate buffer, the analyte solution is introduced and the biosensor is incubated with the solution. A rapid increase in the relative EOT value is observed, which is attributed to the infiltration of the protein solution into the pores and to binding events of the his-tagged protein to the 6H7 aptamer. Subsequently, the target solution is removed and the biosensor is thoroughly rinsed with a buffer to remove unbound species, inducing a sharp decrease in the relative EOT after which a stable signal is attained. Thus, the significant change in EOT, corresponding to a net shift of 40 nm, is attributed to binding of the target protein to the aptamer-functionalized surface.

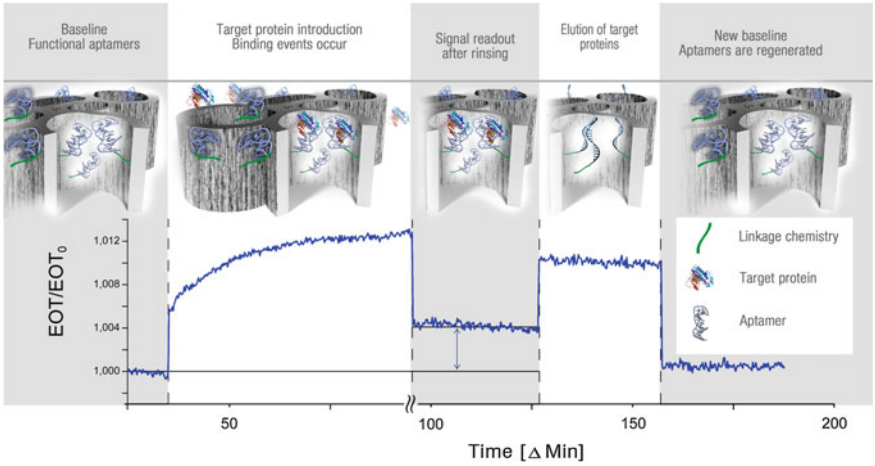

Fig. 4.3 Relative EOT value versus time of 6H7-functionalized $PSiO_2$ during a typical biosensing experiment. A baseline is obtained in buffer solution followed by the introduction of lipase solution, binding events occur and the signal increases rapidly. After a rinse step to remove unbound molecules, a stable readout signal is attained. Competitive elution with 1 M imidazole leads to the release of the captured target protein and the rapid removal of such in the following rinse step. Following a short incubation in the aptamer's selection buffer, the biosensor can be restored for subsequent use. Note that during buffer exchange and rinsing, EOT measurements are briefly paused. Adapted with permission [93]

The stability of the EOT signal during the rinsing step implies that the captured protein molecules are tightly bound to the aptamer under these conditions.

During the 6H7 aptamer selection, gentle elution conditions for the resulting sequence to release the captured target were pre-defined, resulting in an aptamer engineered to undergo reversible changes of confirmation when exposed to high concentrations of imidazole. Therefore, the resulting biosensor can withstand repeated cycles of denaturation and renaturation, exhibiting outstanding stability and reusability for numerous subsequent experiments. Indeed, exposing the biosensor to the elution buffer, see Fig. 4.3, results in an immediate increase in EOT signal (due to the higher refractive index of this buffer solution) and induces the release of the target molecules. Following this step and another thorough rinse of the biosensor, the relative EOT readout returns to its original value and a new cycle can be initiated (see Fig. 4.4).

The notably high selectivity and specificity of the proposed biosensing scheme is demonstrated in several controls: aptamer-conjugated $PSiO_2$ are exposed to non-target protein solutions, mixtures of proteins as well as to complex biological fluids such as bacteria in their culturing medium and bacterial lysates. All these experiments confirmed the very low non-specific adsorption of unrelated molecules on the aptamer-functionalized surface, indicating that the biosensor is suitable for application in real samples.

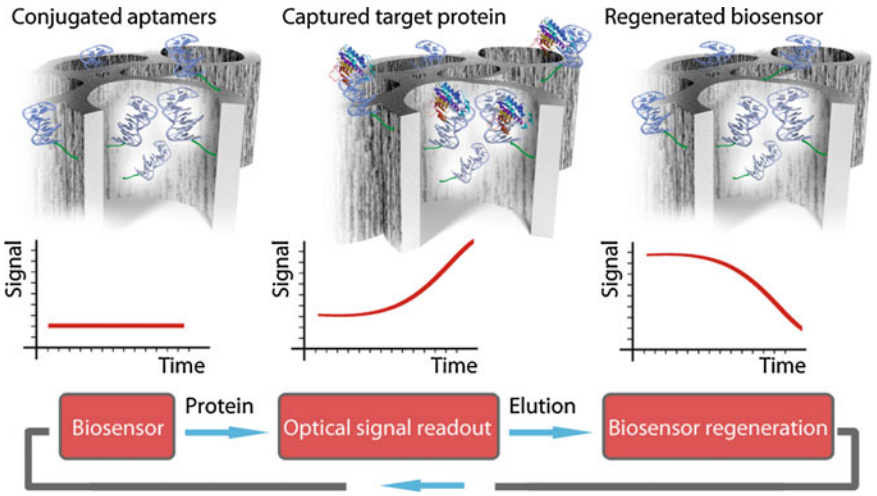

Fig. 4.4 The concept of the aptamer-porous silicon biosensor. Adapted with permission from [93]

A limitation of the presented biosensing scheme lies in the sensitivity of the sensor. Due to the poor dissociation constant of the 6H7 aptamer [69], a linear response could only be shown in the micromolar range. However, as the study has a proof-of-concept character, we expect to adapt this principle for other aptamers displaying nanomolar dissociation constants against highly relevant target molecules. This will allow the design of simple, flexible, inexpensive, robust and portable biosensing platforms combining the superior properties of aptamer capture probes and PSi-optical transducers.

4.3.2 Electrochemical Biosensors

In electrochemical biosensors, the investigated reaction usually produces or consumes an electro-active moiety due to the activity of the recognition element in the device. An important characteristic of these biosensors is a direct spacial contact between the electrochemical transducer and the bioreceptor, enabling a measurement of either current (amperometric), potential or charge accumulation (potentiometric) between the electrodes [122, 123]. These changes in electrical properties of the biosensor system are induced by the occurrence of analyte attachment to the recognition element. A similar technique that does not require labeling, relies on the measurement of impedance spectra. Here, the observed change in the characteristic impedance spectrum of the sensor is solely based on the binding of the target molecule.

The dielectric constant, space-charge distribution and therefore conductance and capacitance of the PSi transducer are the signal-producing properties in different

electrochemical sensing techniques. These depend on the Si-dopant, the interacting surface area (hence layer thickness and porosity), as well as the number of available binding sites [2, 5, 77, 124]. In order to sensitively follow changes of these properties during target capture, a thorough characterization of the biosensor surface in respect to all relevant parameters is essential.

Zhang et al. successfully demonstrated the application of the well-known tetracycline-aptamer in an electrochemical impedance spectroscopy setup. The aptamer is immobilized within $PSiO_2$ structures via standard silanization and coupling chemistry [125, 126]. The sensor's faradic impedance is measured and compared to a neat PSi sample, showing a decrease in impedance due to aptamer attachment. Upon exposure of the aptamer-functionalized $PSiO_2$ to different concentrations of tetracycline, further decrease in impedance is observed, while the neat PSi (no aptamer) retains constant impedance when subject to different target solutions. The recorded results in form of Nyquist plots are fitted as a function of the semicircle-diameter corresponding to the electron-transfer resistance, as presented in Fig. 4.5. The biosensor shows a linear response in the range between 2.079 and 62.37 nM with the lowest concentration detectable of about 2 nM and the maximum of 100 nM, above which the signal plot remains constant. Utilization of PSi as the transducer allows for bioreceptor immobilization in higher densities in comparison to planar surfaces [127] and accordingly improves the biosensor sensitivity. Although, enzyme-linked immunosorbent assay (ELISA) approaches have shown superior sensitivity levels ($\sim$2 ng/ml [128]), aptasensors still offer a number of advantages especially concerning simplicity of the assay and stability of the fabricated sensors. The work by Zhang et al. [125, 126] does not state or investigate the dissociation constant (K_D) of the aptamer sequence obtained in their SELEX process. Therefore, it is not possible to assess whether the detection method or the K_D value might be the limiting factor for the obtained sensitivity. Thus, further

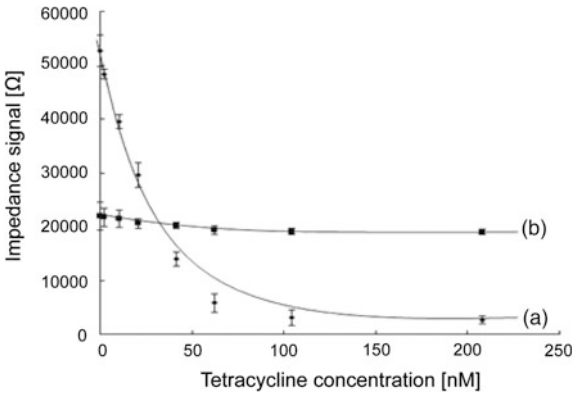

Fig. 4.5 Fitted biosensor signal upon exposure to different target concentrations. Trace **a** shows the response for an aptamer-functionalized PSi biosensor, while trace **b** serves as negative control showing the response of neat PSi (no aptamer). Adapted with permission from [86]

studies using aptamer/target pairs with known dissociation constants in combination with PSi-based impedance assays may result in promising detection schemes, which are highly sensitive yet simple.

A potentiometric PSi-based biosensor for triglyceride (TG) detection was developed by Setzu et al. [85]. As high levels of TG in the bloodstream are linked with cardiovascular problems, there is an increasing demand for simple and rapid TG monitoring systems [129]. The operation principle of the biosensor is the lipase-catalyzed hydrolysis of the TG tributyrin to glycerol and free butyric acid. Fatty acid production induces changes in the solution pH, which are measured using an open circuit potential (OCP) configuration. The enzyme is physisorbed onto an n-type PSi scaffold, which is 50 μm thick. Despite the thickness of the layer, the enzymatic reaction is not limited by the diffusion of tributyrin within the porous film. In fact, the adsorbed lipase follows the Michaelis Menten law, which is widely used to describe enzymatic reactions. It is interesting to mention that the biosensor is reusable and has a relatively long shelf life. Thus, the performance of this biosensing scheme is impressive; however, more work is needed in order to establish a reliable calibration curve, which correlates the change in the OCP to the TG concentration. Nevertheless, this work significantly advances previous potentiometric PSi-based schemes for monitoring of triglycerides [130], in which the enzyme was not loaded into the PSi matrix but rather added to the electrolyte solution together with the tributyrin.

The study by Setzu et al. suggests a promising approach for the detection of analytes, which are the substrates of enzyme-mediated biological reactions. Further studies should optimize the immobilization method (adsorption/covalent immobilization), as well as the enzyme concentration so that the enzymatic reaction will be confined to the linear range of the Michaelis-Menten curve. Also, time of reaction should be optimized and fixed for all measurements.

4.4 Conclusions

In this book chapter, we briefly reviewed novel capture probes and described their properties, emphasizing their advantages and disadvantages when applied in biosensors. We focused on PSi-based biosensors, which combine these new bioreceptors with different transduction schemes. These studies, although few in number, demonstrate the compatibility of PSi with a wide range of novel receptor molecules. As for now, many of the reported biosensors are still in a proof-of-concept stage applying model-systems; nonetheless, we believe that further improvements of the sensors systems will soon enable real applications. PSi, facilitating different transduction strategies, and the broad range of available bioreceptors, both provide a versatile toolbox for developing biosensors that can be tailored to fit the needs of uncountable analytical applications. It is important to keep in mind that for the development of a biosensor, the chosen bioreceptor and PSi-based detection method need to be thoroughly validated for this specific application. It could be

concluded from the given examples, that sensitivity and limit of detection are crucial parameters to determine the applicability of a biosensor. Not only the resolution and sensitivity of the detection have to be considered, but also binding properties of the bioreceptor/target pair as well as possible cross-reactions with other substances involved. Critical studies on these performance-determining issues need to be conducted.

As one of the most promising methods, label-free optical biosensing provides the easiest and most generally applicable method. Excellent examples of effective and reliable biosensors utilizing label-free optical schemes with traditional bioreceptors have already been reported; these biosensing approaches can be further improved by the implementation of novel receptor molecules that will not only enhance the resulting system performance but may also generate new designs (e.g. target-induced dissociation of complementary oligonucleotides from aptamers).

References

1. M.J. Sailor, *Porous Silicon in Practice* (Wiley-VCH, Weinheim, 2011), p. 250
2. A. Jane et al., Porous silicon biosensors on the advance. Trends Biotechnol. **27**(4), 230–239 (2009)
3. L.M. Bonanno, E. Segal, Nanostructured porous silicon-polymer-based hybrids: from biosensing to drug delivery. Nanomedicine **6**(10), 1755–1770 (2011)
4. J. Salonen, V.-P. Lehto, Fabrication and chemical surface modification of mesoporous silicon for biomedical applications. Chem. Eng. J. **137**(1), 162–172 (2008)
5. M. Archer, M. Christophersen, P.M. Fauchet, Macroporous silicon electrical sensor for DNA hybridization detection. Biomed. Microdevices **6**(3), 203–211 (2004)
6. K.A. Kilian, T. Boecking, J.J. Gooding, The importance of surface chemistry in mesoporous materials: lessons from porous silicon biosensors. Chem. Commun. **6**, 630–640 (2009)
7. L.M. Bonanno, L.A. DeLouise, Steric crowding effects on target detection in an affinity biosensor. Langmuir **23**(10), 5817–5823 (2007)
8. L.M. Bonanno, L.A. DeLouise, Tunable detection sensitivity of opiates in urine via a label-free porous silicon competitive inhibition immunosensor. Anal. Chem. **82**(2), 714–722 (2010)
9. N. Massad-Ivanir et al., Engineering nanostructured porous SiO(2) surfaces for bacteria detection via "direct cell capture". Anal. Chem. **83**(9), 3282–3289 (2011)
10. S. Chan et al., Identification of gram negative bacteria using nanoscale silicon microcavities. J. Am. Chem. Soc. **123**(47), 11797–11798 (2001)
11. N. Massad-Ivanir, E. Segal, *12—Porous Silicon for Bacteria Detection*, in *Porous Silicon for Biomedical Applications*, ed. by H.A. Santos (Woodhead Publishing, Finland, 2014), pp. 286–303
12. G. Shtenberg, E. Segal, *Porous Silicon Optical Biosensors*, in *Handbook of Porous Silicon*, ed. by L. Canham, (Springer International Publishing, Switzerland, 2014), pp. 1–11
13. C. Pacholski, Photonic crystal sensors based on porous silicon. Sensors **13**(4), 4694–4713 (2013)
14. K.P.S. Dancil, D.P. Greiner, M.J. Sailor, A porous silicon optical biosensor: detection of reversible binding of IgG to a protein A-modified surface. J. Am. Chem. Soc. **121**(34), 7925–7930 (1999)

15. A. Janshoff et al., Macroporous p-type silicon Fabry-Perot layers. Fabrication, characterization, and applications in biosensing. J. Am. Chem. Soc. **120**(46), 12108–12116 (1998)
16. V.S.-Y. Lin et al., A porous silicon-based optical interferometric biosensor. Science **278** (5339), 840–843 (1997)
17. A. Salis et al., *Porous Silicon-based Electrochemical Biosensors*, in *Biosensors—Emerging Materials and Applications*, ed. by P.A. Serra.(InTech, Croatia, 2011)
18. D.R. Thévenot et al., Electrochemical biosensors: recommended definitions and classification. Biosens. Bioelectron. **16**(1–2), 121–131 (2001)
19. A.P.F. Turner, Current trends in biosensor research and development. Sens. Actuators **17**(3–4), 433–450 (1989)
20. K. Kahn, K.W. Plaxco, *Principles of Molecular Recognition*, in *Recognition Receptors in Biosensors*, ed by M. Zourob (Springer, New York, 2011), pp. 3–46
21. M. Zourob, *Recognition Receptors in Biosensors* (Springer, New York Dordrecht Heidelberg London, 2010)
22. S.A. Piletsky, M.J. Whitcombe (eds.), *Designing Receptors for the Next Generation of Biosensors*. in Springer Series on Chemical Sensors and Biosensors, ed. by G. Urban. Vol. 12 (Springer, Heidelberg, 2013)
23. S. Tonegawa, Somatic generation of antibody diversity. Nature **302**(5909), 575–581 (1983)
24. J.P. Kim et al., Ultrasensitive carbon nanotube-based biosensors using antibody-binding fragments. Anal. Biochem. **381**(2), 193–198 (2008)
25. P. Holliger, P.J. Hudson, Engineered antibody fragments and the rise of single domains. Nat. Biotechnol. **23**(9), 1126–1136 (2005)
26. A.C.A. Roque, C.R. Lowe, M.A. Taipa, Antibodies and genetically engineered related molecules: production and purification. Biotechnol. Prog. **20**(3), 639–654 (2004)
27. K. Shreder, Synthetic haptens as probes of antibody response and immunorecognition. METHODS: A Companion to Methods in Enzymology **20**(3), 372–379 (2000)
28. N.A.E. Hopkins, *Antibody engineering for Biosensor Applications*, in *Recognition Receptors in Biosensors*, ed. by M. Zourob (Springer, New York, 2010), pp. 451–529
29. L.C. Clark, C. Lyons, Electrode systems for continuous monitoring in cardiovascular surgery. Ann. N. Y. Acad. Sci. **102**(1), 29–000 (1962)
30. H.G. Hundeck et al., Calorimetric biosensor for the detection and determination of enantiomeric excesses in aqueous and organic phases. Biosens. Bioelectron. **8**(3–4), 205–208 (1993)
31. B.D. Leca-Bouvier, L.C. Blum, *Enzyme for Biosensing Applications*, in *Recognition Receptors in Biosensors*, ed. by M. Zourob (Springer, New York ,2010), pp. 177–220
32. I. Axarli, A. Prigipaki, N.E. Labrou, Engineering the substrate specificity of cytochrome P450CYP102A2 by directed evolution: production of an efficient enzyme for bioconversion of fine chemicals. Biomol. Eng. **22**(1–3), 81–88 (2005)
33. M. Ostermeier, Engineering allosteric protein switches by domain insertion. Protein Eng. Des. Sel. **18**(8), 359–364 (2005)
34. J.P. Chambers et al., Biosensor recognition elements. Curr. Issues Mol. Biol. **10**, 1–12 (2008)
35. R.E.W. Hancock, H.-G. Sahl, Antimicrobial and host-defense peptides as new anti-infective therapeutic strategies. Nat. Biotech. **24**(12), 1551–1557 (2006)
36. C.D. Fjell et al., Designing antimicrobial peptides: form follows function. Nat. Rev. Drug. Discov. **11**(1), 37–51 (2012)
37. L. Shriver-Lake et al., *Antimicrobial Peptides for Detection and Diagnostic Assays*, in *Designing Receptors for the Next Generation of Biosensors*, ed. by S.A. Piletsky, M. J. Whitcombe (Springer, Heidelberg, 2013), pp. 85–104
38. M.S. Mannoor et al., Electrical detection of pathogenic bacteria via immobilized antimicrobial peptides. Proc Natl Acad Sci U S A **107**(45), 19207–19212 (2010)
39. I.E. Tothill, *Peptides as Molecular Receptors*, in *Recognition Receptors in Biosensors*, ed. by M. Zourob (Springer, New York, 2010), pp. 249–274

40. S. Rotem et al., Analogous oligo-acyl-lysines with distinct antibacterial mechanisms. FASEB J. **22**(8), 2652–2661 (2008)
41. A.P.F. Turner, Biochemistry—biosensors sense and sensitivity. Science **290**(5495), 1315–1317 (2000)
42. J.C. Liao et al., Development of an advanced electrochemical DNA biosensor for bacterial pathogen detection. J. Mol. Diagn. **9**(2), 158–168 (2007)
43. F. Farabullini et al., Disposable electrochemical genosensor for the simultaneous analysis of different bacterial food contaminants. Biosens. Bioelectron. **22**(7), 1544–1549 (2007)
44. Y. Shin, A.P. Perera, M.K. Park, Label-free DNA sensor for detection of bladder cancer biomarkers in urine. Sens. Actuators B-Chem. **178**, 200–2006 (2013)
45. F. Stahl, Analysis of genregulation—DNA chip technology. Chem. unserer Zeit **39**(3), 188–194 (2005)
46. Y.V. Gerasimova, J. Ballantyne, D.M. Kolpashchikov, Detection of SNP-containing human DNA sequences using a split sensor with a universal molecular beacon reporter. Methods Mol. Biol. **1039**, 69–80 (2013)
47. J. Wang, From DNA biosensors to gene chips. Nucleic Acids Res. **28**(16), 3011–3016 (2000)
48. F. Eckstein, G. Gish, Phosphorothioates in molecular-biology. Trends Biochem. Sci. **14**(3), 97–100 (1989)
49. B. Vester, J. Wengel, LNA (Locked nucleic acid): high-affinity targeting of complementary RNA and DNA. Biochemistry **43**(42), 13233–13241 (2004)
50. A. Vainrub, B.M. Pettitt, Coulomb blockage of hybridization in two-dimensional dna arrays. Phys. Rev. E. **66**(4) (2002)
51. A.N. Rao, D.W. Grainger, Biophysical properties of nucleic acids at surfaces relevant to microarray performance. Biomater. Sci. **2**(4), 436–471 (2014)
52. P.E. Nielsen et al., Sequence selective recognition of DNA by strand displacement with a thymine-substituted polyamide. Science **254**, 1498–1500 (1991)
53. E. Mateo-Martí, C.-M. Pradier, *A Novel Type of Nucleic Acid-based Biosensors: the Use of PNA Probes, Associated with Surface Science and Electrochemical Detection Techniques* in *Intelligent and biosensor*, ed. by V.S. Somerset (InTech, Croatia, 2010)
54. A.D. Ellington, J.W. Szostak, In vitro selection of RNA molecules that bind specific ligands. Nature **346**(6287), 818–822 (1990)
55. D.L. Robertson, G.F. Joyce, Selection in vitro of an RNA enzyme that specifically cleaves single-stranded DNA. Nature **344**(6265), 467–468 (1990)
56. C. Tuerk, L. Gold, Systematic evolution of ligands by exponential enrichment: RNA ligands to bacteriophage T4 DNA polymerase. Science **249**(4968), 505–510 (1990)
57. R. Stoltenburg, N. Nikolaus, B. Strehlitz, Capture-selex: selection of dna aptamers for aminoglycoside antibiotics. J. Anal. Methods Chem 415697, 14 (2012)
58. R. Stoltenburg, C. Reinemann, B. Strehlitz, FluMag-SELEX as an advantageous method for DNA aptamer selection. Anal. Bioanal. Chem. **383**(1), 83–91 (2005)
59. A. Nitsche et al., One-step selection of Vaccinia virus-binding DNA aptamers by MonoLEX. BMC Biotechnol. **7**, 48 (2007)
60. D.J. Patel, Structural analysis of nucleic acid aptamers. Curr. Opin. Chem. Biol. **1**(1), 32–46 (1997)
61. T. Hermann, D.J. Patel, Biochemistry—adaptive recognition by nucleic acid aptamers. Science **287**(5454), 820–825 (2000)
62. B. Strehlitz, N. Nikolaus, R. Stoltenburg, Protein detection with aptamer biosensors. Sensors **8**(7), 4296–4307 (2008)
63. J.-G. Walter, F. Stahl, T. Scheper, Aptamers as affinity ligands for downstream processing. Eng. Life Sci. **12**(5), 496–506 (2012)
64. J.-G Walter et al., Aptasensors for small molecule detection. Z. Naturforsch. **67b** 976–986 (2012)
65. M. Loenne et al., *Aptamer-modified Nanoparticles as Biosensors*, in *Biosensors Based on Aptamers and Enzymes—Advances in biochemical engineering/biotechnology*, ed. by M.B. Gu, H.-S. Kim (Springer, Heidelberg, 2014), pp. 121–154

66. A. Heilkenbrinker et al., Identification of the target binding site of ethanolamine binding aptamers and its exploitation for ethanolamine detection. Anal. Chem. **87**(1), 677–685 (2015)
67. N. Hamaguchi, A. Ellington, M. Stanton, Aptamer beacons for the direct detection of proteins. Anal. Biochem. **294**(2), 126–131 (2001)
68. R. Stoltenburg, C. Reinemann, B. Strehlitz, SELEX–a (r)evolutionary method to generate high-affinity nucleic acid ligands. Biomol. Eng. **24**(4), 381–403 (2007)
69. Ö. Kökpinar et al., Aptamer-based downstream processing of his-tagged proteins utilizing magnetic beads. Biotechnol. Bioeng. **108**(10), 2371–2379 (2011)
70. G. Zhu, J.-G. Walter, *Aptamer-Modified Magnetic Beads in Affinity Separation of Proteins*, in *Affinity Chromatography: Methods and Protocols,* 2nd edn. ed. by S. Reichelt (Springer Protocols, Humana Press, 2015), pp. 67–82
71. E.J. Lee et al., Peptide nucleic acids are an additional class of aptamers. Rsc Advances **3**(17), 5828–5831 (2013)
72. R. Bredehorst et al., *Method for determining an unknown PNA sequence and uses thereof*, ed. by E.P. Specification 2005
73. G. Vasapollo et al., Molecularly imprinted polymers: present and future prospective. Int. J. Mol. Sci. **12**(9), 5908–5945 (2011)
74. S.A. Piletsky et al., Substitution of antibodies and receptors with molecularly imprinted polymers in enzyme-linked and fluorescent assays. Biosens. Bioelectron. **16**(9–12), 701–707 (2001)
75. T.A. Sergeyeva et al., Selective recognition of atrazine by molecularly imprinted polymer membranes. Development of conductometric sensor for herbicides detection. Anal. Chim. Acta **392**(2–3), 105–111 (1999)
76. R.J. Umpleby et al., Characterization of the heterogeneous binding site affinity distributions in molecularly imprinted polymers. J. Chromatogr. B-Anal. Technol. Biomed. Life Sci. **804** (1), 141–149 (2004)
77. F.A. Harraz, Porous silicon chemical sensors and biosensors: a review. Sens. Actuators B: Chem. **202**, 897–912 (2014)
78. L.A. DeLouise, P.M. Kou, B.L. Miller, Cross-correlation of optical microcavity biosensor response with immobilized enzyme activity. Insights biosens. sensitivity Anal. Chem. **77**(10), 3222–3230 (2005)
79. Z. Deng, E.C. Alocilja, Characterization of nanoporous silicon-based dna biosensor for the detection of salmonella enteritidis. Sens. J. IEEE **8**(6), 775–780 (2008)
80. S.B. de Leon et al., Neurons culturing and biophotonic sensing using porous silicon. Appl. Phys. Lett. **84**(22), 4361–4363 (2004)
81. M.P. Stewart, J.M. Buriak, Chemical and biological applications of porous silicon technology. Adv. Mater. **12**(12), 859–869 (2000)
82. A. Birner et al., Silicon-based photonic crystals. Adv. Mater. **13**(6), 377–388 (2001)
83. J.E. Lugo et al., Electrochemical sensing of dna with porous silicon layers. J. New Mater. Electrochem. Syst. **10**(2), 113–116 (2007)
84. M.J. Song et al., Electrochemical biosensor array for liver diagnosis using silanization technique on nanoporous silicon electrode. J. Biosci. Bioeng. **103**(1), 32–37 (2007)
85. S. Setzu et al., Porous silicon-based potentiometric biosensor for triglycerides. physica status solidi(a). **204**(5), 1434–1438 (2007)
86. J. Zhang et al., Label-free electrochemical detection of tetracycline by an aptamer nano-biosensor. Anal. Lett. **45**(9), 986–992 (2012)
87. M. Simion et al., Dual detection biosensor based on porous silicon substrate. Mater. Sci. Engi. B-Adv. Funct. Solid-State Mater. **178**(19), 1268–1274 (2013)
88. L.M. Bonanno, L.A. DeLouise, Tunable detection sensitivity of opiates in urine via a label-free porous silicon competitive inhibition immunosensor. Anal. Chem. **82**(2), 714–722 (2009)
89. G. Shtenberg et al., Picking up the pieces: a generic porous si biosensor for probing the proteolytic products of enzymes. Anal. Chem. **85**(3), 1951–1956 (2012)

90. K.A. Kilian et al., Peptide-modified optical filters for detecting protease activity. ACS Nano **1** (4), 355–361 (2007)
91. K.R. Beavers et al. *Porous Silicon Functionalization for Drug Delivery and Biosensing by In Situ Peptide Nucleic Acid Synthesis*. in *Porous Semiconductors—Science and Technology* (Alicante-Benidorm, Spain, 2014)
92. L. Yoo et al., A simple one-step assay platform based on fluorescence quenching of macroporous silicon. Biosens. Bioelectron. **41**, 477–483 (2013)
93. K. Urmann et al., Label-free optical biosensors based on aptamer-functionalized porous silicon scaffolds. Anal. Chem. **87**(3), 1999–2006 (2015)
94. V.M. Starodub et al., Control of myoglobin level in a solution by an immune sensor based on the photoluminescence of porous silicon. Sens. d Actuators B: Chem. **58**(1–3), 409–414 (1999)
95. A.G. Cullis, L.T. Canham, Visible light emission due to quantum size effects in highly porous crystalline silicon. Nature **353**(6342), 335–338 (1991)
96. L.T. Canham, K. (Firm), *Properties of porous silicon EMIS datareviews series no. 18*. ed. by Leigh Canham (Institution of Electrical Engineers, London, 1997)
97. O. Bisi, S. Ossicini, L. Pavesi, Porous silicon: a quantum sponge structure for silicon based optoelectronics. Surf. Sci. Rep. **38**(1–3), 1–126 (2000)
98. G. Gaur, D. Koktysh, S.M. Weiss. Porous silicon biosensors using quantum dot signal amplifiers. Proc. of SPIE 8594, 859408 (2013)
99. X. Fan et al., Sensitive optical biosensors for unlabeled targets: a review. Anal. Chim. Acta **620**(1–2), 8–26 (2008)
100. C. Pacholski et al., Reflective interferometric fourier transform spectroscopy: a self-compensating label-free immunosensor using double-layers of porous SiO2. J. Am. Chem. Soc. **128**, 4250–4252 (2006)
101. L.M. Bonanno, L.A. DeLouise, Whole blood optical biosensor. Biosens. Bioelectron. **23**(3), 444–448 (2007)
102. M.M. Orosco et al., Protein-coated porous-silicon photonic crystals for amplified optical detection of protease activity. Adv. Mater. **18**(11), 1393–1396 (2006)
103. C. Pacholski et al., Biosensing using porous silicon double-layer interferometers: reflective interferometric Fourier transform spectroscopy. J. Am. Chem. Soc. **127**(33), 11636–11645 (2005)
104. A. Ressine, G. Marko-Varga, T. Laurell, *Porous silicon protein microarray technology and ultra-/superhydrophobic states for improved bioanalytical readout*, in *Biotechnology Annual Review*, ed. by M.R. El-Gewely (Elsevier 2007), pp. 149–200
105. L. Danos, R. Greef, T. Markvart, Efficient fluorescence quenching near crystalline silicon from Langmuir-Blodgett dye films. Thin Solid Films **516**(20), 7251–7255 (2008)
106. H.M. Nguyen et al., Efficient radiative and nonradiative energy transfer from proximal cdse/zns nanocrystals into silicon nanomembranes. ACS Nano **6**(6), 5574–5582 (2012)
107. L. Gu, M. Orosco, M.J. Sailor, *Detection of protease activity by FRET using porous silicon as an energy acceptor.* physica status solidi (a), **206**(6) pp. 1374–1376 (2009)
108. J.R. Unruh et al., Orientational dynamics and dye-dna interactions in a dye-labeled dna aptamer. Biophys. J. **88**(5), 3455–3465 (2005)
109. B.P. Ramakers et al., Measurement of the endogenous adenosine concentration in humans in vivo: methodological considerations. Curr. Drug Metab. **9**(8), 679–685 (2008)
110. J. Stagg, M.J. Smyth, Extracellular adenosine triphosphate and adenosine in cancer. Oncogene **29**(39), 5346–5358 (2010)
111. G. Schulte, B.B. Fredholm, Signalling from adenosine receptors to mitogen-activated protein kinases. Cell. Signal. **15**(9), 813–827 (2003)
112. L. Bekar et al., Adenosine is crucial for deep brain stimulation-mediated attenuation of tremor. Nat. Med. **14**(1), 75–80 (2008)
113. L.A. Conlay et al., Caffeine alters plasma adenosine levels. Nature **389**(6647), 136–136 (1997)

114. D.E. Huizenga, J.W. Szostak, A DNA aptamer that binds adenosine and ATP. Biochemistry **34**(2), 656–665 (1995)
115. J. Zhang et al., Aptamer-based multicolor fluorescent gold nanoprobes for multiplex detection in homogeneous solution. Small **6**(2), 201–204 (2010)
116. S. Guo et al., Solid-state label-free integrated aptasensor based on graphene-mesoporous silica-gold nanoparticle hybrids and silver microspheres. Anal. Chem. **83**(20), 8035–8040 (2011)
117. L. Zhang et al., A carbon nanotubes based ATP apta-sensing platform and its application in cellular assay. Biosens. Bioelectron. **25**(8), 1897–1901 (2010)
118. K. Urmann et al. *Highly Generic Aptamer-Based Porous Si Optical Biosensors*. in *Porous Semiconductors—Science and Technology*.(Alicante-Benidorm, Spain, 2014)
119. S.A. Doyle, M.B. Murphy, U.S. Patent *Aptamers and methods for their in vitro selection and uses thereof* 2005
120. G. Zhu et al., Characterization of optimal aptamer-microarray binding chemistry and spacer design. Chem. Eng. Technol. **34**(12), 2022–2028 (2011)
121. J.G. Walter et al., Systematic investigation of optimal aptamer immobilization for protein-microarray applications. Anal. Chem. **80**(19), 7372–7378 (2008)
122. D. Grieshaber et al., Electrochemical biosensors—sensor principles and architectures. Sensors **8**(3), 1400–1458 (2008)
123. D.R. Thevenot et al., Electrochemical biosensors: recommended definitions and classification: biosens Bioelectron. **16**(1–2), 121–131 (2001)
124. F. De Filippo et al., *Measurement of Porous Silicon Dielectric Constant by VUV Laser Harmonic Radiation.* physica status solidi (a), 2000. **182**(1) pp. 261–266
125. J. Zhang et al., Nano-porous light-emitting silicon chip as a potential biosensor platform. Anal. Lett. **40**(8), 1549–1555 (2007)
126. J. Zhang et al., A label free electrochemical nanobiosensor study. Anal. Lett. **42**(17), 2905–2913 (2009)
127. Y.-J. Kim et al., Electrochemical aptasensor for tetracycline detection. Bioprocess Biosyst. Eng. **33**(1), 31–37 (2010)
128. C.C. Weber et al., Broad-spectrum protein biosensors for class-specific detection of antibiotics. Biotechnol. Bioeng. **89**(1), 9–17 (2005)
129. C.S. Pundir, J. Narang, Determination of triglycerides with special emphasis on biosensors: a review. Int. J. Biol. Macromol. **61**, 379–389 (2013)
130. R.R.K. Reddy et al., Estimation of triglycerides by a porous silicon based potentiometric biosensor. Curr. Appl. Phys. **3**(2–3), 155–161 (2003)

Chapter 5
Biomedical Uses of Porous Silicon

Steven J.P. McInnes and Rachel D. Lowe

Abstract The versatility of porous silicon (pSi), due to the myriad of possible structures, ease of chemical modification and inherent biocompatibility, has resulted in it being readily tailored for numerous biomedical applications. Commonly prepared via the anodisation of crystalline silicon wafers in HF electrolyte, pSi can be produced as films, microparticles, nanoparticles and free-standing membranes. The combination of both its unique physical properties and the incorporation of stable surface functionalities have been fundamental to its performance. Through an immense number of modification techniques, numerous species from antibodies to polymers can be integrated into pSi structures. This adaptability has produced materials with an increased half-life both in vitro and in vivo and enabled the development of both targeted detection platforms and local delivery of therapeutic payloads. As a result, modified pSi has been readily applied to a range of biomedical applications including molecular detection, drug delivery, cancer therapy, imaging and tissue engineering.

5.1 Introduction

The emergence of nanomaterials with characteristics different from the bulk material has resulted in an explosion of new applications in many fields, including water purification [1], energy collection/storage [2], and medicine [3]. One such material that has impacted a number of fields is porous silicon (pSi). pSi offers a

S.J.P. McInnes (✉)
ARC Centre of Excellence in Convergent Bio-Nano Science and Technology, Mawson Institute, University of South Australia, 5095 Mawson Lakes, Australia
e-mail: steven.mcinnes@unisa.edu.au

R.D. Lowe (✉)
Biological Micro- and Nanotechnology, Max Plank Institute for Biophysical Chemistry, 37077 Göttingen, Germany
e-mail: rachel.lowe@mpibpc.mpg.de

D. Losic and A. Santos (eds.), *Electrochemically Engineered Nanoporous Materials*, Springer Series in Materials Science 220,
DOI 10.1007/978-3-319-20346-1_5

number of advantages over other nanomaterials including tunable pore dimensions, surface chemistry and degradation rates [4]. In particular, this has allowed pSi to acquire tailored responses to specific biological environments [5], which has significant value for the biomedical field.

Production of various two and three-dimensional pSi forms with different surface chemistries including the integration of polymers has resulted in many new biomedical applications. Exploitation of optical, electrical, photoluminesence and chemical nature of the porous structure has given rise to the development of chemical and biological sensors [6]. Studies with pSi have also focused on optimizing the loading capacity, cell adhesion, biocompatibility and biodegradability for drug delivery and implantation applications. The ability of the pSi to degrade in the body has lead to the fabrication of substrates with specific degradation rates which can be matched to the growth rate of the tissue under repair, leaving no long-term trace in vivo [7–9]. Combining pSi with a wide variety of chemistries and secondary nanoparticle payloads has also lead to the improvement of a wide variety of biomedical imaging modes.

This chapter will examine the properties of porous silicon (pSi) and their exploitation for biomedical applications.

5.2 pSi Fabrication and Properties

5.2.1 Fabrication Procedures

Porous silicon (pSi) is commonly fabricated from bulk silicon by electrochemical etching in ethanol and hydrofluoric acid (HF) mixtures [10]. pSi films can then be easily processed into a variety of forms including membranes, microparticles (MPs) and nanoparticles (NPs). pSi membranes can be formed via the removal of pSi film from bulk silicon through electropolishing, achieved when there is a low concentration of HF or a high current density [11]. Subsequently pSi MPs are produced by fracturing thin pSi membranes via sonication [12–15] or other mechanical forces [16, 17]. Extended sonication or ball milling of etched pSi leads to the formation of pSi nanoparticles (NPs) [18–20]. While electrochemical etching is the most common fabrication method for pSi, to generate pSi without the use of an applied current, stain etching can be used [21, 22]. This method is often employed to introduce porosity to shaped structures and particles that cannot have a current easily applied to them. Other techniques such as photochemical, galvanic, hydrothermal and spark processing can also be used to generate pSi [22]. More details on pSi fabrication and the underlying chemistry and mechanisms can be found in the following literature [23–25] and also reviewed in this book (in Chap. 1 contributed by A. Santos and T. Kumeria).

5.2.2 Porous Structure

There is not just one type of pSi and consequently it possesses an array of unique physical and material characteristics [26]. Different porous structures with distinct pore morphologies can be generated by simply altering fabrication parameters including wafer resistivity, HF concentrations and current densities [23, 27, 28]. Pore sizes range in diameter from a few nanometers to several microns [10]. The various pore size regimes are classified into three categories according to pore diameter; microporous (<2 nm), mesoporous (2–50 nm) and macroporous (>50 nm) [10]. These porous structures enable the generation of high surface areas up to 800 $m^2\ g^{-1}$ [29], which can be exploited to immobilize and load bioactive species, such as proteins and small molecular therapeutics.

Porosity, defined as the void fraction of the total volume, is another feature of pSi that can be tuned using different electrolyte mixtures and current densities [30]. The porosity of pSi has been fabricated as low as 5 % [31] and as high as 95 % [32]. Consequently, by changing the porosity, the refractive index of pSi is also varied between that of bulk silicon and air. Porosity patterns can also be generated both laterally and vertically [26]. A key feature of pSi fabrication is that when etching conditions are changed during the process, the altered conditions only affect the new layer being formed beneath the pSi layers already generated [5]. Varying the formed porosity periodically with depth has resulted in multilayer devices such as rugate filters [33] and optical microcavities [34], which have been utilized for optical detection platforms and in vivo drug release monitoring.

5.2.3 Optical Properties

Initially, visible photoluminescence of pSi was discovered [35] and attributed to quantum confinement effects [36]. Now the emission wavelength can be adjusted through both the visible and infrared ranges [37]. Subsequently, pSi has been used as an optical transducer exploiting reflectance interference, photonic resonance or photoluminescence. Interference patterns resulting from white light reflectance can be monitored to elucidate variations in the effective optical thickness (EOT). EOT, based on the refractive index, is influenced by the binding or removal of species or material within the pores [38]. The specific capture of target molecules via direct binding to complementary probe molecules results in a positive shift in EOT, while negative shifts can result from the release of species from the surface, or oxidation and degradation of the pSi scaffold [39]. Consequently, the ability to tune the optical properties of pSi has been readily exploited for many applications including bio-sensing [40–42], self-reporting drug delivery [43, 44] and imaging [18, 45, 46].

5.2.4 Biocompatibility

pSi has been shown to be biocompatible both in vitro and in vivo [47, 48]. The biodegradability of pSi [49] is dependent not only on the acidity of the environment but the size, porosity and chemical functionality of the pSi substrate [8, 22, 50, 51]. It has been reported to form non-toxic orthosilicic acid ($Si(OH)_4$) in environments typical of those that exist in vivo [52–54]. However, the residence time can range from weeks to months as demonstrated in the study by Cheng et al. [43]. Unmodified particles injected into rabbit's eyes degraded within 3–4 weeks, without evidence of toxicity but both thermal oxidation and hydrosilylation increased the particles stability and subsequently residence time. Therefore, as new variants of pSi are developed their biological response, potential toxicity and residence time [55] needs to be verified.

5.3 pSi Functionalization

The surface chemistry of pSi can be readily functionalized with a number of chemical modification techniques including oxidation, nitridization, silanization, hydrosilylation, carbonization, hydrocarbonization and electrografting. The most common surface functionalization methods routinely employed for biomedical pSi applications will be outlined here. Comprehensive reviews on the broad topic of pSi functionalization can also be found in the literature [22, 56].

5.3.1 Surface Passivation

The performance of pSi as a biomedical material is contingent on both the control and stability of its surface chemistry. Immediately following electrochemical etching the pSi surface is hydride-terminated (Si–H). However, in both air and aqueous media this surface is unstable, rapidly converting to highly unpredictable compositions of native oxide. In order to overcome this undesired surface variability, pSi surfaces have been intentionally oxidized through a number of techniques [57]. Ozonolysis and thermal oxidation are typically employed, resulting in surfaces that are converted primarily to Si–OH and Si–O–Si groups, for the respective methods. pSi surfaces with hydroxyl termination (Si–OH) are stable in atmospheric conditions, and are both hydrophilic and silane chemistry compatible. By contrast, thermal oxide layers are thicker and more bio-inert.

pSi surface passivation is not limited just to oxidation. In a similar manner to thermal oxidation, thermal nitridization is performed by exposing the surface to a nitrogen gas rich atmosphere [58, 59] and has been reported to stabilize the optical properties [60]. Thermal carbonization (TC) and thermal hydrocarbonization (THC)

is attained by flowing of a mixture of N_2 and acetylene over pSi surfaces at elevated temperatures [61, 62]. The benefits of thermal carbonization of pSi include increased thermal and electrical conductivity, as well as enhanced mechanical strength and chemical stability of the pSi substrate [63].

5.3.2 Silanisation

Chemical functionalization of pSi surfaces with Si–OH termination following oxidation can be achieved with alkoxy- or chlorosilanes in ambient conditions or with moderate temperature elevation [64–66]. Through this simple method, functional groups including amines, isocyanates, methacrylates, polyethylene glycols (PEG) and limitless customized functionalities can be introduced to the pSi surface [54, 67–70]. Numerous silanes can be readily purchased or synthesised. They can also easily be modified further via the use of a myriad of commercially available cross-linking agents. Functionalization of pSi with various surface chemistries can also assist protein adsorption, necessary for cell adhesion. The use of PEG functionalities reduce protein and cell adhesion, creating an anti-fouling surface [22]. Although silane functionalization is a quite popular method, the S–O–Si bonds formed can readily undergo hydrolysis, making the surface moderately unstable in aqueous solutions [71], which is not ideal for biosensors and other platforms that rely on targeting interfaces [72].

5.3.3 Hydrosilylation

Derivatization of Si–H terminated pSi directly, via hydrosilylation, is also widely used. Hydrosilylation is performed by exposing the surface to alkyl groups, [57, 73] resulting in a covalent Si–C bond. Numerous methods of Si–C bond formation exist including thermal [74], chemical [75], photochemical [76, 77], electrochemical [78], and microwave assisted methods [79]. The significant benefits of these methods is that they greatly increase the stability of pSi surfaces in aqueous environments by capping oxidative-susceptible sites and allow the introduction of a broad range of chemical functionalities.

5.3.4 Linking Biomolecules

pSi surfaces can also be modified through the incorporation of more complex organic and biomolecular species. Both Si–H and Si–OH groups can be readily functionalized to include reactive groups that allow the attachment of peptides [80], proteins [81, 82], enzymes [83, 84], antibodies [85–87], and DNA [88–90].

Commonly linked species are reactive with either amine and thiol moieties. Examples of common reactive groups include isocyanate [69], epoxy [91], *N*-hydroxysuccinimide (NHS) [77] and sulfhydryl reactive groups [81, 92]. While the above list is not complete, a resource that extensively covers the field of bioconjugation can be found elsewhere [93]. The two key considerations when immobilizing biomolecules are surface coverage and retention of biological activity and properties for the desired application.

5.3.5 Polymers

pSi can also be functionalized with various polymers, either directly onto the surface or in bulk without covalent attachment [94]. To attach polymers directly, functional anchoring points are first created using surface modification techniques, from which polymer grafting can be performed. Polymer grafting can be performed by "grafting from" polymerization involving a surface with a radial forming species that initiates the process [95–97] or the "grafting to" of preformed polymers [98–100] to the surface. The introduction of polymers to the surface of pSi helps to reduce mechanical brittleness [101] and improve stability of pSi substrates in aqueous biological fluids [96]. Furthermore, capping polymer layers can be used to design responsive devices through pH [102, 103], temperature, [70] or potentially ligand binding [104]. The combination of pSi with polymeric materials improves degradation control, drug release kinetics and surface responses to environmental changes, beneficial to advanced drug delivery devices [4, 105], biodegradable materials for implantation [20] or injection [4] and sensing devices [106].

5.3.6 Dual Functionalization

Recent advances in pSi functionalization include the ability to functionalize the surface with dual chemistries both laterally [69, 77, 107] and vertically [108, 109]. To pattern pSi with dual chemistries in a lateral fashion photolithographic techniques are commonly employed for both silanization [69, 107] and hydrosilylation [77]. Photoresist based patterning enables dual functionalized pSi surfaces to be generated for selective protein patterning [77] and cell attachment [69]. This method allows greater control over feature shape and size, with possible feature sizes smaller than conventional microarray technology. The opportunity for application spans a myriad of biological areas such as microarrays, degradable supports for tissue culture and in vitro cell culture materials capable of drug delivery from the underlying pSi reservoir.

The ability to differentially functionalize the upper surface and the internal surface of the porous network has also been achieved. Kilian et al. [109] exploited wettability properties to selectively functionalize the external and internal structure

of pSi. The entire surface was first stabilized by thermal hydrosilylation of 10-succinimidylundecanoate and subsequently an aqueous solution containing GRGDS peptide was introduced to the external surface. Following, the substrate was exposed to an organic solution, which introduced a second chemistry to the internal porous structure, resulting in dual functionalities. Similarly, a method based on click chemistry was used to functionalize the pSi external surface via ligand free click and the internal pores were subsequently functionalized with ligand assisted click [110]. The successful coupling of the GRGDS peptide to the surface was demonstrated, as well as the attachment of endothelial cells. Dual functionalities has also been achieved by isolating hydrosilylation to the top surface of the pores [108]. Firstly, the entire pSi film is thermally oxidized and filled it with octane. The substrate is then exposed to aqueous HF solution, which strips the oxide from the top of the pores, allowing hydrosilylation to occur only on the oxide stripped pore openings. The hydrophobic pore entrance was then used to slow the release of rhodamine, as shown in Fig. 5.1.

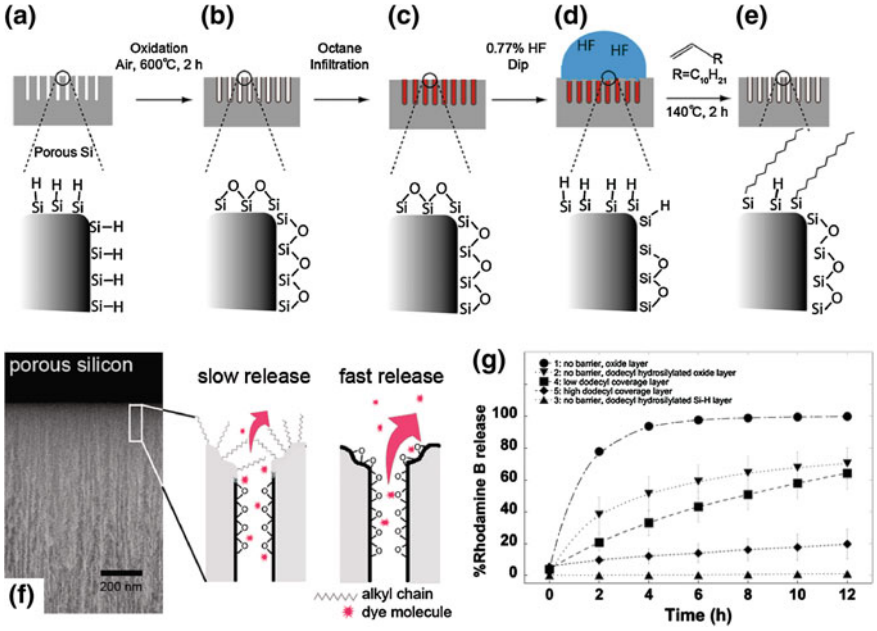

Fig. 5.1 Fabrication of dual functionalized pSi. **a** As fabricated pSi, Si–H terminated, **b** thermally oxidized pSi (600 °C 2 h), **c** infiltration of hydrophobic octane, **d** treatment of octane-infiltrated pSi in aqueous HF to strip the oxide on the external surface of the pSi structure and **e** thermal hydrosilylation of the newly generated external Si–H surface. **f** Schematic representation of the effect of dual functionalization on rhodamine release, including scanning electron microscopy (SEM) side profile image of the pSi network. **g** Release of rhodamine B into PBS from different dual functionalized pSi. Adapted from Wu and Sailor [1]

5.4 pSi in Biomedical Applications

5.4.1 Biomolecular Detection Platforms

pSi has been used as a platform for the detection of many biomedically relevant species including small molecules [111], DNA [82, 112], proteins [42, 113, 114], viruses [115, 116] and bacteria [117]. These methods have typically been demonstrated in the presence of simple aqueous buffers; however, more relevant is the direct analysis of samples with minimal preparation and/or extraction. The work considered here primarily focuses on the application of pSi for the analysis of biofluids and tissues as well as the detection of molecules relevant for biomedical studies.

5.4.1.1 Biosensors

The physical characteristics of pSi, namely large surface area [35, 66], tailored morphological structure [27, 118] and unique optical properties [119], have made it an attractive biosensor surface. pSi biosensors are label free relying on electrical [120–122], electrochemical [123], and optical [82] mechanisms. A few recent reviews comprehensively cover the requirements and applications of pSi biosensors [6, 124–126].

Optical biosensors have been the most prevalent pSi biosensors [127]. These predominantly consist of pSi in the form of thin films [81, 82], microcavities [117, 128], rugate filters [33, 129], Bragg mirrors [38] and waveguides [112, 130]. By utilizing changes in photoluminescence or optical reflectivity of pSi, the detection of proteins [42, 81, 131], enzymatic activity [91, 132, 133], DNA [82, 112, 134], viruses [116] and bacteria [41, 117] have all been shown. The desired selectivity is achieved by chemically tuning the large surface area with biomolecular probes that effectively bind the target molecule from a complex mixture [128]. The resulting environment change, induced by molecule binding, then elicits a detectable spectral shift that requires no labeling [126], broadening the number of targets that can be potentially addressed with this method.

However, the analysis of complex biological samples presents a challenge when considering pSi biosensors as they solely rely on the ability of the surface properties to discriminate the analyte from all other components [135, 136]. Consequently, the modified surface requires robust surface chemistry that limits non-specific binding at physiological pH [72, 81]. One of first demonstrations of complex sample analysis with pSi optical biosensors was the detection of gram negative bacteria [117], using photoluminescent detection. This was achieved by immobilizing a mixture of tetratryptophan ter-cyclopentane (TWTCP) and glycine methyl ester in a 1:10 ratio onto the pSi surface. Diphosphoryl Lipid A, a component in the outer cell membrane of gram negative bacteria, was recognized by TWTCP. In an effort to prevent the four TWTCP amino groups from reacting with the pSi surface and

subsequently blocking the binding receptor, glycine methyl ester was used as the blocking agent. Gram positive bacteria does not contain Lipid A, hence, enabling differential detection between the two cell lysates.

Photoluminescence quenching has also been used to detect the binding of myoglobin to pSi immobilized antibodies in the presence of human serum [137]. The effect of serum dilution was investigated and a detection limit for myoglobin of 10 ng/mL was achieved. The detection of a specific protein in the presence of numerous bacterial proteins ($\sim$2 mg/mL protein content) has also been demonstrated by Ouyang et al. [131]. Their microcavity pSi sensor was immobilized with the Intimin binding domain of the Intimin receptor. The average pore diameter was 120 nm, and the sensor consisted of two eight period Bragg mirrors with a defect layer. A shift in optical reflectance could be observed and quantified when Intimin extracellular domain (Intimin-ECD) was present in *Escherichia coli* cell lysate.

Biofluid analysis has also been shown with the detection of rabbit IgG in both whole blood and serum samples [136]. In this work, both the filtering capabilities and optical parameters of pSi were utilized in a single device. To limit blood clogging and allow sufficient time for the samples to infiltrate the porous network, anti-coagulant was mixed into the samples and the pSi detection platform was maintained in a humidified enclosure. Interference from red blood cells was excluded from the sub 100 nm pores as shown in Fig. 5.2. Also, non-specific protein binding was reduced by bovine serum albumin (BSA) acting as the blocking agent. The specificity of the device with immobilized biotinylated anti-rabbit IgG was tested with a selection of samples including rabbit serum, fetal bovine serum, rabbit blood and human blood. A large wavelength shift was only observed for the target sample, specifically rabbit blood and serum, as shown in Fig. 5.2. Subsequent work by Bonanno et al. measured the presence of small molecules in urine [38]. Sensing relied on competitive binding because the small molecules alone did not result in a detectable change in EOT. This work was further extended to include a blind clinical study [38]. The application of pSi biosensors for the analysis of complex biological samples however is still very limited. An important aspect of the development of pSi biosensors has been the creation of pSi pore sizes greater than 50 nm that allow penetration of biomolecules while maintaining transducer sensitivity [131].

Biosensors comprised of composite materials have also been developed [138]. One recent example is a photonic glucose biosensor that benefited from glucose and pH-responsive surface moieties (thiol-terminated poly(4-vinyl-phenylboronic acid)) grafted onto a porous silicon film [139]. Glucose levels at physiological pH were monitored by changes in effective optical thickness (EOT) caused by changes in the polymers refractive index. A LOD of 0.15 mM was reported, and is lower than current commercially available glucose meters. Interestingly, when glucose in wound fluid was studied, the pH of the solution impacted the observed EOT difference. This suggests the interaction of these sensors in biologically relevant environments is a key parameter to consider for future studies, particularly in the applicability of pSi for implantable biosensors.

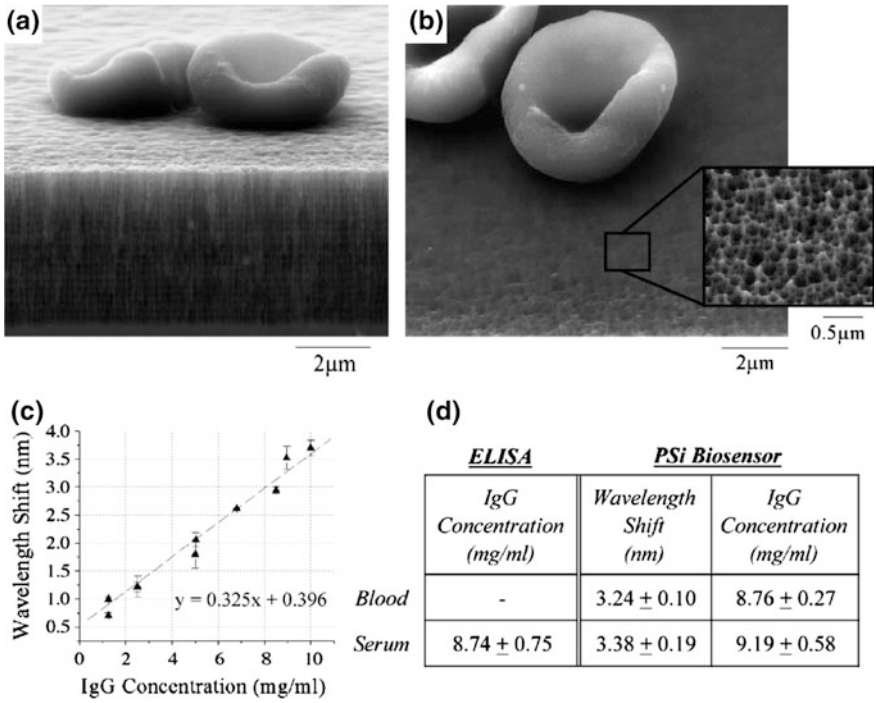

	ELISA	PSi Biosensor	
	IgG Concentration (mg/ml)	*Wavelength Shift (nm)*	*IgG Concentration (mg/ml)*
Blood	-	3.24 ± 0.10	8.76 ± 0.27
Serum	8.74 ± 0.75	3.38 ± 0.19	9.19 ± 0.58

Fig. 5.2 Depiction of the size-exclusion capability of the pSi microcavity biosensor, IgG concentration dependent response and comparative analysis of pSi biosensor and enzyme-linked immunosorbent assay (ELISA) quantification of rabbit IgG in rabbit blood and serum samples. **a** Cross-sectional and **b** top view images of pSi biosensor substrate highlighting erythrocyte exclusion from the porous matrix and subsequently prepared with glutaraldehyde fixation. Inset shows a highly magnified image of the ~88 nm pores. **c** IgG calibration curve showing the wavelength shift for rabbit IgG binding per known rabbit IgG concentrations (st. dev. from n = 9 replicates); **d** comparison of biosensor and ELISA quantification of IgG from the same sample. Male Dutch Belted rabbits were used for blood collection and both the ELISA and the pSi biosensor tests were conducted separately with n = 3 per experiment. Statistical testing (*t*-test) showed ELISA and biosensor results as not statistically different to within 95 % confidence. Adapted from Bonanno and DeLouise [2]

5.4.1.2 Microarrays

Porous silicon microarrays [140] with fluorescent readout have been shown to be amenable to biofluid analysis [141]. Detection of lowly abundant protein biomarkers is made possible by the high surface area of pSi, which increases binding sites and consequently increases sensitivity. The first reported application was the detection of FITC labeled Angiotensin I and II in blood plasma [142]. The ability to either discretely deposit samples and/or antibodies using a piezoelectric microdispenser [140] has allowed array densities of up to 4000 spots/cm^2. This method has

been extended to employ both the sandwich and reverse phase immunoassay [143] approaches typical for enzyme-linked immunosorbent assay (ELISA), which was used to detect Cyclin E from cell and tissue lysates [143].

Predominantly, however, pSi microarrays have been utilised to detect prostate specific antigen (PSA), a biomarker for prostate cancer. PSA has been detected in both spiked serum [141, 144] and clinical serum samples [145]. After optimizing deposited antibody concentrations, limits of detection of 800 fg/mL were achieved. Signal amplification using the incorporation of NPs also has been attempted [146] and PSA detection on an integrated chip with acoustophoresis based separation of serum from whole blood has been shown [147].

Recently, the quantification of α-synuclein in cerebrospinal fluid (CSF) has been presented for Parkinson's disease diagnostics [148]. The study resulted in LOD of 35 pg/mL and an assay dynamic range of 0.01–100 ng/mL in neat CSF, comparable to ELISA, the current standard detection method. As such, this work has demonstrated the possibility for utilizing pSi microarrays to aid in disease diagnosis and the monitoring of potential treatment strategies.

5.4.1.3 Mass Spectrometry Detection

One of the most successful techniques for pSi-based analysis of biological samples and tissues has been mass spectrometry. This was first shown with desorption ionisation on porous silicon (DIOS) [111, 149], which is a derivative of matrix-assisted laser desorption ionization (MALDI) [150, 151]. However, instead of matrix molecules the pSi acts as the energy transfer medium to promote analyte desorption and ionisation resulting in minimised signal suppression and interference in the low mass range ($m/z < 700$). pSi substrates for mass spectrometry are predominately produced via photoelectrochemical etching and their performance is heavily influenced by the resulting porosity and pore depth [152–154]. In addition, solvent acidity and surface chemistry [153, 155, 156] have been shown to improve detection, and in particular modification of the surface chemistry has helped maintain performance following long-term storage of DIOS chips [149, 152].

The detection of biologically relevant molecules with DIOS has encompassed metabolite profiling [149, 157, 158] proteomics [111, 159–161], enzymatic activity monitoring [157, 159, 162, 163], drug discovery [149] and tissue imaging [155, 164, 165]. Since its inception, DIOS it has been regularly used to analyse complex biological mixtures for both biomedical [149, 166] and forensic applications [167, 168]. Significant improvements have been achieved by incorporating different surface functionalities to the pSi, in particular fluorinated entities [149]. Sample preparation prior to mass spectral analysis has also significantly expanded the scope of this application. Based on the principles of solid–liquid extraction, a sample droplet is deposited onto the hydrophobic DIOS surface and subsequently removed. This results in the removal of interfering species such as hydrophilic molecules and salts. This method of preferential adsorption improves analyte detection, and has

been reported to enable the detection of 800 yoctomoles of BSA [149]. Furthermore, the use of affinity molecules chemically bound to the DIOS surface, such as antibodies, makes it possible to probe or enrich specific molecules of interest and further improve the selectivity and sensitivity for the required analytes [67], particularly when analyzing molecules of low abundance. Furthermore, the elimination of sample pre-treatment reduces preparation time and sample volumes, both of which increase throughput.

Reports of DIOS have encompassed both diagnostic and drug discovery applications, including analyzing biological fluids from humans. The identification of catecholamines, dopamine and noradrenaline, from human peripheral blood lymphocyte extract was reported by Kraj et al. [169]. Similarly, the quantitation of salicylate in human serum has been demonstrated in negative ion mode [170]. In this study, however, solid phase extraction (SPE) was employed to clean up the sample prior to analysis. Information regarding the biochemical interactions between proteins and small molecules, important for drug discovery can also be provided by DIOS. In one such study avidin, DI-22 antibody and BSA were covalently linked to the surface and their known small molecule partners (biotin, digoxigenin and atenolol, respectively) were subsequently introduced as a mixture to each of the surfaces [171]. Following exposure to the mixture, mass spectral analysis showed selectivity for the partner, indicating non-covalent interactions between the protein and the small molecule. These investigations traditionally have been conducted with fluorescence, however, with DIOS faster analysis of non-covalent interactions is possible, with the added benefit of not requiring molecule labeling.

Derivatives of DIOS have also been developed where additional species are introduced to the pSi surface, including matrix molecules [172] to improve the process. The most prominent of these methods is nanostructure initiator mass spectrometry (NIMS), involving the application of liquid chemical initiators to the pSi surface prior to introduction of the sample [114, 173]. Initiators are distinct from matrix molecules in that they do not absorb UV energy [174], consequently limiting the chemical noise present in the low mass range of the spectrum. Typically perfluorinated compounds have been used, with the initiator bis(heptadecafluoro-1,1,2,2-tetrahydrodecyl)tetramethyl-disiloxane (bisF17) being preferred [174]. Detection of proteins, peptides, metabolites and drug molecules have all been demonstrated with this NIMS surface [114]. NIMS and its derivatives have successfully been employed for the direct analysis of biofluids, cell lysates and metabolite extraction with limited or no sample preparation [114, 158, 175]. It is important to note that different initiators can result in different profiles of biological samples, resulting from their affinity for extracting specific molecules. For the analysis of biological samples this is beneficial because of their chemical complexity and the prevalence of ion suppression [114]. Detection however, is not limited to biological mixtures, the major impact of NIMS is in tissue and cell imaging as it readily enables biomolecule detection at the surface interface, as will be addressed below.

5.4.1.4 Mass Spectrometry Imaging

As the need for more direct analysis methods has grown, MALDI [176–180] and subsequently DIOS [181, 182] have been applied to tissue and cell profiling. Mass spectrometry imaging (MSI) enables determination of the spatial distribution of molecular species and local concentrations of heterogeneous samples, where each pixel corresponds to an area of lateral resolution [183]. The use of the pSi desorption platform eliminates the negative impacts of MALDI matrix crystals, including reduced spatial resolution and increased horizontal diffusion of molecules [182]. Consequently the reduced sample preparation steps result in high resolution images [165, 183, 184], limited only by laser spot size [182, 185].

Mapping of molecular species in tissue on pSi surfaces has been shown to be feasible with fixed mouse liver tissue embedded in DER 736 epoxy resin [182]. Due to the pSi surface being critical to the desorption and ionization processes, tissue samples were cut into 50 nm slices to enable interaction between the pSi and the laser. In the same study, direct detection of HEK 293 cells was also performed. An added advantage of imaging whole cells on pSi is that they can be directly cultured on the surface, further minimizing sample preparation.

Extensive advancements in the direct analysis of tissue have been made with NIMS, which has been reviewed elsewhere [165, 186]. The method first reported involved a two-step process, consisting of laser ablation to remove a layer from the 12 μm tissue sample followed by interrogation of the surface at a lower energy to acquire mass the spectrum [114]. Thinner slices (<5 μm) are now used which allows immediate analysis of the sample [158]. Follow up studies have involved the use of cationization agents, where coated NIMS surfaces enabled the visualization of brain sterol localization in mouse sections [175]. The localization of lipids in brain tissue has also been demonstrated [187] using just the application of initiator bisF17, enabling glial and neuronal regions in a mouse brain to be distinguished [188] as shown in Fig. 5.3. Additionally, the non-covalent immobilization of the pSi surface with enzymes that interact with tissue samples, termed Nimzyme, has enabled enzyme activity product monitoring [173, 189] expanding the applicability of NIMS even further. The spatial characterization of proteins, peptides, drugs and their metabolites in both cells and tissues using pSi substrates, in particular NIMS, creates the opportunity to unveil unlimited numbers of unknown species, potentially enabling disease diagnosis and biomarker discovery [182, 190].

5.4.1.5 Summary

pSi has been demonstrated as a versatile platform for the detection of biologically relevant molecules including DNA, proteins, metabolites and bacteria. These detection techniques exploit the ability of pSi to retain the analyte of interest and subsequently output a signal. For pSi biosensors the signal is transduced either optically, electrically or electrochemically while pSi microarrays rely on fluorescence readout. The pSi surface in laser based mass spectrometry enables

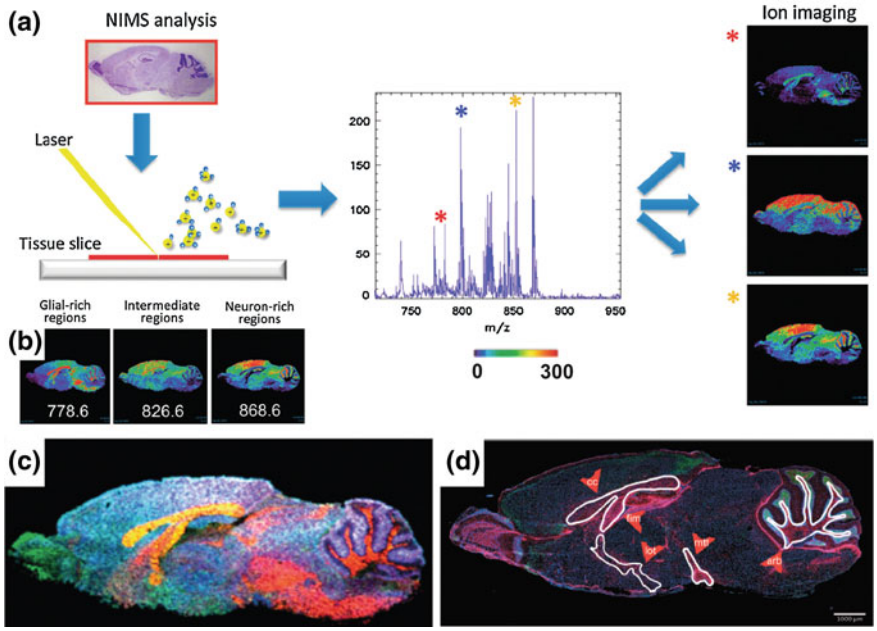

Fig. 5.3 Nanostructure initiator mass spectrometry (NIMS) imaging of a mouse brain showing localization of specific lipids. **a** Schematic showing NIMS imaging, where laser rastering with defined spatial points ionizes metabolites from nanoinitiator-associated tissue slice. Distinct m/z ions can then be mapped to create ion intensity images. **b** Individual ion profiles mapped for *m/z* 778.6, 826.6 and 868.6. **c** Composite overlay of individual ions in **b** with *red*, *green* and *blue* indicating the intensity of the respective ions. **d** Immunohistochemical stain of the brain section showing concentrated glial projections (neuronal nuclei stained with NeuN-*green*, glial projections stained with GFAP-*red* and all nuclei are stained with DAPI-*blue* (*scale* 1 mm). Adapted from Lee et al. [3]

desorption/ionization of the molecules resulting in a mass to charge signal, with mapping capabilities. Further developments of biomolecular detection techniques will continue advances in metabolite and protein profiling, aiding not only diagnostics but lead to a better understanding of disease states and potential therapeutics.

5.4.2 pSi Delivery and Tracking Systems

5.4.2.1 Drug Delivery

The ability to control the physical and chemical properties of pSi has made it a viable delivery system, increasing therapeutic benefits by both targeted delivery and controlled payload release while simultaneously minimizing toxicity and side

effects [191–197]. Here the development of pSi substrates for drug delivery will be covered along with exploration of key advances in vitro and in vivo [20, 198–201].

Factors Affecting PSi Drug Release

Many factors affect the applicability of pSi as a drug delivery platform. In particular it is known that both pore morphology and surface chemistry influence both the loading and release of payloads [105, 202]. The overwhelming influence of the surface chemistry on pSi drug delivery devices has been reviewed extensively by Jarvis et al. [28]. Drug molecules can be loaded into the pore structure by taking advantage of the high surface area, pore volume of the material and the affinity of the pSi to the drug molecule itself [203]. Immobilization methods for pSi include covalent [15, 204], hydrophobic interactions [205, 206], electrostatic binding [105, 207] and physical trapping by oxidation [208], which have been discussed in detail by Haidary et al. [209]. The ability to tune the surface chemistry and binding techniques allows for both hydrophilic and hydrophobic drugs to be loaded [210]. The use of pSi as a drug delivery carrier is particularly important for drugs and proteins that have poor water solubility [28]. When choosing the surface chemistry, potential chemical reactivity of the drug with the substrate should also be considered as it has been shown that some drugs, like antipyrine, catalyze the oxidation of pSi [211].

The typical release mechanism from pSi may occur via either the degradation of the scaffold, for fast degrading pSi or covalently bound drugs, or the diffusion of the drug from the wetted porous structure, for non/slowly degrading pSi structures and non-covalently bound drugs [209]. The first report of oral drug delivery was performed by Foraker et al. [212], using micromachined pSi MPs. The pSi particles acted as permeation enhancers to the tight junctions between intestinal epithelial cells and allowed paracellular transport. This study showed the enhanced uptake of therapeutics when delivered locally by pSi particles, while minimizing the uptake of pathogens and toxins that can occur when permeation enhancers are delivered orally.

In an attempt to control the release properties of pSi surfaces, various surface chemistries have been used to prolong the drug/surface interactions and consequently slow the release [213]. In a study by Salonen et al. [211] the release of five model drugs with different solubilities from thermally oxidized (TO) and thermally carbonised (TC) pSi MPs was monitored at different pH conditions, selected to represent the different conditions in the small intestine. It was observed that loading of TO pSi MPs was much lower than TC pSi MPs due to variances in the pore volume and surface chemistry. The influence of MPs on drug solubility was most pronounced with ibuprofen at pH 5.5 releasing 80 % of the loaded drug within 60 min, in comparison to 240 min for unloaded ibuprofen [211]. Overall, it was observed that MPs increased dissolution of poorly soluble drugs while also delaying the dissolution rate of highly soluble drugs. The release profiles were also generally more consistent across the studied pH range for the particular drug loaded into MPs than the unloaded form. pSi particles hydrosilylated with dodecene [205] also showed that surface changes prolong the release of the steroid dexamethasone

due to the pSi being protected from rapid dissolution. Release profiles were actually a two component system. There was an initial 2-h linear release that was fast, followed by a much slower release phase that lasted approximately 3 days.

The electrostatic attraction between negatively charged pSi and positively charged biomolecules can also be exploited for loading and release. One study has shown the controlled release of 94 % of Bevacizumab, a monoclonal antibody (mAb), raised against vascular endothelial growth factor A, over a 30 day period from oxidized pSi [207]. In this study, no initial burst release was observed and the released mAb was shown to have retained its functionality. Proteins have also been used as a capping layer to control the release of a payload. Perelman et al. [214] used BSA to cap pSi, loaded with vancomycin, at pH 4. Upon switching to pH 7.4, where BSA is soluble, this capping layer was removed and the vancomycin was then released.

The covalent attachment of drug molecules can also avoid rapid diffusion from the pores, prolonging the payload release. It has been shown that the release of covalently bound dye molecules can be triggered by oxidation [15]. The release rate was tuned by the addition of peroxynitrite, which increases the hydrolysis rate of the Si–O backbonds. Similarly, the covalent binding of daunorubicin via EDC/NHS coupled to amino-silanised pSi MPs sustained intraocular release [204]. Extension of this work then demonstrated the ability to tune the release of daunorubicin based on the pore size of the pSi matrix [215].

Biomolecules such as peptides [216] and oligonucleotides [89] have also been combined with pSi for the purpose of delivery. pSi MPs that are capable of direct solid-phase synthesis of oligonucleotides can be generated with cleavable chemical linkers [89]. The oligonucleotides are then slowly released when the support dissolves under physiological conditions, creating the potential to transfect cells and promote desired cellular responses. Surface chemistries therefore can control the identity, amount and in vivo release rate of the payloads and also influence the resorption rate [105]. In addition, multistage delivery systems have been envisaged where they can deliver multiple therapeutic agents in a controlled fashion [217]. These systems will be discussed further in relation to thernaostics.

pSi-Polymer Composites

Attempts to further improve drug release from pSi have included the incorporation of polymers. Integration of the two systems can be achieved by capping [102], coating [218], support [219], and encapsulation with polymers [18, 220]. These introduced polymers layers then can act as a release control mechanism. However, their performance is reliant on a suitable solvent system being available to dissolve the drug of interest, wet the pSi layer and swell the polymer layer [221, 222].

A number of different polymers have been employed to control the release rate of drug from loaded pSi substrates. Repetitive coating with a poly(ε-caprolactone) (PCL) layer of varying thickness has been shown to encapsulate dye-loaded pSi substrates and slow the observed release rate [220]. A pSi film coated with a

cross-linked chitosan hydrogel capping layer has been used to control insulin release for over 100 min, at pH 6, avoiding the typical burst release observed from uncapped pSi [102]. pSi MPs encapsulated with poly(lactide-co-glycolide) (PLGA) have also been shown to extended the release time in vitro of daunorubicin from 14 to 74 days [223]. Recently, a novel development has been reported by McInnes et al. [103] where initiated chemical vapour deposition (iCVD) was used to generate poly methacrylic acid-co-ethylene dimethacrylate (p(MAA-co-EDMA)) coatings on drug-loaded pSi. The iCVD process was demonstrated to coat in a solvent-free environment without the loss of the loaded drug, allowing the pre-loading of sensitive drug payloads (such as proteins and other biomolecules) without the possibility of damage usually incurred by post-polymerisation loading techniques. Thermoresponsive polymers such as PNIPAM have also been integrated with pSi [70, 99]. The thermoresponsive nature of PNIPAM is affected by the thickness of the polymer, which is dependent on polymerization time. In this work, camptothecin (CPT) was released when the lower critical solution temperature (LCST) of the polymer was exceeded and CPT was withheld when below the LCST of the polymer [70]. There are many benefits to this system which would allow the release of a drug payload above the LCST of the polymer, for example, when a wound becomes infected [224, 225].

Embedding pSi MPs into polymer monoliths can also create composite materials. Drug-loaded polymeric blocks, varying in size and shape, have been prepared and pSi MPs were then adhered to the outer surface via localised melting [226]. The blocks self-assemble into networks and it was observed that the release profile of the preloaded $Ru(bpy)_3Cl_2$ varied based on physical structure, spatial organisation, pSi enrichment site and composition of the block network. Furthermore, in a comparative study of three different pSi and PLLA composites, each showed distinct characteristics that affected the release profiles of the drug molecule CPT [227]. Overall, however, the monolithic morphology was calculated to potentially extended CPT release up to 200 days.

Tissue Permeation of PSi

A number of challenges are encountered, including enzymes, the immune system and the cell membrane, when drug delivery platforms are introduced in vivo. In an effort to overcome the cell membrane and deliver molecules such as DNA, proteins, drugs or dyes, pSi has been used as a permeation agent [212, 228]. Two modes are possible, either where permeation is enhanced by the physical presence of large pSi structures or where pSi is processed into MPs or NPs small enough to infiltrate the cells. In the first demonstration of pSi as a delivery device [212], a Caco-2 human epithelial cell monolayer was incubated with particles loaded with fluorescein isothiocyanate (FITC). The permeation of the fluorophore across the cell monolayer was then compared to solutions of FITC in the presence of a permeation enhancer (sodium laurate or sodium caprate) and FITC alone. This resulted in a tenfold or greater increase in transport when particles were present and it was also shown that

the particles did not penetrate or disrupt the cell monolayers integrity. Subsequent studies have confirmed this result, increasing the delivery of furosemide from thermally carbonised pSi MPs [228] and thermally oxidised pSi MPs and NPs delivery of griseofulvin [210], across Caco-2 monolayers without cellular internalisation of particles. In contrast, rapid internalisation of the 1–10 μm MPs was observed when immune response cells, RAW 264.7 macrophages, were incubated.

Extensive studies of a pSi MPs system penetrating cells has been conducted by Serda et al. [229–235]. MPs created using photolithography have been shown to be internalized by human umbilical vein endothelial cells by phagocytosis. Interestingly, cationic, amino-silanized, particles were taken up more readily than oxidised particles. In addition, these MPs could then be loaded with iron oxide NPs for imaging purposes. After internalization of the particles, the cells were monitored and appeared to remain unaffected over several days. To improve blood circulation and targeting, recently pSi MPs were camouflaged with cellular membranes isolated from leukocytes [236] as shown in Fig. 5.4. These particles, termed leukolike vectors (LLV), were able to delay immune system clearance, interact with endothelial cells and deliver a payload across the endothelium. Interestingly, internalization of LLV by human umbilical vein endothelial cells (HUVEC) was observed to be different from that of uncoated particles, see Fig. 5.4.

Luminescent pSi NPs, emitting in the near-infrared, have also been shown to penetrate the cellular membrane of HeLa cells [18]. Their distribution was also monitored in vivo using a mouse model, demonstrating for the first time organ and tumour imaging in live animals with fully biodegradable pSi NPs. Imaging was achieved via the intrinsic luminescence of pSi and hence very low toxicity was observed. Cellular uptake of non-toxic alkyl modified pSi NPs has also been performed [237] with an array of cell lines. The accumulation of the NPs showed only minor differences between the neoplastic cell lines. However, the rate of accumulation for malignant cells were higher compared to normal human primary cells. Particles such as these could exploit the preferential uptake by malignant cells to more effectively deliver chemotherapeutic drugs with minimal side effects in vivo, due to their low toxicity and rapid accumulation in the target cells.

Targeted and Traceable PSi Delivery

Targeted drug release platforms have been developed using monoclonal antibodies. Secret et al. [86] have demonstrated the direct targeting of pSi NPs, by coating camptothecin (CPT) loaded NPs with antibodies to target neuroblastoma, glioblastoma and B lymphoma cells. Successful targeted uptake of the pSi NPs was shown and in all cases the drug-loaded pSi NPs did not affect cells that did not express the specific receptor. The combination of luminescent pSi NPs with the FGK45 antibody has been shown to activate B cells [53]. They demonstrated, for the first time, that the pSi NPs with the agonistic FGK45 antibody lead to 40 % higher activation of the B cells, compared to the FGK45 antibody alone. This effect could lead to a decrease in dosages required.

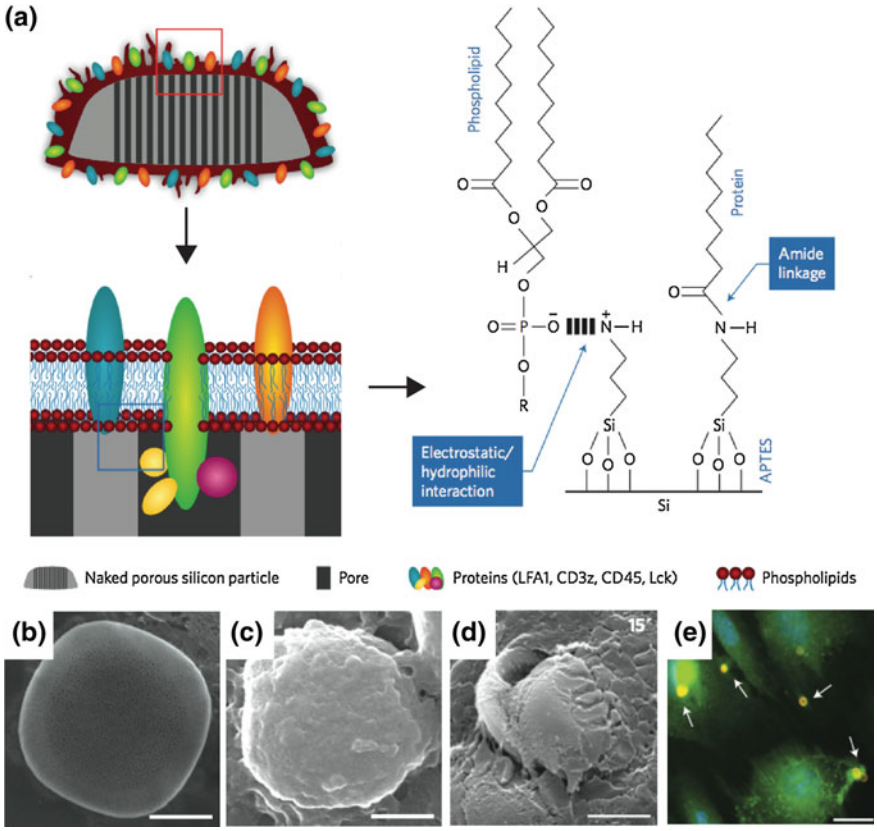

Fig. 5.4 pSi MPs covered in leukocyte-derived membranes internalized by HUVEC cells. **a** Schematic representation of the leukolike vectors (LLV) showing full coverage and sealing of the pSi MPs pores by the leukocyte-derived cell membranes. Scanning electron microscopy (SEM) showing **b** bare pSi MPs (*scale* 1 μm), **c** MPs with leukocyte-derived membrane coatings (*scale* 1 μm) and **d** LLV uptake into HUVEC cells (*scale* 2 μm). **e** pSi MPs, visualized by immunofluorescence, on the surface of HUVEC cells. Reproduced from Parodi et al. [4]

The future of drug delivery relies on the ability to monitor drug release in real time. Optical monitoring of pSi polymer composites could make this possible as shown with the smart patch developed by Koh et al. [238]. In this work, free-standing pSi distributed Bragg reflector (DBR), was cast into a drug containing PMMA solution, and a flexible but robust 140 μm thick device was formed. The photonic pSi films exhibited a reflectance peak that shifted as the caffeine payload was released in vitro. Tailoring the reflection peaks in the range of 500–600 nm gives low optical absorption in human tissue and allows the DBR to potentially be monitored in vivo. Furthermore, the reflectance peak from pSi MP photonic structures has been monitored non-invasively with a charged coupled device (CCD) device when particles were injected into the vitreous of rabbit eyes.

Degradation was monitored over several weeks as the pSi reflectance peak changed from green to blue/violet. Not unexpectedly, it was reported that different surface chemistries, TO and hydrosilylated with 1-dodecene, lead to different life times in vivo. This work was then extended with photonic rugate pSi structures and the release of daunorubicin to retinal pigment cells was monitored [44]. Tracking the reflectance peak showed that it changed linearly with drug release and subsequent pore filling changes. The change in pSi optical properties over the release period was strong enough that a change in the particle colour from red to green could be observed with the naked eye.

5.4.2.2 Cancer Therapy

Cancer, the uncontrolled division of abnormal cells that can affect any part of the body and spread through the blood and lymph systems, is a major health issue worldwide [239]. The effective treatment of cancer has been significantly hindered as our bodies have many physical barriers that naturally exclude foreign materials [240, 241]. Therefore, recent therapies have focused on passive delivery through the enhanced permeability and retention effect (EPR) with NPs below 400 nm [242] The highly disordered "leaky" neovasculature that the tumor cells create to survive [243] is not connected to the lymphatic system [244] and therefore cannot filter small NPs adequately. In addition, targeting the tumor or its vasculature reduces the systemic effects by increasing the local concentration and lowering exposure [243]. The NPs surface can be modified with targeting species, such as monoclonal antibodies [245], peptides [246, 247], RNA [248] or small molecules [249, 250]. In vivo, nanomaterials are rapidly removed by the mononuclear phagocytic system (MPS) and so any introduced species should be non-toxic and readily cleared by the body to avoid systemic toxicity [251]. These size and chemical requirements can all be met by pSi, enabling therapies such as, thermal therapy [252], photodynamic therapy [253] and brachytherapy [254].

Thermal therapy induces cell death by local heating of accumulated metal NPs with external stimuli such as microwave, radio frequencies, ultrasound and laser energy [255, 256]. Hong et al. [257, 258] have demonstrated the ability of pSi to induce photothermal therapy to colon carcinoma (CT-26) both in vitro and in vivo with a NIR laser. Firstly, the study showed in vitro that cell viability after combined (pSi and NIR) therapy was reduced to 6.7 %. Following, it was observed that in vivo the treatment resulted in elimination of the tumors within 5 days, without reoccurrence up to 90 days later. The process is heavily dependent on the accumulation of sufficient NPs at the tumor site. With improvement it could be used to not only treat superficial tumors, but also deeper tumors using radio frequencies to stimulate gold NPs [259] embedded into pSi. In addition, these procedures could be utilized as a two-component systems [200] where the nanoparticle is heated by the external stimuli and subsequently releases a secondary payload. This idea is similar to the work of Ma et al. [260], where gold capped mesoporous silica particles were

used to induce simultaneous chemo and phototherapy through the enhanced release of a DOX payload upon NIR irradiation.

Photodynamic therapy is commonly used to generate cytotoxic singlet oxygen and reactive oxygen species (ROS) from photosensitizers [261]. In this manner, a two-photon initiation was used to generate cytotoxic species from porphyrin modified pSi NPs to induce cell death in human breast cancer cells [253]. In the study, cell death incurred was increased up to 75 % when mannose targeting moieties were also incorporated into covalently linked phorphyrin pSi NPs. It was suspected that this resulted from the mannose moiety increasing cellular internalization of the NPs.

Brachytherapy is the treatment of tumors based on the radiation emitted from an area close to or inside the tumor. BrachySil™, is a porous silicon based brachytherapy treatment where the radioactive ^{32}P isotope incorporated into pSi is introduced through intratumoral injection and high doses of radiation is confined to the local site as β-emission only penetrates 8 mm of tissue [262]. Its ability to reduce tumors was first demonstrated with nude mice models for both pancreatic (2119) and hepatocellular carcinoma xenografts [263]. BrachySil™ is the first product developed by pSiMedica Ltd that went to clinical trials for unresectable hepatocellular carcinomas [254] and successfully reduced the tumor size at both 12 and 24 weeks post implantation. The main advantages of this treatment are that radioactive ^{32}P isotope has only a 2 weeks half life and pSi readily degrades and is excreted by the body after the dose of radiation has been locally delivered.

5.4.2.3 In Vivo Imaging

pSi substrates can be used for in vivo imaging in various modes, such as luminescence [18], magnetic resonance imaging (MRI) [231, 264], positron emission tomography (PET) [265, 266], computed tomography (CT) [200, 233, 263] and intravital microscopy [236, 267]. The benefit of NPs in non-invasive imaging is substantial, as they can carry and concentrate contrast agents, enhancing signal. As such, NP based systems for imaging, including pSi have previously been reviewed [268]. The ability of pSi to image in various modes is dependent on the criteria of the imaging mode and both surface properties and surface modification imparted to the pSi substrate. Summarized here are applications of pSi to imaging and the current in vivo studies.

Imaging in vivo using luminescent pSi NPs (LpSi NPs) has been shown [18, 46]. Luminescent particles emit in the near-infrared (NIR) and are excited with red or NIR radiation or by a two photon NIR excitation. Tissue penetration is maximized in the NIR range, while minimizing the absorption by physiologically species, like hemoglobin, relevant when detecting and imaging deep tissue tumors or other diseases. In one study, dextran coated LpSi NPs were injected into a nude mouse with a MDA-MB tumor and resulted in a passive accumulation of the nanomaterial in the tumor, as shown in Fig. 5.5. In addition, the particles carried and released the anti tumor agent, doxorubicin. Amine terminated LpSi NPs have been shown to be

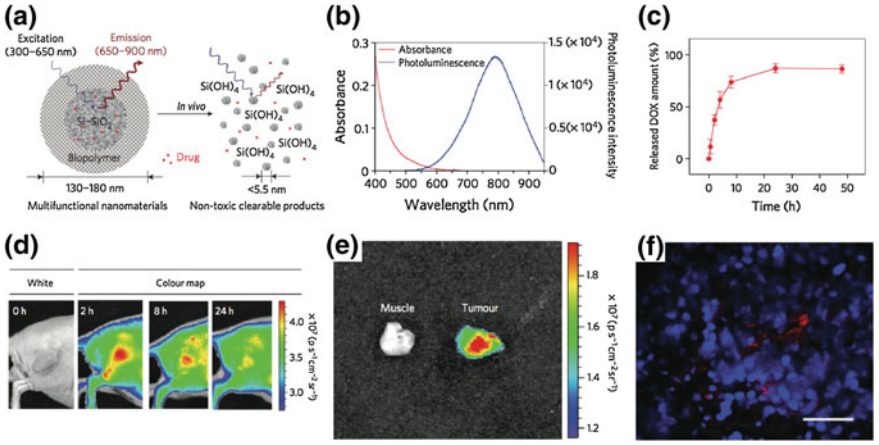

Fig. 5.5 Properties, release profile and passive accumulation in tumor tissue of luminescent pSi NPs (LpSi NPs). **a** Schematic diagram of the LpSi NPs structure and in vivo degradation. **b** Photoluminescence absorbance and emission spectra of LPSi NPs upon UV excitation at 370 nm. **c** Release profile depicting % DOX released into PBS over 50 h at 37 °C. **d** Fluorescence images of an MDA-MB-435 tumor in a mouse model over 24 h after intravenous injection of D-LpSiNPs at 20 mg kg^{-1}. The imaging was performed using a Cy5.5 excitation filter and an ICG emission filter. **e** Ex vivo fluorescence images of the tumor and surrounding muscle after resection from the mouse used in (**d**). **f** Fluorescence image of a tumor section from the mouse in **d** with *red* D-LpSi NPs and *blue* (DAPI stained) cell nuclei (*scale* 100 μm). Adapted from Park et al. [5]

non-toxic, stable over the pH range of 4–14 and resistant to ageing/degradation over several weeks [46]. This development enables the subsequent immobilization of other chemical functionalities, such as antibodies for site-specific targeting. Furthermore, the functionalization of photoluminescent pSi, with species such as PEG [269] has been demonstrated to improve photoluminescence stability and also increasing their longevity for circulation and imaging. However, only particular types of pSi with adequate pore size and porosity are photoluminescent or reflect in the correct wavelength range [5]. Hence, other approaches that use the conjugation of fluorescent dyes or probes to the pSi surface can be used [45] and these probes can be enhanced via the loading of additional agents such as quantum dots [217, 270] and silver nanoparticles [271]. Typically, intravital microscopy has been used to monitor the biodistribution of fluorescent particles [236, 267].

MRI imaging can be enhanced with the use of pSi loaded with gadolinium (Gd) based contrast agents. These agents enhanced sensitivity by improving longitudinal relaxivity, enabling single cell imaging [272]. Gizzatov et al. [264] also used Gd particles in pSi with similar results of improved longitudinal relaxivity of the confined Gd particles when compared to the free Gd. Additionally, no cytotoxicity was observed and it was found that these particles accumulated in ovarian tumors of mice when injected intravenously. Another contrast agent that has been developed recently for imaging is superparamagnetic iron oxide NPs (SPIONs). pSi MPs have since been loaded with SPIONs and trapped using crosslinked

aminosilanisation [231]. SPION loaded pSi MPs have been shown to induce shorter relaxation times and enhance imaging in a concentration dependent manner. In addition, surface aminosilanisation allows the attachment of targeting molecules. This was demonstrated with the attachment of vascular endothelial growth factor receptor 2 (VEGFR-2) and platelet endothelial cell adhesion molecule (PECAM), which were used to target endothelial tissue. pSi NPs have also had iron oxide nanocrystals precipitated into them and used for MRI imaging [273]. In this work, it was also demonstrated that the particles could be stabilized with PEG, with no significant effect on the MRI imaging capabilities.

Nuclear imaging with pSi structures has also been shown with two common modes, PET and single-photon emission computed tomography (SPECT) [251]. Nuclear imaging requires the material to be labeled with a radioactive label, including ^{13}N, ^{11}C, ^{68}Ga, ^{18}F, ^{64}Cu, and ^{124}I for PET modes and ^{99m}Tc, ^{111}In and ^{125}I for SPECT modes [5]. The decay mechanism of the isotope chosen determines the detector required and the relative penetration of the imaging [5]. THC, TC and TO pSi have all been successfully labeled with ^{18}F by the direct substitution of Si–H or oxygen in Si–O–Si bonds with Si–F bonds [274]. THC pSi NPs labeled with ^{18}F has been studied as a tracer in mice through oral, subcutaneous, and intravenous administration routes. It was possible to track the particles through the gastrointestinal tract for 6 h at nanogram quantities [198]. It was also shown that the material released a small amount (<0.6 % ID/g) of ^{18}F into the bone and urine, likely to have occurred via defluorination or dissolution of the NPs. The same NPs, delivered subcutaneously, remained there for 4 h while those delivered intravenously were eliminated to the spleen and liver (only 0.3 %ID/g being found in bone after administration). The Si–F bond exploited here was found to be quite stable to both hydrolytic and enzymatic cleavage. SPECT imaging has been conducted with ^{125}I labeled PEGylated pSi NPs and found that they were almost immediately taken into the spleen and liver of healthy mice. Huhtala et al. [275] have also tracked ^{125}I labeled IGF-1 delivered via THC pSi NPs and observed that the complexed IGF-1 was able to remain in the liver and produce a more sustained release compared to the IGF-1 administered alone. Radio labeling with ^{18}F and ^{125}I is now becoming more popular for monitoring the biodistribution of pSi NPs in vivo [266, 276, 277].

Dual imaging modalities have also been developed using a combination of fluorescence and magnetic properties. Gu et al. [278] achieved this by loading boron activated LpSi MPs with SPIONs, which were locked into the pores by a prolonged thermal oxidation. However, the pores did not close completely and so small drug payload could be subsequently loaded. In this study, the magnetic properties of SPIONS enabled a local site to be targeted, while fluorescence was simultaneously used to track the pSi. Dual magnetic and luminescent pSi NPs has also included the incorporation of cobalt NPs into luminescent pSi via electro-infiltration [279]. Here it was shown that the particles possessed low cytotoxicity and were internalized by human mesenchymal stem cells within 4 h. This method with further tuning and particle development could be used for organelle specific targeting or deep tissue imaging.

5.4.2.4 Theranostic Applications

Theranostics combines the two elements of diagnostics and therapy into one device. Due to the plethora of physical and chemical properties, pSi has significant potential in this area. Investigations into pSi for theranostic applications include optimisation of the device residence time, disease state targeting and on demand payload delivery. Studies that cover two or more of these areas have been briefly covered in earlier sections of this chapter, including Secret et al. [86] and Chiappini et al. [280]. Multistage delivery vehicles have been readily achieved by incorporating pSi devices with targeting molecules. The combination of pSi with a range of different chemistries and NPs allows for the activation of therapy via external stimuli and there are now a myriad of combinations that are being used including magnetic and luminescent pSi [278], QD in pSi MPs [217], photoluminescent pSi NPs [18] and radiolabelled pSi [198].

Another pSi system that has theranostic application is pSi NPs that are photoluminescent and can act as photosensitizers to generate singlet oxygen [281]. Particles of 40–200 nm were created by mechanically grinding pSi in water. These particles were then used to image both a dog thymus and 3T3NIH cells as the particles could penetrate cells within 24 h. Following penetration, the transfected 3T3NIH cells were then irradiated with a 1 mW/cm^2 Hg-lamp for 150 min, resulting in 70 % cell death. This clearly demonstrates that these materials have potential applications in photodynamic therapy (PDT) of cancer. Another theranostic example combined bacteriophage and silicon NPs as a targeting moiety, which were subsequently loaded with SPIONs [282]. It was shown that electrostatically bound targeting system did not interfere with the SPION loading and the prepared particles were able to more efficiently target tumor tissue both in vitro and in vivo. It is expected that a system such as this could be used for cancer therapy, inflammatory conditions and cardiovascular diseases.

5.4.2.5 Summary

Tailoring pSi properties and functionality along with the diverse pSi-polymer hybrid architectures has created an array of delivery carriers that have distinct optical properties, release profiles, degradation rates and mechanical strength. Both pSi degradation and drug release rate are heavily influenced by surface functionality and porosity. Release rates can also be controlled by the incorporation of polymers, in particular the integration of stimuli-responsive polymers. A significant advantage is the ability to switch from passive to accelerated drug release upon the external application of stimuli including heat, magnetism or light. The use of surface functionality and environmental stimuli has enabled the development of new drug delivery systems that provide targeted delivery on demand.

pSi has successfully been used for a wide variety of imaging modes including, MRI, PET, CT and optical techniques. In particular, pSi NPs as contrast agents have been traced and used to deliver therapeutics for localized treatment. Radiolabelled

pSi has also proven effective as sensitive probes for tracking and therapy. The ability to image and simultaneously deliver drug will lead to theranostic applications. The potential to penetrate the leaky vasculature in both passive and targeted approaches with pSi NPs has lead to the more effective delivery of conventional anti-tumor drugs directly to the tumor, minimizing unwanted side-effects. Further development in this area offers the potential to deliver on demand, controlled amounts of drugs, by utilizing both internal biological and/or external stimuli.

5.4.3 Tissue Engineering Scaffolds

Tissue engineering relies on the ability of the biomaterial to become integrated into the body, enabling repair and regeneration of damaged tissue [283, 284]. pSi is one such material that following introduction in vivo can be completely resorbed by the human body, without an immune response [285]. Due to not requiring removal, the degradation rate then plays a significant role in the body's healing process. In addition, pSi substrates have been used to regulate cell behavior by adjusting properties such as surface chemistry and topography [80, 286]. Consequently, pSi has been the focus of intensive studies for a wide variety of implantable devices, which will be reviewed here.

5.4.3.1 pSi Cell Culture

Fundamental to tissue engineering is the material's ability to support cell adhesion, proliferation and differentiation when required [287]. In addition, a high degree of porosity is needed for neovasculization. The first report of cell culture on pSi showed Chinese hamster ovary (CHO) cells adhering to the porous substrates but not to crystalline controls [288, 289]. Since then, numerous studies have been conducted that demonstrate the influence of surface properties, including surface topography and surface chemistry, on cell growth.

The preference elicited by cells for different surface topographies has been shown to control cell growth using patterned topographical regions. Regions with 100 μm squares and 100 μm wide stripes were generated with pore sizes ranging from 50 to 100 nm on both crystalline and polycrystalline substrates [290]. The B50 cells adhered preferentially to the pSi surface rather than the untreated surface, demonstrating a method that used topography alone to define areas of cell growth. The influence of topography on cellular response was then extended to include lateral porosity gradients. Continuous pSi gradients, ranging from 3 μm to 4 nm were used to study the influence of pore size on neuroblastoma cell behaviour [291]. Different effects were observed depending on the specific pore region. Cells in the region of 1–3 μm pores could not use their filopodia to find anchorage points, and were elevated from the surface. As the pore size decreased to 100 nm, the cells were able to produce more protrusions and in the region of pores sizes below

50 nm, the normal neuroblastoma morphology was recovered. Similar work was then conducted by Wang et al. to investigate the attachment and differentiation of mesenchymal stem cells (MSCs) onto pSi lateral gradients [286, 292] as shown in Fig. 5.6. In this work, the nanoscale topographies did not significantly affect cell proliferation, but differentiation was clearly enhanced when pore sizes were decreased to 10–30 nm [286].

In a similar manner, the impact of surface chemistry on cell adhesion and growth has been observed. Modified pSi surfaces, both thermally treated and carbon deposited, were shown to be suitable substrates for an extensive collection of cell lines. Those studied included human retinal endothelial cells, mouse aortic endothelial cells, murine melanomas, B50 and CHO cells [293]. The influence of surface chemistry on cell adhesion, was further demonstrated by Low et al. [54]. In this work, both rat pheochromocytoma cells (PC12) and human lens epithelial cells (SRA 01/04) preferred surfaces that were collagen coated or amino-silanized, rather than those that were oxidised or PEG-silanized. Therefore, cell adhesion can be

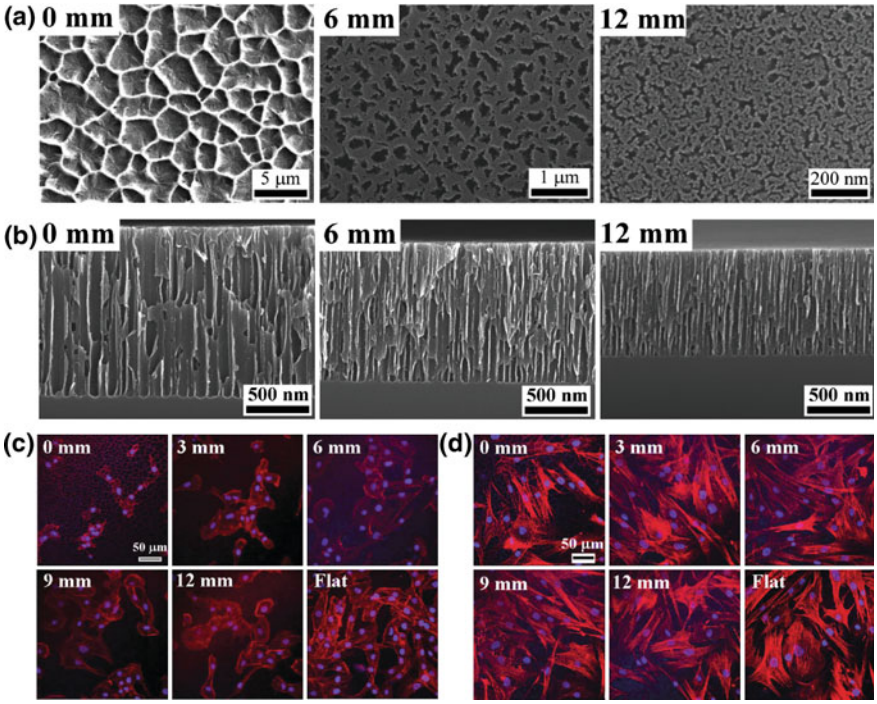

Fig. 5.6 Attachment and differentiation of mesenchymal stem cells (MSCs) on different pSi tophographies generated by an electrical gradient. SEM images of **a** top view and **b** cross section of the surface and pore structure at distances 0, 6, and 12 mm from the electrode position during the etching process. **c** hBMSCs and **d** hASCs on the pSi gradients at 24 h in culture and at 0, 3, 6, 9 and 12 mm along the pSi gradient and also flat Si for comparision. Nuclei staining was performed with DAPI (*blue*) and F-actin was stained with TRITC-Phalloidin (*red*). Adapted from Wang et al. [6]

promoted by coating pSi with proteins and peptides belonging to the extracellular matrix, including collagen, fibronectin and the tripeptide arginine-glycine-aspartate (RGD) [54, 294].

Chemical patterning has also been conducted to control cell growth on pSi substrates. One study, by Khung et al. [295], achieved cell patterning by first modifying the surface with a PEG silane and subsequently ablating the surface in specific regions with the laser of a commercial MALDI mass spectrometer. This method created distinct channels, without the use of a mask, into which SK–N–SH cells could be guided to grow as the remaining PEG surface prevented cells from adhering. An alternative method, that also utilizes PEG to retain cell growth has recently been reported by Sweetman et al. [77]. In this study, UV initiated hydrosilylation was used to pattern an NHS-alkene on pSi that was then functionalized further with fibronectin. The un-reacted pSi areas were then backfilled with a PEG-alkene to prevent cell attachment and consequently it was found that 99 % of cells adhered to the fibronectin regions. The ability to simply pattern bio-elements onto pSi surfaces and subsequently use these surfaces to support mammalian cells will potentially impact a myriad of biomedical applications.

The effect of chemical gradients has also been demonstrated to influence cell growth. This has been shown in one study by electrochemically modifying the surface with ethyl-6-bromohexanoate in a gradient. Cyclic RGD peptide was then coupled to the hydrolyzed ester moieties and followed by incubation with rat MSCs [80]. MSCs were responsive to the gradient, with attachment increasing as cyclic RGD density increased. A lateral porosity gradient in combination with cyclic RGD gradient [294] was generated and MSCs were shown to respond to the orthogonal gradient, although the influence of the RGD density was more dominant than topographical cues during short-term culture. As such, both patterned and gradient surfaces could be used as a screening method to determine the optimal topography and surface molecule density required to support the cellular morphology needed for specific tissue engineering applications.

5.4.3.2 Ophthalmology

The biocompatibility of pSi has been further demonstrated with the implantation of pSi scaffolds into the eyes of animals. In one study, Low et al. implanted both thermally oxidised and amino-silanised pSi membranes under the rat conjunctiva [296]. It was then observed that the pSi eroded slowly, still being visible at 8 weeks with no damage to the surrounding tissue observed. Following that, human lens epithelial cells attached to these porous membranes were implanted into rats and these donor cells were observed to migrate off the supporting substrate into the ocular tissue space.

In a similar manner, Kashanian et al. [20] implanted pSi MPs encapsulated into electrospun PCL fibers in the rat subconjunctival space. Both hydride terminated and oxidised pSi MPs were tested and were observed to actively support epithelial cell attachment with only a mild histiocytic foreign-body reaction, as shown in Fig. 5.7. The pSi component within a flexible PCL component offers the possibility

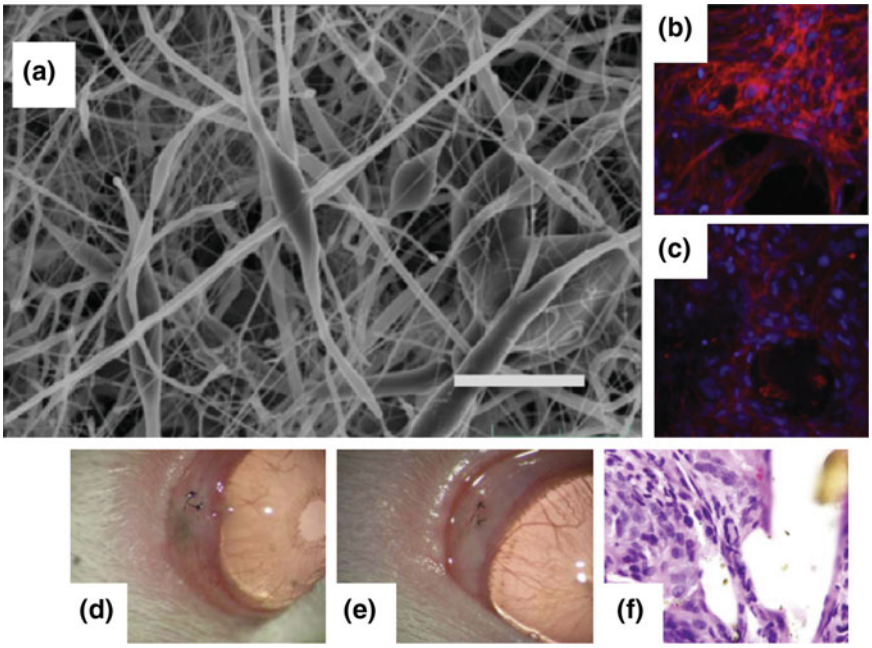

Fig. 5.7 pSi MPs encapsulated in electrospun PCL fibres interaction with cells and implantation into the conjunctival space of a rat. **a** SEM image of composite PCL-pSi electrospun material (*scale* 50 μm). **b** SRA 01/04 cells attached to the composite material after 72 h post seeding and **c** the continued cell adhesion and survival to the composite after 7 days post seeding. Cells were visualized using Hoechst 33342 and Alexa Fluor 594 phalloidin. **d** 1 week and **e** 8 weeks after implantation beneath the conjunctiva of a rat and **f** end-point histology. Adapted from Kashanian et al. [7]

of loading therapeutic or bioactive factors allowing these materials to be also used as a two-stage drug-delivery vehicle.

5.4.3.3 Orthopedics

The discovery that pSi can induce the growth of hydroxyapatite [49, 297] has lead to a number of investigations due to it being the mineral phase of bone development and compatible with osteoblasts [298]. Studies undertaken have involved the deposition of hydroxyapatite on various Si substrates to improve biocompatibility. It was observed that after 4 days in culture, B50 cells preferred the hydroxyapatite-modified pSi, while the optimal surface for CHO cells was modified poly-Si [299]. The growth of hydroxyapatite on pSi has also been shown to accelerate with cathodic bias, providing a better support for cell culture than the equivalent unfunctionalised pSi [300].

The promotion of osteoblast growth, protein-matrix synthesis and mineralization is also heavily influenced by surface morphology [301]. A systematic study on the effects of three different pore sizes (nanoporous, mesoporous and macroporous) showed that macroporous pSi was the most suitable for the reactive oxygen species 17/2.8 osteoblast cell line. The macroporous pSi adhered a higher number of cells, showed cell spreading and after 7 days in culture calcified ECM was present. However, the work did not account for the lack of bioresorption of macroporous pSi and in light of this it should be noted that microporous pSi showed similar results although required a longer incubation time. Interestingly, $Si(OH)_4$ can also promote expression of osteogenic differentiation markers, for example, collagen type I, osteocalcin and alkaline phosphatase [302], adding another benefit to using pSi in bone repair.

pSi-polymer composite materials have also been shown to induce hydroxyapatite growth [303]. The addition of PANi, which is electrically conductive, to pSi-PCL composites [304] was shown to induce hydroxyapatite growth within 7 h when an electrical bias was applied, compared to over a month required for unbiased materials. Furthermore, pSi-PCL scaffolds were shown to support the growth of mouse and human MSCs from bone marrow and subsequently promote their differentiation into osteoblasts. If developed further, these materials could prove very beneficial in orthopedics as they are non-toxic, able to induce hydroxyapatite growth, support cell proliferation and with refinement could lead to fully degradable implantable scaffolds.

5.4.3.4 Delivery of Growth Factors

The ability of pSi and pSi-polymer composite material to be drug delivery reservoirs has been widely demonstrated and this approach could be extended to encompass the inclusion of growth factors. The presence of growth factors can be increased by the delivery of genetic material to the cells to stimulate production or direct delivery of the required growth factor by an implanted material [284]. Due to the high cost [305] of purified growth factors, i.e. bone morphogenic proteins (BMP), fibroblast growth factors (bFGF) and VEGF [284], not many studies have been performed. However, delivery with pSi would prevent denaturation of the growth factors and a constant release profile. Fan et al. have used BSA as a model for growth factors to study the optimization of pSi morphology for the delivery of growth factor for orthopedic applications [306]. Advances in growth factor isolation and production will surely allow these kinds of studies to feature in the coming years.

5.4.3.5 pSi as a Cell Signal Transducer

Attempts to interface pSi with cells for applications such as in vitro biosensors and interfaced neuronal networks have also been made. One study used scanning electron microscopy to study cell morphology of B50 cells on pSi, which was found

to be normal, forming axons, dendrites and intracellular connections [307]. Furthermore, it was determined that the B50 cells rested on a 100 nm thick layer of ECM proteins and there are points along the axons and dendrites where the cells connect to the pSi surface, opening the possibility of direct signal transduction. In another study, *Aplysia* neurons were cultured on oxidized pSi for 1 week, and showed normal passive membrane properties and were able to generate action potentials [308]. The surfaces also demonstrated the ability to monitor neuronal activity using both changes in the photoluminescence (PL) response to voltage changes and the pSi reflectivity response to the presence of acetylcholine.

5.4.3.6 Summary

The ability to tune the degradation of pSi has opened up the possibility to implant scaffolds that can be present in vivo from days to years. Optimization of both surface topography and surface chemistry has been shown to enhance or guide the adhesion, proliferation and differentiation of a variety of mammalian cells. The ability to also incorporate drugs and various growth factors assists in utilizing the complete substrate for the regeneration of damaged tissue. Finally, the use pSi creates the opportunity to monitor cell behavior by utilizing the optical and electronic properties of pSi both in vitro and possibly in vivo.

5.5 Conclusions and Future Trends

Common chemistries for the modification of Si substrates can be applied to pSi. This allows the incorporation of numerous surface functionalities for targeted biomolecular detection as well as the ability to elucidate the spatial localization of unknown species from biological samples. pSi is biocompatible, benefits from a large and tunable drug loading capacity along with favorable bioresoption properties. pSi based materials also require no future surgical intervention after implantation and additional benefits such as the ability to be processed into MPs and NPs allows for a range of delivery routes to be used. The combination of pSi with polymers has lead to an impressive range of new and novel hybrid materials for biomedical applications. These new materials may lead to the development of surgically implantable drug delivery devices that can automatically activate as required, making multiple injections and frequent medical consultations a thing of the past and improving patient care.

The development of new pSi technologies offers increasing opportunities for better diagnostics and targeted disease treatment in the future. The ability to combine multiple functionalities onto pSi NPs in particular is now leading to the development of theranostic applications that can be used for both diagnosis of disease states and subsequent treatment via external stimuli such as hyperthermia or the release/activation of preloaded therapeutic molecules. It is expected that more

smart/active biomaterials will emerge in the coming years that are able to target particular disease states, respond to specific stimuli in vivo and subsequently perform therapeutic actions such as the delivery of drugs or growth factors or removal of toxins or inflammatory markers.

References

1. R. Narayan, Use of nanomaterials in water purification. Mater. Today **13**, 44–46 (2010)
2. N. Linares, A.M. Silvestre-Albero, E. Serrano, J. Silvestre-Albero, J. Garcia-Martinez, Mesoporous materials for clean energy technologies. Chem. Soc. Rev. **43**, 7681–7717 (2014)
3. O.V. Salata, Applications of nanoparticles in biology and medicine. J. Nanobiotechnol. **2**, (2004)
4. S.J.P. McInnes, N.H. Voelcker, Silicon–polymer hybrid materials for drug delivery. Future Med. Chem. **1**, 1051–1074 (2009)
5. H.A. Santos, *Porous Silicon for Biomedical Applications* (Woodhead Publishing Limited, 2014)
6. F.A. Harraz, Porous silicon chemical sensors and biosensors: a review. Sensor. Actuat. B: Chem. **202**, 897–912 (2014)
7. A. Loni, Capping of porous silicon, in *Properties of Porous Silicon*, ed. by L. Canham (Short Run Press, London, 2006)
8. S. Anderson, H. Elliott, D. Wallis, L. Canham, J. Powell, Dissolution of different forms of partially porous silicon wafers under simulated physiological conditions. Phys. Stat. Sol. (A). **197**, 331–335 (2003)
9. L.A.R. Canham, Will a chip everyday keep the doctor away? Phys. World 27–31 (2001)
10. H. Föll, M. Christophersen, J. Carstensen, G. Hasse, Formation and application of porous silicon. Mater. Sci. Eng., R **39**, 93–141 (2002)
11. C. Solanki, R. Bilyalov, J. Poortmans, J.P. Celis, J. Nijs, Effect of the composition of electrolyte on separation of porous silicon film by electrochemical etching. Phys. Stat. Sol. (A). **197**, 507–511 (2003)
12. J.R. Dorvee, A.M. Derfus, S.N. Bhatia, M.J. Sailor, Manipulation of liquid droplets using amphiphilic, magnetic one-dimensional photonic crystal chaperones. Nat. Mater. **3**, 896–899 (2004)
13. J. Link, M. Sailor, Smart dust: self-assembling, self-orienting photonic crystals of porous Si. PNAS **100**, 10607–10610 (2003)
14. J.C. Thomas, C. Pacholski, M.J. Sailor, Delivery of nanogram payloads using magnetic porous silicon microcarriers. Lab Chip **6**, 782–787 (2006)
15. E.C. Wu, J.-H. Park, J. Park, E. Segal, F. Cunin, M.J. Sailor, Oxidation-triggered release of fluorescent molecules or drugs from mesoporous Si microparticles. ACS Nano **2**, 2401–2409 (2008)
16. J. Heinrich, C. Curtis, G. Credo, K. Kavanagh, M. Sailor, Luminescent colloidal silicon suspensions from porous silicon. Science **255**, 66–68 (1992)
17. T. Schmedake, F. Cunin, J. Link, M. Sailor, Standoff detection of chemicals using porous silicon "smart dust" particles. Adv. Mater. **14**, 1270–1272 (2002)
18. J.-H. Park, L. Gu, G. von Maltzahn, E. Ruoslahti, S.N. Bhatia, M.J. Sailor, Biodegradable luminescent porous silicon nanoparticles for in vivo applications. Nat. Mater. **8**, 331–336 (2009)
19. M.H. Kafshgari, A. Cavallaro, B. Delalat, F.J. Harding, S.J.P. McInnes, E. Mäkilä, J. Salonen, K. Vasilev, N.H. Voelcker, Nitric oxide-releasing porous silicon nanoparticles. Nanoscale Res. Lett. **9**, 333–339 (2014)

20. S. Kashanian, F. Harding, Y. Irani, S. Klebe, K. Marshall, A. Loni, L. Canham, D. Fan, K.A. Williams, N.H. Voelcker, J.L. Coffer, Evaluation of mesoporous silicon/polycaprolactone composites as ophthalmic implants. Acta Biomater. **6**, 3566–3572 (2010)
21. K.W. Kolasinski, Silicon nanostructures from electroless electrochemical etching. Cur. Opin. Solid State Mater. Sci. **9**, 73–83 (2005)
22. J. Salonen, V.-P. Lehto, Fabrication and chemical surface modification of mesoporous silicon for biomedical applications. Chem. Eng. J. **137**, 162–172 (2008)
23. O. Bisi, S. Ossicini, L. Pavesi, Porous silicon: a quantum sponge structure for silicon based optoelectronics. Surf. Sci. Rep. **38**, 1–126 (2000)
24. V. Lehmann, Porous silicon preparation: alchemy or electrochemistry? Adv. Mater. **4**, 762–764 (1992)
25. O.I. Ksenofontova, A.V. Vasin, V.V. Egorov, A.V. Bobyl, F.Y. Soldatenkov, E.I. Terukov, V.P. Ulin, N.V. Ulin, O.I. Kiselev, Porous silicon and its applications in biology and medicine. Tech. Phys. **59**, 66–77 (2014)
26. R.J. Martín-Palma, M. Manso-Silván, V. Torres-Costa, Biomedical applications of nanostructured porous silicon: a review. J. Nanophoton. **4**, 042502–042520 (2010)
27. R.L. Smith, S.D. Collins, Porous silicon formation mechanisms. J. Appl. Phys. **71**, R1–R22 (1992)
28. K.L. Jarvis, T.J. Barnes, C.A. Prestidge, Surface chemistry of porous silicon and implications for drug encapsulation and delivery applications. Adv. Colloid Interface Sci. **175**, 25–38 (2012)
29. L.T. Canham, *Properties of Porous Silicon* (Short Run Press, 2006)
30. G. Bomchil, A. Halimaoui, I. Sagnes, P.A. Badoz, Porous silicon: material properties, visible photo-and electroluminescence. Appl. Surf. Sci. **65–66**, 394–407 (1993)
31. B. González-Díaz, R. Guerrero-Lemus, D. Borchert, C. Hernández-Rodríguez, J.M. Martínez-Duart, Low-porosity porous silicon nanostructures on monocrystalline silicon solar cells. Phys. E **38**, 215–218 (2007)
32. D. Bellet, L. Canham, Controlled drying: the key to better quality porous semiconductors. Adv. Mater. **10**, 487–490 (1998)
33. F. Cunin, T.A. Schmedake, J.R. Link, Y.Y. Li, J. Koh, S.N. Bhatia, M.J. Sailor, Biomolecular screening with encoded porous-silicon photonic crystals. Nat. Mater. **1**, 39–41 (2002)
34. S.N.A. Jenie, Z. Du, S.J.P. McInnes, P. Ung, B. Graham, S.E. Plush, N.H. Voelcker, Biomolecule detection in porous silicon based microcavities via europium luminescence enhancement. J. Mater. Chem. B **2**, 7694–7703 (2014)
35. L.T. Canham, Silicon quantum wire array fabrication by electrochemical and chemical dissolution of wafers. Appl. Phys. Lett. **57**, 1046–1048 (1990)
36. A. Sa'ar, Photoluminescence from silicon nanostructures: the mutual role of quantum confinement and surface chemistry. J. Nanophoton. **3**, 032501, 1–42 (2009)
37. L. Pavesi, E. Buzaneva (eds.), Silicon light emmitters: preparation, properties, limitations, and integration with microelectronic circuitry, in *Frontiers of Nano-optoelectronic Systems* (2014)
38. L.M. Bonanno, T.C. Kwong, L.A. DeLouise, Label-free porous silicon immunosensor for broad detection of opiates in a blind clinical study and results comparison to commercial analytical chemistry techniques. Anal. Chem. **82**, 9711–9718 (2010)
39. L.M. Bonanno, E. Segal, Nanostructured porous silicon-polymer-based hybrids: from biosensing to drug delivery. Nanomedicine **6**, 1755–1770 (2011)
40. C. Pacholski, M. Sartor, M.J. Sailor, F. Cunin, G.M. Miskelly, Biosensing using porous silicon double-layer interferometers: reflective interferometric fourier transform spectroscopy. J. Am. Chem. Soc. **127**, 11636–11645 (2005)
41. S.D. Alvarez, M.P. Schwartz, B. Migliori, C.U. Rang, L. Chao, M.J. Sailor, Using a porous silicon photonic crystal for bacterial cell-based biosensing. Phys. Stat. Sol. (A). **204**, 1439–1443 (2007)

42. A. Janshoff, K.-P.S. Dancil, C. Steinem, D.P. Greiner, V.S.Y. Lin, C. Gurtner, K. Motesharei, M.J. Sailor, M.R. Ghadiri, Macroporous p-type silicon Fabry-Perot layers: fabrication, characterization, and applications in biosensing. J. Am. Chem. Soc. **120**, 12108–12116 (1998)
43. L. Cheng, E.J. Anglin, F. Cunin, D. Kim, M.J. Sailor, I. Falkenstein, A. Tammewar, W.R. Freeman, Intravitreal properties of porous silicon photonic crystals: a potential self-reporting intraocular drug-delivery vehicle. Br. J. Ophthalmol. **92**, 705–711 (2008)
44. E.C. Wu, J.S. Andrew, L. Cheng, W.R. Freeman, L. Pearson, M.J. Sailor, Real-time monitoring of sustained drug release using the optical properties of porous silicon photonic crystal particles. Biomaterials **32**, 1957–1966 (2011)
45. E. Tasciotti, B. Godin, J.O. Martinez, C. Chiappini, R. Bhavane, X. Liu, M. Ferrari, Near-infrared imaging method for the in vivo assessment of the biodistribution of nanoporous silicon particles. Mol. Imaging **10**, 56–68 (2011)
46. J.H. Ahire, Q. Wang, P.R. Coxon, G. Malhotra, R. Brydson, R. Chen, Y. Chao, Highly luminescent and nontoxic amine-capped nanoparticles from porous silicon: synthesis and their use in biomedical imaging. ACS Appl. Mater. Interfaces **4**, 3285–3292 (2012)
47. A.P. Bowditch, K. Waters, H. Gale, P. Rice, E.A.M. Scott, L.T. Canham, C.L. Reeves, A. Loni, T.I. Cox, In-vivo assessment of tissue compatibility and calcification of bulk and porous silicon. MRS Proc. **536**, 149–154
48. A. Rosengren, L. Wallman, M. Bengtsson, T. Laurell, N. Danielsen, L. Bjursten, Tissue reactions to porous silicon: a comparative biomaterial study. Phys. Stat. Sol. (A). **182**, 527–531 (2000)
49. L.T. Canham, Bioactive silicon structure fabrication through nanoetching techniques. Adv. Mater. **7**, 1033–1037 (1995)
50. M.J. Sailor, E.J. Lee, Surface chemistry of luminescent silicon nanocrystallites. Adv. Mater. **9**, 783–793 (1997)
51. L. Canham, C. Reeves, J. Newey, M. Houlton, T. Cox, J.M. Buriak, M. Stewart, Derivatised mesoporous silicon with dramatically improved stability in simulated human blood plasma. Adv. Mater. **11**, 1505–1507 (1999)
52. D.M. Reffitt, R. Jugdaohsingh, R.P. Thompson, J.J. Powell, Silicic acid: its gastrointestinal uptake and urinary excretion in man and effects on aluminium excretion. J. Inorg. Biochem. **76**, 141–147 (1999)
53. L. Gu, L.E. Ruff, Z. Qin, M. Corr, S.M. Hedrick, M.J. Sailor, Multivalent porous silicon nanoparticles enhance the immune activation potency of agonistic CD40 antibody. Adv. Mater. **24**, 3981–3987 (2012)
54. S. Low, K. Williams, L. Canham, N.H. Voelcker, Evaluation of mammalian cell adhesion on surface-modified porous silicon. Biomaterials **27**, 4538–4546 (2006)
55. S.M. Moghimi, A.C. Hunter, J.C. Murray, Nanomedicine: current status and future prospects. FASEB J. **19**, 311–330 (2005)
56. J.M. Buriak, Organometallic chemistry on silicon and germanium surfaces. Chem. Rev. **102**, 1271–1308 (2002)
57. J. Song, M. Sailor, Chemical modification of crystalline porous silicon surfaces. Comment. Inorg. Chem. **21**, 69–84 (1999)
58. M. Lai, G. Parish, J. Dell, Y. Liu, A. Keating, Chemical resistance of porous silicon: photolithographic applications. Phys. Stat. Sol. (C). **8**, 1847–1850 (2011)
59. M. Lai, G. Parish, Y. Liu, J.M. Dell, A.J. Keating, Development of an alkaline-compatible porous-silicon photolithographic process. J. Microelectromech. Syst. **20**, 418–423 (2011)
60. T.D. James, A. Keating, G. Parish, C.A. Musca, Low temperature N_2-based passivation technique for porous silicon thin films. Solid State Commun. **149**, 1322–1325 (2009)
61. J. Salonen, V.-P. Lehto, M. Bjorkqvist, E. Laine, L. Niinisto, Studies of thermally-carbonized porous silicon surfaces. Phys. Stat. Sol. (A). **182**, 123–126 (2000)
62. J. Salonen, M. Bjorkqvist, E. Laine, L. Niinisto, Stabilization of porous silicon surface by thermal decomposition of acetylene. Appl. Surf. Sci. **225**, 389–394 (2004)

63. J. Salonen, E. Laine, L. Niinisto, Thermal carbonization of porous silicon surface by acetylene. J. App. Phys. **91**, 456–461 (2002)
64. V.M. Dubin, C. Vieillard, F. Ozanam, J.-N. Chazalviel, Preparation and characterization of surface-modified luminescent porous silicon. Phys. Stat. Sol. (B). **190**, 47–52 (1995)
65. R.C. Anderson, R.S. Muller, C.W. Tobias, Chemical surface modification of porous silicon. J. Electrochem. Soc. **140**, 1393–1396 (1993)
66. M.P. Stewart, J.M. Buriak, Chemical and biological applications of porous silicon technology. Adv. Mater. **12**, 859–869 (2000)
67. R.D. Lowe, E.J. Szili, P. Kirkbride, H. Thissen, G. Siuzdak, N.H. Voelcker, Combined immunocapture and laser desorption/ionization mass spectrometry on porous silicon. Anal. Chem. **82**, 4201–4208 (2010)
68. M.A. Cole, M. Jasieniak, N.H. Voelcker, H. Thissen, R. Horn, H. Griesser, Switchable surface coatings for control over protein adsorption. Biomed. App. Micro. Nanoeng. III, Proc. SPIE. **6416**, 6–10 (2006)
69. M.J. Sweetman, C.J. Shearer, J.G. Shapter, N.H. Voelcker, Dual silane surface functionalization for the selective attachment of human neuronal cells to porous silicon. Langmuir **27**, 9497–9503 (2011)
70. R.B. Vasani, S.J.P. McInnes, M.A. Cole, A.M.M. Jani, A.V. Ellis, N.H. Voelcker, Stimulus-responsiveness and drug release from porous silicon films ATRP-grafted with poly (N-isopropylacrylamide). Langmuir **27**, 7843–7853 (2011)
71. E. Mäkilä, L.M. Bimbo, M. Kaasalainen, B. Herranz, A.J. Airaksinen, M. Heinonen, E. Kukk, J. Hirvonen, H.A. Santos, J. Salonen, Amine modification of thermally carbonized porous silicon with silane coupling chemistry. Langmuir **28**, 14045–14054 (2012)
72. K.A. Kilian, T. Boecking, J.J. Gooding, The importance of surface chemistry in mesoporous materials: lessons from porous silicon biosensors. Chem. Commun. **14**, 630–640 (2009)
73. N. Kim, P. Laibinis, Derivatization of porous silicon by grignard reagents at room temperature. J. Am. Chem. Soc. **120**, 4516–4517 (1998)
74. J. Bateman, R. Eagling, D. Worrall, B. Horrocks, A. Houlton, Alkylation of porous silicon by direct reaction with alkenes and alkynes. Angew. Chem. Int. Ed. **37**, 2638–2685 (1998)
75. J.M. Buriak, M.P. Stewart, T.W. Geders, M.J. Allen, H.C. Choi, J. Smith, D. Raftery, L.T. Canham, Lewis acid mediated hydrosilylation on porous silicon surfaces. J. Am. Chem. Soc. **121**, 11491–11502 (1999)
76. M.P. Stewart, J.M. Buriak, Photopatterned hydrosilylation on porous silicon. Angew. Chem. Int. Ed. **37**, 3257–3260 (1998)
77. M.J. Sweetman, M. Ronci, S.R. Ghaemi, J.E. Craig, N.H. Voelcker, Porous silicon films micropatterned with bioelements as supports for mammalian cells. Adv. Funct. Mater. **22**, 1158–1166 (2012)
78. I. Lees, H. Lin, C. Canaria, C. Gurtner, M. Sailor, G. Miskelly, Chemical stability of porous silicon surfaces electrochemically modified with functional alkyl species. Langmuir **19**, 9812–9817 (2003)
79. R. Boukherroub, A. Petit, A. Loupy, J.-N. Chazalviel, F. Ozanam, Microwave-assisted chemical functionalization of hydrogen-terminated porous silicon surfaces. J. Phys. Chem. B **107**, 13459–13462 (2003)
80. L.R. Clements, P.-Y. Wang, F. Harding, W.-B. Tsai, H. Thissen, N.H. Voelcker, Mesenchymal stem cell attachment to peptide density gradients on porous silicon generated by electrografting. Phys. Stat. Sol. (A). **208**, 1440–1445 (2010)
81. K.-P.S. Dancil, D.P. Greiner, M.J. Sailor, A porous silicon optical biosensor: detection of reversible binding of IgG to a protein A-modified surface. J. Am. Chem. Soc. **121**, 7925–7930 (1999)
82. V. Lin, K. Motesharei, K. Dancil, M.J. Sailor, M.R. Ghadiri, A porous silicon-based optical interferometric biosensor. Science **278**, 840–843 (1997)
83. H.R. Hart, S.E. Létant, S.R. Kane, M.Z. Hadi, S.J. Shields, J.G. Reynolds, New method for attachment of biomolecules to porous silicon. Chem. Commun. 322–323 (2003)

84. J. Drott, K. Lindstrom, L. Rosengren, T. Laurell, Porous silicon as the carrier matrix in microstructured enzyme reactors yeilding high enzyme activities. J. Micromech. Microeng. **7**, 14–23 (1997)
85. T. Laurell, J. Drott, L. Rosengren, K. Lindstrom, Enhanced enzyme activity in silicon integrated enzyme reactors utilizing porous silicon as the coupling matrix. Sensor. Actuat. B: Chem. **31**, 161–166 (1996)
86. E. Secret, K. Smith, V. Dubljevic, E. Moore, P. Macardle, B. Delalat, M.-L. Rogers, T.G. Johns, J.-O. Durand, F. Cunin, N.H. Voelcker, Antibody-functionalized porous silicon nanoparticles for vectorization of hydrophobic drugs. Adv. Healthcare Mater. **2**, 718–727 (2013)
87. B. Guan, A. Magenau, S. Ciampi, K. Gaus, P.J. Reece, J.J. Gooding, Antibody modified porous silicon microparticles for the selective capture of cells. Bioconjug. Chem. **25**, 1282–1289 (2014)
88. D. Holthausen, R.B. Vasani, S.J.P. McInnes, A.V. Ellis, N.H. Voelcker, Polymerization-amplified optical DNA detection on porous silicon templates. ACS Macro Lett. **1**, 919–921 (2012)
89. S.J.P. McInnes, N.H. Voelcker, Porous silicon-based nanostructured microparticles as degradable supports for solid-phase synthesis and release of oligonucleotides. Nanoscale Res. Lett. **7**, 1–10 (2012)
90. C. Steinem, A. Janshoff, V.S.Y. Lin, N.H. Völcker, M. Reza Ghadiri, DNA hybridization-enhanced porous silicon corrosion: mechanistic investigations and prospect for optical interferometric biosensing. Tetrahedron **60**, 11259–11267 (2004)
91. G. Shtenberg, N. Massad-Ivanir, S. Engin, M. Sharon, L. Fruk, E. Segal, DNA-directed immobilization of horseradish peroxidase onto porous SiO2 optical transducers. Nanoscale Res. Lett. **7**, 443 (2012)
92. S.E. Letant, B.R. Hart, S.R. Kane, M.Z. Hadi, S.J. Shields, J.G. Reynolds, Enzyme immobilization on porous silicon surfaces. Adv. Mater. **16**, 689–693 (2004)
93. G.T. Hermanson, *Bioconjugate Techniques* (2008), pp. 1–1233
94. A. Pike, S. Patole, N. Murray, T. Ilyas, B. Connolly, B. Horrocks, A. Houlton, Covalent and non-covalent attachment and patterning of polypyrrole at silicon surfaces. Adv. Mater. **15**, 254–257 (2003)
95. C.B. Gorman, R.J. Petrie, J. Genzer, Effect of substrate geometry on polymer molecular weight and polydispersity during surface-initiated polymerization. Macromolecules **41**, 4856–4865 (2008)
96. S.J.P. McInnes, H. Thissen, N.R. Choudhury, N.H. Voelcker, New biodegradable materials produced by ring opening polymerisation of poly(L-lactide) on porous silicon substrates. J. Colloid Interface Sci. **332**, 336–344 (2009)
97. N. Errien, G. Froyer, G. Louarn, P. Retho, Electrochemical growth of poly (3-dodecylthiophene) into porous silicon layers. Synth. Met. **150**, 255–258 (2005)
98. S. Pace, R.B. Vasani, W. Zhao, S. Perrier, N.H. Voelcker, Photonic porous silicon as a pH sensor. Nanoscale Res. Lett. **9**, 420 (2014)
99. E. Segal, L.A. Perelman, T. Moore, E. Kesselman, M.J. Sailor, Grafting stimuli-responsive polymer brushes to freshly-etched porous silicon. Phys. Stat. Sol. (C). **6**, 1717–1720 (2009)
100. B. Xia, S.-J. Xiao, J. Wang, D.-J. Guo, Stability improvement of porous silicon surface structures by grafting polydimethylsiloxane polymer monolayers. Thin Solid Films **474**, 306–309 (2005)
101. M.S. Yoon, K.H. Ahn, R.W. Cheung, H. Sohn, J.R. Link, F. Cunin, M.J. Sailor, Covalent crosslinking of 1-D photonic crystals of microporous Si by hydrosilylation and ring-opening metathesis polymerization. Chem. Commun. **6**, 680–681 (2003)
102. J. Wu, M.J. Sailor, Chitosan hydrogel-capped porous SiO_2 as a pH responsive nano-valve for triggered release of insulin. Adv. Funct. Mater. **19**, 733–741 (2009)
103. S.J.P. McInnes, E.J. Szili, S.A. Al-Bataineh, J. Xu, M.E. Alf, K.K. Gleason, R.D. Short, N.H. Voelcker, Combination of iCVD and porous silicon for the development of a controlled drug delivery system. ACS Appl. Mater. Interfaces **4**, 3566–3574 (2012)

104. E. Climent, R. Martínez-Máñez, Á. Maquieira, F. Sancenón, M.D. Marcos, E.M. Brun, J. Soto, P. Amorós, Antibody-capped mesoporous nanoscopic materials: design of a probe for the selective chromo-fluorogenic detection of finasteride. ChemistryOpen **1**, 251–259 (2012)
105. E.J. Anglin, L. Cheng, W.R. Freeman, M.J. Sailor, Porous silicon in drug delivery devices and materials. Adv. Drug Deliv. Rev. **60**, 1266–1277 (2008)
106. B.H. King, A. Gramada, J.R. Link, M.J. Sailor, Internally referenced ammonia sensor based on an electrochemically prepared porous SiO_2 photonic crystal. Adv. Mater. **19**, 4044–4048 (2007)
107. M.J. Sweetman, N.H. Voelcker, Chemically patterned porous silicon photonic crystals towards internally referenced organic vapour sensors. RSC Adv. **2**, 4620–4622 (2012)
108. C.-C. Wu, M.J. Sailor, Selective functionalization of the internal and the external surfaces of mesoporous silicon by liquid masking. ACS Nano **7**, 3158–3167 (2013)
109. K.A. Kilian, T. Bocking, K. Gaus, J.J. Gooding, Introducing distinctly different chemical functionalities onto the internal and external surfaces of mesoporous materials. Angew. Chem. Int. Ed. **47**, 2697–2699 (2008)
110. B. Guan, S. Ciampi, G. Le Saux, K. Gaus, P.J. Reece, J.J. Gooding, Different functionalization of the internal and external surfaces in mesoporous materials for biosensing applications using "click" chemistry. Langmuir **27**, 328–334 (2011)
111. J. Wei, J.M. Buriak, G. Siuzdak, Desorption-ionization mass spectrometry on porous silicon. Nature **399**, 243–246 (1999)
112. G. Rong, A. Najmaie, J.E. Sipe, S.M. Weiss, Nanoscale porous silicon waveguide for label-free DNA sensing. Biosens. Bioelectron. **23**, 1572–1576 (2008)
113. B. Wu, G. Rong, J. Zhao, S. Zhang, Y. Zhu, B. He, A nanoscale porous silicon microcavity biosensor for novel label-free tuberculosis antigen-antibody detection. Nano **07**, 1250049–1250057 (2012)
114. T.R. Northen, O. Yanes, M.T. Northen, D. Marrinucci, W. Uritboonthai, J. Apon, S.L. Golledge, A. Nordstrom, G. Siuzdak, Clathrate nanostructures for mass spectrometry. Nature **449**, 1033–1037 (2007)
115. A.M. Rossi, L. Wang, V. Reipa, T.E. Murphy, Porous silicon biosensor for detection of viruses. Biosens. Bioelectron. **23**, 741–745 (2007)
116. S. Chan, Y. Li, L.J. Rothberg, B.L. Miller, P.M. Fauchet, Nanoscale silicon microcavities for biosensing. Mater. Sci. Eng., R **15**, 277–282 (2001)
117. S. Chan, S.R. Horner, P.M. Fauchet, B.L. Miller, Identification of gram negative bacteria using nanoscale silicon microcavities. J. Am. Chem. Soc. **123**, 11797–11798 (2001)
118. P.C. Searson, J.M. Macaulay, S.M. Prokes, The formation, morphology, and optical-properties of porous silicon structures. J. Electrochem. Soc. **139**, 3373–3378 (1992)
119. W. Theiss, Optical properties of porous silicon. Surf. Sci. Rep. **29**, 95–192 (1997)
120. M. Archer, M. Christophersen, P.M. Fauchet, Macroporous silicon electrical sensor for DNA hybridization detection. Biomed. Microdevices **6**, 203–211 (2004)
121. J. Lopez-Garcia, R.J. Martín-Palma, M. Manso, J.M. Martínez-Duart, Porous silicon based structures for the electrical biosensing of glucose. Sensor. Actuat. B: Chem. **126**, 82–85 (2007)
122. O. Meskini, A. Abdelghani, A. Tlili, R. Mgaieth, N. Jaffrezic-Renault, C. Martelet, Porous silicon as functionalized material for immunosensor application. Talanta **71**, 1430–1433 (2007)
123. M.-J. Song, D.-H. Yun, N.-K. Min, S.-I. Hong, Electrochemical biosensor array for liver diagnosis using silanization technique on nanoporous silicon electrode. J. Biosci. Bioeng. **103**, 32–37 (2007)
124. A. Jane, R. Dronov, A. Hodges, N.H. Voelcker, Porous silicon biosensors on the advance. Trends Biotechnol. **27**, 230–239 (2009)
125. S. Dhanekar, S. Jain, Porous silicon biosensor: current status. Biosens. Bioelectron. **41**, 54–64 (2013)

126. B. Gupta, Y. Zhu, B. Guan, P.J. Reece, J.J. Gooding, Functionalised porous silicon as a biosensor: emphasis on monitoring cells in vivo and in vitro. Analyst **138**, 3593–3615 (2013)
127. J. Charrier, M. Dribek, Theoretical study of the factor of merit of porous silicon based optical biosensors. J. Appl. Phys. **107**, 044905 (2010)
128. H. Ouyang, M. Christophersen, R. Viard, B.L. Miller, P.M. Fauchet, Macroporous silicon microcavities for macromolecule detection. Adv. Funct. Mater. **15**, 1851–1859 (2005)
129. J. Chapron, S.A. Alekseev, V. Lysenko, V.N. Zaitsev, D. Barbier, Analysis of interaction between chemical agents and porous Si nanostructures using optical sensing properties of infra-red Rugate filters. Sensor. Actuat. B: Chem. **120**, 706–711 (2007)
130. M. Hiraoui, L. Haji, M. Guendouz, N. Lorrain, A. Moadhen, M. Oueslati, Towards a biosensor based on anti resonant reflecting optical waveguide fabricated from porous silicon. Biosens. Bioelectron. **36**, 212–216 (2012)
131. H. Ouyang, L.A. DeLouise, B.L. Miller, P.M. Fauchet, Label-free quantitative detection of protein using macroporous silicon photonic bandgap biosensors. Anal. Chem. **79**, 1502–1506 (2007)
132. L.A. DeLouise, P.M. Kou, B.L. Miller, Cross-correlation of optical microcavity biosensor response with immobilized enzyme activity. Insights into biosensor sensitivity. Anal. Chem. **77**, 3222–3230 (2005)
133. M.M. Orosco, C. Pacholski, M.J. Sailor, Real-time monitoring of enzyme activity in a mesoporous silicon double layer. Nat. Nanotech. **4**, 255–258 (2009)
134. G. Di Francia, V. La Ferrara, S. Manzo, S. Chiavarini, Towards a label-free optical porous silicon DNA sensor. Biosens. Bioelectron. **21**, 661–665 (2005)
135. L. De Stefano, L. Rotiroti, I. Rendina, L. Moretti, V. Scognamiglio, M. Rossi, S. D'Auria, Porous silicon-based optical microsensor for the detection of l-glutamine. Biosens. Bioelectron. **21**, 1664–1667 (2006)
136. L.M. Bonanno, L.A. DeLouise, Whole blood optical biosensor. Biosens. Bioelectron. **23**, 444–448 (2007)
137. V.M. Starodub, L.L. Fedorenko, A.P. Sisetskiy, N.F. Starodub, Control of myoglobin level in a solution by an immune sensor based on the photoluminescence of porous silicon. Sensor. Actuat. B: Chem. **58**, 409–414 (1999)
138. C.K. Tsang, T.L. Kelly, M.J. Sailor, Y.Y. Li, Highly stable porous silicon-carbon composites as label-free optical biosensors. ACS Nano **6**, 10546–10554 (2012)
139. F.S.H. Krismastuti, W.L.A. Brooks, M.J. Sweetman, B.S. Sumerlin, N.H. Voelcker, A photonic glucose biosensor for chronic wound prognostics. J. Mater. Chem. B **2**, 3972–3983 (2014)
140. A. Ressine, S. Ekström, G. Marko-Varga, T. Laurell, Macro-/nanoporous silicon as a support for high-performance protein microarrays. Anal. Chem. **75**, 6968–6974 (2003)
141. S. Lee, S. Kim, J. Malm, O.C. Jeong, H. Lilja, T. Laurell, Improved porous silicon microarray based prostate specific antigen immunoassay by optimized surface density of the capture antibody. Anal. Chim. Acta **796**, 108–114 (2013)
142. D. Finnskog, A. Ressine, T. Laurell, G. Marko-Varga, Integrated protein microchip assay with dual fluorescent- and MALDI read-out. J. Proteome Res. **3**, 988–994 (2004)
143. A. Ressine, I. Corin, K. Järås, G. Guanti, C. Simone, G. Marko-Varga, T. Laurell, Porous silicon surfaces—a candidate substrate for reverse protein arrays in cancer biomarker detection. Electrophoresis **28**, 4407–4415 (2007)
144. K. Järås, A. Ressine, E. Nilsson, J. Malm, G. Marko-Varga, H. Lilja, T. Laurell, Reverse-phase versus sandwich antibody microarray, technical comparison from a clinical perspective. Anal. Chem. **79**, 5817–5825 (2007)
145. K. Järås, B. Adler, A. Tojo, J. Malm, G. Marko-Varga, H. Lilja, T. Laurell, Porous silicon antibody microarrays for quantitative analysis: measurement of free and total PSA in clinical plasma samples. Clin. Chim. Acta **414**, 76–84 (2012)
146. K. Järås, A.A. Tajudin, A. Ressine, T. Soukka, G. Marko-Varga, A. Bjartell, J. Malm, T. Laurell, H. Lilja, ENSAM: Europium nanoparticles for signal enhancement of antibody microarrays on nanoporous silicon. J. Proteome Res. **7**, 1308–1314 (2008)

147. A. Lenshof, A. Ahmad-Tajudin, K. Järås, A.-M. Sward-Nilsson, L. Aberg, G. Marko-Varga, J. Malm, H. Lilja, T. Laurell, Acoustic whole blood plasmapheresis chip for prostate specific antigen microarray diagnostics. Anal. Chem. **81**, 6030–6037 (2009)
148. S. Lee, E. Silajdzic, H. Yang, M. Bjorkqvist, S. Kim, O.C. Jeong, O. Hansson, T. Laurell, A porous silicon immunoassay platform for fluorometric determination of alpha-synuclein in human cerebrospinal fluid. Microchim. Acta **181**, 1143–1149 (2014)
149. S.A. Trauger, E.P. Go, Z.X. Shen, J.V. Apon, B.J. Compton, E. Bouvier, M.G. Finn, G. Siuzdak, High sensitivity and analyte capture with desorption/ionization mass spectrometry on silylated porous silicon. Anal. Chem. **76**, 4484–4489 (2004)
150. M. Karas, F. Hillenkamp, Laser desorption ionization of proteins with molecular masses exceeding 10000 daltons. Anal. Chem. **60**, 2299–2301 (1988)
151. K. Tanaka, H. Waki, Y. Ido, S. Akita, Y. Yoshida, T. Yoshida, Protein and polymer analyses up to *m/z* 100 000 by laser ionization time-of-flight mass spectrometry. Rapid Commun. Mass Spectrom. **2**, 151–153 (1988)
152. Z.X. Shen, J.J. Thomas, C. Averbuj, K.M. Broo, M. Engelhard, J.E. Crowell, M.G. Finn, G. Siuzdak, Porous silicon as a versatile platform for laser desorption/ionization mass spectrometry. Anal. Chem. **73**, 612–619 (2001)
153. G.H. Luo, Y. Chen, G. Siuzdak, A. Vertes, Surface modification and laser pulse length effects on internal energy transfer in DIOS. J. Phys. Chem. B **109**, 24450–24456 (2005)
154. T.R. Northen, H.-K. Woo, M.T. Northen, A. Nordstroem, W. Uritboonthail, K.L. Turner, G. Siuzdak, High surface area of porous silicon drives desorption of intact molecules. J. Am. Soc. Mass Spectrom. **18**, 1945–1949 (2007)
155. Q. Liu, L. He, Quantitative study of solvent and surface effects on analyte ionization in desorption ionization on silicon (DIOS) mass spectrometry. J. Am. Soc. Mass Spectrom. **19**, 8–13 (2008)
156. R.A. Kruse, X.L. Li, P.W. Bohn, J.V. Sweedler, Experimental factors controlling analyte ion generation in laser desorption/ionization mass spectrometry on porous silicon. Anal. Chem. **73**, 3639–3645 (2001)
157. Z.X. Shen, E.P. Go, A. Gamez, J.V. Apon, V. Fokin, M. Greig, M. Ventura, J.E. Crowell, O. Blixt, J.C. Paulson, R.C. Stevens, M.G. Finn, G. Siuzdak, A mass spectrometry plate reader: monitoring enzyme activity and inhibition with a desorption/ionization on silicon (DIOS) platform. ChemBioChem **5**, 921–927 (2004)
158. O. Yanes, H.-K. Woo, T.R. Northen, S.R. Oppenheimer, L. Shriver, J. Apon, M.N. Estrada, M.J. Potchoiba, R. Steenwyk, M. Manchester, G. Siuzdak, Nanostructure initiator mass spectrometry: tissue imaging and direct biofluid analysis. Anal. Chem. **81**, 2969–2975 (2009)
159. J.J. Thomas, Z.X. Shen, J.E. Crowell, M.G. Finn, G. Siuzdak, Desorption/ionization on silicon (DIOS): a diverse mass spectrometry platform for protein characterization. PNAS **98**, 4932–4937 (2001)
160. E.P. Go, W. Uritboonthai, J.V. Apon, S.A. Trauger, A. Nordstrom, G. O'Maille, S.M. Brittain, E.C. Peters, G. Siuzdak, Selective metabolite and peptide capture/mass detection using fluorous affinity tags. J. Proteome Res. **6**, 1492–1499 (2007)
161. D. Finnskog, K. Järås, A. Ressine, J. Malm, G. Marko-Varga, H. Lilja, T. Laurell, High-speed biomarker identification utilizing porous silicon nanovial arrays and MALDI-TOF mass spectrometry. Electrophoresis **27**, 1093–1103 (2006)
162. D.B. Wall, J.W. Finch, S.A. Cohen, Comparison of desorption/ionization on silicon (DIOS) time-of-flight and liquid chromatography/tandem mass spectrometry for assaying enzyme-inhibition reactions. Rapid Commun. Mass Spectrom. **18**, 1482–1486 (2004)
163. S.Y. Xu, C.S. Pan, L.G. Hu, Y. Zhang, Z. Guo, X. Li, H.F. Zou, Enzymatic reaction of the immobilized enzyme on porous silicon studied by matrix-assisted laser desorption/ionization-time of flight-mass spectrometry. Electrophoresis **25**, 3669–3676 (2004)
164. M. Ronci, D. Rudd, T. Guinan, K. Benkendorff, N.H. Voelcker, Mass spectrometry imaging on porous silicon: investigating the distribution of bioactives in marine mollusc tissues. Anal. Chem. **84**, 8996–9001 (2012)

165. M.P. Greving, G.J. Patti, G. Siuzdak, Nanostructure-initiator mass spectrometry metabolite analysis and imaging. Anal. Chem. **83**, 2–7 (2011)
166. K.P. Law, Laser desorption/ionization mass spectrometry on nanostructured semiconductor substrates: DIOS and QuickMass. Int. J. Mass Spectrom. **290**, 72–84 (2010)
167. A.Y. Lim, J. Ma, Y.C.F. Boey, Development of nanomaterials for SALDI-MS analysis in forensics. Adv. Mater. **24**, 4211–4216 (2012)
168. R.D. Lowe, G.E. Guild, P. Harpas, P. Kirkbride, P. Hoffmann, N.H. Voelcker, H. Kobus, Rapid drug detection in oral samples by porous silicon assisted laser desorption/ionization mass spectrometry. Rapid Commun. Mass Spectrom. **23**, 3543–3548 (2009)
169. A. Kraj, J. Jarzebinska, A. Gorecka-Drzazga, J. Dziuban, J. Silberring, Identification of catecholamines in the immune system by desorption/ionization on silicon. Rapid Commun. Mass Spectrom. **20**, 1969–1972 (2006)
170. S. Okuno, Y. Wada, Measurement of serum salicylate levels by solid-phase extraction and desorption/ionization on silicon mass spectrometry. J. Mass Spectrom. **40**, 1000–1004 (2005)
171. L. Hu, S. Xu, C. Pan, H. Zou, G. Jiang, Preparation of a biochip on porous silicon and application for label-free detection of small molecule-protein interactions. Rapid Commun. Mass Spectrom. **21**, 1277–1281 (2007)
172. Q. Liu, Y. Xiao, C. Pagan-Miranda, Y.M. Chiu, L. He, Metabolite imaging using matrix-enhanced surface-assisted laser desorption/ionization mass spectrometry (ME-SALDI-MS). J. Am. Soc. Mass Spectrom. **20**, 80–88 (2009)
173. T.R. Northen, J.-C. Lee, L. Hoang, J. Raymond, D.-R. Hwang, S.M. Yannone, C.-H. Wong, G. Siuzdak, A nanostructure-initiator mass spectrometry-based enzyme activity assay. PNAS **105**, 3678–3683 (2008)
174. H.-K. Woo, T.R. Northen, O. Yanes, G. Siuzdak, Nanostructure-initiator mass spectrometry: a protocol for preparing and applying NIMS surfaces for high-sensitivity mass analysis. Nat. Protoc. **3**, 1341–1349 (2008)
175. G.J. Patti, H.-K. Woo, O. Yanes, L. Shriver, D. Thomas, W. Uritboonthai, J.V. Apon, R. Steenwyk, M. Manchester, G. Siuzdak, Detection of carbohydrates and steroids by cation-enhanced nanostructure-initiator mass spectrometry (NIMS) for biofluid analysis and tissue imaging. Anal. Chem. **82**, 121–128 (2010)
176. R.M. Caprioli, T.B. Farmer, J. Gile, Molecular imaging of biological samples: localization of peptides and proteins using MALDI-TOF MS. Anal. Chem. **69**, 4751–4760 (1997)
177. P. Chaurand, S.A. Schwartz, R.M. Caprioli, Profiling and imaging proteins in tissue sections by MS. Anal. Chem. **76**, 86A–93A (2004)
178. J. Franck, K. Arafah, M. Elayed, D. Bonnel, D. Vergara, A. Jacquet, D. Vinatier, M. Wisztorski, R. Day, I. Fournier, M. Salzet, MALDI imaging mass spectrometry: state of the art technology in clinical proteomics. Mol. Cell. Proteomics **8**, 2023–2033 (2009)
179. A. Thomas, P. Chaurand, Advances in tissue section preparation for MALDI imaging MS. Bioanalysis **6**, 967–982 (2014)
180. L.A. McDonnell, R.M.A. Heeren, Imaging mass spectrometry. Mass Spectrom. Rev. **26**, 606–643 (2007)
181. R.A. Kruse, S.S. Rubakhin, E.V. Romanova, P.W. Bohn, J.V. Sweedler, Direct assay of Aplysia tissues and cells with laser desorption/ionization mass spectrometry on porous silicon. J. Mass Spectrom. **36**, 1317–1322 (2001)
182. Q. Liu, Z. Guo, L. He, Mass spectrometry imaging of small molecules using desorption/ionization on silicon. Anal. Chem. **79**, 3535–3541 (2007)
183. A. Roempp, B. Spengler, Mass spectrometry imaging with high resolution in mass and space. Histochem. Cell Biol. **139**, 759–783 (2013)
184. R.J.A. Goodwin, S.R. Pennington, A.R. Pitt, Protein and peptides in pictures: imaging with MALDI mass spectrometry. Proteomics **8**, 3785–3800 (2008)
185. B. Spengler, M. Hubert, Scanning microprobe matrix-assisted laser desorption ionization (SMALDI) mass spectrometry: instrumentation for sub-micrometer resolved LDI and MALDI surface analysis. J. Am. Soc. Mass Spectrom. **13**, 735–748 (2002)

186. R. Calavia, F.E. Annanouch, X. Correig, O. Yanes, Nanostructure initiator mass spectrometry for tissue imaging in metabolomics: future prospects and perspectives. J Proteomics **75**, 5061–5068 (2012)
187. R.M. Sturm, T. Greer, R. Chen, B. Hensen, L. Li, Comparison of NIMS and MALDI platforms for neuropeptide and lipid mass spectrometric imaging in C. borealis brain tissue. Anal. Methods **5**, 1623–1628 (2013)
188. D.Y. Lee, V. Platt, B. Bowen, K. Louie, C.A. Canaria, C.T. McMurray, T. Northen, Resolving brain regions using nanostructure initiator mass spectrometry imaging of phospholipids. Integr. Biol. **4**, 693–699 (2012)
189. K. Deng, T.E. Takasuka, R. Heins, X. Cheng, L.F. Bergeman, J. Shi, R. Aschenbrener, S. Deutsch, S. Singh, K.L. Sale, B.A. Simmons, P.D. Adams, A.K. Singh, B.G. Fox, T.R. Northen, Rapid kinetic characterization of glycosyl hydrolases based on oxime derivatization and nanostructure-initiator mass spectrometry (NIMS). ACS Chem. Biol. **9**, 1470–1479 (2014)
190. S.S. Rubakhin, J.C. Jurchen, E.B. Monroe, J.V. Sweedler, Imaging mass spectrometry: fundamentals and applications to drug discovery. Drug Discovery Today **10**, 823–837 (2005)
191. G.R. Castro, B. Panilaitis, D.L. Kaplan, Emulsan, a tailorable biopolymer for controlled release. Bioresour. Technol. **99**, 4566–4571 (2008)
192. S.T. Andreadis, D.J. Geer, Biomimetic approaches to protein and gene delivery for tissue regeneration. Trends Biotechnol. **24**, 331–337 (2006)
193. C. Elvira, A. Gallardo, J. San Roman, A. Cifuentes, Covalent polymer-drug conjugates. Molecules **10**, 114–125 (2005)
194. S. Sharma, A. Jasper Nijdam, P. Sinha, R. Walczak, X. Liu, M. Cheng, M. Ferrari, Controlled-release microchips. Expert Opin. Drug Deliv. **3**, 379–394 (2006)
195. K. Soppimath, T. Aminabhavi, A. Kulkarni, W. Rudzinski, Biodegradable polymeric nanoparticles as drug delivery devices. J. Controlled Release **70**, 1–20 (2001)
196. K.C. Wood, J.Q. Boedicker, D.M. Lynn, P.T. Hammond, Tunable drug release from hydrolytically degradable layer-by-layer thin films. Langmuir **21**, 1603–1609 (2005)
197. T. Tsukagoshi, Y. Kondo, N. Yoshino, Preparation of thin polymer films with controlled drug release. Colloids Surf., B **57**, 219–225 (2007)
198. L.M. Bimbo, M. Sarparanta, H.A. Santos, A.J. Airaksinen, E. Mäkilä, T. Laaksonen, L. Peltonen, V.-P. Lehto, J. Hirvonen, J. Salonen, Biocompatibility of thermally hydrocarbonized porous silicon nanoparticles and their biodistribution in rats. ACS Nano **4**, 3023–3032 (2010)
199. M. Kovalainen, J. Mönkäre, M. Kaasalainen, J. Riikonen, V.-P. Lehto, J. Salonen, K.-H. Herzig, K. Järvinen, Development of porous silicon nanocarriers for parenteral peptide delivery. Mol. Pharm. **10**, 353–359 (2013)
200. H. Shen, J. You, G. Zhang, A. Ziemys, Q. Li, L. Bai, X. Deng, D.R. Erm, X. Liu, C. Li, M. Ferrari, Cooperative, nanoparticle-enabled thermal therapy of breast cancer. Adv. Healthcare Mater. **1**, 84–89 (2012)
201. R. Xu, Y. Huang, J. Mai, G. Zhang, X. Guo, X. Xia, E.J. Koay, G. Qin, D.R. Erm, Q. Li, X. Liu, M. Ferrari, H. Shen, Multistage vectored siRNA targeting ataxia-telangiectasia mutated for breast cancer therapy. Small **9**, 1799–1808 (2013)
202. J. Salonen, A.M. Kaukonen, J. Hirvonen, V.-P. Lehto, Mesoporous silicon in drug delivery applications. J. Pharm. Sci. **97**, 632–653 (2008)
203. C.A. Prestidge, T.J. Barnes, C.-H. Lau, C. Barnett, A. Loni, L. Canham, Mesoporous silicon: a platform for the delivery of therapeutics. Expert Opin. Drug Deliv. **4**, 101–110 (2007)
204. J. Chhablani, A. Nieto, H. Hou, E.C. Wu, W.R. Freeman, M.J. Sailor, L. Cheng, Oxidized porous silicon particles covalently grafted with daunorubicin as a sustained intraocular drug delivery system. Invest. Ophthalmol. Vis. Sci. **54**, 1268–1279 (2013)
205. E.J. Anglin, M.P. Schwartz, V.P. Ng, L.A. Perelman, M.J. Sailor, Engineering the chemistry and nanostructure of porous silicon fabry-pérot films for loading and release of a steroid. Langmuir **20**, 11264–11269 (2004)

206. L. Vaccari, D. Canton, N. Zaffaroni, R. Villa, M. Tormen, E. di Fabrizio, Porous silicon as drug carrier for controlled delivery of doxorubicin anticancer agent. Microelectron. Eng. **83**, 1598–1601 (2006)
207. J.S. Andrew, E.J. Anglin, E.C. Wu, M.Y. Chen, L. Cheng, W.R. Freeman, M.J. Sailor, Sustained release of a monoclonal antibody from electrochemically prepared mesoporous silicon oxide. Adv. Funct. Mater. **20**, 4168–4174 (2010)
208. N.L. Fry, G.R. Boss, M.J. Sailor, Oxidation-induced trapping of drugs in porous silicon microparticles. Chem. Mater. **26**, 2758–2764 (2014)
209. S.M. Haidary, E.P. Córcoles, N.K. Ali, Nanoporous silicon as drug delivery systems for cancer therapies. J. Nanomater **2012**, 1–15 (2012)
210. L.M. Bimbo, E. Mäkilä, T. Laaksonen, V.-P. Lehto, J. Salonen, J. Hirvonen, H.A. Santos, Drug permeation across intestinal epithelial cells using porous silicon nanoparticles. Biomaterials **32**, 2625–2633 (2011)
211. J. Salonen, L. Laitinen, A. Kaukonen, J. Tuura, M. Bjorkqvist, T. Heikkila, K. Vaha-Heikkila, J. Hirvonen, V.-P. Lehto, Mesoporous silicon microparticles for oral drug delivery: loading and release of five model drugs. J. Controlled Release **108**, 362–374 (2005)
212. A. Foraker, R. Walcazak, M. Cohen, T. Boiarski, C. Grove, P. Swaan, Microfabricated porous silicon particles enhance paracellular delivery of insulin across intestinal Caco-2 cell monolayers. Pharm. Res. **20**, 110–116 (2003)
213. C.-H. Lee, L.-W. Lo, C.-Y. Mou, C.-S. Yang, Synthesis and characterization of positive-charge functionalized mesoporous silica nanoparticles for oral drug delivery of an anti-inflammatory drug. Adv. Funct. Mater. **18**, 3283–3292 (2008)
214. L.A. Perelman, C. Pacholski, Y.Y. Li, M.S. VanNieuwenhze, M.J. Sailor, pH-triggered release of vancomycin from protein-capped porous silicon films. Nanomedicine **3**, 31–43 (2008)
215. H. Hou, A. Nieto, F. Ma, W.R. Freeman, M.J. Sailor, L. Cheng, Tunable sustained intravitreal drug delivery system for daunorubicin using oxidized porous silicon. J. Controlled Release **178**, 46–54 (2014)
216. M. Kilpeläinen, J. Mönkäre, M.A. Vlasova, J. Riikonen, V.-P. Lehto, J. Salonen, K. Järvinen, K.-H. Herzig, Nanostructured porous silicon microparticles enable sustained peptide (Melanotan II) delivery. Eur. J. Pharm. Biopharm. **77**, 20–25 (2011)
217. E. Tasciotti, X. Liu, R. Bhavane, K. Plant, A.D. Leonard, B.K. Price, M.M.-C. Cheng, P. Decuzzi, J.M. Tour, F. Robertson, M. Ferrari, Mesoporous silicon particles as a multistage delivery system for imaging and therapeutic applications. Nat. Nanotech. **3**, 151–157 (2008)
218. M.P. Schwartz, A.M. Derfus, S.D. Alvarez, S.N. Bhatia, M.J. Sailor, The smart petri dish: a nanostructured photonic crystal for real-time monitoring of living cells. Langmuir **22**, 7084–7090 (2006)
219. L.A. DeLouise, P.M. Fauchet, B.L. Miller, A.A. Pentland, Hydrogel-supported optical-microcavity sensors. Adv. Mater. **17**, 2199–2203 (2005)
220. I. Batra, J.L. Coffer, L.T. Canham, Electronically-responsive delivery from a calcified mesoporous silicon structure. Biomed. Microdevices **8**, 93–97 (2006)
221. H. Tsuji, K. Sumida, Poly(L-lactide): v. effects of storage in swelling solvents on physical properties and structure of poly(L-lactide). J. Appl. Polym. Sci. **79**, 1582–1589 (2001)
222. A. Hatefi, D. Knight, B. Amsden, A biodegradable injectable thermoplastic for localised camptothecin delivery. J. Pharm. Sci. **93**, 1195–1204 (2004)
223. K. Nan, F. Ma, H. Hou, W.R. Freeman, M.J. Sailor, L. Cheng, Porous silicon oxide-PLGA composite microspheres for sustained ocular delivery of daunorubicin. Acta Biomater. **10**, 3505–3512 (2014)
224. T.R. Dargaville, B.L. Farrugia, J.A. Broadbent, S. Pace, Z. Upton, N.H. Voelcker, Sensors and imaging for wound healing: a review. Biosens. Bioelectron. **41**, 30–42 (2013)
225. S. Pace, R.B. Vasani, F. Cunin, N.H. Voelcker, Study of the optical properties of a thermoresponsive polymer grafted onto porous silicon scaffolds. New J. Chem. **37**, 228–235 (2012)

226. P. Mukherjee, M.A. Whitehead, R.A. Senter, D. Fan, J.L. Coffer, L.T. Canham, Biorelevant mesoporous silicon/polymer composites: directed assembly, disassembly, and controlled release. Biomed. Microdevices **8**, 9–15 (2006)
227. S.J.P. McInnes, Y. Irani, K.A. Williams, N.H. Voelcker, Controlled drug delivery from composites of nanostructured porous silicon and poly(L-lactide). Nanomedicine **7**, 995–1016 (2012)
228. A.M. Kaukonen, L. Laitinen, J. Salonen, J. Tuura, Enhanced in vitro permeation of furosemide loaded into thermally carbonized mesoporous silicon (TCPSi) microparticles. Eur. J. Pharm. Biopharm. (2007)
229. R.E. Serda, B. Godin, E. Blanco, C. Chiappini, M. Ferrari, Multi-stage delivery nano-particle systems for therapeutic applications. Biochim. Biophys. Acta Gen. Subj. **1810**, 317–329 (2011)
230. R.E. Serda, J. Gu, R.C. Bhavane, X. Liu, C. Chiappini, P. Decuzzi, M. Ferrari, The association of silicon microparticles with endothelial cells in drug delivery to the vasculature. Biomaterials **30**, 2440–2448 (2009)
231. R.E. Serda, A. Mack, M. Pulikkathara, A.M. Zaske, C. Chiappini, J.R. Fakhoury, D. Webb, B. Godin, J.L. Conyers, X.W. Liu, J.A. Bankson, M. Ferrari, Cellular association and assembly of a multistage delivery system. Small **6**, 1329–1340 (2010)
232. R.E. Serda, A. Mack, A.L. van de Ven, S. Ferrati, K. Dunner Jr, B. Godin, C. Chiappini, M. Landry, L. Brousseau, X. Liu, A.J. Bean, M. Ferrari, Logic-embedded vectors for intracellular partitioning, endosomal escape, and exocytosis of nanoparticles. Small **6**, 2691–2700 (2010)
233. R.E. Serda, S. Ferrati, B. Godin, E. Tasciotti, X. Liu, M. Ferrari, Mitotic trafficking of silicon microparticles. Nanoscale **1**, 250–259 (2009)
234. R. Serda, Particle platforms for cancer immunotherapy. Int. J. Nanomed. **8**, 1683–1696 (2013)
235. R.E. Serda, C. Chiappini, D. Fine, E. Tasciotti, M. Ferrari, Porous silicon particles for imaging and therapy of cancer. Nanotechnol. Life Sci. (2009)
236. A. Parodi, N. Quattrocchi, A.L. van de Ven, C. Chiappini, M. Evangelopoulos, J.O. Martinez, B.S. Brown, S.Z. Khaled, I.K. Yazdi, M.V. Enzo, L. Isenhart, M. Ferrari, E. Tasciotti, Synthetic nanoparticles functionalized with biomimetic leukocyte membranes possess cell-like functions. Nat. Nanotech. **8**, 61–68 (2013)
237. N.H. Alsharif, C.E.M. Berger, S.S. Varanasi, Y. Chao, B.R. Horrocks, H.K. Datta, Alkyl-capped silicon nanocrystals lack cytotoxicity and have enhanced intracellular accumulation in malignant cells via cholesterol-dependent endocytosis. Small **5**, 221–228 (2009)
238. Y. Koh, S. Jang, J. Kim, S. Kim, Y. Ko, S. Cho, H. Sohn, DBR PSi/PMMA composite materials for smart patch application. Colloids Surf. A: Physicochem. Eng. Aspects **313–314**, 328–331 (2008)
239. A.M. Minino, S.L. Murphy, J. Xu, K.D. Kochanek, Deaths: final data for 2008. Nat. Vital Stat. Rep. **59**, 1–127 (2012)
240. Y. Wakai, J. Matsui, K. Koizumi, S. Tsunoda, H. Makimoto, I. Ohizumi, K. Taniguchi, S. Kaiho, H. Saito, N. Utoguchi, Y. Tsutsumi, S. Nakagawa, Y. Ohsugi, T. Mayumi, Effective cancer targeting using an anti-tumor tissue vascular endothelium-specific monoclonal antibody (TES-23). Jpn. J. Cancer Res. **91**, 1319–1325 (2000)
241. W.R. Sanhai, J.H. Sakamoto, R. Canady, M. Ferrari, Seven challenges for nanomedicine. Nat. Nanotech. **3**, 1–4 (2008)
242. Y.H. Bae, K. Park, Targeted drug delivery to tumors: myths, reality and possibility. J. Controlled Release **153**, 198–205 (2011)
243. E. Ruoslahti, S.N. Bhatia, M.J. Sailor, Targeting of drugs and nanoparticles to tumors. J. Cell Biol. **188**, 759–768 (2010)
244. R.K. Jain, Transport of molecules, particles, and cells in solid tumors. Annu. Rev. Biomed. Eng. **1**, 241–263 (1999)

245. L. Brannon-Peppas, J.O. Blanchette, Nanoparticle and targeted systems for cancer therapy. Adv. Drug Deliv. Rev. (2012)
246. O.H. Aina, R. Liu, J.L. Sutcliffe, J. Marik, C.X. Pan, K.S. Lam, From combinatorial chemistry to cancer-targeting peptides. Mol. Pharm. **4**, 631–651 (2007)
247. O.H. Aina, T.C. Sroka, M.-L. Chen, K.S. Lam, Therapeutic cancer targeting peptides. Biopolymers **66**, 184–199 (2002)
248. V. Bagalkot, L. Zhang, E. Levy-Nissenbaum, S. Jon, P.W. Kantoff, R. Langer, O.C. Farokhzad, Quantum dot—aptamer conjugates for synchronous cancer imaging, therapy, and sensing of drug delivery based on bi-fluorescence resonance energy transfer. Nano Lett. **7**, 3065–3070 (2007)
249. V. Lebret, L. Raehm, J.-O. Durand, M. Smaïhi, M.H.V. Werts, M. Blanchard-Desce, D. Méthy-Gonnod, C. Dubernet, Folic acid-targeted mesoporous silica nanoparticles for two-photon fluorescence. J. Biomed. Nanotechnol. **6**, 176–180 (2010)
250. M. Gary-Bobo, Y. Mir, C. Rouxel, D. Brevet, I. Basile, M. Maynadier, O. Vaillant, O. Mongin, M. Blanchard-Desce, A. Morère, M. Garcia, J.-O. Durand, L. Raehm, Mannose-functionalized mesoporous silica nanoparticles for efficient two-photon photodynamic therapy of solid tumors. Angew. Chem. Int. Ed. **50**, 11425–11429 (2011)
251. H.A. Santos, L.M. Bimbo, B. Herranz, M.-A. Shahbazi, J. Hirvonen, J. Salonen, Nanostructured porous silicon in preclinical imaging: moving from bench to bedside. J. Mater. Res. **28**, 152–164 (2012)
252. C. Hong, C. Lee, In vitro cell tests of pancreatic malignant tumor cells by photothermotherapy based on DMSO porous silicon colloids. Laser Med. Sci. **29**, 221–223 (2014)
253. E. Secret, M. Maynadier, A. Gallud, A. Chaix, E. Bouffard, M. Gary-Bobo, N. Marcotte, O. Mongin, El, K. Cheikh, V. Hugues, M. Auffan, C. Frochot, A. Morère, P. Maillard, M. Blanchard-Desce, M.J. Sailor, M. Garcia, J.-O. Durand, F. Cunin, Two-photon excitation of porphyrin-functionalized porous silicon nanoparticles for photodynamic therapy. Adv. Mater. **26**, 7643–7648 (2014)
254. A.S.-W. Goh, A.Y.-F. Chung, R.H.-G. Lo, T.-N. Lau, S.W.-K. Yu, M. Chng, S. Satchithanantham, S.L.-E. Loong, D.C.-E. Ng, B.-C. Lim, S. Connor, P.K.-H. Chow, A novel approach to brachytherapy in hepatocellular carcinoma using a phosphorous32 (32P) brachytherapy delivery device—a first-in-man study. Int. J. Radiat. Oncol. Biol. Phys. **67**, 786–792 (2007)
255. L.C. Kennedy, L.R. Bickford, N.A. Lewinski, A.J. Coughlin, Y. Hu, E.S. Day, J.L. West, R.A. Drezek, A new era for cancer treatment: gold-nanoparticle-mediated thermal therapies. Small **7**, 169–183 (2011)
256. D.K. Chatterjee, P. Diagaradjane, S. Krishnan, Nanoparticle-mediated hyperthermia in cancer therapy. Ther. Deliv. **2**, 1001–1014 (2011)
257. C. Hong, J. Lee, M. Son, S.S. Hong, C. Lee, In-vivo cancer cell destruction using porous silicon nanoparticles. Anticancer Drugs **22**, 971–977 (2011)
258. C. Hong, J. Lee, H. Zheng, S.S. Hong, C. Lee, Porous silicon nanoparticles for cancer photothermotherapy. Nanoscale Res. Lett. **6**, 321 (2011)
259. P. Puvanakrishnan, J. Park, D. Chatterjee, S. Krishnan, J.W. Tunnell, In vivo tumor targeting of gold nanoparticles: effect of particle type and dosing strategy. Int. J. Nanomed. **7**, 1251–1258 (2012)
260. M. Ma, H. Chen, Y. Chen, X. Wang, F. Chen, X. Cui, J. Shi, Au capped magnetic core/mesoporous silica shell nanoparticles for combined photothermo-/chemo-therapy and multimodal imaging. Biomaterials **33**, 989–998 (2012)
261. C.A. Robertson, D.H. Evans, H. Abrahamse, Photodynamic therapy (PDT): a short review on cellular mechanisms and cancer research applications for PDT. J. Photochem. Photobiol. B **96**, 1–8
262. L.T. Canham, D. Ferguson, Porous silicon in brachytherapy, in *Handbook of Porous Silicon*, ed. by L.T. Canham (2014)

263. K. Zhang, S.L.E. Loong, S. Connor, S.W.K. Yu, S.-Y. Tan, R.T.H. Ng, K.M. Lee, L. Canham, P.K.H. Chow, Complete tumor response following intratumoral 32P BioSilicon on human hepatocellular and pancreatic carcinoma xenografts in nude mice. Clin. Cancer Res. **11**, 7532–7537 (2005)
264. A. Gizzatov, C. Stigliano, J.S. Ananta, R. Sethi, R. Xu, A. Guven, M. Ramirez, H. Shen, A. Sood, M. Ferrari, L.J. Wilson, X. Liu, P. Decuzzi, Cancer Lett. **352**, 1–5 (2014)
265. A.M. Kallinen, M.P. Sarparanta, D. Liu, E.M. Mäkilä, J.J. Salonen, J.T. Hirvonen, H.A. Santos, A.J. Airaksinen, In vivo evaluation of porous silicon and porous silicon solid lipid nanocomposites for passive targeting and imaging. Mol. Pharm. **11**, 2876–2886 (2014)
266. M. Sarparanta, L.M. Bimbo, J. Rytkönen, E. Mäkilä, T.J. Laaksonen, P. Laaksonen, M. Nyman, J. Salonen, M.B. Linder, J. Hirvonen, H.A. Santos, A.J. Airaksinen, Intravenous delivery of hydrophobin-functionalized porous silicon nanoparticles: stability, plasma protein adsorption and biodistribution. Mol. Pharm. **9**, 654–663 (2012)
267. A.L. van de Ven, P. Kim, O. Haley, J.R. Fakhoury, G. Adriani, J. Schmulen, P. Moloney, F. Hussain, M. Ferrari, X. Liu, S.-H. Yun, P. Decuzzi, Rapid tumoritropic accumulation of systemically injected plateloid particles and their biodistribution. J. Controlled Release **158**, 148–155 (2012)
268. J. Niu, X. Wang, J. Lv, Y. Li, B. Tang, Luminescent nanoprobes for in-vivo bioimaging. Trends Anal. Chem. **58**, 112–119 (2014)
269. D. Gallach, G.R. Sanchez, A.M. Noval, M.M. Silvan, G. Ceccone, R.J.M. Palma, V.T. Costa, J.M.M. Duart, Materials science and engineering B. Mater. Sci. Eng., B **169**, 123–127 (2010)
270. C. Chiappini, E. Tasciotti, J.R. Fakhoury, D. Fine, L. Pullan, Y.-C. Wang, L. Fu, X. Liu, M. Ferrari, Tailored porous silicon microparticles: fabrication and properties. ChemPhysChem **11**, 1029–1035 (2010)
271. M. Hernandez, G. Recio, R.J. Martin-Palma, J.V. Garcia-Ramos, C. Domingo, P. Sevilla, Surface enhanced fluorescence of anti-tumoral drug emodin adsorbed on silver nanoparticles and loaded on porous silicon. Nanoscale Res. Lett. **7**, 364–370
272. J.S. Ananta, B. Godin, R. Sethi, L. Moriggi, X. Liu, R.E. Serda, R. Krishnamurthy, R. Muthupillai, R.D. Bolskar, L. Helm, M. Ferrari, L.J. Wilson, P. Decuzzi, Geometrical confinement of gadolinium-based contrast agents in nanoporous particles enhances T1 contrast. Nat. Nanotech. **5**, 815–821 (2010)
273. T. Nissinen, S. Näkki, M. Latikka, M. Heinonen, T. Liimatainen, W. Xu, R.H.A. Ras, O. Gröhn, J. Riikonen, V.-P. Lehto, Facile synthesis of biocompatible superparamagnetic mesoporous nanoparticles for imageable drug delivery. Micropor. Mesopor. Mat. **195**, 2–8 (2014)
274. M. Sarparanta, E. Mäkilä, T. Heikkila, J. Salonen, E. Kukk, V.-P. Lehto, H.A. Santos, J. Hirvonen, A.J. Airaksinen, ^{18}F-labeled modified porous silicon particles for investigation of drug delivery carrier distribution in vivo with positron emission tomography. Mol. Pharm. **8**, 1799–1806 (2011)
275. T. Huhtala, J. Rytkönen, A. Jalanko, M. Kaasalainen, J. Salonen, R. Riikonen, A. Närvänen, Native and complexed IGF-1: biodistribution and pharmacokinetics in infantile neuronal ceroid lipofuscinosis. J. Drug Deliv. **2012**, 626417 (2012)
276. M.P. Sarparanta, L.M. Bimbo, E.M. Mäkilä, J.J. Salonen, P.H. Laaksonen, A.M.K. Helariutta, M.B. Linder, J.T. Hirvonen, T.J. Laaksonen, H.A. Santos, A.J. Airaksinen, The mucoadhesive and gastroretentive properties of hydrophobin-coated porous silicon nanoparticle oral drug delivery systems. Biomaterials **33**, 3353–3362 (2012)
277. J. Rytkönen, R. Miettinen, M. Kaasalainen, V.-P. Lehto, J. Salonen, A. Närvänen, R. Miettinen, Functionalization of mesoporous silicon nanoparticles for targeting and bioimaging purposes. J. Nanomater. **2012**, 2–9 (2012)
278. L. Gu, J.-H. Park, K.H. Duong, E. Ruoslahti, M.J. Sailor, Magnetic luminescent porous silicon microparticles for localized delivery of molecular drug payloads. Small **6**, 2546–2552 (2010)
279. A. Muñoz-Noval, V. Sánchez-Vaquero, V. Torres-Costa, D. Gallach, V. Ferro-Llanos, J. J. Serrano, M. Manso-Silván, J.P. García-Ruiz, F. del Pozo, R.J. Martín-Palma, Hybrid

luminescent/magnetic nanostructured porous silicon particles for biomedical applications. J. Biomed. Opt. **16**, 025002–025008 (2011)
280. C. Chiappini, E. Tasciotti, R.E. Serda, L. Brousseau, X. Liu, M. Ferrari, Mesoporous silicon particles as intravascular drug delivery vectors: fabrication, in-vitro, and in-vivo assessments. Phys. Stat. Sol. (C). **8**, 1826–1832 (2010)
281. L.A. Osminkina, K.P. Tamarov, A.P. Sviridov, R.A. Galkin, M.B. Gongalsky, V.V. Solovyev, A.A. Kudryavtsev, V.Y. Timoshenko, Photoluminescent biocompatible silicon nanoparticles for cancer theranostic applications. J. Biophoton. **5**, 529–535 (2012)
282. S. Srinivasan, J.F. Alexander, W.H. Driessen, F. Leonard, H. Ye, X. Liu, W. Arap, R. Pasqualini, M. Ferrari, B. Godin, Bacteriophage associated silicon particles: design and characterization of a novel theranostic vector with improved payload carrying potential. J. Mater. Chem. B **1**, 5218–5229 (2013)
283. R. Lanza, R. Langer, J. Vacanti, *Principles of Tissue Engineering*, 3rd edn. (Elsevier Inc., 2007)
284. Y. Ikada, Challenges in tissue engineering. J. R. Soc. Interface **3**, 589–601 (2006)
285. S.J.P. McInnes, N.H. Voelcker, Porous silicon–polymer composites for cell culture and tissue engineering applications, in *Porous Silicon for Biomedical Applications*, ed. by H.A. Santos (Woodhead Publishing Limited, 2014), pp. 420–469
286. P.-Y. Wang, L.R. Clements, H. Thissen, A. Jane, W.-B. Tsai, N.H. Voelcker, Screening mesenchymal stem cell attachment and differentiation on porous silicon gradients. Adv. Funct. Mater. **22**, 3414–3423 (2012)
287. J.F. Mano, G.A. Silva, H.S. Azevedo, P.B. Malafaya, R.A. Sousa, S.S. Silva, L.F. Boesel, J. M. Oliveira, T.C. Santos, A.P. Marques, N.M. Neves, R.L. Reis, Natural origin biodegradable systems in tissue engineering and regenerative medicine: present status and some moving trends. J. R. Soc. Interface **4**, 999–1030 (2007)
288. S. Bayliss, L. Buckberry, P. Harris, C. Rousseau, Nanostructured semiconductors: compatibility with biomaterials. Thin Solid Films **297**, 308–310 (1997)
289. S.C. Bayliss, P.J. Harris, L.D. Buckberry, C. Rousseau, Phosphate and cell growth on nanostructured semiconductors. J. Mater. Sci. Lett. **16**, 737–740 (1997)
290. A.V. Sapelkin, S.C. Bayliss, B. Unal, A. Charalambou, Interaction of B50 rat hippocampal cells with stain-etched porous silicon. Biomaterials **27**, 842–846 (2006)
291. Y.L. Khung, G. Barritt, N.H. Voelcker, Using continuous porous silicon gradients to study the influence of surface topography on the behaviour of neuroblastoma cells. Exp. Cell Res. **314**, 789–800 (2008)
292. P.-Y. Wang, L.R. Clements, H. Thissen, S.-C. Hung, N.-C. Cheng, W.-B. Tsai, N.H. Voelcker, Screening the attachment and spreading of bone marrow-derived and adipose-derived mesenchymal stem cells on porous silicon gradients. RSC Adv. **2**, 12857–12865 (2012)
293. A. Angelescu, I. Kleps, M. Mihaela, M. Simion, T. Neghina, S. Petrescu, N. Moldovan, C. Panduraru, A. Raducanu, Porous silicon matrix for applications in biology. Rev. Adv. Mater. Sci. **5**, 440–449 (2003)
294. L.R. Clements, P.-Y. Wang, W.-B. Tsai, H. Thissen, N.H. Voelcker, Electrochemistry-enabled fabrication of orthogonal nanotopography and surface chemistry gradients for high-throughput screening. Lab Chip **12**, 1480–1486 (2012)
295. Y.-L. Khung, S.D. Graney, N.H. Voelcker, Micropatterning of porous silicon films by direct laser writing. Biotechnol. Prog. **22**, 1388–1393 (2008)
296. S.P. Low, N.H. Voelcker, L.T. Canham, K.A. Williams, The biocompatibility of porous silicon in tissues of the eye. Biomaterials **30**, 2873–2880 (2009)
297. L.T. Canham, C.L. Reeves, Apatite nucleation on low porosity silicon in acellular simulated body fluids. Mat. Res. Soc. Symp. Proc. **414**, 189 (1995)
298. V. Chin, B.E. Collins, M.J. Sailor, S.N. Bhatia, Compatibility of primary hepatocytes with oxidized nanoporous silicon. Adv. Mater. **13**, 1877 (2001)
299. S.C. Bayliss, R. Heald, D.I. Fletcher, L.D. Buckberry, The culture of mammalian cells on nanostructured silicon. Adv. Mater. **11**, 318–321 (1999)

300. A. Sánchez, J. González, A. García-Piñeres, M.L. Montero, Nano-hydroxyapatite colloid suspension coated on chemically modified porous silicon by cathodic bias: a suitable surface for cell culture. Phys. Stat. Sol. (C). **8**, 1898–1902 (2011)
301. W. Sun, J.E. Puzas, T.-J. Sheu, X. Liu, P.M. Fauchet, Nano- to microscale porous silicon as a cell interface for bone-tissue engineering. Adv. Mater. **19**, 921–924 (2007)
302. D.M. Reffitt, N. Ogston, R. Jugdaohsingh, H.F.J. Cheung, B.A.J. Evans, R.P.H. Thompson, J.J. Powell, G.N. Hampson, Orthosilicic acid stimulates collagen type 1 synthesis and osteoblastic differentiation in human osteoblast-like cells in vitro. Bone **32**, 127–135 (2003)
303. M. Whitehead, D. Fan, P. Mukherjee, G. Akkaraju, L. Canham, J. Coffer, High-porosity poly (ε-caprolactone)/mesoporous silicon scaffolds: calcium phosphate deposition and biological response to bone precursor cells. Tissue Eng. **14**, 195–206 (2008)
304. M.A. Whitehead, D. Fan, G.R. Akkaraju, L.T. Canham, J.L. Coffer, Accelerated calcification in electrically conductive polymer composites comprised of poly(ε-caprolactone), polyaniline, and bioactive mesoporous silicon. J. Biomed. Mater. Res. **83A**, 225–234 (2007)
305. M.N. Rahaman, D.E. Day, B.S. Bal, Q. Fu, S.B. Jung, L.F. Bonewald, A.P. Tomsia, Acta Biomater. **7**, 2355–2373 (2011)
306. D. Fan, E. De Rosa, M.B. Murphy, Y. Peng, C.A. Smid, C. Chiappini, X. Liu, P. Simmons, B.K. Weiner, M. Ferrari, E. Tasciotti, Mesoporous silicon-PLGA composite microspheres for the double controlled release of biomolecules for orthopedic tissue engineering. Adv. Funct. Mater. **22**, 282–293 (2011)
307. A.H. Mayne, S.C. Bayliss, P. Barr, M. Tobin, L.D. Buckberry, Mayne 2000. Phys. Stat. Sol. (A). **182**, 505–513 (2000)
308. S.B.-T. de-Leon, R. Oren, M.E. Spira, N. Korbakov, S. Yitzchaik, A. Sa'ar, Porous silicon substrates for neurons culturing and bio-photonic sensing. Phys. Stat. Sol. (A). **202**, 1456–1461 (2005)

Chapter 6
Porous Silicon in Drug Delivery Applications

Joakim Riikonen, Wujun Xu and Vesa-Pekka Lehto

Abstract Several beneficial features needed in an efficient drug delivery device can be combined relatively easily in nanostructured porous silicon drug carrier. The latest results obtained to verify the feasibility of mesoporous silicon as a versatile drug carrier are highlighted in the present chapter. The encouraging results presented concern high amounts of loaded cargos, stabilization of the cargo, improved dissolution, triggered release of the cargos, improved permeation, biocompatibility (non-toxicity), biodegradation and targeting of the nanoparticles.

6.1 Introduction

Nanotheranostics has been recognized to be a promising methodology especially for fatal diseases such as cancer, cardiovascular diseases and AIDS. It enables various approaches utilized in nanomedicine, and is defined as an application of nanotechnology to diagnose, treat and prevent diseases at cellular and molecular level. Frequently, nanotechnological approaches developed for medicine take advantage of various nano-sized drug carriers such as polymer conjugations, dendrimers, micelles, liposomes, metal and inorganic nanoparticles, carbon nanotubes, nanoparticles of biodegradable polymers. The functionalities embedded in these nano-ensembles include long residence times in systemic circulation, targetability of the carriers, intracellular delivery and triggered release of the diagnostic and therapeutic agents for bio-imaging and therapy.

Among other nanomaterials, mesoporous silicon (pSi) has obtained only limited attention in drug delivery mainly because of the specific top-down method used to produce the material. However, number of study reports has increased exponentially during the last years (Fig. 6.1), because of several beneficial features of pSi as a drug carrier. For example, integration of various functions into

J. Riikonen · W. Xu · V.-P. Lehto (✉)
Department of Applied Physics, University of Eastern Finland, Kuopio, Finland
e-mail: vesa-pekka.lehto@uef.fi

D. Losic and A. Santos (eds.), *Electrochemically Engineered Nanoporous Materials*, Springer Series in Materials Science 220,
DOI 10.1007/978-3-319-20346-1_6

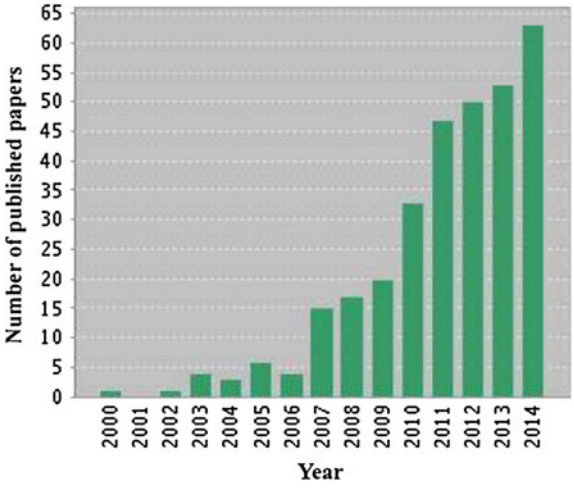

Fig. 6.1 Number of the published papers based on the information adopted from Web of Science on 7th December, 2014. The key words used for the topic were "drug", "delivery", "porous" and "silicon". The five most cited papers (cited 1155 times all together) have been prepared by the groups of Sailor (2), Lehto (2) and Ferrari (1)

pSi nanoparticles is reasonably easy due to the inorganic nature of the carrier and the well-known chemistry of silicon. Loading of therapeutic compounds, or cargo, into confined spaces of nanoporous inorganic materials can radically change their physico-chemical properties and biofate when delivered intravenously. In addition, the protection of the cargos against harsh conditions and/or the enzymatic degradation in vivo, together with possibilities of crossing biological barriers and active targeting make pSi nanoparticles attractive carriers for drug delivery purposes.

The present chapter focuses on the latest results obtained to manifest the feasibility of mesoporous silicon as a versatile drug carrier. The encouraging results include high amounts of loaded cargos, stabilization of the cargos, improved dissolution, triggered release of the cargos, improved permeation, biocompatibility (non-toxicity), biodegradation and targeting of the nanoparticles. The chapter is divided into sections concerning enhanced dissolution of poorly water-soluble drugs, sustained release of peptides or other therapeutics, and targeted drug delivery that mainly is related to cancer treatments. These manifold examples emphasize the great variety of ways pSi can be exploited in biomedical applications because of its easy tunability. Also safety experiments made with various micro- and nanoparticles are reviewed briefly. Even though pSi seems to be considerably safe material to be administrated via different routes the overall safety studies are limited in number. The results published so far are mainly based on in vitro studies and the clinical investigations are extremely rare. Overall, the material is still in the preclinical phase. The first pSi product for clinical assessments was related to localized radiotherapy (brachytherapy) for unresectable hepatocellular and pancreatic carcinoma where the beta-emitter ^{32}P was immobilized in pSi (http://www.psivida.com/).

pSivida Corp. is also performing clinical investigations to treat back of the eyes but there is no detailed descriptions available on the constituent of the medical devices. Most of the pSi material for biomedical applications has been produced from single crystal silicon wafers and thus the material is still relatively expensive. There should be more emphasis also in the large scale production of pSi fulfilling the requirements of good manufacturing practices (GMP).

6.2 Enhanced Dissolution

Using pSi to enhance dissolution of poorly soluble drugs was one of the earliest adaptations of pSi in drug delivery [42]. Poor aqueous solubility of drugs is a major problem in modern pharmaceutical industry. It has been estimated that 30–90 % of all potential drug candidates suffer from poor solubility which can cause poor bioavailability and rejection of the drug candidate from the development program [22, 48, 59]. Due to the low equilibrium solubility of some drugs, drug concentrations within the gastrointestinal track remain low. The equilibrium solubility can only be improved by changing the chemical structure of the drug or the properties of the liquid in which the drug dissolves. However, unless the drug has very poor absorption, the limiting factor of absorption is often the dissolution rate rather than the equilibrium concentration (class II drugs of Biopharmaceutics Classification System) [38]. Poorly soluble drugs also have slow dissolution rate, since the dissolution rate of a drug dm/dt is proportional to its solubility according to Noyes-Whitney Equation:

$$\frac{dm}{dt} = A\frac{D}{d}(C_S - C_b), \tag{6.1}$$

where m is the mass of the dissolved drug, t is time, A is the area of dissolution, i.e., the surface area of the interface between the solid drug and the liquid, D is the diffusion coefficient, d is the thickness of the boundary layer, i.e., the thickness of the liquid layer between the bulk liquid and the solid surface, C_s is the apparent solubility, and C_b is the drug concentration in the bulk liquid. Because of the slow dissolution rate, the drug concentration of a poorly soluble drug in the gastrointestinal track does not often raise to sufficient levels during the relevant time period leading to poor bioavailability. However, the bioavailability can be increased by increasing the dissolution rate.

Several approaches have been taken to improve dissolution rate of poorly soluble drugs. These include amorphization, solid dispersions, crystal engineering, particle size reduction and lipid formulations [38]. The common problem in many of these approaches is the poor stability of the formulation. For example, amorphous drugs tend to recrystallize within time. Another complication is that many of these approaches need a very specific formulation which requires considerable

formulation effort for each drug individually. The main advantages of using pSi to enhance the dissolution rate of drugs are that the formulations are very stable and can be used for a variety of drugs with minimal changes in the formulation.

Loading a drug into pores of mesoporous silicon divides the drug physically into small volumes or compartments. The drug inside the pores is, therefore, in a state which is very different from the crystalline bulk state. If the loading degree is relatively low, the drug forms a thin layer on the pore surfaces (Fig. 6.2) [32]. The drug remains in non-crystalline state which, in absence of strong drug-wall interactions, has a higher apparent solubility than the crystalline state. Theoretically, apparent solubility of various amorphous drugs has been estimated to be 10–1600 times higher than the solubility of the stable crystalline form [14]. However, with typical amorphous formulations the solubility advantage is usually highly reduced in real situations because of the recrystallization of the amorphous drug during dissolution [14]. Another advantage of the drug loaded as a thin layer on pSi, is the high increase in the area of dissolution. Because dissolution area in this case is close to the surface area of the pSi, which might be several hundreds of m^2/g, the increase in the dissolution area is in the order of 1000-fold compared to drug microparticles. On the other hand, the thickness of the diffusion layer d in (6.1) increases because of the loading. Before the loaded drug can diffuse into the free liquid volume, it has to diffuse out of the pores. However, the typical thickness of the diffusion layer is in the same order of magnitude as the typical size of pSi microparticles (from few micrometers to few tens of micrometers) and, therefore, the increase in the diffusion layer does not slow down the dissolution significantly. Therefore, according to (6.1), theoretical initial dissolution rate of the drug from pSi can be expected to be from thousands to million times faster than from pure crystalline drug microparticles.

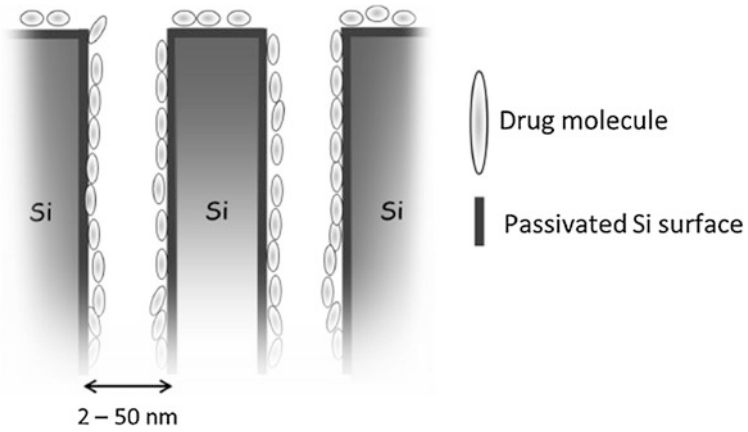

Fig. 6.2 Schematic drawing of the cross section of pSi where the drug molecules are adsorbed on the passivated silicon surface. The *scale bar* indicates the pore diameters in the mesoporous scale

Loading drug so that it forms only a thin layer on pore surfaces leads to rather low loading degrees typically in the region of a few weight percents. However, one of the main advantages of pSi is that very high loading degrees can be used. For example higher than 50 % loading degree has been reported for ibuprofen in pSi [39]. This reduces the amount of porous material needed in the formulation thereby reducing the costs, volume of the formulation for a single dose and also risks for possible adverse effects. When loading degree is increased the drug begins to form thicker layers on pore surfaces. Already long before 100 % filling, the free space at the center of the pore will be partially filled by the drug. This is because the surface area and, therefore, the free energy of the drug are minimized as the drug forms larger particles in the pores rather than a thin layer with large surface area. When larger particles form in the pores, the area of the dissolution decreases. The area between liquid and drug during dissolution is no longer close to the surface area of the pSi but is close to the area of the pore openings and the surface area advantage is lost.

Increasing the loading degree may also cause crystallization of the drug [39]. Crystallization in the pores may take place if the dimensions of the drug inside the pores are large enough. If the dimensions are smaller than the size of the critical nucleus, crystallization of the drug is not energetically favorable and will not take place. However, if the dimensions of the drug inside the pores are larger than the diameter of the critical nucleus crystallization can take place. This can happen if the drug fills the cross-section of the pores which are wider than the size of the critical nucleus or if the drug forms a layer thicker than the size of the critical nucleus (in relatively large mesopores). Even if the crystallization may be energetically favorable it may be very slow process. Considering the drug divided into millions of separate pores, the crystallization of drug in each pore needs to nucleate separately whereas for a large drug particle only one nucleus is needed for crystallization of the entire particle. For example, crystallization of ibuprofen in pSi has been observed to take several weeks in some cases [39]. Although the drug crystallizes in the pores, it does not mean that the increased apparent solubility is lost. Apparent solubility of the drug crystals inside the pores is lower than that of the amorphous state but remains higher than bulk crystals due to the small size of the drug crystals [43]. The advantage of having drug in the pores as small nanocrystals compared to free nanoparticles is that in the pores the nanocrystals will not aggregate into larger particles and the material is easier to handle. It should also be noted that the crystal form that the drug forms inside the pores might not be the most stable form. Drug may form crystals in metastable forms, or the stable form in the pores might be different than the one in bulk [13]. Completely new polymorphs which have not been found in the bulk have also been observed in the pores [13].

Crystallization of ibuprofen has been studied in the pores of porous silicon with various pore sizes [39]. The drug was shown to crystallize in pores with average pore diameters between 11 and 75 nm. However, not all the drug was crystallized, but a non-crystalline layer existed between the crystalline core and pore wall. The thickness of the layer was found to be dependent on the surface properties of the pores. Because of this non-crystalline layer crystallinity of ibuprofen in the pores

depended on the pore diameter. In pores with small pore diameter, and therefore large surface area, a large part of the loaded ibuprofen was in the non-crystalline layer and the crystallinity was as low as 50 %. In large pores with low surface area, only small part of the drug was in the non-crystalline layer and therefore the crystallinity was high, up to 94 %.

A remarkable benefit in using pSi for enhancing dissolution of poorly soluble drugs is that it does not rely on any kinds of chemical interactions between the carrier and the drug. The drug is physically deposited in the material and the enhanced dissolution results from physical properties of the material, high surface area and high apparent solubility. Because the system is not dependent on the chemical properties of the drug it can be applied to several different drugs with minimal changes in the formulation making the formulation considerably easier than with many other delivery systems. Indeed, various poorly soluble drugs have been loaded into pSi including, ibuprofen, griseofulvin, furosemide, indomethacin, celecoxib, itraconazole, ethionamide and saliphenylhalamide [25, 42, 53, 58]. Loading into pSi significantly improved the in vitro dissolution of all the above mentioned drugs compared with their macrocrystalline counterpart. The extent of the improvement varies and is likely to depend on numerous variables such as pH [42], loading degree, final concentration of a release medium, mixing, etc. Some of the most impressive improvements in the dissolution rates have shown the decrease in time required for 100 % release by a factor of 40, and a 15 fold increase in the amount of the dissolved drug after 60 min of release [42, 53].

In addition to enhanced dissolution, other advantages of using pSi carrier for poorly soluble drugs have been observed. Dissolution of drugs has been noticed to become less pH-dependent, which could reduce the variation in drug adsorption due to variation of pH in the gastrointestinal track [42]. Also the permeability of drugs has been improved because of the loading into pSi [21, 53]. This effect is most likely a result of high local drug concentration next to the cell monolayer in vitro experiments promoting absorption [21]. Furthermore, loading into pSi has been shown to lower the cytotoxicity of the loaded drug and even affect the drug metabolism [53].

pSi has been shown to be an efficient carrier of poorly soluble drugs not only in vitro but also in vivo. In oral administration of indomethacin, a 100 % bioavailability was achieved with indomethacin loaded pSi microparticles whereas only 54 and 77 % was achieved with pure indomethacin and commercial formulation (Indocid), respectively [58]. Interestingly, the pSi loaded indomethacin outperformed the commercial formulation in vivo despite the fact that the commercial formulation had faster dissolution in vitro. The authors also reported good in vitro–in vivo correlation for indomethacin loaded in PSi, which makes it possible to predict in vivo absorption from in vitro dissolution profile. Further evidence on applicability of pSi in drug delivery of poorly soluble drugs was given by a study in which celecoxib was orally administered to rats [57]. Again, drug loaded in pSi showed superior pharmacokinetics compared with pure drug and a commercial formulation (Celebrex).

The potential of pSi as a carrier of poorly soluble drugs has been amply demonstrated in vitro. Various drugs loaded in pSi have shown significantly enhanced dissolution and also improved permeability, and reduced toxicity has been observed. More research in vivo is required to understand the behavior of the carrier system in real biological systems. For this purpose, the possibility to label the pSi particles and study their residence time in the gastrointestinal track after oral administration with imaging modalities is an attractive option [45]. With the excellent preliminary in vivo results and the clear benefits of the delivery system such as high loading degrees, good physical stability and easy formulation, the future of the pSi in this sense seems promising.

6.3 Sustained Release

The latest in vivo studies in which pSi has been developed to obtain sustained release are mainly concentrated on intraocular drug delivery or subcutaneous peptide delivery. Several approaches have been utilized to sustain or even control the release of therapeutically active compounds from formulations where pSi has been mainly used as a drug reservoir. pSi particles can be modified physically and chemically to modulate the release kinetics of the cargo but quite often various coatings have also been used on pSi particles to trigger the release externally or internally. When sustained or controlled release from pSi is desired, the approaches can be divided in four categories:

1 Mechanical hindrance; the release is affected by the pore size and structure,
2 Electrostatic interaction; the pore surfaces are modified to exhibit strong electrostatic attraction towards cargo molecules,
3 Chemical conjugation; covalent bond between the pore surfaces and the cargo molecules is formed and the release usually takes place through degradation of the carrier, and
4 Pore capping; the pore openings are closed with triggerable plugs.

Intraocular delivery of therapeutics is the most advanced biomedical application of pSi where in vivo experiments have been frequently performed. Sailor et al. has extensively studied and developed pSi microparticles to release different therapeutics relevant to ocular diseases in a prolonged manner. In one of their latest studies [16], they have covalently conjugated daunorubicin to the carboxyl groups on the surface of fully oxidized pSi. The release rates (from days to months) observed in the living eye vitreous was directly related to the pore diameter, which, in turn, affected the total degradation rate of the pSi microparticles. The covalent bonding of daunorubicin did not destroy the therapeutic efficacy of the released drug. The particles were also screened for ocular safety for 6 months after the intravitreal injection [15]. Reduced ocular toxicity of daunorubicin was observed, which was due to its prolonged release from microparticles that were visible in the eyes for >6 months. In another study, doxorubicin was also covalently conjugated

to the carboxyl groups of pSi [7]. The loading degree obtained (6 % w/w) can be considered extremely high as a chemisorbed monolayer of the drug was formed on pSi. The release was dominated by the degradation of pSi and lasted for 3 months. Polymer (PLGA) coating was another approach to obtain sustained release [35]. Here, the composite microparticles were produced with solid-in-oil-in-water method and the release of daunorubicin was observed for 74 days. In all the above mentioned studies, pSi was totally oxidized to prevent the possible incompatibility of the cargo molecules with the carrier. The same research group has also developed a self-reporting intraocular drug delivery vehicle based on 1-D photonic crystal of pSi [6]. Here, the surface of pSi was passivated with 1-undecylenic acid via hydrosilylation and attached covalently with daunorubicin. The drug released from the particles was recognized to be even more therapeutically effective than the as-received daunorubicin in the inhibition of the growth of retinal pigment epithelial (ARPE-19) cells.

pSi has been systematically developed also for sustained delivery of subcutaneously administrated peptides. In one of the first studies from Lehto et al., ghrelin antagonist was loaded in thermally hydrocarbonized pSi microparticles [24]. The pharmacological activity (food intake and blood pressure) and the cytokine activity were monitored in vivo. The loading degree was high (20 % w/w), the peptide released from the carrier was biologically active and the peptide released showed prolonged effects for several hours compared with the peptide administered as a solution. The cytokine levels in plasma did not rise indicating no acute inflammatory effects. Furthermore, peptide melanotan II was utilized in a corresponding study where heart rate and water consumption were monitored [23]. Peptide YY3-36 (PYY) was used to screen the effect of different surface chemistries of pSi on the plasma concentrations of the peptide in vivo [28]. The studied microparticles were all negatively charged but they differed in the hydrophobicity. The carboxyl modified surface gave the most sustainable release of PYY but pSi with oxidized surface gave the best bioavailability for the peptide. In this case, the absolute bioavailability was 100 % and the relative bioavailability (relative to the peptide solution also administrated subcutaneously) was as high as 250 %. The most interesting results were obtained when the size of pSi carrier was reduced in nano-scale [27]. With PYY loaded carboxyl derivatized pSi nanoparticles the absolute bioavailability was 100 % and the release of PYY lasted for 4 days after subcutaneous delivery compared to a mere 12 h for peptide solution (Fig. 6.3). As a conclusion, pSi nanoparticles had high peptide loading capacity and acted as depots in the subcutaneous space controlling the peptide release and protecting the peptide from rapid elimination. It is noteworthy that in all of these studies the peptides were loaded in pSi with a gentle immersion method the interaction between the cargo and the carrier being electrostatic and/or hydrophobic in nature. As high as 45 % w/w loading degree was obtained [17].

A multistage drug delivery vector based on pSi has been developed by Ferrari et al. already for years. The vector is based on a material produced with a lithographic method through electrochemical etching [51]. The production method is quite complicated but the particles produced are well defined in size, shape

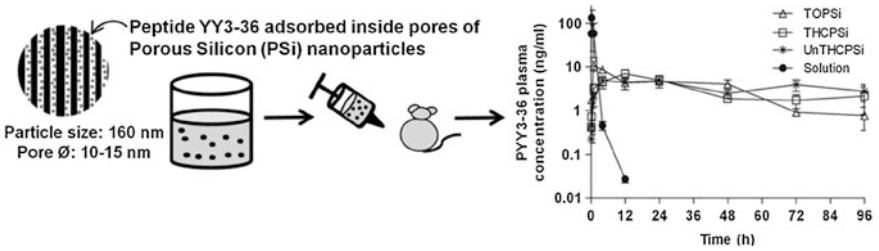

Fig. 6.3 Peptide PYY3-36 was loaded in the pSi nanoparticles with different hydrophobic nature. Loading was performed with a simple immersion method resulting in a loading efficiency close to 100 % based on physical adsorption. As a result, sustained release for 4 days without burst effect and absolute bioavailability of 100 % was obtained. Reprinted with permission of ACS Publications [27]

(discoidal) and porous properties. The vector has been utilized, e.g., in intravenous delivery of small interfering RNA (siRNA) for improved chemotherapy. In one of the first studies, siRNA was incorporated in neutral nanoliposomes and loaded in pSi microparticles (>1 μm in diameter) for intravenous administration in orthotopic mouse model of ovarian cancer. Sustained gene silencing for >3 weeks was observed resulting in reduced tumor weight with no significant increase in cytokine production. The vectors were not observed to accumulate in tumor, instead, these micrometer-sized particles accumulated in the liver and spleen due to reticuloendothelial system. Obviously, the function of the vector was based on the fact that the vector was able to protect siRNA from degradation and renal extraction when entrapped within capillary spaces of the liver and spleen. Slow release was due to the gradual degradation of the vector with subsequent release of siRNA that reached the tumor and gave sustained pharmacological effect. On the other hand, in a further study, the multistage vector was recognized to accumulate in metastatic ovarian cancer tissues and caused the inhibition of the growth of both metastatic SKOV3ip2 and chemotherapy-resistant HeyA8 ovarian tumors when delivered in combination of paclitaxel or docetaxel [49]. The study showed that pSi based delivery vector is an effective drug carrier to overcome multiple biological barriers (like multidrug resistance) which are normally huge obstacles for siRNA therapeutics. siRNA was also loaded in discoidal pSi microparticles which were first oxidized, functionalized with isocyanate group and subjected to polyethyleneimine (PEI) conjugation [64]. PEI as a cationic polymer enabled effective electrostatic complexation with anionic siRNA inside the pores of pSi. Due to the gradual degradation of pSi matrix, the release of the PEI/siRNA complexes took place in a sustained manner. The complexes were internalized by the cells in vitro and they were able to escape from the endosomal/lysosomal compartments resulting in gene knockdown against the target cancer gene.

Intracellular delivery of macromolecules was also studied by Lehto et al. in a study where pSi nanoparticles were first passivated with oxidation and grafted with amine groups [40]. Splice correction oligonucleotides (SCO) were loaded in pSi

by means of electrostatic interaction and finally cell penetrating peptides (CPP) were added into the formulation. The biological effect was verified in vitro with splice correction assay and confocal microscopy. The nanoparticles were actively internalized by the cells also without CPP, but CPP facilitated the endosomal escape of SCO to give the biological effect. Furthermore, SCO/CPP complexes inside the pores were stabilized against enzymatic digestion.

Sustained release of therapeutics is an important aspect also in tissue engineering and wound healing devices. Materials used for these purposes need to promote cell differentiation and proliferation, but they could also deliver compounds to specifically promote cell growth and reduce risks of inflammation and other adverse effects. To this end, Voelcker et al. have developed several stimulus-sensitive constituents based on pSi. In one of their latest studies, they utilized a temperature sensitive polymer ploy(*N*-isopropylacrylamide) (PNIPAM) that has the lower critical temperature of ~35 °C [54]. The polymer was grafted on silanized pSi film using controlled radical polymerization technique. Interferometric reflectance spectroscopy was used to study the function of the polymers on pSi with different porous properties at different temperatures. The polymer was able to modulate the release of the model drug (camptothecin) so that the release was markedly (1.9 times) enhanced at temperatures above the critical temperature due to the conformational rearrangements in the polymer layer. The authors foresaw the potential of the biodevice developed especially for cell sheet engineering scaffolds for localized and controlled release of therapeutics. In another study, the same group realized the capping of the pores with a pH responsive polymer film via initiated chemical vapor deposition [33]. Due to the "gentle" nature of the coating method, the drug (camptothecin) could be loaded in the pores of the pSi film before the coating without any degradation of the drug. At low pH the diffusion of the drug molecules through the polymer layer was slow and at neutral conditions the diffusion, i.e., the release, was fast.

A microfluidic assembly to produce microcomposite constituents with monodispersive spherical morphology has been introduced by Santos et al. the first study being related to encapsulation of thermally hydrocarbonized pSi microparticles within lipid matrix [30]. Prolonged drug release of both hydrophilic and hydrophobic drugs with enhanced cytocompatibility was obtained. In a further study, they have utilized pH responsive polymer (hypomellose acetate succinate) as the polymeric matrix to prevent the release under acidic conditions in a formulation intended for *per oral* administration [29]. Atorvastatin was loaded in pSi microparticles which were encapsulated in the polymer where celecoxib was dissolved. The release in vitro was well controlled over the intended pH value for both of the drugs.

Even though fancy release profiles can be obtained in vitro, in most cases the carriers are still not working in vivo as expected. Biological barriers in vivo are much more complicated than what can be realized in vitro. For example, when nanoparticles are injected intravenously they are instantly covered with various plasma proteins. This protein corona determines the biofate of the particle and may totally override the originally intended function. The release profiles determined

with buffer solutions might be far from the reality as release in vivo is taking place in a totally different environment which is even dynamically changing. Thus, to obtain relevant information about in vitro in vivo correlation (IVIVC) the studies published in high impact journals should always contain in vivo evaluation even though the results might not be positive regarding the functionality of the carrier system. This is the way the pSientists are able to learn from other researchers' works, trials and errors, and finally be able to surpass the complex barriers of the human body.

6.4 Targeting

As the feature of an ideal nanocarrier for therapeutics, the carrier should recognize the therapeutic target and the release kinetics of the loaded drug should be precisely controlled. The drug should not be leaking out from the carrier during the circulation in blood vessels, but it should be released quickly from the carrier after reaching the pathological site and recognizing the target. This type of smart drug delivery method is considered as targeted drug delivery, which not only reduces side effects to healthy tissues but also improves the therapeutic effect. Targeted drug delivery is one of the most distinguishing features for nanomedicine as compared to traditional medicine.

6.4.1 Passive Targeting

Passive targeting is mainly applied in cancer therapy and it takes advantage of unique pathophysiological characteristics of defective tumor vessels. Tumor blood vessels are generally leaky due to the discontinuity of the endothelium, i.e., there are many pores on the tumor microvessel with diameters varying from 100 nm to several micrometers depending on the tumor type [18]. Nanoparticles can extravasate through the pores and accumulate in tumors when they flow in tumor blood vessels. This passive phenomenon is recognized as the enhanced permeability and retention (EPR) effect (Fig. 6.4a). Particle size, surface charge, stealthy coating and particle shape are the most important factors in optimizing the passive targeting. The size of nanoparticles should be smaller than 400 nm to extravasate through the leaky vasculature in a tumor but be bigger than 10 nm to avoid filtration by the kidneys. However, particles bigger than 100 nm are easily captured by the liver. Thus, the ideal particle size is between 10 and 100 nm [8]. The charge of the particles should be neutral or anionic for efficient evasion of the renal elimination. Because a long residence time of the nanoparticles in the systemic circulation is the most important factor for the passive targeting, the nanoparticles should have stealthy coating such as polyethylene glycol (PEG) to hide them from the reticulo-endothelial system (RES) or mononuclear phagocyte system (MPS) of the

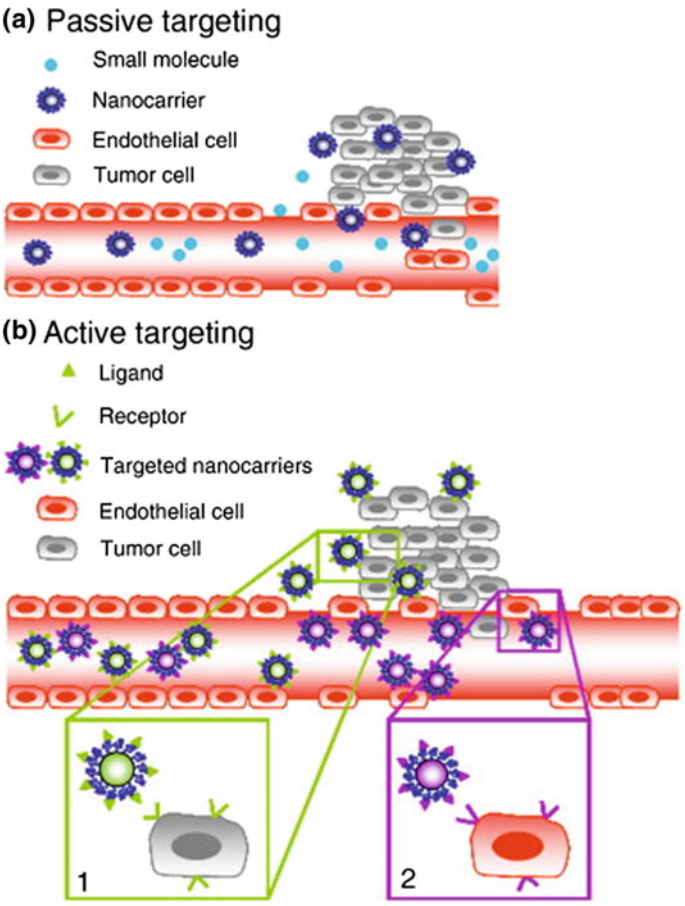

Fig. 6.4 Illustration of passive targeting and active targeting in drug delivery. **a** Passive targeting of nanocarriers. Nanocarriers reach tumors selectively through the leaky vasculature surrounding the tumors. **b** Active targeting strategies. Ligands grafted on the surface of nanocarriers bind to receptors (over) expressed by (*1*) cancer cells or (*2*) angiogenic endothelial cells. Reprinted with permission of Elsevier [8]

body [8]. Also the shape of the nanoparticles has significant influence on the targeting tendency [1, 12]. It has been found that accumulation of discoidal pSi nanoparticles in breast tumor was five times higher compared to spherical particles with similar size [12].

There is only limited number of in vivo studies made with pSi nanoparticles regarding passive targeting, and no systematic study on the effect of the pSi particle sizes on their biodistribution has been conducted. In one study, the in vivo passive targeting of pSi nanoparticles was investigated with solid lipid encapsulated pSi nanoparticles [20]. These nanoparticles were slightly accumulated in tumors (tumor-to-liver ratio 0.24 ± 0.09 %). However, because the solid lipids were

physically coated on the surface of the nanoparticles by utilization of hydrophobic interaction, the stability of the nanocomposite was poor during the circulation in blood vessels. The solid lipid coating on the surface of the nanoparticles cannot prevent the immune recognition, resulting in a short circulation time of the developed nanocomposite.

Previous clinical therapies with other carrier systems have proven passive targeting to be feasible for targeted drug delivery. Nevertheless, it still suffers from several limitations, e.g., it is difficult to control the targeting due to the random nature of the accumulation. Furthermore, certain tumors do not exhibit an EPR effect, and the permeability of vessels may not be the same throughout a single tumor.

6.4.2 Active Targeting

Active targeting utilizes ligands grafted on the surface of nanoparticles to bind to the receptors expressed preferentially at the pathological cells/tissues. Therefore, the drug-loaded nanoparticles can selectively accumulate in the disease sites to achieve targeted drug delivery (Fig. 6.4b). The affinity ligands of antibodies [46], peptides [56] or small molecules like folic acid [62] are grafted on the surface of the nanoparticles via a variety of conjugation chemistries. The potential of pSi in targeted drug delivery has been demonstrated by various ligand conjugations [2, 41, 62]. For example, Rytkönen et al. studied the active targeting capability of pSi by grafting antibodies against glutathione *S*-transferase (anti-GST) in human plasma [41]. The pSi nanoparticles with anti-GST bound to GST-agarose nearly 35-fold compared with the control nanoparticles with human-IgG. The targeting potential of pSi to breast cancer was studied by conjugating an amide-modified hyaluronic acid (HA^+) covalently on the surface of pSi nanoparticles [2]. The conjugation of HA^+ on nanoparticles not only improved colloidal stability in plasma but also enhanced the cellular interactions and internalization: the fluorescence signal of the conjugated undecylenic acid treated pSi nanoparticles was 30-fold higher for MDA-MB-231 cells in the flow cytometer analysis compared to their negative controls. The active targeting of pSi was also demonstrated with folic acid modification [62]. In Fig. 6.5, significantly higher uptake was found for HeLa cells, but not for MCF-7. After adding 1 mM free folic acid to saturate the receptors, the uptake of nanoparticles into Hela cells was clearly reduced. However, addition of folic acid did not affect the uptake of nanoparticles into MCF-7 that does not have folate receptors on the cell membrane.

The active targeting strategy can be divided into targeting of cancer cells and targeting of tumoral endothelium. The examples above demonstrated the ability of pSi nanoparticles to target the receptors on cancer cells. The targeted drug delivery to endothelium in solid tumors can result in death of tumor cells by the lack of oxygen and nutrients. Recently, Wang et al. utilized this approach in vitro and introduced targeting moieties (iRGD and RGDS) on PSi nanoparticles via

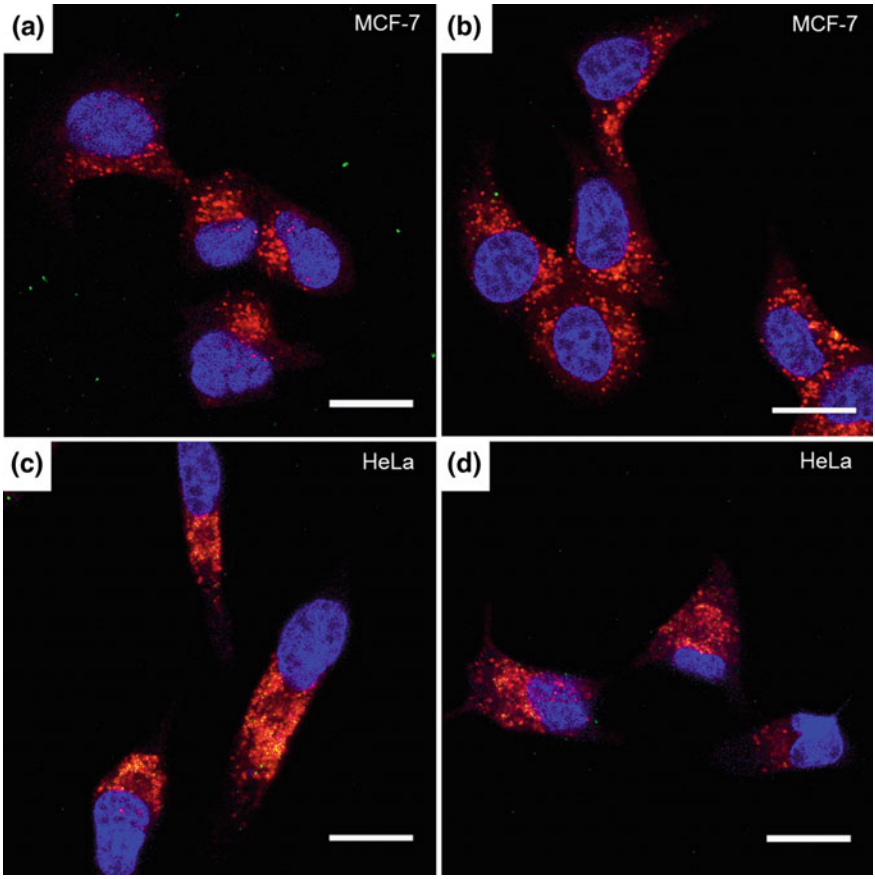

Fig. 6.5 Fluorescence confocal microscopy images of folic acid modified pSi nanoparticles internalized into MCF-7 (folate receptor-negative) and Hela (folate receptor-postitive) cells after 1 h incubation without (**a**, **c**) and with (**b**, **d**) addition of 1 mM free folic acid. The *scale bar* is 20 μm. To visualize the intracellular compartments, the nucleus (*blue*) and endosomes (*red*) were stained and the nanoparticles were labelled (*green*). Reprinted with permission of ACS [62]

copper-free azide-alkyne cycloaddition [56]. The peptide-functionalized nanoparticles enhanced the endothelial cell internalization compared to the amine modified nanoparticles.

Because of the cellular heterogeneity both within and among tumor sites, the active targeting based on a single approach might not be efficient for cancer therapy in some cases [9, 63]. For example, in pancreatic tumors, the targeting only to endothelial cells may not be enough for efficient active delivery due to a general hypovascularization of the lesion. Therefore, dual active targeting has been developed for more effective cancer therapy. Yokoi et al. decorated the surface of pSi nanoparticles with Ly6C antibody for dual-targeting to endothelial cells and macrophages in the stroma of human pancreatic cancers [63]. The in vivo study

showed that 9.8 ± 2.3 % of injected Ly6C targeting nanocarriers accumulated in the pancreatic tumors at 4 h after administration, as opposed to 0.5 ± 1.8 % with non-targeted nanocarriers.

It should be noticed, that regarding various targeting strategies of cancer, passive and active targeting have often been considered to be options to each other even though they should be considered as complementary to each other. Namely, the passive targeting stemming from the EPR effect because of the big gap junctions between the endothelial cells of the vascular system in tumors and the lack of their lymphatic drainage is always needed to get the carriers/vectors into contact with the cancer cells. After this process the targeting moieties (antibodies, ligands) are eventually able to facilitate the internalization of the carrier in the right type of the cells, i.e., cancer cells.

6.4.3 Environment-Responsive Nanoparticles

Development of environment-responsive nanoparticles is a novel strategy for targeted drug delivery. These nanoparticles are responsive to some environmental variables that are found in specific tissues of human body. For example, there are different pH values and enzymes in stomach and intestinal tract, which can be utilized to achieve targeted drug delivery upon *per oral* administration [29]. Zhang et al. utilized a microfluidic technique to fabricate multistage drug delivery system by encapsulating pSi nanoparticles within a polymer matrix [64]. The drugs (fluorouracil and celecoxib) were loaded into the nanoparticles for synergistic therapy of colon cancer. Mucoadhesive polymer was conjugated to the pSi nanoparticles and this entity in turn was encapsulated in pH-responsive polymer to control the drug release. The encapsulated drugs were not released in acidic medium due to the protection of polymer coating. When the surrounding pH was increased to 6.5–7.4, the pH-responsive polymer was dissolved and the release of the drugs took place. The in vitro experiments proved the expected function of the constituent.

Moreover, the abnormal metabolic mechanism of tumors produces a special microenvironment as compared with healthy tissues: The extracellular pH (6.4–6.8) of tumor tissues is lower than that of healthy tissues (pH = 7.4). Also, the endosomal/lysosomal compartments within cells have a low pH (5.0–6.0) [10]. Therefore, it is a promising strategy to develop pH-sensitive nanoparticles for targeted cancer therapy. In a recent study, undecylenic acid and folic acid modified pSi nanoparticles were prepared for tumor targeting and pH-responsive drug release [62]. When the pH value of release medium was around 7, the –COOH groups of the undecylenic acid conjugated on the pSi surface were ionized to COO^- groups while the anticancer drug doxorubicin (DOX) has a positive charge. DOX molecules were confined into the pores because of electrostatic attraction and thus the drug release was very slow. When pH of the release medium changed to 5, the ionized $–COO^-$ groups were gradually protonated to neutral –COOH. The electrostatic attraction decreased and DOX was released in a pH triggered manner.

Although the active targeting or environment-responsive drug delivery strategy looks very promising, they are still far away from the practical clinical applications. For example, in active targeting, the retention and uptake of nanoparticles by cancer cells can indeed be augmented as a result of receptor-mediated endocytosis, but only after the nanoparticles have extravasated from the vasculature [26]. Therefore, an efficient passive process is a very important precondition for active targeting, in which the nanoparticles should possess long circulation time in body. Also, active targeting may anchor nanoparticles to tumor cells next to the leaky vessels, decreasing the efficiency of diffusion, depth of penetration and uniformity of distribution [50]. Moreover, the conjugation of ligands makes the process of nanoparticles preparation more complicated and thus it is more difficult to control the homogeneity of different batches. Therefore, the nanomedicines currently approved for clinical applications are relatively simple and generally lack active targeting. However, the increasing number of in vitro and in vivo experiments has proven that active targeting has a great potential for drug delivery. Because the nanomedicine is still in its infancy and human body is a complicated system, more systematic and detailed studies are needed to find an optimized way for active targeting in drug delivery.

6.5 Miscellaneous

As discussed earlier, pSi can provide enhanced dissolution, sustained release and targeted delivery of drugs. Although majority of drug delivery studies related to pSi focus on these purposes, pSi can provide more versatile functions as a drug carrier. A particularly interesting feature of the material is that it can be tailored to be a self-reporting delivery system [60]. In this system, drug release from the particles can be monitored by measuring the visible light reflectance spectrum of the particles. This system exploits the possibility to easily fabricate 1-D photonic crystals based on pSi with layers of alternating refractive index. The reflectance spectrum of this kind of material depends on the refractive index of the material inside the pores. As the drug is replaced by release medium, the refractive index inside the pores changes and a shift in the reflectance spectrum is observed. A linear dependency between the peak reflectance wavelength and the amount of released drug has been observed [60]. Therefore, the amount of released drug can be observed by an optical measurement. This kind of system is especially beneficial in intraocular drug delivery where optical monitoring of the particles can be conveniently realized.

Possibility to image pSi particles and determine their biofate is essential in theranostic applications. Imaging of the pSi particles can be based on several properties or features of the particles. The intrinsic photoluminescence of pSi can be exploited in imaging without the need to attach additional fluorescent molecules on the particles [37]. The feasibility of this system was demonstrated for imaging of tumors in mice [37]. However, it is unlikely to lead into good results in humans if the tissues to be imaged lie deep in the body due to the absorption of the excitation

and the emission radiation in the visible or near infrared region. Absorption is less problematic in magnetic resonance imaging (MRI). MRI can be utilized with pSi by incorporating pSi with paramagnetic species such as superparamagnetic iron oxide or gadolinium [11, 36]. Another possibility of imaging the pSi drug carriers is attaching a radioactive label for positron emission tomography (PET) imaging [45].

A new application of pSi is to use it in vaccines for immune activation. pSi can function as a safe vehicle for delivering antigenic peptides or adjuvants for the immune system to induce an immune response. It has been shown that pSi microparticles can be used to deliver viral specific antigenic peptides to antigen presenting cells which further present the antigenic peptides to T-cells [19]. In this study, pSi particles significantly enhanced the immune reaction against the antigenic peptides. Similar effect was achieved with 50 fold smaller dose of loaded peptide compared to the free peptide. The improvement was ascribed to prolonged release of peptides from the phagocytosed pSi particles internalized in the antigen presented cells. pSi can also be used as a carrier of adjuvants [34]. Unlike common adjuvant alum, monophosphoryl lipid A loaded pSi particles were shown to increase secretion of Th1 cytokines in vivo which is important in immune response against cancer cells. Indeed, the loaded pSi microparticles were shown to inhibit tumor growth in mice.

6.6 Safety Aspects

Biocompatibility of pSi is a prerequisite when the material is developed for drug delivery applications. Unlike bulk silicon, pSi has been shown to exhibit good biocompatibility because it degrades completely in aqueous solutions into non-toxic silicic acid [37, 61]. Following the first biocompatibility evaluation of pSi in 1995 [5]. Several studies have been carried out to investigate the safety of the materials in different applications [3, 4, 31, 47].

The cytotoxicity of pSi related to oral drug delivery was evaluated in vitro employing Caco-2 intestinal cell line [44]. The particle size and the surface chemistry of pSi microparticles were considered to be the key factors regarding their toxicity. The smaller pSi particles showed higher cytotoxicity and the particles with oxidized surface were less cytotoxic than the carbonized particles. Moreover, cytotoxicity of pSi particles was observed to be dose-dependent. Under the used experimental conditions (particle sizes >25 μm), the non-toxic threshold concentration for carbonized particles was <2 mg ml^{-1} and for oxidized particles <4 mg ml^{-1}. The animal experiments demonstrated that no adverse effects on rats were observed in a study where indomethacin was loaded in oxidized pSi microparticles and administrated orally [58].

Thermally oxidized and aminosilane modified pSi films were implanted into rat eyes to study the biocompatibility in the eye [31]. When implanted under the rat conjunctiva, the pSi films did not erode the underlying or overlying tissue. The implant underwent slow dissolution, but remained visible at the operating

microscope for over 8 weeks. End-stage histology indicated the presence of a thin fibrous capsule surrounding the implant, but little evidence of any local accumulation of acute inflammatory cells or vascularization was observed.

The biocompatibility of pSi for drug delivery to the heart has also been investigated [52]. In this study, micro- and nanoparticles of thermally hydrocarbonized and oxidized microparticles were tested in the heart tissue. The results indicated that both particle types had good in vivo biocompatibility; no influence on hematological parameters and no considerable changes in cardiac function before and after myocardial infarction were observed during the period of 1 week post-injection. The effect of surface chemistry on the biocompatibility was observed in heart tissue. Local injection of hydrocarbonized microparticles into the myocardium led to significantly greater activation of inflammatory cytokines and fibrosis promoting genes compared to oxidized micro- and nanoparticles. However, both particles showed no significant effect on myocardial fibrosis at 1 week post-injection.

To further understand the immunotoxicity of pSi in drug delivery, a comprehensive study was carried out with Raji (B-cell), Jurkat (T-cell), U937 (monocyte) and RAW264.7 (macrophage) both in vitro and in vivo [47]. The results showed that cytotoxicity of nanoparticles was prompted more by the surface charge than by the hydrophilicity/hydrophobicity of the surface. For similar surface charges, hydrophilic particles (oxidized and carbonized particles) were less cytotoxic than hydrophobic particles (hydrocarbonized particles). No notable changes were observed in the serum level of biochemical and hematological factors even though mild renal steatosis, glomerular degeneration, hepatic central vein dilation and white pulp shrinkage in spleen were observed.

Cytokines are group of signaling molecules and responsive to infection, immune responses and inflammation. The analysis of cytokine release in vivo is a good way to evaluate the safety of pSi particles for drug delivery. The cytokine levels after a subcutaneous administration of thermally hydrocarbonized pSi were similar to those assayed after 0.9 % NaCl injections at 6 h except for IL-1α suggesting possible slight tissue damage probably because of the large size of microparticles [24]. However, the intravenous injection of the same type of nanoparticles did not cause significant change of plasma cytokine concentrations in mice [55]. As the positive control, lipopolysaccharide increased plasma concentrations of most cytokines significantly.

6.7 Future Prospects

Three bottlenecks for wider research activities in development of porous silicon for biomedical and drug delivery applications and especially for their commercialization can be recognized. The first one is related to the limited availability of pSi material particularly when it comes to nanoparticles. There is, or has been, only few companies found through web search that produce and sell pSi micro- and nanoparticles (e.g., EM-Silicon Nano-Technologies and Vesta Ceramics) and the prices

are remarkably high in relation to a budget of a typical research group. This is presumably the reason why only a considerably small number of research laboratories are studying pSi in drug delivery as they have their own manufacturing facilities. The lack of the companies producing and selling pSi is due to the balance between supply and demand. If the demand is high enough, also the investment to the large scale manufacturing system becomes profitable. On the other hand, if there are no appropriate large scale manufacturing facilities of the material, no drug development company will base their R&D projects upon the material especially if there is already a proved material/technology available for the purpose. The researcher needs to consider closely what the requirements of the applications are and what features are essential for the materials so that the goal of their study can be reached. The beneficial properties of pSi have been highlighted above but the researcher needs to be critical when choosing the most potential material/technology for his/her need.

The second bottleneck is the safety issue related to every novel nanomaterial especially when used as biomaterial. There is a lot of research work done on the field nowadays and as there is already a product (BrachySil™) and more to come in clinical trials, the threshold for the safety concern should become smaller and smaller. As the thorough safety screening is application specific and demands huge resources these are out of the everyday focus of a common academic researcher.

The third bottleneck is the intellectual property rights (IPR) issue. When researchers are collaborating with drug development companies the rights should be directed to the company. Basically, the drug delivery field is open for pSi and there are no overall limitations to utilize pSi except in certain specific types of material in specific applications. However, the freedom to operate need to be verified already before the start of the research project.

Summa summarum, pSi is able to combine several beneficial features needed in drug delivery that it seems likely that there will be more commercial medical devices based on pSi on the market in future. This needs systematic approaches and more thorough research especially in vivo. At least the trend is promising as the research activity is still increasing exponentially.

References

1. G. Adriani, M.D. de Tullio, M. Ferrari, F. Hussain, G. Pascazio, X. Liu, P. Decuzzi, The preferential targeting of the diseased microvasculature by disk-like particles. Biomaterials **33**, 5504–5513 (2012)
2. P.V. Almeida, M.A. Shahbazi, E. Mäkilä, M. Kaasalainen, J. Salonen, J. Hirvonen, H.A. Santos, Amine-modified hyaluronic acid-functionalized porous silicon nanoparticles for targeting breast cancer tumors. Nanoscale **6**, 10377–10387 (2014)
3. S.H.C. Anderson, H. Elliott, D.J. Wallis, L.T. Canham, J.J. Powell, Dissolution of different forms of partially porous silicon wafers under simulated physiological conditions. Phys. Status Solidi A **197**, 331–335 (2003)

4. L.M. Bimbo, M. Sarparanta, H.A. Santos, A.J. Airaksinen, E. Mäkilä, T. Laaksonen, L. Peltonen, V.P. Lehto, J. Hirvonen, J. Salonen, Biocompatibility of thermally hydrocarbonized porous silicon nanoparticles and their biodistribution in rats. ACS Nano **4**, 3023–3032 (2010)
5. L.T. Canham, Bioactive silicon structure fabrication through nanoetching techniques. Adv. Mater. **7**, 1033–1037 (1995)
6. L. Cheng, E. Anglin, F. Cunin, D. Kim, M.J. Sailor, I. Falkenstein, A. Tammewar, W.R. Freeman, Intravitreal properties of porous silicon photonic crystals: A potential self-reporting intraocular drug-delivery vehicle. Br. J. Ophthalmol. **92**, 705–711 (2008)
7. J. Chhablani, A. Nieto, H. Hou, E.C. Wu, W.R. Freeman, M.J. Sailor, L. Cheng, Oxidized porous silicon particles covalently grafted with daunorubicin as a sustained intraocular drug delivery system. Invest. Ophthalmol. Visual Sci. **54**, 1268–1279 (2013)
8. F. Danhier, O. Feron, V. Préat, To exploit the tumor microenvironment: passive and active tumor targeting of nanocarriers for anti-cancer drug delivery. J. Controlled Release **148**, 135–146 (2010)
9. E.C. Dreaden, S.W. Morton, K.E. Shopsowitz, J. Choi, Z.J. Deng, N. Cho, P.T. Hammond, Bimodal tumor-targeting from microenvironment responsive hyaluronan layer-by-layer (LbL) nanoparticles. ACS Nano **8**, 8374–8382 (2014)
10. W. Gao, J.M. Chan, O.C. Farokhzad, PH-responsive nanoparticles for drug delivery. Mol. Pharm. **7**, 1913–1920 (2010)
11. A. Gizzatov, C. Stigliano, J.S. Ananta, R. Sethi, R. Xu, A. Guven, M. Ramirez, H. Shen, A. Sood, M. Ferrari, L.J. Wilson, X. Liu, P. Decuzzi, Geometrical confinement of Gd(DOTA) molecules within mesoporous silicon nanoconstructs for MR imaging of cancer. Cancer Lett. **352**, 97–101 (2014)
12. B. Godin, C. Chiappini, S. Srinivasan, J.F. Alexander, K. Yokoi, M. Ferrari, P. Decuzzi, X. Liu, Discoidal porous silicon particles: fabrication and biodistribution in breast cancer bearing mice. Adv. Funct. Mater. **22**, 4225–4235 (2012)
13. B.D. Hamilton, J.M. Ha, M.A. Hillmyer, M.D. Ward, Manipulating crystal growth and polymorphism by confinement in nanoscale crystallization chambers. Acc. Chem. Res. **45**, 414–423 (2012)
14. B.C. Hancock, M. Parks, What is the true solubility advantage for amorphous pharmaceuticals? Pharm. Res. **17**, 397–404 (2000)
15. K.I. Hartmann, A. Nieto, E.C. Wu, W.R. Freeman, J.S. Kim, J. Chhablani, M.J. Sailor, L. Cheng, Hydrosilylated porous silicon particles function as an intravitreal drug delivery system for daunorubicin. J. Ocul. Pharmacol. Ther. **29**, 493–500 (2013)
16. H. Hou, A. Nieto, F. Ma, W.R. Freeman, M.J. Sailor, L. Cheng, Tunable sustained intravitreal drug delivery system for daunorubicin using oxidized porous silicon. J. Controlled Release **178**, 46–54 (2014)
17. A. Huotari, W. Xu, J. Mönkäre, M. Kovalainen, K.H. Herzig, V.P. Lehto, K. Järvinen, Effect of surface chemistry of porous silicon microparticles on glucagon-like peptide-1 (GLP-1) loading, release and biological activity. Int. J. Pharm. **454**, 67–73 (2013)
18. R.K. Jain, T. Stylianopoulos, Delivering nanomedicine to solid tumors. Nat. Rev. Clin. Oncol. **7**, 653–664 (2010)
19. A. Jiménez-Periáñez, B. Abos Gracia, J. López Relaño, C.M. Diez-Rivero, P.A. Reche, A. Jiménez-Periáñez, E. Martínez-Naves, M. Gómez Del Moral, E. Martínez-Naves, Mesoporous silicon microparticles enhance MHC class i cross-antigen presentation by human dendritic cells. Clin. Dev. Immunol. **2013**, 362163 (2013)
20. A.M. Kallinen, M.P. Sarparanta, D. Liu, E.M. Mäkilä, J.J. Salonen, J.T. Hirvonen, H.A. Santos, A.J. Airaksinen, In vivo evaluation of porous silicon and porous silicon solid lipid nanocomposites for passive targeting and imaging. Mol. Pharm. **11**, 2876–2886 (2014)
21. A.M. Kaukonen, L. Laitinen, J. Salonen, J. Tuura, T. Heikkilä, T. Limnell, J. Hirvonen, V.P. Lehto, Enhanced in vitro permeation of furosemide loaded into thermally carbonized mesoporous silicon (TCPSi) microparticles. Eur. J. Pharm. Biopharm. **66**, 348–356 (2007)

22. Y. Kawabata, K. Wada, M. Nakatani, S. Yamada, S. Onoue, Formulation design for poorly water-soluble drugs based on biopharmaceutics classification system: basic approaches and practical applications. Int. J. Pharm. **420**, 1–10 (2011)
23. M. Kilpeläinen, J. Mönkäre, M.A. Vlasova, J. Riikonen, V.P. Lehto, J. Salonen, K. Järvinen, K.H. Herzig, Nanostructured porous silicon microparticles enable sustained peptide (Melanotan II) delivery. Eur. J. Pharm. Biopharm. **77**, 20–25 (2011)
24. M. Kilpeläinen, J. Riikonen, M.A. Vlasova, A. Huotari, V.P. Lehto, J. Salonen, K.H. Herzig, K. Järvinen, In vivo delivery of a peptide, ghrelin antagonist, with mesoporous silicon microparticles. J. Controlled Release **137**, 166–170 (2009)
25. P. Kinnari, E. Mäkilä, T. Heikkilä, J. Salonen, J. Hirvonen, H.A. Santos, Comparison of mesoporous silicon and non-ordered mesoporous silica materials as drug carriers for itraconazole. Int. J. Pharm. **414**, 148–156 (2011)
26. D.B. Kirpotin, D.C. Drummond, Y. Shao, M.R. Shalaby, K. Hong, U.B. Nielsen, J.D. Marks, C.C. Benz, J.W. Park, Antibody targeting of long-circulating lipidic nanoparticles does not increase tumor localization but does increase internalization in animal models. Cancer Res. **66**, 6732–6740 (2006)
27. M. Kovalainen, J. Mönkäre, M. Kaasalainen, J. Riikonen, V. Lehto, J. Salonen, K. Herzig, K. Järvinen, Development of porous silicon nanocarriers for parenteral peptide delivery. Mol. Pharm. **10**, 353–359 (2013)
28. M. Kovalainen, J. Mönkäre, E. Mäkilä, J. Salonen, V.P. Lehto, K.H. Herzig, K. Järvinen, Mesoporous silicon (PSi) for sustained peptide delivery: effect of PSi microparticle surface chemistry on peptide YY3-36 release. Pharm. Res. **29**, 837–846 (2012)
29. D. Liu, H. Zhang, B. Herranz-Blanco, E. Mäkilä, V. Lehto, J. Salonen, J. Hirvonen, H.A. Santos, Microfluidic assembly of monodisperse multistage pH-responsive polymer/porous silicon composites for precisely controlled multi-drug delivery. Small **10**, 2029–2038 (2014)
30. D. Liu, L.M. Bimbo, E. Mäkilä, F. Villanova, M. Kaasalainen, B. Herranz-Blanco, C.M. Caramella, V.P. Lehto, J. Salonen, K.H. Herzig, J. Hirvonen, H.A. Santos, Co-delivery of a hydrophobic small molecule and a hydrophilic peptide by porous silicon nanoparticles. J. Controlled Release **170**, 268–278 (2013)
31. S.P. Low, N.H. Voelcker, L.T. Canham, K.A. Williams, The biocompatibility of porous silicon in tissues of the eye. Biomaterials **30**, 2873–2880 (2009)
32. E. Mäkilä, M.P.A. Ferreira, H. Kivelä, S. Niemi, A. Correia, M. Shahbazi, J. Kauppila, J. Hirvonen, H.A. Santos, J. Salonen, Confinement effects on drugs in thermally hydrocarbonized porous silicon. Langmuir **30**, 2196–2205 (2014)
33. S.J.P. McInnes, E.J. Szili, S.A. Al-Bataineh, J. Xu, M.E. Alf, K.K. Gleason, R.D. Short, N.H. Voelcker, Combination of iCVD and porous silicon for the development of a controlled drug delivery system. ACS Appl. Mater. Interfaces **4**, 3566–3574 (2012)
34. I. Meraz, C.H. Hearnden, X. Liu, M. Yang, L. Williams, D.J. Savage, J. Gu, J.R. Rhudy, K. Yokoi, E.C. Lavelle, R.E. Serda, Multivalent presentation of MPL by porous silicon microparticles favors T helper 1 polarization enhancing the anti-tumor efficacy of doxorubicin nanoliposomes. PLoS ONE, **9**, (2014)
35. K. Nan, F. Ma, H. Hou, W.R. Freeman, M.J. Sailor, L. Cheng, Porous silicon oxide-PLGA composite microspheres for sustained ocular delivery of daunorubicin. Acta Biomater. **10**, 3505–3512 (2014)
36. T. Nissinen, S. Näkki, M. Latikka, M. Heinonen, T. Liimatainen, W. Xu, R.H.A. Ras, O. Gröhn, J. Riikonen, V.P. Lehto, Facile synthesis of biocompatible superparamagnetic mesoporous nanoparticles for imageable drug delivery. Microporous Mesoporous Mater. **195**, 2–8 (2014)
37. J.H. Park, L. Gu, G. Von Maltzahn, E. Ruoslahti, S.N. Bhatia, M.J. Sailor, Biodegradable luminescent porous silicon nanoparticles for in vivo applications. Nat. Mater. **8**, 331–336 (2009)

38. C.W. Pouton, Formulation of poorly water-soluble drugs for oral administration: physicochemical and physiological issues and the lipid formulation classification system. Eur. J. Pharm. Sci. **29**, 278–287 (2006)
39. J. Riikonen, E. Mäkilä, J. Salonen, V.P. Lehto, Determination of physical state of drug molecules in mesoporous silicon with different surface chemistries. Langmuir **25**, 6137–6142 (2009)
40. J. Rytkönen, P. Arukuusk, W. Xu, K. Kurrikoff, U. Langel, V. Lehto, A. Närvänen, Porous silicon-cell penetrating peptide hybrid nanocarrier for intracellular delivery of oligonucleotides. Mol. Pharm. **11**, 382–390 (2014)
41. J. Rytkönen, R. Miettinen, M. Kaasalainen et al., Functionalization of mesoporous silicon nanoparticles for targeting and bioimaging purposes. J. Nanomater (2012)
42. J. Salonen, L. Laitinen, A. Kaukonen, J. Tuura, M. Björkqvist, T. Heikkilä, K. Vähä-Heikkilä, J. Hirvonen, V.P. Lehto, Mesoporous silicon microparticles for oral drug delivery: loading and release of five model drugs. J. Controlled Release **108**, 362–374 (2005)
43. H.A. Santos, L. Peltonen, T. Limnell, J. Hirvonen, Mesoporous materials and nanocrystals for enhancing the dissolution behavior of poorly water-soluble drugs. Curr. Pharm. Biotechnol. **14**, 926–938 (2013)
44. H.A. Santos, J. Riikonen, J. Salonen, E. Mäkilä, T. Heikkilä, T. Laaksonen, L. Peltonen, V.P. Lehto, J. Hirvonen, In vitro cytotoxicity of porous silicon microparticles: effect of the particle concentration, surface chemistry and size. Acta Biomater. **6**, 2721–2731 (2010)
45. M. Sarparanta, E. Mäkilä, T. Heikkilä, J. Salonen, E. Kukk, V. Lehto, H.A. Santos, J. Hirvonen, A.J. Airaksinen, ^{18}F-labeled modified porous silicon particles for investigation of drug delivery carrier distribution in vivo with positron emission tomography. Mol. Pharm. **8**, 1799–1806 (2011)
46. E. Secret, K. Smith, V. Dubljevic, E. Moore, P. Macardle, B. Delalat, M. Rogers, T.G. Johns, J. Durand, F. Cunin, N.H. Voelcker, Antibody-functionalized porous silicon nanoparticles for vectorization of hydrophobic drugs. Adv. Healthcare Mater. **2**, 718–727 (2013)
47. M.A. Shahbazi, M. Hamidi, E.M. Mäkilä, H. Zhang, P.V. Almeida, M. Kaasalainen, J.J. Salonen, J.T. Hirvonen, H.A. Santos, The mechanisms of surface chemistry effects of mesoporous silicon nanoparticles on immunotoxicity and biocompatibility. Biomaterials **34**, 7776–7789 (2013)
48. P. Sharma, W.A. Denny, S. Garg, Effect of wet milling process on the solid state of indomethacin and simvastatin. Int. J. Pharm. **380**, 40–48 (2009)
49. H. Shen, C. Rodriguez-Aguayo, R. Xu, V. Gonzalez-Villasana, J. Mai, Y. Huang, G. Zhang, X. Guo, L. Bai, G. Qin, X. Deng, Q. Li, D.R. Erm, B. Aslan, X. Liu, J. Sakamoto, A. Chavez-Reyes, H. Han, A.K. Sood, M. Ferrari, G. Lopez-Berestein, Enhancing chemotherapy response with sustained EphA2 silencing using multistage vector delivery. Clin. Cancer Res. **19**, 1806–1815 (2013)
50. T. Sun, Y.S. Zhang, B. Pang, D.C. Hyun, M. Yang, Y. Xia, Engineered nanoparticles for drug delivery in cancer therapy. Angew. Chem. Int. Ed. Engl. **53**, 12320–12364 (2014)
51. E. Tasciotti, X. Liu, R. Bhavane, K. Plant, A.D. Leonard, B.K. Price, M.M.C. Cheng, P. Decuzzi, J.M. Tour, F. Robertson, M. Ferrari, Mesoporous silicon particles as a multistage delivery system for imaging and therapeutic applications. Nat. Nanotechnol. **3**, 151–157 (2008)
52. M.A. Tölli, M.P.A. Ferreira, S.M. Kinnunen, J. Rysä, E.M. Mäkilä, Z. Szabó, R.E. Serpi, P.J. Ohukainen, M.J. Välimäki, A.M.R. Correia, J.J. Salonen, J.T. Hirvonen, H.J. Ruskoaho, H.A. Santos, In vivo biocompatibility of porous silicon biomaterials for drug delivery to the heart. Biomaterials **35**, 8394–8405 (2014)
53. N. Vale, E. Mäkilä, J. Salonen, P. Gomes, J. Hirvonen, H.A. Santos, New times, new trends for ethionamide: in vitro evaluation of drug-loaded thermally carbonized porous silicon microparticles. Eur. J. Pharm. Biopharm. **81**, 314–323 (2012)
54. R.B. Vasani, S.J.P. McInnes, M.A. Cole, A.M.M. Jani, A.V. Ellis, N.H. Voelcker, Stimulus-responsiveness and drug release from porous silicon films ATRP-grafted with poly(N-isopropylacrylamide). Langmuir **27**, 7843–7853 (2011)

55. M.A. Vlasova, J. Rytkönen, J. Riikonen, O.S. Tarasova, J. Mönkäre, M. Kovalainen, A. Närvänen, J. Salonen, K. Herzig, V. Lehto, K. Järvinen, Nanocarriers and the delivered drug: effect interference due to intravenous administration. Eur. J. Pharm. Sci. **63**, 96–102 (2014)
56. C.F. Wang, E.M. Mäkilä, M.H. Kaasalainen, D. Liu, M.P. Sarparanta, A.J. Airaksinen, J.J. Salonen, J.T. Hirvonen, H.A. Santos, Copper-free azide-alkyne cycloaddition of targeting peptides toporous silicon nanoparticles for intracellular drug uptake. Biomaterials **35**, 1257–1266 (2014)
57. F. Wang, T.J. Barnes, C.A. Prestidge, Celecoxib confinement within mesoporous silicon for enhanced oral bioavailability. Mesoporous Biomater. **1**, 1–15 (2014)
58. F. Wang, H. Hui, T.J. Barnes, C. Barnett, C.A. Prestidge, Oxidized mesoporous silicon microparticles for improved oral delivery of poorly soluble drugs. Mol. Pharmaceutics **7**, 227–236 (2010)
59. C.Y. Wu, L.Z. Benet, Bull. Tech. Gattefosse **99**, 9–16 (2006)
60. E.C. Wu, J.S. Andrew, L. Cheng, W.R. Freeman, L. Pearson, M.J. Sailor, Real-time monitoring of sustained drug release using the optical properties of porous silicon photonic crystal particles. Biomaterials **32**, 1957–1966 (2011)
61. W. Xu, J. Riikonen, V.P. Lehto, Mesoporous systems for poorly soluble drugs. Int. J. Pharm. **453**, 181–197 (2013)
62. W. Xu, J. Rytkönen, S. Rönkkö, T. Nissinen, T. Kinnunen, M. Suvanto, A. Närvänen, V. Lehto, A nanostopper approach to selectively engineer the surfaces of mesoporous silicon. Chem. Mater. **26**, 6734–6742 (2014)
63. K. Yokoi, B. Godin, C.J. Oborn, J.F. Alexander, X. Liu, I.J. Fidler, M. Ferrari, Porous silicon nanocarriers for dual targeting tumor associated endothelial cells and macrophages in stroma of orthotopic human pancreatic cancers. Cancer Lett. **334**, 319–327 (2013)
64. H. Zhang, D. Liu, M. Shahbazi, E. Mäkilä, B. Herranz-Blanco, J. Salonen, J. Hirvonen, H.A. Santos, Fabrication of a multifunctional nano-in-micro drug delivery platform by microfluidic templated encapsulation of porous silicon in polymer matrix. Adv Mater. **26**, 4497–4503 (2014)

Chapter 7
Sensing and Biosensing Applications of Nanoporous Anodic Alumina

Tushar Kumeria and Abel Santos

Abstract Nanoporous anodic alumina (NAA) is fabricated by a simple yet cost-effective self-ordering anodization process of aluminium foils, which yields highly ordered and columnar nanopores. These ordered pores impart NAA with unique optical and electrochemical properties, which have been intensively researched to develop smart, efficient, cost-competitive and portable yet complex sensing and biosensing systems. This chapter provides detailed fundamentals of sensing techniques and recent advances in development of NAA based sensing and biosensing technologies.

7.1 Introduction

Sensing devices allow users to determine, what and how much a substance of interest is present in an industrial, environmental or a biological sample [1]. One, very simple and most commonly used such device out of several hundred other devices is a portable glucometer, which measures blood sugar level of a patient subject [2]. Nanotechnology, since its advent has been pushing the boundaries and giving rise to a new paradigm in smart and portable sensing devices. Solid state sensors based on nanoporous substrates are a good example of this. Nanoporous substrates such as porous silicon, nanoporous anodic alumina, titania nanotube arrays, and track etched porous polymer membranes have been commonly employed as substrates for advanced sensing devices [3–5]. As described in previous chapters, NAA possesses unique structural, chemical, optical, thermal and mechanical properties, and biocompatibility besides controllable geometry and exploitable surface chemistry [6, 7]. Owing to these properties, NAA has emerged as an attractive material for development of sensing tools for chemicals with

T. Kumeria (✉) · A. Santos
School of Chemical Engineering, The University of Adelaide,
North Engineering Building, 5005 Adelaide, Australia
e-mail: tushar.kumeria@adelaide.edu.au

D. Losic and A. Santos (eds.), *Electrochemically Engineered Nanoporous Materials*, Springer Series in Materials Science 220,
DOI 10.1007/978-3-319-20346-1_7

relevance for industry, environment and biomedicine. NAA has been coupled with a wide range of optical and electrochemical techniques such as photoluminescence (PL), surface plasmon resonance (SPR), surface enhanced Raman spectroscopy (SERS), reflectometric interference spectroscopy (RIfS), electrochemical impedance spectroscopy (EIS), etc. to fabricate highly sensitive and selective detection systems [3, 6, 8]. This chapter deals with fundamental understanding of various optical, electrochemical and other sensing techniques coupled with NAA and represents most recent advances in the development and applications of NAA based sensing and biosensing platforms.

7.2 Optical Sensors Based on NAA

Notice that, the interaction of light and NAA is highly dependent on its structural and chemical nature. In this regard, NAA displays exceptional optical properties including reflectance, transmittance, absorbance, photoluminescence, and wave-guiding, which can be easily utilized to design and fabricate a new generation of optical sensing and biosensing devices [8]. As for this, NAA based optical sensing tools have recently been explored for a broad range of analytical applications including environmental and clinical analysis, industrial and food control, and defence and homeland security [3, 6, 9]. The next four sections of our chapter will be focused on some of the optical sensing techniques, including PL, SPR, SERS, and RIfS, which have been majorly applied to fabricated sensing devices using NAA as substrate (Fig. 7.1).

7.2.1 Photoluminescence Spectroscopy (PL)

Photoluminescence (PL) is a commonly used term for phenomenon of absorption of radiation energy and subsequent emission of light by materials. Absorption of energy from a radiation by a luminescent center results in excitation of electron to higher energy level, which emits/releases energy in the form of light during the process of returning to the ground state [1]. PL based sensing generally relies on quenching or shift in PL peak on attachment of target entity to the PL substrate. This is due to generation of a competing pathway for electron to return back excited state to ground state that is also called non-radiative relaxation or intermediate energy levels having different radiative energy [14]. Readers should refer to [1, 10] for details for fundamental understanding of photoluminescence. Decades of research and development in this field have given us the ability to design materials with excitation and emission wavelength ranges *ad-lib*. Therefore, PL based sensing and biosensing devices occupy a prominent place among the optical devices due to its excellent sensitivity (i.e. down to single molecule detection) and the required selectivity. The first report on emission of light from NAA was by Braun [15] while

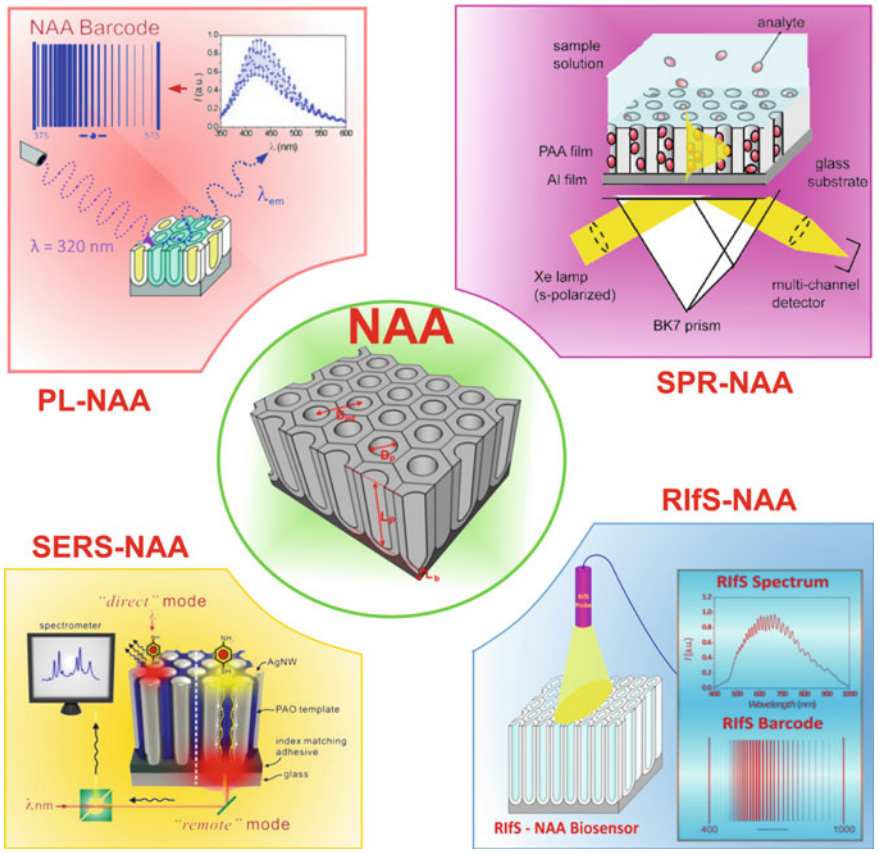

Fig. 7.1 A schematic showing all four optical sensing techniques coupled with NAA for developing highly sensitive optical sensors (adapted with permission from [10–13])

passing positive potential through aluminium/oxide/electrolyte system against platinum cathode [15–17]. This phenomenon is called galvanoluminescence (GL) and has been extensively researched during the last century. Despite, several years of research the GL phenomenon is not yet completely understood due to the complex system required for GL to occur. GL from nanoporous anodic aluminium oxide is influenced by parameters including the nature of the electrolyte (organic or inorganic), metal surface properties (nature, purity, and pretreatment), anodization conditions (temperature and concentration of the electrolyte, current density, and voltage of anodization), and so on. The general observations are that GL increases with higher temperature, concentration, anodization voltage, and current density. Figure 7.2 presents GL plots of NAA displaying effect of annealing temperature and electrolyte concentration (i.e. phosphoric acid in this case). This is due to increase in number of electrons in excited state on increasing electrolyte concentration, temperature, current density, and voltage. As for pretreatment, the highest GL is

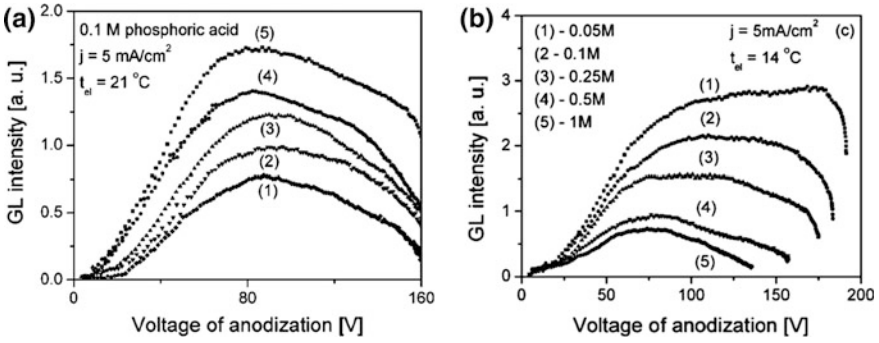

Fig. 7.2 GL intensity plots for NAA displaying intensity of GL against voltage for **a** different annealing temperature (*1*) 75 °C; (*2*) 150 °C; (*3*) 250 °C; (*4*) 350 °C; (*5*) 450 °C; and **b** varying electrolyte concentrations (adapted with permission from [17])

obtained from NAA prepared on degreased Al whereas it decreases on cleaned samples and almost disappears for electropolished samples. This suggests that surface defects and impurities imparted in the oxide film during anodization are responsible for GL [17–21].

GL pawed the way for advances of photoluminescence (PL) from NAA, which was reported several decades ago. A large number of studies have been concentrated on understanding the PL properties of NAA, however, the mechanism of its origin is still not clear [22, 23]. However, the generally accepted mechanism behind PL in NAA is thought to be the presence oxygenated impurities and inherent defects of Al_2O_3 forming NAA. These flaws in chemical structure of NAA are also referred to as photoluminescent field centres. There are three types of PL field centres depending upon the type of oxygen vacancies (i) *F* centres, which are oxygen vacancies with two electrons and rely on the amount of carboxylate impurities incorporated into the AAO structure from the acid electrolyte in the course of the anodization process, (ii) F^+ centres, which are oxygen vacancies with single electron and related with ionized oxygen vacancies in the AAO structure, and (iii) F^{++} centres, which are oxygen vacancy without an electron and are not stable [22, 24–27]. Similar to GL, PL is also influenced by anodization parameters as anodization voltage, electrolyte, thermal treatment, pore widening time, and anodization regime [26, 28, 29]. As for this, it has been reported that PL intensity for NAA fabricated using oxalic acid electrolyte is higher than NAA fabricated using sulphuric acid or phosphoric acid electrolyte [30, 31]. As mentioned above the main contribution to PL of NAA is from oxygen containing species (F^+ centres), hence, anodization in oxalic acid imparts the maximum oxygen impurities. Post anodization thermal treatment and pore widening of NAA display a similar trend in PL intensity, which increases initially but starts decreasing after a critical point [30, 32, 33]. The major advantage of NAA based PL sensing devices is that, unlike other materials such as porous silicon, the PL spectrum remains stable without any passivation process. Apart from exceptional stability of NAA, its unique PL

fingerprint with high degree of sensibility, biocompatibility, ability to act as a container to accommodate target molecules and measure their PL response with high resolution has made it even more attractive as a sensing substrate.

PL sensing using NAA as substrate could either be through label molecules (i.e. dyes, Q-dots) or without labels (i.e. label-free). Label based PL sensing generally results in changes in intensity whereas label-free sensors rely of shift in the peak in its PL spectrum. It has been reported that confinement of luminescent molecules inside the nanopores results in enhancement of the PL signal [34]. First reports on label based PL-NAA sensing observed that adsorption of organic dye (Morin) and proteins (Trypsin: Try and Human Serum Albumin: HSA) results in enhancement in PL signal [35, 36]. They also found that their PL peak positions are similar to that of dye itself in ethanol solution but the PL intensity of embedded dye-Try or dye-HAS is much higher than that of dye alone, which was attributed to the formation of morin-Al complex and coexistence of morin and Try or HAS in the NAA pores. Another innovative label based PL sensing approach by Feng et al. studied DNA hybridization using quantum dots as labels [37]. In this study, positively charged 3-aminopropyl dimethylethoxysilane functionalised NAA are subjected to layer-by-layer deposition of positively or negatively charged dendrimers and ZnCdSe quantum dots. Changes in PL intensity are monitored to detect hybridization of DNA complementary to ssDNA immobilized onto ZnCdSe quantum dots inside NAA pres.

A label-free PL-NAA sensing approach was adopted by Santos et al. who developed an optical barcode sensing systems [10, 38]. Interestingly, interference like fringes/oscillations related to Fabry–Pérot effect are observed during label-free PL-NAA sensing, which produces an amplification of the PL oscillations by an enhancement of the photoluminescence at wavelengths corresponding to the optical modes of the cavity formed by the Air-NAA-Al system. The PL spectrum of NAA is shown in Fig. 7.3a with narrow and well-resolved fringes, which are highly useful for biosensing purposes. The number, intensity and position of these oscillations can be tuned by modifying the pore length and diameters (i.e. by changing the effective medium). Figure 7.3b shows a schematic diagram of a label-free PL-NAA sensor tested for detection of target entities as organic dyes, enzymes and glucoses, which displays a shift in PL peaks towards higher wavelength. Furthermore, these fringes can generate PL barcodes to be used as target fingerprints. PL barcodes enable development of smart optical biosensors for a broad range of analytes.

7.2.2 Surface Plasmon Resonance (SPR) and Localized Surface Plasmon Resonance (LSPR)

The first report on plasmonic drop on a grating dates back to 1902 but it was thought of as an anomaly in the spectrum. Later, a large drop in reflectivity spectrum when illuminating a thin metal film was observed by Thurbadar [39] but he did not relate it

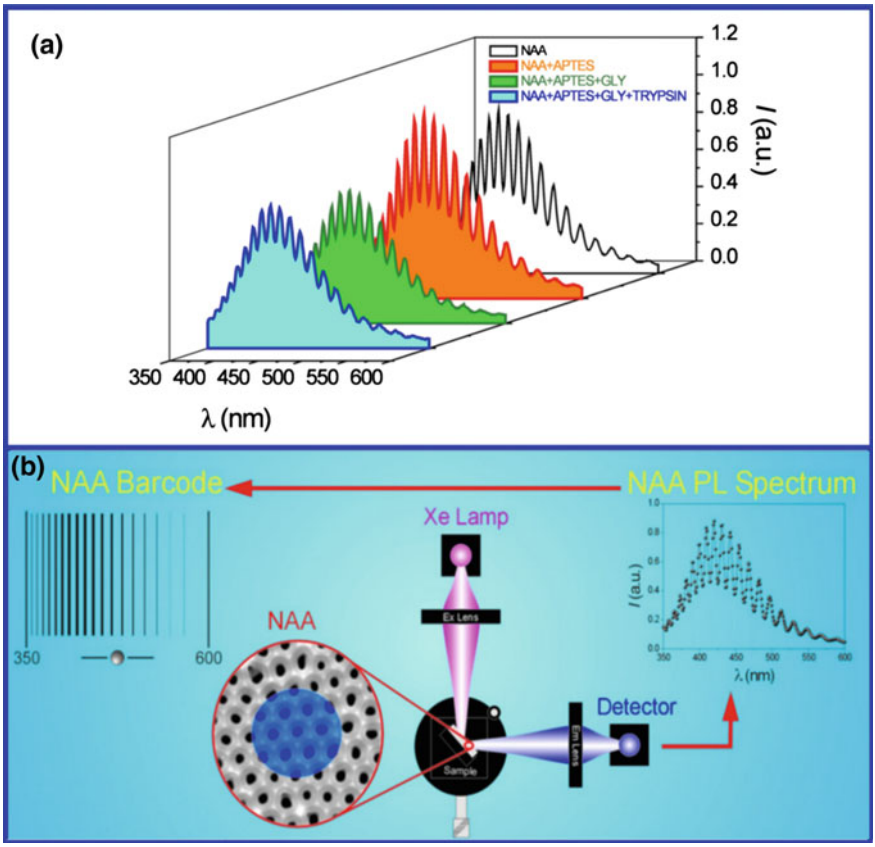

Fig. 7.3 **a** PL spectrum of NAA showing Fabry–Pérot fringes and step-wise changes in PL on attachment of trypsin side the pores. **b** Typical PL setup used for recording luminescence of NAA substrate along with the FP fringes that can be converted to PL barcode (adapted with permission from [38])

to plasmon resonance [39]. However, Otto [40] correlated this drop in reflectivity spectrum to excitation of surface plasmons [41]. Kertschmann, in the same year, reported excitation of surface plasmons in a different configuration (i.e. attenuated total internal reflection) [42]. It was only late 1970 when surface plasmons were employed for characterization of thin films and monitor process at metal boundaries [43, 44]. A surface plasmon is an electromagnetic wave that propagates along the boundary between a dielectric and a metal and behaves like quasi-free electron plasma [45]. The propagation constant of an SP, β, can be expressed as:

$$\beta = \frac{\omega}{c}\sqrt{\frac{\varepsilon_M \varepsilon_D}{\varepsilon_M + \varepsilon_D}} \tag{7.1}$$

where ω is the angular frequency, c is the speed of light in vacuum, and εD and εM are dielectric functions of the dielectric and metal, respectively. For this equation for SP to hold true the real part of εM should be negative and its absolute value smaller than εD [45]. These conditions are successfully satisfied at different wavelengths for several metals of which gold and silver are the most commonly employed in SPR biosensors [46]. The real and imaginary parts of the propagation constant describe spatial periodicity and attenuation of an SP in the direction of propagation, respectively. The electromagnetic field of an SP is confined at the metal-dielectric boundary and decreases exponentially into both media. As shown in Fig. 7.4a, the vast majority of the field of an SP is concentrated in the dielectric, thus the propagation constant of the SP is extremely sensitive to changes in the effective refractive index of the dielectric. After the first study of monitoring a biological reaction in 1980s, surface plasmon resonance (SPR) is recognized as the most popular analytical method used to probe biological interactions in real-time [47]. The advances in SPR technique over the last three decades have led to the development of SPR systems capable of in situ measurements of a wide range of surface interactions including ligand binding affinity, association/dissociation kinetics, affinity constant, and highly sensitive surface concentration measurements [48–50]. SPR systems are mainly based on a Kretschmann configuration, where surface plasmons are excited by an evanescent electromagnetic wave generated by the light incident on the surface of a prism coated with a thin layer of metal, mostly gold or silver [46].

NAA based SPR biosensors are mostly based on thin metallic film coated prism (i.e. Kretschmann configuration). The metal coated prism is subsequently coated by aluminium (Al) which is anodized to grow a NAA layer. The surface plasmons of a NAA layer on a prism surface rely strongly on the effective refractive index of the adjacent medium within distances of approximately 200 nm from the metal film. The effective refractive index of the porous layer is easily manipulated by replacing the medium filling the pores making it possible to use SPR with NAA for detecting biological binding events [6]. Figure 7.4c shows a schematic diagram of a typical SPR configuration used for SPR-NAA biosensing systems. These SPR-NAA devices have been utilized to monitor the adsorption and desorption of bovine serum albumin at varying pH values and formation of self assembled monolayers (SAMs) [51, 52]. Yamaguchi et al. developed a simpler yet sensitive SPR-NAA device by directly depositing Al onto a prism, which was then anodized to generate a nanoporous layer of 200 nm thick. The plasmons were excited in the remaining underlying unanodized Al (17 nm) metal layer [53]. The performance of the prepared device was measured by detecting formation of $Fe[Bphen]_3^{2+}$. Koutsioubas et al. fabricated a similar NAA-based SPR sensors to detect the formation of SAMs of octadecyl-phosphonic acid (ODP) [54]. NAA-SPR sensors have also been demonstrated for quantitative analyses of biological molecules and biological events as enzymatic kinetics [55]. This was achieved by growing a 3 μm thick NAA layer with pores of diameter approximately 60 nm that acted as container for immobilization of enzymes (invertase). Subsequently, the enzyme-substrate was flowed over the invertase modified NAA through the flow cell and the digested

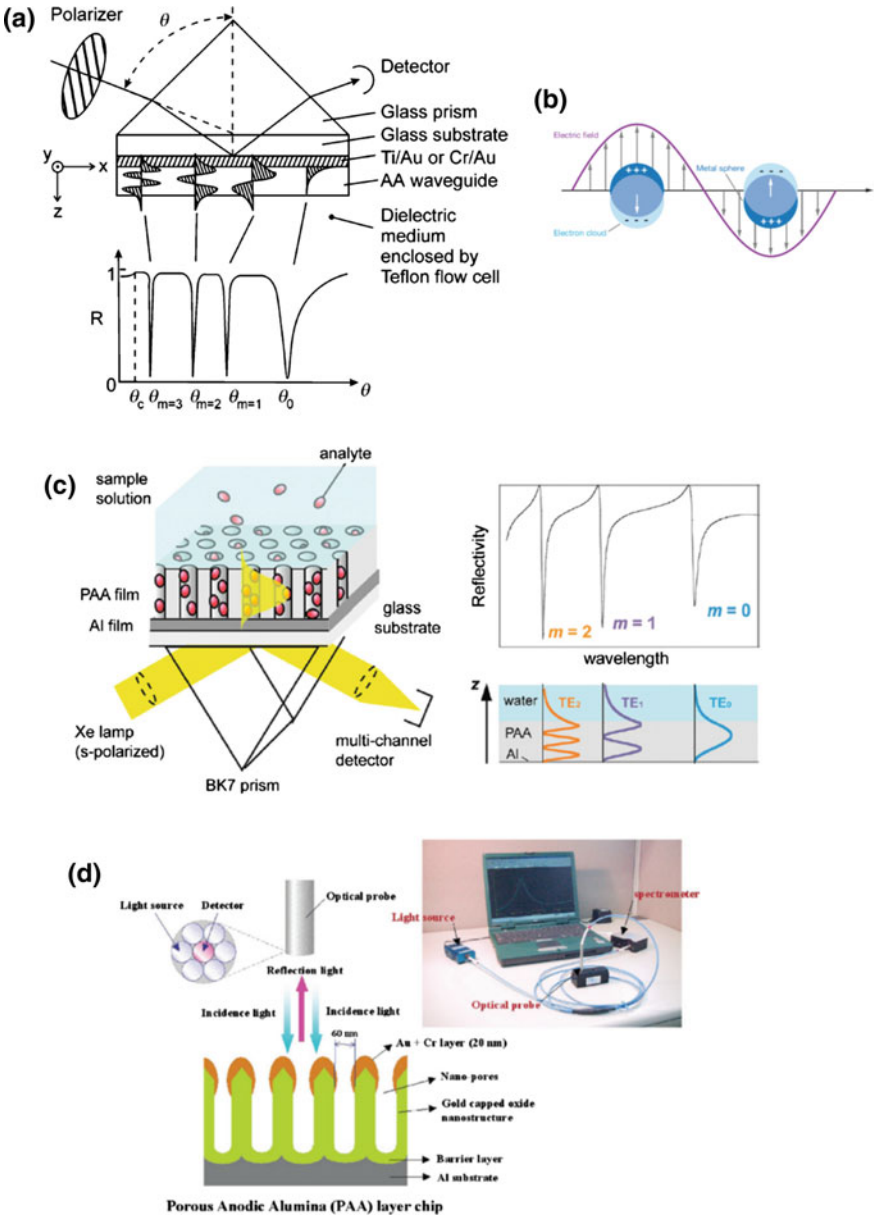

Fig. 7.4 Schematic of **a** excitation of the surface plasmon and waveguide modes showing very sharp dips when reflectivity (R) is measured as a function of the angle of incidence (õ). **b** Localized surface plasmon. **c** NAA based SPR system with excitation of plasmon and waveguide modes similar to planar films in **a** and **d** LSPR device formed by coating top surface of NAA with gold for highly sensitive detection of analytes along with the digital photo of the original setup used for measuring LSPR from NAA based substrates (adapted with permission from [11, 52, 59, 61])

product was detected by SPR. Activity of immobilized invertase was determined with different concentrations of sucrose at pH ranging from 3 to 6.5, with maximum activity at pH 4.5. SPR revealed biphasic type kinetics for both the adsorption of the enzyme and degradation of the substrate. In another study, real-time and in situ monitoring of the grafting of polymer (i.e. poly(*g*-benzyl-*L*-glutamate: PBLG) within the nanopores of NAA was studied using SPR [56]. The study shows conformal alignment of PBLG inside the nanopores of NAA which could be attributed to confinement of polymer chains inside the pores. This was later confirmed by comparing the results obtained with NAA and planar silicon dioxide surface.

Another form of SPR, optical wave-guiding mode (OWG) is generated when pore diameters of NAA is 0.1 times smaller than the wavelength of the incident light resulting in confinement of the light optical modes [11]. Nano dimensional pore diameter of NAA also minimises scattering loses at visible and longer wavelength, which is important for sensitive probing of binding of biomolecules inside the pores. The geometry of NAA is shown to have an exquisite control over surface plasmons of OWG-NAA biosensors, which can be used to tune and optimize the plasmonic characteristics of the OWG-NAA sensor for specific applications. Knoll's group reported on modification of NAA substrate for OWG sensing with atomic layer deposition and polymer grafting for designing and optimizing OWF-NAA sensors for detection of biomolecules [56, 57]. They also demonstrated a strategy for mounting bulk anodized AAO thin films on heterogeneous solid-supports suitable for OWG sensing that even works on a curved metallic substrates [58].

Metal nanoparticles, especially gold and silver display a new type of SPR known as localized SPR (LSPR or LPR). During localized surface plasmons, due to size restrictions, light interacts with particles/structures of dimensions much smaller than the incident wavelength. This constricted interaction of light leads to oscillation of plasmons locally around the nanoparticle with a frequency known as the localized surface plasmon (LSPR). Like SPR, LSPR is sensitive to changes in the local refractive index or dielectric medium (Fig. 7.4b). The changes in the local environment are measured through an LSPR wavelength-shift. Angle resolved variant of the LSPR sensing setup is also possible. The localized plasmons resonance is highly dependent on the material, size, and shape of the nanoparticles/structures. Apart from the aforementioned parameters LSPR is also highly dependent on the organization of metal nanoparticles/structures, which can leads to enhancement of LSPR signals [3, 59, 60]. The major advantages of LSPR systems in comparison to conventional SPR are that it is simple, inexpensive and portable system that does not require a Kretschmann configuration (i.e. the prism element is not necessary). NAA possesses hexagonally organized pores with controllable diameter. Therefore, coating of noble metal by thermal deposition or sputter deposition or other assembly methods results in highly ordered arrays of metallic nanoparticles (i.e. nanocaps) like structure on the top surface of AAO. As stated above that organized metal nanostructures display enhanced LSPR signal thus, making NAA a very popular substrate for designing LSPR devices. Figure 7.4d shows a LSPR-NAA

sensor fabricated by coating gold to generate gold-capped NAA substrate for monitoring antigen-antibody binding and an actual optical system used for measuring LSPR signal. LSPR-NAA sensors have been successfully utilized for highly sensitive and specific detection of proteins (e.g. BSA, avidin, DNA and thrombin) or biomolecular binding events (i.e. biotin-avidin), nucleotide hybridization, and 5-fluorouracil-anti-5-fluorouracil [3, 6, 8]. Gold nanocaps formation was first demonstrated by kim et al. by simply depositing gold on top surface of NAA substrate using thermal deposition technique [61]. These gold nanocaps displayed strong LSPR signal that was highly sensitive to the changes in the refractive index of the surrounding environment. This high sensitivity toward changes in local refractive index enables this system to efficiently detect up to picomolar quantities of un-labeled oligonucleotides. The same strategy to form gold nanocaps on the top surface of NAA was also used to develop an immunosensor featuring anti-CRP (C-reactive protein, a cardiac and inflammatory biomarker) antibody immobilised on the gold nanocaps for detection of CRP antigen [62].

This system displayed an extremely low limit of detection for CRP antigen at concentration 1 fg/mL due to LSPR enhancement of the optical signals similar to previous study. In a different approach Hiep et al. deposited gold nanoparticles on the surface of NAA to form active sites for exciting LSPR signal to detect binding between biomolecules such as biotin–avidin and 5-fluorouracilant-5-fluorouracil [63]. A LSPR active NAA substrate was fabricated by commonly used two step anodization process and incubated with a cationic polymer (Poly-allylamine) to impart positive charge on its surface. Next, this positively charged NAA substrate was immersed in plasmonic gold nanoparticle (AuNPs) solution (negatively charged) to attach AuNPs on NAA surface. Au nanoparticles were observed to be trapped into the pores of NAA. The LSPR spectrum was enhanced for these AuNPs embedded NAA LSPR substrates in both experimental and simulation studies due to formation of Fabry–Perot interference cavity between Air:AuNPs-NAA:Al system. The performance of this composite LSPR substrate was measured by introducing liquids with different refractive indices [64]. Similar type of plasmonic AuNPs-NAA composite substrate was combined with electrochemical system for sensitive detection of toxic peptide (i.e. melittin, the venom from the honey bees) with a lower limit of detection (LOD) in nanograms/mL range (i.e. 10 ng/mL) [65].

7.2.3 Surface-Enhanced Raman Scattering Spectroscopy (SERS)

The phenomenon named as Raman scattering effect was first experimentally discovered by C.V. Raman and K.S. Krishnan in India and reported in their 1928 Nature paper [66]. The paper reports that the inelastic scattering effect characterized by “its feebleness in comparison with the ordinary scattering” and this “feeble”

phenomenon is now called Raman scattering. The excitation (or relaxation) of vibrational modes of a molecule result in change in wavelength that is observed in photon that undergoes Raman scattering. Every molecule has a different and specific Raman spectrum due to difference in the vibrational energies of the functional groups it contains. However, the intensity of the Raman signal is dependent on the magnitude of polarizability of the molecule which changes with vibration of functional groups (i.e. displacement of constituent atoms from their equilibrium position). Therefore, aromatic molecules display a more intense Raman scattering than aliphatic molecules. The inherent shortcoming of Raman scattering is that its typically 14 magnitude order smaller than the fluorescence, therefore, Raman signal are shadowed by fluorescence emission in most cases [67]. In 1977, Jeanmaire and Van Duyne observed enhancement of the Raman scattering signal when the target scatterer is placed on or near a roughened noble-metal substrate [68]. This strong enhancement of Raman signal is most often related to localized surface plasmon resonance (LSPR) that causes enhancement of local electromagnetic field around a plasmonic nanoparticle/structure (i.e. the so-called "hot spots" or "hot junctions") [69]. These intense electromagnetic fields induce greater dipole movement (i.e. vibrational energies) in the target Raman scatterer, and accordingly, the intensity of the inelastic scattering increases. This enhanced inelastic scattering process on roughened or organized plasmonic noble metal nanoparticle/substrate is known as surface enhanced Raman scattering (SERS). Notice that, SERS phenomenon can generate Raman signal enhancement within the order of 10^6 of the typical Raman signal of the target Raman scatterer. This makes SERS an extremely sensitive system for qualitative and quantitative detection of trace amounts of target Raman scattering molecules [70]. NAA has gained huge attention as a substrate for developing SERS based sensing systems because of its well-defined nanoporous structure (i.e. controlled nanoscale roughness), reliable reproducibility, cost-competitive fabrication, high optical transparency, minimal light scattering and large surface area. Similar to LSPR, SERS-NAA devices are also mostly fabricated by evaporating or sputtering a metallic layer of silver or gold on the top or bottom side of NAA substrates to generate a periodic metallic nanometric structures with controlled geometry. Furthermore, the ability to control and tune the pore structure of NAA enables tuning and optimization of SERS properties of these SERS-NAA substrates at wills for specific sensing applications [71]. The SERS enhancement factor (G) can be calculated to evaluate the enhancement ability of such substrates. The enhancement factor is given by:

$$G = (I_{ads}/N_{ads})/(I_{bulk}/N_{bulk}) \tag{7.2}$$

where I_{ads} is the intensity of a vibration mode in SERS spectrum, and I_{bulk} is the intensity of the same mode in normal Raman spectrum. N_{ads} and N_{bulk} is the number of molecules probed in SERS spectrum and in normal Raman spectrum, respectively [72].

Raman signal enhancements in the range of 10^5–10^6 have been reported on NAA substrates decorated with gold and silver nanoparticles grafted onto or in situ

synthesized inside NAA nanopores [71–73]. Ko et al. introduced metal nanoparticle decorated nanocanal arrays of uniformly aligned vertical cylindrical pores of NAA membranes [68]. For this, the inner surface of commercially available NAA membrane (i.e. pore diameter: 200 nm, thickness: 60 μm) was first modified with poly(diallyldimethylammonium chloride) (PDDA) polyelectrolyte using spin coating followed by incubation with AuNPs (∼32 nm) to generate "hot spots" inside NAA pores (Fig. 7.5a). These SERS-NAA substrates were then employed for the detection of trace amounts of 2,4-dinitrotoluene (2,4-DNT, TNT-based plastic explosive) with modest Raman cross-section. It has been reported that this class of compound is usually not detected by conventional Raman measurements. With this metal nanoparticle decorated NAA substrate they achieved a Raman signal enhancement of order 1.1×10^6. They also found SERS performance of AuNPs decorated NAA for detection of 2,4-DNT was superior. A similar strategy was reported to decorate NAA with silver nanoparticles (AgNPs) and the performance of the resulting SERS-NAA substrate was measured by detecting of p-aminothiophenol [72]. This AgNPs-NAA based SERS substrate displays an enhancement factor of 5×10^5. Another study reports on detection mercapto-based Raman reporter (i.e. 4-mercaptopyridine) on silver nanoparticles decorated NAA membrane with Raman enhancement of a factor 2.7×10^5 [74]. This study utilized we established metal electrodeposition technique to prepare silver nanoparticles along the NAA pore walls. Other studies have used NAA as template to grow metal nanostructures as nanowires and nanotubes which can be used to develop highly sensitive SERS sensors [74, 75]. For this, Lee et al. used NAA with varying pore diameter, layer thickness and interpore distance to prepare silver nanowires inside NAA pores by electrodeposition and measured their performance by studying the adsorption of 4-aminobenzenethiol [76]. They demonstrate the overwhelming dependence of SERS on plasmonic excitation of metal nanostructure and on the nanogeometry of the substrate used for the application. Electroless deposition has also been used to make SERS active NAA/Au nanotube array composite and was used to study formation of 3-mercaptobenzoic acid SAMs [75]. NAA templates have been used as mask for deposition to grow 3D multi-layered Au cone-like and nanodots arrays by vacuum evaporation deposition with precise control over shape and geometry by adjusting the geometrical features of NAA [77, 78]. Pyridine, an important solvent and reagent for pharmaceutical and agrochemical applications, was used as a Raman scatterer to probe its sensing performance.

7.2.4 Reflectometric Interference Spectroscopy (RIfS)

Reflectometric interference spectroscopy (RIfS) is a label-free and highly sensitive optical detection method that is based on the interaction of white light with films at micrometer scale. In this technique, white light is shined on a thin film and reflected at the two interfaces of the thin film resulting in amplification of the reflected light signal at wavelengths corresponding to the optical modes of the Fabry–Pérot

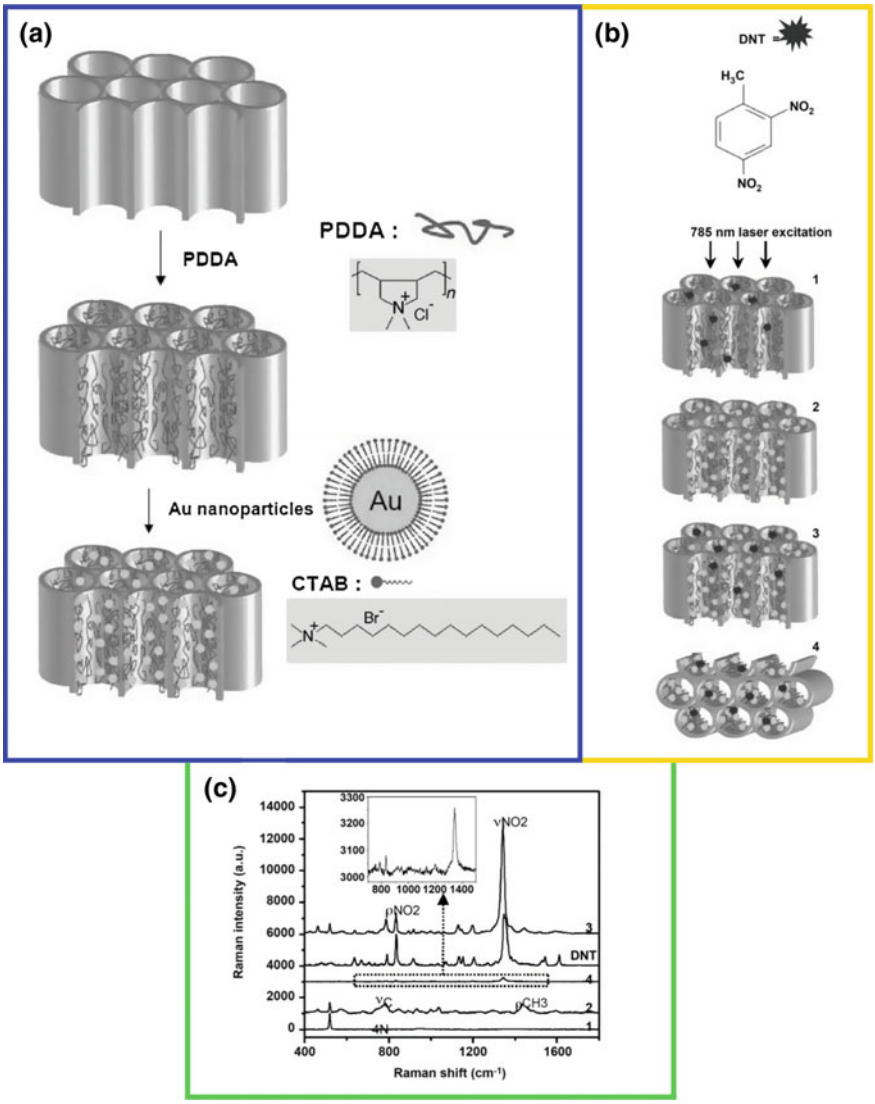

Fig. 7.5 Schematic demonstrating procedure of **a** decorating NAA with AuNPs. **b** Chemical structure of 2,4-DNT and schematic of Raman measurement of 2,4-DNT with different laser excitation angles parallel (*1*, *2*, *3*) and perpendicular (*4*) to the pore axes and **c** the Raman spectrum of DNT powder and 1000 ppm 2,4-DNT on each substrate shown schematically in (**b**) (adapted with permission from [71])

(FP) cavity formed by the thin film-surrounding medium system (i.e. the Fabry–Pérot effect) [79]. Reflectometric interference is very efficiently utilized by nature to provide structural colors to living organisms (e.g. butterfly wings, beetle shell and others) and mineral rocks (e.g. abalone shells) [80]. This phenomenon was coupled

with synthetic thin films by Gauglitz's group in late 1980 [81]. They fabricated polymer and metal oxide thin films to obtain interference spectrum by monitoring the reflection. The reflection spectrum of these thin films presents intense and well-resolved interference fringes with alternate maxima and minima (Fig. 7.6a). The wavelength of each interference fringe is governed by the Fabry–Pérot relationship

$$EOT = 2n_{eff}L\cos\theta = m\lambda \tag{7.3}$$

Here, *EOT* is the effective optical thickness of the thin film, n_{eff} is its effective refractive index, L is the actual thickness of the film, m is the order of interference maxima in the interference spectrum at wavelength λ, and θ is the angle of incidence [80, 82]. It is clear from (7.3) that any change in the effective refractive index or thickness of the thin film will be translated to a shift in the interference maximum. For the solid thin films, like used by Gauglitz's groups rely on changes in thickness of films due to swelling or deswelling of the polymer films or addition of another layer of biological molecules for metal oxide thin films (during the biological recognition reaction) [82, 83]. Reflectometric interference spectroscopy was coupled with nanoporous substrates (i.e. porous silicon, nanoporous anodic alumina, and titanina nanotube arrays) in late 1990s by Sailor's group [84–86]. These nanoporous films possess very high surface area for analyte-receptor reaction and rely on changes in effective refractive index due to attachment of target molecules inside their pores. Similar to solid thin films, nanoporous thin films also display shift in interference fringe wavelength as a result of target attachment. Pan and co-worker (2003), for the first time, had developed a highly sensitive NAA-RIfS sensing platform for label-free detection of DNAs hybridization with sensitivity to 1 nanomol levels [87]. The first major report on NAA based RIfS sensor was published in 2009 by Sailor's group [86]. In this study, they not only introduced NAA as RIfS active substrate but also resolved the shifts of the interference maximum by establishing the effective optical thickness, which is calculated by applying fast Fourier transform (FFT) to the interference spectrum. The details of calculations of the FFT Gaussian peak corresponding to *EOT* of the Fabry–Pérot cavity is provided in ref [4]. This label-free NAA-RIfS immunosensor monitors the capturing of target antigens (i.e. sheep IgG) by their specific antibodies (i.e. rabbit anti-sheep IgG) immobilized inside NAA pores [86]. NAA not only offers several advantages over other nanoporous substrates (i.e. pSi and titania nanotubes arrays) as better chemical and mechanical stability, ease of surface modification, and controllable and defined nanoporous structure but also presents well-resolved interference peaks in the RIfS spectrum. RIfS-NAA can be used for both quantitative and qualitative analysis with capabilities to follow an analyte-receptor binding event in real-time and in situ by following the changes in *EOT* (Fig. 7.6b). NAA in combination with RIfS has been developed to detect gases, organic molecules, metal ions and biologically relevant molecules [3, 6, 8]. An et al. studied the effect of pored diameter of NAA on the interference signals [88]. The performance of RIfS with NAA having different pores was monitored by following the changes in the effective

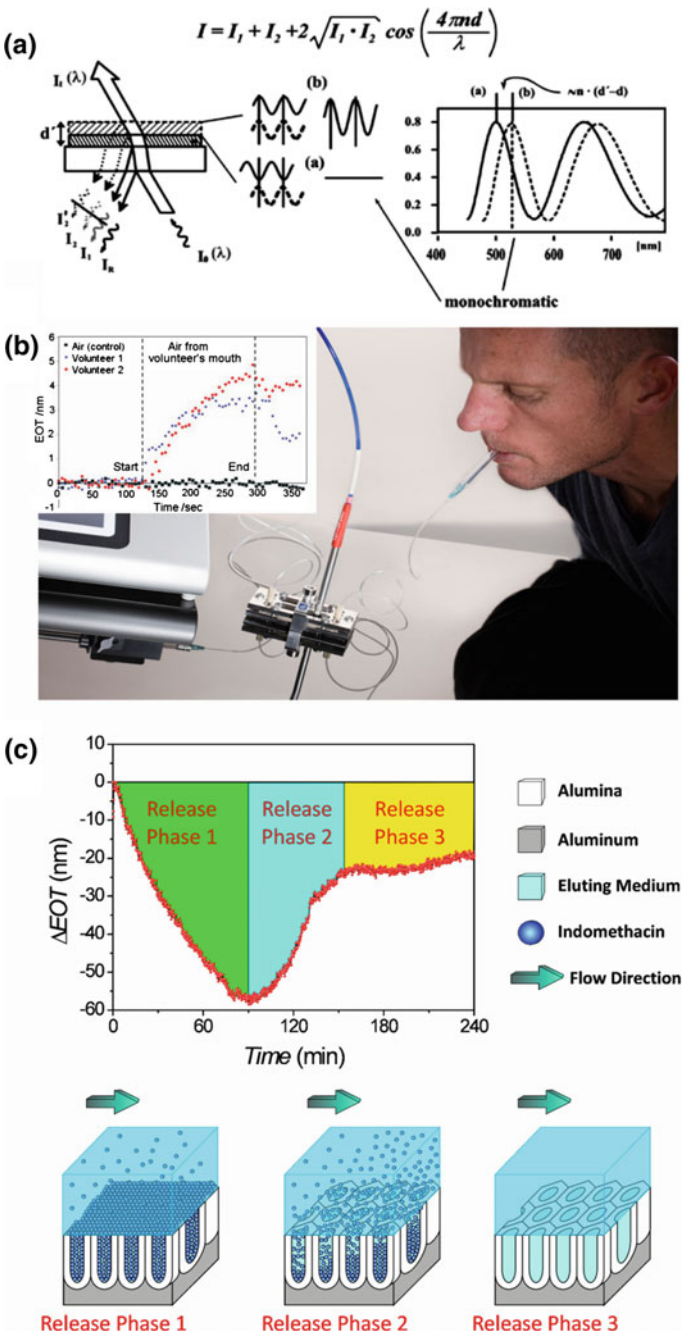
(a)
$I = I_1 + I_2 + 2\sqrt{I_1 \cdot I_2}\cos\left(\frac{4\pi nd}{\lambda}\right)$
monochromatic
(b)
Air (control)
Volunteer 1
Volunteer 2
Air from volunteer's mouth
EOT /nm
Start
End
Time /sec
(c)
Release Phase 1
Release Phase 2
Release Phase 3
ΔEOT (nm)
Time (min)
Alumina
Aluminum
Eluting Medium
Indomethacin
Flow Direction
Release Phase 1
Release Phase 2
Release Phase 3

◀ **Fig. 7.6** **a** Schematic illustrating the principle of reflectometric interference spectroscopy. **b** Microfluidic setup for NAA based oral malodor measurements with inset showing the real time EOT changes on introduction of air from volunteer's mouth and **c** real time drug release curve from NAA measured using RIfS under dynamic conditions and the schematic describing three phases of release (adapted with permission from [82, 91, 95])

optical thickness on adsorption of BSA and PSA (prostate specific antigen) antigen onto RIfS-NAA substrate. As expected NAA substrate with higher pore diameter displayed better sensing characteristics as it can hold larger amount of analytes inside the pores (i.e. higher changes in effective refractive index of NAA thin film). A more detailed study on controlling the RIfS signal of NAA depending on its structural features was performed by Kumeria et al., where they manipulated parameters such as pore diameter, pore length, and surface coatings [89]. Their conclusion was that the RIfS signal is dependent on the aspect ratio of pores instead of individually on pore diameter or length. Also, the observed that interference signal is highly enhanced on depositing a thin film (5–10 nm) of metals (i.e. gold, silver, chromium etc.) by thermal or sputter coating. In their next studies, Kumeria et al. used the optimum NAA structure for RIfS to develop sensor for detection of volatile sulphur compounds (i.e. VSCs: hydrogen sulphide gas) and hydrogen gas [90, 91]. Selectivity towards volatile sulfur compound was achieved by depositing metallic gold on NAA surface where hydrogen was selectively detected by a thin platinum film. Biomedical application of this structure was displayed by detecting VSCs in human oral malodor (Fig. 7.6b). For this, a special microfluidic device was designed, consisting of a cavity capable of holding Au coated NAA substrate and a micron level channel for delivery of analyte to the Au coated NAA chip. Kumeria et al. utilized the same microfluidic device and optimized NAA substrate to develop a sensor for detecting and quantifying circulating tumour cells (CTCs) in buffer and blood samples [92]. For this, NAA chips were coated with ultrathin layer of gold and subsequently functionalized with anti-EpCAM antibodies that specifically capture the CTCs, and changes in *EOT* were used to monitor the capturing of CTCs in real-time. The major advantage of this device was its ability to capture and detect CTCs without any pre-enhancement step. This RIfS-NAA device showcased high selectivity toward CTCs and a limit of detection down to 1000 cell/mL of buffer. Finally, the ability of this system to detect CTCs in human blood was also proven. Dronov et al. studied platinum-coated NAA to act as an interferometric transducer and found that metal coating on NAA surface drastically improves the signal to noise ratio [93]. Their results also revealed that the NAA based RIfS substrates provide much stable signal over time in comparison to porous silicon substrate. Ability of NAA based RIfS sensing system to detect toxic metal ions was recently demonstrated by Kumeria et al. by capturing and detecting gold (III) ions on mercapto-silane modified NAA substrate [94]. The widespread use of gold (III) has made it necessary to have devices for regulatory check for its concentration in our biological and environmental ensembles as gold (III) ions can cause severe damage to essential organs as liver, kidney, nervous system and others. This approach combines portability of RIfS setup with high surface are of NAA and high affinity

of mercapto groups towatds gold (III) ions to develop an ultrasensitive and selective sensor for Au^{3+} ions. In this study, NAA substrates were chemically modified with 3-mercaptopropyl-tirethoxysilane (MPTES) using chemical vapor deposition technique to impart the NAA with selectively gold (III) ions. The sensor displays a linear range between 0.1–80 μm and a lower limit of detection 0.1 μm which was assessed through a series of experiments. The real-life application of NAA-RIFS sensor was assessed by successfully detecting gold (III) ions in tap water and phosphate buffer solution (PBS).

On the contrary, application of RIfS-NAA for release of molecules such as drugs from NAA pores was displayed by Kumeria et al., where the monitored release of a model drug indomethacin from NAA using RIfS. In this study, the release of indomethacin was measured in real-time under dynamic flow conditions using the aforementioned microfluidic setup (Fig. 7.6c) [95]. The drug release mechanism was observed to be diffusion-controlled and the rate of release as a function of the flow rate (i.e. the faster flow rate results in faster drug release). Recently, the performance of NAA based RIfS and PL (photoluminescence) sensing was compared by Santos et al. [13]. First, most optimal NAA structure with highest optical signal was obtained by calculating the ratio of height to width of the measured peak in effective optical thickness for both RIfS and PL. Then the performance of this NAA structure for detection of biomolecules under non-specific (i.e. pore filling with glucose solutions of different concentrations) and specific (i.e. attachment of L-cysteine on APTES modified NAA chips) binding conditions was assessed. Note that, PL based sensing system displayed better sensing performance (i.e. linearity, higher sensitivity toward analytes and lower limit of detection) for both the binding conditions in comparison to RIfS-NAA sensing system. Macias et al. employed structural engineering capabilities of NAA to fabricated a bilayered funnel-like NAA-RIfS sensing platform, which generates a complex reflectivity spectrum [96]. In coherence with previous studies their results also suggest a significant in RIfS signal on coating the top surface of the NAA with an ultrathin metallic gold layer. They estimated the performance of this bilayer-NAA based RIfS sensing system by detecting BSA molecules. The advantage of the bilayer system is that effective optical thickness changes only take place only in the peak corresponding to layer where molecules have attached or infiltrated based on size exclusion.

Kumeria et al. recently fabricated rugate filters (i.e. photonic crystals) based on NAA using a pseudo-sinusoidal anodization profile, which results in a continues gradient in effective refractive index of the layer (Fig. 7.7) [97, 98]. Four different types of NAA rugate filters (NAA-RF) were prepared varying the anodization parameters and most sensitive NAA-RF was selected by studying the shift in stop band peak. After that, the most sensitive NAA-RF was use for highly sensitive detection of toxic mercury (Hg (II)) ions. For this, NAA-RFs were functionalized with 3-mercaptopropyl-trimethoxy silane (MPTMS) to impart it selectivity towards Hg (II) ions. Real life application of this NAA-RF based RIfS sensing system was displayed by measuring Hg (II) ions in tap water, PBS, and water from River Torrens (South Australia, Australia). Although, a large number of efforts have already been made in this field but there is still plenty of scope for new

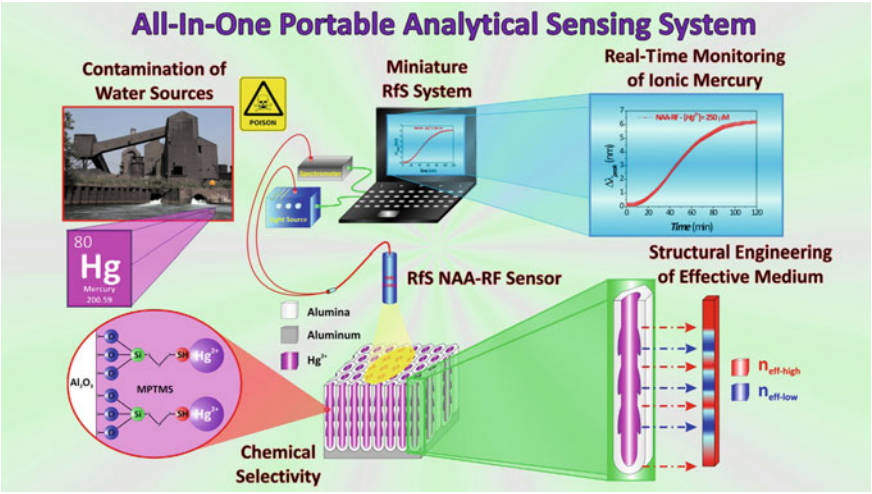

Fig. 7.7 A schematic describing NAA-RF based portable mercury ion sensing platform (adapted with permission from [98])

developments where our group is still working on and we believe RIfS-NAA based sensing system have a great potential for industrial, environmental, and biomedical applications.

7.3 NAA Based Electrochemical Sensors

Electrochemical sensors, depending on their principle of detection, can be divided into several types including voltammetric (i.e. changes in potential), amperometric (i.e. changes in current), impedometric (i.e. opposition of a circuit to flow of current), capacitive, and resistive [3, 99]. Although, NAA is inherently insulating, the composite of NAA with electrically conducting materials or redox active species have successfully been used to develop voltammetric or amperometric sensors. NAA in the form of membrane after removal of barrier layer have been realized as flow through impedometric or capacitive or resistive sensors.

7.3.1 Voltammetric and Amperometric NAA Sensors

Nanoporous anodic alumina can potentially support a large number of capture probes immobilized in its pores due to the large surface area. This is an excellent characteristic for developing membrane type amperometric or voltammetric nanosensor platform, which allows higher interaction between analyte and capture probe

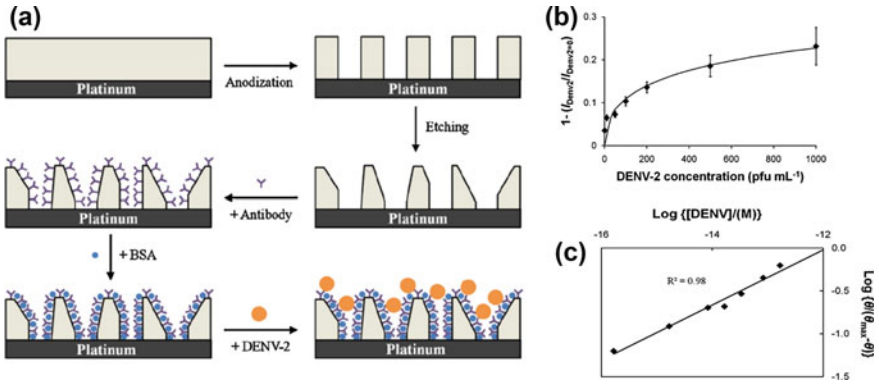

Fig. 7.8 **a** Design of NAA based electrochemical nanobiosensor for detection of DENV-2 Dengue virus. **b** NAA nanosensor's response toward different concentrations of DENV-2 in 0.1 M phosphate and **c** its corresponding linear calibration curve in log values (adapted with permission from [108])

molecules while flowing through the pores. As mentioned before, NAA is an electrical insulator but its pores can be modified with a conductive layer or a redox active species to transform them into electro-active elements. Composite of NAA with several metal or metal oxide deposition (Au, Pt, SnO_2), carbon nanotubes (CNT), conductive polymers (polypyrole) or other electrochemically active materials (Prussian blue) have previously been reported for electrochemical sensing of gas detection (vinil chloride, ammonia, formaldehyde), glucose, hydrogen peroxide, cholesterol, nucleotides and proteins, enzymatic activity, and detection of cells (viruses, bacteria and cancer cell) [3, 99–106]. The electron transfer to the electrode is carried either indirectly via redox mediator between the NAA substrate and the immobilized molecules or directly by attached conducting linkers using voltammetric and amperometric methods.

Most significant contribution to NAA based electrochemical sensors has come from Toh's group who developed a series of NAA based electrochemical immunosensors by growing NAA layer onto a conducting Pt substrate. The inner surface of NAA-Pt pores were functionalized with antibodies specific to either dengue virus or West Neil virus (WNV) or glucose oxidase (Fig. 7.8) [107–109]. The antibody-antigen reaction was probed by measuring the AC voltammetry signal of a redox indicator (i.e. ferrocenemethanol). In simple terms attachment of specific target molecule inside impedes the diffusion of the redox mediator therefore resulting in low voltammetry signal. A three-electrode system was employed which comprised of a platinum auxiliary electrode (diameter 2 mm), silver-silver chloride reference electrode, and alumina membrane working electrode. A lower limit of detection of 100 ng/L, 4 pg/mL, 2 viral particles per 100 mL, and 1 pfu/mL were reported for glucose oxidase, WNV proteins, WNV particles, and dengue viruses, respectively [107–109]. Similar to antibody-antigen reaction hybridization of complementary target DNA with DNA probe immobilized inside the NAA pores influences the ionic conductivity of NAA pores [110]. This approach was adopted by Toh's group for

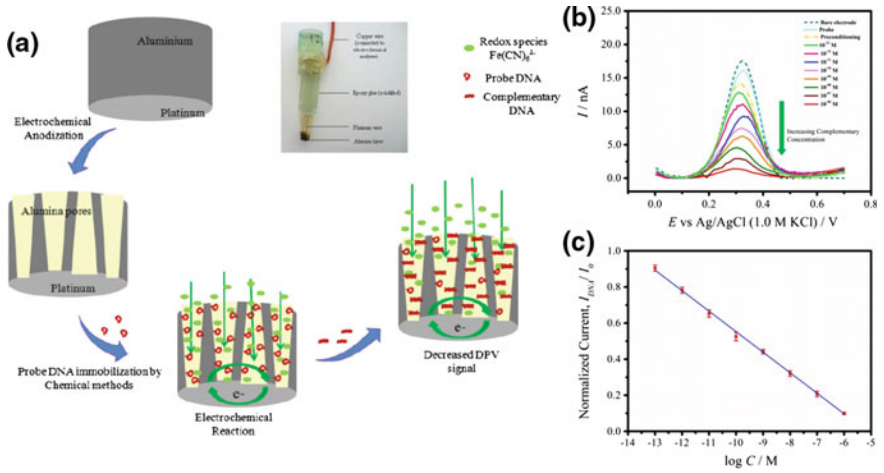

Fig. 7.9 **a** Scheme of construction of NAA based electrochemical DNA sensors. **b** Current signal response of bare electrode toward increasing concentration of complementary target and **c** its corresponding calibration curve (adapted with permission from [110])

development of a nucleotide biosensor, where signal was derived from redox species $Fe(CN)_6^{4-}$ across single wire Pt electrode. The biosensor displays a broad linear range of over 7 orders of magnitude with ultralow detection limit of 3.1×10^{-13} M (Fig. 7.9). Another NAA membrane based DNA biosensor was constructed by Toh's group using 5′-aminated DNA probes immobilized onto the alumina pore walls. The hybridization of target and probe DNA immobilized inside the pores influences the pore size and thus the ionic conductivity of the NAA membrane. This DNA sensor displays a linear range of over 6 order of magnitude a lower detection limit of 9.55×10^{-12} M for 31 Mer ssDNA extracted from dengue virus [106]. The detection limits obtained in the aforementioned DNA sensors was found sufficient to challenge commercially used RT-PCR method for detection of dengue virus.

The sensing characteristics of voltammetric and amperometric NAA sensors have been improved by modification of pores with Prussian blue (PB) or iron hexacyanoferrate polymer based on their unique ion-exchange and electrocatalytic properties [111]. For example, nanoelectrode arrays of Prussian blue (PB) were electrochemical deposited into highly ordered pores of a gold coated NAA membrane (Fig. 7.10). These highly ordered PB arrays act inside NAA as an ensemble of closely packed nanoelectrodes, which highly improve the analytical performances of glucose detection by electro-catalytically reducing enzymatically liberated H_2O_2. The resulting glucose biosensor showed excellent performance with a broad linear concentration range over three orders of magnitude and a low detection limit of 1 μM [112]. Similar, PB-NAA sensors have been also successfully demonstrated for ion-selective detection of Na^+ and K^+ ions [111, 113, 114]. Wong et al. recently reported the development of a unique self-powered PB-NAA amperometric nanotube sensor for detection of hydrogen peroxide and glucose [115]. This sensor

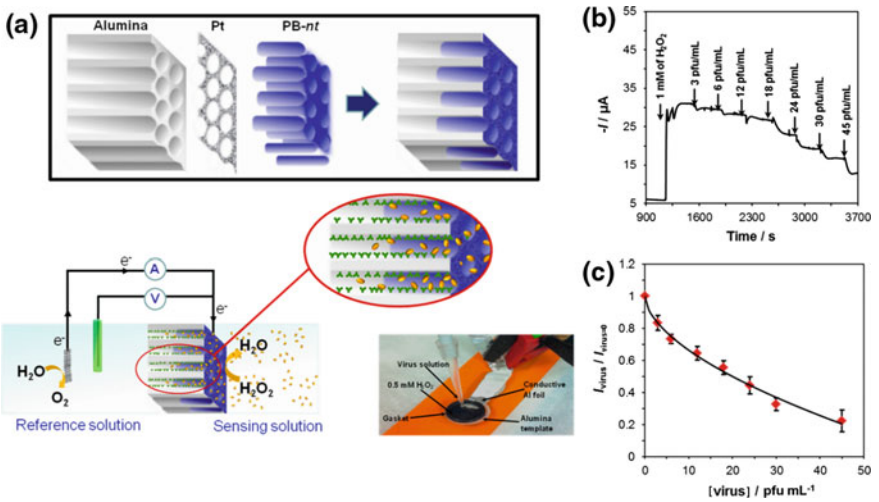

Fig. 7.10 **a** Schematic describing process of depositing Prussian blue nanotubes inside NAA pore and their use for virus sensing. **b** Typical closed-circuit steady-state current response of a PB nt based sensor toward DENV-2 virus and **c** its corresponding calibration plot showing normalized closed-circuit steady-state current versus virus concentration (adapted with permission from [116])

employs selective anodic and cathodic reactions with suitable thermodynamic potentials considering the reactions taking place at the sensing and auxiliary electrodes, which are modified with appropriate mediators or enzymes. In this case, the PB nanotubes reduce hydrogen peroxide and are reduced themselves by electron flow from the counter reaction taking place at the auxiliary electrode. This strategy presents improved the lower detection limit of 0.1 μM H_2O_2 and linear range up to 80 μM. This same strategy was recently adapted for highly sensitive detection of dengue virus serotype-2 (DENV-2) [116]. The resulting sensor displays an extremely fast reaction time of less than 5 min and outstanding lower detection limit of 0.04 pfu/mL, which is comparable to conventional used PCR setup.

7.3.2 Impedance, Capacitance, Conductance, and Resistance Based NAA Sensors

Electrochemical Impedance Spectroscopy (EIS) has gained tremendous increase in its popularity in recent years due to its applicability in determination of the double-layer capacitance and in AC polarography, characterization of electrode processes and biosensing applications. EIS studies the system response to the application of periodic small amplitude AC pulses at different frequencies. In simple terms, EIS measures the dielectric properties of a material as result of interaction of the applied electric field (at different frequencies) and the generated electric dipole moment of the material. The removal of oxide barrier layer from

NAA pore bottom reduces the electrical resistance and allows flow of ionic current through the pores. Therefore, NAA can act as a flow through sensor as the attachment of target species onto the capture probe inside the NAA pores hinders the transport of ionic species across the membrane influencing the electric dipole of the structure. Other advantage of the large internal surface area of NAA pores is its ability to immobilize large amounts of capture probes for binding target species and this binding event can be sensitively detected using impedance measurements. Equivalent circuits based on different models can be generated to fit the experimental data and understand the electric behaviour and properties of NAA. NAA based impedance sensors have been used for detection and study of DNA hybridization, protein and lipid membrane interactions, cancer cells, viruses, and bacteria [3].

A DNA based impedance sensor was reported by Takmakov et al., in which they efficiently utilized high resistance of hydrothermally treated (HT) NAA to shrink the pore mouth [117]. The complementary ssDNA capture probe attachment to HT NAA membranes was achieved by first modifying NAA surface with 3-aminopropyltrimethoxysilane (APTES) followed by activation of amine terminals with glutaraldehyde (GTA) and incubation with DNA probe. Target DNA hybridization with the complementary ssDNA, covalently immobilized inside the pores, results in an increase in impedance signal by more than 50 % whereas a noncomplementary ssDNA does not show any measurable change in impedance. Wang et al. demonstrated a novel complementary ssDNA immobilization process inside NAA pores and its application for highly sensitive detection of *Escherichia coli* O157:H7 DNA [118]. The immobilization of complementary ssDNA probe inside NAA pores occurred through a dynamic polymerase-extending (PE) DNA hybridization procedure, where hybridization takes place in presence of Taq polymerase (enzyme) and deoxynucleotide triphosphates (dNTPs: monomers of DNA) under controlled temperature conditions. The impedance sensor works in a manner that PE assisted growth extends the target DNA to the length equal to complementary DNA and this hybridized DNA structure efficiently blocks the flow of ionic species across the NAA membrane. They investigated the changes in ionic conductivity during the DNA hybridization using cyclic voltammetry and impedance spectroscopy and report a low detection limit up to a few hundreds of picomol for DNA obtained from *Escherichia coli* O157:H7 DNA.

A microchip based NAA impedance sensor for detection of food pathogens like *Escherichia coli* O157:H7 and *Staphylococcus aureus* was reported by Tan et al. [118]. In this study, specific antibodies for the abovementioned targets were immobilized onto NAA membrane surface using 3-glycidoxypropyl)trimethoxysilane (GPMS) functionalization and this chip was packed in a polydimethylsiloxane microchip. This microfluidic NAA based impedance sensor achieved rapid bacteria detection (<2 h) with the sensitivity up to 10^2 CFU/ml. A simplified electrochemical impedance sensor for detection of dengue virus was recently reported, where, NAA membrane itself acted as working and counter electrode after coating both the sides with a submicron layer of platinum [119]. The changes in the membrane resistance were measured using EIS, which displayed a good correlation with the

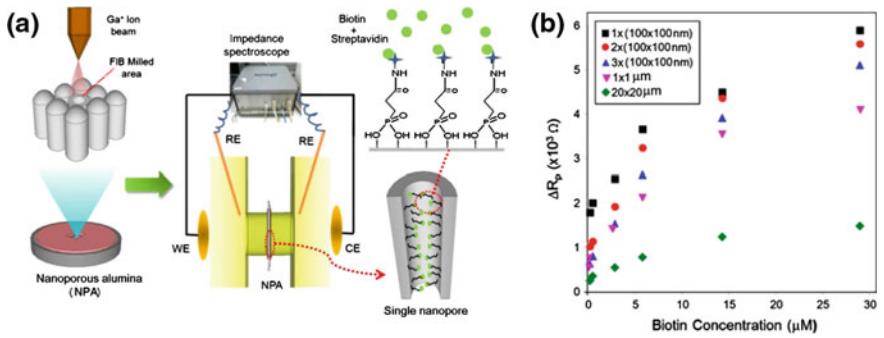

Fig. 7.11 **a** Schematic of NAA based impedance sensors for recognition of streptavidin and biotin interaction with selective area of pores opened with FIB and **b** graph showing changes of the pore resistance against various concentration of biotin for areas of pore opened using FIB (adapted with permission from [120])

concentration of the dengue 2 and dengue 3 viruses (PFU/mL), with detection limits 0.230 PFUmL and 0.710 PFU/mL respectively. Recently, our group also reported on effect of NAA geometry (i.e. pore diameter, pore length, and number of open pores) on its EIS properties [120, 121]. For the first study, Focused ion beam (FIB) was used to specifically mill out the barrier layer of NAA in area ranging from 1 µm × 1 µm to 100 µm × 100 µm, to open a selective number of pore (Fig. 7.11) [120]. The sensing performance of this FIB etched system was also studied using the streptavidin to biotin model analyte-receptor reaction. The results reveal that the lowest limit of detection (i.e. 0.2 µM) was achieved using the NAA with the largest area of pores opened by FIB. In the next study, NAA membranes with pore diameters in range 25–65 nm and lengths from 4 to18 µm were analysed for sensing capabilities using a model protein analyte-receptor reaction (i.e. streptavidin to biotin) [121]. The NAA membranes with pore diameter 25 nm and pore length up to 10 µm displayed the best sensing performance.

NAA, due to its high thermal stability, surface area, and affinity towards gases and vapours, has become an attractive substrate to develop gas or humidity sensing devices. In an example, Juhász et al. fabricated a capacitance and resistance based CMOS-MEMS chip for measuring relative humidity (RH) using NAA layers grown on silicon wafers [122]. Two different sensors, namely: (a) capacitance based and (b) resistance based, were fabricated by growing two types of electrodes on the NAA surface (i.e. a vapour-permeable palladium layer and a gold grid). The aim of this study was to produce a cheap, reliable, low-power and CMOS-MEMS process compatible RH sensor. The highest sensitivity of this capacite RH sensors (i.e. 15 pF/RH%) was found to be much better than most off-the shelf commercial humidity sensors. An environmental capacitive sensor based on NAA was displayed by Jin et al, where model environmental pollutant polychlorinated biphenyls (PCBs) were successfully quantified [123]. The cylindrical pores of NAA provide large surface area for adsorption of PCBs which in turn can lead to enhancement of capacitive response. PCBs can be adsorbed onto NAA pore walls just by simply

dropping a methanolic solution of PCBs (i.e. 3,3′,4,4′-tetrachlorobiphenyl: PCB77). This simple NAA based capacitive sensor also displays a good response to PCB77 even under nonspecific interferent like benzene. The lower detection limit for PCB77 was calculated at 8×10^{-8} M at room temperature. A parallel plate capacitor model was used to understand the behaviour of capacitance in the NAA sensor, which shows an exponential increase of capacitance with the increasing PCB77 concentration. Nanocomposite of NAA with tungsten trioxide was used to develop a resistance based sensor for toxic gases (i.e. nitrogen dioxide, ammonia and ethanol) [124]. This type of sensor also displayed increment in resistance with increasing concentration of the toxic gases. Apart from gas sensing, NAA based conductivity sensors have been used to detection DNA hybridization and enzyme activity. The DNA sensor measured changes in ionic conductance as result of DNA hybridization inside NAA pores [125]. In other study, NAA based conductance sensor was utilized for establishing the activity of enzyme immobilized (urease in this case) inside NAA pores [126]. This support that NAA based electrochemical sensors can be used for both qualitative and quantitative detection of Analytes or measuring kinetics of an analyte-receptor reaction or enzyme-substrate reaction.

7.4 Miscellaneous NAA Based Sensing Systems

7.4.1 Matrix Assisted Laser Desorption/Ionization and Electrospray Ionization

Mass spectrometry (MS) has become the key analytical tool used for biomolecular analysis and proteomics. Development of techniques such as matrix assisted laser desorption ionization (MALDI) and electrospray ionization (ESI) are two great milestones in the history of MS, which extended MS analysis to a large group of previously intractable biological molecules. Both, MALDI and ESI are soft ionization techniques that proved to be highly efficient for generation of gas-phase ions of fragile and non-volatile molecular complexes including peptides/proteins, oligosaccharides, oligonucleotides, and synthetic polymers [127, 128]. While MALDI is a laser-based ionization method, ESI uses electrospray of a solvent directed towards the sample under ambient conditions. In MALDI, the matrix plays a key role by absorbing the laser light energy and causing a small molecular target to desorb and ionize which are subsequently detected by MS. In contrast, ESI the sample is introduced with suitable solvent as charged nebulized droplets, which are made to undergo desolvation to obtain gas-phase ions for analysis by MS [128]. The application of NAA for MALDI and ESI was explored with the aim to overcome the inherent problem of conventional MALDI systems including interfering signal from matrix itself and non-uniformity of signal due to poor cocrystallization of sample with matrix. Therefore, NAA based desorption ionization systems mostly do not require a matrix and are referred also to as matrix free laser desorption ionization (i.e. LDI) or surface assisted LDI (i.e. SALDI). Similarly, NAA based

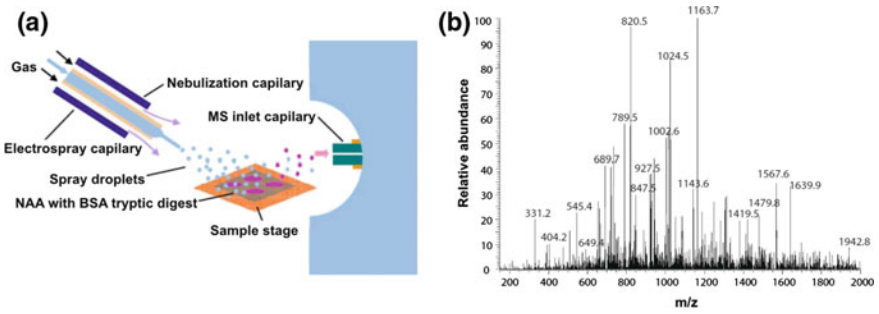

Fig. 7.12 **a** Schematic of the DESI MS experimental setup as describe by Knapp's group and **b** DESI MS mass spectrum of BSA tryptic digests on nanoporous alumina surface (adapted with permission from [132])

ESI systems are referred to as desorption electrospray ionization (DESI) [129]. Additionally, NAA can hold large sample volumes crystallized inside the cylindrical pores enhancing the signal intensity in the MS and protect the protein from harsh ambient conditions preventing the sample from degradation for months even when kept in air.

A matrix free NAA-LDI system was explored by Nayak and Knapp for analysis of BSA tryptic digest. The main aim of this study was to establish the effect of NAA pore structure (i.e. pore diameter and thickness) and thickness of surface gold coating on MS signal intensities [130]. They found the most optimum NAA for LDI application to have pore diameter, thickness, and surface gold coating of less than 600 nm, greater than 100 nm and thicker than 90 nm, respectively. The same group also compared the performance of NAA based substrates with polymeric membranes for DESI-MS analysis of reserpine and BSA tryptic digest. It was observed that NAA offers much superior performance in terms of signal intensity and low limit of detection in comparison to the polymer counterparts (Fig. 7.12) [131]. They also combined DESI with LDI to have a dual ionization and MS analysis setup and found that DESI-LDI observes more peptides DESI or LDI performed alone. The number of ionized peptides observed was comparable to the ones observed with combination of MALDI and ESI [129].

Another study using SALDI (i.e. surface layer assists desorption and ionization) based on platinum coated highly ordered NAA explored to obtain high signal-to-noise ratio of protonated angiotensin I ions in the MS spectrum obtained by 337-nm ultraviolet laser irradiation. They studied variations in pore geometries and density and found that laser intensities required to generate ions directly related to porosity [132]. Surface platinum layer was observed to desorb and ionize the angiotensin I and verapamil at low laser intensities to achieve femtomole level sensitivity. Moreover, small proteins and glycoproteins such as 24-kDa trypsinogen and 15-kDa ribonuclease B could also be ionized with sufficient sensitivity using this Pt coated NAA substrate. Due to high surface-to-volume ratio, biocompatibility, and unique ionic properties, NAA has been used to selectively enrich

phosphorylated peptides from a mixture of synthetic peptides and tryptic digest product of β-casein and directly analyse using LDI [133]. NAA displays strong incorporation ability for phosphate anion, which was used to enrich phosphopeptides with a high efficiency and selectivity. This system could satisfactorily detect the tryptic digest product of β-casein at a concentration as low as 4×10^{-9} M which is a great improvement over the MS signal from non-enriched peptide mixture.

7.4.2 *Surface Acoustic Wave and Quartz Crystal Microbalance Nanosenors*

NAA substrates, have been applied in other sensing techniques such as surface acoustic wave (SAW), and quartz crystal microbalance (QCM) [134, 135]. NAA based SAW sensors are prepared by depositing and anodizing a film of aluminium between two interdigitated electrodes [136]. Acoustic signal of a specific frequency generated by one electrode (source) is sent through active region (NAA in this case) to the collector electrode. Decays/delays in the frequency/phase of the acoustic that occur during its transit through active region are detected the collector electrode and any change in the phase delay and frequency decay can be used as a sensing parameter. NAA-SAW sensors have been used for detection for ammonia, and humidity [135, 137].

QCM-NAA sensors have been prepared by depositing and anodizing a film of aluminium on quartz substrate. This NAA-quartz structure is subjected to a known frequency that is in resonance with the prepared structure any addition/depletion in mass results in the change in this resonance frequency which is monitored for detection of analyte. Sensing characteristics NAA based QCM sensors have been determined and they have been used detection of highly sensitive sensing tools for detection and observing hysteresis curve for capillary condensation of vapours of organic molecules, water vapours (humidity) and activity of urease for urea detection [126, 134, 138, 139].

7.5 Conclusions

This chapter provides fundamental understanding of a number of sensing techniques including optical, electrochemical and others and also gives a detailed summary of recent studies coupling these sensing techniques with NAA. We envisage that future reports on structural and chemical modifications of NAA will facilitate the development of even smarter and advanced sensing devices. Finally we can conclude there is a bright opportunity for development of miniature sensing devices based on NAA as lab-on-a chip systems for point of care diagnostics, industrial, and environmental applications.

Acknowledgments Financial support from Australian Research Council (DE14010054) and the School of Chemical Engineering of The University of Adelaide are greatly acknowledged.

References

1. R.B. Thompson, *Fluorescence Sensors and Biosensors* (CRC Press, 2005)
2. S. Carrara, G. De Micheli, *Nano-Bio-sensing* (Springer, 2011)
3. A. Santos, T. Kumeria, D. Losic, Nanoporous anodic aluminum oxide for chemical sensing and biosensors. Trac Trends Anal. Chem. **44**, 25–38 (2013)
4. M.J. Sailor, *Porous Silicon in Practice: Preparation, Characterization and Applications* (Wiley, 2012)
5. M.J. Madou, S.R. Morrison, *Chemical Sensing with Solid State Devices* (Elsevier, 2012)
6. T. Kumeria, A. Santos, D. Losic, Nanoporous anodic alumina platforms: engineered surface chemistry and structure for optical sensing applications. Sensors **14**(7), 11878–11918 (2014)
7. W. Lee, S.-J. Park, Porous anodic aluminum oxide: anodization and templated synthesis of functional nanostructures. Chem. Rev. **114**(15), 7487–7556 (2014)
8. A. Santos, T. Kumeria, D. Losic, Nanoporous anodic alumina: a versatile platform for optical biosensors. Materials **7**(6), 4297–4320 (2014)
9. F.S. Ligler, C.A.R. Taitt, *Optical Biosensors: Present and Future* (Gulf Professional Publishing, 2002)
10. A. Santos et al., Nanoporous anodic alumina barcodes: toward smart optical biosensors. Adv. Mater. **24**(8), 1050–1054 (2012)
11. K. Hotta, A. Yamaguchi, N. Teramae, Nanoporous waveguide sensor with optimized nanoarchitectures for highly sensitive label-free biosensing. ACS Nano **6**(2), 1541–1547 (2012)
12. S.J. Lee, M. Moskovits, Remote sensing by plasmonic transport. J. Am. Chem. Soc. **134**(28), 11384–11387 (2012)
13. A. Santos, T. Kumeria, D. Losic, Optically optimized photoluminescent and interferometric biosensors based on nanoporous anodic alumina: a comparison. Anal. Chem. **85**(16), 7904–7911 (2013)
14. K.N. Shinde et al., Basic mechanisms of photoluminescence, in *Phosphate Phosphors for Solid-State Lighting* (Springer, 2012), pp. 41–59
15. F. Braun. Wied. H. D. Ann. **65** 361–364 (1898)
16. S. Ikonopisov, Problems and contradictions in galvanoluminescence, a critical review. Electrochim. Acta **20**(10), 783–793 (1975)
17. S. Stojadinovic et al., Luminescence during the electrochemical oxidation of aluminum, in *Electrodeposition and Surface Finishing*, ed. by S. Djokic (Springer, 2014), p. 241
18. S. Tajima et al., Nature of luminescence during galvanostatic anodizing of high purity aluminium. Electrochim. Acta **22**(8), 845–849 (1977)
19. L.D. Zeković, V. Urošević, B. Jovanić, Investigation of anodic alumina by a photoluminescence method: I. Thin Solid Films **105**(2), 169–176 (1983)
20. B. Kasalica et al., Nature of galvanoluminescence of oxide films formed by aluminum anodization in inorganic electrolytes. J. Phys. Chem. C **111**(33), 12315–12319 (2007)
21. S. Stojadinovic et al., Structural and luminescence characterization of porous anodic oxide films on aluminum formed in sulfamic acid solution. Appl. Surf. Sci. **255**(5), 2845–2850 (2008)
22. S. Stojadinovic et al., The effect of annealing on the photoluminescent and optical properties of porous anodic alumina films formed in sulfamic acid. Appl. Surf. Sci. **256**(3), 763–767 (2009)
23. G. Huang et al., Strong blue emission from anodic alumina membranes with ordered nanopore array. J. Appl. Phys. **93**(1), 582–585 (2003)

24. Y. Mei et al., Color centers vs electrolytes for Si-based porous anodic alumina. Phys. Lett. A **324**(5), 479–483 (2004)
25. G. Huang et al., On the origin of light emission from porous anodic alumina formed in sulfuric acid. Solid State Commun. **137**(11), 621–624 (2006)
26. S. Stojadinovic et al., Luminescence properties of oxide films formed by anodization of aluminum in 12-tungstophosphoric acid. Electrochim. Acta **55**(12), 3857–3863 (2010)
27. Y. Mei et al., Nanoscale islands and color centers in porous anodic alumina on silicon fabricated by oxalic acid. Appl. Surf. Sci. **230**(1), 393–397 (2004)
28. G. Huang et al., Dependence of blue-emitting property on nanopore geometrical structure in Al-based porous anodic alumina membranes. Appl. Phys. A **81**(7), 1345–1349 (2005)
29. S. Stojadinovic et al., Photoluminescent properties of barrier anodic oxide films on aluminum. Thin Solid Films **519**(11), 3516–3521 (2011)
30. A. Santos et al., Structural tuning of photoluminescence in nanoporous anodic alumina by hard anodization in oxalic and malonic acids. Nanoscale Res. Lett. **7**(1), 1–11 (2012)
31. Y. Du et al., Preparation and photoluminescence of alumina membranes with ordered pore arrays. Appl. Phys. Lett. **74**(20), 2951–2953 (1999)
32. I. Vrublevsky et al., Photoluminescent behavior of heat-treated porous alumina films formed in malonic acid. Appl. Surf. Sci. **256**(7), 2013–2017 (2010)
33. M. Ghrib et al., Effect of annealing on photoluminescence and optical properties of porous anodic alumina films formed in sulfuric acid for solar energy applications. Appl. Surf. Sci. **258**(12), 4995–5000 (2012)
34. H. Elhouichet et al., Energy transfer in porous anodic alumina/rhodamine 110 nanocomposites. J. Lumin. **132**(9), 2232–2234 (2012)
35. R. Jia et al., Enhanced photoluminescence properties of morin and trypsin absorbed on porous alumina films with ordered pores array. Solid State Commun. **130**(6), 367–372 (2004)
36. R.-P. Jia et al., Photoluminescence spectra of human serum albumen and morin embedded in porous alumina membranes with ordered pore arrays. J. Phys.: Condens. Matter **15**(49), 8271 (2003)
37. C.L. Feng et al., Graded-bandgap quantum-dot-modified nanotubes: a sensitive biosensor for enhanced detection of DNA hybridization. Adv. Mater. **19**(15), 1933–1936 (2007)
38. A. Santos et al., Photoluminescent enzymatic sensor based on nanoporous anodic alumina. ACS Appl. Mater. Interfaces **4**(7), 3584–3588 (2012)
39. T. Turbadar, Complete absorption of light by thin metal films. Proc. Phys. Soc. Lond. **73**(1), 40–44 (1959)
40. A. Otto, Excitation of nonradiative surface plasma waves in silver by the method of frustrated total reflection. Zeitschrift fur Physik **216**, 398–410 (1968)
41. R.B. Schasfoort, A.J. Tudos, *Handbook of Surface Plasmon Resonance* (Royal Society of Chemistry, 2008)
42. I. Pockrand et al., Optical properties of organic dye monolayers by surface plasmon spectroscopy. J. Chem. Phys. **69**(9), 4001–4011 (1978)
43. I. Pockrand et al., Exciton–surface plasmon interactions. J. Chem. Phys. **70**(7), 3401–3408 (1979)
44. J. Homola, Present and future of surface plasmon resonance biosensors. Anal. Bioanal. Chem. **377**(3), 528–539 (2003)
45. P. Pattnaik, Surface plasmon resonance. Appl. Biochem. Biotechnol. **126**(2), 79–92 (2005)
46. B. Liedberg, C. Nylander, I. Lunström, Surface plasmon resonance for gas detection and biosensing. Sens. Actuators **4**, 299–304 (1983)
47. X. Guo, Surface plasmon resonance based biosensor technique: a review. J. Biophotonics **5**(7), 483–501 (2012)
48. M.C. Estevez et al., Trends and challenges of refractometric nanoplasmonic biosensors: a review. Anal. Chim. Acta **806**, 55–73 (2014)
49. R.J. Green et al., Surface plasmon resonance analysis of dynamic biological interactions with biomaterials. Biomaterials **21**(18), 1823–1835 (2000)

50. A.G. Koutsioubas et al., On the implementation of nano-structured materials in surface plasmon resonance sensors. Mater. Sci. Eng., B **165**(3), 270–273 (2009)
51. K.H.A. Lau et al., Highly sensitive detection of processes occurring inside nanoporous anodic alumina templates: a waveguide optical study. J. Phys. Chem. B **108**(30), 10812–10818 (2004)
52. A. Yamaguchi, K. Hotta, N. Teramae, Optical waveguide sensor based on a porous anodic alumina/aluminum multilayer film. Anal. Chem. **81**(1), 105–111 (2008)
53. A.G. Koutsioubas et al., Nanoporous alumina enhanced surface plasmon resonance sensors. J. Appl. Phys. **103**(9), (2008)
54. A. Dhathathreyan, Real-time monitoring of invertase activity immobilized in nanoporous aluminum oxide. J. Phys. Chem. B **115**(20), 6678–6682 (2011)
55. K.A. Lau, H. Duran, W. Knoll, In situ characterization of N-carboxy anhydride polymerization in nanoporous anodic alumina. J. Phys. Chem. B **113**(10), 3179–3189 (2009)
56. L.K. Tan et al., Atomic layer deposition of TiO_2 to bond free-standing nanoporous alumina templates to gold-coated substrates as planar optical waveguide sensors. J. Phys. Chem. C **112**(45), 17576–17580 (2008)
57. T.D. Lazzara, K. Aaron Lau, W. Knoll, Mounted nanoporous anodic alumina thin films as planar optical waveguides. J. Nanosci. Nanotechnol. **10**(7), 4293–4299 (2010)
58. K.A. Willets, R.P. Van Duyne, Localized surface plasmon resonance spectroscopy and sensing. Annu. Rev. Phys. Chem. **58**, 267–297 (2007)
59. K.M. Mayer et al., A label-free immunoassay based upon localized surface plasmon resonance of gold nanorods. ACS Nano **2**(4), 687–692 (2008)
60. D.-K. Kim et al., Label-free DNA biosensor based on localized surface plasmon resonance coupled with interferometry. Anal. Chem. **79**(5), 1855–1864 (2007)
61. S.-H. Yeom et al., Highly sensitive nano-porous lattice biosensor based on localized surface plasmon resonance and interference. Opt. Express **19**(23), 22882–22891 (2011)
62. H.M. Hiep, H. Yoshikawa, E. Tamiya, Interference localized surface plasmon resonance nanosensor tailored for the detection of specific biomolecular interactions. Anal. Chem. **82**(4), 1221–1227 (2010)
63. H.M. Hiep et al., Immobilization of gold nanoparticles on aluminum oxide nanoporous structure for highly sensitive plasmonic sensing. Jpn. J. Appl. Phys. **49**(6S), 06GM02 (2010)
64. H.M. Hiep et al., Label-free detection of melittin binding to a membrane using electrochemical-localized surface plasmon resonance. Anal. Chem. **80**(6), 1859–1864 (2008)
65. C. Raman, K. Krishnan, Polarisation of scattered light-quanta. Nature **122**(3066), 169–169 (1928)
66. C.L. Haynes, A.D. McFarland, R.P.V. Duyne, Surface-enhanced Raman spectroscopy. Anal. Chem. **77**(17), 338 A–346 A (2005)
67. K. Kneipp, M. Moskovits, H. Kneipp, Surface-enhanced Raman scattering. Phys. Today **60**(11), 40 (2007)
68. D. Cialla et al., Surface-enhanced Raman spectroscopy (SERS): progress and trends. Anal. Bioanal. Chem. **403**(1), 27–54 (2012)
69. X. Lang et al., Tunable silver nanocap superlattice arrays for surface-enhanced Raman scattering. J. Phys. Chem. C **115**(49), 24328–24333 (2011)
70. H. Ko, V.V. Tsukruk, Nanoparticle-decorated nanocanals for surface-enhanced raman scattering. Small **4**(11), 1980–1984 (2008)
71. Z. Lu et al., Deposition of Ag nanoparticles on porous anodic alumina for surface enhanced Raman scattering substrate. J. Raman Spectrosc. **40**(1), 112–116 (2009)
72. R. Kodiyath et al., Assemblies of silver nanocubes for highly sensitive SERS chemical vapor detection. J. Mater. Chem. A **1**(8), 2777–2788 (2013)
73. N. Ji et al., Fabrication of silver decorated anodic aluminum oxide substrate and its optical properties on surface-enhanced Raman scattering and thin film interference. Langmuir **25**(19), 11869–11873 (2009)
74. L. Velleman et al., Raman spectroscopy probing of self-assembled monolayers inside the pores of gold nanotube membranes. Phys. Chem. Chem. Phys. **13**(43), 19587–19593 (2011)

75. S.J. Lee et al., Surface-enhanced Raman spectroscopy and nanogeometry: The plasmonic origin of SERS. J. Phys. Chem. C **111**(49), 17985–17988 (2007)
76. T. Kondo et al., Surface-enhanced Raman scattering on multilayered nanodot arrays obtained using anodic porous alumina mask. J. Photochem. Photobiol., A **221**(2), 199–203 (2011)
77. T. Kondo, H. Masuda, K. Nishio, SERS in ordered array of geometrically controlled nanodots obtained using anodic porous alumina. J. Phys. Chem. C **117**(6), 2531–2534 (2012)
78. G. Gauglitz, J. Ingenhoff, Design of new integrated optical substrates for immuno-analytical applications. Fresen. J. Anal. Chem. **349**(5), 355–359 (1994)
79. T. Kumeria, L. Parkinson, D. Losic, Bioinspired microchip nanoporous interferometric sensor for sensing and biosensing applications. Micro Nanosyst. **3**(4), 290–295 (2011)
80. G. Gauglitz et al., Spectral interference refractometry by diode array spectrometry. Anal. Chem. **60**(23), 2609–2612 (1988)
81. G. Gauglitz, Direct optical sensors: principles and selected applications. Anal. Bioanal. Chem. **381**(1), 141–155 (2005)
82. G. Gauglitz, Direct optical detection in bioanalysis: an update. Anal. Bioanal. Chem. **398**(6), 2363–2372 (2010)
83. V.S.-Y. Lin et al., A porous silicon-based optical interferometric biosensor. Science **278** (5339), 840–843 (1997)
84. K.-S. Mun et al., A stable, label-free optical interferometric biosensor based on TiO_2 nanotube arrays. ACS Nano **4**(4), 2070–2076 (2010)
85. S.D. Alvarez et al., A label-free porous alumina interferometric immunosensor. ACS Nano **3** (10), 3301–3307 (2009)
86. S. Pan, L.J. Rothberg, Interferometric sensing of biomolecular binding using nanoporous aluminum oxide templates. Nano Lett. **3**(6), 811–814 (2003)
87. H.C. An, J.Y. An, B.-W. Kim, Improvement of sensitivity in an interferometry by controlling pore size on the anodic aluminum oxide chip pore-widening technique. Korean J. Chem. Eng. **26**(1), 160–164 (2009)
88. T. Kumeria, D. Losic, Controlling interferometric properties of nanoporous anodic aluminium oxide. Nanoscale Res. Lett. **7**(1), 1–10 (2012)
89. T. Kumeria, D. Losic, Reflective interferometric gas sensing using nanoporous anodic aluminium oxide (AAO). Phys. Status Solidi (RRL)-Rapid Res. Lett. **5**(10–11), 406–408 (2011)
90. T. Kumeria, L. Parkinson, D. Losic, A nanoporous interferometric micro-sensor for biomedical detection of volatile sulphur compounds. Nanoscale Res. Lett. **6**(1), 1–7 (2011)
91. T. Kumeria et al., Label-free reflectometric interference microchip biosensor based on nanoporous alumina for detection of circulating tumour cells. Biosens. Bioelectron. **35**(1), 167–173 (2012)
92. R. Dronov et al., Nanoporous alumina-based interferometric transducers ennobled. Nanoscale **3**(8), 3109–3114 (2011)
93. T. Kumeria, A. Santos, D. Losic, Ultrasensitive nanoporous interferometric sensor for label-free detection of gold (III) ions. ACS Appl. Mater. Interfaces **5**(22), 11783–11790 (2013)
94. T. Kumeria et al., Real-time and in situ drug release monitoring from nanoporous implants under dynamic flow conditions by reflectometric interference spectroscopy. ACS Appl. Mater. Interfaces **5**(12), 5436–5442 (2013)
95. G. Macias et al., Gold-coated ordered nanoporous anodic alumina bilayers for future label-free interferometric biosensors. ACS Appl. Mater. Interfaces **5**(16), 8093–8098 (2013)
96. T. Kumeria et al., Structural and optical nanoengineering of nanoporous anodic alumina rugate filters for real-time and label-free biosensing applications. Anal. Chem. **86**(3), 1837–1844 (2014)
97. T. Kumeria et al., Nanoporous anodic alumina rugate filters for sensing of ionic mercury: toward environmental point-of-analysis systems. ACS Appl. Mater. Interfaces **6**(15), 12971–12978 (2014)

98. M. Pumera, *Nanomaterials for Electrochemical Sensing and Biosensing* (CRC Press, 2014)
99. E. Ekanayake, D.M. Preethichandra, K. Kaneto, Polypyrrole nanotube array sensor for enhanced adsorption of glucose oxidase in glucose biosensors. Biosens. Bioelectron. **23**(1), 107–113 (2007)
100. G. Jeon et al., Electrically actuatable smart nanoporous membrane for pulsatile drug release. Nano Lett. **11**(3), 1284–1288 (2011)
101. R.E. Sabzi, K. Kant, D. Losic, Electrochemical synthesis of nickel hexacyanoferrate nanoarrays with dots, rods and nanotubes morphology using a porous alumina template. Electrochim. Acta **55**(5), 1829–1835 (2010)
102. S. Ansari et al., Glucose sensor based on nano-baskets of tin oxide templated in porous alumina by plasma enhanced CVD. Biosens. Bioelectron. **23**(12), 1838–1842 (2008)
103. Y. Zhang et al., A novel electrochemical sensor for formaldehyde based on palladium nanowire arrays electrode in alkaline media. Electrochim. Acta **68**, 172–177 (2012)
104. E. Stura et al., Anodic porous alumina as mechanical stability enhancer for LDL-cholesterol sensitive electrodes. Biosens. Bioelectron. **23**(5), 655–660 (2007)
105. V. Rai et al., Ultrasensitive cDNA detection of dengue virus RNA using electrochemical nanoporous membrane-based biosensor. PLoS ONE **7**(8), e42346 (2012)
106. G. Koh et al., Development of a membrane-based electrochemical immunosensor. Electrochim. Acta **53**(2), 803–810 (2007)
107. M.S. Cheng et al., Development of an electrochemical membrane-based nanobiosensor for ultrasensitive detection of dengue virus. Anal. Chim. Acta **725**, 74–80 (2012)
108. B.T. Nguyen et al., Membrane-based electrochemical nanobiosensor for the detection of virus. Anal. Chem. **81**(17), 7226–7234 (2009)
109. V. Rai, J. Deng, C.-S. Toh, Electrochemical nanoporous alumina membrane-based label-free DNA biosensor for the detection of Legionella sp. Talanta **98**, 112–117 (2012)
110. B.T.T. Nguyen, J.Q. Ang, C.-S. Toh, Sensitive detection of potassium ion using Prussian blue nanotube sensor. Electrochem. Commun. **11**(10), 1861–1864 (2009)
111. Y. Xian et al., Template synthesis of highly ordered Prussian blue array and its application to the glucose biosensing. Biosens. Bioelectron. **22**(12), 2827–2833 (2007)
112. J.Q. Ang, B.T.T. Nguyen, C.-S. Toh, A dual K^+/Na^+ selective Prussian blue nanotubes sensor. Sens. Actuators B: Chem. **157**(2), 417–423 (2011)
113. J.Q. Ang et al., Ion-selective detection of non-intercalating Na^+ using competitive inhibition of K<$^+$ intercalation in Prussian blue nanotubes sensor. Electrochim. Acta **55**(27), 7903–7908 (2010)
114. L.P. Wong, Y. Wei, C.-S. Toh, Self-powering amperometric sensor and biosensor. J. Electroanal. Chem. **671**, 80–84 (2012)
115. Y. Wei, L.P. Wong, C.-S. Toh, Fuel cell virus sensor using virus capture within antibody-coated nanochannels. Anal. Chem. **85**(3), 1350–1357 (2013)
116. P. Takmakov, I. Vlassiouk, S. Smirnov, Hydrothermally shrunk alumina nanopores and their application to DNA sensing. Analyst **131**(11), 1248–1253 (2006)
117. L. Wang et al., A novel electrochemical biosensor based on dynamic polymerase-extending hybridization for E. coli O157: H7 DNA detection. Talanta **78**(3), 647–652 (2009)
118. F. Tan et al., A PDMS microfluidic impedance immunosensor for E. coli O157: H7andStaphylococcus aureusdetection via antibody-immobilized nanoporous membrane. Sens. Actuators B: Chem. **159**(1), 328–335 (2011)
119. A.E.K. Peh, S.F.Y. Li, Dengue virus detection using impedance measured across nanoporous aluminamembrane. Biosens. Bioelectron. **42**, 391–396 (2013)
120. K. Kant et al., Characterization of impedance biosensing performance of single and nanopore arrays of anodic porous alumina fabricated by focused ion beam (FIB) milling. Electrochim. Acta (2014)
121. K. Kant et al., Impedance nanopore biosensor: influence of pore dimensions on biosensing performance. Analyst **139**(5), 1134–1140 (2014)
122. L. Juhász, J. Mizsei, Humidity sensor structures with thin film porous alumina for on-chip integration. Thin Solid Films **517**(22), 6198–6201 (2009)

123. Z. Jin et al., A novel porous anodic alumina based capacitive sensor towards trace detection of PCBs. Sens. Actuators B: Chem. **157**(2), 641–646 (2011)
124. V. Khatko et al., Tungsten trioxide sensing layers on highly ordered nanoporous alumina template. Sens. Actuators B: Chem. **118**(1), 255–262 (2006)
125. X. Wang, S. Smirnov, Label-free DNA sensor based on surface charge modulated ionic conductance. ACS Nano **3**(4), 1004–1010 (2009)
126. Z. Yang, S. Si, C. Zhang, Study on the activity and stability of urease immobilized onto nanoporous alumina membranes. Microporous Mesoporous Mater. **111**(1–3), 359–366 (2008)
127. L.H. Cohen, A.I. Gusev, Small molecule analysis by MALDI mass spectrometry. Anal. Bioanal. Chem. **373**(7), 571–586 (2002)
128. R.B. Cole, *Electrospray and MALDI Mass Spectrometry: Fundamentals, Instrumentation, Practicalities, and Biological Applications* (Wiley, 2011)
129. R. Nayak et al., Dual desorption electrospray ionization—laser desorption ionization mass spectrometry on a common nanoporous alumina platform for enhanced shotgun proteomic analysis. Anal. Chem. **80**(22), 8840–8844 (2008)
130. R. Nayak, D.R. Knapp, Effects of thin-film structural parameters on laser desorption/ionization from porous alumina. Anal. Chem. **79**(13), 4950–4956 (2007)
131. A. Sen et al., Use of nanoporous alumina surface for desorption electrospray ionization mass spectrometry in proteomic analysis. Biomed. Microdevices **10**(4), 531–538 (2008)
132. Y. Wada, T. Yanagishita, H. Masuda, Ordered porous alumina geometries and surface metals for surface-assisted laser desorption/ionization of biomolecules: possible mechanistic implications of metal surface melting. Anal. Chem. **79**(23), 9122–9127 (2007)
133. Y. Wang et al., Highly efficient and selective enrichment of phosphopeptides using porous anodic alumina membrane for MALDI-TOF MS analysis. J. Am. Soc. Mass Spectrom. **18**(8), 1387–1395 (2007)
134. I. Goubaidoulline, G. Vidrich, D. Johannsmann, Organic vapor sensing with ionic liquids entrapped in alumina nanopores on quartz crystal resonators. Anal. Chem. **77**(2), 615–619 (2004)
135. M. Sato et al., Sensitivity of an anadically oxidized aluminium film on a surface acoustic wave sensor to humidity. Sens. Actuators B: Chem. **20**(2–3), 205–212 (1994)
136. Y.L. Rao, G. Zhang, Enhancing the sensitivity of SAW sensors with nanostructures. Curr. Nanosci. **2**(4), 311–318 (2006)
137. O.K. Varghese et al., Ammonia detection using nanoporous alumina resistive and surface acoustic wave sensors. Sens. Actuators B: Chem. **94**(1), 27–35 (2003)
138. I. Goubaidoulline et al., Simultaneous determination of density and viscosity of liquids based on quartz-crystal resonators covered with nanoporous alumina. J. Appl. Phys. **98**(1), (2005)
139. Z. Yang et al., Piezoelectric urea biosensor based on immobilization of urease onto nanoporous alumina membranes. Biosens. Bioelectron. **22**(12), 3283–3287 (2007)

Chapter 8
Chemical and Structural Modifications of Nanoporous Alumina and Its Optical Properties

Agnieszka Brzózka, Anna Brudzisz, Katarzyna Hnida and Grzegorz D. Sulka

Abstract A growing scientific interest in the fabrication of porous anodic aluminum oxide (AAO) films and their further applications for the fabrication of various devices, has given rise to many studies of porous alumina properties. Highly ordered porous alumina exhibits some unique physical and optical characteristics, especially in the visible spectrum. These properties are of technological importance for applications in the fields of micro and nanotechnology.

8.1 Introduction

In recent decades, anodic aluminum oxide (AAO) has attracted scientific and technological interest due to its numerous applications. The protective AAO layer on aluminum increases its oxidation resistance [1], and after incorporation of organic or metallic pigments can act as a decorative layer [2]. As the insulator with a large surface area, porous alumina is used in electrolytic capacitors [3]. The most common application of AAO is its use as a template for fabrication of nanowires [4], nanodots [5], nanotubes [6], porous membranes [7], etc. [8]. The porous AAO membranes are also used as molecular sieves [9] and masks for selective etching [10]. In recent years, more and more attention has been devoted to optical properties of nanoporous AAO films. Due to the specific interaction of light with a porous medium, an incident light beam can be (i) reflected from the AAO surface or from the Al_2O_3/Al interface, (ii) absorbed by the oxide structure, (iii) transmitted across the pore walls, and also (iv) reflected inside the nanopores [11] as shown in Fig. 8.1.

A. Brzózka · A. Brudzisz · G.D. Sulka (✉)
Department of Physical Chemistry and Electrochemistry, Faculty of Chemistry, Jagiellonian University in Krakow, Ingardena 3, 30060 Krakow, Poland
e-mail: sulka@chemia.uj.edu.pl

K. Hnida
AGH University of Science and Technology, Academic Centre for Materials and Nanotechnology, al. A. Mickiewicza 30, 30-059 Krakow, Poland

D. Losic and A. Santos (eds.), *Electrochemically Engineered Nanoporous Materials*, Springer Series in Materials Science 220,
DOI 10.1007/978-3-319-20346-1_8

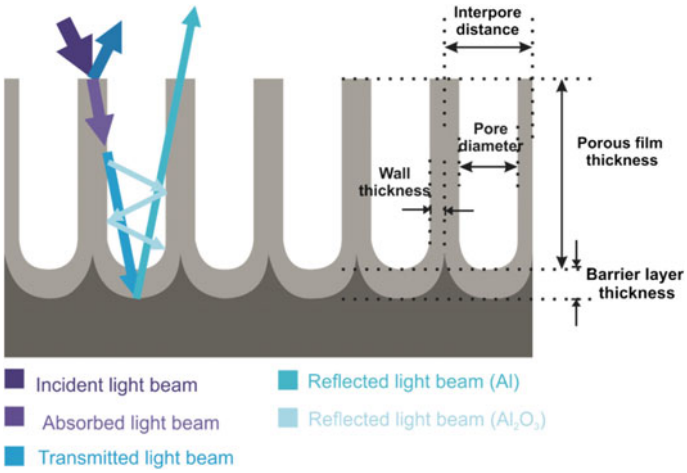

Fig. 8.1 Schematic representation of different phenomena occurring when a light beam incident on the AAO surface and selected characteristic parameters of the AAO film which affect its optical properties

All interactions of the incident light beam with porous AAO depends considerably on the characteristic geometrical parameters of AAO (e.g., pore diameter, interpore distance, wall thickness, oxide layer thickness) and its chemical composition.

It is widely recognized that freestanding AAO films are transparent in the UV-visible range [12]. Porous alumina exhibits a blue photoluminescence band, with the emission bands being attributed to optical transition in the singly ionized oxygen vacancies or to electrolyte impurities embedded in the porous alumina membranes. The previous studies have shown that the photoluminescence of porous alumina relies upon such fabrication parameters as the electrolyte type, anodization voltage, pore diameter, thermal treatment, and anodization regime. It is possible to tune the photoluminescent behavior of AAO by simple modification of the characteristic geometrical parameters of porous alumina. A relatively new approach is to use a pulse anodization, which has been developed for the formation of well-ordered porous alumina with periodically modulated pore diameter. Due to the fact that porous alumina films with modulated diameters have typically a structure based on a stack of thin transparent dielectric layers with alternating high and low refractive indices, they have found applications as distributed Bragg reflectors which offer a high reflectance similar to metallic mirrors. Modification of the optical properties of the porous alumina films can be realized by changing the anodization conditions (e.g., voltage, electrolyte composition, temperature) and by chemical treatment of AAO after anodization (e.g., etching, coloring with dyes, sandblasting, modification by metal nanoparticles, pore filling with polymers).

Highly ordered porous anodic aluminum oxide can be synthesized via two-step anodization of aluminum in acidic electrolytes. The process of AAO membrane formation is relatively simple and inexpensive. AAO formed by the self-organized

anodization of aluminum consists of regularly arranged hexagonal cells with parallel nanopores at their centers [8]. Depending on the anodizing conditions (concentration and type of the electrolyte, applied potential, temperature, and anodizing time), this electrochemical process results in typical nanoporous oxide structures with the pore diameter ranging from about 10 to over 300 nm and the corresponding interpore distance varies in a range of about 35–500 nm.

8.2 Structural Engineering of AAO

During the electrochemical anodization of aluminum carried out in acidic electrolytes including sulfuric acid [13–16], oxalic acid [4, 17] and phosphoric acid [18], anodic aluminum oxide (AAO) with a periodic hexagonal structure can be produced by a self-organized process. Through strict control of anodization conditions it is possible to obtain porous alumina with well-defined characteristic geometrical parameters such as pore diameter, interpore distance (cell diameter), wall thickness, and barrier layer thickness. All geometrical parameters of AAO are easily controllable by anodization conditions (type of electrolyte, anodizing potential or current, time, temperature, and agitation speed) and by post-anodization treatment (etching and annealing) [8].

For self-ordered porous AAO it was found that the interpore distance, pore diameter and barrier layer thickness increase linearly with anodizing potential. The proportionality constants for AAOs formed by conventional mild anodization (MA) processes are 2.5 nm V^{-1} for the interpore distance, 1.29 nm V^{-1} for the pore diameter and 1.2 nm V^{-1} for the barrier layer thickness [8, 19]. In case when hard anodizing (HA) conditions are applied, the interpore distance and barrier layer thickness depend also linearly on the anodizing potential with proportionality constants of about 1.8–2.1 and 0.6–1.0 nm V^{-1}, respectively [19]. On the other hand, the pore diameter of AAOs formed by hard anodization at potentiostatic conditions depends on the anodizing current density [19, 20].

The chemical composition of the AAO membranes is strongly dependent on the type and concentration of electrolyte used for anodization, anodizing potential, current density and temperature [8]. For typical acids used as the anodizing electrolyte (H_2SO_4, H_3PO_4 and $H_2C_2O_4$), incorporation of the acid anions occurs due to their migration in an electric field during the anodizing process. The mechanical properties of AAO such as hardness, elasticity, wear resistance and durability, are determined by the presence of water and embedded anions [19]. The alumina obtained by anodization has a different chemical composition across the pore depth. In other words, the concentration of incorporated ions is much higher at the external oxide layer formed at the beginning of anodization (high acid concentration) than that at the electrolyte/oxide interface where the oxide layer is formed at the end of anodization (low acid concentration) [21]. It is generally accepted that pore walls of AAO have a duplex structure with regard to chemical composition [22]. The outer layer close to the pore channel is rich in the incorporated ions due to the contact

with the electrolyte. The inner layer of pore walls is substantially made of pure Al_2O_3. As-prepared AAO is amorphous and contains water. The water content in porous alumina depends on the anodizing conditions. Annealing of AAO, depending on the applied temperature, may lead to the removal of embedded water from the pore walls, thermal decomposition of build-in anions or a phase transition from amorphous to crystalline. The internal pore structure of nanoporous AAO can be engineered by controlling anodization conditions or by applying an appropriate post-anodization treatment. For instance, by control of the applied anodizing potential it is possible to obtain Y-branched [23–27], multi-branched [27–29] and hierarchically branched pore structures [30–35] as well as periodically modulated nanopore diameters along the pore axes [20, 36–48].

It is widely recognized that for the mild anodization of aluminum performed in sulfuric, oxalic, and phosphoric acid the interpore distance depends on the applied potential with a proportionality constant of about 2.5 nm V^{-1} [8]. Therefore, the reduction of the applied potential by a factor of $1/\sqrt{2}$ during anodization results in branching of stem pores and, consequently, porous AAO with Y-branched nanopores is formed [25]. The AAO structures with a few generations of branched pores can be obtained by further sequential reductions of anodizing potentials by the same factor (Fig. 8.2). The reduction of the anodizing potential by a factor of $1/\sqrt{n}$, where n is a number of branches, results in a n-branched nanopores.

The ordered nanoporous AAO with a complex internal pore structure can be formed by combining the mild and hard anodizations in a process of so called pulse anodization [43]. This approach allows for a continuous modulation of internal pore diameter along the pore axis. The principle of the pulse anodization is based on applying a relatively long low potential/current pulses (MA regime) followed by short high potential/current pulses (HA regime). The length of MA and HA segments in AAO structure are fully controlled by varying anodizing time and MA, HA conditions (applied potential/current). The schematic representation of the applied potential–time waveforms used for the pulse anodization of aluminum is shown in Fig. 8.3a. The effect of applying of HA and MA pulses on the structure of porous anodic alumina is shown in Fig. 8.3b. Figure 8.3c shows the cross-sectional

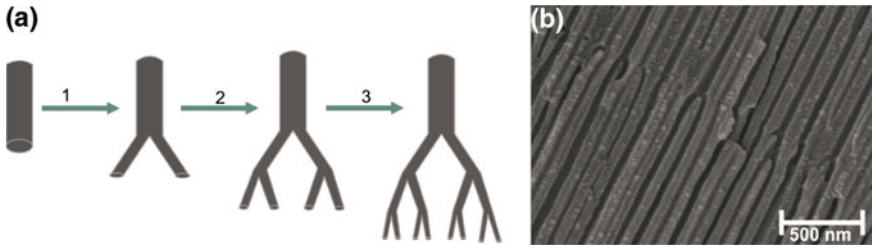

Fig. 8.2 Schematic representation of the anodization procedure used for the fabrication of AAO with hierarchical Y-branched nanopores (*1*, *2*, *3* subsequent reduction of the potential by a factor of $1/\sqrt{2}$) (**a**) together with a SEM microphotograph of the cross-section of porous AAO with Y-branched nanopores (**b**)

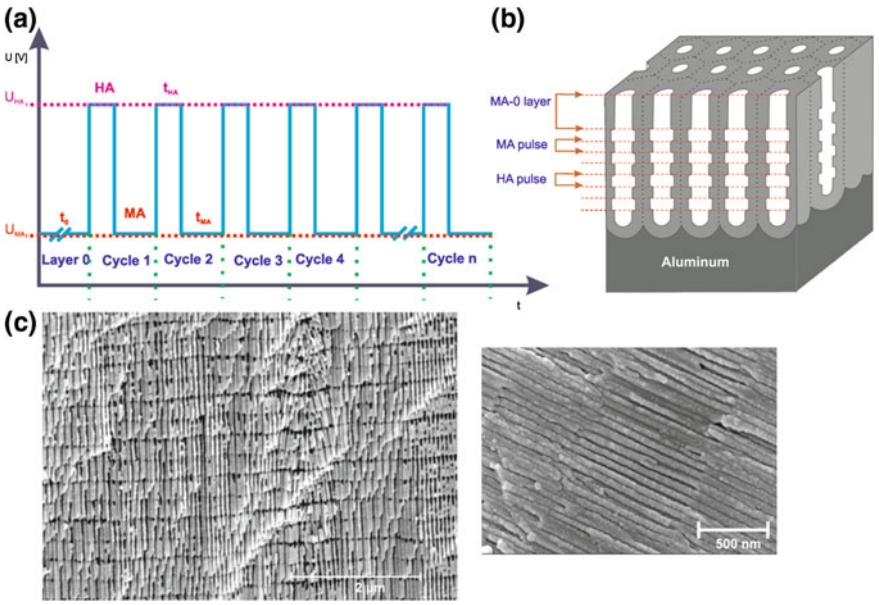

Fig. 8.3 Pulse anodization of aluminum for pore diameter modulations. Typical voltage signal applied during the pulse anodization of aluminum, where U_{MA} and U_{HA} are the anodizing potentials used to achieve mild anodizing (MA) and hard anodizing (HA) conditions, respectively (**a**). Schematic representation of AAO structure grown after a few HA and MA pulses (**b**). SEM microphotograph showing the cross-sectional views of prepared AAO layers produced by pulse anodization in 0.3 M H_2SO_4 at U_{MA} = 25 V and U_{HA} = 32 V (**c**)

views of AAO layers formed by pulse anodization in 0.3 M H_2SO_4 with a potential waveform varied between U_{MA} = 25 V and U_{HA} = 32 V.

Porous alumina with shaped pore geometries and complex pore architectures can be fabricated by periodic anodization. The concept of periodic anodization is based on the application of a periodically oscillating signal in either potentiostatic or galvanostatic mode during the anodization process. The periodic anodization of aluminum with controlled anodizing potential followed by subsequent chemical etching can lead to a periodically branched nanopores [30–32]. In this method, the anodization potential decreases linearly to a certain value of the anodizing potential, and then increases sinusoidally to the initial value of the potential. By repeating this process, a periodic structure with a main (stem) channel and branched channels is formed. The straight stem channel is formed during the high-voltage duration and each stem channel branches into several small channels during the low-voltage duration [30, 35]. The process of periodic anodization is shown in Fig. 8.4. Some modifications of the applied potential signal wave were also proposed to slightly engineer the internal pore geometry [35, 49–52]. For instance, the linear decrease in the applied potential occurring in time t_1 (as denoted in Fig. 8.5) was split into two periods with different linear slopes [35]. For the fabrication of anodic alumina with

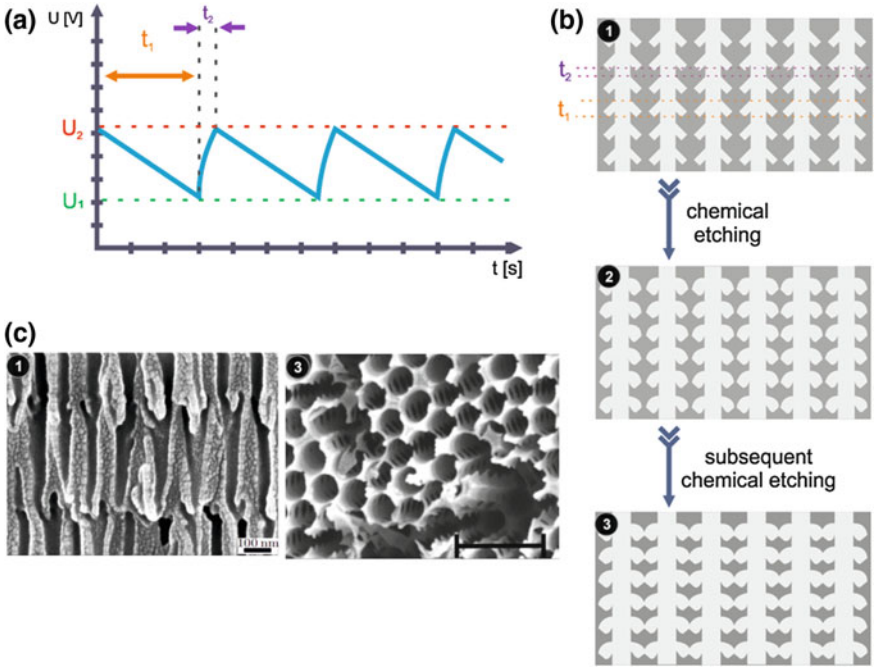

Fig. 8.4 Schematic illustration of the synthesis process for a porous anodic alumina oxide with periodically branched nanopores. Typical voltage signal applied during the periodic anodization of aluminum (**a**). Schematic representation of AAO structure grown after (*1*) a few cycles of periodic anodization and (*2*, *3*) subsequent chemical etching (**b**). SEM microphotograph showing the cross-sectional views of prepared AAO layers by (*1*) periodic anodization and (*3*) after subsequent chemical etching (**c**). **c** reprinted with permission from [32]

2-branched channels, the oxidation potential was periodically reduced by a factor of $1/\sqrt{2}$ (~ 0.71). Figure 8.5 shows schematic representation of the applied potential wave and scheme of the internal geometry of pores with a bilayered structure consisting of the layer with one large channel (layer I) and layer with two small channels (layer II). The layer I is formed during high-voltage anodization (≥ 0.71 U_H, t_1 and t_2). When the applied potential is reduced to $\sim 0.71 U_H$, the channels in the layer I begin to branch into small channels. The small channels grow during the time t_3.

Losic et al. [45, 46] for the first time demonstrated that by applying during anodization periodically oscillating current signals with different profiles, amplitudes and periods, it is possible to perform structural modulation of AAO and to control the internal geometry of nanopores. Figure 8.6 shows the concept of cyclic anodization.

They showed that this approach allows to control the internal geometry of pores by a slow change of anodization conditions (voltage or current) between the MA and HA modes using periodically oscillating signals. This is in contrast with the

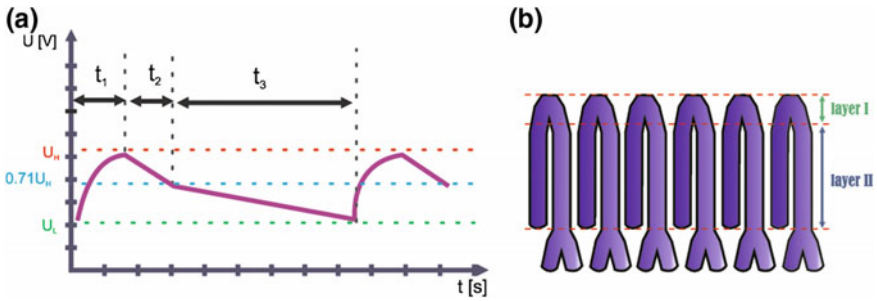

Fig. 8.5 Schematic representation of the synthesis of AAO membranes with a bilayered structure. Typical voltage signal applied during the periodic anodization of aluminum (**a**) and the scheme of the high-quality AAO prepared under the newly-designed periodic oxidation voltage (**b**). Adapted with permission from [35]

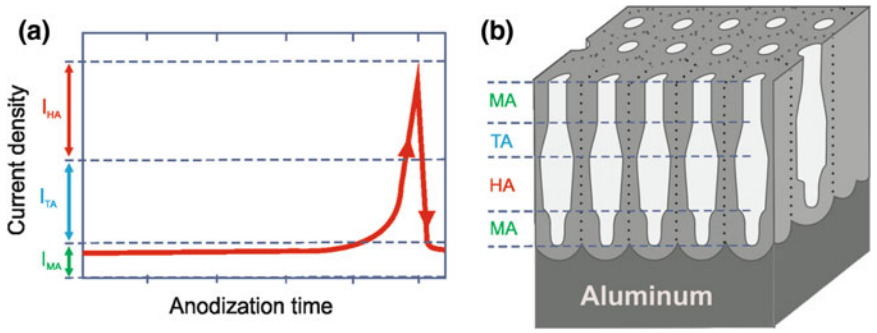

Fig. 8.6 Schematic representation of cyclic anodization of aluminum. Typical current signal applied in a single anodization cycle showing different anodization conditions (I_{MA} mild anodization current, I_{TA} transitional anodization current, and I_{HA} hard anodization current) during the process (**a**). Schematic representation of the AAO structure grown after the MA, TA and HA pulses (**b**)

concept of the pulse anodization [37, 43], where the changes between the MA and HA modes are very fast.

The modulation of the pore diameter can be also obtained by spontaneous current oscillations during hard anodization performed in an unstirred electrolyte [20, 47, 53]. The current oscillations usually appear when stirring is stopped. The observed oscillatory behavior is directly related to the diffusion of the electrolyte from the bulk solution to the bottom of the nanopores. During oxidation of aluminum under the HA regime, oxygen-containing anionic species at the bottom of pores are rapidly consumed, what is indicated by an increase in ionic current and, consequently, a large concentration gradient of anions along the pore channels is established. Depletion of anions at the pore bottoms results in retardation of the

oxidation process and thus to a decrease in current density. A new cycle starts when ions from the bulk solution will influx to the reaction interface at the bottom of pores.

The another approach to alter the internal pore structure is based on alternating repetition of anodization and pore-widening process. This method allows the synthesis inverted-cone-shaped [54–57] and step-shaped pores [26, 54, 58–60]. Figure 8.7 shows schematic illustration of the fabrication of AAO with cone-shaped and step-shaped pores. To fabricate the AAO with inverted cone-shape nanopores, repeated alternating anodization and pore widening treatments should be performed [54–57]. The shape and size of the pores in this process depends on both the anodization and etching conditions. Typically 5–7 full cycles are required to obtain desired pore shape. The main disadvantage of the method is that it leads to AAOs with very low aspect ratios (not exceeding 5). In addition, the combination of anodization and pore widening processes is used to form the AAO with step-shaped pores [26, 54, 58–60]. The procedures includes anodization followed by chemical etching of formed pore walls and finally, the sample is anodized once again for a short of time. Moreover, the AAO with reversed step-shaped pores can be

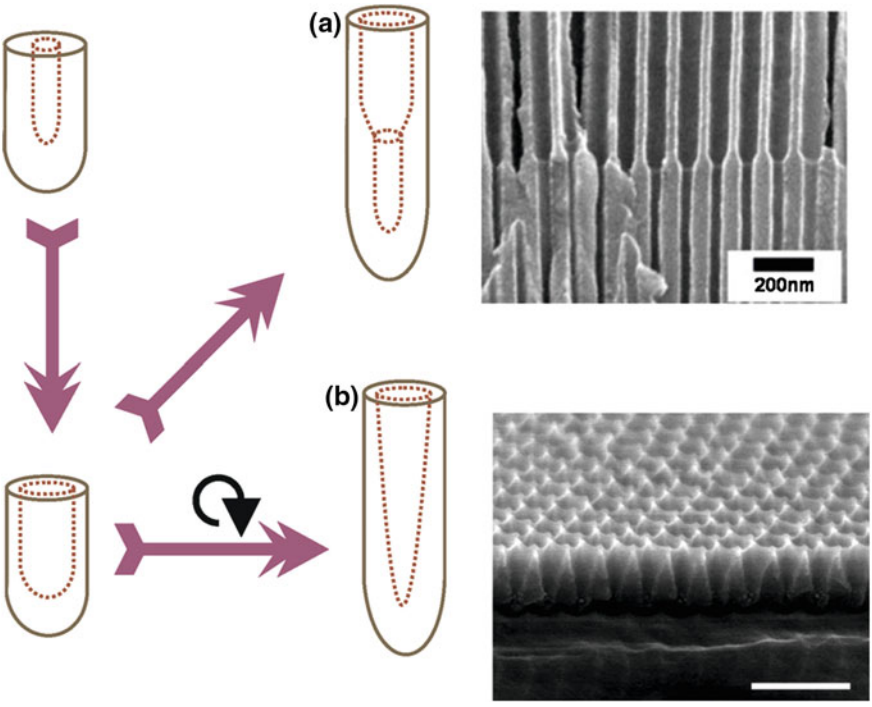

Fig. 8.7 Schematic diagram of fabrication process for the multi-step structure in single pore. Fabrication of step-shaped (**a**) and conical (**b**) pore structure. **a** and **b** reprinted with permission from [56, 58], respectively

fabricated by changing the electrolyte and applied potential during anodization [37, 59]. In turn, serrated nanopores with periodic intervals are formed in AAO when oxygen bubbles are periodically generated during anodization [61–63].

8.3 Optical Response of AAO to Light

When a beam of light is incident on the surface of porous alumina the following physical phenomena can be observed: reflection of light from the air/Al_2O_3 interface and Al_2O_3/Al interface [11, 64–75], partial absorption [11, 68, 76–87] or transmission [11, 12, 71, 77, 88–104] the remaining beam along the pores walls. Those effects were schematically shown in Fig. 8.1.

8.3.1 Reflection and Transmission in AAO

A very significant application of porous anodic aluminum oxide is its use as a decorative and protective coating. Porous alumina films can produce bright colors on reflections in the visible light range but their saturation is relatively low [73]. The low color saturation of AAO on the Al substrate is due to the fact that aluminum highly reflects visible light. A good way to change the AAO color or increase its saturation is (i) sputtering a thin metallic layer (e.g. Ag [33, 68, 105], Cr [105] and Pt [106]), (ii) deposition of metallic nanowires in the pores (Ni [107–109], Co [110], and Ag [33]), (iii) removal of the aluminum substrate after anodization [73, 74], and (iv) modification of internal pore structure [105–110]. The reflection of light from the porous alumina layers is affected by many factors including residues of the Al substrate [73, 74], pore diameter [64, 67], thickness of AAO [66, 69, 71, 73–75], and the existence of other molecules and compounds in the pores or on the AAO surface [101, 105–108, 110].

Xu et al. [73, 74] studied the effect of remaining aluminum substrate on the optical properties of porous anodic alumina oxide. Figure 8.8 shows schematically the interaction of the incident light beam with the porous AAO film before (Fig. 8.8a) and after (Fig. 8.8b) removal of the aluminum substrate. The color of AAO film with the supporting Al substrate mainly comes from the interference of two beams reflected from the air/Al_2O_3 interface and Al_2O_3/Al interface. The phase difference is related only with the optical path difference. After removal of the supporting Al layer, except the phase difference caused by the path difference there is additional a phase change difference between the two reflections. Therefore, the removal of the Al substrate affects the observed color of AAO. Figure 8.8c illustrates this effect. The observed pink color corresponds to the AAO film on the Al substrate while the deep green area in the center of the sample shows the AAO film after the removal of the Al substrate. This indicates that the reflected light from the

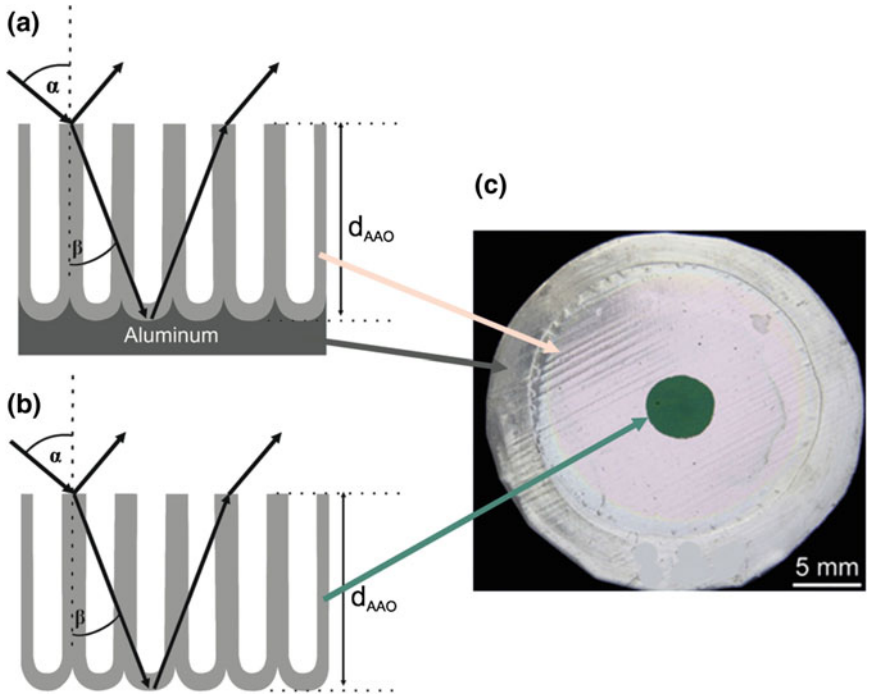

Fig. 8.8 Schematic interaction of the light beam with a porous AAO film before (**a**) and after **b** removal of the Al substrate. Optical photograph of the AAO film after a partial removal of Al substrate in the center of the sample (**c**). Reprinted with permission from [74]

alumina/Al interface has an important effect on the color of AAO. The color can be altered by changing of incident angle as is expected by Bragg's equation [73].

Reflectance of AAO films depends also on the thickness of the anodic alumina oxide layer [66, 69, 71, 73, 74]. The thickness of the aluminum oxide layer can be controlled by anodization time [69, 73, 74], and temperature [66]. By varying the anodizing time, it is possible to modulate reflectance of AAO. Figure 8.9 shows the influence of oxide thickness on the reflectance spectra for the AAO with or without the remaining Al layer. By increasing the anodization time, the thickness of the oxide layer increases and a red shift in the peak position is observed for both types of AAO samples. On the other hand, as was previously mentioned, the removal of the Al layer results in a blue shift of the peak position.

The reflectance spectrum of the porous AAO film depends on the pore diameter of the AAO membrane [64, 67]. Kant et al. [67] studied the influence of pore diameter of AAO on its reflectance. The pores of different sizes were generated on the same sample along a longitudinal direction by a non-uniform anodization of unpolished aluminum alloy. The SEM microphotographs taken at different parts of the sample show that the nanopores are aligned in parallel lines in the same manner as rows are distributed on the rolled and unpolished Al foil (Fig. 8.10a–e).

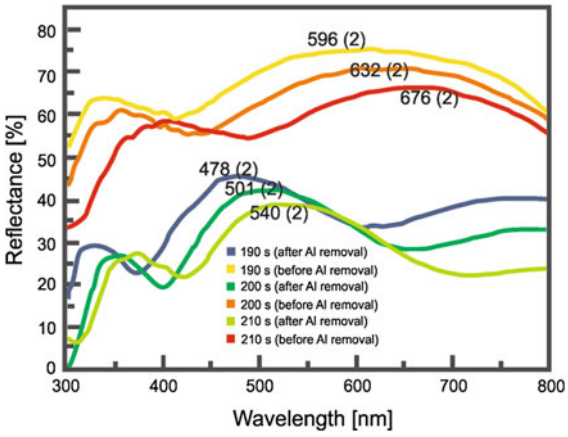

Fig. 8.9 Reflectance spectra of the AAO films before (*top*) and after (*bottom*) removal of the Al layer for different anodizing durations: 210, 200, and 190 s. Reprinted with permission from [74]

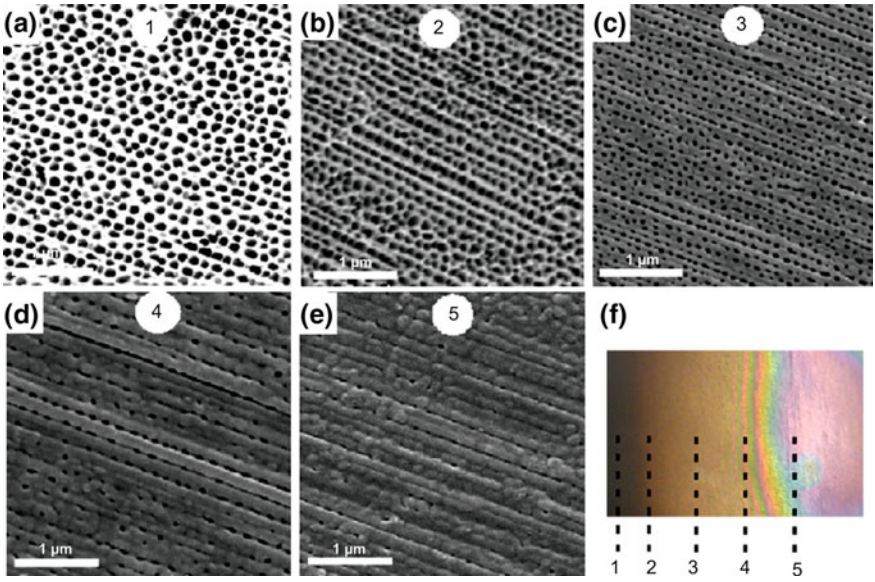

Fig. 8.10 SEM microphotographs of the AAO surface with different pore diameters at different locations on the tilted electrode formed by anodization of low purity Al foil (**a**–**e**). The anodization was performed in 0.3 M phosphoric acid at the current density of 100 mA cm^{-2} and 0 °C. The angle between electrodes was 45°. Photo of the prepared AAO surface with marked locations (*1*–*5*) where SEM images were acquired (**f**). Reprinted with permission from [67]

Figure 8.10f shows the photo of the prepared AAO sample. A gradual change of color from golden to pink corresponding to the gradual change of pore diameter is visible.

Ghrib et al. [64] studied the effect of annealing temperature on the reflectance spectra of AAO. It was found that the reflectance of AAO increases from about 80 to 96 %, respectively before and after annealing at 650 °C. The increase in reflectance of the annealed AAO is caused by decreasing porosity of alumina and modification of the structure leading to higher packing density.

The observed reflectance spectra depend also on which side of the AAO membrane was tested (Fig. 8.11) [111]. As can be seen, the reflected light shows complementary colors, while the transmitted light presents similar colors. The corresponding reflectance and transmittance spectra of the AAO sample are presented in Fig. 8.11e. In the reflectance spectra some oscillations are clearly visible and their presence can be ascribed to a complex interference occurring in the AAO film.

As was shown in Fig. 8.1 the incident beam light can be also partially reflected inside the nanopores of the anodic film, and therefore the AAO can be treated as a Fabry-Pérot interferometer [112]. Consequently, well resolved fringe patterns (oscillations) result from Fabry-Pérot interference of the light reflected from multiple interfaces can be observed in the reflectance spectrum as shown in Fig. 8.11 [111, 113, 114]. The signal oscillations are commonly observed also in transmission [12] and photoluminescence spectra [67, 115–117] of AAO films.

The transmittance spectra tested from the top and the back sides of the AAO membrane are nearly the same. These result correlates perfectly with the observed similar color of the sample (see Fig. 8.11). A strong absorption below 350 nm visible in the transmittance spectra (Fig. 8.11e) is induced by a supporting glass substrate. In general, porous anodic aluminum oxide is transparent to visible light, however, its permeability depends on many factors such as type and amount of

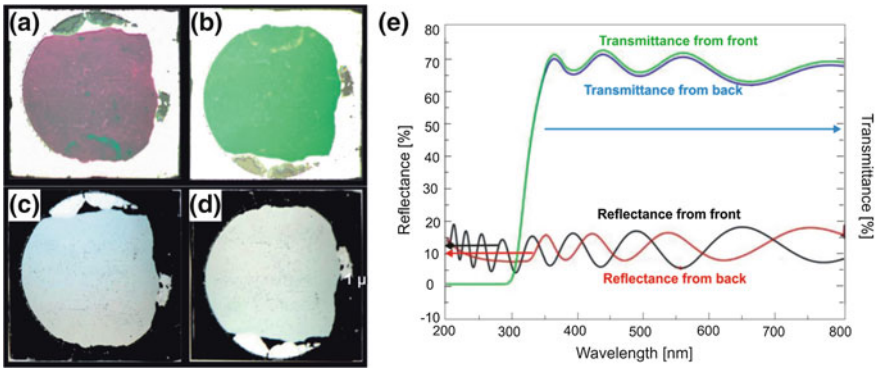

Fig. 8.11 Reflectance (**a**, **b**) and transmittance (**c**, **d**) photographs taken from the top side (**a**, **c**) and back side (**b**, **d**) of the AAO membrane together with the corresponding reflectance and transmittance spectra (**f**). Reprinted with permission from [111]

incorporated impurities [77, 87, 93, 95–98, 103, 104, 118], thickness of the oxide layer [12, 71, 89, 95, 102, 103], and pore diameter [12, 88, 89, 91, 93, 94, 103, 119]. Not surprisingly, it was shown that the increased transmittance of AAO film with increased pore diameter is attributed to the decreased refractive index of AAO layer. It was also reported that during the heat treatment impurities incorporated in the AAO structure are removed and phase transitions occurred [95]. As a result of that, a decrease in the number of absorption centers and increase in transmission are observed [103, 119]. The transparency of porous anodic alumina films in the visible light range is very important for LCD panel applications [90].

8.3.1.1 Absorption in AAO

The beam of light incident on the surface of porous anodic alumina can be absorbed. The absorption of the incident beam depends on the film thickness [11], pore diameter [11], impurities in the oxide structure [19, 76–78, 80, 83, 85, 87, 91, 120, 121], impurities in the pores [81, 94], and post annealing process [83]. Absorption of incident light beam on the porous AAO film depends also on the structural characteristic of anodic aluminum oxide [11, 91] and beam incident angle [11]. The AAO films synthesized at different anodization conditions have different dimensional features (pore diameter, wall thickness, etc.). Therefore, the incident light beam interacts with the AAO surfaces with different geometrical parameters and light is absorbed in different degree. Figure 8.12a shows the influence of porous film thickness on the optical path length of incident beam and the number of

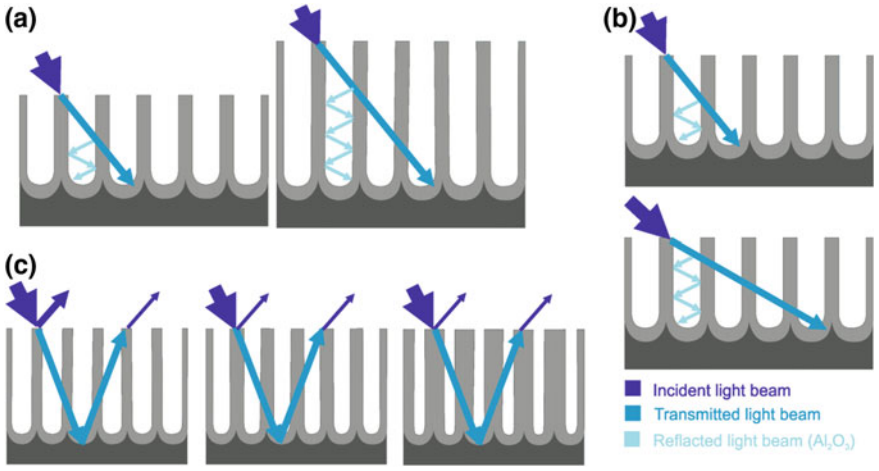

Fig. 8.12 Diagram showing the influence of the AAO thickness (**a**) and incident angle (**b**) on the passage length of penetrated beam and the number of reflections inside the pores. Influence of pores area percentage (porosity) on the reflected beams intensity (**c**). Reprinted with permission from [11]

reflections inside the pores. For the light beam incident on the porous AAO surfaces with different film thicknesses it can be seen that absorption increases with increasing AAO thickness [11, 91]. It comes from the fact that the incident beam becomes weaker when passing across the increasing number of pore walls. In addition, as the pore length increases more reflections occur inside the nanopores. Figure 8.12b shows the effect of incident angle on the optical path length of light beam and the number of reflections inside the nanopores. It can be seen also that optical absorption increases with increasing incident angle. With increasing incident angle the light beam passes across the higher number of pore walls. Figure 8.12c shows the effect of porosity of the AAO layer on its optical properties. According to Moghadam et al. [11] light absorption in AAO increases with decreasing porosity, and then after reaching the maximum for about 15 % decreases with a further porosity decrease. The poor absorption of light observed for the sample with the highest porosity was attributed to a high pore fraction which make it easier for the incident beam to access the high reflective Al surface. According to this hypothesis, the reduction of AAO porosity diminishes the intensity of reflected beams to the point when the thickness of pore walls is large enough to provide a significant planar surface area on AAO top for enhanced light reflection.

It is widely recognized that during anodization of aluminum in acidic electrolytes, acid anions are incorporated into the AAO structure [8, 19]. Due to the larger size and lower mobility of acid anions compared with O^{2-} and OH^{-}, the acid anions migrate in the electric field during anodization from the solution to anode and their content decreases from the outer to the inner layer of the pore walls [8, 77]. The anions incorporated into the AAO film play a role of absorption centers to the incident light beam. Recently Fan et al. reported that with decreasing concentration of $C_2O_4^{2-}$ ions an increase in the refractive index and absorption coefficient was observed [77].

Li et al. [83] recorded the absorption spectra for the AAO membranes formed in oxalic acid and sulfuric acid. The absorption spectrum for the oxalic AAO membrane showed an additional absorption band at 294 nm when compared to that for the sulfuric AAO membrane. It was considered that this absorption band is derived from $C_2O_4^{2-}$ ions which are incorporated in the AAO structure. The samples annealed above 550 °C do not absorb at 294 nm and it is associated with a heat-dissolution of $C_2O_4^{2-}$ in the AAO membrane [81]. With increasing annealing temperature, the intensity of both absorption bands at 370 and 254 nm, increases, reaches a maximum (at 480 and 550 °C, respectively), and then decreases. The observed changes in intensity of the absorption bands were attributed to effective number of oxygen vacancies in the oxide structure. In addition, as the annealing temperature increases the shift of absorption bands to shorter wavelengths was reported. In turn, this phenomenon was ascribed to the release of internal stress of the AAO film.

Fan et al. [77] examined the role of $C_2O_4^{2-}$ anion impurities on absorption coefficient. The absorption spectra of the AAO films with different thicknesses were recorded. It was found that the absorption band gradually broadens as the thickness of AAO film increases. Such behavior is caused by increasing amount of $C_2O_4^{2-}$

anion impurities incorporated in AAO films. Gao et al. [78–80] obtained similar results. They conducted anodization of aluminum in oxalic acid, sulfuric acid, and in a mixture of oxalic and sulfuric acids. The results indicated that the absorption spectra for the oxalic AAO film showed the absorption bands, in contrast to the sulfuric AAO film. Yang et al. [87] studied the influence of sulfosalicylic acid (SSA) presence in the electrolyte on the optical properties of porous anodic alumina membranes. For this purpose, they conducted anodization of aluminum in the different mixtures of sulfosalicylic acid and sulfuric acid. The recorded absorption spectra in the UV-Vis range showed that for the sample prepared in sulfuric acid only, an absorption band edge of alumina was observed as previously reported [78–80, 83]. For the AAO films obtained through anodization in the mixed electrolytes (H_2SO_4 + SSA) absorption bands at about 343 and 248 nm were observed. It was revealed that the intensity of the absorption bands in the absorption spectra of the AAO films, increases with increasing of concentration of SSA. These results indicate that the AAO samples obtained by anodization in various acidic electrolytes have a different intrinsic structural characteristics.

The absorption of the incident light beam on the porous AAO film can be enhanced by other ions [84, 122] incorporated during anodization in the oxide structure. The absorption of light in the UV-Vis region can be enhanced by incorporated Cr^{3+} ions [84, 121]. The absorption bands are associated with three electron transitions of Cr^{3+} in α-Al_2O_3 [84]. Similar results were obtained by Stępniowski et al. [121].

The absorption centers of AAO films can be changed by thermal annealing. Efeoglu et al. [76] studied the anodization of aluminum sputtered on Si substrate in oxalic acid. To deactivate the absorption centers, the AAO films were thermally annealed at 250–950 °C. It was found that the optical activity of the AAO film is attributed to oxygen-related defects and partly to impurities that may be originated from oxalic acid. As can be seen in Fig. 8.13 the absorption is sensitive to a high density of defect levels within the band gap. The theoretical band gap of Al_2O_3 is around 200 nm, however the effective absorption within the band gap is evident and becomes stronger after annealing at 550 °C. Such a strong absorption is related with an increase in oxygen defect density to the highest level. With a further temperature increase the tails decrease at 950 °C and, finally disappear at 1050 °C. It indicates that the annealing above 1000 °C results in a less defected material and Al_2O_3 becomes optically transparent from deep UV to NIR region.

8.4 Photoluminescence Properties of AAO

8.4.1 The Origin of Optical Centers in AAO

The optical properties of aluminum oxide have attracted the attention of scientists since the 70s of the last century, however, the first report on the photoluminescence (PL) properties of nanoporous AAO appeared in 1999 [123]. Since then, many

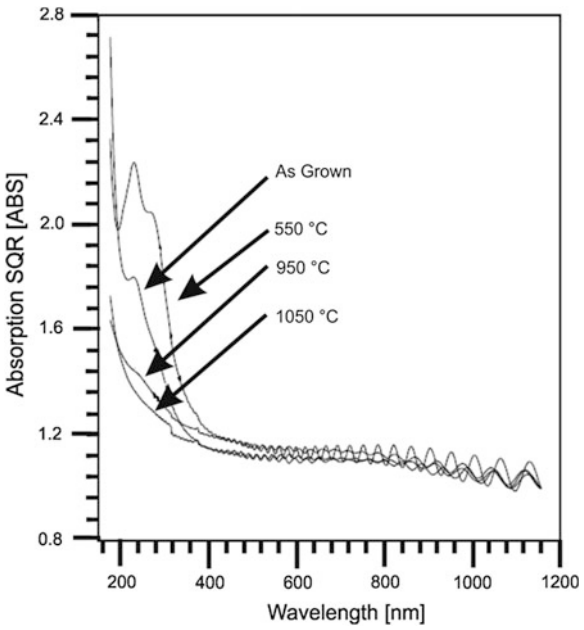

Fig. 8.13 Optical absorption of Al_2O_3 for different annealing temperatures. Reprinted with permission from [76]

studies have been done to clarify the mechanism of PL spectra and to determine the parameters which affect the optical properties of AAO [79, 124, 125]. The initial studies have primarily focused on the determination of types of optical centers present in the structure of porous alumina oxide obtained through anodization. For this purpose, the obtained PL spectra were compared with the corresponding results for sapphire [85, 126, 127]. In 2003, Gao et al. [79] found that the photoluminescence properties of AAO are induced by electrolyte ions incorporated into the oxide structure during anodization. Recently, it has been postulated that the PL mechanism of the anodic aluminum oxide is complex and depends on both the optical center distribution and embedded anions.

Optical centers dispersed in the porous structure of anodic aluminum oxide are associated with the presence of oxygen vacancies. Depending on the type of electrolyte used for anodization, it is possible to produce oxide coating containing two or more layers [8, 19]. The outer layer (which is in contact with the electrolyte or air) contains a higher amount of impurities (e.g. embedded ions or structural defects) than the inner layer close to the cell boundaries (Fig. 8.14) [128]. During anodization OH^- ions are transferred to the vicinity of the oxide/metal interface, where are converted to O^{2-} ions which react with Al to form Al_2O_3 and oxygen vacancies. Generally, the concentration of oxygen vacancies in the formed AAO film is inversely proportional to the concentration of hydroxide ions in the electrolyte. Huang et al. found that the photoluminescence properties of porous alumina correspond to more than one type of optical centers [129]. Besides F^+ defects, being oxygen vacancies with one electron and giving an intensive peak in PL spectra, it is

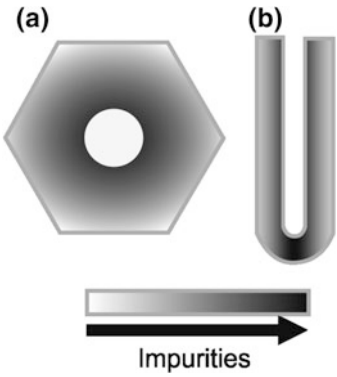

Fig. 8.14 The layered structure of AAO nanopore: top (**a**) and cross-sectional (**b**) view. Reprinted with permission from [128]

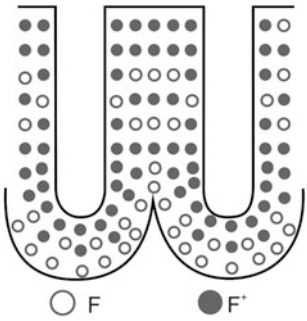

Fig. 8.15 Arrangement of optical centers in the porous structure of the AAO. After [94, 129]

also possible to observe F centers (doubly ionized oxygen vacancies) and less likely unstable F^{++} centers (vacancies without electrons) [94, 129–131]. Figure 8.15 presents a distribution model of different type of optical centers in AAO. According to previous research [94, 129], F^{+} centers are located mainly in the outer layer of AAO, while the F type centers are distributed in the inner oxide layer.

The second factor influencing the PL spectrum is the previously mentioned effect of incorporated acid-anions that contaminate the outer oxide layer next to the pores [99, 101, 122, 132–134]. The incorporation of acid anions during the anodization is possible due to their inward migration under an electric field toward the oxide/metal interface. Acid anions, formed by the dissociation of the anodizing electrolyte can be incorporated into the structure of oxide during its growth, and may replace O^{2-} in the oxide [12]. Due to the influence of a high electric field or by Joule heating inside the pores, incorporated oxalate ions can be transformed into optical centers

[104, 135]. For example, during anodization in oxalic acid the following reactions take place (8.1, 8.2):

$$^{3}/_{2}H_2O \rightarrow 3H^+ + {}^{3}/_{2}O^{2-} \tag{8.1}$$

$$HC_2O_4^- \rightarrow C_2O_4^{2-} + H^+ \tag{8.2}$$

As a result, the O^{2-} ion in the oxide layer could be easily substituted by the oxalate anion. The similar situation is in the case when other acids are used for anodization. The concentration of incorporated ions depends on the conditions of anodization i.e. the type and concentration of the electrolyte, temperature and applied anodizing potential. In the following subsections, the factors affecting the shape of the peaks, their spectral shift and PL intensity of AAO will be throughly discussed.

8.4.2 Factors Affecting PL of AAO

Among the factors having a significant impact on photoluminescence spectra of anodized alumina, special attention should be given to the following:

a. purity and polishing of the starting material
b. anodizations regimes: mild and hard anodizations
c. pore diameter and porosity of AAO, which depend on the anodization conditions (type of electrolyte, applied potential, temperature, etc.)
d. thickness of the oxide layer
e. etching and widening of pores
f. post-annealing of AAO
g. different internal pore structure of AAO
h. modification of the AAO surface and pore walls with nanoparticles
i. filling the pores of AAO with metals/oxides/polymers/dyes organic compounds, etc.

8.4.2.1 Purity and Polishing of the Starting Material

The purity of the aluminum foil and the preparation of the starting material for anodization significantly affect the quality of obtained AAO nanostructures. Pershukevich et al. [136] carried out a study on the anodization of aluminum alloy and high-purity Al foil. It was shown that the recorded photoluminescence spectra are comparable and the type of active centers does not depend on the purity of the starting material. On the other hand, Kokonou et al. [137] reported that the intensity of the PL spectrum of the AAO film obtained in citric acid by anodization of the

aluminum alloy containing 1 % of Si was lower compared to the PL intensity of the AAO from pure aluminum.

The pre-treatment of the starting material has a huge impact on the quality of nanopore order and presence of defects, and consequently, on the PL spectrum [138]. It was found that the PL spectra are affected by the electropolishing pre-treatment mainly by the type of the used electropolishing mixture. A red shift in the PL spectra was observed for the Brytale solution compared to the perchloric acid-alcohol solution used for electropolishing samples anodized at 40 V. The opposite shift in PL spectra was noticed for the higher anodizing potentials. When the defect density (pore disorder) of AAO increases a red shift in the PL spectrum is observed due to probable enhanced accommodation of F centers at defects [138]. This is attributed to increased number of pentagons and hexagons with missing pores and, consequently, to a large number of metallic protrusions (hills) which change the relative curvatures of the electrolyte/oxide interface with respect to the oxide/metal interface. In the aftermath of that the field distribution at the barrier layer is different from the rest of the oxide, electrostriction, volume expansion stresses and flow of the oxide are different at the defects.

8.4.2.2 Anodizing Regimes: Mild and Hard Anodizations

It is worth mentioning that the anodizing protocol influences the photoluminescence spectra of AAO films. It was found that the PL intensity of the AAO formed in the mixture of oxalic acid and ethanol is higher under mild anodization regime than under hard anodization conditions (Fig. 8.16) [139]. It has been shown that the presence of ethanol as a coolant does not affect significantly the PL spectra (curves 1 and 2 in Fig. 8.16). The AAO sample obtained in the same electrolyte but at 130 V has much lower PL intensity (curve 3). There is also observable a shift of the peak position from 440 to 490 nm. Both decline of intensity and red shift can be attributed to the reduction of single ionized oxygen vacancies [139]. The optical properties of the AAO films formed by hard anodizations performed at different anodizing conditions will be discussed in detail below.

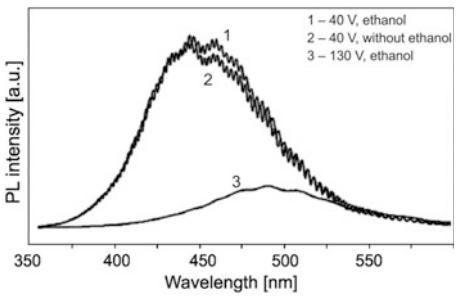

Fig. 8.16 PL spectra obtained for the nanoporous AAO films received by hard anodization of Al foil in 0.1–0.5 M oxalic acid with and without ethanol. Reprinted with permission from [139]

8.4.2.3 Anodization Conditions

Depending on the electrolyte used for anodization it is possible to obtain AAO structures with different geometrical parameters, i.e. pore diameter, interpore distance, porous oxide layer thickness, porosity etc. [4, 87, 97–99, 118, 121, 122, 134, 136, 140–143]. The photoluminescence properties of AAO formed in commonly used acid electrolytes such as sulfuric, oxalic and phosphoric acid, were studied in detail [137, 144–148]. It has been proven that the AAO films obtained in oxalic acid have a different photoluminescence excitation mechanism than those formed in phosphoric or sulfuric acid [137, 145]. The comparison of photoluminescent spectra for AAO samples formed in oxalic, sulfuric and phosphoric acid is shown in Fig. 8.17. Clearly, the intensity of the PL spectrum for the AAO anodized in oxalic acid is much higher compared to other electrolytes. Deconvolution of this spectrum obtained for AAO anodized in oxalic acid showed the presence of three peaks associated with the presence of the different optical centers namely F (435 nm), F^+ (398 nm) and oxalate impurities (473 nm) [145]. The observed high intensity of the spectrum is caused by the high concentration of oxygen vacancies. Oxalic acid belongs to the dihydric acids group. The presence of σ bonds and especially delocalized π bonds are responsible for easy excitation of incorporated oxalate ions in the ultraviolet region [100]. Therefore, high intensity of the PL spectra of AAO formed in oxalic acid can be explain by combining the effect of high concentration of oxygen vacancies and the luminescence properties of oxalate ions due to the presence of delocalized electrons of π bonds. On the other hand, low PL intensity of AAOs obtained in sulfuric and phosphoric acid is caused by the presence of two optical centers F and F^+, and much smaller contribution of embedded acid anions in the spectrum. Shi et al. showed that photoluminescence intensity of AAO prepared in phosphoric acid is higher compared to those obtained in sulfuric acid. This is due to the increased incorporation of PO_4^{3-} ions compared to SO_4^{2-} [132].

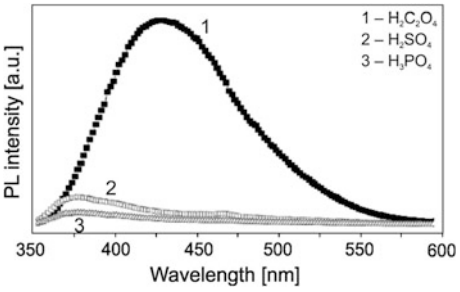

Fig. 8.17 PL spectra obtained for porous AAO by anodization in optimal conditions in: (*1*) 0.3 M oxalic acid, 40 V, 11 °C, (*2*) 0.3 M sulfuric acid, 25 V, 6 °C, (*3*) 10 % phosphoric acid, 60 V, 6 °C. Reprinted with permission from [145]

In 2003, Li et al. [144] postulated that the origin of photoluminescence from AAO obtained in sulfuric and oxalic acid is the same. It is widely recognized that $C_2O_4^{2-}$ and SO_4^{2-} ions incorporate during anodization into the oxide layers. Recently, it has been revealed that not only the oxalic impurities but also the sulfuric and sulfosalicylic impurities incorporated in AAOs can be converted into luminescent centers and both affect the PL properties of AAOs [87, 149]. In order to demonstrate the influence of oxalate and sulfate anions on the PL spectra of AAOs, a number of experiments on Al anodization in various mixtures of these acids was performed [78, 80, 133, 146, 149]. The obtained PL spectra are shown in Fig. 8.18. Besides the typical emissions centered at 370, 385 and 470 nm, Li et al. observed the new emission peak at 290 and 325 nm for AAOs anodized in sulfuric acid and oxalic acid, respectively. The same PL peaks appeared when the AAO sample was formed in the mixed solution of both acids [149]. Furthermore, as the volume ratio of acids changes the intensity of both peaks changes as well. With the increase of SO_4^{2-} concentration in the electrolyte, the intensity of peak centered at 325 nm initially increases ($V_{sulf}/V_{ox} < 6$), and then decreases ($V_{sulf}/V_{ox} > 6$). The opposite tendency was observed for the 290 nm emission. In order to understand the PL behavior it is necessary to analyze the mechanism of energy transfer in AAO formed during anodization in a mixture of acids (Fig. 8.19). According to Li et al., the process of energy transfer can be divided into three stages: (1) absorption of photon energy by electrons, (2) thermal relaxation of electrons to a lower energy level, e.g. impurity levels of sulfate and/or oxalate ions, (3a) the spontaneous radiation of energy by decay from the impurity energy levels (S or C) to the ground state and (3b) nonradiative energy transfer between the impurity levels of SO_4^{2-} and $C_2O_4^{2-}$ accompanied by the weakened emission 3a and enhanced emission 3b [149]. Due to the incorporation of both types of ions in the oxide structure, step 3b is the most favored. According to the data published by Wang et al., the intensity of

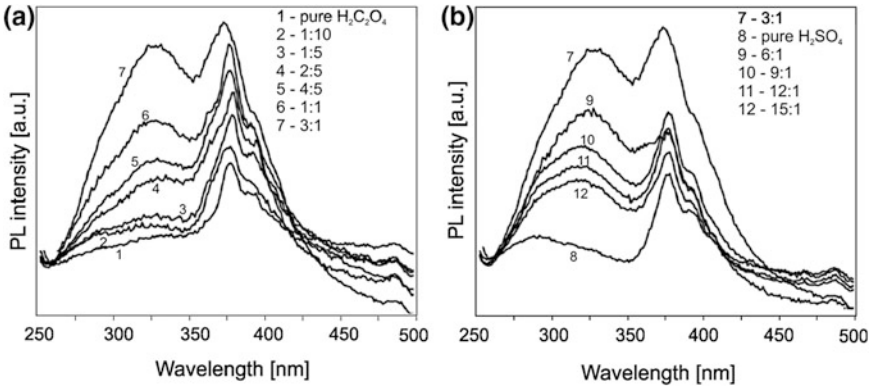

Fig. 8.18 Comparison of PL spectra for AAO obtained in the mixture of 0.3 M sulfuric acid and 0.3 M oxalic acid: **a** *(1)* pure oxalic acid, *(2)* 1:10, *(3)* 1:5, *(4)* 2:5, *(5)* 4:5, *(6)* 1:1, *(7)* 3:1, **b** *(8)* pure sulfuric acid, *(9)* 6:1, *(10)* 9:1, *(11)* 12:1, *(12)* 15:1 the volume ratio of sulfuric to oxalic acid. Reprinted with permission from [149]

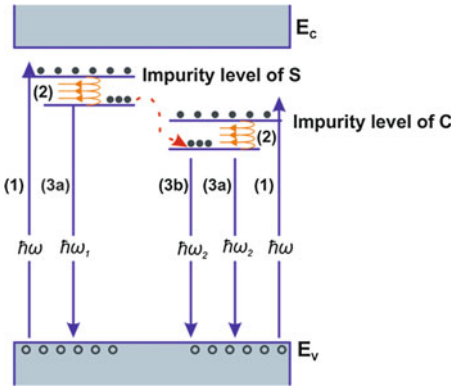

Fig. 8.19 Energy transfer mechanism in porous alumina with embedded SO_4^{2-} and $C_2O_4^{2-}$ ions. Reprinted with permission from [149]

Table 8.1 The effect of electrolyte used for anodization on the position of the maxima of the peaks in the PL spectrum

Electrolyte	Anodization conditions	PL peaks position	Type of optical centers	References
0.3 M chromic acid	20–50 V, 50 °C	255 nm, 350 nm	Embedded chromate ions	[121]
0.01 M citric acid	15 mA cm^{-2}, 17 °C	425 nm	F^+	[99]
		460 nm	F	
1 wt% citric acid	Room temperature	550–580 nm	F^+	[137]
0.8 M malonic acid	80 V, 18 °C	440–450 nm	Embedded malonate ions	[118]
0.8 M malonic acid	6 mA cm^{-2}, 18 °C	438 nm	Embedded malonate ions	[134]
		501 nm	F^{2+}	
0.3 M sulfamic acid	30 V, 24 °C	460 nm	F	[98]
0.4 M tartaric acid	6 mA cm^{-2}, 18 °C	440–450 nm	Embedded tartarate ions	[143]
2 wt% sulfuric acid + 0.02 M Cu^{2+} + 0.02 M EDTA	15–21 V, 15 °C	280 nm	Embedded Cu-EDTA anionic species	[122]
		320 nm		
		>360 nm	F	

peak in the PL spectrum for the AAO obtained in the mixture of sulfuric and oxalic acids depends mainly on the concentration of oxalate ions [133]. Changes in the content of SO_4^{2-} anions can, however, cause a shift of the peak towards lower wavelengths (410 nm → 345 nm). When the concentration of the sulfate anions remains constant, a decrease of peak intensity with increasing concentration of $C_2O_4^{2-}$ ions is observed [133].

Although the most commonly used acids for the anodization are sulfuric, oxalic and phosphoric acid, scientists have tested other electrolytes as well, for example: chromic acid [121], citric acid [99, 137], malonic acid [118, 134], sulfamic acid

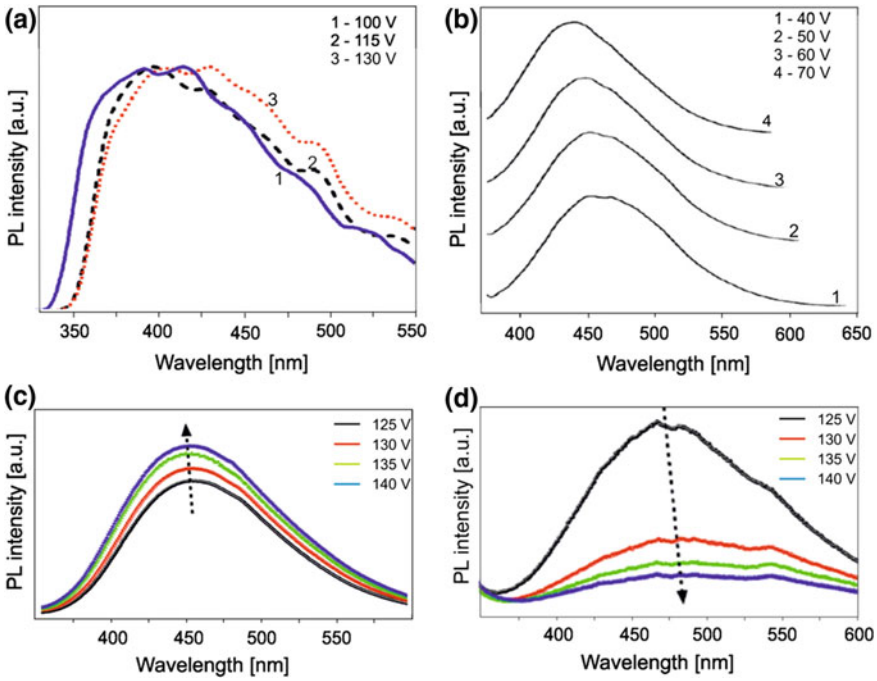

Fig. 8.20 The influence of anodizing potential on the peak position in the PL spectrum for AAO obtained by mild anodization in: 85 wt % H_3PO_4, 1 °C (**a**), 0.3 M $H_2C_2O_4$, 1 °C (**b**), and by hard anodization in: 0.3 M oxalic acid (**c**), 1.7 M malonic acid (**d**). Reprinted with permission from [150] (**a**), [138] (**b**), and [142] (**c** and **d**)

[98], tartaric acid [143], electrolyte containing the Cu-EDTA complex [122], etc. Clearly, the AAOs obtained in all these electrolytes exhibit differences in the PL spectra especially in peak positions (see Table 8.1). This is mainly related with differences in the electronic structure of embedded ions.

It has been proven that the anodization potential greatly affects the position of the peaks in the PL spectrum and, thereby, the type and arrangement of optically active centers in the porous oxide structure. Nourmohammadi et al. [150] showed that during anodization performed in phosphoric acid, an increase in anodization potential up to 115 V causes a slight red shift of the PL peak (Fig. 8.20a). The increase in applied anodizing potential results in the formation of optically active defects which subband gaps are in the range of visible light. Deconvolution of the PL spectra showed the presence of the five components [150]. Similar studies were performed for the AAOs obtained in oxalic acid [138]. Figure 8.20b shows the effect of potential used for anodization in oxalic acid on the peak position in the PL spectra. A significant shift towards the longer wavelengths (similarly to that observed for AAO membranes formed in phosphoric acid) was observed with increasing anodization potential (40 → 70 V). Despite the large number of published papers on photoluminescence properties of AAO obtained in sulfuric acid,

there is no conclusive research on the effect of anodizing potential on the PL peak position. It should be noted, that the potential of anodization influences not only the geometric parameters of AAO, but also the thickness of resulting oxide and, thus, the amount of incorporated acid ions from the electrolyte. Santos et al. conducted a study on the effect of anodizing potential on optical properties of the AAO films formed by hard anodization of aluminum in oxalic acid and malonic acid [142]. They showed that for oxalic acid with increasing potential of hard anodization from 125 to 140 V (Fig. 8.20c) a slight increase in the intensity of the PL peak can be observed [142]. For the AAOs formed in malonic acid at the same potential range, the decrease in the peak intensity and the red shift of peak were observed with increasing anodization potential (Fig. 8.20d).

Another parameter that significantly affects the growth of oxide during anodization and, consequently, PL properties of AAO is temperature. Green et al. have demonstrated that during anodization in oxalic acid the increase in temperature from 2 to 20 °C results in a 10 nm red shift [66]. As mentioned previously, the photoluminescence properties of AAO are affected by the presence of oxygen vacancies and acid ions impurities. As shown by Stępniowski et al., the lower the anodization temperature the less ions from the electrolyte are incorporated into the oxide structure [121]. It can therefore be concluded that for the AAO films obtained at low temperatures the predominant optical centers are single ionized vacancies (F^+). Increasing anodizing temperature leads to an increase in current density during anodization process, and thus enhances the ability of oxygen vacancies to capture electrons (conversion of optical centers from F^+ on F). Therefore, a higher density of F centers should be expected for higher anodizing temperature (lower energy PL peak) [66].

8.4.2.4 Thickness of the Oxide Layer

The thickness of oxide layer obtained by anodization depends directly on the total amount of charge involved in the electrochemical process. Consequently, for a steady-state conditions of anodization, the thickness of the porous oxide layer increases with increasing anodization time [141]. The thickness of the oxide layer has an obvious impact on the shape and intensity of the PL spectrum. For the AAOs obtained in phosphoric acid (t = 11–40 h), Novrmohammadi et al. found that the thicker the alumina layer the widen the whole emission PL spectrum is (Fig. 8.21a) [150]. Moreover, a peak shift toward shorter wavelengths was observed. According to the model shown in Fig. 8.15, the distribution of the F and F^+ optical centers is not uniform in the oxide structure. Thus, the longer the anodization process and, consequently, the thicker the resulting oxide layer, the greater the possibility of creation new point defects. It is worth mentioning that applying a potential to the electrode for a long period of time may cause conversion of the F^+ centers into the neutral F centers by trapping electrons from negatively charged electrolyte anions.

The effect of anodization time and hence thickness of the oxide layer on PL of AAOs formed in oxalic acid was studied by Chen et al. [124]. It was found that for anodizations shorter than 15 min (oxide thickness of about 850 nm) a small red shift

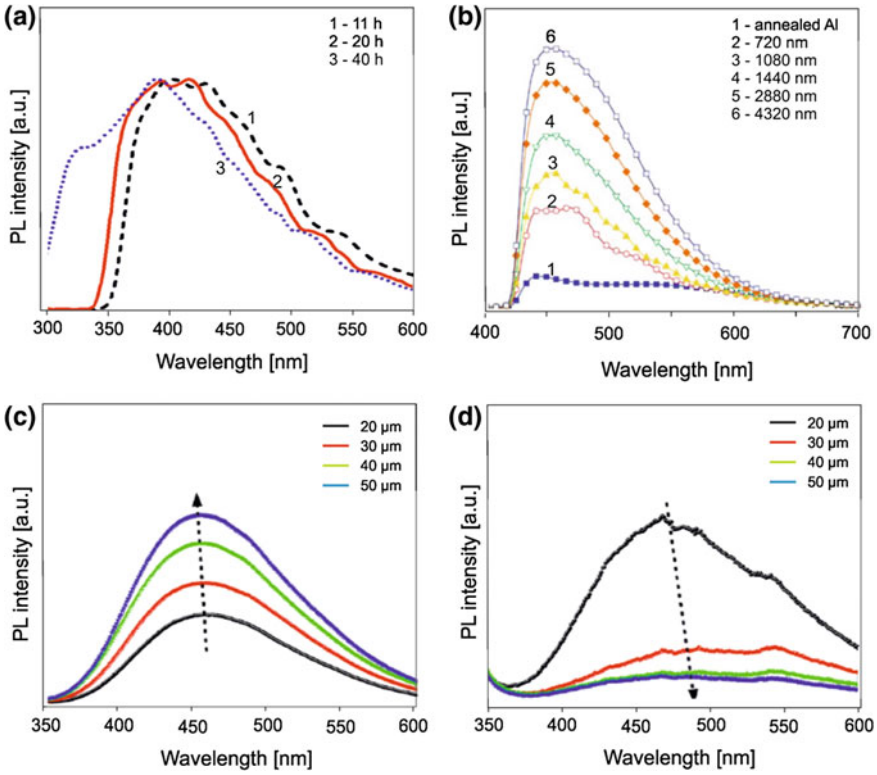

Fig. 8.21 The influence of anodizing time on PL spectra of AAO obtained by mild anodization in: phosphoric acid (85 wt%, 1 °C, 100 V) (**a**), oxalic acid (0.3 M, 20 °C, 40 V) (**b**), or by hard anodization in: oxalic acid (0.3 M, 0 °C, 120–140 V) (**c**), and malonic acid (1.7 M, 0 °C, 120–140 V) (**d**). Reprinted with permission from [150] (**a**), [124] (**b**), and [142] (**c** and **d**)

of the PL peak occurs (Fig. 8.21b). On the other hand, for anodizations longer than 15 min the peak shift is not observed, but the intensity of PL peak gradually increases with increasing oxide thickness [124]. The most plausible explanation for these results is increasing number of optical centers within the increased depth of the pores. More than this, for the prolonged anodization AAO is longer exposed for oxalate anions, and higher concentration of oxalate impurities can be incorporated in the oxide structure. The results presented by Chen et al. are consistent with the findings of other researchers who studied the effect of the membrane thickness on the PL of AAO fabricated in oxalic acid under the mild anodization [151] and hard anodization (Fig. 8.21c) [142] conditions.

Surprisingly, for the AAOs formed by hard anodization in malonic acid the opposite correlation between the oxide thickness and the PL peak intensity was observed. The thicker the AAO layer, the lower PL peak intensity (Fig. 8.21d). In addition, upon increase of the oxide layer a red shift (longer wavelengths) in the PL peak position was reported.

8.4.2.5 Etching and Widening of Pores

The characteristic parameters of porous AAO are affected not only by the conditions of anodization, but also by post-anodizing treatment such as etching and widening of pores [4, 140]. The pore etching process changes significantly the geometric parameters of the AAO and consequently the PL spectra [94]. Liu et al. studied the effect of pore etching in 5 % H_3PO_4 on the PL properties of AAO formed in oxalic acid [94]. It was found that the applied etching procedure increases the pore diameter of AAO from about 40 to nearly 100 nm. With increasing pore diameter of AAO (increasing porosity) an increase in the intensity of the PL peak was noticed (Fig. 8.22a). The observed increase in the peak intensity, by a factor of 1/3, was attributed to better access to the F^+ centers in the walls of enlarged pores. A slight blue shift in the peak position was also observed. Stojadinovic et al. studied

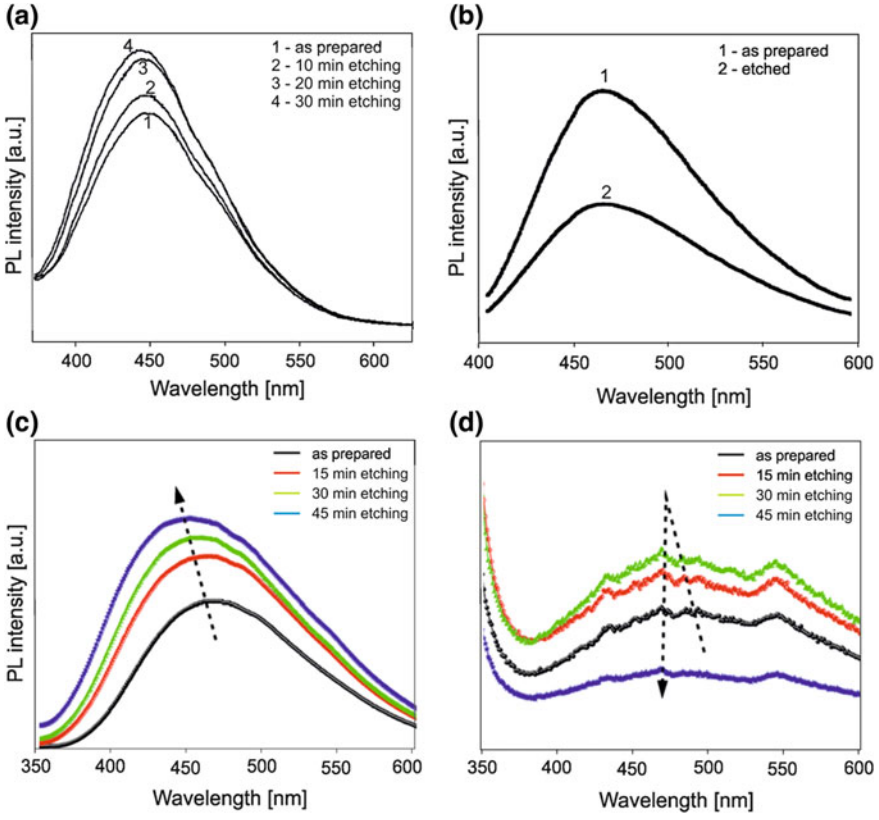

Fig. 8.22 The influence of etching time on PL spectra of AAO obtained by mild anodization in oxalic acid (0.3 M, 40 V) (**a**), sulfamic acid (0.3 M, 30 V) (**b**) and by hard anodization in oxalic acid (0.3 M, 120–140 V) (**c**) and malonic acid (1.7 M, 120–140 V) (**d**) . Reprinted with permission from [94] (**a**), [98] (**b**), and [142] (**c** and **d**)

the effect of short-time etching on the intensity and peak position of photoluminescence spectra for AAOs obtained through anodization in sulfamic acid [98]. It was shown that the chemical etching results in the removal of the thin oxide layer of the pore walls (outer layer), and consequently reduction of the peak intensity in the PL spectrum was observed (Fig. 8.22b). Stojadinovic et al. postulated that the intensity of PL band decreases due to the removal of adsorbed water on pore walls. The similar effect of pore etching on PL was reported for AAOs formed in sulfuric acid [115].

For the AAOs obtained by hard anodization in oxalic acid, a slight blue shift in the peak position and noticeable linear increase of the PL peak intensity with the pore diameter were reported (Fig. 8.22c) [142]. These results are in agreement with the PL data obtained for AAOs formed by mild anodization performed in oxalic acid. When porous anodic oxide was formed by hard anodization in malonic acid, a complex effect of pore etching on PL spectra was observed (Fig. 8.22d) [142]. It was shown that the intensity of PL peak linearly increases until 10 min of pore widening (pore diameter of 111 nm), and then abruptly decreases between 10 and 15 min (pore diameter of 116 nm).

8.4.2.6 Postannealing

Numerous research on annealing the AAO films in the context of their photoluminescence properties have been made in order to determine the origin and type of optical centers existing in the porous oxide structure. In 1999, Du et al. observed that the PL intensity of AAO formed in sulfuric and oxalic acid can be enhanced by a heat treatment [123]. For the AAO membranes obtained in sulfuric and oxalic acid, the intensity of the PL band increases with the annealing temperature up to 400 and 500 °C, respectively [64, 83, 104, 123, 144, 152, 153]. The intensity of the PL peak for the AAOs formed in sulfamic acid increases with annealing temperature, and at about 300 °C reaches its maximum value, followed by the PL intensity decrease with a further temperature increase [98]. The increase in the PL intensity was assigned to the formation of new oxygen vacancies in the newly formed (during annealing) aluminum oxide by the reaction of remaining aluminum with oxygen diffusing from air and/or located in the AAO layer. Above the annealing temperature of 500 °C for the AAO formed in oxalic acid and 400 °C for sulfuric acid, the intensity of the peaks in the PL spectrum decrease. Du et al. attributed this effect to the enhanced rate of oxygen vacancy annihilation compared to the rate of their formation [123]. As it was shown by Sun et al. and then proven by other investigators, dehydration, decomposition of embedded anion impurities, and amorphous-crystalline phase transition occur during annealing of AAO formed in oxalic acid [77, 85, 95, 98, 100, 153, 154]. Figure 8.23 shows typical thermogravimetric analysis (TG) and differential thermal analysis (DTA) curves for the AAOs obtained through anodization in 0.3 M oxalic acid [154]. The weight loss observed in the Sect. 8.1 (up to 100 °C) is caused by the desorption of weakly bound water from the AAO surface and pore walls [153, 154]. At temperatures

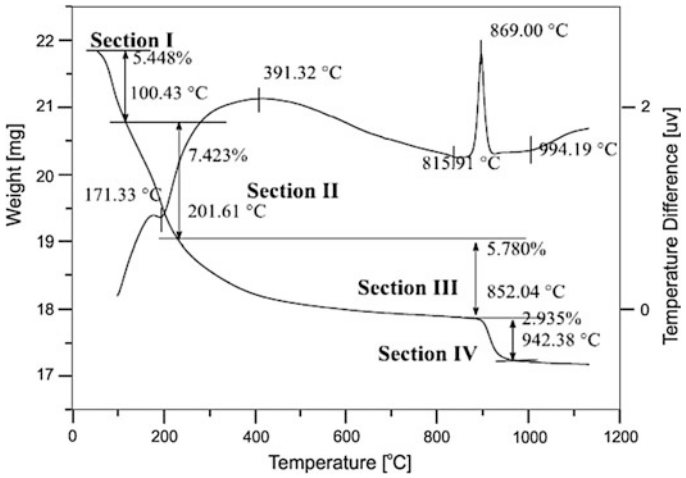

Fig. 8.23 TG and DTA curves for the AAO layer obtained by anodization in 0.3 M oxalic acid at 40 V. Reprinted with permission from [154]

higher than 171 °C (Sect. 8.2), the removal of structural water from hydroxide and oxy-hydroxide of aluminum is observed. In the Sect. 8.3, from 200 to 852 °C, the decomposition of oxalic impurities takes place. It is believed that the decomposition of metal oxalates, according to the reaction (8.3) [155], occurs at temperatures above 350 °C [153].

$$(COOH)_2 \xrightarrow{T} CO_2 + CO + H_2O \tag{8.3}$$

According to Mukhurov et al., CO_2 is not chemically bound to oxide but only trapped in the crystal structure [146]. This assumption was confirmed by the IR spectra analysis for the annealed AAO film. The progressive decomposition of embedded oxalate ions (above 500 °C), and continuous ordering of Al and O atoms in the crystal structure result in immobilization of CO_2 in the oxide lattice (aluminum–carboxylate complex) [109, 147] and lead to decrease in the intensity of PL spectra. In the Sect. 8.4, the phase transitions to γ–Al_2O_3 (above 800 °C) and then to α-Al_2O_3 (at 1100 °C) are observed [104]. During the former transformation, the –OH groups in crystalline structure of γ–Al_2O_3 are lost [104, 146, 153]. At the temperature of about 930 °C, the decompositions of aluminum carbonate ($Al_2(CO_3)_3$) and $Al_2(C_2O_4)_3$ took place [153, 154]. Typical PL spectra of the AAOs annealed at different temperatures are shown in Fig. 8.24 [154].

A significant influence of incorporated ions on photoluminescence properties of the AAOs formed by anodization in malonic acid and tartaric acid was reported by Vrublevsky et al. (Fig. 8.25) [134, 143]. Similarly to the AAOs obtained in oxalic acid, the AAOs formed in malonic acid and tartaric acid exhibit a substantial change in the intensity of PL peaks with annealing temperature. For temperatures higher

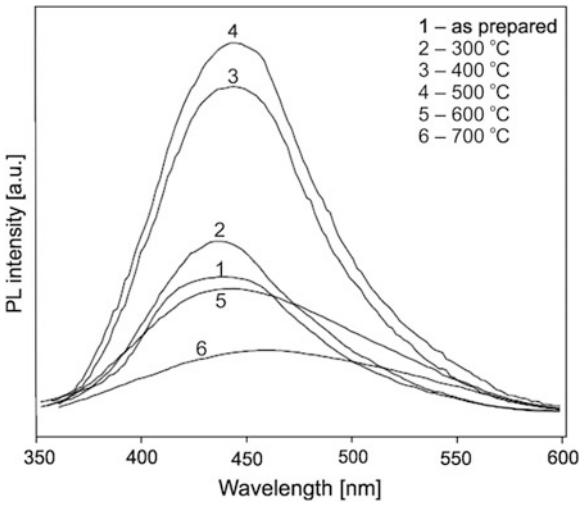

Fig. 8.24 PL spectra for AAOs obtained by anodization in 0.3 M $H_2C_2O_4$ at 40 V and annealed at different temperatures. Reprinted with permission from [154]

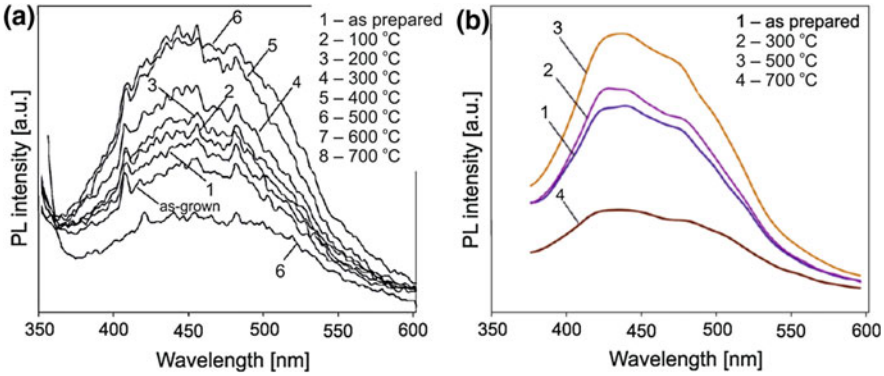

Fig. 8.25 PL spectra for AAOs obtained through anodization in malonic acid (0.8 M, 6 mA cm^{-2}, 18 °C) (**a**), tartaric acid (0.4 M, 6 mA cm^{-2}, 18 °C) (**b**) and then annealed at different temperatures. **a** and **b** reprinted with permission from [134, 143], respectively

than 600 °C, a drastic decrease in the intensity of the PL peak, due to the decomposition of organic ions to CO_2, is observed [118, 143]. Deconvolution of the PL spectra obtained for the AAOs formed in malonic acid and annealed at temperatures not exceeding 600 °C indicated two peaks centered at 437 and 502 nm. Vrublevsky et al. proposed that the peak at 437 nm originates from the optical centers with incorporated malonate ions, which decompose at higher temperatures, while the peak observed at 502 nm comes from the defects in the oxide structure caused by a lattice mismatch and difference in the coefficients of thermal expansion between alumina and incorporated acid impurities [134].

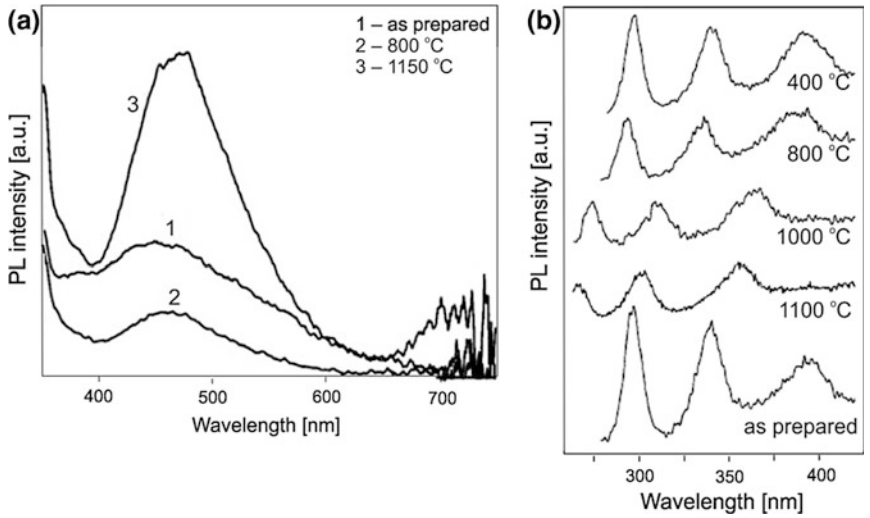

Fig. 8.26 The influence of annealing temperature on the PL spectra of porous alumina obtained through anodization in sulfuric acid of the aluminum foil (**a**) and 400 nm Al film on Si (**b**). **a** and **b** reprinted with permission from [85, 156], respectively

For the AAO films obtained in sulfuric acid, a different effect of the annealing temperature (in the range 800–1150 °C) on the PL intensity was observed (Fig. 8.26a) [85]. After annealing at 800 °C, the less intense PL peak of the AAO compared to the spectrum of the as-prepared AAO was observed. When the annealing temperature was raised to 1150 °C a sharp increase in PL intensity was detected. This kind of variation in the photoluminescence intensity with thermal processing was attributed to (i) partial oxidation of the AAO surface by atmospheric oxygen at 800 °C resulting in a reduction in the density of divacancies and, consequently, decreasing PL intensity, and (ii) thermal decomposition of incorporated sulfate ions, occurring at temperatures between 950–1230 °C, and resulting in the removal of decomposition products from the oxide structure what increases the concentration of oxygen vacancies in the oxide [85]. The presence of decomposition products, mainly SO_2 and O_2, was confirmed by IR analyses. It is worth noting that the position of the PL peak does not change with annealing temperature. In analogy to the PL spectra observed for sapphire, Mukhurov et al.[85] proposed that the photoluminescence properties of the AAO obtained through anodization in sulfuric acid are affected mostly by concentration and distribution of oxygen vacancies F_2^+, F_2, F_2^{2+}, while the effect of embedded SO_4^{2-} ions is negligible.

The different results on the annealing temperature influence on the PL of AAOs formed in sulfuric acid was reported by Wu et al. [156]. It was found that the porous thin AAO layers on p-Si substrate show three strong PL bands at 295, 340, and 395 nm. A blue shift of these peaks and decrease in their intensity were observed with increasing annealing temperature (Fig. 8.26b) [156]. It was also shown that the

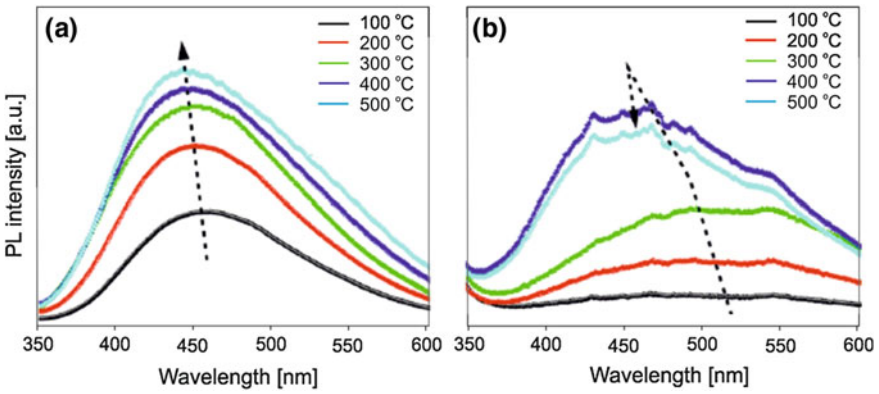

Fig. 8.27 The influence of annealing temperature on the PL spectra of porous alumina obtained through hard anodization in oxalic acid (0.3 M, 120–140 V) (**a**) and malonic acid (1.7 M, 120–140 V) (**b**). Reprinted with permission from [142]

heat-treatment time and the type of gas used for this process affect the intensity of the PL peaks. According to Wu et al., the photoluminescence activity of the AAO on Si substrate depends mainly on the presence of oxygen vacancies F^+.

Figure 8.27 shows the PL spectra of AAO samples formed in oxalic acid and malonic acid by hard anodization and annealed at different temperatures. Similarly to the PL spectra for the AAOs anodized under the mild anodization conditions in oxalic acid, an increase in the PL peak intensity and a slight blue shift of the peak position with annealing temperature were observed [142]. For the AAO obtained in malonic acid by hard anodization, the intensity of the PL peak gradually increases up to 400 °C, and then decreases at 500 °C. The changes in the PL peak intensity are related to the thermal decomposition of malonic and oxalic acid impurities located at the pore walls (i.e. outer layer). In both types of AAOs, the PL peak is shifted towards shorter wavelengths as a result of the decomposition of superficial impurities at low temperatures, which allows increase the light emission from the outer layer [142].

8.4.3 Applications of AAO Photoluminescence

Photoluminescence spectra of the porous alumina is stable in time and therefore it is not necessary to cover AAO films with protecting layers. PL spectra of AAO may change due to alteration of geometric parameters, modification of the oxide surface or filling the pores with some substances. Last type of modification has been used in optical biosensors. Due to the Fabry-Pérot effect in the PL spectrum of AAO modified with organic particles, oscillations appear. These oscillations can be converted into a barcode (Fig. 8.28a). The more oscillations in the PL spectrum the

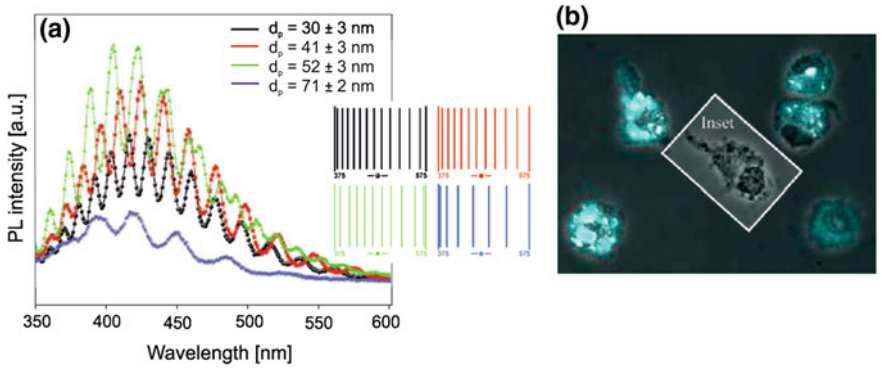

Fig. 8.28 Examples of practical application of photoluminescent properties of AAO in biological barcodes (**a**) and fluorescent biological labeling (**b**). **a** and **b** reprinted with permission from [157, 161], respectively

more strokes in the code, so it is possible to increase the sensitivity of the sensor to the determined molecule [157]. With a large stability, sensitivity and biocompatibility, porous AAO was applied in the determination of DNA [158], glucose [157, 159], organic dyes [157, 160], enzymes [157] or amino acid [159]. The photoluminescence properties of AAO also allow use it as a fluorescent biological label for i.e. dendritic cells (Fig. 8.28b) [161]. This is possible by controlling the distribution of the oxygen vacancies and alumina nanoparticles in a porous film. The optical properties of AAO enable the use of it as color display decorations or in anti-counterfeiting technology [86].

8.5 Photonic Crystals and Bragg Reflectors

Photonic crystals are structures in which refractive index varies periodically in space. This variation of refractive index is obtained by combining at least two different materials/dielectrics with different refractive indices. There are three groups of photonic crystals-1D, 2D, and 3D, depending on how many spatial directions are involved in refractive index changes. The incident light beam on the photonic crystal will be scattered because of the refractive index variation in the structure. As long as the wavelength of the electromagnetic radiation is much larger than the lattice constant of the photonic crystal, the structure behaves as an effective medium. However, if the wavelength is comparable with the periodicity of the photonic crystal, Bragg scattering occurs and light beam with a particular frequency (or wavelength) that radiates the crystal could be totally reflected. Similar to the X-ray diffraction, the Bragg scattering can be interpreted as constructive interference of scattered waves, which are emitted by parallel lattice planes of the photonic crystal. The energy range corresponding to frequencies at which the light is reflected (not allowed to be transmitted) is called the photonic band gap.

In one-dimensional photonic crystals, periodic modulation of the permeability occurs in two directions [162]. Such structures can be used as the Bragg grating, antireflection coatings, and Bragg stacks [44]. It was shown that porous one-dimensional photonic crystals or Bragg stacks can be fabricated by periodic altering the potential during the anodization process [163]. Two-dimensional photonic crystals have the periodic permeability in two directions while the third direction is uniform. Therefore, 2D photonic crystals can have a large variety of configurations. An interesting example of 2D photonic crystals is porous silicon [164], and porous alumina [165, 166]. Three-dimensional photonic crystals have periodic permeability in three directions, hence the number of possible configurations is very high [167]. 3D photonic crystals are found in nature, for example opal and diamond [168].

The ordered nanoporous AAO films are intrinsically 2D photonic crystals with photonic band gaps centered at wavelengths in the range of near infrared (IR) and visible light [169]. A great advantage of this type of photonic crystals is almost a non-limited depth of pores and, consequently, large aspect ratio. For photonic crystal applications, porous alumina with a perfect nanopore order, is usually fabricated by one-step anodizing of the pre-patterned Al foil. There are a number of reports on 2D photonic band gap crystals made of AAO with a typical internal pore structure i.e. parallel pores with uniform diameter along their depth [170–178]. It was shown that AAO photonic crystals exhibit a photonic band gap between 600 and 1350 nm. The influence of the pore diameter of AAO with 500 or 100 nm intervals on the band gap position was investigated in detail [174]. On the other hand, it was reported that with decreasing interpore distance of the AAO photonic crystal a red shift in the transmission dip is observed [170, 172].

A number of interesting observations have been recently made on birefringence occurring in 2D photonic crystals based on AAO layers. The birefringence is often defined as a difference in the normal and tangential refraction indices or in other words as the maximum difference between refractive indices exhibited by the material. It was found that quasi-ordered porous anodic aluminum oxide has anisotropy on the scale of the wavelength of light, and therefore shows birefringence in the visible region [179–182]. The effect of pore diameter of the AAO film on refractive index and birefringence was detailed examined by Lutich et al. [183]. It was demonstrated that AAO films could offer a wide range of refractive index and birefringence values for optical device applications. It was shown for the low porosity range that the birefringence increases (29–39 %), with the porosity increase from 0.033 to 0.062 [183]. These results were confirmed by Gong et al. who observed that for the increasing pore diameter in the range of about 13–37 nm, the birefringence of the AAOs increases from 0.02 to 0.06 [65].

Photonic crystals made of anodic alumina with periodically branched nanopores were prepared by adjusting the anodizing cell voltage periodically during electrochemical oxidation and followed by chemical etching [30]. To enlarge the main and branched channels the samples were etched in a phosphoric acid solution for an appropriate time. Figure 8.29 shows the optical photograph of porous alumina membranes before and after chemical etching for different times. Figure 8.29a shows that the AAO sample after anodization and before chemical etching (sample 1) is

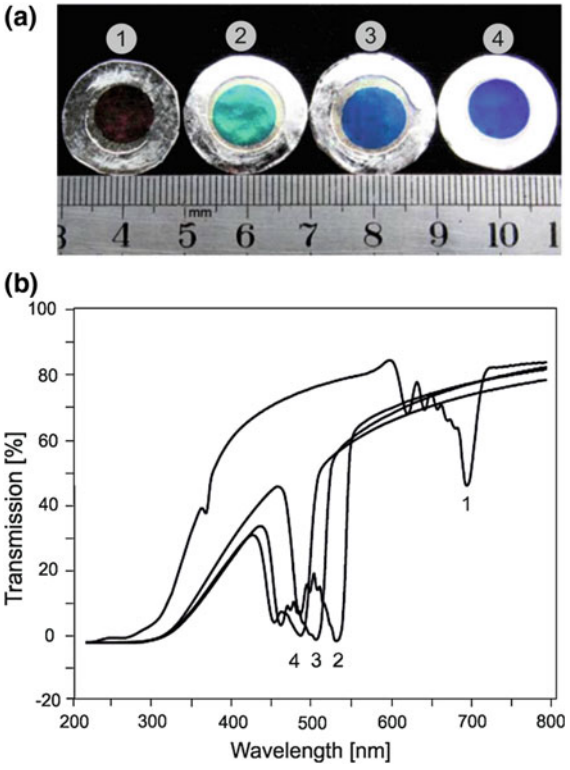

Fig. 8.29 Optical photograph of porous anodic alumina membranes (*1*) before, and after chemical etching for: (*2*) 15 min, (*3*) 18 min and (*4*) 20 min (**a**), and the corresponding optical transmission spectra (**b**). Reprinted with permission from [30]

almost transparent, while the samples after chemical etching are green (sample 2) and blue (samples 3 and 4). The bright colors come from optical reflections from the AAO membranes which occur at wavelengths corresponding to the forbidden photonic band gap region. The observed effect of the chemical etching duration on the color of AAO samples may originate from the different sizes pores (different effective dielectric constants). The existence of photonic band gap in those porous membranes is also confirmed by the transmission spectra recorded before and after chemical etching for 15, 18, and 20 min (Fig. 8.29b). For wavelengths lower than 400 nm, a low transmission was observed for all samples. This behavior was caused by a strong reflection and absorption of alumina. The transmission spectrum of the sample without chemical etching (sample 1) shows only a weak peak at 700 nm. As the etching time was prolonged (samples 2–4), a gradual blue shift in position of the peak was observed. The intensity of transmission light decreases with increasing etching time because of the increasing porosity of AAO. The similar results for photonic crystals made of AAO with branched pores were reported by Hu et al. [184].

In a similar manner using cyclic anodization with a slightly modified voltage signal (see Fig. 8.5), the photonic crystals based on AAOs were synthesized by Su et al. [35]. In order to study if the photonic band gaps of the fabricated photonic crystals based on the AAOs are tunable and controllable, the transmission spectra

were recorded for the samples with different thicknesses (different times, t_3) of the branched channel layer (layer II). It was found that the photonic band gaps of the AAO photonic crystals are tunable and controllable in the wavelength range from 350 to 1330 nm. In addition, it was shown that the peak shifts to longer wavelengths when the thickness of layer II increases.

One of the most remarkable accomplishments of the fabrication of photonic crystals with very narrow photonic band gaps located in the near infrared region was reported by Shang et al. [185]. Using the cyclic anodization with a compensation potential mode, they prepared the photonic crystals based on AAOs with narrow photonic band gaps which the full width at half maximum was only 30 nm. The transmission spectra showed that the AAO-based photonic crystal is transparent (about 90 %) in the region out of the band gap and reflects the transmitted light only in the center of the band gap at 1150 nm. This photonic crystal was used also as a sensor for detection of ethanol vapor [185]. Recently, the same research group reported fabrication of the AAO-based photonic crystals with extremely narrow (full width at half maximum less than 10 nm) photonic band gaps which centers were located at 440 and 652 nm [186]. It is worth mentioning that the observed asymmetric line-shape profiles of the photonic band gaps were attributed to Fano resonance between the photonic band gap state of photonic crystal and continuum scattering state of the porous structure [186].

Distributed Bragg reflectors are one-dimensional photonic structures which can be considered as a stack of thin layers of transparent dielectric with alternating high and low refractive indices. Such layered structures exhibit a high reflectance similar to metallic mirrors [187]. As number of alternating layers increases in the Bragg reflector, the stop band enlarges and sharpens [188]. The spectral width of the reflected wavelength ($d\lambda_{Bragg}$) (at full width at half maximum) is proportional to the reflected wavelength (λ_{Bragg}) [189] and decreases when the number stacks (N) increases according to

$$d\lambda_{Bragg} = \frac{2\lambda_{Bragg}}{N} \tag{8.4}$$

Furthermore, the intensity of the reflected light depends on the number of stacks (N), and the low (n_L) and high (n_H) refractive indices of the alternating layers [190].

The cyclic anodization technique was also used to synthesize distributed Bragg reflectors based on nanoporous anodic alumina [34]. The cyclic anodization approach results in an in-depth modulation of the pore geometry and, consequently, the refractive index. Four different potential profiles (potential wave structures) in which the amount of charge passing in stage b (horizontal upper line in the voltage profile) was different and varied from 0 to 4 °C (Fig. 8.30a). Rahman et al. studied the effect of the applied potential profile and pore-widening treatment on photonic band gaps. The transmittance spectra for the potential profiles with the passing charge of 1 C is presented in Fig. 8.30b.

As can be seen, the transmittance decreases and is blue shifted when the pore-widening time increases. It can be ascribed to increasing porosity of AAO and to scattering losses produced by the irregular interfaces between cycles [34].

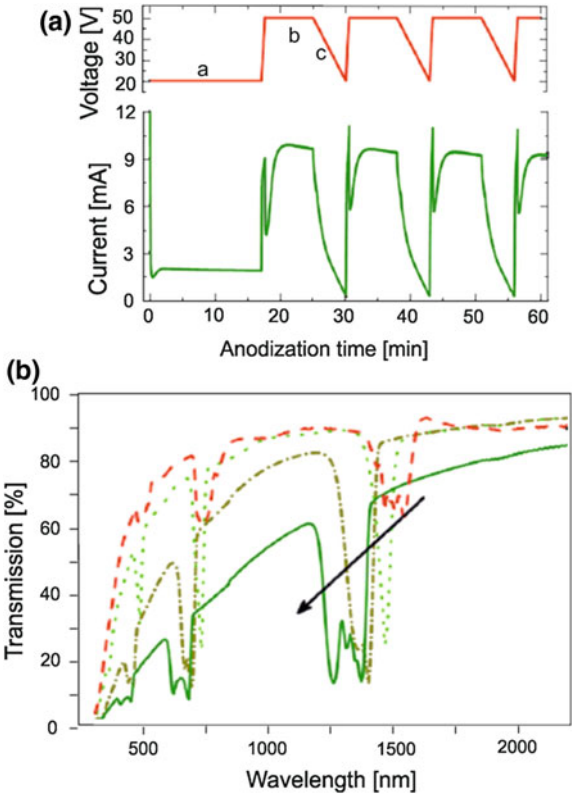

Fig. 8.30 Applied voltage profiles (*red*) and measured current transients (*green*) (**a**) and transmittance spectra (**b**) of the sample with passing charge of 1 C for different pore widening times. Reprinted with permission from [34]

Using cyclic anodizations performed at different temperatures ranging from 6 to 18 °C, Zheng et al. synthesized the AAO-based Bragg reflectors with the transmission peak covering almost any wavelength range of the visible light region [50]. It was found that as anodizing temperature increases, a red shift in the transmission peak is observed. On the other hand, the same researchers demonstrated that by adjusting the anodizing potential waveform applied during cyclic anodization, the first Bragg condition peak of the AAO-based Bragg reflectors could be modulated from 727 to 1200 nm [49].

A remarkable distributed Bragg reflector based on nanoporous anodic aluminum oxide and fabricated by pulse anodization in a sulfuric acid solution was recently presented by Sulka and Hnida [44]. Taking into account the fact that pore diameter of AAO, can be tuned by the applied potential under a constant potential regime (or current density under a constant current regime), the authors used pulse anodization of aluminum with periodic pulses in alternating regimes of mild (MA) and hard anodizations (HA) for the synthesis of the AAO with modulated pore diameter. It was shown that the designed AAO structure consists of alternating high and low refractive index layers and behaves as a distributed Bragg mirror reflecting light in two different ranges of wavelength (Fig. 8.31). Such behavior is extremely

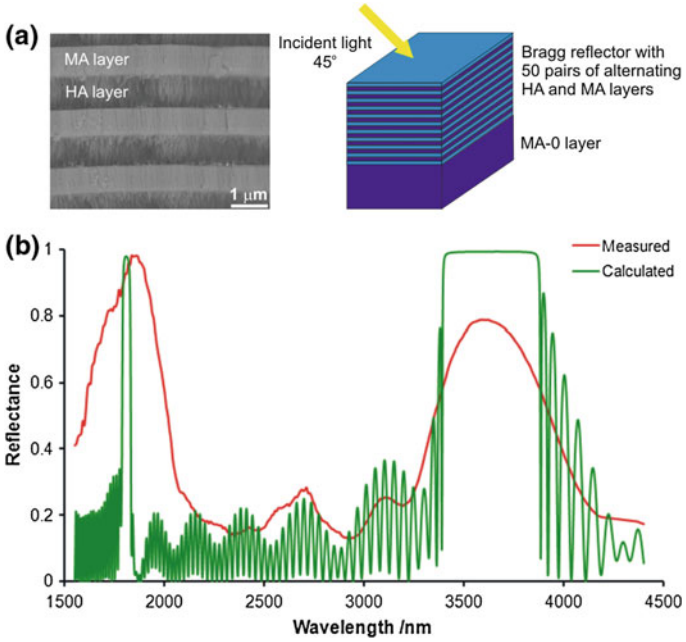

Fig. 8.31 SEM cross-sectional view and schematic diagram of the Bragg reflector with 50 pairs of alternating HA and MA layers (**a**) together with the measured and calculated reflectance spectra of the designed mirror (**b**). The alternating high (MA) and low (HA) index layers have thicknesses of 750 and 800 nm, respectively. The thickness of the initial MA layer (MA-0 layer) was 7500 nm. After [44]

important in optical communication lines where two separate spectral bands of high reflectivity in the infrared region are desired.

Guo et al. [188] studied influence of number of periods in the Bragg stack on the transmittance spectra. The AAO-based Bragg reflectors were formed by pulse anodization at the constant current regime. By periodical modulation of the current density they precisely controlled the porosity and thickness of each layer in the AAO structure. They showed that the reflected light intensity increases, and its position is blue shifted when in number of alternating layers in the Bragg stack increases.

8.6 Chemical Modification of AAO

The porous anodic alumina films are optically transparent, however, the optical properties of AAO can be easily modified by the presence of different guest molecules/materials, i.e. metallic and inorganic nanoparticles, metallic and polymer nanowires, xerogels and other compounds. It is also possible to deposit metallic or inorganic thin layers on the surface of AAO films in order to change their UV-Vis

and photoluminescence spectra. The inorganic species immobilized on the surface, incorporated or embedded into the oxide structure can also modify the optical properties of AAO. The AAO with organic substances adsorbed on the surface of pore walls can be used for optical sensing applications [128, 191–193].

The AAO membranes are used not only as templates for the synthesis nano-sized materials but also, in the presence of an electron accepting guest organic molecules, as a convenient light-energy collecting materials for both energy and electron transport from AAO to nanopore-embedded inorganic quantum dots and nanowires. The mechanism of the ultrafast excited state deactivation from the host AAO to the guest molecules and inorganic nanostructures can be associated with charge transfer, Förster energy transfer, and nano-surface energy transfer [194]. Optical properties of the AAO with different guest molecules and materials have been extensively studied in recent years, therefore, only the most important examples will be presented here.

8.6.1 Nanowires in AAO

8.6.1.1 Metal Nanowires in AAO

In recent years, many researches took an effort to thoroughly investigate the optical properties of AAO films with metallic nanowires (NWs) embedded inside the pores. In this regard many AAO-NWs composites based on deposited metals such as Ag [33, 195–202], Au [200, 202–207], Co [110, 208], Cu [209], Fe [210], Ni [107–109, 211, 212], and Sn [213] were investigated. In addition, the AAO composites with multilayered Au/Ag nanowires [202] and heterojunction nanowires such as Au nanowires with a thin top layer of Ag [199] or Ag nanowires with a thin AgI segment [214] were also fabricated.

It is widely recognized that as-grown anodic oxide films on aluminum are optically transparent. For practical applications, therefore, the process of anodization is followed by AC electrodeposition of metallic layers into the AAO nanopores (electrolytic coloring). Due to the fact, that metallic NWs deposited in the AAO exhibit distinctive reflection peaks in the UV-Vis, it is possible to investigate optical properties of such materials by UV-Vis spectroscopy. Structural colors originate from the constructive interference among reflecting light having different optical pathlengths, namely the light reflected from the air/AAO interface and the light reflected from the air/metal or AAO/Al interface (Fig. 8.32) [107, 109]. It is worth mentioning that different reflection spectra are observed when the light is incident on the bottom side of the AAO-NWs composite films [33]. In case when the light is incident on the bottom side of the composite film, the beam is considerably attenuated during propagation through the metallic (e.g., Ag) layer. When the reduced diffraction light of the porous alumina propagates through the Ag layer again, the diffraction is suppressed seriously. The deposited metal layer enhances the color saturation of the composite film. It is attributed to partial adsorption of the

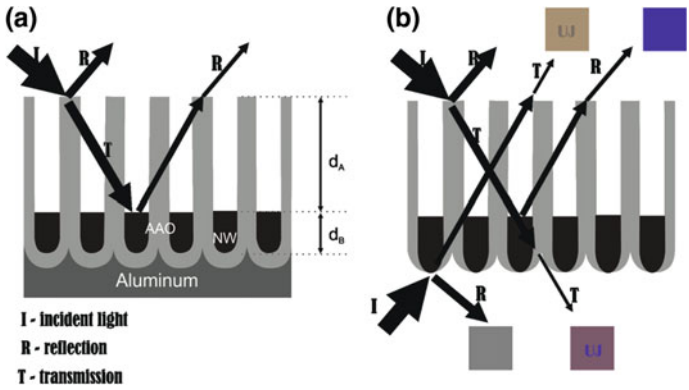

Fig. 8.32 Scheme of interference of reflected lights on AAO filled with NWs

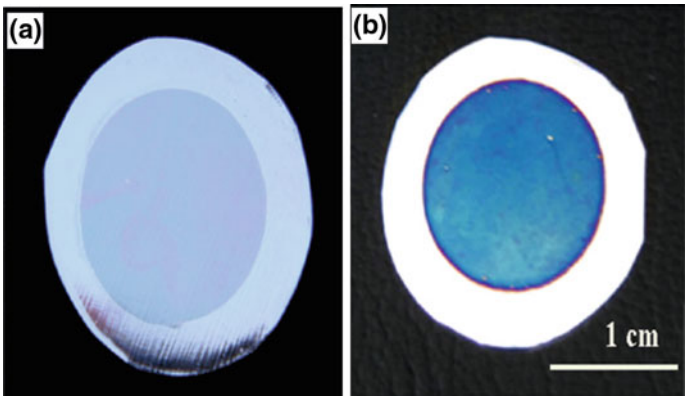

Fig. 8.33 Photographs (**a**) of the AAO film anodized for 11 min and (**b**) AAO film with deposited Ni NWs. Reprinted with permission from [109]

incident and reflected light from the AAO/Al interface by loose metallic nanograins (Fig. 8.33).

The optical properties of AAO with embedded NWs depend upon the thickness of the oxide layer (depth of pores), thickness of the deposited metallic layer (length of NWs) and the quality of deposit (size of metallic grains, compactness etc.). Therefore, the optical properties of AAO-NWs can be changed by altering the conditions of anodization (i.e. applied potential, anodization time) and deposition of NWs (i.e. current density of deposition). The colors of the AAO-NWs composite films vary with increasing the thickness of the sample [109] and depend on the observable angle [109, 124]. It is widely recognized that the wavelength of maximum reflectance decreases (blue shift is observed) with increasing incident angle. For the same sample, the reflection spectra collected at different incident angles exhibit peaks at different wavelengths. For instance, the color of the same ultra-thin

AAO-Ni NWs sample gradually changes from reddish-brown to green when the incident angle increases [109].

In order to better understand this effect, Bragg's law has to be considered

$$2d\sin\theta = n\lambda \tag{8.5}$$

where d, n, θ and λ are lattice spacing, an order of diffraction, diffraction angle and wavelength, respectively. For the constant lattice spacing, detected reflection wavelengths depend on the observable angle. Different order of diffraction is represented by different reflection peaks in the spectrum. Since the thickness of the AAO layer affects d value, the color of the metal plates could be controlled by anodizing time (Fig. 8.34). Zhang et al. observed a red-shift in the peak positions with increasing anodizing time and, consequently, film thickness of the samples [109, 110, 208, 210]. The length of deposited nanowires also affects the observed color of the fabricated AAO-NWs composites [107].

It is widely recognized that noble metal nanostructures (e.g., Ag and Au nanoparticles, nanorods, and nanowires) show characteristic absorption peaks, known as localized surface plasmon resonance (LSPR), being a result of the collective oscillation of the conduction electrons in nanostructures with the incident electromagnetic field [215–217]. There are two main consequences of existing the LSPR: (i) selective photon absorption and (ii) generation of locally enhanced or amplified electromagnetic fields at the nanoobject surface. The LSPR for noble metal nanostructures occurs in the visible and IR regions of the spectrum and can be measured by UV-Vis-IR absorption spectroscopy. The LSPR band of a noble metal nanostructure relies on its size, shape, composition and its surrounding medium

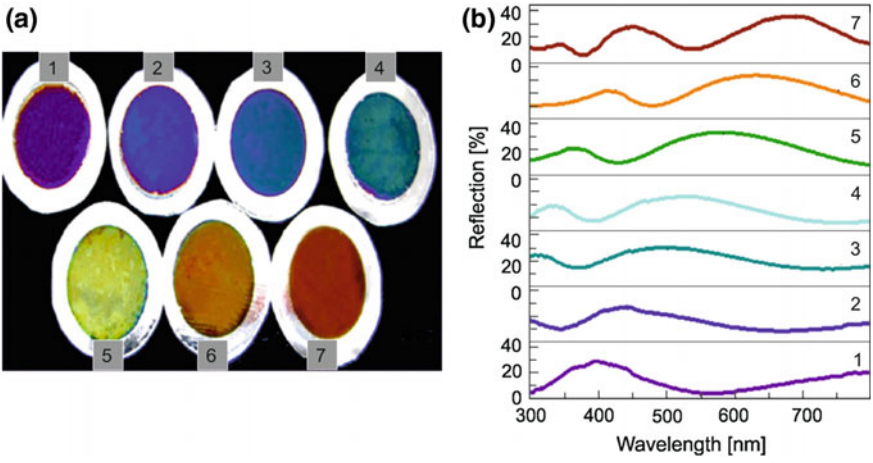

Fig. 8.34 Photographs of AAO films with deposited Ni NWs taken in natural light at nearly normal incidence (**a**). The AAO films were formed at different anodizing times: (*1*) 9 min , (*2*) 10 min , (*3*) 11 min , (*4*) 12 min , (*5*) 13 min , (*6*) 14 min , (*7*) 15 min (*7*). The corresponding UV-Vis reflection spectra of the AAO-NWs nanocomposite films (**b**). Adapted with permission from [109]

(refractive index of environment) [191, 216]. In particular, nanowires show two LSPR peaks corresponding to the transverse and the longitudinal resonance mode. The transverse resonance mode is related to the electron motion perpendicular to the nanowire long axes and can be excited with the light having an electric-field component perpendicular to it. On the other hand, the longitudinal resonance mode is related to the electron oscillations along the nanowire axes and requires p-polarized light to be excited with a component of the incident electric field along the nanowire [205]. For Au nanowires embedded into the AAO membrane, the transverse mode resonance occurs at fixed wavelength of about 520 nm, whereas the longitudinal mode wavelength shifts towards near infrared (from 700 to 900 nm) with an increase in the nanowire length (from 260 to 360 nm) [200, 204, 205]. A slight red shift in the longitudinal peak position was reported for the composite films containing Au nanowires with the diameter of 20 nm and length ranging from 75 to 330 nm (Fig. 8.35) [206]. The transverse plasmon bands at about 360–390 nm for the Ag-based [195, 199, 200] and at 560–580 nm for the Cu-based AAO-NWs [209, 218] composite were observed. The longitudinal peak for these AAO-NWs composite films is typically observed at broad wavelength range of 500–845 nm [199, 200, 218]. The diameter of embedded nanowires has the influence only on the longitudinal peak position. When the diameter of Ag nanowires increases in the range between 22 and 40 nm, and consequently aspect ratio of NWs decreases, a gradual blue-shift of the longitudinal peak from 734 to 509 nm is observed (Fig. 8.36a) [199, 207]. Similar behavior was also reported for Au NWs embedded in the AAO membrane [207]. On the other hand, for the Au-Ag alloy nanowires deposited in the AAO membranes, the position of the transverse peak was found to dependent linearly on the NW composition varying between 390 nm for pure Ag and 520 nm for pure Au (see Fig. 8.36b) [199]. The same position of transverse resonance peak (520 nm) for the AAO-Au NWs composite film was observed by Yan et al. in the photoluminescence spectrum [203]. Surprisingly, they observed a significant suppression or quench of the PL intensity of the AAO-Au

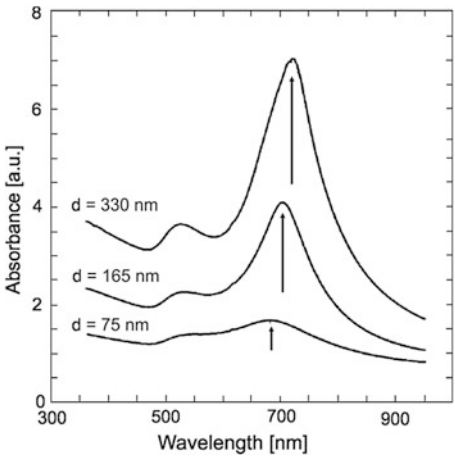

Fig. 8.35 Transmission data for P-polarized light at 60° angle of incidence and various Ni nanowire lengths in the AAO-NWs composites. Reprinted with permission from [206]

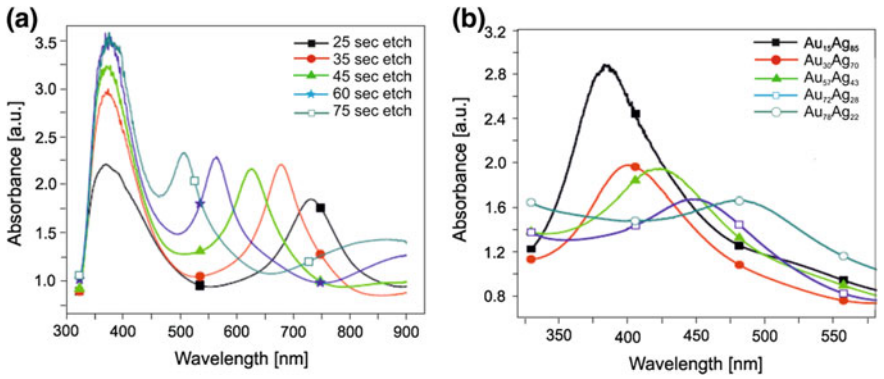

Fig. 8.36 Effect of changing nanorod diameter (aspect ratio) on the transmission spectra of 400 nm long silver NWs embedded in a 450 nm thick film of porous AAO with a 60 nm interpore distance. The angle of TM polarized incidence was 40° in all cases (**a**). Transverse resonance peaks for the 24 nm diameter and 300 nm long AAO-Ag NWs composites with different Au-Ag compositions (**b**). Reprinted with permission from [199]

NWs composite in comparison with the PL spectrum for the pure AAO film. This quenching was attributed to an efficient fluorescent resonance energy transfer (FRET) between the plasmonic absorption of the Au nanowire array and the PL band of the AAO membrane. This phenomenon depends on the donator acceptor separation which is small, due to the spatial proximity of the nanowires and the AAO.

Recently, it has been demonstrated that metal NWs embedded vertically in a dielectric medium, such as AAO, can change the propagation of light and can exhibit negative refraction in the visible wavelengths or infrared region [197, 200, 201]. As was mentioned previously, the AAO-NWs composite films have two surface plasmon resonances (LSPR): a longitudinal LSPR and transverse LSPR. It is widely recognized that the AAO-NWs composite should be excited with higher wavelengths (with TM polarized light) than the longitudinal resonance mode in order to observed negative refraction phenomenon [219]. This type of materials with such extraordinary optical properties do not exist in the nature and are known as negative index metamaterials. Typical applications for these materials include the development of next-generation optical devices such as flat lens and superlenses, waveguiding, as well as imaging, optical communication, and biosensing [197, 205, 219, 220].

As it was mentioned earlier, the ideally ordered nanopore array of AAO can be directly used as a 2D photonic crystal material in the near infrared (IR) and visible wavelength regions [178]. The theoretical studies showed that negative refraction can also be achieved in some 2D photonic crystals [201, 219, 221]. Moreover, by incorporating silver or gold into AAO template with various pore diameter, photonic crystal band gap or the TM polarization can be tuned from near-infrared to visible region for AAO with 100 and 200nm diameter, respectively [222]. The

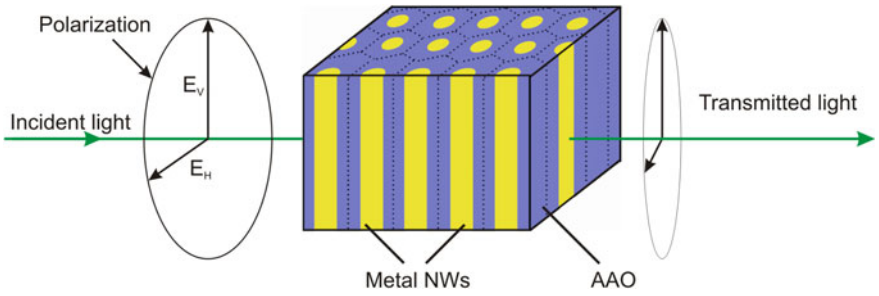

Fig. 8.37 Schematic illustration of a wire grid micropolarizer made of the AAO-NWs composite. The micropolarizer transmits the light polarized vertically (E_V) and attenuates the light polarized horizontally (E_H)

Table 8.2 Characteristics of various AAO-based micropolarizes

Type	Pore diameter (filled with metal) (nm)	Wavelength (μm)	Extinction ratio (dB)	Insertion loss (dB)	References
Ag/AAO	90	1.0–2.2	25–26	0.77	[226]
Co/AAO	20	1.3	22	n.a.	[227]
Cu/AAO	20	1.25–1.46	24.9–14.9	n.a.	[209]
	90	1.0–2.2	24–32	0.5	[228]
Ni/AAO	30	1.3	30	2–4	[229]
	70	1.0–2.5	25–30	1.07	[230]
Pb/AAO	40	1.0–2.2	17–18	0.4	[231]

n.a. Not available data

theoretical concept has been recently demonstrated in practice. When AAO template is filled with a metallic component, e.g. Ag [197], Au [223], new metal-dielectric photonic crystals with negative refraction index were fabricated.

It is widely recognized that anodic porous alumina exhibits anisotropic optical properties. In case when its channels are filled with a metallic material starts to behave as a wire-grid micrpolarizer (Fig. 8.37) [224, 225]. A number of studies have documented the fabrication of micropolarizers from AAO membranes filled with Ag [226], Co [227], Cu [209, 228], Ni [229, 230], and Pb [231]. The optical characteristics of fabricated micropolarizes is summered in Table 8.2.

8.6.1.2 Polymer Nanowires in AAO

Although various polymers are often deposited inside the pores of AAO membranes, the optical properties such composite materials are rather occasionally studied except the following polymer NWs embedded in AAO films: poly (2,5-dibutoxy-1,4-phenylenevinylene) (DBO-PPV) [232], poly(2,3-diphenyl)phenylene vinylene) (DP-PPV) [233], poly[2-methoxy-5-(20-ethyl-hexyloxy)-

p-phenylene vinylene] (MEH-PPV) [poly[2-methoxy-5-(20-ethyl-hexyloxy)-p-phenylene vinylene] (MEH-PPV) [233–237], poly[3-(2-methoxyphenyl)thiophene] (PMP-Th) [120, 238], poly(3-hexylthiophene) (P3HT) [239, 240], and poly (N-vinylcarbazole)/tris(8-hydroxyquinoline) aluminum composite (PVK-Alq_3) [241]. As can be seen, mainly conjugated polymers are deposited due to their high potential to be applied in light-emitting diodes, solar cells, and optoelectronic devices. In the nanoscale, the polymer chains exhibit intrinsically anisotropic properties, such as luminescence polarization and highly directional charge transport [242].

The preparation of the conjugated polymer nanostructures (e.g., nanotubes and nanowires) in AAO templates is not really problematic, and impregnation or wetting processes as well as chemical and electrochemical techniques are commonly used. The optical properties of the conjugated polymers embedded in AAOs are remarkably different from those in films, as a result of preferential axial orientation of the polymer chains within the nanowires/nanotubes, possible isolation of the polymer chains and chemical interaction between both components [120, 233–235, 239, 243]. As shown in photoluminescence studies, the optical properties can be altered by adjusting the diameter of the nanopores of AAO, and the type and concentration of the polymer solution used for polymerization [235–237]. Nguyen et al. demonstrated that the polarity of solvent has a strong influence on the chain conformation, which in turn, affects the PL yield [237]. It was found that polymer chains fill the nanopores in a form of polymer bunch and the number of the polymer chains in the bunch depends on both: the concentration of polymer solution and the pore diameter of AAO [234]. When the concentration of polymer solution increases bunches of chains in nanopores are more compact and contain larger number of polymer chains. As a result of enhanced interchain interactions, the number of the energy levels increases and a red shift in the PL spectrum is observed [234].

The most important factor which influences the optical properties of AAO membranes with embedded polymer nanowires is a size confinement effect. The isolation of polymer chains embedded in the nanopores of AAO membranes is directly responsible for the blue shifts in the PL spectra and great enhancements in photoluminescence intensity [120, 232, 233, 236, 238]. The effective conjugation length of polymers in the AAO nanopores is much shorter than in the film and, therefore, the optical energy gap is larger. Furthermore, the blue shift depends on the pore diameter of the AAO membrane (Fig. 8.38). It was found that the lower the pore diameter is, the more evident effect is observed [120, 234, 237]. A little blue-shift in PL for the samples with small pore size is related with a high portion of the ordered polymeric chains (regular, compact packing and alignment of chains) inside the nanopores. It was also suggested that the observed PL intensity enhancement is a result of (i) Förster energy transfer from oxygen vacancies in AAO, acting as donors, to polymer molecules, acting as acceptors [120, 238] or (ii) higher density of polymeric material embedded into the nanopores [240]. Therefore, a lack of oxygen vacancies in the AAO prepared in sulfuric acid is the main reason for a lower energy transfer efficiency and, consequently, lower intensity of the PL spectra [120, 238].

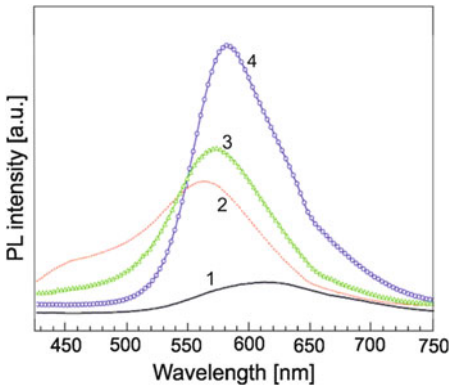

Fig. 8.38 Photoluminescence of the (*1*) PMP-Th film electropolymerized on Pt and AAO-PMP-Th composites with a AAO pore diameter of: (*2*) 60 nm , (*3*) 70 nm , and (*4*) 80 nm . Reprinted with permission from [238]

Chemical interactions between polymer and the AAO walls influence considerably the optical properties of the conjugated polymer nanostructures embedded into the AAO membranes. The Lewis acid/base and hydrogen-bonding-type interactions between conjugated polymers and AAO membranes significantly affect the optical properties of theses composites compared to bulk materials [233, 236, 241]. Kong et al. suggested that the aromatic rings and the ether groups in the MEH-PPV chains interact with the Lewis acid Al centers on the surfaces of the nanopore walls via electron donation, and with the Brønsted acid surface hydroxyl groups via a hydrogen-bonding-type interactions [233, 234, 236]. Consequently, the planar conformations of the polymer chains is destroyed and the short conjugation of the conjugated polymer in the nanopores appeared. As a result of this preferable alignment of the polymer chains, a blue shift is observed in the PL spectrum. The effect of chemical interactions between polymer chains and AAO surface is often accompanied by the size confinement effect [234].

From the photoluminescence studies it was revealed that for some nanocoposites (e.g., AAO-PMP-Th [120, 238], AAO-DBO-PPV [232]), the nano-size effect is only responsible for the blue shift of the PL peaks, while for other nanocomposites (e.g., AAO-MEH-PPV [234, 236], AAO-PVK-Alq_3 [241]) the interaction between the AAO and polymer chains or both mentioned effects influence the PL behavior.

8.6.2 Nanoparticles in AAO

Optical properties of nanoparticles (NPs) embedded into the AAO membranes were extensive studied. Many AAO-NPs composites based on deposited metals such as Ag [244–251], Au [252–261], and other materials e.g. PbS [262], TiO_2 [263], and

ZnO [264, 265] were investigated. In general, the optical properties of such systems depend on the type of nanoparticle material, particle size, surrounding material and particle interactions. The effective medium theory predicted, that even large amount of metal nanoparticles can be transparent, because the wavelength of light is much larger than their dimensions [252]. The anodic porous alumina membranes are especially useful as templates to produce small nanoparticles [266] and, due to the optical transparency of AAO, to investigate optical properties of nanoparticles [254].

The nanoparticles in the nanoporous AAO membranes can be deposited randomly or as layered structures as shown in Fig. 8.39 [250, 259]. As was demonstrated, the layered structure of deposited Ag NPs influences the LSPR peak in absorption spectra [250, 259, 260]. The absorption was dependent on the number of layers of Ag NPs. With an increase in the number of NP layers the intensity of the absorption peak increased and its position shifted from 450 to 400 nm (Fig. 8.39). The observed blue shift originates from the surface-plasmon coupling between the Ag NPs closely arranged in the AAO membrane. Sandrock et al. considered the plasmon resonance of the AAO-NPs composites with two layers of gold spheres, rods and rod-sphere pairs [259]. The influence of spacing between particles on the optical properties of the paired sphere composites was investigated. It was found that the plasmon resonance peak position does not change when the distance between NPs is larger than three particle diameters. However, when the interparticle spacing is smaller than the NP diameter, a red-shift and broadening of the peak can be observed. The smaller distance between sphere nanoparticles, the higher plasmon resonance [259, 260].

The size of NPs embedded into the AAO membrane is also important. When the Au particle diameter exceeds 200 nm, the AAO-NPs composite films are transparent in IR spectrum but opaque in near IR and visible range [252, 253]. The

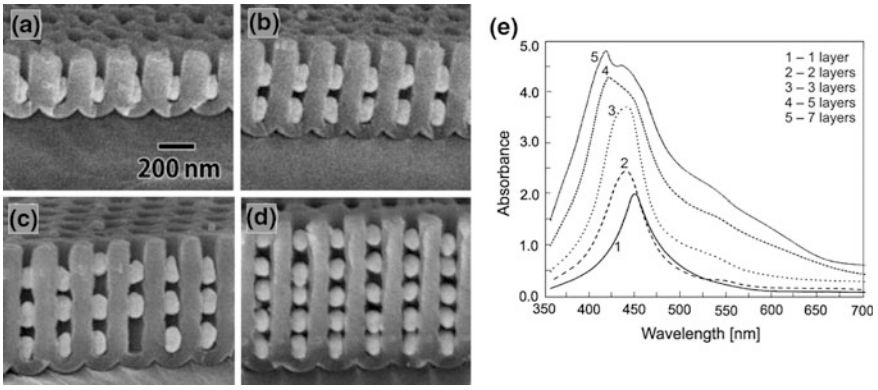

Fig. 8.39 SEM images of the layered structure of Ag NPs in the AAO membrane. One layer (**a**), two layers (**b**), three layers (**c**), and five layers of Ag nanoparticles (**d**) in the AAO membranes and their corresponding absorption spectra (**e**). Reprinted with permission from [250]

composites with the smaller particle diameter than 50 nm and aspect ratio of 1 are fully transparent in NIR and UV-Vis spectrum, except the strong absorption band of about 520 nm typical for LSPR of Au NPs [252]. Moreover, it is possible to design color of these composites by changing the shape of nanoparticles. With decreasing diameter of nearly spherical Au NPs (from 60 to 30 nm) a blue shift in the resonance peak was noticed [253]. For the rod-like Au nanoparticles (aspect ratio larger than 1) embedded in the AAO, in the intensity of the Au plasmon resonance increases and the peak shifts to lower wavelengths with increasing aspect ratio of NPs [252, 254, 255]. All those observation are consistent with effective medium theory formulated by Maxwell-Garnett theory [255, 258, 267, 268].

Moreover, the optical properties of Au nanoparticles embedded in the AAO membrane can be altered by heat treatment of the nanocomposite up to 400 °C, however, the effect is observable only for the NPs with irregular shape [255]. A low-temperature heating induces changes in the size and shape of Au nanoparticles and, consequently, affects the optical properties without interference from nanoparticle coalescence (Fig. 8.40). This is possible because each nanoparticle is confined to its own nanopore. The low aspect ratio (much lower than 3) Au nanoparticles have irregular structure (shape and size), however, after the heat treatment at low temperatures, they become dense and spherical. A blue shift in the plasmon band is observed with increasing annealing temperature (Fig. 8.40). On the other hand, no considerable changes in the optical absorption spectra with

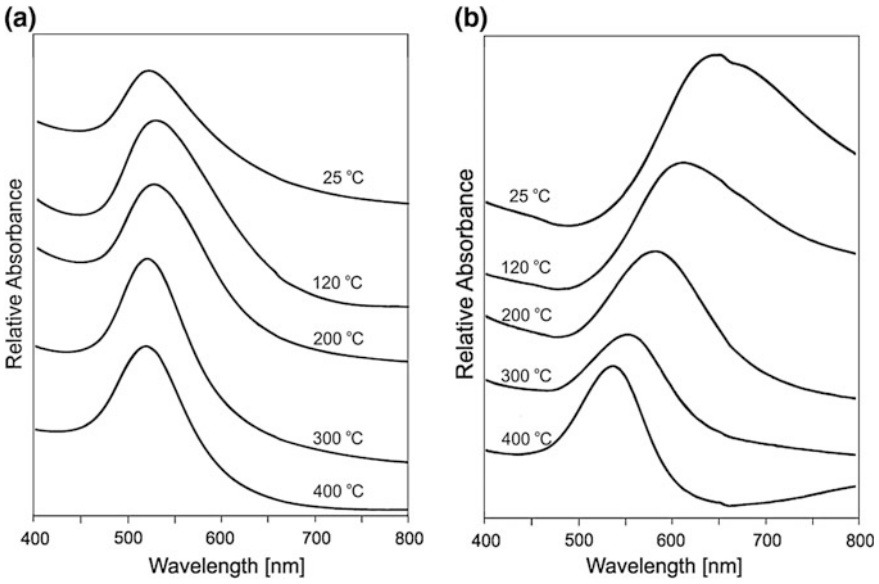

Fig. 8.40 Absorption spectra obtained before and after heating the AAO-Au NPs composites with Au NPs aspect ratio of about 3 (**a**) and 1 (**b**). The annealing temperatures were as indicated. Reprinted with permission from [255]

increasing annealing temperature were observed for the particles with the aspect ratio of about 3 [255]. Hu et al. studied the reflectivity of the AAO membranes containing Ag NPs and they observed the reduced reflectivity at the wavelength of ~465 nm caused by the strong plasmonic absorption [247]. The aggregation of NPs, accompanied by a considerable increase in their size (from 10 to 40 nm), was observed upon annealing. In contrast to the results reported by Hulteen et al. [255] for Au NPs, they [247] found that the increasing temperature of annealing shifts the plasmon absorption peak of Ag towards longer wavelengths. A similar red shift in the position of plasmon absorption peak (from 395 to 432 nm) with increasing diameter of Ag nanoparticles (from 46 to 90 nm) embedded in the AAO membranes was observed by Huang et al. [245].

As it was shown in Fig. 8.39, metallic nanoparticles can be deposited in the AAO membrane at the bottom of pores. Huang et al. studied absorption properties of the AAO-NPs composites at the bottom side of the AAO membranes [244]. The remaining aluminum layer was removed and Ag NPs were illuminated through the existing barrier layer of AAO (Fig. 8.41). The effect of the thinning of the barrier layer on absorption properties was studied for different thicknesses of the barrier layer ranging from about 15 to 0 nm. From the obtained spectra it was revealed that decreasing the barrier layer thickness shifts the LSPR peak location from 435 to 398 nm. The observed red-shift in the excitation spectra of the AAO-Ag NPs composites was attributed to higher refractive index of AAO as compared to refractive index of air or vacuum.

Various inorganic nanoparticles were loaded into the pores of AAO membranes and optical properties such composites were studied. For instance, an intense blue PL emission peaked around 450–485 nm was observed after ZnO nanoparticles

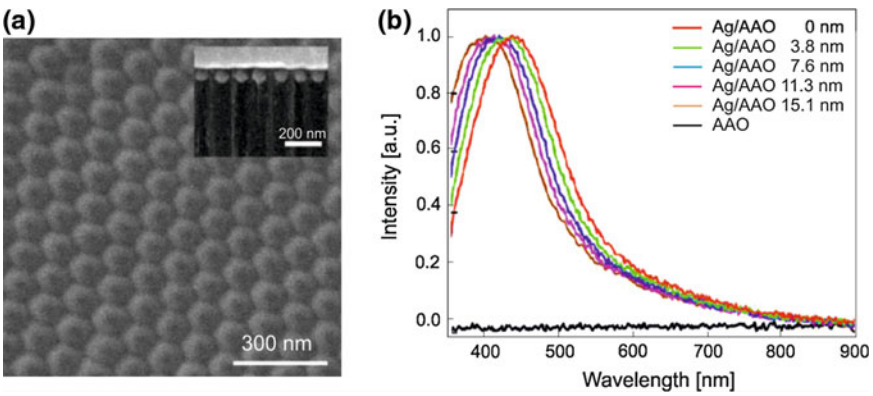

Fig. 8.41 SEM image of the bottom side of the AAO-Ag NPs film (**a**). *Inset* Cross-sectional SEM image of the Ag/AAO substrate where the back-end alumina layer has been chemically etched for 30 min to reduce the layer thickness to 3.8 nm. Silver nanoparticles were deposited inside the tube-like nanochannels. The extinction spectra of an AAO film without Ag and Ag/AAO films with different etching times for thinning the back-end alumina layer (**b**). Reprinted with permission from [244]

embedded into the AAO films [264, 265]. The PL intensity of the AAO-Zn NPs composite was 20 times higher than that of the nanostructured thin ZnO film. The luminescence enhancement was attributed to the increased number of singly ionized oxygen vacancies (F^+ centers) in the ZnO nanoparticles located in the pores of the AAO membrane [264, 265]. In general, blue shifts in absorption spectra were observed for the composites with embedded ZnO, PbS and TiO_2 nanoparticles [262, 263, 265]. This phenomenon was ascribed to the size confinement effect occurring in the AAO-NPs composites.

8.6.3 Xerogels in AAO

One of the simplest method used for the synthesis of luminescence materials is deposition of xerogels into the pores of the AAO membranes by a sol-gel technique. Generally, solutions are deposited inside the pores of AAO by spinning and during subsequent heat treatment xerogels (dry gels) are formed in nanopores. So far, the application of sol–gel techniques on AAO was used for the preparation of xerogels such as: Eu-doped Al_2O_3 [269, 270], Tb_2O_3-doped Al_2O_3 [271, 272], Y-doped Al_2O_3 [273], Er_2O_3-doped Fe_2O_3 [274], Er-doped In_2O_3 [275], Eu-doped In_2O_3 [269], Tb-doped SiO_2 [272, 276], Er_2O_3-doped TiO_2 [180, 274, 277–282], Eu_2O_3-doped TiO_2 [269, 278, 283–289], Tb-doped TiO_2 [180], Tb_2O_3-doped TiO_2 [277, 290, 291], and Tb-doped ZrO_2 [272]. All these nanocomposite materials exhibit enhanced photoluminescence compared to xerogels fabricated on planar substrates [269, 288–290]. It is widely recognized that PL of lanthanides from the AAO-xerogel composites increases with the thickness of AAO (Fig. 8.42a) [285, 290] and, for some excitation wavelength, increases with the number of xerogel layers deposited inside the AAO nanopores (Fig. 8.42b) [278, 282, 288, 290, 291], and even with the concentration of lanthanides in xerogels (Fig. 8.42c) [270, 271, 278, 290]. However, the PL spectra of the AAO-xelogel composites strongly depend on the annealing temperature e.g., [271, 273, 282, 290–292], etc.

8.6.4 Metallic and Other Layers Deposited on the AAO Surface

A controllable synthesis of nanoporous metals with a high degree of regularity in a form of metallic thin layers or nanomeshes has attracted recently much attention due to interest in fundamental optics and applications. The ordered metallic nanohole arrays demonstrate novel and unusual optical properties such as localized surface plasmon resonance (LSPR) due to surface corrugation at the subwavelength scale, which is significantly different from surface plasmon polaritons (SPPs) of planar surfaces [216, 217]. Since the LSPR is responsible for the electromagnetic-field enhancement that leads to surface-enhanced Raman scattering (SERS), this

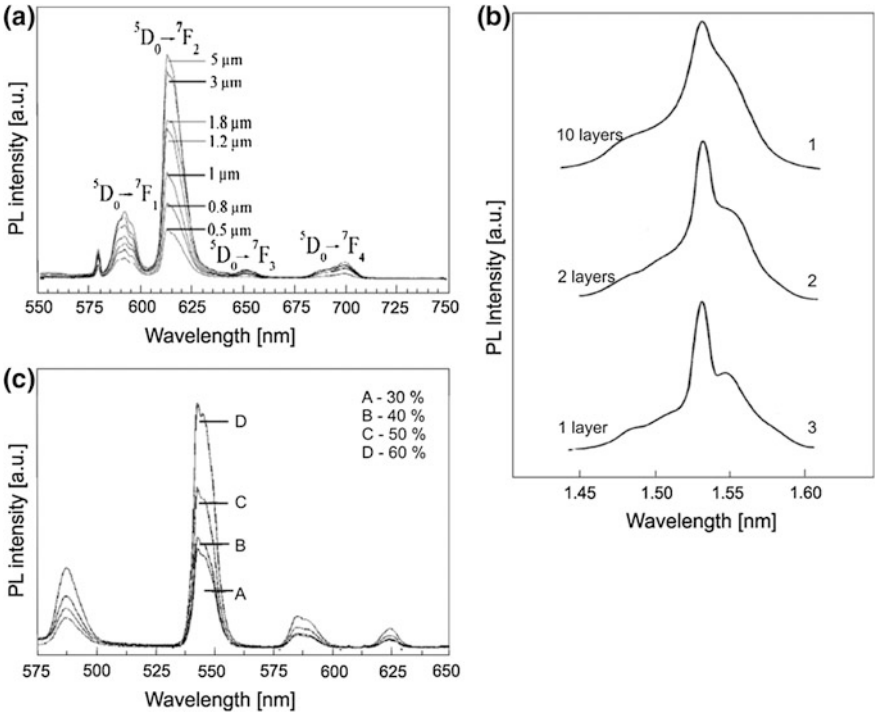

Fig. 8.42 Photoluminescence spectra of AAO-xerogels composites with one layer of the Eu-doped TiO_2 xerogel deposited at the AAOs with different thicknesses (**a**), different numbers of Er-doped TiO_2 xerogel layers deposited at the AAOs (**b**), and one layer of the Tb_2O_3-doped Al_2O_3 xerogels containing different Tb_2O_3 contents (**c**). Reprinted with permission from [285] (**a**), [282] (**b**), and [271] (**c**)

technique is commonly used for probing the thin metal films on the AAO membranes with adsorbed various molecules [293, 294]. These unique properties of metallic nanoporous arrays have generated potential applications in the field of antireflection materials, high-density capacitors and electrodes, photonic crystals, wave guides and lasing materials. A great variety of chemo- and biosensors based on absorbance, reflection, fluorescence, chemiluminescence, surface plasmon resonance and Raman scattering properties of the metal-coated AAO films were developed [128, 191, 193, 295–300].

Although the fabrication of nanoporous metal and metal oxide layers on AAO membranes has been widely explored over the last decades, the investigation of the optical properties is rather limited to noble metal layers. The studies on the optical properties of nanoporous metal layers deposited on the AAO membranes include such metals as: Ag [68, 105, 294, 301–303], Au [114, 193, 296–298, 303–306], Cr [105, 307], Fe [105], Ni [105], Pt [106, 308, 309], and Ti [105]. More recently, the optical properties of thin $Si_{1-x}Ge_x$ [310] and TiO_2 [307] layers deposited on the AAO membranes were also studied.

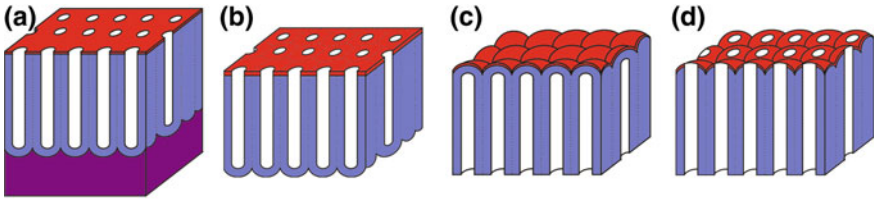

Fig. 8.43 Schematic structures of AAOs with the deposited thin layers on: the *top side* of the anodized sample (**a**), the *top side* of the membrane after Al removal (**b**), the barrier layer of the membrane (**c**), the barrier layer of the membrane with opened pores (**d**)

In general, nanoporous anodic alumina may be used in various variants as a substrate for the deposition of thin metallic layers (Fig. 8.43). However, the most frequently utilized is the mechanically stable AAO with the remaining aluminum layer-structure (a) (Fig. 8.43a).

UV-Vis absorption of the structures (b) – (d) (Fig. 8.43b–d) covered with sputtered Ag layers was studied in detail [294, 301, 302]. The observed distinct surface bands in the UV-Vis absorption spectra (e.g., different shape and position of the band) were attributed to differences in the shape and size of deposited Ag nanoparticles. In addition, the PL spectra recorded to the (b) – (d) composites showed a broad emission band centered at ~500 nm, with the luminescence intensity increasing in the order (b) < (d) < (c) [301]. It is worth mentioning that for the pure AAO membrane intensity of the PL peak was the highest among all the spectra and the PL band was centered at 470 nm that is typical for the membranes obtained by anodization in oxalic acid. Yao et al. reported transmission spectra of the AAO samples coated with Au films (type (c) and (d)) [303]. It was stated that transmittance of the samples decreases in comparison with the un-coated AAO films because the Au layer creates a mirror-like surface and blocks most of the incident light. For the (d) structures with partially opened pores, a strongly enhanced transmission peak in the visible light range was observed and ascribed to LSPR of Au [303]. The highly ordered AAO films with higher porosities exhibit stronger the transmission enhancement effect. When the interpore distance in the AAO membranes decreases the effect weakens [303].

Similarly to NWs deposited inside the AAO membranes, the composite consisting of metallic or other inorganic layers deposited on the AAO membrane can be considered as a layered structure with different refractive indices (Fig. 8.44). Therefore, light interaction with such a structure, and especially interference enhancement can be described by the Bragg reflection principle (8.6)

$$2(n_d d_d \cos\theta_d + n_{AAO} d_{AAO} \cos\theta_{AAO}) = m\lambda \tag{8.6}$$

where n_d, d_d, d_{AAO}, θ_d and θ_{AAO} are effective reflective index of the deposited film, thickness of the deposited film, pore-depth in AAO (thickness of the AAO film), refractive angle in the deposited film and refractive angle in the AAO membrane,

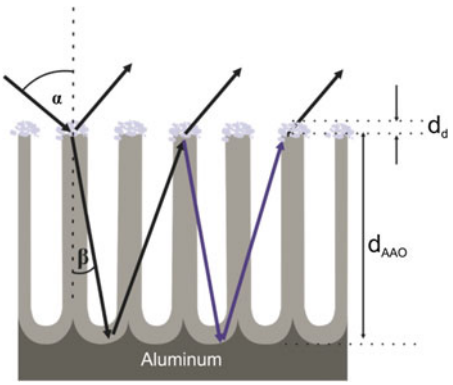

Fig. 8.44 Schematic of reflectance from a porous AAO membrane with deposited thin metallic layer

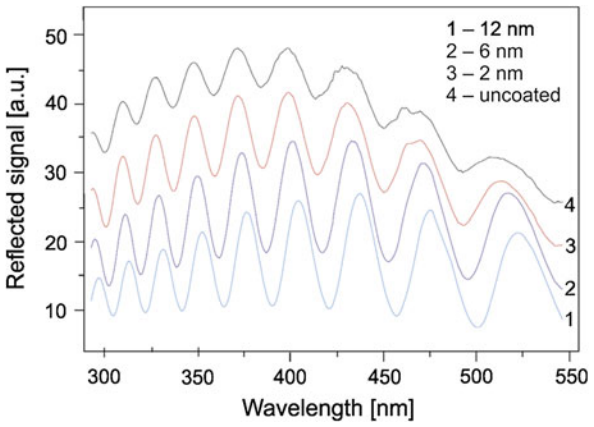

Fig. 8.45 Reflectance spectra of AAO films with different thicknesses of the deposited Pt layer. The pore diameter and thickness of the AAO film was 31 and 1600 nm, respectively. Reprinted with permission from [106]

respectively. All of the wavelengths which fits the equation will be strongly enhanced (at certain frequencies) and the others will be quenched, resulting in distinguish color of the sample [311]. Thus, the interference enhancement depends on the optical path difference, thickness of the AAO film, effective reflective index of the AAO structure (porosity), and incident angle.

The AAO film covered with thin metallic layer can be treated as a Fabry-Pérot interferometer containing nanometer size cavities [112]. Therefore, the reflectance signal varies upon the changes of the effective refractive index in cavities. As a result, oscillations in the reflectance spectrum are observed [106]. Fabry-Pérot interference of reflected light from the AAO membranes covered with thin metal layer forms the maximum peaks whose sharpness is determined by the effective thickness of the metal-coated AAO membranes (see Fig. 8.45) and by optical loss during propagation and reflection inside the sample [114, 191, 305–307]. Recently, a series of oscillations in the reflectance spectra was also demonstrated for the bilayered AAO structure (two layers with different pore diameters and consequently different porosities) covered with a thin Au layer [304].

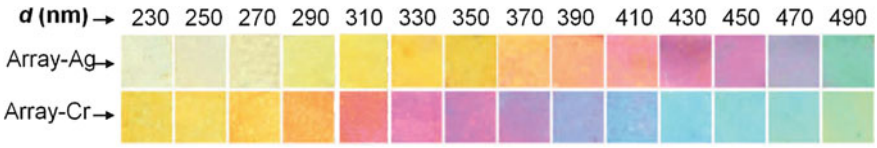

Fig. 8.46 Colors of AAO films with sputtering Ag and Cr layers. The thickness of the AAO film (pore depth, d) was ranged from 230 to 490 nm with 20-nm interval. The pore diameter and interpore distance of AAO was 40 and 100 nm, respectively. Reprinted with permission from [105]

One of the most effective method to change the color of the anodized AAO sample is to precisely control the thickness of the AAO film (pore depth, d_{AAO}). Wang et al. demonstrated that the best effect and the most distinct colors can be obtained by sputtering thin (c.a.7 nm) Ag and Cr layers on the surface of the AAO films. Due to the different refractive indices of Cr and Ag, the structures with the same pore depth exhibit different colors (Fig. 8.46) [105, 307]. As expected colors of AAO films coated with thin metal layers can be also tuned by the depth of pores in the AAO membrane. It was demonstrated that the colors of the AAO membranes anodized for longer period of time or using higher anodization potentials, and then covered with a metal layer, tend to become brighter due to increased thicknesses of the AAO layers [68, 308]. The structural color of the metal-coated AAO films can be alter by changing pore diameter of AAO [308]. The changing of incident angle is also a very effective procedure to tune color of the AAO membranes coated with thin films other than metals, e.g. TiO_2 [307].

8.6.5 Other Guest Molecules and Compounds in AAO

The presence of other ions, guest molecules, dyes and compounds inside the nanopores of the AAO membranes affects their optical properties. It is a direct result of interaction of the guest with the exposed aluminum atoms in the pores of the AAO films. The diversity in optical behavior of the modified AAO membranes is related mainly with a different nature of the immobilized/embedded/deposited guest and, therefore, different interactions with the alumina. The following examples are far from a complete list of possible chemical modifications of nanopores which influence the optical properties of AAO membranes, e.g., Cr^{3+} ions [84], Eu^{3+} ions [312], Tb^{3+} ions [312, 313], CdS [314], Ru(II)(4,4′-dicarboxyl-2,2′-bipyridyl)$_2$(SCN)$_2$) dye [315], $[Ru(dpp)_3]^{2+}$ (dpp = 4,7-diphenyl-1,10-phenanthroline) [316], siloxane with repeating Si_3OSiH and Si_3SiH moieties [266], Alizacin red S [317], 8-anilino-1-naphtalene-sulfonic acid [318], 7-diethyl amino-4-methylcumarin [318], diiodofluorescein [317], tetraiodofluorescein [317], 8-hydroxyquinoline [319, 320], Rhodamine B [321], Rhodamine 6G [87, 318, 322], Rhodamine110 (Rh110) [323], paraterphenyl and perylene [324], *N,N′*-diphenyl-*N, N′*-bis(3-methylpheny-l,1′-biphenyl-4,4′-diamine) (TPD) + 5 % rubrene (5,6,11,12-

tetraphenylnaphthacene) [325], tetrhydroxyflavanol [326], morin (3,5,7,2′,4′-pentahydroxyflavone) [327–329], morin-human serum albumen (HSA) [327], morin-human immunoglobulin (IgN) [329], morin-lysozyme (lys) [330], morin-trypsin (Try) [328].

Kurashima et al. [81] studied the saturable absorption effect of semiconducting single-wall carbon nanotubes for mode-locking devices of short pulse lasers. The optical absorption spectra of AAO membranes with different amount of carbon nanotubes were compared. The optical absorption spectra in a near-infrared showed that the absorption of the AAO membranes could be controlled by the content of the nanotubes in the pores.

As a general remark can be concluded that the porous alumina enhances considerably the photoluminescence intensity of the studied systems.

Acknowldgments Some of the research presented here was supported by the National Science Centre (Grant No. 2011/01/N/ST5/02510).

References

1. K.P. Han, J.L. Fang, Decorative-protective coatings on aluminum. Surf. Coat. Tech. **88**, 178–182 (1996)
2. L. Anicai, A. Meghea, C. Sirean, L. Dima, Analysis of electrochemically coloured aluminium anodic films by diffuse reflectance spectra. Mater. Sci. Forum **185–188**, 489–496 (1995)
3. F. Behzadi, M. Moradi, H.R. Karimi-Alavijeh, A. Gharavi, The effect of anodization voltage and surface morphology on the capacitance properties of Al-Al_2O_3-Al nanocapacitors. Vacuum **99**, 204–210 (2014)
4. G.D. Sulka, A. Brzózka, L. Zaraska, M. Jaskuła, Through-hole membranes of nanoporous alumina formed by anodizing in oxalic acid and their applications in fabrication of nanowire arrays. Electrochim. Acta **55**, 4368–4376 (2010)
5. T. Gao, J.C. Fan, G.W. Meng, Z.Q. Chu, L.D. Zhang, Thin Au film with highly ordered arrays of hemispherical dots. Thin Solid Films **401**, 102–105 (2001)
6. K. Nielsch, F.J. Castaño, S. Matthias, W. Lee, C.A. Ross, Synthesis of cobalt/polymer multilayer nanotubes. Adv. Eng. Mater. **7**, 217–221 (2005)
7. H. Masuda, H. Tanaka, N. Baba, Preparation of porous material by replacing microstructure of anodic alumina film with metal. Chem. Lett. **19**, 621–622 (1990)
8. Sulka, G.D.: *Highly ordered anodic porous alumina formation by self-organised anodising and template-assisted fabrication of nanostructured materials*, ed. by A. Eftekhari. Nanostructured Materials in Electrochemistry (Wiley-VCH, 2008), pp. 1–116
9. S.A. Bagshaw, T.J. Pinnavaia, Mesoporous alumina molecular sieves. Angew. Chem. Int. Ed. Engl. **35**, 1102–1105 (1996)
10. M.D. Henry, S. Walavalkar, A. Homyk, A. Scherer, Alumina etch masks for fabrication of high-aspect-ratio silicon micropillars and nanopillars. Nanotechnology **20**, 255305 (2009)
11. H. Moghadam, A. Samimi, Solar absorptivity of nano-porous anodic alumina (NPAA): effects of structural features. J. Porous Mater. **21**, 331–336 (2014)
12. W.L. Xu, H. Chen, M.J. Zheng, G.Q. Ding, W.Z. Shen, Optical transmission spectra of ordered porous alumina membranes with different thicknesses and porosities. Opt. Mater. **28**, 1160–1165 (2006)

13. G.D. Sulka, S. Stroobants, V. Moshchalkov, G. Borghs, J.-P. Celis, Synthesis of well-ordered nanopores by anodizing aluminum foils in sulfuric acid. J. Electrochem. Soc. **149**, D97–D103 (2002)
14. G.D. Sulka, M. Jaskuła, Defects analysis in self-organized nanopore arrays formed by anodization of aluminium at various temperatures. J. Nanosci. Nanootechnol. **6**, 3803–3811 (2006)
15. G.D. Sulka, K.G. Parkoła, Anodising potential influence on well-ordered nanostructures foremd by anodisation of aluminium in sulphuric acid. Thin Solid Films **515**, 338–345 (2006)
16. G.D. Sulka, K.G. Parkoła, Temperature infuence on well-ordered nanopore grown by anodization of auminium in sulphuric acid. Electrochim. Acta **52**, 1880–1888 (2007)
17. G.D. Sulka, W.J. Stępniowski, Structural features of self-organized nanopore arrays formed by anodization of aluminum in oxalic acid at relatively high temperatures. Electrochim. Acta **54**, 3683–3691 (2009)
18. L. Zaraska, G.D. Sulka, M. Jaskuła, The effect of n-alcohols on porous anodic alumina formed by self-organized two-step anodizing of aluminum in phosphoric acid. Surf. Coat. Technol. **204**, 1729–1737 (2010)
19. W. Lee, S.-J. Park, Porous anodic aluminum oxide: anodization and templated synthesis of functional nanostructures. Chem. Rev. **114**, 7487–7556 (2014)
20. W. Lee, J.-C. Kim, U. Gösele, Spontaneous current oscillations during hard anodization of aluminum under potentiostatic conditions. Adv. Funct. Mater. **20**, 21–27 (2010)
21. H. Han, S.J. Parh, J.S. Jang, H. Ryu, K.J. Kim, S. Baik, W. Lee, In situ determination of the pore opening point during wet-chemical etching of the barrier layer of porous anodic aluminum oxide: nonuniform impurity distribution in anodic oxide. ACS Appl. Mater. Interfaces **5**, 3441–3448 (2013)
22. G.E. Thompson, R.C. Furneaux, G.C. Wood, Electron microscopy of ion beam thinned porous anodic films formed on aluminium. Corros. Sci. **18**, 481–498 (1978)
23. G. Meng, F. Han, X. Zhao, B. Chen, D. Yang, J. Liu, Q. Xu, M. Kong, X. Zhu, Y.J. Jung, Y. Yang, Z. Chu, M. Ye, S. Kar, R. Vajtai, P.A. Ajayan, A general synthetic approach to interconnected nanowire/nanotube and nanotube/nanowire/nanotube heterojunctions with branched topology. Angew. Chem. Int. Ed. **48**, 7166–7170 (2009)
24. Y.T. Tian, G.W. Meng, T. Gao, S.H. Sun, T. Xie, X.S. Peng, C.H. Ye, L.D. Zhang, Alumina nanowire arrays standing on a porous anodic alumina membrane. Nanotechnology **15**, 189–191 (2004)
25. L. Zaraska, E. Kurowska, G.D. Sulka, M. Jaskuła, Porous alumina membranes with branched nanopores as templates for fabrication of y-shaped nanowire arrays. J. Solid State Electrochem. **16**, 3611–3619 (2012)
26. K.O. Jeong, Y.C. Choi, J. Kim, J.K. Han, S.A. Yang, S.D. Bu, Porous alumina templates with various shaped nanochannels. J. Korean Phys. Soc. **51**, S105–S110 (2007)
27. G. Meng, Y.J. Jung, A. Cao, R. Vajtai, P.M. Ajayan, Controlled fabrocation of hierarchically branched nanopores, nanotubes, and nanowires. Proc. Nat. Acad. Sci. **102**, 7074–7078 (2005)
28. W. Cheng, M. Steinhart, U. Gösele, R.B. Wehrspohn, Tree-like alumina nanopores generated in a non-steady-state anodization. J. Mater. Chem. **17**, 3493–3495 (2007)
29. A.Y.Y. Ho, H. Gao, Y.C. Lam, I. Rodríguez, Controlled fabrication of multitiered three-dimensional nanostructures in porous alumina. Adv. Funct. Mater. **18**, 2057–2063 (2008)
30. B. Wang, G.T. Fei, M. Wang, M.G. Kong, D. Zhang, Preparation of photonic crystals made of air pores in anodic alumina. Nanotechnology **18**, 1–4 (2007)
31. J. Ferré-Borrull, M.M. Rahman, J. Pallarès, L.F. Marsal, Tuning nanoporous anodic alumina distributed-Bragg reflectors with the number of anodization cycles and the anodization temperature. Nanoscale Res. Lett. **9**(416), 1–6 (2014)
32. Z.-Y. Ling, S.-S. Chen, X. Hu, X. Hu, Y. Li, Optical transmission spectra of anodic aluminum oxide membranes with a dual layer-by-layer structure. Chinese Phys. Lett. **26**, 1–3 (2009)

33. X. Hu, Y.J. Pu, Z.Y. Ling, Y. Li, Coloring of aluminum using photonic crystals of porous alumina with electrodeposited Ag. Opt. Mater. **32**, 382–386 (2009)
34. M.M. Rahman, L.F. Marsal, J. Pallares, J.F. Borrull, Tuning the photonic stop bands of nanoporous anodic alumina-based distributed Bragg reflectors by pore widening. ACS Appl. Mater. Interfaces **5**, 13375–13381 (2013)
35. Y. Su, G.T. Fei, Y. Zhang, P. Yan, H. Li, G.L. Shang, L.D. Zhang, Controllable preparation of the ordered pore arrays anodic alumina with high-quality photonic band gaps. Mater. Lett. **65**, 2693–2695 (2011)
36. C.K. Chung, R.X. Zhou, T.Y. Liu, W.T. Chang, Hybrid pulse anodization for the fabrication of porous anodic alumina films from commercial purity (99 %) aluminium at room temperature. Nanotechnology **20**(055301), 1–5 (2009)
37. W. Lee, R. Ji, U. Gösele, K. Nielsch, Fast fabrication of long-range ordered porous alumina membranes by hard anodization. Nat. Mater. **5**, 741–747 (2006)
38. W. Lee, K. Schwirn, M. Steinhart, E. Pippel, R. Scholz, U. Gösele, Structural engineering of nanoporous anodic aluminium oxide by pulse anodization of aluminium. Nat. Nanotechnol. **3**, 234–239 (2008)
39. W. Lee, R. Scholz, U. Gösele, A continuous process for structurally well-defined Al_2O_3 nanotubes based on pulse anodization of aluminum. Nano Lett. **8**, 2155–2160 (2008)
40. W. Lee, J.-C. Kim, Highly ordered porous alumina with tailor-made pore structures fabricated by pulse anodization. Nanotechnology **21**, 1–8 (2010)
41. K. Pitzschel, J.M. Montero Moreno, J. Escrig, O. Albrecht, K. Nielsch, J. Bachmann, Controlled introduction of diameter modulations in arrayed magnetic iron oxide nanotubes. ACS Nano **3**, 3463–3468 (2009)
42. K. Schwirn, W. Lee, R. Hillebrand, M. Steinhart, K. Nielsch, U. Gösele, Self-ordered anodic aluminum oxide formed by H_2SO_4 hard anodization. ACS Nano **2**, 302–310 (2008)
43. G.D. Sulka, A. Brzózka, L. Liu, Fabrication of diameter-modulated and ultrathin porous nanowires in anodic auminum oxide templates. Electrochim. Acta **56**, 4972–4979 (2011)
44. G.D. Sulka, K. Hnida, Distributed Bragg reflector based on porous anodic alumina fabricated by pulse anodization. Nanotechnology **23**, 1–8 (2012)
45. D. Losic, M. Lillo, D. Losic, Porous alumina with shaped pore geometries and complex pore architectures fabricated by cyclic anodization. Small **5**, 1392–1397 (2009)
46. D. Losic, D. Losic, Preparation of porous anodic alumina with periodically perforated pores. Langmuir **25**, 5426–5431 (2009)
47. M. Noormohammadi, M. Moradi, M.A. Kashi, A. Ramazani, Y. Mayamai, Structural engineering of nanoporous alumina by controlling the anodization voltage during the spontaneous current oscillation in hard anodization. Surf. Coat. Tech. **223**, 104–109 (2013)
48. M. Raoufi, H. Schonherr, Improved synthesis of anodized aluminum oxide with modulated pore diameters for the fabrication of polymeric nanotubes. RSC Adv. **3**, 13429–13436 (2013)
49. W.J. Zheng, G.T. Fei, B. Wang, Z. Jin, L.D. Zhang, Distributed Bragg reflector made of anodic alumina membrane. Mater. Lett. **63**, 706–709 (2009)
50. W.J. Zheng, G.T. Fei, B. Wang, L.D. Zhang, Modulation of transmission spectra of anodized alumina membrane distributed Bragg reflector by controlling anodization temperature. Nanoscale Res. Lett. **4**, 665–667 (2009)
51. A. Santos, L. Vojkuvka, M. Alba, V.S. Balderrama, J. Ferre-Borrull, J. Pallares, L.F. Marsal, Understanding and morphology control of pore modulations in nanoporous anodic alumina by discontinuous anodization. Phys. Status Solidi A **209**, 2045–2048 (2012)
52. C.K. Chung, M.W. Liao, O.K. Khor, Fabrication of porous anodic aluminum oxide by hybrid pulse anodization at relatively high potential. Microsyst. Technol. **20**, 1827–1832 (2014)
53. W. Lee, The anodization of aluminum for nanotechnology applications. JOM **62**, 57–63 (2010)
54. T. Nagaura, F. Takeuchi, S. Inoue, Fabrication and structural control of anodic alumina films with inverted cone porous structure using multi-step anodizing. Electrochim. Acta **53**, 2109–2114 (2008)

55. T. Nagaura, F. Takeuchi, Y. Yamauchi, K. Wada, S. Inoue, Fabrication of ordered Ni nanocones using a porous anodic alumina template. Electrochem. Comm. **10**, 681–685 (2008)
56. Y. Yamauchi, T. Nagamura, A. Ishikawa, T. Chikyow, S. Inoue, Evolution of standing mesochannels on porous anodic alumina substrates with designed conical holes. J. Am. Chem. Soc. **130**, 10165–10170 (2008)
57. A. Yamaguchi, K. Hotta, N. Teramae, Optical waveguide sensor based on a porous anodic alumina/aluminum multilayer film. Anal. Chem. **81**, 105–111 (2009)
58. W.S. Im, Y.S. Cho, G.S. Choi, F.C. Yu, D.J. Kim, Stepped carbon nanotubes synthesized in anodic aluminum oxide templates. Diam. Relat. Mater. **13**, 1214–1217 (2004)
59. R. Krishnan, C.V. Thompson, Monodomain high-aspect-ratio 2D and 3D ordered porous alumina structures with independently controlled pore spacing and diameter. Adv. Mater. **19**, 988–992 (2007)
60. Y.T. Tian, G.M. Meng, G.Z. Wang, F. Phillipp, S.H. Sun, L.D. Zhang, Step-shaped bismuth nanowires with metal-semiconductor junction characteristics. Nanotechnology **17**, 1041–1045 (2006)
61. Y.C. Sui, D.R. Acosta, J.A. Gonzalez-Leon, A. Bermudez, J. Feuchtwanger, B.Z. Cui, J.O. Flores, J.M. Saniger, Structure, thermal stability, and deformation of multibranched carbon nanotubes synthesized by CVD in the AAO template. J. Phys. Chem. B **105**, 1523–1527 (2001)
62. Y.C. Sui, J.A. Gonzales-Leon, A. Bermudez, J.M. Saniger, Synthesis of multi branched carbon nanotubes in porous anodic aluminum oxide template. Carbon **39**, 1709–1715 (2001)
63. X. Zhu, L. Liu, Y. Song, H. Jia, H. Yu, X. Xiao, X. Yang, Oxygen bubble mould effect: serrated nanopore formation and porous alumina growth. Monatsh. Chem. **139**, 999–1003 (2008)
64. M. Ghrib, R. Ouertani, M. Gaidi, N. Khedher, M.B. Salem, H. Ezzaouia, Effect of annealing on photoluminescence and optical properties of porous anodic alumina films formed in sulfuric acid for solar energy applications. Appl. Surf. Sci. **258**, 4995–5000 (2012)
65. S. Gong, A. Stolz, G. Myeong, E. Dogheche, A. Gokarna, S. Ryu, D. Decoster, Y. Cho, Effect of varying pore size of AAO films on refractive index and birefringence measured by prism coupling technique. Opt. Lett. **36**, 4272–4274 (2011)
66. S. Green, J.A. Badan, M. Gilles, A. Cortes, G. Riveros, D. Ramirez, H. Gomez, E. Quagliata, E.A. Dalchiele, R.E. Marotti, Optical properties of nanoporous Al_2O_3 obtained by aluminum anodization. Phys. Status Solidi A **4**, 618–621 (2007)
67. K. Kant, S.P. Low, A. Marshal, J.G. Shapter, D. Losic, Nanopore gradients on porous aluminum oxide generated by nonuniform anodization of aluminum. ACS Appl. Interfaces **2**, 3447–3454 (2010)
68. Y. Liu, H.H. Wang, J.E. Indacochea, M.L. Wang, A colorimetric sensor based on anodized aluminum oxide (AAO) substrate for the detection of nitroaromatics. Sensor. Actuat. B-Chem. **160**, 1149–1158 (2011)
69. A. Markovics, G. Nagy, B. Kovacs, Reflection-based sensor for gaseous ammonia. Sensor. Actuat. B-Chem. **139**, 252–257 (2009)
70. A. Markovics, B. Kovacs, Fabrication of optical chemical ammonia sensors using anodized alumina supports and sol-gel method. Talanta **109**, 101–106 (2013)
71. L.F. Marsal, L. Vojkouvka, J. Ferre-Borrull, T. Trifonov, J. Pallares, Optical characterization of self-ordered porous alumina membranes of various thicknesses. Phys. Status Solidi C **4**, 1918–1922 (2007)
72. J. Marthe, E. Meillot, G. Jeandel, F. Enguehard, J. Ilavsky, Enhancement of scattering and reflectance properties of plasma-sprayed alumina coatings by controlling the porosity. Surf. Coat. Tech. **220**, 80–84 (2013)
73. Q. Xu, H.-Y. Sun, Y.-H. Yang, L.-H. Liu, Z.-Y. Li, Optical properties and color generation mechanism of porous anodic alumina films. Appl. Surf. Sci. **258**, 1826–1830 (2011)
74. Q. Xu, Y. Yang, J. Gu, Z. Li, H. Sun, Influence of Al substrate on the optical properties of porous anodic alumina films. Mater. Lett. **74**, 137–139 (2012)

75. W. Zaghdoudi, M. Gaidi, R. Chtourou, Microstructural and optical properties of porous alumina elaborated on glass substrate. J. Mater. Eng. Perform. **23**, 869–874 (2013)
76. H. Efeoglu, T. Karacali, K. Meral, I.Y. Erdogan, Y. Onganer, Anodization of aluminium thin films on p++ Si and annihilation of strong luminescence from Al_2O_3. J. Lumin. **130**, 157–162 (2010)
77. D.H. Fan, G.Q. Ding, W.Z. Shen, M.J. Zheng, Anion impurities in porous alumina membranes: existence and functionality. Micropor. Mesopor. Mater. **100**, 154–159 (2007)
78. T. Gao, G.-W. Meng, L.-D. Zhang, Origin of the blue luminescence in porous anodic alumina films formed in oxalic acid solutions. Chinese Phys. Lett. **20**, 713–716 (2003)
79. T. Gao, G.-W. Meng, L.-D. Zhang, Blue luminescence in porous anodic alumina films: the role of the oxalic impurities. J. Phys.: Condens. Matter **15**, 2071–2079 (2003)
80. T. Gao, G.-W. Meng, L.-D. Zhang, Ultraviolet photoluminescence of porous anodic alumina films. Chinese Sci. Bull. **48**, 1090–1092 (2003)
81. Y. Kurashima, Y. Yokota, I. Miyamoto, H. Katura, Y. Sakakibara, Mode-locking nanoporous alumina membrane embedded with carbon nanotube saturable absorber. Appl. Phys. Lett. **94**(223102), 1–3 (2009)
82. Y.X. Gan, X. Zeng, L. Su, L. Yang, B.J. Gan, L. Zhang, Synthesis and enhanced light absorption of alumina matrix nanocomposites containing multilayer oxide nanorods and silver nanoparticles. Mater. Res. Bull. **46**, 1828–1836 (2011)
83. Y. Li, G.H. Li, G.W. Meng, L.D. Zhang, F. Phillipp, Photoluminescence and optical absorption caused by the f^+ centres in anodic alumina membranes. J. Phys.: Condens. Matter **13**, 2691–2699 (2001)
84. T. Li, S. Yang, L. Huang, J. Zhang, B. Gu, Y. Du, Strong photoluminescence from Cr^{3+} doped porous anodic alumina. J. Phys.: Condens. Matter **16**, 2463–2469 (2004)
85. N.I. Mukhurov, S.P. Zhvavyi, I.V. Gasenkova, S.N. Terekhov, P.P. Pershukevich, V.A. Orlovich, Photoluminescence of F-centers in films of anodic alumina. J. Appl. Spectrosc. **77**, 549–555 (2010)
86. C. Xu, Q. Xue, Y. Zhong, Y. Cui, L. Ba, B. Zhao, N. Gu, Photoluminescent blue-shift of organic molecules in nanometre pores. Nanotechnology **13**, 47–50 (2002)
87. Y. Yang, Q. Gao, Influence of sulfosalicylic acid in the electrolyte on the optical properties of porous anodic alumina membranes. Phys. Lett. A **333**, 328–333 (2004)
88. S. Garabagiu, G. Mihailescu, Thinning anodic aluminum oxide films and investigating their optical properties. Mater. Lett. **65**, 1648–1650 (2011)
89. G. Peitao, X. Zhilin, X. Yiyu, H. Caihua, Z. Lixin, Morphology and transmittance of porous alumina on glass substrate. Appl. Surf. Sci. **257**, 3307–3312 (2011)
90. C. Hong, T.T. Tang, C.-Y. Hung, R.-P. Pan, W. Fang, Liquid crystal alignment in nanoporous anodic aluminum oxide layer for LCD panel applications. Nanotechnology **21**, 1–10 (2010)
91. C.H. Jeon, D.H. Kim, Y.S. Lee, J.K. Han, Y.C. Choi, S.D. Bu, H.Y. Shin, S. Yoon, Strong pore-size dependence of the optical properties in porous alumina membranes. J. Korean Phys. Soc. **63**, 1789–1793 (2013)
92. L.-R. Zhao, J. Wang, Y. Li, Ch-W Wang, F. Zhou, W.-M. Liu, Anodic aluminum oxide films formed in mixed electrolytes of oxalic and sulfuric acid and their optical constants. Physica B **405**, 456–460 (2010)
93. Y. Katsuta, A. Yasumori, K. Wada, K. Kurashima, S. Suehara, S. Inoue, Three-dimensionally nanostructured alumina film on glass substrate: anodization of glass surface. J. Non-Cryst. Solids **354**, 451–455 (2008)
94. Y.-F. Liu, Y.-F. Tu, S.-Y. Huang, J.-P. Sang, X.-W. Zou, Effect of etch-treatment upon the intensity and peak position of photoluminescence spectra for anodic alumina films with ordered nanopore array. J. Mater. Sci. **44**, 3370–3375 (2009)
95. S. Jeon, D.-H. Kang, G.W. Lee, Difference of optical properties between porous alumina and sapphire using two-substrate method at elevated temperature. Curr. Appl. Phys. **13**, 1594–1599 (2013)

96. C.-H. Peng, C.-C. Hwang, C.-S. Hsiao, Structure and photoluminescence properties of strong blue-emitting alumina film developed from a liquid sol at low temperature. J. Alloy. Compd. **491**, 129–132 (2010)
97. S. Stojadinovic, I. Belca, M. Tadic, B. Kasalica, Z. Nedic, L. Zekovic, Galvanoluminescence properties of porous oxide films formed by anodization of aluminum in malonic acid. J. Electroanal. Chem. **619–620**, 125–130 (2008)
98. S. Stojadinovic, Z. Nedic, I. Belca, R. Vasilic, B. Kasalica, M. Petkovic, L. Zekovic, The effect of annealing on the photoluminescent and optical properties of porous anodic alumina films formed in sulfamic acid. Appl. Surf. Sci. **256**, 763–767 (2009)
99. S. Stojadinovic, R. Vasilic, Z. Nedic, B. Kasalica, I. Belca, L. Zekovic, Photoluminescen properties of barrier anodic oxide films on aluminum. Thin Solid Films **519**, 3516–3521 (2011)
100. I. Vrublevsky, A. Jagminas, S. Hemeltjen, W.A. Goedel, Effect of heat treatment on the structure of incorporated oxalate species and photoluminescent properties of porous alumina films formed in oxalic acid. J. Solid State Electrochem. **254**, 7326–7330 (2008)
101. I.A. Vrublevsky, K.V. Chernyakova, A. Ispas, A. Bund, N. Gaponik, A. Dubavik, Photoluminescence properties of heat-treated porous alumina films formed in oxalic acid. J. Lumin. **131**, 938–942 (2011)
102. J. Wang, C.-W. Wang, Y. Li, W.-M. Liu, Optical constans of anodic aluminum oxide films formed in oxalic acid solution. Thin Solid Films **516**, 7689–7694 (2008)
103. Z. Xia, Q. Xu, P. Guo, R. Wu, Laser-induced damage characteristic of porous alumina optical films. Opt. Commun. **284**, 4033–4037 (2011)
104. W.L. Xu, M.J. Zheng, S. Wu, W.Z. Shen, Effects of high-temperature annealing on structural and optical properties of highly ordered porous alumina membranes. Appl. Phys. Lett. **85**, 4364–4366 (2004)
105. X. Wang, H. Zhang, D. Zhang, Y. Ma, H.-J. Fecht, J.Z. Jiang, Color tuning by local sputtering metal nanolayer on microstructured porous alumina. Microsc. Res. Techniq. **75**, 698–701 (2012)
106. Y. Zhang, S.J. Son, H. Ju, Anodized aluminum oxide membranes of tunable porosity with platinum nanoscale-coating for photonic application. Curr. Appl. Phys. **12**, 1561–1565 (2012)
107. H.M. Chen, C.F. Hsin, R.-S. Liu, S.-F. Hu, C.-Y. Huang, Controlling optical properties of aluminum oxide using electrochemical deposition. J. Electrochem. Soc. **154**, K11–K14 (2007)
108. F. Davione, P.A. Galione, J.R. Ramos-Barrado, D. Leinen, F. Martin, E.A. Dalchiele, R.E. Marotti, Modeling of gradient index solar selective surfaces for solar thermal applications. Sol. Energy **91**, 316–326 (2013)
109. J.-J. Zhang, Z.-Y. Li, Z.J. Zhang, T.-S. Wu, H.-Y. Sun, Optical and magnetic properties of porous anodic alumina/Ni nanocomposite films. J. Appl. Phys. **113**(244305), 1–5 (2013)
110. J.-J. Zhang, Z.-Y. Li, H.-M. Zhang, H. Xue, H.-Y. Sun, Optical and magnetic properties of porous anodic alumina films embedded with Co nanowires. Chinese Phys. B **22**(087805), 1–4 (2013)
111. K. Huang, Y. Li, Z. Wu, C. Li, H. Lai, J. Kang, Asymmetric light reflectance effect in AAO on glass. Opt. Express **19**, 1301–1309 (2011)
112. T. Zhang, Z. Gong, R. Giorno, L. Que, A nanostructured Fabry-Pérot interferometer. Opt. Express **18**, 20282–20288 (2010)
113. F. Trivinho-Strixino, H.A. Guerreio, C.S. Gomes, E.C. Pereira, F.E.G. Guimaraes, Active waveguide effects from porous anodic alumina: an optical sensor proposition. Appl. Phys. Lett. **97**(011902), 1–3 (2010)
114. L.P. Hernandez-Eguia, J. Ferre-Borrull, G. Macias, J. Pallares, L.F. Marsal, Engineering optical properties of gold-coated nanoporous anodic alumina for biosensing. Nanoscale Res. Lett. **9**, 1–8 (2014)
115. G.S. Huang, X.L. Wu, G.G. Siu, P.K. Chu, On the origin of light emission from porous anodic alumina formed in sulfuric acid. Solid State Commun.**137**, 621–624 (2006)

116. K. Huang, L. Pu, Y. Shi, P. Han, R. Zhang, Y.D. Zheng, Photoluminescence oscillations in porous alumina films. Appl. Phys. Lett. **89**(201118), 1–2 (2006)
117. S. Gardelis, A.G. Nassiopoulou, V. Giannetta, M. Theodoropoulou, Photoluminescence-induced oscillations in porous anodic aluminum oxide films grown on Si: effect of the interface and porosity. J. Appl. Phys. **107**(113104), 1–5 (2010)
118. I. Vrublevsky, A. Jagminas, S. Hemeltjen, W. Goedel, Behavior of acid species during heat treatment and re-anodizing of porous alumina films formed in malonic acid. J. Solid State Electrochem. **13**, 1873–1880 (2009)
119. K.-W. Lee, T.-H. Yang, W.-L. Lu, M.-P. Houng, Fabricating 20 cm × 20 cm porous template using anodic aluminum oxide. Integr. Ferroelectr. **143**, 47–57 (2013)
120. X. Liu, F. Xu, Z. Li, W. Zhang, Photoluminescence of poly(thiophene) nanowires confined in porous anodic alumina membrane. Polymer **49**, 2197–2201 (2008)
121. W.J. Stępniowski, M. Norek, M. Michalska-Domańska, A. Bombalska, A. Nowak-Stępniowska, M. Kwaśny, Z. Bojar, Fabrication of anodic aluminium oxide with incorporated chromate ions. Appl. Surf. Sci. **259**, 324–330 (2012)
122. W.J. Stępniowski, M. Norek, M. Michalska-Domańska, A. Nowak-Stępniowska, A. Bombalska, M. Włodarski, Z. Bojar, Incorporation of copper chelate ions into anodic alumina walls. Mater. Lett. **106**, 242–245 (2013)
123. Y. Du, W.L. Cai, C.M. Mo, J. Chen, L.D. Zhang, X.G. Zhu, Preparation and photoluminescence of alumina membranes with ordered pore arrays. Appl. Phys. Lett. **74**, 2951–2953 (1999)
124. J.H. Chen, C.P. Huang, C.G. Chao, T.M. Chen, The investigation of photoluminescence centers in porous alumina membranes. Appl. Phys. A-Mater. **84**, 297–300 (2006)
125. J. Hohlbein, U. Rehn, R.B. Wehrspohn, In-situ optical characterization of porous alumina. Phys. Status Solidi A **201**, 803–807 (2004)
126. K.H. Lee, J.H. Crawford Jr, Luminescence of the F-center in sapphire. Phys. Rev. B **19**, 3217–3221 (1979)
127. S. Jheeta, D.C. Jain, R. Kumar, F. Singh, K.B. Garg, Photoluminescence study of swift heavy ion (SHI) induced defect centers in sapphire. J. Nucl. Mater. **353**, 190–192 (2006)
128. A. Santos, T. Kumeira, D. Losic, Nanoporous anodic alumina: a versatile platform for optical biosensors. Materials **7**, 4297–4320 (2014)
129. G.S. Huang, X.L. Wu, Y.F. Mei, X.F. Shao, Strong blue emission from anodic alumina membranes with ordered nanopores. J. Appl. Phys. **93**, 582–585 (2003)
130. M.E. Nasir, B. Hamilton, Measurement of the physical and electronic properties of ordered nanoporous alumina using XUV excitation spectroscopy. J. Phys. D Appl. Phys. **42**(195404), 1–7 (2009)
131. T.-E. Nee, C.-H. Fang, J.-C. Wang, P.-L. Fan, J.-A. Jiang, Characterization of the anomalous luminescence properties from self-ordered porous anodic alumina with oxalic acid electrolytes. Thin Solid Films. **518**, 1439–1442 (2009)
132. Y.-L. Shi, X.-G. Zhang, H.-L. Li, Enhanced photoluminescence of Eu(III)-anchored porous anodic alumina films. Spectrosc. Lett. **34**, 419–426 (2001)
133. J. Wang, C.-W. Wang, S.-Y. Li, F. Zhou, The effect of oxalic and sulfuric ions on the photoluminescence of anodic aluminium oxide formed in a mixture of sulfuric and oxalic acid. Appl. Phys. A-Mater. **94**, 939–942 (2009)
134. I. Vrublevsky, A. Jagminas, S. Hemeltjen, W.A. Goadel, Photoluminescent behavior of heat-treated porous alumina films formed in malonic acid. Appl. Surf. Sci. **256**, 2013–2017 (2010)
135. Y. Yamamoto, N. Baba, S. Tajima, Coloured materials and photoluminescence centres in anodic film on aluminium. Nature **289**, 572–574 (1981)
136. P.P. Pershukevich, D.V. Shabov, V.P. Osipov, J. Schreiber, V.A. Lapina, Luminescence properties of oxide coatings of aluminum alloys. J. Appl. Spectrosc. **78**, 524–533 (2011)
137. M. Kokonou, A.G. Nassiopoulou, A. Travlos, Structural and photoluminescence properties of thin alumina films on silicon, fabricated by electrochemistry. Mater. Sci. Eng. B-Adv. **101**, 65–70 (2003)

138. A. Rauf, M. Mehmood, M. Ahmed, M. Hasan, M. Aslam, Effects of ordering quality of the pores on the photoluminescence of porous anodic alumina prepared in oxalic acid. J. Lumin. **130**, 792–800 (2010)
139. Y.B. Li, M.J. Zheng, L. Ma, High-speed growth and photoluminescence of porous anodic alumina films with controllable interpore distances over a large range. Appl. Phys. Lett. **91** (073109), 1–3 (2007)
140. Y. Li, M. Zheng, M. Li, W. Shen, Fabrication of highly ordered nanoporous alumina films by stable high-field anodization. Nanotechnology **17**, 5101–5105 (2006)
141. L. Zaraska, G.D. Sulka, M. Jaskuła, Anodic alumina membranes with defined pore diameters and thicknesses obtained by adjusting the anodizing duration and pore opening/widening time. J. Solid State Electrochem. **15**, 2427–2436 (2011)
142. A. Santos, M. Alba, M.M. Rahman, P. Formentin, J. Ferre-Borrull, J. Pallares, L.F. Marsal, Structural tuning of photoluminescence in nanoporous anodic alumina by hard anodization in oxalic and malonic acids. Nanoscale Res. Lett. **7**, 1–11 (2012)
143. I.A. Vrublevsky, K.V. Chernyakova, A. Ispas, A. Bund, S. Zavadski, Optical properties of thin anodic alumina membranes formed in a solution of tartaric acid. Thin Solid Films **556**, 230–235 (2014)
144. G.H. Li, Y. Zhang, L.D. Zhang, Wavelength dependent photoluminescence of anodic alumina membranes. J. Phys.: Condens. Matter **15**, 8663–8671 (2003)
145. Z. Li, K. Huang, Blue luminescence in porous anodic alumina films. J. Phys.: Condens. Matter **19**, 1–7 (2007)
146. N.I. Mukhurov, S.P. Zhvavyi, S.N. Terekhov, A.Y. Panarin, I.F. Kotova, P.P. Perhukevich, I. A. Khodasevich, I.V. Gasenkova, V.A. Orlovich, Influence of electrolyte composition on photoluminescent properties of anodic aluminum oxide. J. Appl. Spectrosc. **75**, 214–218 (2008)
147. G.G. Khan, A.K. Singh, K. Mandal, Structure dependent photoluminescence of nanoporous amorphous anodic aluminium oxide membranes: role of F^+ center defects. J. Lumin. **134**, 772–777 (2013)
148. Y.F. Mei, G.G. Siu, J.P. Zou, X.L. Wu, Color centers vs electrolytes for Si-based porous anodic alumina. Phys. Lett. A **324**, 479–483 (2004)
149. Y. Li, Ch-W Wang, L.-R. Zhao, W.-M. Liu, Photoluminescence properties of porous anodic aluminium oxide membranes formed in mixture of sulfuric and oxalic acid. J. Phys. D Appl. Phys. **42**(045407), 1–5 (2009)
150. A. Nourmohammadi, S.J. Asadabadi, M.H. Yousefi, M. Ghasemzadeh, Photoluminescence emission of nanoporous anodic aluminum oxide films prepared in phosphoric acid. Nanoscale Res. Lett. **7**, 1–7 (2012)
151. Z. Li, K. Huang, Optical properties of alumina membranes prepared by anodic oxidation process. J. Lumin. **127**, 435–440 (2007)
152. S. Shingubara, Fabrication of nanomaterials using porous alumina templates. J. Nanopart. Res. **5**, 17–30 (2003)
153. X. Sun, F. Xu, Z. Li, W. Zhang, Photoluminescence properties of anodic alumina membranes with ordered nanopore arrays. J. Lumin. **121**, 588–594 (2006)
154. Z. Li, K. Huang, The effect of high-temperature annealing on optical properties of porous anodic alumina formed in oxalic acid. Luminescence **22**, 355–361 (2007)
155. Y. Han, L. Cao, F. Xu, T. Chen, Z. Zheng, K. Qian, W. Huang, Quantitative investigation in the influence of oxalic impurities on photoluminescence properties of porous AAOs. Mater. Chem. Phys. **129**, 1247–1251 (2011)
156. J.H. Wu, X.L. Wu, N. Tang, X.M. Bao, Strong ultraviolet and violet photoluminescence form Si-based anodic porous alumina films. Appl. Phys. A-Mater. **72**, 735–737 (2001)
157. A. Santos, G. Macias, J. Ferre-Borrull, J. Pallares, J.F. Marsal, Photoluminescent enzymatic sensor based on nanoporous anodic alumina. ASC Appl. Mater. Interfaces **4**, 3584–3588 (2012)
158. C.-L. Feng, Z. Zhong, M. Steinhart, A.-M. Caminade, J.-P. Majoral, W. Knoll, Graded-bangap quantum-dot-modified nanotubes: a sensitive biosensor for enhnanced detection of DNA hybridization. Adv. Mater. **19**, 1933–1936 (2007)

159. A. Santos, T. Kumeria, D. Losic, Optically optimized photoluminescent and interferometric biosensors base on nanoporous anodic alumina: a comparison. Anal. Chem. **85**, 7904–7911 (2013)
160. S.-J. Yuan, Q.-S. Li, Z.-F. Pan, Y.-F. Dong, Q.-T. Wang, H.-H. Ji, Photoluminescence spectra of organic dyes embedded in porous alumina. Chin. J. Semicond. **22**, 1406–1410 (2001)
161. X. Wu, S. Xiong, J. Guo, L. Wang, C. Hua, Y. Hou, P.K. Chu, Ultrathin amorphous alumina nanoparticles with quantum-confined oxygen-vacancy-induced blue photoluminescence as fluorescent biological labels. J. Phys. Chem. C **116**, 2356–2362 (2012)
162. Y. Cao, J.O. Schenk, M.A. Fiddy, Third order nonlinear effect near a degenerate band edge. Optic. Photo. Lett. **1**, 1–7 (2008)
163. M.E. Calvo, S. Colodrero, N. Hidalgo, G. Lozano, C. Lopez-Lopez, O. Sanchez-Sobrado, H. Miguez, Porous one dimensional photonic crystals: novel multifunctional materials for environmental and energy applications. Energ. Environ. Sci. **4**, 4800–4812 (2011)
164. M.J.A. De Dood, E. Snoeks, A. Moroz, A. Polman, Design and optimization of 2D photonic crystal waveguides based on silicon. Opt. Quant. Electron. **34**, 145–159 (2002)
165. J. Choi, Y. Luo, R.B. Wehrspohn, R. Hillebrand, J. Schilling, U. Gösele, Perfect two-dimensional porous alumina photoni crystals with duplex oxide layer. J. Appl. Phys. **94**, 4757–4762 (2003)
166. A. Sato, Y. Pennec, T. Yanagishita, H. Masuda, W. Knoll, B. Djafari-Rouhani, G. Fytas, Cavity-type hypersonic phononic crystals. New J. Chem. **14**(113032), 1–13 (2012)
167. J.D. Joannopoulos, S.G. Johnson, J.N. Winn, R.D. Meade, *Photonic Crystals* (Princeton University Press, Molding the Flow of Light, 2008)
168. T. Maka, D.N. Chigrin, S.G. Romanov, C.M. Sotomayor Torres, Three dimensional photonic crystals in the visible regime. Prog. Electromagn. Res. **41**, 307–335 (2003)
169. R.B. Wehrspohn, J. Schilling, Electrochemically prepared pore arrays for photonic-crystal applications. MRS Bull. **26**, 623–626 (2001)
170. H. Masuda, M. Ohya, H. Asoh, M. Nakao, M. Nohtomi, T. Tamamura, Photonic crystal using anodic porous alumina. J. Appl. Phys. **38**, L1403–L1405 (1999)
171. H. Masuda, M. Ohaya, K. Nishio, H. Asoh, M. Nakao, M. Nohtomi, A. Yakoo, T. Tamamura, Electrochemically prepared pore arrays for photonic-crystal applications. Jpn. J. Appl. Phys. **39**, L1039–L1041 (2000)
172. H. Masuda, M. Ohya, H. Asoh, K. Nishio, Photonic band gap in naturally occurring ordered anodic porous alumina. Jpn. J. Appl. Phys. **40**, L1217–L1219 (2001)
173. H. Masuda, M. Yamada, F. Matsumoto, S. Yokoyama, S. Mashiko, M. Nakao, K. Nishio, Lasing from two-dimensional photonic crystals using anodic porous alumina. Adv. Mater. **18**, 213–216 (2006)
174. J. Choi, K. Schilling, K. Nielsch, R. Hillebrand, M. Reiche, R.B. Wehrspohn, U. Gösele, Large-area porous alumina photonic crystals via imprint method. Mat. Res. Soc. Symp. Proc. **722**, 2.1–2.6 (2002)
175. H. Masuda, T. Kondo, K. Nishio, Functional optical devices using highly ordered hole array architectures of anodic porous alumina. Proc. SPIE **8204**, 820414 (2011)
176. I. Mikulskas, S. Juodkazis, R. Tomasiunas, J.G. Dumas, Aluminum oxide photonic crystals grown by a new hybrid method. Adv. Mater. **13**, 1574–1577 (2001)
177. V. Mizeikis, I. Mikulskas, R. Tomasionas, S. Juodkazis, S. Matsuto, H. Misawa, Optical characteristics of two-dimensional photonic crystals in anodic aluminum oxide films. Jpn. J. Appl. Phys. **43**, 3643–3647 (2004)
178. R.B. Wehrspohn, A.P. Li, K. Nielsch, F. Müller, W. Erfurth, U. Gösele, Highly ordered alumina films: pore growth and applications. Electrochem. Soc. 271–282 (2000)
179. M. Saito, M. Miyagi, Anisotropic optical loss and birefrigence of anodized alumina film. J. Opt. Soc. Am. A **6**, 1895–1900 (1989)
180. G.K. Maliarevich, I.S. Molchan, N.V. Gaponenko, A.V. Mudryi, S.V. Gaponenko, A.A. Lutich, G.E. Thompson, Optoelectronic applications of lantanide-doped sol-gel products and porous anodic alumina. J. Soc. Inf. Display **14**, 583–588 (2006)

181. A.A. Lutich, I.S. Molchan, N.V. Gaponenko, S.V. Gaponenko, Scattering, propagation and polarization changes of light in nanoporous anodic alumina. Proc. SPIE **6258**, 1–9 (2006)
182. A.A. Lutich, I.S. Molchan, N.V. Gaponenko, Briefringence in porous anodic aluminum oxide. Opt. Spectrosc. **97**, 817–821 (2004)
183. A.A. Lutich, M.B. Danailov, S. Volchek, V.A. Yakovtseva, V.A. Sokol, S.V. Gaponenko, Birefringence of nanoporous alumina: dependence on structure parameters. Appl. Phys. B-Lasers Opt. **84**, 327–331 (2006)
184. X. Hu, Z.-Y. Ling, S.-S. Chen, X.-X. He, Influence of light scattering on transmission spectra of photonic crystals of anodized alumina. Chinese Phys. Lett. **25**, 3284–3287 (2008)
185. G.L. Shang, G.T. Fei, Y. Zhang, P. Yan, S.H. Xu, L.D. Zhang, Preparation of narrow photonic bandgaps located in the near infrared region and their applications in ethanol gas sensing. J. Mater. Chem. C **1**, 5285–5291 (2013)
186. G.L. Shang, G.T. Fei, Y. Zhang, P. Yan, S.H. Xu, H.M. Ouyang, L.D. Zhang, Fano resonance in anodic aluminium oxide based photonic crystals. Sci. Rep. **4**, 1–6 (2014)
187. L. Pavesi, Porous silicon dielectric multilayers and microcavities. Riv. Nuovo Cimento **20**, 1–76 (1997)
188. D.-L. Guo, L.-X. Fan, F.-H. Wang, S.-Y. Huang, X.-W. Zou, Porous anodic aluminum oxide Bragg stacks as chemical sensors. J. Phys. Chem. C **112**, 17952–17956 (2006)
189. M. Francon, *Optical Interferometry* (Academic Press, New York ,1966), p. 178
190. J. Hawkes, I. Latimer, *Lasers: Theory and Practice* (Prentice-Hall , Lebanon, 1995), p. 222
191. T. Kumeria, A. Santos, D. Losic, Nanoporous anodic alumina platforms: engineered surface chemistry and structure for optical sensing applications. Sensors **14**, 1187–11918 (2014)
192. K. Malek, A. Brzózka, A. Rygula, G.D. Sulka, SERS imaging of silver coated nanostructured Al and Al_2O_3 substrates. The effect of nanostructure. J. Raman Spectrosc. **45**, 281–291 (2014)
193. S.-H. Yeom, O.-G. Kim, B.-H. Kang, K.-J. Kim, H. Yuan, D.-H. Kwon, H.-R. Kim, S.-W. Kang, Highly sensitive nano-porous lattice biosensor based on localized surface plasmon resonance and interference. Opt. Express **19**, 22882–22891 (2011)
194. A. Makhal, S. Sarkar, S.K. Pal, H. Yan, D. Wulferding, F. Cetin, P. Lemmens, Ultrafast excited state deactivation of doped porous anodic alumina membranes. Nanotechnology **23**, 1–8 (2012)
195. R.-L. Zong, J. Zhou, Q. Li, B. Du, B. Li, M. Fu, X.-W. Qi, L.-T. Li, Synthesis and optical properties of silver nanowire arrays embedded in anodic alumina membrane. J. Phys. Chem. B **108**, 16713–16716 (2004)
196. Z.-K. Zhou, X.-R. Su, X.-N. Peng, L. Zhou, Sublinear and superlinear photoluminescence from Nd doped anodic aluminum oxide templates loaded with Ag nanowires. Opt. Express **16**, 18028–18033 (2008)
197. J. Yao, Z. Liu, Y. Liu, Y. Wang, C. Sun, G. Bartal, A.M. Stacy, X. Zhang, Optical negative refraction in bulk metamaterials of nanowires. Science **321**, 930 (2008)
198. P.R. Evans, R. Kullock, W.R. Hendren, R. Atkinson, R.J. Pollard, L.M. Eng, Optical transmission properties and electric field distribution of interacting 2D silver nanorod arrays. Adv. Funct. Mater. **18**, 1075–1079 (2008)
199. P.R. Evans, W.R. Hendren, R. Atkinson, R.J. Pollard, Optical transmission measurements of silver, silver-gold alloy and silver-gold segmented nanorods in thin film alumina. Nanotechnology **19**, 1–8 (2008)
200. L. Menon, W.T. Lu, A.L. Friedman, S.P. Bennett, D. Heiman, S. Sridhar, Negative index metamaterials based on metal-dielectric nanocomposites for imaging applications. Appl. Phys. Lett. **93**(123117), 1–3 (2008)
201. X. Ao, S. He, Negative refraction of left-handed behaviour in porous alumina with infiltrated silver at an optical wavelength. Appl. Phys. Lett. **87**(101112), 1–3 (2005)
202. A. Yasui, M. Iwasaki, T. Kawahara, H. Tada, S. Ito, Color properties of gold-silver alternate nanowires electrochemically grown in the pores of aluminum anodic oxidation film. J. Colloid Interf. Sci. **293**, 443–448 (2006)

203. H. Yan, P. Lemmens, D. Wulferding, J. Shi, K.D. Becker, C. Lin, A. Lak, M. Schilling, Tailoring defect structure and optical absorption of porous anodic aluminium oxide membranes. Mater. Chem. Phys. **135**, 206–211 (2012)
204. M. Es-Souni, S. Habouti, Ordered nanomaterial thin films via supported anodized alumina templates. Front. Mater. **1**, 1–9 (2014)
205. A.V. Kabashin, P. Evans, S. Pastkovsky, W. Hendren, G.A. Wurtz, R. Atkinson, R. Pollard, V.A. Podolskiy, A.V. Zayats, Plasmonic nanorod metamaterials for biosensing. Nat. Mater. **8**, 867–871 (2009)
206. R. Atkinson, W.R. Hendren, G.A. Wurtz, W. Dickson, A.V. Zayats, P. Evans, R.J. Pollard, Anisotropic optical properties of arrays of gold nanorods embedded in alumina. Phys. Rev. B **73**(235402), 1–8 (2006)
207. P. Evans, W.R. Hendren, R. Atkinson, G.A. Wurtz, W. Dickson, A.V. Zayats, R.J. Pollard, Growth and properties of gold and nickel nanorods in thin film aumina. Nanotechnology **17**, 5746–5753 (2006)
208. Q. Xu, W.-J. Ye, S.-Z. Feng, H.-Y. Sun, Synthesis and properties of iridescent Co-containing anodic aluminum oxide films. Dyes Pigments **111**, 185–189 (2014)
209. H.J. Tang, F.Q. Wu, H.L. Wang, Y.H. Wei, Q.S. Li, Microstructure and optical properties of Cu/Al_2O_3 nanoarray composite structure. J. Appl. Phys. **100**(064316), 1–4 (2006)
210. J.-J. Zhang, X. Hou, L.-H. Liu, H.-Y. Sun, Optical and magnetic properties of PAA@Fe nanocomposite films. AIP Adv. **3**, 072116, 1–6 (2013)
211. E. Wäckelgård, A study of the optical properties of nickel-pigmented anodic alumina in the infrared region. J. Phys.: Condens. Matter **8**, 5125–5138 (1996)
212. L. Arurault, G. Zamora, V. Vilar, P. Winterton, R. Bes, Electrical behaviour, characteristics and properties of anodic aluminium oxide films coloured by nickel electrodeposition. J. Mater. Sci. **45**, 2611–2618 (2010)
213. R. Akolkar, Y.-M. Wang, H.-H. Kuo, Kinetics of the electrolytic coloring process on anodized aluminum. J. Appl. Electrochem. **37**, 291–296 (2007)
214. C. Liang, K. Terabe, T. Tsuruoka, M. Osada, T. Hasegawa, M. Aono, AgI/Ag heterojunction nanowires: facile electrochemical synthesis, photoluminescence, and enhanced ionic conductivity. Adv. Funct. Mater. **17**, 1466–1472 (2007)
215. E. Hutter, J.H. Fendler, Exploitation of localized plasmon resonance. Adv. Mater. **16**, 1685–1706 (2004)
216. S.K. Ghosh, T. Pal, Interparticle coupling effect on the surface plasmon resonance of gold nanoparticles: from theory to applications. Chem. Rev. **107**, 4749–4862 (2007)
217. W.L. Barnes, A. Dereux, T.W. Ebbesen, Surface plasmon subwavelength optics. Nature **424**, 824–830 (2003)
218. R.-L. Zong, J. Zhou, B. Li, M. Fu, S.-K. Shi, L.-T. Li, Optical properties of transparent copper nanorod and nanowire arrays embedded in anodic aumina oxide. J. Chem. Phys. **123** (094710), 1–5 (2005)
219. W.T. Lu, S. Sridhar, Superlens imaging theory for anisotropic nanostructured metamaterials with broadband all-angle negative refraction. Phys. Rev. B **77**(233101), 1–4 (2008)
220. X. Hu, C.T. Chan, Photonic crystals with silver nanowires as a near-infrared superlens. Appl. Phys. Lett. **85**, 1520–1522 (2004)
221. X. Zhang, Absolute negative, refraction and imaging of unpolarized electromagnetic waves by two-dimensional photonic crystals. Phys. Rev. B **70**(205102), 1–6 (2004)
222. O. Takayama, M. Cada, Two-dimensional metallo-dielectric photonic crystals embedded in anodic porous alumina for optical wavelengths. Appl. Phys. Lett. **85**, 1311–1313 (2004)
223. D. Pullini, P. Repetto, S. Bernard, L. Doskolovich, P. Perlo, Rigorous calculations and fabrication by self-assembly techniques of 2D subwavelength structures of gold for photonic applications. Appl. Optics **44**, 5127–5130 (2005)
224. M. Saito, M. Miyagi, Micropolarizer using anodized alumina with implanted metallic columns: theoretical analysis. Appl. Optics **28**, 3529–3533 (1989)

225. J. Zhang, Y. Yan, X. Co, L. Zhang, Microarrays of silver nanowires embedded in anodic alumina membrane templates: size dependence of polarization characteristics. Appl. Optics **45**, 297–304 (2006)
226. Y.T. Pang, G.W. Meng, Q. Fang, L.D. Zhang, Silver nanowire array infrared polarizers. Nanotechnology **14**, 20–24 (2003)
227. H.J. Tang, F.Q. Wu, S. Zhang, Optical properties of Co/Al_2O_3 nano-array composite structure. Appl. Phys. A-Mater. **85**, 29–32 (2006)
228. Y.T. Pang, G.W. Meng, Y. Zhang, Q. Fang, L.D. Zhang, Copper nanowire arrays for infrared polarizer. Appl. Phys. A-Mater. **76**, 533–536 (2003)
229. M. Saito, M. Kirihara, T. Taniguchi, M. Miyagi, Micropolarizer made of the anodized alumina film. Appl. Phys. Lett. **55**, 607–609 (1989)
230. Y.-T. Pang, G.-W. Meng, W.-J. Shan, Q. Fang, L.-D. Zhang, Micropolarizer of ordered Ni nanowire arrays embedded in porous anodic alumina membrane. Chinese Phys. Lett. **30**, 144–147 (2003)
231. Y.-T. Pang, G.-W. Meng, L.-D. Zhang, Y. Qin, X.-Y. Gao, A.-W. Zhao, Q. Fang, Arrays of ordered Pb nanowires and their optical properties for laminated polarizers. Adv. Funct. Mater. **12**, 719–722 (2002)
232. Y. Zhao, D. Yang, C. Zhou, Q. Yang, D. Que, Photoluminescence properties of the composite of porous alumina and poly(2,5-dibutoxy-1,4 phenylenevinylene). J. Lumin. **105**, 57–60 (2003)
233. D. Qi, K. Kwong, K. Rademacher, M.O. Wolf, J.F. Young, Optical emission of conjugated polymers adsorbed to nanoporous alumina. Nano Lett. **3**, 1265–1268 (2003)
234. F. Kong, X.L. Wu, G.S. Huang, Y.M. Yang, R.K. Yuan, C.Z. Yang, P.K. Chu, G.C. Siu, Optical emission from Nano-poly[2-methoxy-5-(2-ethyl-hexyloxy)-p-phenylene vinylene] arrays. J. Appl. Phys. **98**(074304), 1–4 (2005)
235. F. Kong, G.S. Huang, Y.M. Yang, C.Z. Yang, X.M. Bao, R.K. Yuan, Conformation and luminescence characteristics of nano-poly[2-metoxy-5-(20-ethyl-hexyloxy)-p-phenylene vinylene] in two-dimensional arrays. J. Polym. Sci. Part B: Polym. Phys. **44**, 3037–3041 (2006)
236. F. Kong, Y. Yang, X. Zhang, B. Lin, Z. Qi, T. Qiu, Effect of absorption to nanopore on optical properties of conjugated polymers in porous anode alumina. J. Appl. Phys. **109** (044309), 1–5 (2011)
237. T.P. Nguyen, S.H. Yang, P. Le Rendu, H. Khan, Optical properties of poly(2-methoxy-5-(2′-ethyl-hexyloxy)-phenylene vinylene) deposited on porous alumina substrates. Compos. Part A-Appl. Sci. Manuf. **36**, 515–519 (2005)
238. X. Liu, F. Xu, Z. Li, J. Zhu, W. Zhang, Synthesis and optical properties of Poly[3-(2-methoxyphenyl)thiophene] nanowires confined in porous anodic alumina membrane. Opt. Mater. **30**, 1861–1866 (2008)
239. K.M. Coakley, B.S. Srinivasan, J.M. Ziebarth, C. Goh, Y. Liu, M.D. McGehee, Enhanced hole mobility in regioregular polythiophene infiltrated in straight nanopores. Adv. Funct. Mater. **15**, 1927–1932 (2005)
240. J. Martin, M. Campoy-Quiles, A. Nogales, M. Garriga, M.I. Alonso, A.R. Goni, M. Martin-Gonzales, Poly(3-hexylthiophene) nanowires in porous alumina: internal structure under confinement. Soft Matter **10**, 3335–3346 (2014)
241. H.-W. Shin, E.-J. Shin, S.Y. Cho, S.-L. Oh, Y.-R. Kim, Enhanced energy transfer within pvk/alq3 polymer nanowires induced by the interface effect of nanochannels in porous alumina membrane. J. Phys. Chem. C **111**, 15391–15396 (2007)
242. T.Q. Nguyen, J. Wu, V. Doan, B.J. Schwartz, S.H. Tolbert, Control of energy transfer in oriented conjugated polymer-mesoporous silica composites. Science **288**, 652–656 (2000)
243. S. Moynihan, D. Iacopino, D. O'Carroll, P. Lovera, G. Redmond, Template synthesis of highly oriented polyfluorene nanotube arrays. Chem. Mater. **20**, 996–1003 (2008)
244. C.-H. Huang, H.-Y. Lin, S. Chen, C.-Y. Liu, H.-C. Chui, Y. Tzeng, Electrochemically fabricated self-aligned 2-D silver/alumina arrays as reliable SERS sensors. Opt. Express **19**, 11441–11450 (2011)

245. C.-H. Huang, H.-Y. Lin, Y. Tzeng, C.-H. Fan, C. Lu, C.-Y. Li, C.-W. Huang, N.-K. Chen, H.-C. Chui, Optical characteristics of pore size on porous anodic aluminium oxide films with embedded silver nanoparticles. Sensor. Actuat. A-Phys.**180**, 49–54 (2012)
246. N. Ji, W. Ruan, C. Wang, Z. Lu, B. Zhao, Fabrication of silver decorated anodic aluminum oxide substrate and its optical properties on surface-enhanced raman scattering and thin film interference. Langmuir **25**, 11869–11873 (2009)
247. Q. Hu, H.H. Lee, D.-Y. Jeong, Y.-S. Kim, K.-B. Kim, J. Xu, T.-S. Yoon, Reflectivity spectra and colors of porous anodic aluminum oxide containing silver nanoparticles by plasmonic absorption. J. Nanosci. Nanotechnol. **12**, 1979–1983 (2012)
248. G. Giallongo, C. Durante, R. Pilot, D. Garoli, R. Bozio, F. Romanto, A. Gennaro, G.A. Rizzi, G. Granozzi, Growth and optical properties of silver nanostructures obtained on connected anodic aluminum oxide templates. Nanotechnology **23**(325604), 1–10 (2012)
249. H.-H. Wang, C.-Y. Liu, S.-B. Wu, N.-W. Liu, C.-Y. Peng, T.H. Chan, C.-F. Hsu, J.-K. Wang, Y.L. Wang, Highly raman-enhancing substrates based on silver nanoparticle arrays with tunable sub-10 nm gaps. Adv. Mater. **18**, 491–495 (2006)
250. T. Kondo, K. Nishio, H. Masuda, Mutilayered three-dimensional structures of Ag nanoparticles in anodic porous alumina. Jpn. J. Appl. Phys. **49**(025002), 1–3 (2010)
251. S. Ye, Y. Hou, R. Zhu, S. Gu, J. Wang, Z. Zhang, S. Shi, J. Du, Synthesis and photoluminescence enhancement of silver nanoparticles decorated porous anodic alumina. J. Mater. Sci. Technol. **27**, 165–169 (2011)
252. C.A. Foss, L.H. Gabor, J.A. Stockert, C.R. Matrin, Optical properties of composite membranes containing arrays of nanoscopic gold cylinders. J. Phys. Chem. **96**, 7497–7499 (1992)
253. C.A. Foss, G.L. Hornyak, J.A. Stockert, C.R. Martin, Template-synthesized nanoscopic gold particles: optical spectra and the effects of particle size and shape. J. Phys. Chem. **98**, 2963–2971 (1994)
254. G.L. Hornyak, C.J. Patrissi, R. Martin, Fabrication, characterization, and optical properties of gold nanoparticle/porous alumina composites: the nonscattering Maxwell-Garnett limit. J. Phys. Chem. B **101**, 1548–1555 (1997)
255. J.C. Hulteen, C.J. Patrissi, D.L. Miner, E.R. Crosthwait, E.B. Oberhauser, C.R. Martin, Changes in the shape and optical properties of gold nanoparticles contained within alumina membranes due to low-temperature annealing. J. Phys. Chem. B **101**, 7727–7731 (1997)
256. C.K. Preston, M. Moskovits, Optical characterization of anodic aluminum oxide films containing electrochemically deposited metal particles. 1. Gold in phosporic acid anodic aluminum oxide films. J. Phys. Chem. **97**, 8495–8503 (1993)
257. T. Sawitowski, Y. Miquel, A. Heilmann, G. Schmid, Optical properties of quasi one-dimensional chains of gold nanoparticles. Adv. Funct. Mater. **11**, 435–440 (2001)
258. V.G. Stoleru, E. Towe, Plasmon resonant Au nanospheres and nanorods in anodic alumina matrix. Microelectron. Eng. **81**, 358–365 (2005)
259. M.L. Sandrock, C.A. Foss, Synthesis and linear optical properties of nanoscopic gold particle pair structures. J. Phys. Chem. **103**, 11398–11406 (1999)
260. M.L. Sandrock, M. El-Kouedi, M. Gluodenis, C.A. Foss, Optical properties of nanoparticle pair structures. Mat. Res. Soc. Symp. Proc. **635**, C2.1.1–C2.1.10 (2001)
261. S.M. Marinakos, L.C. Brousseau, A. Jones, D.L. Feldheim, Template synthesis of one-dimensional Au, Au-poly(pyrrole), and poly(pyrrole) nanoparticle arrays. Chem. Mater. **10**, 1214–1219 (1998)
262. J.-H. Chen, C.-G. Chao, J.-C. Ou, T.-F. Liu, Growth and characteristics of lead sulfide nanocrystals produced by the porous alumina membrane. Surf. Sci. **601**, 5142–5147 (2007)
263. Y. Ishikawa, Y. Matsumoto, Electrodeposition of TiO_2 photocatalyst into porous alumite prepared in phosphoric acid. Solid State Ionics **151**, 213–218 (2002)
264. G. Shi, C.M. Mo, W.L. Cai, L.D. Zhang, Photoluminescence of ZnO nanoparticles in alumina membrane with ordered pore arrays. Solid State Commun. **115**, 253–256 (2000)

265. T. Gao, G. Meng, Y. Tian, Y. Sun, X. Liu, L. Zhang, Photoluminescence of ZnO nanoparticles loaded into porous anodic alumina hosts. J. Phys.: Condens. Matter **14**, 12651–12656 (2002)
266. G. Schmid, Materials in nanoporous alumina. J. Mater. Chem. **12**, 1231–1238 (2002)
267. J.C. Maxwell Garnett, Colours in metal glasses and in metallic films. Philos. Trans. R. Soc. London A **203**, 385–420 (1904)
268. J.C. Maxwell Garnett, Colours in metal glasses, in metallic films, and in metallic solutions. II. Philos. Trans. R. Soc. London A **205**, 237–288 (1906)
269. R. Kudrawiec, A. Podhorecki, N. Mirowska, J. Misiewicz, I. Molchan, N.V. Gaponenko, A. A. Lutich, S.V. Gaponenko, Photoluminescence investigation of Europium-doped alumina, titania and indium sol–gel-derived films in porous anodic alumina. Mater. Sci. Eng. B-Adv. **105**, 53–56 (2003)
270. I.S. Molchan, N.V. Gaponenko, R. Kudrawiec, J. Misiewicz, L. Bryja, G.E. Thompson, P. Skeldon, Visible luminescence from europium-doped alumina sol-derived films confined in porous anodic alumina. J. Alloy. Compd. **341**, 251–254 (2002)
271. N.V. Gaponenko, I.S. Molchan, O.V. Sergeev, G.E. Thompson, A. Pales, P. Skeldon, R. Kudrawiec, L. Bryja, J. Misiewicz, J.C. Pivin, B. Hamilton, E.A. Stepanova, Enhancment of green terbium-related photoluminescence from higly doped microporous alumina xerogels in mesoporous anodic alumina. J. Electrochem. Soc. **149**, H49–H52 (2002)
272. J.C. Pivin, N.V. Gaponenko, I. Molchan, R. Kudrawiec, J. Misiewicz, L. Bryja, G.E. Thompson, P. Skeldon, Comparsion of terbium photoluminescence from ion implanted and sol–gel-derived films. J. Alloy. Compd. **341**, 272–274 (2002)
273. A. Podhorodecki, M. Banski, J. Misiewicz, J. Serafińczuk, N.V. Gaponenko, Influence of annealing on excitation of terbium uminescence in $YAlO_3$ films deposited onto porous anodic alumina. J. Electrochem. Soc. **157**, H628–H632 (2010)
274. N.V. Gaponenko, D.M. Unuchak, A.V. Mudryi, G.K. Malyarevich, O.B. Gusev, M.V. Stepikhova, L.V. Krasilnikova, A.P. Stupak, S.M. Kleshcheva, M.I. Samoilovich, M.Y. Tsvetkov, Modification of erbium photoluminescence excitation spectra for the emission wavelength 1.54 μm in mesoscopic structures. J. Lumin. **121**, 217–221 (2006)
275. A. Podhorodecki, R. Kudrawiec, J. Misiewicz, N.V. Gaponenko, D.A. Tsyrkunov, 1.54 μm photoluminescence from Er-doped sol-gel derived In_2O_3 films embedded in porous anodic alumina. Opt. Mater. **28**, 685–687 (2006)
276. N.V. Gaponenko, O.V. Sergeev, V.E. Borisenko, J.C. Pivin, P. Skeldon, G.E. Thompson, B. Hamolton, J. Misiewicz, L. Bryja, R. Kudrawiec, A.P. Stupak, E.A. Stepanova, Terbium photoluminescence in polysiloxane films. Mater. Sci. Eng. B-Adv. **81**, 191–193 (2001)
277. S.A. Klimin, E.P. Chukalina, M.N. Popova, E. Antic-Fidancev, P. Aschehoug, N.V. Gaponenko, L.S. Molchan, D.A. Tsyrkunov, Absorption and emission spectra of erbium-doped titania xerogels confined on porous anodic alumina. Phys. Lett. A **323**, 159–163 (2004)
278. N.V. Gaponenko, I.S. Molchan, D.A. Tsyrkunov, G.K. Maliarevich, M. Aegerter, J. Puetz, N. Al.-Dahoudi, J. Misiewicz, R. Kudrawiec, V. Lambertini, N. Li Pira, P. Repetto, Optical and structural properties of sol gel derived materials embedded in porous anodic alumina. Microelectron. Eng. **81**, 255–261 (2005)
279. M.T. Tsvetkov, S.M. Kleshcheva, M.I. Samoilovich, N.V. Gaponenko, A.N. Shushunov, Erbium photoluminescence in opal matrix and porous anodic alumina nanocomposites. Microelectron. Eng. **81**, 273–280 (2005)
280. N.V. Gaponenko, G.K. Malyarevich, D.A. Tsyrkunou, E.A. Stepanova, A.V. Mudrui, O.B. Gusev, E.I. Terukov, M.V. Stepikhova, L.V. Krasilnikova, Y.N. Drozdov, Optical properties of erbium-doped xerogels embedded in porous anodic alumina. Opt. Mater. **28**, 688–692 (2006)
281. M.I. Samoilovich, M.Y. Tsvetkov, S.M. Kleshcheva, A.V. Guryanov, Y.I. Chigirinskii, N.V. Gaponenko, L.I. Ivleva, A.F. Belyanin, Erbium luminescence in 3D- and 2D-mesoporous matrices. Proc. SPIE **5450**, 508–516 (2004)

282. N.V. Gaponenko, O.V. Sergeev, E.A. Stepanova, V.M. Parkun, A.V. Mudryi, H. Gnaser, J. Misiewicz, R. Heiderhoff, L.J. Balk, G.E. Thompson, Optical and structural characterization of erbium-doped TiO_2 xerogels films processed on porous anodic alumina. J. Electrochem. Soc. **148**, H13–H16 (2001)
283. N.V. Gaponenko, I.S. Molchan, A.A. Lutich, S.V. Gaponenko, Enhanced luminescence of europium in porous anodic alumina films. Solid State Phenom. **97–98**, 251–258 (2004)
284. I.S. Molchan, N.V. Gaponenko, R. Kudrawiec, J. Misiewicz, G.E. Thompson, Influence of porous anodic alumina matrix upon europium luminescence from sol–gel-derived films. Mater. Sci. Eng. B-Adv. **105**, 37–40 (2003)
285. R. Kudrawiec, J. Misiewicz, L. Bryja, I.S. Molchan, N.V. Gaponenko, Photoluminescence investigation of porous anodic alumina with spin–on europium-containing titania sol-gel films. J. Alloy. Compd. **341**, 211–213 (2002)
286. S. Molchan, E.A. Stepanova, G.E. Thompson, P. Skelton, N.V. Gaponenko, Europium photolumiescence in titania xerogel on porous anodic aluminum. Proc. SPIE **4511**, 58–60 (2001)
287. N.V. Gaponenko, I.S. Molchan, G.E. Thompson, P. Skeldon, A. Pakes, R. Kudrawiec, L. Bryja, J. Misiewicz, Photoluminescence of Eu-doped titania xerogel spin-on deposited on porous anodic alumina. Sensor. Actuat. A-Phys. **99**, 71–73 (2002)
288. I.S. Molchan, N.V. Gaponenko, R. Kudrawiec, J. Misiewicz, G.E. Thompson, P. Sheldon, Luminescence from sol-gel-derived europium-doped films confined in mesoporous anodic alumina. J. Electrochem. Soc. **151**, H16–H20 (2004)
289. A. Peng, E. Xie, C. Jia, R. Jiang, H. Lin, Photoluminescence properties of TiO_2:Eu^{3+} thin films deposited on different substrates. Mater. Lett. **59**, 3866–3869 (2005)
290. N.V. Gaponenko, J.A. Davidson, B. Hamilton, P. Skeldon, G.E. Thompson, X. Zhou, J.C. Pivin, Strongly enhanced Tb luminescence from titania xerogels solids mesoscopocally confined in porous anodic alumina. Appl. Phys. Lett. **76**, 1006–1008 (2000)
291. N.V. Gaponenko, Sol-gel-derived films in meso-porous matrices: porous silicon, anodic alumina and artificial opals. Synth. Met. **124**, 125–130 (2001)
292. A. Podhorodecki, N.V. Gaponenko, M. Banski, M.V. Rudenko, L.S. Khoroshko, A. Sieradzki, J. Misiewicz, Green emission from barium-strontium titanate matrix introduced into nano-porous anodic alumina. Opt. Mater. **34**, 1570–1574 (2012)
293. T. Qiu, W. Zhang, X. Lang, Y. Zhou, T. Cui, P.K. Chu, Controlled assembly of highly raman-enhancing silver nanocap arrays templated by porous anodic alumina membranes. Small **5**, 2333–2337 (2009)
294. R.J. Walsh, G. Chumanov, Silver coated porous alumina as a new substrate for surface-enhanced raman scattering. Appl. Spectrosc. **55**, 1695–1700 (2001)
295. A.M. Md Jani, D. Losic, N.H. Voelcker, Nanoporous anodic aluminium oxide: advances in surface engineering and emerging applications. Prog. Mater. Sci. **58**, 636–704 (2013)
296. K. Hotta, A. Yamaguchi, N. Teramae, Properties of a metal clad waveguide sensor based on a nanoporous-metal-oxide/metal multilayer film. Anal. Chem. **82**, 6066–6073 (2010)
297. K. Hotta, A. Yamaguchi, N. Teramae, Nanoporous waveguide sensor with optimized nanoarchitectures for highly sensitive label-free biosensing. ACS Nano **6**, 1541–1547 (2012)
298. D. Kim, K. Kerman, M. Salto, R.R. Salthulurl, T. Endo, S. Yamamura, Y.-Y. Kwon, E. Tamlya, Label-free DNA biosensor based on localized surface plasmon resonance coupled with interferometry. Anal. Chem. **79**, 1855–1864 (2007)
299. A. Santos, T. Kumeria, D. Losic, Nanoporous anodic aluminum oxide for chemical sensing and biosensors. Trends Anal. Chem. **44**, 25–38 (2013)
300. A. Santos, V.S. Balderrama, M. Alba, P. Formentin, J. Ferre-Borrull, J. Pallares, L.F. Marsal, Nanoporous anodic alumina barcodes: toward smart optical biosensing. Adv. Mater. **24**, 1050–1054 (2012)
301. S.N. Terekhov, P. Mojzes, S.M. Kachan, N.I. Mukhurov, S.P. Zhvavyi, A.Y. Panarin, I.A. Khodasevich, V.A. Orlovich, A. Thorel, F. Grillon, P.Y. Turpin, A comparative study of surface-enhanced raman scattering from silver-coated anodic aluminum oxide and porous silicon. J. Raman Spectrosc. **42**, 12–20 (2011)

302. J. Wang, L. Huang, H. Tong, L. Zhai, L. Yuan, L. Zhao, W. Zhang, D. Shan, A. Hao, X. Feng, Perforated nanocap array: facile fabrication process and efficient surface enhanced raman scattering with fluorescence suppression. Chinese Phys. B **22**, 047301-1-047301-5 (2013)
303. Z. Yao, M. Zheng, L. Ma, W. Shen, The fabrication of ordered nanoporous metal films based on high field anodic alumina and their selected transmission enhancement. Nanotechnology **19**(465705), 1–7 (2008)
304. G. Macias, L.P. Hernandes Eguia, J. Ferre Borrull, J. Pallares, L.F. Marsal, Gold-coated ordered nanoporous, anodic alumina bilayers for future label–free interferometric biosensors. Appl. Mater. Interfaces **5**, 8093–8098 (2013)
305. T. Kumeria, L. Parkinson, D. Losic, A nanoporous interferometric micro-sensor for biomedical detection of volatile sulphur compounds. Nanoscale Res. Lett. **6**, 1–7 (2011)
306. T. Kumeria, M.D. Kurkuri, K.R. Diener, L. Parkinson, D. Losic, Label-free reflectometric interference microchip biosensor based on nanoporous alumina for detection of circulating tumour cells. Biosens. Bioelectron. **35**, 167–173 (2012)
307. X. Wang, D. Zhang, H. Zhang, Y. Ma, J.Z. Jiang, Tuning color by pore depth of metal-coated porous alumina. Nanotechnology **22**(305306), 1–6 (2011)
308. J. Li, Z. Zhu, Y. Hu, J. Zheng, J. Chu, W. Huang, Numerical and experimental study of the structural color by widening the pore size of nanoporous anodic alumina. J. Nanomater. **819432**, 1–10 (2014)
309. Y. Wada, T. Yanagishita, H. Masuda, Ordered porous alumina geometries and surface metals for surface-assisted laser desorption/ionization of biomolecules: possible mechanistic implications of metal surface melting. Anal. Chem. **79**, 9122–9127 (2007)
310. H. Hu, D. He, The properties of $Si_{1-x}Ge_x$ nanodot arrays prepared by plasma-enhanced CVD on porous alumina templates. Chem. Vapor. Depos. **12**, 751–754 (2006)
311. S. Kinoshita, S. Yoshioka, Structural colors in nature: the role of regularity and irregularity in the structure. Chem. Phys. Chem. **6**, 1442–1459 (2005)
312. N.V. Gaponenko, Y.V. Hluzd, G.K. Maliarevich, I.S. Molchan, G.E. Thompson, S. Dabboussi, H. Elhouichet, S.Y. Prislopski, A.A. Lutich, Room-temperature photoluminescence from porous anodic alumina films with embedded terbium and europium species. Mater. Lett. **63**, 621–624 (2009)
313. S. Dabboussi, H. Elhouichet, C. Bouzidi, G.K. Maliarevich, N.V. Gaponenko, M. Oueslati, Excitation and emission processes of Tb^{3+} in porous anodic alumina. Appl. Surf. Sci. **255**, 4255–4258 (2009)
314. S.P. Mondal, A. Dhar, S.K. Ray, Optical properties of CdS nanowires prepared by DC electrochemical deposition in porous alumina template. Mater. Sci. Semicond. Process. **10**, 185–193 (2007)
315. Y.L. Shi, J. Wang, H.L. Li, Photoluminescence effect of ru dye on alumina membranes with ordered pore arrays. Appl. Phys. A-Mater. **75**, 423–426 (2002)
316. J.W. Gregory, K. Asai, M. Kameda, T. Liu, J.P. Sullivan, A review of pressure-sensitive paint for high-speed and unsteady aerodynamics. Proceed. Inst. Mech. Eng. Part G: J. Aerospace Eng. **222**, 249–290 (2008)
317. Y.-Q. Cheng, Y.-Z. Yang, C.-R. Niu, D.-Y. Miao, X.-G. Chen, Z.-D. Hu, Photoluminescence characteristics of several fluorescent molecules on nanometer porous alumina film. Acta Chim. Sinica **62**, 183–187 (2004)
318. Y. Yang, H.-Y. Li, H.-L. Chen, X.-M. Bao, Luminescence study of fluorescent dye impregnated into si-based nanoporous alumina. Chem. J. Chinese Univ. **23**, 768–771 (2002)
319. C. Xu, C. Xu, Q. Xue, L. Ba, B. Zhao, N. Gu, Y. Cui, Spectral behavior of 8-hydroxyquinoline aluminum in nanometer-sized holes of porous alumina. Chinese Sci. Bull. **46**, 1839–1841 (2001)
320. Y.-F. Dong, Q.-S. Li, Photoluminescent sectra of 8-hydroxyquinoline aluminum embedded in porous alumina. Acta Phys.Sinica **51**, 1645–1648 (2002)
321. A. Moadhen, H. Elhouichet, L. Nosova, M. Ouslati, Rhodamine B absorbed by anodic porous alumina: stokes and anti-stokes luminescence study. J. Lumin. **126**, 789–794 (2007)

322. I. Miura, Y. Okada, S. Kudoh, M. Nakata, Organic electroluminescence in porous alumina. Jpn. J. Appl. Phys. **43**, 7552–7553 (2004)
323. H. Elhouichet, N. Harima, H. Koyama, N.V. Gaponenko, Energy transfer in porous anodic alumina/rhodamine 110 nanocomposites. J. Lumin. **132**, 2232–2234 (2012)
324. A. Kukhto, E. Kolesnik, A. Mozalev, M. Taoubi, Luminescent properties of organic compounds in nanodimensional aluminium oxide structures. Proc. SPIE **3573**, 513–515 (1998)
325. H.J. Peng, Y.L. Ho, X.J. Yu, H.S. Kwok, Enhanced coupling of light from organic light emitting diodes using nanoporous films. J. Appl. Phys. **96**, 1649–1654 (2004)
326. S. Wang, H. Luo, Y. Wang, G. Gong, The effect of nanometer size of porous anodic aluminum oxide on adsorption and fluorescence of tetrahydroxyflavanol. Spectrochim. Acta B **59**, 1139–1144 (2003)
327. R.-P. Jia, Y. Shen, H.-Q. Luo, X.-G. Chen, Z.-D. Hu, D.-S. Xue, Photoluminescence spectra of human serum albumen and morin embedded in porous alumina membranes with ordered pore arrays. J. Phys.: Condens. Mater. **15**, 8271–8279 (2003)
328. R.P. Jia, Y. Shen, H.Q. Luo, X.G. Chen, Z.D. Hu, D.S. Xue, Enhanced photoluminescence properties of morin and trypsin absorbed on porous alumina films with ordered pores array. Solid State Commun. **130**, 367–372 (2004)
329. R.P. Jia, Y. Shen, H.Q. Luo, X.G. Chen, Z.D. Hu, D.S. Xue, Photoluminescence behaviors of morin-human immunoglobulin on porous anodized aluminum oxide films. Thin Solid Films **471**, 264–269 (2005)
330. R.P. Jia, Y. Shen, H.Q. Luo, X.G. Chen, Z.D. Hu, D.S. Xue, Enhanced photoluminescence properties of morin and trypsin absorbed on porous alumina films with ordered pores array. Solid State Commun. **233**, 343–351 (2004)

Chapter 9
Titania Nanotubes for Solar Cell Applications

Naoum Vaenas, Thomas Stergiopoulos and Polycarpos Falaras

Abstract Nanotubular structures have been established in the literature as advanced porous materials presenting high potential for practical applications and innovative devices. Due to their lengthwise growth, self-organized titania nanotubes belong to the family of 1D materials and continue to be at the forefront of the research activity. In this chapter a thorough analysis of the electrochemical preparation of self-organized titania nanotubes, as well as their application in dye-sensitized solar cells is presented.

9.1 Electrochemical Synthesis of the TiO_2 Nanotubes

9.1.1 Titanium Dioxide (TiO_2)

Titania (TiO_2) is a mineral oxide which is mainly sourced from the ore ilmenite ($FeTiO_3$). The most common use of titania is as a white pigment, in cosmetics, toothpastes, sunscreens, self-cleaning materials and food (E171). The production in TiO_2 pigment on the year 2012 touches the 7.000 tons worldwide, according to the U.S. Geological Survey [1]. Titanium dioxide is chemically and biologically stable, non-toxic and easily producible with low cost (selling price for the crude ore of $11.75 per kilogram [1]). TiO_2 is founded in several crystal forms, but the best known are the anatase, rutile and brookite. The crystal structure of the anatase belongs to the tetragonal system and its basic building unit is the octahedral Fig. 9.1 [2]. Rutile is thermodynamically the most stable form, anatase is however preferred for energy applications, because it has better electrical characteristics [3]. TiO_2 has reflective index n = 2.5, band gap E_g = 3.0–3.2 eV [4] and is an n type semiconductor, due to crystal defects (oxygen vacancies, Ti^{3+} ions) [5].

N. Vaenas · T. Stergiopoulos · P. Falaras (✉)
Institute of Nanoscience and Nanotechnology (INN), National Centre for Scientific Research Demokritos, 153 10 Agia Paraskevi Attikis, 60037, Athens, Greece
e-mail: p.falaras@inn.demokritos.gr

D. Losic and A. Santos (eds.), *Electrochemically Engineered Nanoporous Materials*, Springer Series in Materials Science 220,
DOI 10.1007/978-3-319-20346-1_9

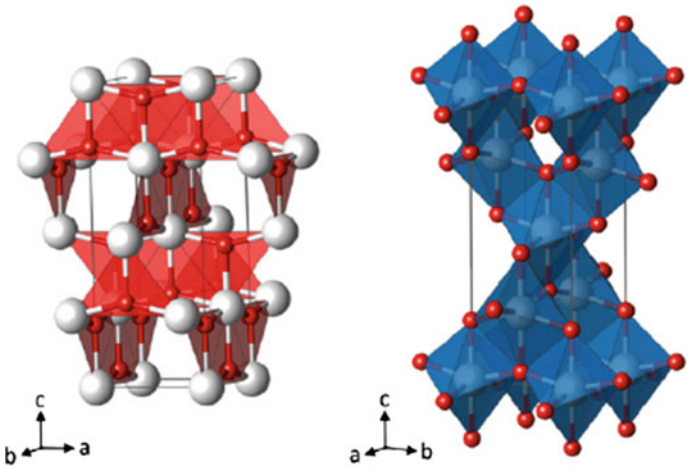

Fig. 9.1 Planar Ti_3O building-block representation (*left*) and TiO_6 octahedral (*right*) for the TiO_2 anatase phase (Ti *white*, O *red*) [2]

9.1.2 Brief Review on the Electrochemical Synthesis of the TiO_2 Nanotubes

The discovery of the carbon nanotubes [6] stimulated intensive research activity in a wide range of materials round this special morphology. Nanotubes have been established in the literature as an advanced 1D structure. Metal oxide nanotubes (including titania ones) belong in the same family of 1D materials (together with nanowires and nanorods), due to their lengthwise growth [7]. A lot of works in the literature have taken advantage of their 1D character and their unique properties (including vectorial electron transport and discovery of an antenna Raman effect [8]) to apply them in promising solar energy conversion to electricity applications, exploiting the transport directionality that they offer to the photogenerated charges [9, 10].

There are literature reports on the electrochemical preparation of the titania nanoporous materials since 1987 [11], but a real impulse was given in 1999 by Zwilling and co-workers [12, 13] in their original works about the anodic oxidation of titanium and its alloys in acidic electrolytes. Self-assembled titania nanotubes are easily prepared by anodic oxidation of a titanium substrate, in fluoride based electrolytes [14]. The potential applications of the TNTs cover a wide research range, including photovoltaics [15], photocatalysis [16], photoelectrolysis [17], gas sensing [18], biomedical implants [19] and batteries [20].

Up to date the anodic oxidation of Ti in Fluoride (F^-) rich environments has been passed though three phases. In the first generation the synthesis was performed in acidic (HF) water based electrolytes [21, 22], but due to highly corrosive solutions the nanotubes' thickness were confined to some hundred of nanometers.

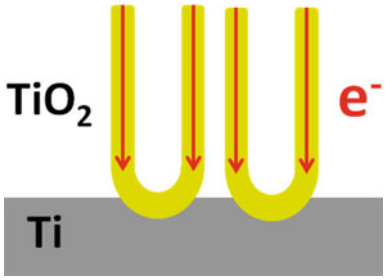

Fig. 9.2 Representation of the vectorial electron transport along the nanotubes axis

The second generation nanotubes were grown in buffered neutral electrolytes which contained NaF, KF or NH_4F instead of HF [23], thus the thickness of TNTs layers was increased and reached some micrometers. It was although, the third growth generation of nanotubes in organic polar electrolytes (mainly ethylene glycol) almost free of water [24], that enables the development of thick layers/membranes (1 mm) [25] and in a variety of morphologies (single wall, double wall, multilayer and branched nanotubes) [26–29].

Even nowadays, the anodically prepared TNTs continue to be at the forefront of the research activity [30]. Figure 9.2 displays a representation of the self-organized and oriented nanotube arrays and highlights their major assets. The nanotubes are particularly favorable in energy applications due to their unique electrical and structural properties [31]. The existence of a continuous wall eliminates the grain boundaries, minimizes the electron trapping/detrapping and ensures the vectorial electron transport without significant losses [32].

On the other hand the electrochemical preparation provides easily controllable 1-D morphology at the nanoscale; in fact, the nanotube can be modified in order to be easily accessible for doping, infiltration and diffusion concepts [33, 34, 35].

9.1.3 Anodic Oxidation of Titanium

The Fig. 9.3 presents an electrochemical cell and the final product of the titanium anodic oxidation, the TiO_2 nanotubes. The electrochemical configuration is constituted by a temperature (T) controlled and inert to chemicals (made by Teflon-PTFE) cell, the electrolyte, the two electrodes and an external source. The apparatus is supplied either by constant potential (potentiostatic oxidation) [14], or by constant current (galvanostatic oxidation) [36]. The working electrode (anode) is a titanium foil and the counter electrode (cathode) is usually a platinum foil or mesh. The electrolyte is consists of the main solvent (e.g., a polar organic compound-ethylene glycol), the co-solvent (H_2O) and the supporting electrolyte (NH_4F). Each one of these parameters plays a crucial role on the nanotubes growth. The temperature governs the growth and the dissolution rate and subsequently the length of the nanotubular film [37]. The applied bias (V)/current (J) induces the

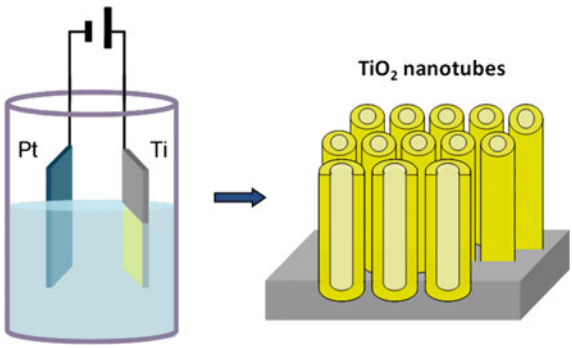

Fig. 9.3 Electrochemical cell (*left*) and shaped TiO_2 nanotubes (*right*)

Table 9.1 Correlation of the NTs' features with the anodization parameters

Cell	NTs					
	Thickness	Diameter	Wall	Growth rate	Dissolution rate	Optimum NTs
V/J ↑	↑	↑	↑	↑	↑	Depending on the morphology in quest, generally a tuning of all the parameters should be done
NH_4F ↑	↑	–	↓	↑	↑	
H_2O ↑	↓	↑	↑	↓	↓	
t ↑	↑	–	↓	↓	–	
T ↑	↑	–	↓	↑	↑	

Faradaic (ionic) current, controls the tube diameter, the thickness of the nanotubes walls and the growth rate [38]. The main solvent (ethylene glycol) is responsible for the conductivity, the PH and the kinetics of the ions within the electrolyte [39, 40]. The co-solvent (H_2O) determines the conductivity, controls the thickness of the nanotubes walls, offers the oxygen for the oxidation of titanium and manages the growth rate [41]. The supporting electrolyte NH_4F causes the titanium etching (nanotubular morphology) and the dissolution of TiO_2 [42]. Additionally, of the same importance is the duration of the oxidation (t), adjusting the length of the nanotubular film [43]. As it is concluded and indicated in the Table 9.1, most of these parameters are interrelated; therefore in order to achieve the desirable morphology a balance is need to set up among them.

Once the two electrodes have been immersed in the electrolyte and the cell has biased the oxidation begins. The anodization procedure has three main stages, as shown in the Fig. 9.4.

In the initial stage (i), during the first 1–2 min, an abrupt decay of current happens, due to the formation of a compact TiO_2 layer (blue color) at the Ti surface (gray color) [44]. Thereafter, owing to some "weak" points on the compact TiO_2 layer, the electrolyte's fluoride ions/F^- (and the oxygen ions too) start to penetrate through it; when the ions reach the Ti/TiO_2 interface, they start to create a new porous-tubular layer (yellow color), this transition lasts 10–15 min (ii) [44]. At the

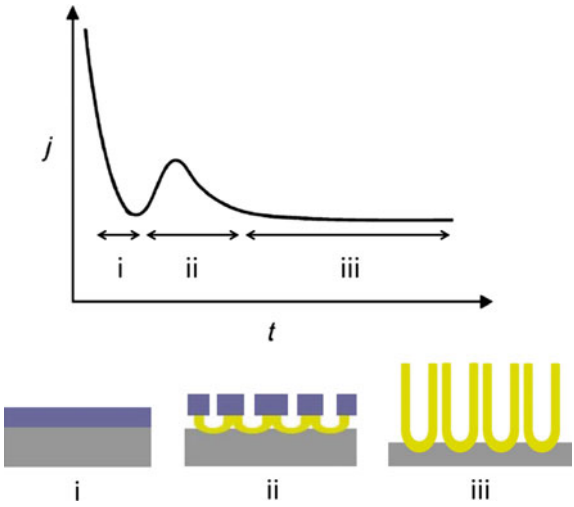

Fig. 9.4 The potentiostatic anodization's evolution in three stages and the corresponding current density-Time (j-t) graph

third stage (iii), a quasi steady state is established; the anodic current remains almost constant and the tubes continue to grow further [44].

During the anodization certain electrochemical reactions occur inside the cell. The Ti anode is oxidized-losing electrons (TiO_2 formation) and on the Pt cathode the reduction of the hydrogen ions occurs, gaining electrons (H_2 gas released); the sum of these two processes is (9.1), the total redox reaction that takes place in the cell.

$$Ti + 4H^+ \rightarrow Ti^{4+} + 2H_2 \tag{9.1}$$

$$Ti + 2H_2O \rightarrow TiO_2 + 2H_2 \tag{9.2}$$

$$TiO_2 + 6F^- + 4H^+ \rightarrow TiF_6^{-2} + 2H_2O \tag{9.3}$$

The reactions (9.2) and (9.3) describe the chemical way that the oxide is composed and dissociated respectively. Specifically, (9.2) is the overall electric field driven oxidation of the metal at the oxide/metal interface [41] and (9.3) is the field assisted oxide dissolution at the electrolyte/oxide interface [45]. Nanotubes' generation is possible only when a balance between these two competitive reactions is settled. If the dissolution rate is too high, the Ti/TiO_2 are solvatized in the electrolyte and only corrosion is observed; on the other hand when the dissolution rate is negligible, only a thick TiO_2 compact layer is detected [44]. It is clear now that the chemical dissolution of TNTs plays a key role in the formation of nanotubes.

Taking a closer look at the mechanistic model of nanotubes array development in Fig. 9.5 [46, 47], one could note a few crucial points. In Fig. 9.5a the fluoride and the oxygen anions transport through the oxide (due to small ionic radius) and cause the etching and the oxidation (growth rate) of the Ti (2); simultaneously, at the electrolyte/oxide interface the TiO_2 is dissolved (dissolution rate) according to (3).

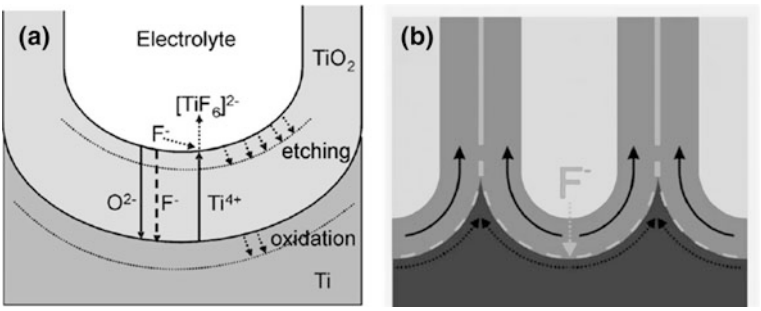

Fig. 9.5 Mechanistic model for the nanotubes development (**a**), flow mechanism for the upwards oxide's expansion (**b**) [44, 46]

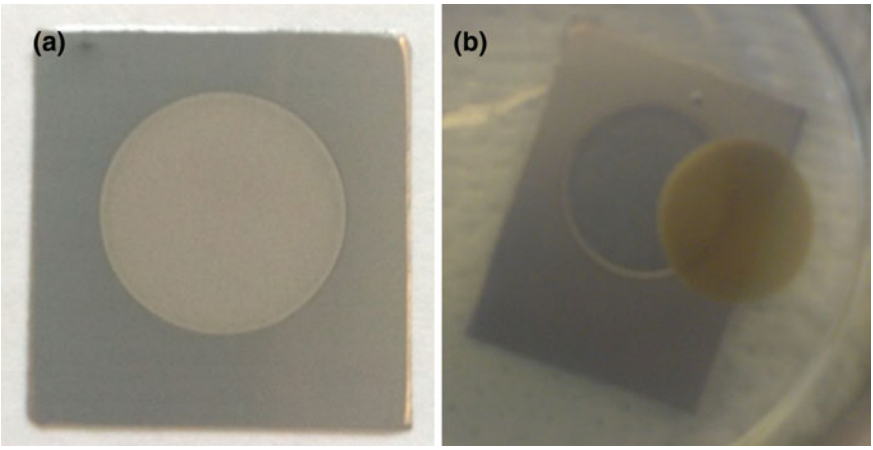

Fig. 9.6 Photos of an anodize Ti foil (*circular part*) (**a**), detached TNT film (membrane) (**b**)

When the growth rate becomes equal to the dissolution rate (after prolonged anodization) the development of the tubes stops [48]. Figure 9.5b presents the flow mechanism, that the oxide's volume is expanded from the bottom where is composed to the top of the tubes [46]. The last remark concerns the formation of nanotubes instead of a nanoporous structure. The precise origin remains under delegation, but it is believed that this separation is due to the weaker and more soluble outer parts of nanotubes [49].

So far, TNTs have been displayed in many representations schematically, but how do the nanotubes look like macroscopically and microscopically? Figure 9.6 shows the photos of an anodized titanium foil (a) and a nanotubular film (membrane) that has detached from the Ti substrate [50]. The circular anodized area (yellow circuit) is about 1.32 cm^2. The microscopically view of the Fig. 9.7 is more interesting; some impressive oxide architectures are shown in different perspectives.

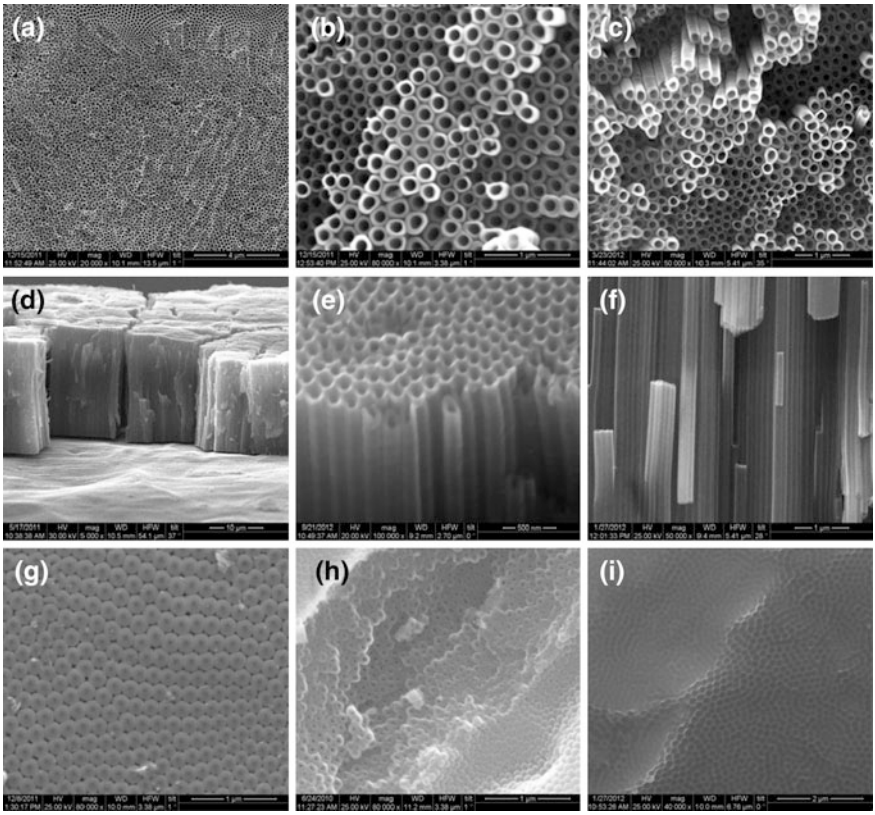

Fig. 9.7 SEM (scanning electron microscopy) images of the TiO_2 nanotubes. Top surface of NTs (**a–c**), cross section of the NTs (**d–f**), bottom of the NTs (**g**, **h**), patterned Ti foil after the detach of TiO_2 nanotubular film-membrane (**i**)

The Fig. 9.7a–c and d–f SEM (scanning electron microscopy) demonstrate a few homogeneous top surfaces and cross sections correspondingly, of some self assembled titania nanotube samples, in various magnifications and perspectives. Image (g) shows the bottom of the NTs after the detachment of the TiO_2 film from the Ti foil (which has a patterned area now-(i)) and last (h) is again a view of the nanotubes' bottom with some caps to have been removed. As soon as the TNTs have been developed they are amorphous, but with the optimum annealing they can obtain the preferable crystallinity [51, 52].

Finalizing this chapter about the anodization procedure, there is enough room for one last comment; it is almost "seductive" the way that the electrochemistry can be at the same time so effective and creative.

9.2 Dye Solar Cell (DSC)

9.2.1 Front Side Illuminated DSCs

Dyesol is one of the global leading companies in the development of DSC technology [53]. Head researchers in Dyesol's R&D department H. Desilvestro and D. Milliken believe that by 2018, it is possible DSCs and in particular solid state DSCs will reach efficiencies of 20 % (30 % is the maximum theoretical attainable efficiency for single junction cell) [54] with a parallel cost reduction. Characteristically, it is expected that the DSCs' manufacturing cost will be much lower than that of the Si PV. Also, Dyesol has performed and surpassed a lot of durability tests (5000 h DSC stability at elevated temperature, according to its announcement in the EMRS 2013 Strasburg meeting) with a view to certification of the international standards before the products commercialization. The PV market is rapidly expanding and soon (the next 20 years) [55] the solar generated electricity will be one of the most economical (half that of coal $99.60 per MWh) and at the same time a source of green energy. DSC technology includes a series of advantages: low energy and cost manufacturing process, wide use of abundant non toxic materials in small quantities, increased energy collection in real world solar conditions and incorporation in building structures (windows, roofs) with high aesthetical and variable results [53]. Today, cutting-edge DSC technology still stays on track since its birth on 1991.

The Dye Solar Cell has a multilayer-sandwich structure, Fig. 9.8. In basic realization a DSC comprises a layer of nano-particulate titania [56] formed on a transparent electrically conducting substrate (conductive glass-TCO) and photosensitized by a monolayer of Ruthenium complex dye [57]. An electrolyte, based on an Iodide-tri-iodide redox system [58] is placed between the layer of photosensitized titania and a second electrically conducting catalytic substrate [59].

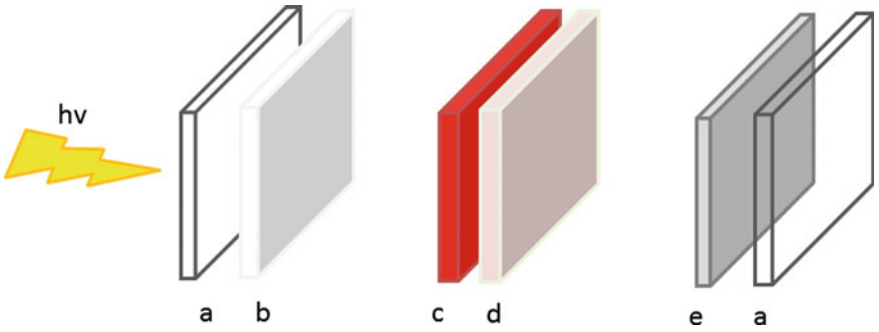

Fig. 9.8 Schematic overview of the DSC multilayer structure: TCO (**a**); TiO_2 (**b**); Dye (**c**); Redox Electrolyte (**d**); Pt Catalyst (**e**)

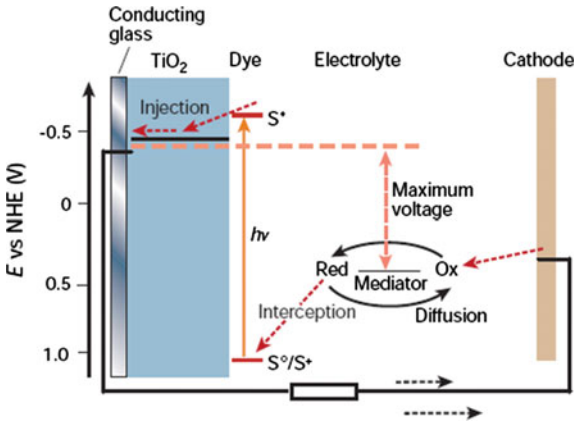

Fig. 9.9 Principle of operation and energy level scheme of the dye-sensitized nanocrystalline solar cell. Reprinted from [60] (Courtesy of P. Bonhôte/EPFL-LPI). Permission requested

The exciting trick of the sensitization of a transparent semiconductor (TiO_2) with a visible light absorbing dye lies in the heart of DSC's operation mechanism, Fig. 9.9 [60]. The dye is excited after a photon absorption, (9.4) [60] and injects an electron into the conduction band of the TiO_2, (9.5) [61]. Then the electron, following a random walk characterized by trapping/detrapping mechanism, is transported from one TiO_2 nanoparticle to another [62] till it arrives at the conductive substrate, in which it is collected from the external circuit. The oxidized state of the dye is restored to its ground state by an electron transfer from the electrolyte, (9.6) [63]. The regenerative cycle is completed at the cathode where the electrolyte is also regenerated by receiving electron from the external circuit, (9.7) [63].

$$S + hv \rightarrow S^* \tag{9.4}$$

$$S^* \rightarrow S^+ + e^-_{CB} \tag{9.5}$$

$$S^+ + 3I^- \rightarrow S + I_3^- + e^- \tag{9.6}$$

$$I_3^- + 2e^- \rightarrow 3I^- \tag{9.7}$$

However, it should be noted that the current generation is a competitive (time dependant) process, among the forward (9.4)–(9.7) reactions and some recombination reactions, which are illustrated in Fig. 9.10 [64]. The cell's kinetics depend on each component (e.g. the solvent of the redox couple) and the interface reactions. All these define the whole cell performance [65].

The film morphology is of vital importance and TiO_2 must fulfill some crucial criteria in order to be an appropriate substrate. The total film thickness usually is about 10 μm, with nanoparticles of 10–30 nm and optimum porosity round to 50–60 % [66].

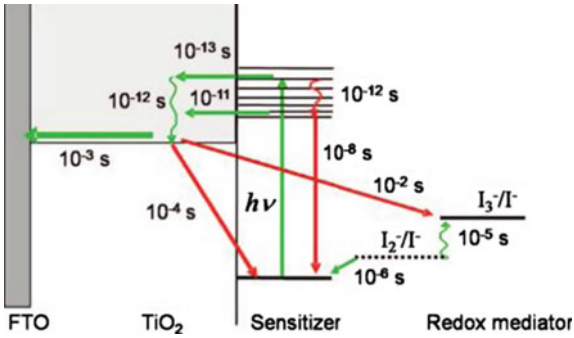

Fig. 9.10 Kinetics of a Ru-based sensitized TiO_2 solar cell with I^-/I_3^- redox mediator. Typical time constants for the forward reactions (*green arrow*) and the loss-recombination reactions (*red arrow*). Reprinted with permission from [64]. Copyright 2001, American Chemical Society

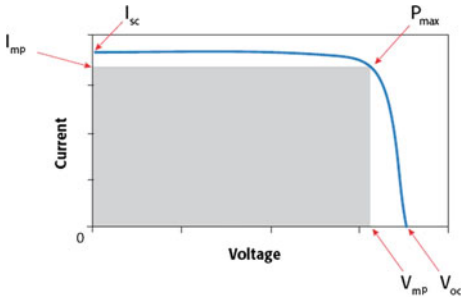

Fig. 9.11 Characteristic I-V curve of a PV and the corresponding electrical parameters

In order to evaluate PVs at any stage of the production, laboratorial or commercial, the cell's performance must be known as well as the rest of the electrical parameters that are estimated from the I-V curve, Fig. 9.11.

The overall solar to electrical energy conversion efficiency (η) for a solar cell is given by (9.8) [67], by the photocurrent density measured at short-circuit (Jsc), the open-circuit photovoltage (Voc), the fill factor of the cell (FF) and the power of the incident light (Pin). The fill factor can attain values between 0 and 1 and is defined by the ratio of the maximum power point (Pmax) divided by the (Voc * Jsc) product according to (9.9) [68]. The maximum power point (Pmax) is obtained as the product of the maximum current density and voltage (Jmp * Vmp). The Pin is the input solar irradiance (1000 W/m^2—AM (air mass) 1.5 G) [69, 70], this value is equal to the solar radiation on a shiny day when the sun is at zenith.

$$\eta = J_{sc} V_{oc} FF / P_{in} \tag{9.8}$$

$$FF = P_{max} / J_{sc} V_{oc} \tag{9.9}$$

Concluding this part, it would be fair to pay some attention on the driving force behind the solar cells' energy generation. The origin of the photovoltaic effect comes from the difference between the semiconductor's Fermi level and the electrochemical potential of the electrolyte, designated as maximum voltage in Fig. 9.9. With respect to the cell's operation conditions the V_{oc} is defined by (9.10) [71], which is one of the most important equations in the theory of photovoltaics.

$$V_{oc} = \frac{K_B T}{e} \log\left(\frac{I_{SC} + I_O}{I_O}\right) \tag{9.10}$$

where, K_B is Boltzmann's constant, T the absolute temperature, e the electron charge, I_{sc} the short circuit current and I_o the dark or saturation current.

9.2.2 Back Side Illuminated DSCs

The main difference between the front and the back side illuminated DSCs is in the direction of the incident light, at the latter the light harvesting is realized though the counter electrode (cathode), Fig. 9.12a, b. This special characterization-preparation technique has led many groups to exploit the advantages of an alternative to glass substrate [72]. Titanium is one of the most preferable substrates, due to the low cost and the elevated conductivity in contrast to the TCO [73]. Furthermore the use of a flexible Ti foil permits its surface to be easily manipulated (roughen), in order to increase the light scattering. As a result, there are a lot of works in which the use of a titanium substrate in combination with composite TiO_2 layers [74, 75] has driven to highly efficient (PCE values up to 8.5 %) back illuminated DSCs [76].

The back illuminated DSCs based on anodically oxidized Ti foils is a distinct category of cells, that take advantage of the unique nanotubular morphology, Fig. 9.12a. The single nanotubular cells have attained efficiencies of about 6 % [77, 78] and when they were subjected to a post treatment (commonly, decoration with TiO_2 nanoparticles) [79], reached the considerable efficiency of 8 % [80, 81].

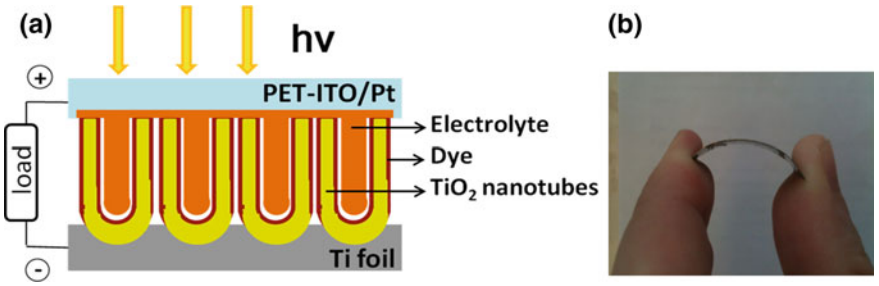

Fig. 9.12 Scheme of a flexible back illuminated DSC, based on TiO_2 nantubes (**a**) and the corresponding functional cell with total thickness lower than 1 mm (**b**)

The highest yield in the classic front side illuminated nanoparticulate DSCs is around 12 %, this means that, the back side illuminated nanotubular DSCs remaining with about 30 % lower efficiencies. This decrease in efficiency is fully justified by light losses on the back illumination mode due to the reflection from the Pt layer at the counter electrode and the light absorption from the electrolyte [82]. Nevertheless, very recently, Prof. Patrik Schmuki (Erlangen, Germany) in a plenary lecture at the 65th Annual Meeting of the ISE (31/8-5/9, Lausanne, Switzerland), presented a power conversion efficiency reaching ~11 %, with a Jsc as high as 22 mA cm^{-2}. Such an enhanced performance justifies increased interest and hopes of practical application for these monodimensional nanostructures.

However, a direct comparison between the nanoparticulate and the nanotubular DSCs will highlight the assets of the last Fig. 9.13. The nanotubes offer a straight path with reduced grain boundaries for directed electron transport, in contradiction to the random walk on the nanoparticles [83]. The open pores of the nanotubes facilitate the electrolyte diffusion (even if it is solvent free with low viscosity), on the contrary the nanoparticulate photoelectrodes hinder the electrolyte's percolation [84]. Additionally, the coarse top surface of the tubes scatters the light better than the smooth nanoparticulate surface [85].

Nevertheless, the nanotubular DSCs have not succeeded up to date, to cope with the high prospects for really enhanced efficiencies. The reasons for that, are grounded in the fabrication procedure. According to the exceptional studies of Boschloo [86] and Schemuttenmaer [87], the state distribution within the band gap of the nanotubes differs substantially from the nanoparticles. The density of the shallow traps-states (Ti^{3+} defects due to oxygen vacancies, interstitial Ti and F^{-} ions) is extended and forms impurity bands 1 eV below the conduction band edge, which result in a vast number of exciton-like traps [87]. Also, in NTs the Fermi level and the deep traps (surface states) [88], are localized lower in the band gap than in the NPs; possibly because of a p-type doping (N and C atoms that come from the anodization electrolyte), that compensates the TNTs n-type semiconductivity by the possession of acceptor states above the valence band. Taking into consideration these notes it is understandable now why the NTs have comparable transport times to the NPs, despite their higher degree of orientation that provides them with higher electron life times [84, 89].

The importance of ordering [90] is unexceptionable, but some critical factors [91] both, in the oxidation procedure and in the post treatment should be taken into account. The geometry of the tubes directly affects the DSCs performance. The nanotube wall has to be thick enough for a space charge layer to form for faster electron transportation and reduced recombination [92]. An estimated critical wall thickness is about 30–40 nm. There is also an optimum nanotube length for effective electron collection in consideration of dye loading capacity and electron diffusion length [93]. In back-side illuminated DSCs, the optimal length and pore diameter can be found as a function of the total porosity. It is strongly believed that the porosity of the nanotubular photoelectrodes must be the same as those made from nanoparticles, around 50–60 %. After that the ranges of the affordable values for the length is from 10 to 40 μm [94] and for the pore diameter from 30 to 90 nm [95].

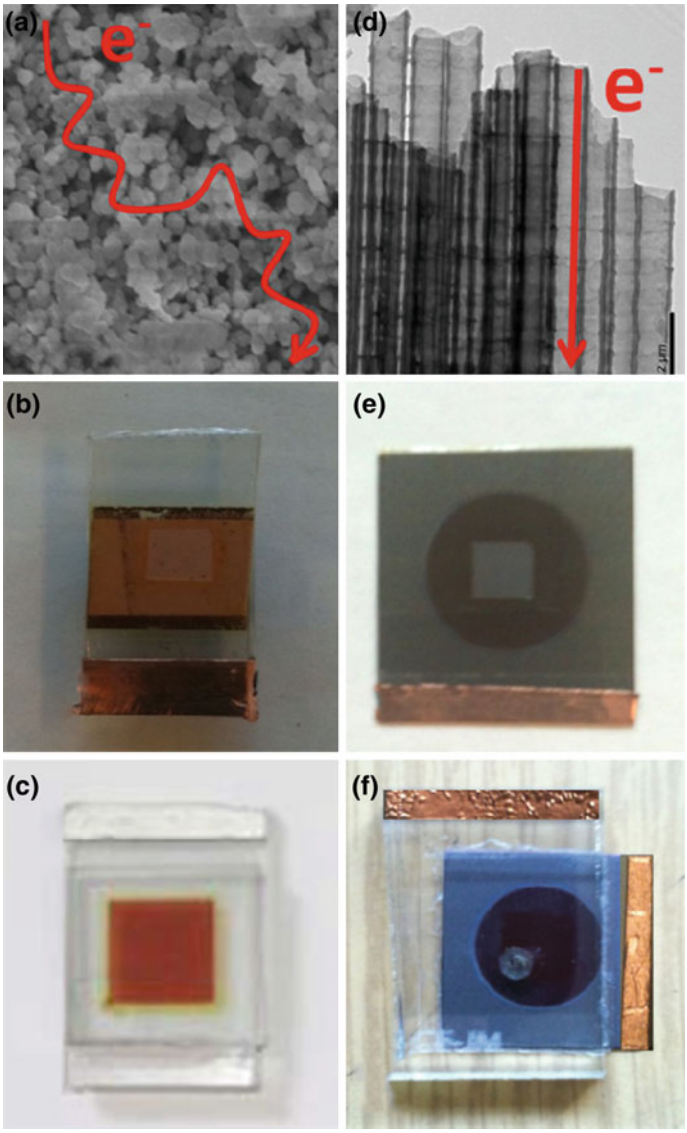

Fig. 9.13 Electron transport in a nanoparticulate (**a**) and a nanotubular (**d**) TiO_2 layer. Images of a nanoparticulate front side illuminated photoelectrode (**b**) and the corresponding sealed DSC (**c**). Accordingly the nanotubular photoelectrode (**e**) and the back illuminated DSC (**f**)

Another tricky point, which has caused a lot of debates [97], is the removing of the structural disorder ("nanograss" dissolved NTs due to extended anodization) from the NTs' surface. Nanograss blocks entering of the dye and the electrolyte inside the NTs and reduces the transport of the electrons due to the increased surface

recombination. Last but not least, is the importance of the post treatments and mainly the annealing. Only a few works have been published which correlate the NTs annealing conditions with the DSCs' efficiency and features [96, 97]. Probably, annealing is one of the best ways to control the trap distribution within the TiO_2 band gap and subsequently to raise the cells' performance.

Acknowledgments This research has been co-financed by the European Social Fund and Greek national funds through the Operational Program "Education and Lifelong Learning" in the framework of ARISTEIA I (AdMatDSC/1847) and THALES (NANOSOLCEL/377756). Financial support from the European Union (Marie Curie Initial Training Network DESTINY/FP7—Grant Agreement 316494) is also acknowledged.

References

1. USGS. www.usgs.gov
2. M. Landmann, E. Rauls, W.G. Schmidt, The electronic structure and optical response of rutile, anatase and brookite TiO_2. J. Phys.: Condens. Matter **24**, 195503 (2012)
3. X. Chen, S.S. Mao, Titanium dioxide nanomaterials: synthesis, properties, modifications, and applications. Chem. Rev. **107**, 2891 (2007)
4. U. Diebold, The surface science of titanium dioxide. Surf. Sci. Rev. **48**, 53 (2003)
5. C. Di Valentin, G. Pacchioni, A. Selloni, Reduced and n-type doped TiO_2: nature of Ti^{3+} species. J. Phys. Chem. C **113**, 20543 (2009)
6. S. Lijima, Helical microtubules of graphitic carbon. Nature **354**, 56 (1991)
7. W.-G. Kim, S. Nair, Membranes from nanoporous 1D and 2D materials: a review of opportunities, developments, and challenges. Chem. Eng. Sci. **104**, 908 (2013)
8. V. Likodimos, T. Stergiopoulos, P. Falaras, Phase composition, size, orientation, and antenna effects of self-assembled anodized titania nanotube arrays: a polarized micro-Raman investigation. J. Phys. Chem. C **112**, 12687 (2008)
9. S. Banerjee, S.K. Mohapatra, P.P. Das, M. Misra, Synthesis of coupled semiconductor by filling 1D TiO_2 nanotubes with CdS. Chem. Mater. **20**, 6784 (2008)
10. C.A. Grimes, O.K. Varghese, G.K. Mor, M. Paulose, X. Feng, Photonic fuels and photovoltaics: application of self-assembled 1D TiO_2 nanotube/wire arrays. *Abstracts of Papers of the American Chemical Society, Meeting Abstract: 39-FUEL 239* (2010), p. 21
11. M. Assefpour-Dezfuly, C. Vlachos, E.H. Andrews, Oxide morphology and adhesive bonding on titanium surfaces. J. Mater. Sci. **19**, 3626 (1984)
12. V. Zwilling, M. Aucouturier, E. Darque-Ceretti, Anodic oxidation of titanium and TA6 V alloy in chromic media. An electrochemical approach. Electrochim. Acta **45**, 921 (1999)
13. V. Zwilling, E. Darque-Ceretti, A. Boutry-Forveille, D. David, M.Y. Perrin, M. Aucouturier, Structure and physicochemistry of anodic oxide films on titanium and TA6 V alloy. Surf. Interface Anal. **27**, 629 (1999)
14. A.G. Kontos, A.I. Kontos, D.S. Tsoukleris, V. Likodimos, J. Kunze, P. Schmuki, P. Falaras, Photo-induced effects on self-organized TiO_2 nanotube arrays: the influence of surface morphology. Nanotechnology **20**, 045603 (2009)
15. T. Stergiopoulos, A. Valota, V. Likodimos, Th Speliotis, D. Niarchos, P. Skeldon, G.E. Thompson, P. Falaras, Dye-sensitization of self-assembled titania nanotubes prepared by galvanostatic anodization of Ti sputtered on conductive glass. Nanotechnology **20**, 365601 (2009)

16. A.G. Kontos, A. Katsanaki, T. Maggos, V. Likodimos, A. Ghicov, D. Kim, J. Kunze, C. Vasilakos, P. Schmuki, P. Falaras, Photocatalytic degradation of gas pollutants on self-assembled titania nanotubes. Chem. Phys. Lett. **490**, 58 (2010)
17. P.P. Das, S.K. Mohapatra, M. Misra, Photoelectrolysis of water using heterostructural composite of TiO_2 nanotubes and nanoparticles. J. Phys. D Appl. Phys. **41**, 245103 (2008)
18. L.X. Yang, S.L. Luo, Q.Y. Cai, S.Z. Yao, A review on TiO_2 nanotube arrays: fabrication, properties, and sensing applications. Chin. Sci. Bull. **55**, 331 (2010)
19. S. Minagar, C.C. Berndt, J. Wanga, E. Ivanova, C. Wen, A review of the application of anodization for the fabrication of nanotubes on metal implant surfaces. Acta Biomater. **8**, 2875 (2012)
20. W. Guo, X. Xue, S. Wang, C. Lin, Z.L. Wang, An integrated power pack of dye-sensitized solar cell and li battery based on double-sided TiO_2 nanotube arrays. Nano Lett. **12**, 2520 (2012)
21. J. Bai, B. Zhou, L. Li, Y. Liu, Q. Zheng, J. Shao, X. Zhu, W. Cai, J. Liao, L. Zou, The formation mechanism of titania nanotube arrays in hydrofluoric acid electrolyte. J. Mater. Sci. **43**, 1880 (2008)
22. R. Beranek, H. Hildebrand, P. Schmuki, Self-organized porous titanium oxide prepared in H_2SO_4/HF. Electrolytes. Electrochem. Solid St. **6**, B12 (2003)
23. Q. Cai, M. Paulose, O.K. Varghese, C.A. Grimes, The effect of electrolyte composition on the fabrication of self-organized titanium oxide nanotube arrays by anodic oxidation. J. Mater. Res. **20**, 230 (2005)
24. S.P. Albu, A. Ghicov, J.M. Macak, P. Schmuki, 250 μm long anodic TiO_2 nanotubes with hexagonal self-ordering. Phys. Stat. Sol. (RRL) **1**, R65 (2007)
25. M. Paulose, H.E. Prakasam, O.K. Varghese, L. Peng, K.C. Popat, G.K. Mor, T.A. Desai, C.A. Grimes, TiO_2 nanotube arrays of 1000 ím length by anodization of titanium foil: phenol red diffusion. J. Phys. Chem. C **111**, 14992 (2007)
26. H. Mirabolghasemi, N. Liu, K. Lee, P. Schmuki, Formation of 'single walled' TiO_2 nanotubes with significantly enhanced electronic properties for higher efficiency dye-sensitized solar cells. Chem. Commun. **49**, 2067 (2013)
27. Y. Ji, K-C. Lin, H. Zheng, J-j. Zhu, A.C.S. Samia, Fabrication of double-walled TiO_2 nanotubes with bamboo morphology via one-step alternating voltage anodization. Electrochem. Commun. **13**, 1013 (2011)
28. H.-J. Oh, I.-K. Kim, K.-W. Jang, J.-H. Lee, S. Lee, C.-S. Chi, Influence of electrolyte and anodic potentials on morphology of titania nanotubes met. Mater. Int. **18**, 673 (2012)
29. S.P. Albu, D. Kim, P. Schmuki, Growth of aligned TiO_2 bamboo-type nanotubes and highly ordered nanolace. Angew Chem. Int. Ed. **47**, 1916 (2008)
30. S. Kurian, H. Seo, H. Jeon, Significant enhancement in visible light absorption of TiO_2 nanotube arrays by surface band gap tuning. J. Phys. Chem. C **117**, 16811 (2013)
31. W. Wei, G. Oltean, C.-W. Tai, K. Edström, F. Björeforsa, L. Nyholma, High energy and power density TiO_2 nanotube electrodes for 3D Li-ion microbatteries. J. Mater. Chem. A **1**, 8160 (2013)
32. A.E. Mohamed, S. Rohani, Modified TiO_2 nanotube arrays (TNTAs): progressive strategies towards visible light responsive photoanode, a review. Energy Environ. Sci. **4**, 1065 (2011)
33. Y-C. Nah, I. Paramasivam, P. Schmuki, Doped TiO_2 and TiO_2 nanotubes: synthesis and applications. Chem. Phys. Chem. **11**(201), 2698 (2010)
34. S.L. Lim, Y. Liu, G. Liu, S.Y. Xu, H.Y. Pan, E.-T. Kang, C.K. Ong, Infiltrating P3HT polymer into ordered TiO_2 nanotube arrays. Phys. Status Solidi. A **208**, 658 (2011)
35. Y. Zhuo, L. Huang, Y. Ling, H. Li, J. Wang, Preliminary investigation of solution diffusive behavior on V-doped TiO_2 nanotubes array by electrochemical impedance spectroscopy. J. Nanosci. Nanotechnol. **13**, 954 (2013)
36. H. Habazaki, Y. Konno, Y. Aoki, P. Skeldon, G.E. Thompson, Galvanostatic growth of nanoporous anodic films on iron in ammonium fluoride-ethylene glycol electrolytes with different water contents. J. Phys. Chem. C **114**, 18853 (2010)

37. G.D. Sulkaa, J. Kapusta-Kołodzieja, A. Brzozkab, M. Jaskuła, Anodic growth of TiO_2 nanopore arrays at various temperatures. Electrochim. Acta **104**, 526 (2013)
38. A. Valota, M. Curioni, D.J. Leclere, P. Skeldon, P. Falaras, G.E. Thompson, Influence of applied potential on titanium oxide nanotube growth. J. Electrochem. Soc. **157**, K243 (2010)
39. S. Yoriya, C.A. Grimes, Self-assembled anodic TiO_2 nanotube arrays: electrolyte properties and their effect on resulting morphologies. J. Mater. Chem. **21**, 102 (2011)
40. X. Feng, J.M. Macak, P. Schmuki, Robust self-organization of oxide nanotubes over a wide ph range. Chem. Mater. **19**, 1534 (2007)
41. S. Berger, J. Kunze, P. Schmuki, A.T. Valota, D.J. LeClere, P. Skeldon, G.E. Thompson, Influence of water content on the growth of anodic TiO_2 nanotubes in fluoride-containing ethylene glycol electrolytes. J. Electrochem. Soc. **157**, C18 (2010)
42. Y. Ku, Y.S. Chen, W.M. Hou, Y.C. Chou, Effect of NH_4F concentration in electrolyte on the fabrication of TiO_2 nanotube arrays prepared by anodization. Micro Nano Lett. **7,** 939 (2012)
43. K. Shankar, G.K. Mor, H.E. Prakasam, S. Yoriya, M. Paulose, O.K. Varghese, C.A. Grimes, Highly-ordered TiO_2 nanotube arrays up to 220 μm in length: use in water photoelectrolysis and dye-sensitized solar cells. Nanotechnology **18**, 065707 (2007)
44. P. Roy, S. Berger, P. Schmuki, TiO_2 nanotubes: synthesis and applications. Angew. Chem. Int. Ed. **50**, 2904 (2011)
45. Z. Su, W. Zhou, Formation, morphology control and applications of anodic TiO_2 nanotube arrays. J. Mater. Chem. **21**, 8955 (2011)
46. J.M. Macak, H. Tsuchiya, A. Ghicov, K. Yasuda, R. Hahn, S. Bauer, P. Schmuki, TiO_2 nanotubes: self-organized electrochemical formation, properties and applications. Curr. Opin. Solid St. M. **11**, 3 (2007)
47. J.M. Macak, H. Hildebrand, U. Marten-Jahns, P. Schmuki, Mechanistic aspects and growth of large diameter self-organized TiO_2 nanotubes. J. Electroanal. Chem. **621**, 254 (2008)
48. G.K. Mor, O.K. Varghese, M. Paulose, K. Shankar, C.A. Grimes, A review on highly ordered, vertically oriented TiO_2 nanotube arrays: fabrication, material properties, and solar energy applications. Sol. Energy Mat. Sol. C. **90**, 2011 (2006)
49. S. Berger, S.P. Albu, F. Schmidt-Stein, H. Hildebrand, P. Schmuki, J.S. Hammond, D.F. Paul, S. Reichlmaier, The origin for tubular growth of TiO_2 nanotubes: a fluoride rich layer between tube-walls. Surf. Sci. **605**, L57 (2011)
50. K.-L. Li, Z.-B. Xie, S. Adams, A reliable TiO_2 nanotube membrane transfer method and its application in photovoltaic devices. Electrochim. Acta **62**, 116 (2012)
51. D. Fanga, Z. Luob, K. Huanga, D.C. Lagoudas, Effect of heat treatment on morphology, crystalline structure and photocatalysis properties of TiO_2 nanotubes on Ti substrate and freestanding membrane. J. Electroanal. Chem. **637**, 6 (2009)
52. Y. Liao, W. Que, P. Zhong, J. Zhang, Y. He, A facile method to crystallize amorphous anodized TiO_2 nanotubes at low temperature. ACS Appl. Mater. Interfaces **3**, 2800 (2011)
53. Dyesol. www.dyesol.com
54. H.J. Snaith, Estimating the maximum attainable efficiency in dye-sensitized solar cells. Adv. Funct. Mater. **20**, 13 (2010)
55. EIA. www.eia.gov
56. N. Alexaki, T. Stergiopoulos, A.G. Kontos, D.S. Tsoukleris, A.P. Katsoulidis, P.J. Pomonis, D.J. LeClere, P. Skeldon, G.E. Thompson, P. Falaras, Mesoporous titania nanocrystals prepared using hexadecylamine surfactant template: crystallization progress monitoring, morphological characterization and application in dye-sensitized solar cells. Micropor. Mesopor. Mater. **124**, 52 (2009)
57. G.C. Vougioukalakis, A.I. Philippopoulos, T. Stergiopoulos, P. Falaras, Contributions to the development of ruthenium-based sensitizers for dye-sensitized solar cells. Coordin. Chem. Rev. **255**, 2602 (2011)
58. T. Stergiopoulos, P. Falaras, Minimizing energy losses in dye-sensitized solar cells using coordination compounds as alternative redox mediators coupled with appropriate organic dyes. Adv. Energy Mater. **2**, 616 (2012)

59. A.V. Katsanaki, H.S. Karayianni, M.-C. Bernard, D.S. Tsoukleris, P. Falaras, Preparation and characterization of nanocrystalline Pt/TCG counterelectrodes for dye-sensitized solar cells. J. Sol. Energy Eng. **130**, 041008 (2008)
60. M. Grätzel, Photoelectrochemical cells. Nature **414**, 338 (2001)
61. L. Peter, 'Sticky Electrons' Transport and interfacial transfer of electrons in the dye-sensitized solar cell. Acc. Chem. Res. **42**, 1839 (2009)
62. K. Park, Q. Zhang, D. Myers, G. Cao, Charge transport properties in TiO_2 network with different particle sizes for DSCs. ACS Appl. Mater. Interfaces **5**, 1044 (2013)
63. T. Stergiopoulos, Spectroscopic characterization of photoelectrochemical solar cells. PhD thesis, University of Patras (2006)
64. G. Boschloo, A. Hagfeldt, Characteristics of the iodide/triiodide redox mediator in dye-sensitized solar cells. Acc. Chem. Res. **42,** 1819 ((2009))
65. A.J. Frank, N. Kopidakis, J.V.D. Lagemaat, Electrons in nanostructured TiO_2 solar cells: transport, recombination and photovoltaic properties. Coordin. Chem. Rev. **248**, 1165 (2004)
66. A. Hagfeldt, G. Boschloo, L. Sun, L. Kloo, H. Pettersson, Dye-sensitized solar cells. Chem. Rev. **110**, 6595 (2010)
67. M. Grätzel, Dye-sensitized solar cells. J. Photochem. Photobiol. C **4**, 145 (2003)
68. M. Grätzel, Recent advances in sensitized mesoscopic solar cells. Acc. Chem. Res. **42**, 1788 (2009)
69. F.O. Lenzmann, J.M. Kroon, Recent advances in dye-sensitized solar cells. Adv. Optoelectron. 2007 (2007)
70. Photovoltaic Education. www.pveducation.org
71. M.A. Omar, *Elementary Solid State Physics* (Book Addison-Wesley, London, 1975)
72. H.-G. Yun, B.-S. Bae, M.G. Kang, A simple and highly efficient method for surface treatment of Ti substrates for use in dye-sensitized solar cells. Adv. Energy Mater. **1**, 305 (2011)
73. J.M. Kroon, N.J. Bakker, H.J.P. Smit, P. Liska, K.R. Thampi, P. Wang, S.M. Zakeeruddin, M. Gratzel, A. Hinsch, S. Hore, U. Wurfel, R. Sastrawan, J.R. Durrant, E. Palomares, H. Pettersson, T. Gruszecki, J. Walter, K. Skupien, G.E. Tulloch, Nanocrystalline dye-sensitized solar cells having maximum performance. Prog. Photovolt: Res. Appl. **15**, 1 (2007)
74. T.-Y. Tsai, C.-M. Chen, S.-J. Cherng, S.-Y. Suen, An efficient titanium-based photoanode for dye-sensitized solar cell under back-side illumination. Prog. Photovolt: Res. Appl. **21,** 226 (2013)
75. S. Ito, N.-L. C. Ha, G. Rothenberger, P. Liska, P. Comte, S.M. Zakeeruddin, P. Pechy, M.K. Nazeeruddin, M. Gratzel, High-efficiency (7.2 %) flexible dye-sensitized solar cells with Ti-metal substrate for nanocrystalline-TiO_2. Photoanode Chem. Commun. **14** 4004 (2006)
76. J. An, W. Guo, T. Ma, Enhanced photoconversion efficiency of all-flexible dye-sensitized solar cells based on a ti substrate with TiO_2 nanoforest underlayer. Small **8**, 3427 (2012)
77. P. Roy, S.P. Albu, P. Schmuki, TiO_2 nanotubes in dye-sensitized solar cells: higher efficiencies by well-defined tube tops. Electrochem. Commun. **12**, 949 (2010)
78. L-L. Li, C.-Y. Tsai, H.-P. Wu, C.-C. Chen, E.W.-G. Diau, Fabrication of long TiO_2 nanotube arrays in a short time using a hybrid anodic method for highly efficient dye-sensitized solar cells. J. Mater. Chem. **20,** 2753 (2010)
79. N. Mir, K. Lee, I. Paramasivam, P. Schmuki, Optimizing TiO_2 nanotube top geometry for use in dye-sensitized solar cells. Chem. Europ. J. **18**, 11862 (2012)
80. J. Wang, Z. Lin, Dye-sensitized TiO_2 nanotube solar cells with markedly enhanced performance via rational surface engineering. Chem. Mater. **22**, 579 (2010)
81. M. Ye, X. Xin, C. Lin, Z. Lin, High efficiency dye-sensitized solar cells based on hierarchically structured nanotubes. Nan. Lett. **11,** 3214 (2011)
82. J.Y. Kim, J.H. Noh, K. Zhu, A.F. Halverson, N.R. Neale, S. Park, K.S. Hong, A.J. Frank, General strategy for fabricating transparent TiO_2 nanotube arrays for dye-sensitized photoelectrodes: illumination geometry and transport properties. ACS Nano **5**, 2647 (2011)
83. P. Roy, D. Kim, K. Lee, E. Spiecker, P. Schmuki, TiO_2 nanotubes and their application in dye-sensitized solar cells. Nanoscale **2**, 45 (2010)

84. K. Zhu, N.R. Neale, A. Miedaner, A.J. Frank, Enhanced charge-collection efficiencies and light scattering in dye-sensitized solar cells using oriented TiO_2 nanotubes arrays. Nano Lett. **7**, 69 (2007)
85. M. Yutao, L. Yuan, X. Xurui, L. Xueping, Z. Xiaowen, Synthesis of TiO_2 nanotubes film and its light scattering property. Chin. Sci. Bull. **50**, 1985 (2005)
86. R. Mohammadpour, A. Irajizad, A. Hagfeldt, G. Boschloo, Comparison of trap-state distribution and carrier transport in nanotubular and nanoparticulate TiO_2 electrodes for dye-sensitized solar cells. Chem. Phys. Chem. **11**, 2140 (2010)
87. C. Richter, C.A. Schmuttenmaer, Exciton-like trap states limit electron mobility in TiO_2 nanotubes. Nat. Nanotechnol. **5**, 769 (2010)
88. J. Bisquert, F. Fabregat-Santiago, I. Mora-Sero, G. Garcia-Belmonte, S. Gimenez, Electron lifetime in dye-sensitized solar cells: theory and interpretation of measurements. J. Phys. Chem. C **113**, 17278 (2009)
89. J.R. Jennings, A. Ghicov, L.M. Peter, P. Schmuki, A.B. Walker, Dye-sensitized solar cells based on oriented TiO_2 nanotube arrays: transport, trapping, and transfer of electrons. J. Am. Chem. Soc. **130**, 13364 (2008)
90. J.P. Gonzalez-Vazquez, V. Morales-Flórez, J.A. Anta, How important is working with an ordered electrode to improve the charge collection efficiency in nanostructured solar cells? J. Phys. Chem. Lett. **3**, 386 (2012)
91. A. Ghicov, S.P. Albu, R. Hahn, D. Kim, T. Stergiopoulos, J. Kunze, C.-A. Schiller, P. Falaras, P. Schmuki, TiO_2 nanotubes in dye-sensitized solar cells: critical factors for the conversion efficiency. Chem. Asian J. **4**, 520 (2009)
92. L. Sun, S. Zhang, X. Sun, X. He, Effect of the geometry of the anodized titania nanotube array on the performance of dye-sensitized solar cells. J. Nanosci. Nanotechnol. **10**, 4551 (2010)
93. P. Zhong, W. Que, Y. Liao, J. Zhang, X. Hu, Improved performance in dye-sensitized solar cells by rationally tailoring anodic TiO_2 nanotube length. J. Alloys Compd. **540**, 159 (2012)
94. C.-C. Chen, H.-W. Chung, C.-H. Chen, H.-P. Lu, C.-M. Lan, S.-F. Chen, L. Luo, C.-S. Hung, E. W.-G. Diau, Fabrication and characterization of anodic titanium oxide nanotube arrays of controlled length for highly efficient dye-sensitized solar cells. J. Phys. Chem. C **112**, 19151 (2008)
95. N. Liu, K. Lee, P. Schmuki, Small diameter TiO_2 nanotubes vs. nanopores in dye sensitized solar cells. Electrochem. Commun. **15**, 1 (2012)
96. S.P. Albu, H. Tsuchiya, S. Fujimoto, P. Schmuki, TiO_2 nanotubes—annealing effects on detailed morphology and structure. Eur. J. Inorg. Chem. **2010**, 4351 (2010)
97. K. Zhu, N.R. Neale, A.F. Halverson, J.Y. Kim, A.J. Frank, Effects of annealing temperature on the charge-collection and light-harvesting properties of TiO_2 nanotube-based dye-sensitized solar cells. J. Phys. Chem. C **114**, 13433 (2010)

Chapter 10
Titania Nanotubes for Local Drug Delivery from Implant Surfaces

Karan Gulati, Masakazu Kogawa, Shaheer Maher, Gerald Atkins, David Findlay and Dusan Losic

Abstract The principal challenge for bone therapy is to deliver an effective dose of therapeutic agent (for example antibiotic or anti-cancer drug) to the affected site within bone, while sparing other organs. The solution to this dilemma is to deliver drug locally within the bone; hence various surface/therapeutic modifications of the conventional bone implants have been suggested to achieve this. Implants composed of biocompatible materials and loaded with active therapeutics thus provide one possible option for effective bone therapy. This chapter showcases the challenges that an electrochemically nano-engineered bone implant based on titania nanotubes must overcome to survive and deliver therapeutics in conditions such as infections and cancer of bone. The fabrication of titania nanotubes, the therapeutic loading and release, ex vivo and in vivo investigations; all are reviewed in terms of effectiveness for therapeutic action. Also discussed are the potential advances of titania nanotube technology and the future research directions to address additional clinical problems.

10.1 Introduction

Implants represent a class of medical devices that correct diseased tissues/organs or modify physical features for cosmetic purposes. These biomaterials upon insertion inside the patient's body are placed inside/over the tissue of concern and face many challenges for acceptance and survival in the human body. These challenges include extensive inflammation, bacterial invasion and poor bio-integration with the

K. Gulati · S. Maher · D. Losic (✉)
School of Chemical Engineering, University of Adelaide, Adelaide, Australia
e-mail: dusan.losic@adelaide.edu.au

M. Kogawa · G. Atkins · D. Findlay
Discipline of Orthopaedics & Trauma, University of Adelaide, Adelaide, Australia

S. Maher
Faculty of Pharmacy, Assiut University, Assiut, Egypt

D. Losic and A. Santos (eds.), *Electrochemically Engineered Nanoporous Materials*, Springer Series in Materials Science 220,
DOI 10.1007/978-3-319-20346-1_10

traumatized tissue. This chapter will primarily focus on hard tissue implants, especially bone implants composed of titanium and its alloys, with the use of nano-engineering to enhance features for improved acceptance and survival of these implants. Metal implants are used in bone to provide fracture fixation or replacement of diseased joints. These bone implants, in the form of screws or plates or artificial joints, are composed of various metals and alloys such as stainless steel, titanium, tantalum and cobalt-chrome. Titanium and some of its alloys have been shown to possess good bio-integration with human bone, while on the other hand being corrosion resistant; have been widely used and extensively researched.

Internal and external fixation devices that are used to provide fracture stability during healing can fail in a number of ways [1]. They may bend or break or they may serve as substrates for bacterial colonization, with the most sinister form being biofilms which are typically resistant to antibiotics. These challenges adversely affect bone healing and furthermore can lead to serious consequences, including repeat surgery, amputation and even death. The conventional way to cater to any issues arising from implant fixation involves systemic drug administration, which involves exposing all body tissues to high levels of sometimes toxic drugs, in order to achieve efficacious therapeutic levels at the affected site. In the case of fractures, impaired blood supply may further exacerbate the problem of systemic delivery of drug to the affected site [2]. These limitations translate to ineffective therapeutic action at the site required while more potent drugs are introduced into the patient's body. Figure 10.1 summarizes the challenges for bone implants' acceptance and survival; and also how systemic therapy is unable to cater to such conditions. A simple solution could be having active therapeutics released directly at the site they are required at the bone implant interface. This local drug delivery (LDD) concept has opened the way for research aiming to achieve optimum therapeutic efficacy from the surface of the implant.

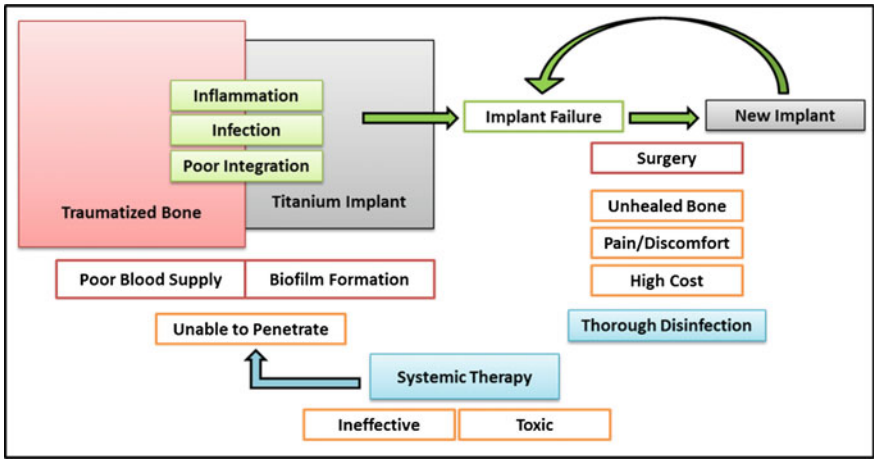

Fig. 10.1 Challenges associated with conventional bone implants and systemic drug delivery

This chapter showcases the suitability of titania nanotubes as the therapeutic extension for current bone implants aiming at achieving controlled local drug delivery of a variety of active drugs, catering to different bone conditions from severe fractures, bone infection to more complex bone cancers. Also detailed are the latest therapeutic advancements like multiple sequential drug release, delayed release to several months, in-built sensing and the various ex vivo and in vivo investigations carried out to establish the same. An overview to this book chapter can be seen from some of our previous review articles [4, 5].

Inability of therapeutics to penetrate biological barriers to reach the target site in effective concentrations suggests the need for local drug delivery (LDD). While systemic DD can be toxic to the patient's body in an attempt to reach a local therapeutic window, it may nevertheless remain ineffective in infected bone, tumors or brain disorders [3, 4]. In LDD, an active therapeutic loaded matrix is surgically inserted adjacent to the affected tissue/organ, and active molecules will be released directly where they are desired, with a release kinetics that can be controlled by various strategies [5–8]. The selection of the drug releasing matrix will relate to its applicability, for instance: prevention of infection at a fractured bone will also require mechanical support, while for brain drug delivery an implant with minimal invasiveness is desired.

LDD has the potential to not only improve the acceptance/survival of conventional implants, but also to open new windows towards effective therapy for conditions like: osteoporosis, osteomyelitis (bone infection), bone cancers etc. [9]. The LDD is well suited to scenarios where drug administration is unable to reach effectively. The material of choice for delivering drugs depends on many factors, which include the need for mechanical support, and whether the implant should be bio-resorbable or bio-integrating [10]. Polymers are an attractive choice for any kind of therapeutic application, with ease of fabrication, control of functionality, and the capacity to store substantial amounts of therapeutics. However for applications where mechanical support is also desired, metals are more appropriate. This review will focus on hard-tissue implant modifications capable of releasing therapeutics locally, to prevent inflammation, infection and poor integration. Also new generation of bone implants aiming towards enhanced/multiple functionalities that can cater to multiple conditions will be showcased.

10.2 Surface Modification of Conventional Bone Implants

The surface of implants is the first site of contact with the surrounding tissues. Appropriate surface characteristics in terms of roughness, chemical and biological functionality are desired to modulate the immune responses (foreign body response/FBR) and to enhance implant integration into the surrounding tissue. As a result various surface modification strategies have been investigated for Ti implant surfaces to achieve enhanced therapeutic functionality [11].

10.2.1 Surface Roughness

The role of surface roughness on implant integration has been investigated, which has led to numerous attempts aiming at finding the most suitable surface enhancement strategy [12]. Various in vitro/in vivo experiments and mathematical derivations conclude that micro-meter range roughness (hemispherical pits 1.5 μm deep and 4 μm wide) provides the most active implant surface to enhance implant bio-integration with the surrounding tissue [12–14]. To create micro-meter surface roughness, various approaches have been tested, including sand-blasting, acid-etching, electrochemical anodisation and plasma reaction.

For blasting, the metal implants are bombarded with abrasive particles under high pressure; however for application as biomaterials, the particle choice is critical. Alumina, titania and hydroxyapatite particles are generally applied to maintain biocompatibility, with HAP being the ideal choice for also enabling the biological responses relevant for bone cell adhesion [15–18]. Strong acids like HNO_3, HCl, H_2SO_4 and HF have also been utilized to etch titanium implant surfaces to render micro scale roughness; which has promoted bone cell functioning, translating to improved osseointegration [19]. Etching using HF further enhances these features by incorporation of fluoride ions, which have been shown to enhance implant integration with the healing bone [20].

The third technique, electrochemical anodisation enables growth of a thick oxide layer in order to enhance anti-corrosion properties. The procedure involves exposure of metal implant surfaces to appropriate solutions (sulphuric, phosphoric, acetic acid etc.) under the influence of voltage. The thickness and characteristics (mechanical, chemical etc.) of the resultant oxide film can easily be controlled by varying anodisation parameters, such as electrolyte concentration, temperature and voltage. Furthermore, anodisation at very high voltages (>100 V) for extended durations (spark anodisation or micro-arc oxidation) results in an irregular micro-porous oxide layer with improved mechanical properties [21]. Also, soaking these micro-porous implants in simulated body fluid (SBF) can lead to HAP growth, which can further enhance bioactivity of the implant [22].

Another approach to induce micro-scale roughness to the implant surfaces is plasma assisted spraying of titania, zirconia or alumina. The spraying also enhances the wear resistance of the implants and offers control over the surface chemistry; however some studies have demonstrated that usage of zirconia and alumina compromises the osseointegration abilities of the implant [23]. Besides the added complexity of plasma spraying, the poor control over resulting structural roughness for sand blasting and acid treatment, anodisation offers greater advantages that can directly contribute towards enhanced osseointegration. The above mentioned approaches render the surface micro-rough, which can enhance implant bonding with the surrounding tissue, but for substantial therapeutic loading and deep osseointegration with the hard tissue: nano-scale roughness is desired.

10.2.2 Biological Enhancements

When an implant is inserted, implant-tissue interactions start via protein adsorption [24]. These protein interactions also initiate an electrochemical reaction at the implant surface, which oxidizes metallic implants, often leading to increased oxide thickness with time [25]. With the aim of implant technology being rapid healing and implant integration, modulating these protein interactions can decide the survival or failure of the implant. This modulation can be achieved for example by, deposition of bioactive species like Ca, P ions or growth factors. The continuous electrochemical reactions at the bone-implant interface (BII) also result in metal corrosion and hence release of such byproducts has been detected in the implant vicinity, serum and urine of patients [26, 27]. Study has also indicated that metal ions can adversely affect bone turnover and repair mechanisms [28]. As a result, implant surfaces that avoid ion discharge are desirable, to allow bioactive species released by the implant to enhance cell function and promote quicker healing.

Several biopolymers coated onto titanium implants have been investigated for enhancing implant integration, modulating protein interactions and also inducing specific cell behaviors [29]. These approaches include impregnation of biomolecules or growth factors into porous ceramics, biodegradable polymers (polylactides) and natural polymers (collagen/fibrin). These biopolymer coatings, in combination with active osteoinductive growth factors like BMPs (bone morphogenetic proteins), can further enhance biomechanics and bone remodeling at the bone-implant interface, ultimately leading to quicker bone healing [30]. Also CaP coatings on titanium implants have demonstrated improved bone cell responses, which can further be enhanced by immobilizing growth factors on these coatings [31]. These bioactive modifications, ensuring appropriate cell behavior without any toxicity, increase the implant integration and the healing rates. However, the inappropriate release kinetics of biomolecules, demonstration of short-term osseointegration and the unexplained degradation of biopolymers demand further investigation. Bioactivity, combined with increased surface roughness of metal implants, offers suitable mechanical/biological features for implant integration and acceptance.

10.2.3 Drug Releasing Implants

With the aim to enable LDD from the surfaces of Ti implants, the simplest and earliest of attempts included simple coating/adsorption of active drugs on titanium surfaces (commercial pure titanium and micro-rough), bone cements and polymers. Several studies report prevention of infection by impregnation of potent antibiotics into bone cements [32]. However, studies have indicated compromised longevity of bone implants, mainly due to poor mechanical strength of the cement (for methyl methacrylate) [33]. Also poor and/or uncontrolled release kinetics from the cement, inadequate osseointegration and the development of antibiotic resistance by the

bacteria, are claimed as other limitations encountered with antibiotic incorporated solutions [34].

Micro-rough Ti implant surfaces, particularly with the inclusion of calcium phosphate, can aid in bone growth and osseointegration, and also possess adequate mechanical strength for load bearing bone implant situations. Antibiotics can easily be adsorbed onto HAP modified Ti surfaces to provide in situ release that can simultaneously cater to both osseointegration and prevention of bacterial infection [35]. Alternate approaches include immobilizing potent antibiotics (like vancomycin, daptomycin etc.) directly onto the Ti implant surfaces to prevent bacterial adhesion and biofilm formation. Besides conventional anti-bacterial drugs, antimicrobial peptides have also been attached to Ti to enable effective bactericidal effects without any chance of toxicity or bacterial resistance [36].

10.2.4 Research Gap: Combining Roughness, Bioactivity and Drug Release

While different approaches have been researched to include appropriate roughness, enabled bioactivity and drug release, seldom are these implant requirements integrated into one tailorable technology. Reports have suggested that adequate nano-scale roughness and bioactive surface modification are required to recruit bone cells to enhance osseointegration, while the therapeutic loading and release can cater to preventing extensive inflammation and bacterial infection. Incorporation of CaP crystals onto the micro-scale and nano-scale titanium surface caters to the roughness and bioactivity; furthermore inclusion of therapeutics into the same modified implant often faces challenges like: inappropriate loading amounts, poor kinetics and unreproducible results. While nano-rough Ti surfaces offer both mechanical strength and improved bioactivity, the therapeutic effect still remains a hurdle.

The challenges with adsorption strategy of antibiotics remain inadequate loading amounts and unpredictable release kinetics, while for covalently attached drugs there remains only limited action immediately adjacent to the implant. Antibiotic release also decides the fate of the implant, as very high local concentration can compromise the bone healing and too early consumption can re-trigger the bacterial invasion. To achieve higher loading amounts of therapeutics, deep integration of payloads into the implant surface modification is desired; and for effective therapy slow and delayed release kinetics are required.

To permit control over the amount of therapeutic loaded with easy tailoring of the nano-rough surfaces, new nano-engineering approaches to fabricate nano-tubular/nano-porous surfaces have been suggested as superior implant modifications to permit enhanced therapeutic action. In particular electrochemically engineered methods based on simple and scalable anodisation process have been extensively explored including porous silicon, nano-pororus anodic alumina and

nanotubular titania [10]. These nanostructured materials have been applied for various medical applications including: drug delivery from implant surfaces and biosensing.

10.2.5 Electrochemically Anodised Implant Surfaces

Among the various nano-porous/-tubular modifications performed using electrochemical anodisation (EA), nanotubular titania (TiO_2) or titania nanotubes (TNTs) have been most successful in terms of its easy integration into the implant industry. This is because the majority of bone and dental implants are composed of titanium and its alloys. The formation of nanotubes or pores on the implant surface via EA is not only a cost-effective and simple process, but also permits easy control over the properties of the fabricated structures (diameters, lengths, structure etc.) [4, 5, 9]. Besides the proven biocompatibility, TNTs have also been shown to possess adequate bioactivity (enhanced cellular functions) and enable substantial drug loading amounts and achieve favourable release kinetics (to be discussed in the following sections) [9, 10]. These features of EA and TNTs make an ideal implant modification technology that can aim at most common bone implant challenges and also can enable effective local drug elution.

10.3 Titania Nanotubes (TNTs)

Titania or titanium dioxide nanotubes (TNTs) generated by electrochemical anodisation of Ti surface represent very remarkable nanostructures which due to its wide range properties (such as corrosion resistance, biocompatibility, tailorable dimensions, ease of functionalization etc.) are extensively explored since last decade for a variety of applications. They are hollow cylindrical, vertically oriented and hexagonally arranged arrays of nanotubes composed of TiO_2 [4]. Like tiny test-tubes they are open at top and closed at bottom and can be fabricated with controllable dimensions (diameters 10–300 nm and lengths 0.5–300 μm) [4, 5]. TNTs can be synthesized in many forms: on titanium substrates, self-supporting TNT membranes and loose/agglomerated in a solution, with more details in the following sections.

10.3.1 Applications of TNTs

Titania nanotubes offer a wide range of properties that enable their use for further diverse biomedical applications as summarized [37]:

(a) Catalysis, purification and biosensing
(b) Bioactive surfaces suitable for

i. accelerated hydroxyapatite formation
ii. enhanced functioning for mesenchymal stem cells, osteoblasts/osteoclasts and hematopoietic cells
iii. improved osseointegration

(c) Drug releasing implants

i. substantial loading of various therapeutics and localized release
ii. ability to achieve triggered and delayed release patterns.

10.3.2 Fabrication of TNTs

Following the first report of TNT fabrication on alumina templates, numerous methods for fabrication of TNTs have been applied. These include: alternate template methods, sol-gel method, hydro/solvothermal, and atomic layer deposition (ALD) [38–45]. The above mentioned methods yield loose nanotubes in solution or bundled in agglomerates, with limited control over nanotube dimensions. These limit the use of the fabricated TNTs for applications in electronics and medical technology, as they cannot be aligned or arranged in a regular reproducible fashion onto a substrate. The most suitable technique for fabricating self-ordered TNTs in an array onto a titanium substrate with strict control over the dimensions is via electrochemical anodisation. This method is very cost-effective and can be extended to any shape of titanium substrate. The electrochemical setup with titanium (as anode) and an alternate metal (cathode), when immersed in appropriate electrolyte and connected to substantial voltage results in two possible reactions: metal dissolution or oxide formation. When the balance between these two reactions is established, porous metal oxide is formed, which in special experimental conditions will result in self-ordering into nanotubular arrays [37]. Many factors determine the quality and dimensions of TNTs: voltage/time of anodisation, water content, pH, temperature and electrolyte composition.

Since the first report in 1999 by Zwilling et al., numerous investigations have been carried out to optimize the TNT fabrication using electrochemical anodisation to achieve improved ordering and higher growth rates [44, 45]. The first attempt resulted in TNT lengths of only 0.5 μm as a result of extensive dissolution in chromic acid electrolyte containing HF [44]. In this pioneering attempt, the role of fluoride species in the fabrication of TNTs was established. However the resulting nanotube structures lacked ordering and uniformity. The 2nd generation of TNT fabrication reported significant improvements, with longer nanotube lengths (5–7 μm) due to reduced dissolution rates [46–48]. In this study, fabrication of TNTs was achieved in pH controlled aqueous buffered electrolyte containing fluoride species and the relation between nanotube properties (size, organization and crystal

structure) and anodisation conditions (electrolyte composition, pH, voltage/current, time etc.) was confirmed [46–48]. Furthermore, to achieve higher growth rates, non-aqueous polar organic solvents (dimethyl sulfoxide, formamide, ethylene glycol, or diethylene glycol) plus fluoride ions were investigated as anodisation electrolytes [49, 50]. This development marked the 3rd generation and yielded TNTs with lengths up to 1000 μm. The most optimum anodisation parameters to obtain long, well-ordered and close-packed TNT structures are: organic viscous electrolytes and anodisation voltage of 80–120 V. More recently TNT fabrication has also been reported in fluoride-free electrolytes [51].

Besides the cylindrical nanotubular arrangement of TiO_2 post anodisation, various other nanostructures have also been reported like: branched tubes, nanolace, bamboo-type nanotubes, inner tubes and multi-layered nanotubes [52]. However such altered nanotube structures obtained as a result of voltage/current oscillations during the anodisation procedure have not been explored for any specific application. Recently, the effect of UV-Vis irradiation on the anodisation of Ti was studied, which yielded TNTs with larger diameters and thicker walls as compared to the conventionally fabricated TNTs [42]. Similar enhancements were also observed with ultrasound irradiation during Ti anodisation [43].

10.3.3 Substrate Choice

Most of the research utilising TNTs on Ti has been focused on anodisation of flat Ti foil, however in recent years other shapes of Ti substrates have also been investigated to fabricate TNTs. These include Ti wires, hollow tubes, meshes etc., which are proposed for various applications [53–56]. Being able to use a range of shapes of Ti substrate for fabricating TNTs opens a new window for integration of the technology into established medical implant devices. For example, TNTs fabricated on curved surfaces of Ti wires can provide a 3D release of therapeutics once implanted inside the patient [57–59]. This not only enhances the spread or the reach of the released therapeutics but also with minimal surface area (in comparison with planar substrate), it represents simpler implantation surgery and therefore easier integration with the surrounding tissue. Ti wires incorporating TNTs have been proposed for anti-infection fracture fixation pins to replace stainless steel wire implants, and also as dopamine releasing brain therapeutic implants [54, 57]. The curved surfaces also mean easy integration into the current bone implants (screws, plates, pins etc.) and brain electrodes (wire, pins); as most of these implantable devices represent curved surfaces (Fig. 10.2). Such fabrication advances have also been shown to address challenges associated with treating conditions such as bone cancer, infection and inflammation, as ‘in-bone’ therapeutic implants [59]. Yu et al. in 2011 reported TNT fabrication on Ti wires, followed by complete dissolution of wire core; thus yielding loose core-shell TNT structures [53]. The novel TNT structures in this study were proposed as photo-anodes for solar-cell application. Another investigation of TNTs on curved surfaces was reported by Zeng et al.,

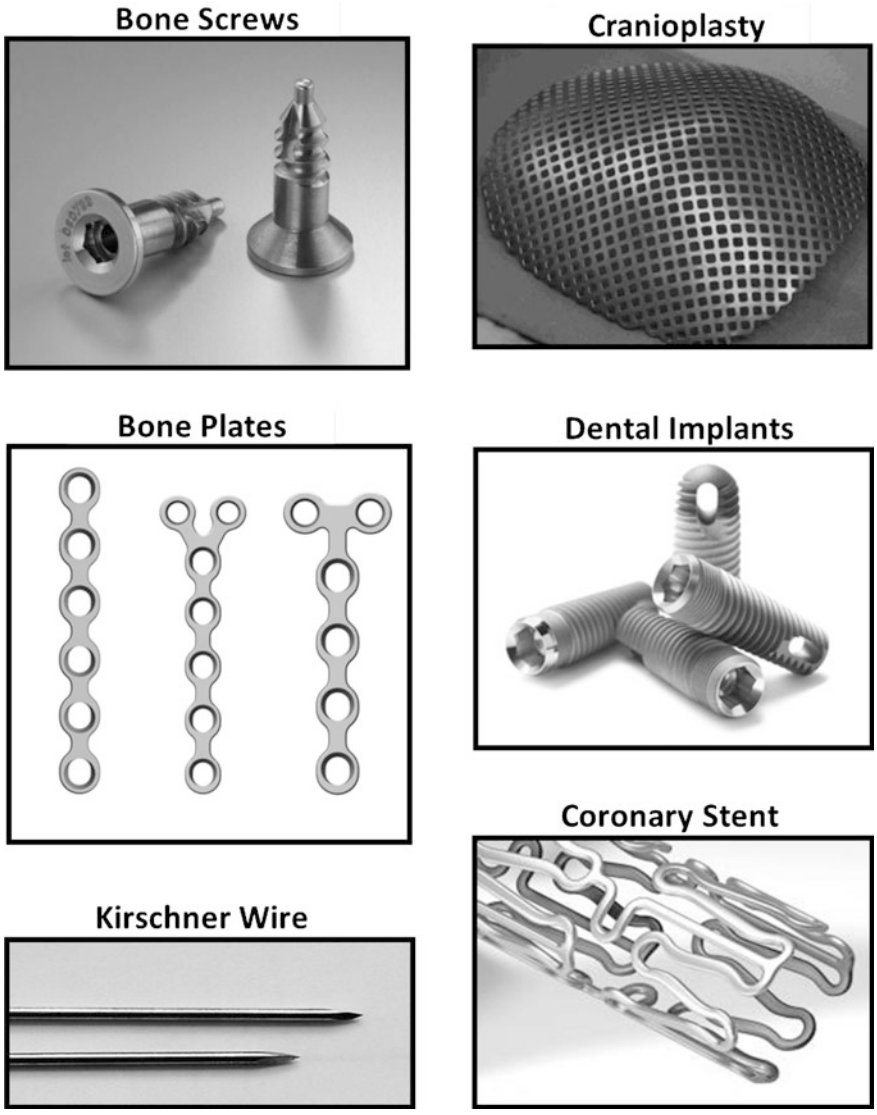

Fig. 10.2 Various metal implants catering to various conditions from fixing fractured bones to correcting blocked arteries

where they fabricated TNTs on Ti mesh using neutral electrolyte composed of ammonium sulphate and ammonium fluoride [55]. The influence of various anodisation parameters like fluoride concentration, voltage and time on TNT structure was also investigated. Sun et al. explored the anodisation of hollow Ti cylinders, showing the influence of electrode orientation on the nanotube features [56] (Fig. 10.3).

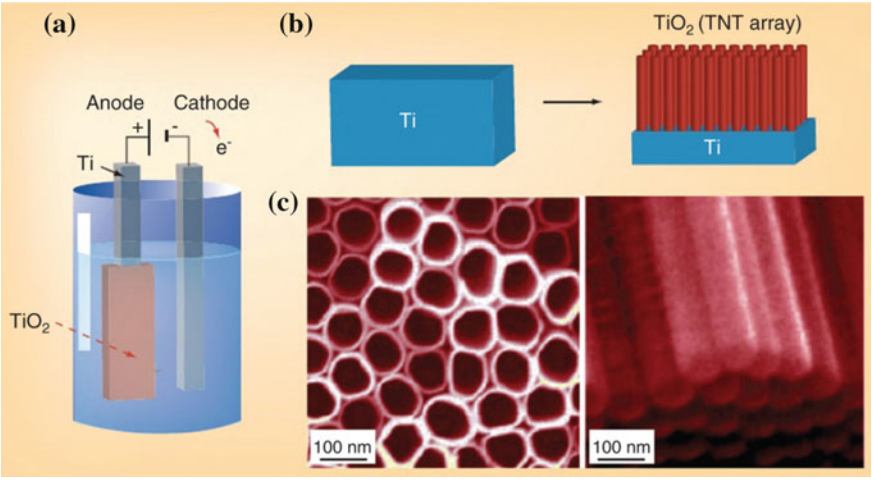

Fig. 10.3 Fabrication of titania nanotubes (TNTs) on titanium substrate. **a**, **b** Scheme showing the electrochemical anodisation of Ti substrates resulting in self-ordering of TNTs on Ti, and **c** SEM images showing open pores and close bottoms of the TNTs. Reproduced with permission from [5]

Titanium alloys with Al, V, Ta, Zr etc. have been shown to offer enhanced bio-mechanical characteristics as compared to cpTi [60]. Moreover, Ti alloys cover a high percentage of the implant market and as a result several surface modification strategies have been attempted on these surfaces [60]. With the advent of nano-technology and confirmed reports of nano-topography (particularly anodised porous or tubular structures) providing advantages over micro-range roughness, many attempts to extend this technology to Ti alloys have been investigated. Macak et al. reported electrochemical anodisation of biomedical Ti alloy Ti-6Al-7Nb and Ti-6Al-4 V and obtained nanotubes composed of mixed oxides, which were grown to several hundred nanometers [61]. Similar observations have also been reported for other alloys including Ti-28Zr-8Nb and Ti-35Zr [62, 63]. In another study by Jha et al., rapid breakdown anodisation (RBA) was utilised to fabricate oxide nanotubes on three Ti alloys: TiNb, TiZr and TiTa [64]. This ultra-fast anodisation procedure was carried out in a chloride-perchlorate electrolyte at 40 V and resulted in mixed oxide nanotubes of several tens of micrometers length [64]. Other investigations have aimed at synthesizing TiO_2 nanotubes on biomedical alloys [65, 66]. TNTs were fabricated on Ti-4Zr-22Nb-2Sn alloy and were demonstrated for drug delivery ability by Liang et al. [65]. The TiO_2 nanotubes or TNTs were loaded with minocycline hydrochloride antibiotic via immersion technique and the release profile was compared with nanotubes formed under different voltage [65].

10.3.4 TNTs' Suitability for LDD Applications

Incorporation of TNTs into implants composed of Ti and its alloys has resulted in a new generation of implants that can release drugs locally to target common implant challenges and hard to reach conditions like bone infection and cancers [10]. While proposing any implant modification, biocompatibility is the first criteria it must fulfil and as a result various biocompatibility and toxicity studies have been carried out using TNT modified Ti surfaces [67, 68]. Studies have shown that bone cell functions like adhesion and differentiation are enhanced on TNT-modified Ti surfaces as compared to normal Ti surfaces [69, 70]. This clearly translates into achieving short-term and long-term osseointegration, which means implant survival and quicker bone healing. Alternate studies with bacteria, endothelial cells, macrophages etc. have also demonstrated interesting results with TNT-modified Ti surfaces that further cater to wide range of conditions encountered by a typical hard tissue implant like: bacterial infection, inadequate bonding, extensive inflammation and so on [70–74].

Also TNTs represent an ideal platform to achieve local therapeutic effects, as its vacant volume can be loaded with substantial therapeutic amounts which can later be released with favourable kinetics. Many investigations have shown loading of various antibiotics, proteins, growth factors etc., which represent varied water solubilities, weights, chemical functionalities and cater to wide range of therapeutic conditions. Furthermore TNT dimensions can easily be controlled using various EA parameters like voltage, time, water content, temperature etc. [9]. This is turn allows for easy control of the amount of drug loaded and its release kinetics. The ease of chemical and biological functionalization of TNTs further allows the abovementioned features to be enhanced. Hence, TNT fabrication on Ti implants has been recognised as the most promising modification strategy to enable implant success and local therapeutics [5, 9, 69, 71].

10.4 Therapeutic Release from TNT/Ti Implants

Implant loosening due to inappropriate osseointegration and bacterial infection can contribute to implant failure [75]. Moreover, appropriate modulation of the immune response ensures implant acceptance in the patient's body. To cater to these conditions, various therapeutic molecules (anti-inflammatory, antibiotic and osseointegrating) in various formulations can be incorporated inside of TNTs to achieve elution locally at the traumatised site. Various active molecules in substantial amounts are loaded inside TNTs and later tested for various cell functions with an aim to attract and promote specific cell responses.

10.4.1 Modulating Immune Responses

10.4.1.1 Foreign Body Response

Immediately after implantation, proteins from the ECM (extra-cellular matrix) and blood adhere onto the implant surface (Fig. 10.4a). The tissue damage by surgical placement of implant and the quick adsorption/conformation of proteins on its surface determines the immune response [3, 76]. Hence the focus of biomaterial design has been on inert materials in order to reduce the cell-material interactions, hence resulting in lowered FBR (foreign body response) which often causes fibrous tissue encapsulation of implants [76]. More recently, it has been reported that some cell interactions might actually be advantageous for the implant acceptance and survival, particularly for Ti bone implants [77, 78]. This deliberate modulation of immune responses by modified implant surfaces can enhance the bone cell functions, ultimately leading to improved osseointegration and bone healing. The immune response modulation can be achieved via various surface enhancements aiming towards: (a) limiting adhesion, activation and fusion of macrophages to FBGCs (foreign body giant cells) by surface roughness/topography, and (b) attachment or loading of bioactive species like growth factors/anti-inflammatory drugs [76].

10.4.1.2 TNTs and Immune Responses

Ainslie et al. reported that the inflammatory response at titanium surfaces can be reduced by rendering the surface nano-rough [79]. They compared the human monocyte viability/morphology, various inflammatory cytokines and reactive oxygen species generation, between flat and nanostructured surfaces [79]. In a similar study by Smith et al., short and long term in vitro immune responses of TNTs were explored using human blood lysate (with leukocytes, thrombocytes and erythrocytes), and were compared with medical grade Ti [80]. The immune cell study with relevant cells (monocyte, macrophage and neutrophil) revealed reduced short and long term cell functionalities (viability, adhesion, proliferation etc.) on TNTs, again signifying the role of nanostructuring in immune response modulation [80].

10.4.1.3 Loading Bioactive Species in TNTs

Besides modifying the surface features, many studies were dedicated to loading/releasing anti-inflammatory drugs from TNTs/Ti in an attempt to reduce immune responses. Aninwene et al. loaded dexamethasone inside TNTs via physical adsorption and deposition from simulated body fluid (SBF) [81]. They showed enhanced osteoblast functions and the role of SBF loading in delaying the release of drugs. Alternatively, other anti-inflammatory drugs like ibuprofen, sodium naproxen etc. have been investigated via various loading strategies for

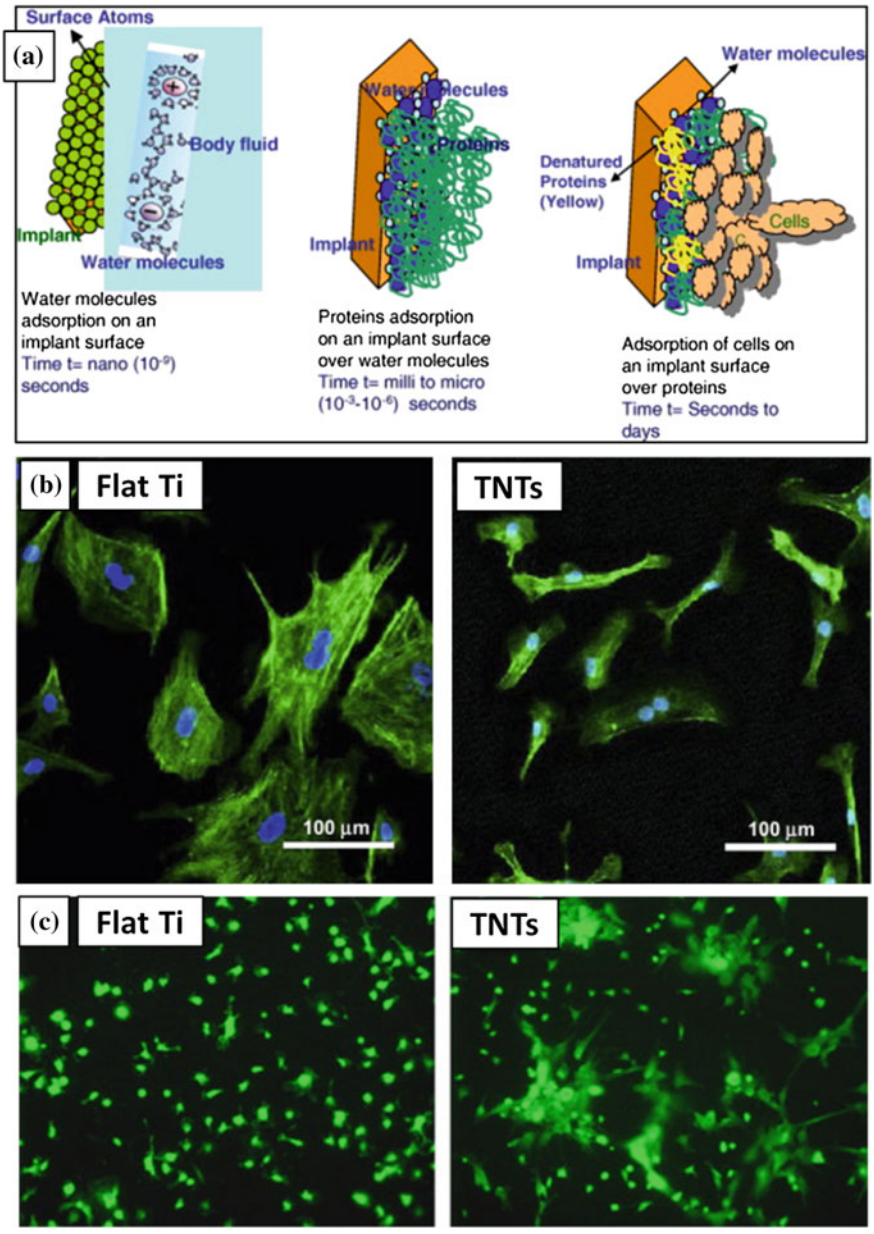

Fig. 10.4 Various cellular functions on TNTs. **a** Cellular events at the bone-implant interface upon implant placement at the traumatized bone [3], **b** varied cellular morphologies for Bovine aortic endothelial cells cultured on flat Ti and TNTs [72], and **c** cluster formation of live marrow stromal cells on TNTs as compared to flat Ti [70]. Reproduced with permission from [3, 70, 72]

achieving favourable release kinetics from TNTs [82, 83]. Also various advanced drug release approaches like biopolymer coating on drug loaded TNTs, micellar encapsulation of drugs and multiple therapeutic releases have been explored, using anti-inflammatory indomethacin as the model drug [69, 84, 85].

Very recently, in vitro testing of TNTs and cp Ti with macrophages [RAW264.7] in both standard and pro-inflammatory conditions, revealed reduced inflammation of macrophages for TNTs [73]. The model used bacterial LPS (lipopolysaccharide)-induced inflammation and strongly indicated that TNTs are capable of modulating macrophage responses without the need of any therapeutic modification. In vivo investigations are needed to optimize surface modifications to suitably modulate immune reactions that do not compromise implant acceptance and survival.

10.4.2 Preventing Bacterial Infection

10.4.2.1 Implants and Bacterial Infection

Many attempts have been made to improve implant surfaces to promote adjacent cell functions; however while doing so bacterial attachment may also be encouraged. Post implantation, the host's immune system coats the implants with serum proteins in an effort to recruit tissue repair cells. This same mechanism is also utilized by pathogens to invade and infect the traumatized site [86]. Gristina et al. suggested the competition between host's cells and the pathogenic bacteria to reach the implant site determines the fate of the implant [87]. Besides strict sterile implant surgeries, there is a high chance of infection: 2–30 % for transcutaneous fracture correction pins, 13 % for bone supplements, and 2–5 % for spinal infections [88]. Hence there is need for effective local antibiotic therapy from implants to avoid bacterial attachment and invasion. The common pathogens related to implant infections are *S. aureus*, *S. epidermidis* and *Pseudomonas aeruginosa* [89, 90].

10.4.2.2 Bacterial Attachment on TNTs

As mentioned in previous sections, TNTs represent a remarkable surface modification that can promote bone cell functions; however studies have revealed that nanotubular and nanotextured Ti surfaces can cause increased bacteria attachment as compared with nano-rough and conventional Ti surfaces (Fig. 10.5a) [91]. In the study by Puckett et al., three reasons for enhanced bacterial attachment on TNTs were postulated: (a) presence of Fluoride ions (mainly from anodisation electrolyte), (b) increased number of dead bacteria, and (c) amorphous nature of nanotubes [91]. Loading of various antibacterial compounds in TNTs seems an appropriate solution, however some groups investigated various properties and structural enhancements of TNTs in order to find a suitable TNT surface setting that could

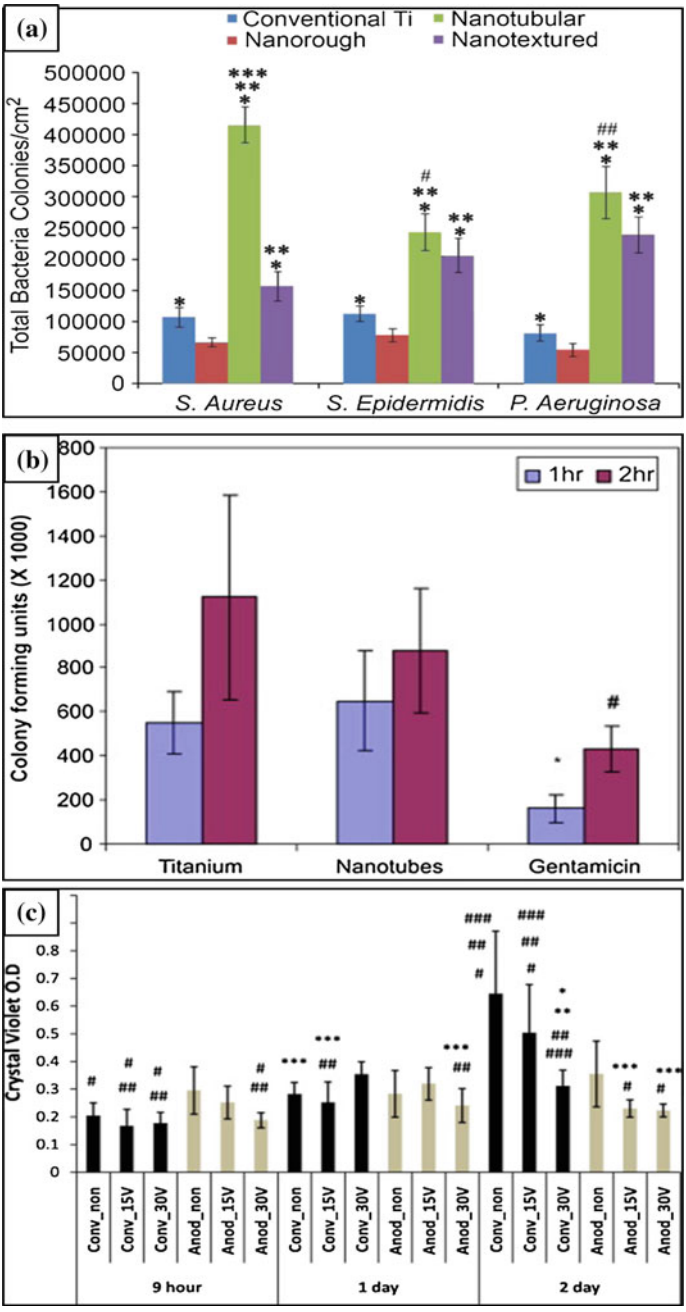
(a)
Conventional Ti
Nanotubular
Nanorough
Nanotextured
Total Bacteria Colonies/cm2
500000
450000
400000
350000
300000
250000
200000
150000
100000
50000
0
S. Aureus
S. Epidermidis
P. Aeruginosa
(b)
1hr
2hr
Colony forming units (X 1000)
1800
1600
1400
1200
1000
800
600
400
200
0
Titanium
Nanotubes
Gentamicin
(c)
Crystal Violet O.D
0.8
0.7
0.6
0.5
0.4
0.3
0.2
0.1
0
Conv_non
Conv_15V
Conv_30V
Anod_non
Anod_15V
Anod_30V
9 hour
1 day
2 day

◀ **Fig. 10.5** Antibacterial effect from TNTs. **a** Increased bacterial colonies on TNT surfaces as compared to other controls: data signify the need to include antibacterial effect in TNTs [91], **b** reduced *S. epidermis* adhesion on gentamicin loaded TNTs [71], and **c** the effect of electrical stimulation on adhesion of *S. aureus* on TNTs and Ti [101]. Reproduced with permission from [71, 91, 101]

itself prove to be bacteria repelling. The concept is that combining bacteria repelling TNTs and the antibiotic elution from the TNTs would give long lasting anti-bacterial effects beyond elution of the drug. Ercan et al. investigated the effect of various TNT diameters and heat treatment on various bone implant related bacteria [92]. They reported that heat treated TNTs (500 °C/2 h) and large pore diameters (60–80 nm) significantly reduced the number of live and dead bacteria attached. It is noteworthy to mention here that the number of both live and dead bacteria must be reduced when testing microbial attachment, as the dying bacteria are known to release proteins that can attract other live cells [93].

10.4.2.3 Antibiotic Loaded TNTs

Many active anti-bacterial compounds have been explored for incorporation into TNTs and achieving appropriate release kinetics to render the surfaces bacteriostatic and bactericidal. There are numerous examples of these loaded molecules like antibiotics, metal ions, anti-microbial peptides and biopolymer coatings [4, 5, 9]. The simplest approach is loading substantial amounts of antibiotics inside of TNTs and achieving release kinetics sufficient to eradicate any bacteria, without compromising bone cell activity. Popat et al. demonstrated the effect of different loaded amounts of gentamicin on reducing *S. epidermidis* adhesion and proved that antibiotic loading did not interfere with osteoblast functions (Fig. 10.5b) [71]. Furthermore, in vivo studies with vancomycin loaded TNTs implanted in rats for 30 days revealed enhanced anti-bacterial activity with increased biocompatibility [94].

Another important aspect that needs to be addressed is the antibiotic resistance, which often makes the most potent conventional antibiotic unable to act against the invading bacteria especially the methicillin-resistant *Staphylococcus aureus* (MRSA) [95]. If untreated, this type of infection can lead to serious consequences, and repeated systemic drug administration or local elution will be totally wasteful and in fact might result in decreased osseointegration. This demands local elution of alternative medicine that can overcome antibiotic resistance without compromising implant integration. As a result, antimicrobial peptides (AMPs) were explored for TNTs as a way to achieve maximum antibacterial effect [95, 96]. TNTs loaded with AMPs HHC-36 were tested against *S. aureus* and almost 99.9 % bactericidal effect was achieved [96].

10.4.2.4 Metal NPs/Ions Loaded TNTs

Besides the established antibiotics, metal ions, especially silver ions and nanoparticles (NPs), have also been investigated by loading inside TNTs, due to their proven antimicrobial activity. Zhao et al. incorporated different concentrations of Ag NPs inside TNTs by simple soaking of nanotube samples in $AgNO_3$ solutions followed by UV irradiation, and evaluated the Ag NPs release kinetics in PBS in vitro [97]. They confirmed the adherence of Ag NPs to TNT inner walls and observed complete bacteria killing in the initial few days and the prevention of bacterial adhesion for over 30 days [97]. The nanoparticle release did cause cytotoxicity but since its loading amount and release can be controlled, this side-effect can be considerably lowered. Similar antibacterial effects were also observed for TNTs loaded with Zinc ions with an added benefit of enhanced osseointegration [98] (Fig. 10.6).

10.4.2.5 Biopolymer Coated TNTs

Some biopolymers are inherently antibacterial, for example Chitosan, and coating these polymers onto TNT surfaces could mean long term antibacterial effects until the polymer completely degrades. This strategy has been used by our group to demonstrate the long term antibacterial effect of these Chitosan coated TNTs with and without the presence of antibiotics [99]. TNTs/Ti were loaded with the potent

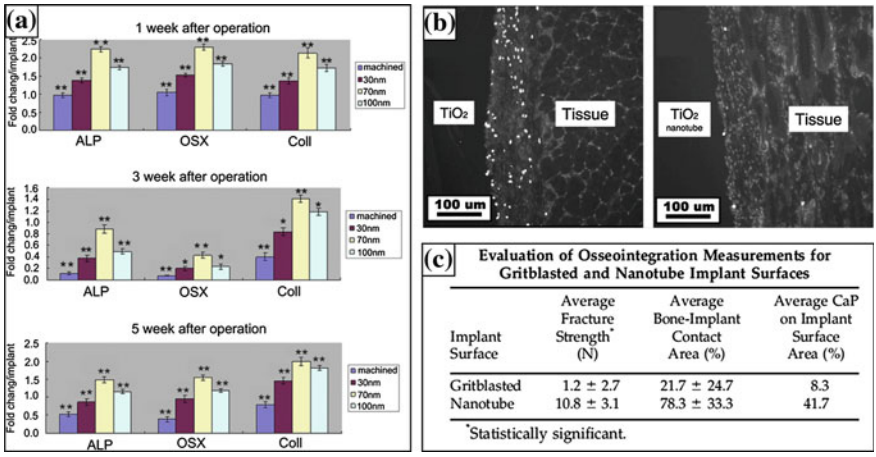

Fig. 10.6 Evidence of enhanced osseointegration with TNT implants in vivo. **a** Enhanced mRNA expression for osteogenesis-related genes for TNTs as compared to machined Ti [161], **b** anti-nitrotyrosine stained (*white*) cells (micrographs) post 1 week implantation suggests favourable soft tissue response [162], and **c** various measurements at the bone-implant interface post in vivo implantation suggests improved osseointegration for TNT implants [74]. Reproduced with permission from [74, 161, 162]

antibiotic gentamicin encapsulated in TPGS (d-α-tocopheryl polyethylene glycol 1000 succinate) micelles, followed by polymer coating of Chitosan and PLGA [poly(lactic-co-glycolic acid)], and later the antibacterial properties were investigated by testing with gram-positive bacteria (*S. epidermidis*). The results confirmed delayed release of antibiotics, significantly reduced bacterial attachment and biofilm formation for Chitosan coated gentamicin loaded TNTs, with simultaneously enhanced bone cell adhesion. Another study showed long term antibacterial activity against *E. Coli* for chitosan coatings on selenium electro-deposited TNTs [100].

10.4.2.6 Advance Anti-bacterial Effects with TNTs

In another study by Webster's group, Ercan et al. showed electricidal effect of TNTs by electrically stimulating TNTs each day for 1 h using 15 and 30 V, with *S. Aureus* seeded onto the various TNT samples and controls [101]. They also reported enhanced biofilm formation on TNT surfaces after 1, 4 and 8 h, which can be explained by increased fibronectin adsorption as compared to bare titanium surfaces. Upon electrical stimulation for both the TNTs and the control Ti samples, the biofilm formation was reduced and this effect was directly proportional to the voltage used (Fig. 10.5c). The electricidal mechanism is based on generation of electrolysis byproducts and electric field driven cell damage and detachment [102]. This unique approach of preventing bacterial attachment is innovative but its effectiveness in actual traumatized bone conditions needs to be investigated, as there remains a risk of disrupting the health of the healing tissue.

With various potent antibiotics or antibacterial metal ions loaded inside TNTs, the release kinetics is often neglected in the investigations and the antibacterial effects are only evaluated for a period of a few weeks. A sudden drop in antibiotic concentration can re-trigger the bacterial attachment and a very high initial dosage can prove toxic to the surrounding tissue, which can impair the healing mechanism. For metal ions the issue with toxicity is another hurdle to overcome before proceeding into clinical stages. In further sections of this chapter, mechanisms to obtain favorable release of antibiotics (along with other therapeutics) will be discussed in detail.

10.4.3 Enhancing Osseointegration

10.4.3.1 Implant Integration

Enhanced bone cell function at the bone-implant interface ensures appropriate integration of the implant with the bone, or osseointegration. This is essential when it comes to bone implants and prevents implant loosening/micromotion, which can contribute to implant failure [103]. As discussed in previous sections, nano-rough surfaces, particularly nanotubular Ti promotes bone cell functions, leading to improved osseointegration as compared to conventional and micro-machined

Ti surfaces [70, 104]. Reports have indicated that TNT surfaces' ability to initially absorb high amount of vitronectin (protein that facilitates osteoblast adhesion) from serum is the key for this morphology to be most suitable for bone implant applications [103]. Besides the surface topography, bone cell adhesion/proliferation can also be enhanced by incorporating bone forming species like: growth factors, biopolymers and hydroxyapatite (HAP) [9].

10.4.3.2 Effect of Nanotopography

It has been well established by many researchers that nano-scale roughness, particularly nano-tubular or nano-porous structures, promotes bone cell functions that lead to promoting osseo-integration, in comparison with bare or micrometer-rough surfaces [105]. In a pioneering study by Popat et al., enhanced short- and long-term in vitro osseointegration was confirmed on TNT modified Ti surfaces [70]. Adherence, proliferation and differentiation of bone marrow stromal cells (MSCs) and in vivo biocompatibility studies by implantation of TNT/Ti in Lewis rats showed enhanced adhesion, proliferation, ALP activity and bone matrix deposition, which all translates to improved osseointegration and bone healing [70]. Moreover no chronic inflammation or fibrosis was observed for in vivo studies [70]. Upon implantation in the frontal skull of domestic pigs, TNT surfaces again demonstrated excellent bone-integration characteristics in comparison with untreated Ti [106]. Higher collagen type-1 expression and enhanced bone cell functions were also confirmed for the TNT substrates [106].

10.4.3.3 Incorporation of NPs and Biopolymers

Surface modifications were also investigated on already bone-forming TNT surfaces in an attempt to enhance this feature. Neupane et al. reported incorporation of gelatin-stabilized Au NPs, which enhanced the osteoblast adhesion/spread and also the movement of the cell filopodia inside the functionalised TNTs [107]. In separate studies, similar enhanced bone-forming features were reported from TNT/Ti implants loaded with Zinc and Strontium [98, 108]. Other strategies to enhance osteogenic characteristics of TNTs were investigated using biopolymers like Chitosan and PLGA, which have proven bone forming abilities. Our group has investigated the effect of Chitosan and PLGA coatings on drug loaded TNTs on bone cell functions [69]. Bone cell adhesion and spread were found to be significantly improved on the biopolymer coated nanotubes. The easily controllable polymer thickness dominates the degradation kinetics, which in turn allows tailoring the implants for long term osseointegration. Chen et al. reported electrodeposition of Selenium inside TNTs followed by spin coating of Chitosan and later obtained osseointegrating and anti-cancer features from Chitosan and Se, respectively [100]. These concepts require additional studies to examine aspects such as

polymeric degradation, toxicity of metal ions/NPs and in vivo osseointegration, in order to prove their effectiveness.

10.4.3.4 Hydroxyapatite Deposition On/Inside TNTs

Hydroxyapatite (HA) formation on implant surfaces can increase osseointegration and hence TNTs were investigated for various treatments in order to provide fast kinetics of HAP formation. Kunze et al. reported that TNTs with anatase structure provide a better environment for the growth of stable carbonated HA layers upon SBF exposure, when compared with amorphous TNTs and TiO_2 layers [109]. In a novel study by Kar et al., incorporation of HA on TNTs was achieved by a pulsed electro-deposition technique [110]. TNTs were exposed to an alkaline environment to template the surface for HA deposition, followed by electrodeposition of calcium phosphate and later annealed in order to improve bond strength of the nanocrystalline HA on TNTs [110].

Kodama et al. reported HA deposition inside of TNTs by alternate immersion method (AIM), employing TNT immersion cycles in solutions containing calcium hydroxide and diammonium hydrogen phosphate [111]. This methodology confirmed accelerated growth of HA particles on/inside the treated-TNTs in SBF environments, permits control over HA deposition weight, and showed improved mineralization rates [111, 112]. Other approaches to prepare TNTs for quicker HA deposition involved NaOH treatment in order to form nanoscale sodium titanate structure, which was observed to accelerate HA growth and simultaneously enhance osteoblast growth/adherence [113]. In addition to the abovementioned strategies, bone integration can also be enhanced using the SBF loading technique. This allows an added benefit of any therapeutic to be loaded inside TNTs, while simultaneously recruiting calcium phosphate crystals from SBF solution containing the drug [81].

10.4.3.5 Loading Growth Factors

Various types of growth factors can cater to various aspects of osseointegration, and are divided as: osteogenic (bone morphogenetic proteins BMPs), angiogenic (vascular endothelial growth factor VEGF), inflammatory (corticosteroids, NSAIDs: non-steroidal anti-inflammatory drugs), and systemic factors (calcitonin, Vitamin D) [114]. As expected, the simple loading and releasing of these designated bio-molecules will guarantee enhanced osseointegration. Lai et al. conjugated BMP-2 on polydopamine functionalised TNTs of various diameters [115]. Immunofluorescence staining of various bone proteins and MSCs culturing on BMP-modified TNTs confirmed surface characteristics appropriate for cellular functions, promotion of ALP activity and mineralisation [115]. Furthermore, in an attempt to control release, Hu et al. reported multilayered coatings of gelatin and chitosan on BMP2-loaded TNTs and obtained enhanced osteoblast differentiation

of MSCs [116]. Bisphosphonates represent another class of growth factors that prevent bone loss and are widely used to treat conditions like bone metastasis, Paget's disease etc. [117]. In separate studies, bisphosphonates pamidronate and ibandronate were successfully loaded inside TNTs in an attempt to reduce bone resorption activity [117, 118]. Upon implantation in tibias of Wistar rats, anodised and heat treated Ti surface with ibandronate were compared with machined Ti, anodised and heat treated Ti [118]. After 2 and 4 weeks, enhanced type1 collagen and osteocalcin expression was confirmed on ibandronate loaded TNTs, which translates into improved osseointegration [118]. Furthermore, in separate studies, CCN2 (connective tissue growth factor) fragment and peptide sequence KRSR (lysine-arginine-serine-arginine) loaded TNTs were also found to enhance the integration of the implants [119, 120].

10.5 Advanced LDD Systems Using TNTs

The release of therapeutic payloads from inside of the TNTs into the surrounding physiological media is governed by Fick's first law of diffusion, which is influenced by size, weight, charge of the drug molecules and the dimensions, charge, chemistry of the TNTs [9]. Other factors include pH, temperature etc. The drug releasing implants must have favourable release kinetics which permits further control over it, such that special conditions can be targeted. Also zero-order release kinetics is the most preferred as the drug is released at a uniform constant rate, which is free from time/concentration dependence. As soon as the drug loaded TNTs come in contact of the media, the huge concentration gradient leads to very quick diffusion of drug molecules (initial burst release/IBR). This IBR causes large amounts of the drug to be released which can be very toxic for the surrounding cells and can further adversely affect the bone cell adhesion and osseointegration. As a result many attempts have been reported towards obtaining tailorable and controlled drug release from TNTs, with optimum initial release and delayed overall release. Other advanced therapeutic features demand catering to multiple conditions at the same time, in-built sensing and externally triggered drug release. These advanced features with TNT/Ti implants are summarized in Fig. 10.7.

10.5.1 Controlling Drug Release

10.5.1.1 Varying TNT Dimensions

Since electrochemical anodisation permits good control over the TNT dimensions, this in turn can be utilised to manage the available vacant volume of TNTs that can be filled with drug containing solution. These simple structural modification strategies have been explored and have been recognised as the simplest way to

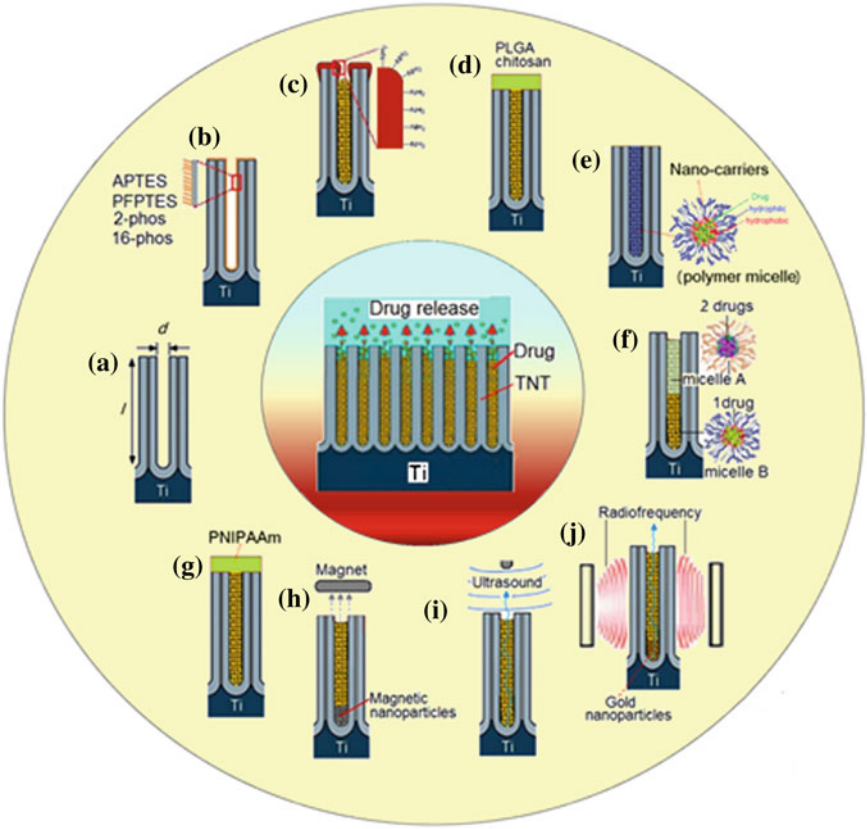

Fig. 10.7 Scheme depicting various approaches for controlling drug release from TNT/Ti implants: **a** TNT dimensions, **b** surface functionalisation, **c** plasma polymerisation to reduce open pore size, **d** biopolymer dip coating on TNTs, **e** drug encapsulation in polymeric micelles, and **f** multi-drug loading. Triggered drug delivery systems based on: **g** temperature, **h** magnetic field, **i** ultrasound, and **j** radiofrequency. Only single nanotube structure is shown to present an array of TNTs. *PLGA* Poly(lactic-co-glycolic acid); *Ti* Titanium; *TNTs* Titania nanotubes. Reproduced with permission from [9]

manage the amount of drug loaded and released from the TNTs [78]. TNTs with various nanotube lengths (25–100 μm) but with fixed diameter (110 nm) were fabricated on flat Ti foil by varying the anodisation time from 30 to 120 min [85]. Indomethacin (water insoluble drug) was loaded in the samples and in vitro drug release was carried out in PBS media. The drug loading capacity (as determined by TGA: thermo-gravimetric analysis) of 15 and 26 %, and the overall release for 6 and 23 days was confirmed for TNTs with lengths of 25 and 100 μm respectively. This observation correlates with the literature which suggests that longer tube lengths offer more vacant space, which means more drug amounts could be loaded and hence longer release times are obtained [121]. The similar effect was also

observed for increasing diameters for NAA, which can very well be applied to TNTs [85]. Moreover for varied lengths, the drug loading did not differ significantly which points out the inability to target deeper loading of drugs into the TNTs. Moreover these studies highlighted several limitations for controlling drug loading/release by TNT dimensions, as there exists a trade-off between loading amounts and the release kinetics. And these characteristics must be optimized in designing a drug releasing implant depending on drug properties and the disease conditions. Using nanoporous substrates with higher aspect ratios, these limitations can be addressed. Furthermore, alterations in the TNT structure achieved by special (periodic) anodisation conditions resulting in: periodic, double-walled, bamboo-type, nanolace and branched TiO_2 nanostructures; can also be explored towards simultaneously improving drug loading and release characteristics.

In another study by Peng et al. the effect of TNT dimensions on elution of various size molecules (large protein BSA-bovine silver albumin, and smaller size sirolimus and paclitaxel) was investigated [122]. The study demonstrated the ability of TNTs to control release of small molecule drugs to several weeks and for large proteins to several months. Also for TNT diameter of 100 nm and above, the drug elution mainly depended on the lengths of TNTs: longer TNTs further delaying the release. However the only limitation in this approach is the relation between loading amounts and release behaviour. Longer and wider TNTs mean maximum drug occupancy but very quick burst release and; shorter and narrower TNTs mean low drug amounts but considerably lowered burst release. More approaches aiming towards maximising the available TNT volume for higher drug loading and also reducing the open pore diameters of TNTs are desired for better control over the release behaviours.

10.5.1.2 Improved Drug Loading Strategies

Titania nanotubes (average diameters 30–100 nm and lengths 1–100 μm) represents a very narrow vacant capillary like structure where substantial amount of drug loading is very difficult. This generally has two consequences: poor loading amounts and since the loading is restricted to occupying the volume near the open pores, release kinetics with large burst release are obtained. Another challenge with the drug loading methodology especially with sensitive bioactive species like growth factors and proteins is the possible deactivation or denaturation of these molecules. Strategies to optimise loading are summarised below.

Yao et al. explored a co-precipitation loading technique by loading penicillin based antibiotics from SBF, thereby also incorporating calcium phosphate crystals inside TNTs [123]. The release was delayed to over 3 weeks, while for simple physical adsorption the release lasted for only 150 min [123]. On the other hand, Santo et al. compared the soaking and vacuum loading strategies for doxorubicin loading inside TNTs [124]. The release lasted for over 30 days for vacuum loaded drug, as compared to 7 days for loading by soaking, and also drug localisation investigations revealed that for the soaking method 90 % of the drug remained in

the inter-nanotube spacing whereas 97 % of the drug occupied the nanotube interior for the vacuum method. This study established vacuum assisted drug impregnation as the most suitable strategy to load substantial drug amounts and achieve delayed release. In another study enhanced drug loading efficiency for tetracycline-hydrochloride (TCH) was observed when TCH loaded silica xerogel was incorporated into TNTs [125].

When it comes to loading and releasing sensitive drugs like hormones or growth factors, their loading methodology or poor stability can easily inactivate them. Our group pioneered using polymeric micelles to encapsulate various drugs (different functions, molecular weights, water solubilities etc.) before loading inside TNTs, in an attempt to also simultaneously delay the release behaviour [84, 85]. In the study by Aw et al. substantial amounts of indomethacin was encapsulated in 4 different types of polymeric micelles: (a) Pluronic F127®, (b) TPGS (d-α-tocopheryl polyethylene glycol 1000 succinate), (c) DGP 2000 (1,2-distearoyl-sn-glycero-3-phosphoethanolamine-N-[methoxy(poly ethylene glycol)-2000]), and (d) DGP 5000 (1,2-distearoyl-sn-glycero-3 phosphoethanolamine-N-[methoxy(poly ethylene glycol)-5000] [84]. The in vitro drug release studies confirmed delaying the release to 4–8 weeks with zero-order kinetics. The strategy of encapsulation allows further control over release kinetics by tailoring nanotube dimensions, size and interfacial properties of micelles. Furthermore these nano-drug carriers can be utilised to load multiple therapeutics, and also achieve sequential and triggered release [126–128].

10.5.1.3 Chemical Functionalization of TNTs

Altering the interaction of drug molecules with the surface of TNTs via surface functionalization to render the surface hydrophobic or hydrophilic can significantly change the drug release kinetics. Self-assembled monolayers (SAMs) of 2-carboxyethyl-phosphonic acid (2-phos) and 16-phosphono hexadecanoic acid (16-phos) were used to functionalize TNTs prior to loading the anti-inflammatory drug indomethacin [85]. The in vitro release confirmed a delayed release pattern in increasing order as: 16-phos < unmodified TNT (control) < 2-phos. This observation confirmed that the hydrophilic surface modification (2-phos) results in longer release as compared to hydrophobic modification (16-phos) which allowed easy diffusion of the drug molecules incorporate in the TNTs. Furthermore, the easy SAM technique allows the use of a wide variety of functional groups and tunable interfacial/binding characteristics, which can be utilised to achieve superior loading and releasing properties from nanoporous implant modifications.

Another chemical modification approach presented by Song et al. was to fabricate amphiphilic TNTs with a hydrophobic cap on hydrophilic TNTs [129]. The fabrication involved hydrophobic modification (octadecylphosphonic acid) after the 1st anodisation step, followed by a 2nd anodisation and hydrophilic modification (3-Aminopropyl triethoxysilane), thereby resulting in unique amphiphilic structures with hydrophilic TNTs with hydrophobic caps towards the open pores. Four drug

loading approaches for horseradish peroxide (HRP) were studied: (a) immersion loading, (b) immersion + hydrophobic cap, (c) covalently attached HRP (via APTES/vitamin C monolayer linker), and (d) covalently attached HRP + hydrophobic cap. The removal of the hydrophobic cap by UV illumination allowed greater control over the release kinetics, whereas the untreated TNTs with HRP [sample (a)] had much greater burst release amounts. This unique approach demonstrated the ability to control release of drugs from TNTs based on chemical functionalization that respond to external triggers like UV irradiation.

10.5.1.4 Polymeric Modifications

After TNTs were established as suitable implant modifications with the added features of biocompatibility and drug release, the focus shifted towards delaying/controlling the release to address real implant challenges. Controlling release by structural modification had limitations and as a result other approaches were tried. The open pore of TNTs acts like an interface between the bulk titanium and the surrounding bone microenvironment and upon contact with the physiological media results in quick diffusion of loaded molecules. Polymer modification of TNTs offers many benefits such as easy control over thickness/covering of the TNTs, and also by inclusion of biopolymers, anti-bacterial and osseointegration characteristics can be included. In an attempt to reduce/control the release, the open pores are modified by various polymer strategies, as discussed in the following sections.

10.5.1.5 Polymeric Capping on TNTs

Plasma polymerisation (PP) has been extensively utilised by our group to extend the release of therapeutics from nano-porous substrates like Nano-porous anodic alumina (NAA) and TNTs (Fig. 10.8a) [85, 130]. An ultrathin layer of poly(allylamine) PAa can easily be deposited by plasma-assisted polymerisation of the monomer allylamine onto the drug loaded TNTs. The PAa is highly polar in nature as it contains primary amines which can further be functionalised to control drug release amounts [131]. Thickness of PAa can easily be controlled by varying the plasma exposure time using the PP, which itself represents a single step, fast and scalable technique. For instance modifying NAA, PP for 50 and 120 s delayed the release of vancomycin (hydrophilic antibiotic) to approximately 200 and 500 h respectively [130]. On the contrary for the unmodified NAA, the entire drug amount was released within 45 min. This technique can also be extended to other nanoporous and nanotubular substrates like TNTs, alternate polymers and various therapeutics (of different sizes and chemistries) like: proteins, anti-inflammatory drugs, anti-cancer drugs, growth factors etc.

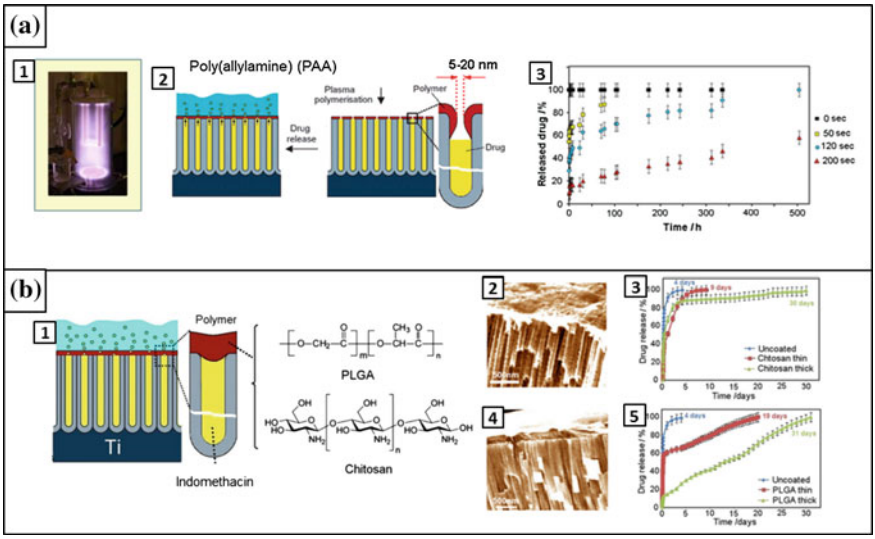

Fig. 10.8 Polymer modifications on drug loaded nano-porous implants for controlling release. **a** Plasma polymerisation (*1*) of allylamine to reduce open pore size of NAA (*2*), controlled release of vancomycin based on various plasma deposition times (*3*) [130]. The concept can also be extended to TNTs/Ti. **b** Dip-coating of biopolymers PLGA and Chitosan on indomethacin loaded TNTs (*1*) and the release based on the thickness of the polymer coating (*2–5*) [69]. *NAA* Nano-porous anodic alumina; *PLGA* Poly(lactic-co-glycolic acid); *Ti* Titanium; *TNTs* Titania nanotubes. Reproduced with permission from [69, 130]

Furthermore, PAa deposited on TNTs has also been reported as an easy functionalization strategy to enable: layer-by-layer assembly (LbL) [electrostatic adsorption of poly(sodium styrenesulfonate) (PSS)], and a protein-resistant surface [covalent coupling of poly(ethylene glycol) (PEG)] [131]. This report demonstrated the ability of the PP technique to modify the physicochemical characteristics (surface reactivity and wettability) of the TNTs by selecting an appropriate plasma polymer and the functional group [131]. This in turn can assist in designing controllable drug releasing implants based on TNTs with suitable interfacial properties that improve the current implants significantly.

Besides the reported benefits of using PP to enhance features of drug-releasing TNT/Ti implants, the PP technique has several disadvantages. These include: time consuming calibration (relation between various plasma conditions and deposited film thickness), costly equipment and technical knowledge requirement; which can possibly mean its limited integration into the current TNT biomedical applications. As a result easy and cost-effective methodology based on simple dip-coating of biopolymers on drug loaded TNTs has been suggested as a superior alternative to PP [69].

10.5.1.6 Polymer Coating on TNTs

In an attempt to overcome the limitations of the plasma polymerisation to delay release kinetics from TNTs, and achieve simultaneously enhanced bioactivity and osseointegrating ability: dip coating of biopolymers: Chitosan and PLGA onto drug loaded TNTs was investigated by our group (Fig. 10.8b) [69]. Dip coating represents an easy and cost-effective approach, by which tuneable coating thickness for various solutions on the substrate can be achieved. Chitosan and PLGA were dip-coated onto indomethacin loaded TNTs (120 nm diameter, 50 μm length) and later were examined for drug releasing abilities and bone cell functions. For the initial burst release of indomethacin (1st 6 h of in vitro release), only 35 and 12 % of the drug was released for the Chitosan- and PLGA-modified TNTs respectively; as compared to 77 % for the bare TNTs. Furthermore, Chitosan- and PLGA-modified TNTs delayed the overall release to over 30 days and on the contrary for unmodified TNTs the entire drug amount was released in about 4 days (Fig. 10.8b). Hence, the ability to use dip-coated biopolymers on TNTs to improve drug releasing features was established. Also demonstrated was the ability to control the dip-coated polymer thickness which relates to the drug release kinetics. Another feature showcased in this report was the simultaneously enhanced osteoblast adhesion and functions on the biopolymer-modified TNTs as compared to the controls of TNTs/Ti and bare Ti. The release of therapeutic agent was dependent on the degradation of the polymeric film, and future work is required to investigate polymeric degradation rates in relation with the release kinetics. In an extension to this work, using the combination of micelle encapsulated antibiotics and biopolymer coatings; the release could further be tailored and enhanced anti-bacterial effects were reported [99]. Multilayered coating of gelatin and chitosan on BMP-2 loaded TNTs has also been demonstrated to control the release, thereby preventing initial wastage of active agents and achieving longer sustained release patterns [116].

10.5.2 Triggered Release

Some conditions in an already traumatized bone scenario, such as bacterial invasion, require immediate local drug action and any delay might result in severe complications such as biofilm formation and osteomyelitis. These can cause implant failure, re-surgery and in worst cases even amputation and death. This calls for an additional feature in-built in a drug eluting implant, which upon trigger (external or internal) can quickly release effective therapeutic dosage. This triggered system can offer other functionalities such as reduced waste of drugs, easily triggered action without the need of invasive surgeries, and overall low costs and complications. As a result, many researchers have combined external triggers, including light, temperature, magnetic/electric fields, radio/ultrasonic frequencies, etc. into TNT drug releasing implants, as discussed below.

10.5.2.1 Temperature

Certain conditions such as bacterial infection, inflammation and cancer, changes the physiological characteristics of the affected cells/tissue like pH, temperature, sugar level, oxygen content, etc. [132]. Utilising these features as a trigger would mean automatic release of therapeutics without the need to administer any external trigger. Moreover, with various polymers already offering this functionality, its integration into the TNT modified implants can open new possibilities towards internally-triggered therapies. Cai et al. reported the deposition of temperature-responsive hydrogel (composed of polymers poly N-isopropylacrylamide or PNIPAAm and polyacrylamide or PAAm) on Vitamin B2 loaded TNTs to enable temperature responsive release [133]. The LCST (lower critical solution temperature) of PNIPAAm/PAAm composite hydrogel is 38 °C, which means at a temperature <38 °C the hydrogel remains in a highly water-swollen state; however at a temperature >38 °C the hydrogel will collapse and release water. This feature was used to design the TNT implant that can release high drug amounts in conditions like inflammation, where the local temperature rises to around 38.3–38.5 °C. Drug release data confirmed the effect of temperature on triggering the release of the model drug. For a time period of 8 days the amount of model drug released from hydrogel modified TNTs was found to be <20 % at 25 °C and >70 % at 38 °C.

10.5.2.2 Photo-catalytic

Shreshtha et al. utilised the photocatalytic activity of TNTs, by loading of model drug (violet-blue fluorescent marker) via suitable linker molecules (silane coupling agents) inside magnetic TNTs (TNTs doped with magnetic Fe_3O_4 NPs) [134]. Upon exposure to UV, the chain scission of anchoring groups caused release of drugs, and as the UV exposure was stopped the release was terminated.

10.5.2.3 Magnetic Field

Aw et al. reported a TNT drug releasing system, which upon magnetic field exposure can quickly administer high local dosage of anti-inflammatory drug indomethacin [127]. Dopamine conjugated iron-oxide NPs were loaded inside of TNTs and later the micelle encapsulated drug was loaded in a layered fashion. When a magnetic field trigger was applied, the magnetic NPs were force-released from inside of TNTs and during release they pushed the drug carriers out of the TNTs. A 100 % release of encapsulated drug was achieved in just 1–1.5 h of magnetic stimuli. This strategy offers many advantages such as various active biomolecules (targeting ligands or dyes) can be attached to dopamine and magnetic NPs. This can be used for live imaging using NMR (nuclear magnetic resonance)

for improved diagnostics. However, when dealing with magnetic triggered systems, there remains a risk of accidental trigger from surrounding magnetic fields encountered in a daily routine.

10.5.2.4 Electric Field

Sirvisoot et al. designed a very advanced drug eluting device that can release active drugs when an electric field is applied [135, 136]. To achieve this, they conjugated antibiotics (penicillin and streptomycin) and anti-inflammatory drug (dexamethasone) with polypyrrole, which was later electrodeposited on MWCNTs (multi-walled carbon nanotubes) modified TNT surface. On applying external voltage, about 80 % of the therapeutics could be released and the TNT/MWCNT modification was proposed as a trigger enabled drug eluting implant.

10.5.2.5 Ultrasonic Trigger

In another study by our group; ultrasonic waves were used as a trigger to enable easy control over the drug release [128]. The study demonstrates triggered release of drug carriers [TPGS polymeric micelles encapsulating anti-inflammatory drug indomethacin] loaded inside TNT/Ti, using ultrasound waves (USW) produced using a sonication probe placed inside the releasing medium (PBS). The release could easily be controlled by various USW parameters such as time, intensity and amplitude and hence can be tailored to meet special therapeutic requirements. This study demonstrates an easy trigger approach that can be integrated into current implant technology as the precise transfer of ultrasound energy can be achieved inside the human body without damaging any tissues or organs.

10.5.2.6 Radiofrequency

More recently, triggered release of drugs carriers from TNTs fabricated on Ti wires using radiofrequency (RF) was shown by our group [137]. It involved loading of gold NPs inside TNTs, followed by the loading of polymeric micelle (tocopheryl PEG succinate) encapsulated indomethacin. Au NPs were used as energy transmitting species due to their ability to vibrate and heat up under the influence of RF energy. Upon RF exposure from the customized RF generator, the transmittance of vibration/heat energy from the NPs to the drug molecules enabled its release. Within 2.5 h, 92 % of the drug was released for a 5 min RF exposure, whereas in the absence of any trigger only 31 % of drug was released. Furthermore the release kinetics can be modified by varying RF energy parameters and the amount of Au NPs.

10.5.3 Multiple Therapies from TNTs

Some conditions like bone infections or cancer require multiple therapeutics in order to achieve effective treatment. Moreover, inclusion of more than one type of therapeutics inside TNTs could address various issues at the same time. These multi-drug releasing implants could improve current implant technology and have been extensively explored by our group [126]. The common challenge that must be addressed for multiple drug delivery from the implant surface includes: shielding sensitive drugs and ability to control release of each drug. Using polymeric nano-carriers for encapsulation of individual therapeutics prior to loading inside TNTs can effectively realize multiple therapies locally.

Active therapeutics encapsulated in totally biodegradable polymeric micelles were loaded inside TNTs in a layered fashion to achieve sequential release of multiple therapeutics [126]. Water insoluble (anti-inflammatory indomethacin and anti-fungal itraconazole) and water soluble (antibiotic gentamicin) drugs were encapsulated in regular ((d-α-tocopherol polyethylene glycol 1000: TPGS) and inverted micelles [1,2-distearoyl-sn-glycero-3-phosphoethanolamine-N [methoxy (poly ethylene glycol)-2000: DGP 2000] respectively. Then loading of these drug carriers in TNTs was performed in a layered manner resulting in immiscible layers containing different drugs (Fig. 10.9a). Upon immersion in PBS, the release was obtained in a sequential time-dependent pattern. The top layer of payloads containing hydrophobic drugs in regular micelles (TPGS) were released initially (until the 5th day), followed by release of hydrophilic drug in inverted micelles (DGP 2000) (Fig. 10.9b). Furthermore, the loading amount of various drugs and release kinetics of each drug can be managed by controlling TNT dimensions, micellar encapsulation and loading strategies. This advanced feature can prove beneficial to address challenges with severe bone conditions, where synergistic action of various drugs might be required for instance: promoting osseointegration but preventing any bacterial attachment.

10.5.4 TNTs with In-Built Bio-sensing

If a sensing feature can be integrated into the TNT drug releasing implant, drug can be released in response to biological requirements. This could enable clinicians to detect in a timely manner abnormalities such as bacterial invasion or extensive inflammation and to respond with triggered release for a quick therapeutic effect. Sirvisoot et al. have proven that MWCNTs grown out of TNTs improve bone cell functions [138]. To further advance the study, electrochemical features of these implants were measured in a solution containing extracellular components released by osteoblasts [139]. These electrochemical data can easily be translated to determine the health of the surrounding bone cells, and any abnormal features like inflammation or infection can be timely detected and addressed.

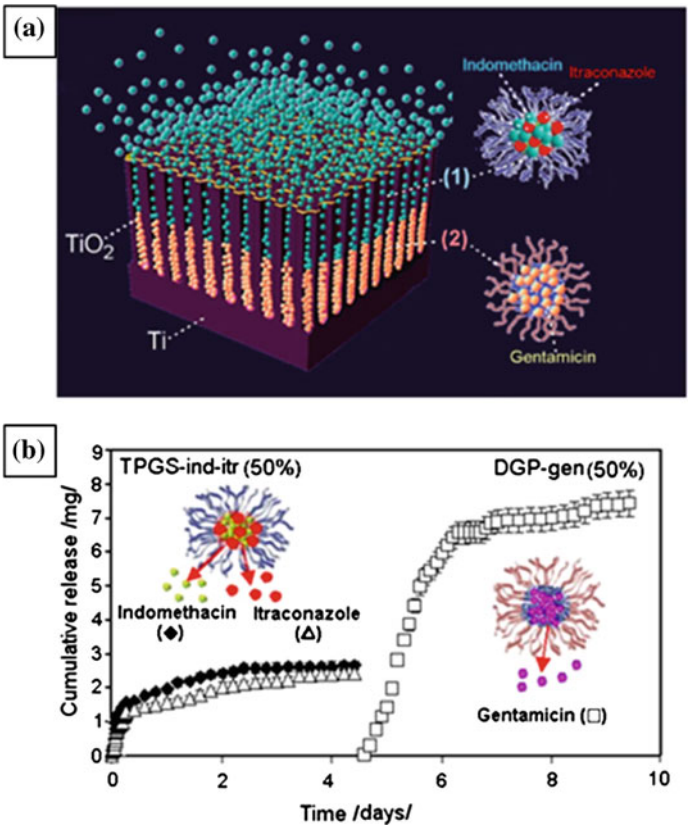

Fig. 10.9 Multi-drug delivery with sequential release from TNT/Ti implants. **a** Concept of loading hydrophilic and hydrophobic drugs encapsulated in micelles inside TNTs forming two immiscible layers, and **b** in vitro drug release plot confirming sequential release of multiple therapeutics in different phases. Reproduced with permission from [126]

10.6 Additional Investigations for TNT DD

10.6.1 Ex Vivo

Ex vivo investigations bridge the gap between in vitro and in vivo investigation and are regarded as an intermediate step prior to entering into animal studies. It enables improved control over various conditions for cells or tissues taken from animals, while minimising the number of animals to be sacrificed and the costs associated with it. A unique system for maintaining 3D cancellous bones ex vivo, with the ability to apply/record stress-strain in real-time, was devised by Jones and Smith [140, 141]. This system can be utilised to test various parameters of bone implants in the context of a maintained bone micro-architecture and cells viability.

Furthermore, media flow and the force parameters (stress cycles, frequency etc.) can easily be managed to replicate in vivo conditions, with the bone also subjected to body weight and loading. Thus, bone implants inserted inside bone cores ex vivo can enable effective mechanical and biological testing of the implants.

In an attempt to quantify the release of drugs from TNT/Ti wire within trabecular bone, our group inserted dye-loaded implants inside the bone cores perfused with media, using the Zetos® system [58]. Hydrophilic fluorescent dye Rhodamine B was loaded inside the TNTs prior to their insertion inside the bovine trabecular bone cores. The release of dye from the TNTs directly inside the bone micro-environment was quantified using fluorescence microscopy (Fig. 10.10a). The release from TNTs in various planes inside the bone core, and the dependence of release on various flow rates of the culture media was demonstrated. This novel study assisted in defining the appropriate kinetics of drugs inside the bone matrix that can result in an optimum therapeutic effect. This information can also aid in optimising the local drug eluting implants to meet specific therapeutic requirements.

10.6.2 In Vivo

In vivo investigations are ultimately necessary to prove whether implants can work and are biocompatible. The key understanding of what molecular events occur when an implant is surgically inserted into bone is crucial before any consideration of human trials. As a result, various in vivo investigations have been carried out to prove the suitability and effectiveness of using TNTs to enhance bone healing in various animal models [5, 9, 10, 142].

10.6.2.1 TNTs for Osseointegration

Various in vivo investigations have been made targeting one or the other hard-tissue implant criteria. Among these, optimizing implant osseointegration, especially in a traumatized bone scenario is very challenging. von Wilmowsky et al. explored the role of TNTs on peri-implant bone formation, by implantation of TNT modified Ti implants in the frontal skull of domestic pigs [106]. In this pioneering study, TNT/Ti implants were compared with cpTi implants, using various characterizations like peri-implant bone formations, immune-histochemistry and bone-implant contact. The results confirmed increased collagen type-1 expression for TNT modified implants (at time periods: day 7, day 14 and day 30) and also enhanced bone cell functions (Fig. 10.10b). Also the TNT modification survived the shearing forces experienced during surgical implantation, clearly demonstrating the TNTs suitability to enhance bone implant features.

In another study by Bjursten et al., TNTs- and TiO_2 gridblasted-modified Ti surfaces were compared for bone bonding strength by implantation in rabbit tibias for 4 weeks [74]. The tests confirmed up to 9-times enhanced bone bonding

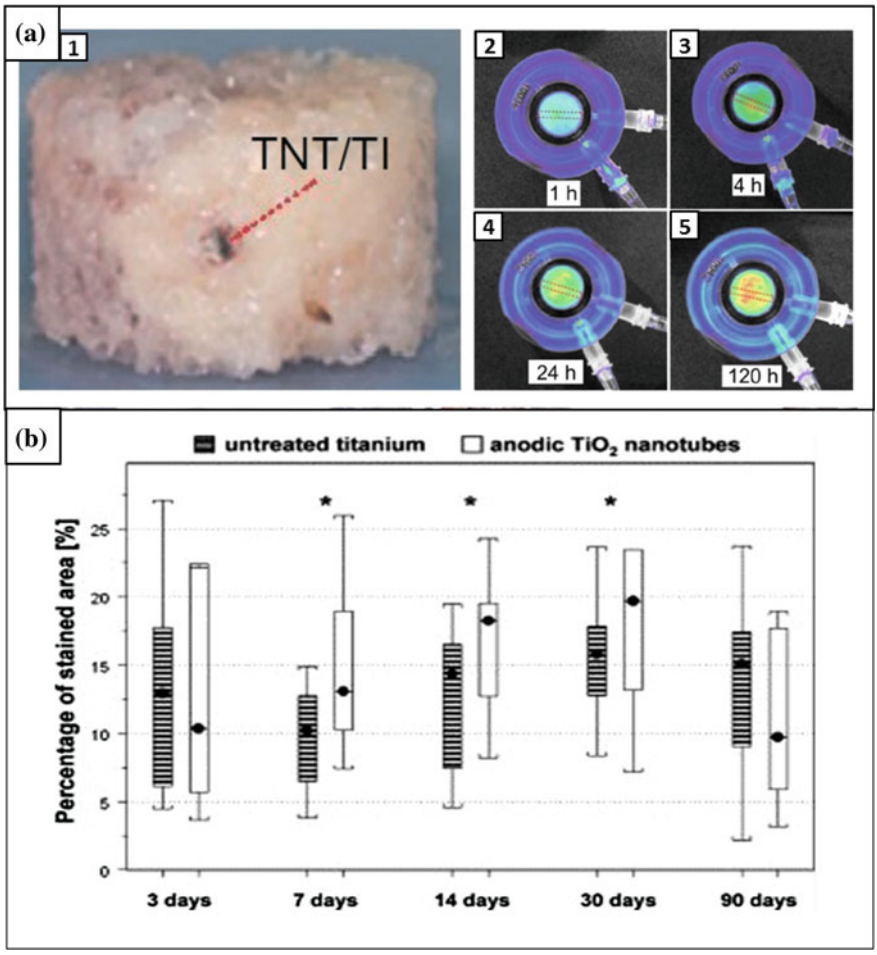

Fig. 10.10 Ex vivo and in vivo investigations of TNT/Ti for bone implant applications. **a** Image of bovine trabecular bone core (*1*) inserted with dye releasing TNT/Ti wire implant, and the dye diffusion at various time-periods (*2*–*5*) inside the bone matrix as visualised by fluorescence microscopy. Bone explant was maintained in the ex vivo setting using the Zetos™ system [58]. **b** TNT/Ti implanted in the front skull of the pig in vivo: significantly higher collagen type-1 expression for TNT/Ti as compared to bare Ti at different days [106]. Results confirm suitability of TNTs to enhance bone formation around implant surfaces. Reproduced with permission from [58, 106]

strength for TNT-surfaces, and furthermore larger bone-implant contact area and increased Ca/P levels on TNT modified implants. Similarly, upon implantation in the mandibles of ovariectomized sheep for 12 weeks, TNTs demonstrated improved osseointegration as revealed by micro-CT, histomorphometry and biomechanical investigations [143]. This evidence clearly establishes TNTs as a realistic, cost-effective modification for conventional bone implants, which enhances bone cell functions that translates into quicker bone healing and implant integration.

10.6.2.2 Loading Osseointegrating Molecules

The abovementioned osseointegrating features of TNTs can further be enhanced by incorporation of growth factors that promote integration/bone cell functions. These might be desired in compromised situations such as osteoporotic fractures. An in vivo study by Vandamme et al. provided molecular evidence that reasserted the need to modify implant surfaces for delivering potent growth factors/hormones to improve bone integration [144]. Lee et al. reported an animal experimental study for evaluating the effect of bisphosphonates on anodised (TNTs) and heat-treated (HT) Ti implant surfaces upon implantation in both tibias of male Wistar rats [118]. Samples were loaded with ibandronate and upon completion of the study (2 and 4 weeks) levels of osseointegration were determined after using a removal torque test and micro-CT, and expression of collagen type 1 and osteocalcin. The results revealed increased biocompatibility, bone formation and osseointegration for the treated TNT surface.

Harmankaya et al. immobilized two potent osteoporotic drugs raloxifene (RLX) and alendronate (ALN) in nanoporous oxide films generated on Ti screws and evaluated the in vitro release kinetics and osteogenic response in vivo in rat tibia [145]. Results confirmed enhanced bone fixation in drug loaded samples post 28 days of implantation. For RLX-incorporated nanopores stronger bone-remodelling action and improved apatite formation; and for ALN-incorporated increased bone density was observed. This study demonstrated the ability to enhance implant fixation or osseointegration by engineering nanoporous surfaces containing appropriate drugs.

Park et al. evaluated the bone response around TNTs modified with FGF (fibroblast growth factor) and human fibronectin (FN) fragment. Modified implants (TNTs with FGF-FN) plus the controls (TNTs only) were surgically implanted inside the holes drilled in the tibia of New Zealand white rabbits [146]. Histomorphometric analysis and removal torque test after 12 weeks of implantation revealed increased osseointegration. These studies confirm that TNT modifications per se provide an osseointegrating interface as compared to commercial Ti implants. Also these features could easily be enhanced by loading of growth factors into TNTs. However the research only represents the initial phase of osseointegration (few weeks to months) and more in vivo investigations of longer duration are required to establish the role of TNTs in long term integration, thereby contributing to implant acceptance and survival.

10.7 Alternate Therapies Using TNTs

10.7.1 Dental Applications

Ti and its alloys are routinely used as implants to correct dental complications. The challenges with dentistry include: caries control, tooth remineralization, periodontal disease, root-canal infections, etc. Like bone implants, dental implants often need

re-correctional surgeries mainly due to bacterial invasion and poor osseointegration, which can cost several thousand dollars. Implant stability and long-term bone regeneration are prerequisites to prevent any bone/tissue damage due to implant loosening and bacterial infection [147]. As a result, various bioactive modifications have been applied on dental implants to improve osseointegration and prevent bacterial infection [148]. These challenges make TNTs suitable modifications for Ti dental implants to achieve delayed release of active therapeutics, while the nano-topography simultaneously attends to increasing osseointegration.

In an attempt to prevent bacterial infection by quick but firm soft tissue seal formation around dental implants, TNTs on Ti surface was modified by loading Ag NPs and FGF-2 growth factor [149]. Upon cell study with human gingival fibroblasts (HGFs), the modified surfaces enhanced HGF functions with negligible cytotoxicity (Fig. 10.11b) [149]. In another strategy aiming towards enhancing osseointegration, Lee et al. loaded N-acetyl cysteine (NAC) in TNTs and investigated its effect on bone formation in vitro and in vivo [150]. Reduced inflammation and oxidative stress-related defence was observed with MC 3T3-E1 cells in vitro; and new bone formation was confirmed upon implantation in rat mandible in vivo [150]. Furthermore to confirm electrochemical stability of TNTs in saliva conditions encountered by implants in dental setting, Demetrescu et al. characterized TNTs in artificial saliva and explored fibroblast cell behaviour [151]. For the TNT surfaces, cell adhesion was promoted and also corrosion/electrical parameter evaluation revealed improved stability in artificial saliva, thereby confirming applicability of TNTs to modify dental implants.

10.7.2 Anti-cancer Therapy

Cancers often metastasize from breast, prostate or lungs to other hard tissues like bone, or may arise in bone (e.g. osteosarcoma). Bone metastases destroy bone, increase the risk of fractures and can induce hypercalcemia. Treating bone cancers can involve radiotherapy/chemotherapy, hormone therapy, and administration of bisphosphonates or orthopaedic surgery. Since TNTs have been recognised an appropriate drug eluting bone implant coatings, several researchers have aimed at targeting cancers via this approach.

Two different loading strategies were used to load doxorubicin inside of TNTs: soaking and wet vacuum impregnation. Doxorubicin release was monitored at 23 and 37 °C for loaded TNTs and Ti flat foils (controls) [124]. The results confirmed 7 days release for soaking and 30 days for vacuum-assisted loading. Fluorescence Correlation Spectroscopy (FCS) analysis was performed to explore the drug localization using different loading strategies and the results confirmed that for soaking 90 % of the drug was loaded in inter-nanotube spaces, while for vacuum loading 97 % of the drug occupied nanotube interior. This further explains the varied release profile obtained for two different loading conditions.

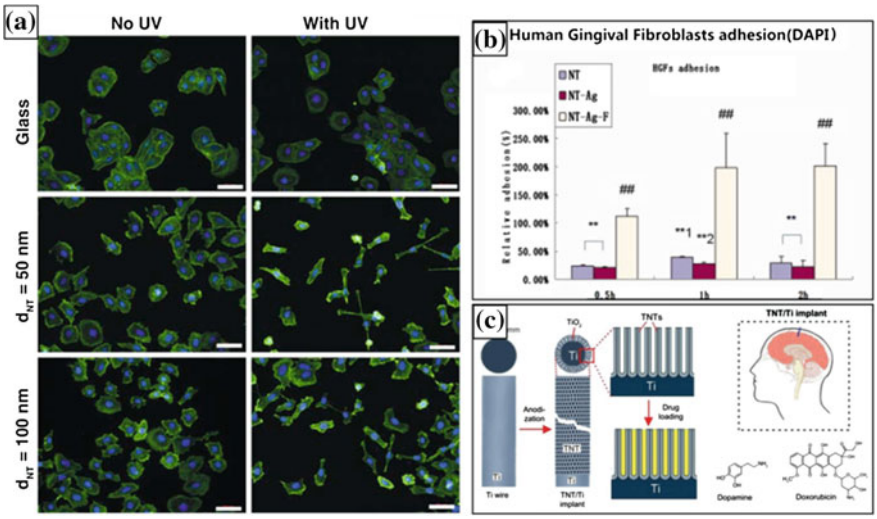

Fig. 10.11 TNTs for wide range therapeutic applications. **a** Photocatalytic cancer killing using UV irradiation on TNT surfaces (fluorescence images of cultured HeLa G cancer cells) [152], **b** adhesion of Human Gingival Fibroblasts (HGF) on various TNT surfaces modified with Ag nanoparticles and Fibroblast Growth Factor-2 (FGF-2) [149], and **c** concept for applying TNTs on Ti wires as tiny implants for brain therapy [57]. Reproduced with permission from [57, 149, 152]

Also recently our group proposed TNTs on Ti wires as drug eluting implants for 'in-bone therapeutics', where the release is 3D from the implant surface [59]. In one such attempt, active anticancer drug doxorubicin was loaded in TNT/Ti wires in substantial amounts. The in vitro release confirmed only a 25 % initial burst release, whereas the overall release lasted for around 8 days. In another study by Chen et al., selenium was electrodeposited inside TNTs, followed by coating of Chitosan so as to delay the release of Se [100]. Culturing of healthy and cancerous osteoblasts on these surfaces in vitro inhibited the growth of cancerous osteoblasts and promoted the function of healthy osteoblasts. On the other hand, Chitosan coating delayed the release of Se to about 21 days.

Kalbacova et al. studied the effect of UV irradiation on TNTs for killing cancer cells [152]. HeLa G cancer cells were cultured on TNTs (different diameters 50 and 100 nm), followed by 5 min UV exposure [152]. Post photocatalysis on TNTs the cancer cells changed morphology with some elongations, whereas the controls of cells cultured on glass retained their morphology (Fig. 10.11a). Lactate dehydrogenase (LDH) activity (which correlates with the number of dead cells) confirmed a higher cell damage caused by 100 nm TNTs. This study demonstrated the photocatalytic killing of the cancer cells achieved by UV irradiation. However, X-rays can also be used to generate the same effect. Loose TNT-like fragments/TiO_2 whiskers (with three-dimensional mesoporous structure) have also been demonstrated as nano-vehicles for carrying active anti-cancer drug daunorubicin (DNR) for anti-tumor functions [153]. Studies with the human hepatocarcinoma

cell line suggested increased cellular uptake of DNR and enhanced anti-tumor efficiency. Also shown was photocatalytic growth inhibition of cancer cells.

10.7.3 Localized Brain Drug Delivery

Besides the applicability of TNTs drug eluting implants for various correctional/therapeutic roles for hard tissues like bone or teeth, many alternative applications has also been shown by some groups. The ease of fabrication, cost effectiveness, biocompatibility, controlled therapeutic release, ease of functionalization and favourable cellular responses make TNTs an ideal implant modification to apply to treat various tissues where conventional systemic therapy fails to deliver effective dosage.

Brain drug delivery represents a very complex setting for bypassing the blood brain barrier, as a result effective therapy still remains a challenge. Polymer implants with active drugs (for e.g. Gliadel® Wafers) showed localised delivery of chemotherapeutics, and offered 2–3 weeks of release post implantation for effective treatment of malignant glioma. However, the polymeric wafer offered few limitations like unpredictable release profiles, polymeric degradation, and need of invasive surgery for implantation [10]. In such a complex tissue, TNTs on Ti can offer various advantages; particularly for treatment/study of neurodegenerative disorders which involves insertion of Ti prosthetic microelectrode devices inside the specific brain tissue to trigger desirable neurological functions [154]. The use of Ti offers high mechanical stability as compared to brittle Si (used for similar application) which can result in very serious consequences upon fracture inside the brain; and furthermore TNT fabrication on these microelectrodes can enhance the therapeutic functions as well. As a result, a new therapy for treating brain conditions like tumour and neurodegenerative disorders was developed by our group, where TNTs were fabricated on Ti wires and proposed as drug releasing implants for brain (Fig. 10.11c) [57]. Substantial amounts of anticancer drug doxorubicin and neurotransmitter dopamine were loaded inside TNTs/Ti wire and the favourable release dosages were obtained in in vitro release experiments [57]. Furthermore, the release can be tailored via nanotube dimensions or by coating of biopolymers to several weeks [85].

In another novel study, Wang et al. labelled loose TNT-fragments with FITC (fluorescein isothiocyanate) and later cultured mouse neural stem cells on them [155]. Confocal microscopy confirmed that for 24 h incubation FITC-TNTs was present around the cell nuclei without crossing the karyotheca, and after 48 h the FITC-TNTs crossed the karyotheca to enter the nuclei of neural stem cells [155]. However more investigations are required for understand the mechanism of cellular uptake (particularly in vivo); this approach showed the promise of using loose TNTs as therapeutic nano-carriers.

10.8 Challenges with TNT DD

10.8.1 Mechanical Stability

Ti offers more appropriate mechanics with human bone as compared to alternative implant material choice like stainless steel, Ti–Al alloys etc. However, with the advent of nanotechnology nanotubular/nanoporous modifications of the conventional surfaces, are established as ideal implant coatings to enable drug loading/release, while also offering increased bioactivity. Most such investigations are focused on enhancing drug releasing features, bone cell functions and meeting special therapeutic requirements. Since bone represents a load bearing organ, mechanical stability of the advanced nano-engineered implants is often neglected. Well suited for range of therapies and even promoted osseointegration, TNTs must succeed in the mechanical testing of load-bearing scenarios to be able to proceed into clinical stages. Stability of TNTs on Ti implants is crucial, and any delamination or disintegration of TiO_2 nanotube fragments can initiate toxic responses. Furthermore, studies are required to test the stability of the TNT arrays on various Ti substrates in different mechanical settings. This can easily be achieved via using the Zetos® System to test the influence of various stress cycles upon the implant structure and morphology. On the other hand, in vivo investigations with TNT-modified implants have reported the ability of TNTs to withstand the shearing forces experienced during surgery, which makes this implant modification strategy suitable for load bearing situations [106].

10.8.2 Toxicity

Every biomaterial must pass the safety regulations issued by respective organisations to be approved as safe medical device that does not initiate any undesirable side effects during the course of the implant lifetime [156, 157]. These regulations vary worldwide and different testing criteria are taken into consideration; however the most basic of such requirements are toxicity due to leaching of ions or particles to the surrounding tissue, and the ultimate fate of these materials in the human body (accumulation or clearance). With these evaluations nanomaterials often face challenges mainly due to unexplored mechanisms behind cellular uptake, immune responses, accumulation in body or clearance from body.

Titanium has been detected in the serum of patients with bone fixative implants, which raises alarms for the safety of the new generation of TNT/Ti drug releasing implants [158]. Many cellular studies have established that TNTs on Ti possess no toxicity, in terms of adverse immune responses and are proven to be highly biosafe and biocompatible. However most such investigations are performed in in vitro and ex vivo settings, with a very limited number of in vivo studies reported. The safe use of TNTs as implant modifications to achieve suitable functionality without

causing any toxic side effects needs to be demonstrated [159]. Toxicology studies (on dermal fibroblasts and human lung epithelial cells) with nanoscale titania particles have been performed, which indicated cytotoxicity and inflammation for concentrations of 100 μg/ml [160]. This effect was found to be directly proportional to the exposure time and increases upon UV irradiation. Ultimately, in vivo investigations are required both short time (few weeks or months) as well as the life time of a hard tissue implant, which may be >10–15 years.

10.9 Conclusion and Future Directions

The following points summarize the research and development required for TNT containing implants to achieve effective therapy:

(a) Fabrication optimization of TNTs on curved Ti surfaces like wires with improved stability for possible in-bone therapies
(b) Mechanical testing of TNT anodic films in terms of stability and adherence to underlying substrate in load bearing situations
(c) Understanding the cellular mechanisms that promote the various cell functions on TNTs in comparison with alternate nano-rough surfaces
(d) Ex vivo drug release modelling inside the bone matrix for effective therapeutic action without causing any adverse effect
(e) Bacterial studies in vivo to address challenges like retriggered bacterial invasion and antibiotic resistance
(f) Long-term in vivo investigations (several months to years) to establish suitability of TNTs to integrate with the traumatised bone
(g) In vivo testing of various advanced implant features, such as delayed drug release, multiple therapies and triggered release
(h) Research towards the possible toxicity of TNTs for situations where loose TNTs can detach from the implant surface
(i) Inclusion of biopolymers and other biomimetic approaches to enable quicker bone healing and implant acceptance
(j) Integration of an effective diagnostic/sensing features into the TNT implant in in vivo conditions

To summarize, titania nanotubes have been established as a suitable Ti implant modification that offers the ability to achieve local drug release to address various pathologies. The drug release can be tailored for specific applications, such as fractures, infections and bone cancers. Advanced features like multiple drug delivery, triggered release and in-built sensing functions can also be integrated using the TNT modification of implants, although these demand more research and development. The TNT implants must also overcome the barriers of stability, toxicity and long-term integration but the approach of TNT modified drug-eluting implants holds a bright future in realizing effective therapies in a range of skeletal and soft tissue conditions.

Acknowledgments The authors acknowledge the financial support of ARC DP 120101680, FT 110100711, and The University of Adelaide. SM was supported in part by a pre-doctoral fellowship from the Egyptian Ministry of Higher Education.

References

1. S.B. Goodman, Z. Yao, M. Keeney, F. Yang, The future of biologic coatings for orthopaedic implants. Biomaterials **34**(13), 3174–3183 (2013)
2. A.K. Jain, R. Panchagnula, Skeletal drug delivery systems. Int. J. Pharm. **206**(1–2), 1–12 (2000)
3. M. Geetha, A.K. Singh, R. Asokamani, A.K. Gogia, Ti based biomaterials, the ultimate choice for orthopaedic implants—A review. Prog. Mater. Sci. **54**(3), 397–425 (2009)
4. D. Losic, S. Simovic, Self-ordered nanopore and nanotube platforms for drug delivery applications. Expert. Opin. Drug Deliv. **6**(12), 1363–1381 (2009)
5. K. Gulati, M.S. Aw, D. Findlay, D. Losic, Local drug delivery to the bone by drug-releasing implants: perspectives of nano-engineered titania nanotube arrays. Ther. Deliv. **3**(7), 857–873 (2012)
6. B. Trajkovski, A. Petersen, P. Strube, M. Mehta, G.N. Duda, Intra-operatively customized implant coating strategies for local and controlled drug delivery to bone. Adv. Drug Deliv. Rev. **64**(12), 1142–1151 (2012)
7. H. Buchholz, R. Elson, E. Engelbrecht, H. Lodenkamper, J. Rottger, A. Siegel, Management of deep infection of total hip replacement. Bone Joint J. **63-B**(3), 342–353 (1981)
8. D.A. Puleo, A. Nanci, Understanding and controlling the bone–implant interface. Biomaterials **20**(23–24), 2311–2321 (1999)
9. D. Losic, M. S. Aw, A. Santos, K. Gulati, M. Bariana, Titania nanotube arrays for local drug delivery: recent advances and perspectives. Expert Opin. Drug Deliv. 1–25 (2014)
10. A. Santos, M. Sinn Aw, M. Bariana, T. Kumeria, Y. Wang, D. Losic, Drug-releasing implants: current progress, challenges and perspectives. J Mater. Chem. B **2**(37), 6157–6182 (2014)
11. R. Bosco, J. Van Den Beucken, S. Leeuwenburgh, J. Jansen, Surface engineering for bone implants: A trend from passive to active surfaces. Coatings **2**(3), 95–119 (2012)
12. S. Bauer, P. Schmuki, K. Von Der Mark, J. Park, Engineering biocompatible implant surfaces: Part I: materials and surfaces. Prog. Mater. Sci. **58**(3), 261–326 (2013)
13. S. Hansson, M. Norton, The relation between surface roughness and interfacial shear strength for bone-anchored implants. A mathematical model. J. Biomech. **32**(8), 829–836 (1999)
14. K. Kieswetter, Z. Schwartz, T.W. Hummert, D.L. Cochran, J. Simpson, D.D. Dean, B.D. Boyan, Surface roughness modulates the local production of growth factors and cytokines by osteoblast-like MG-63 cells. J. Biomed. Mater. Res. **32**(1), 55–63 (1996)
15. S. Stea, L. Savarino, A. Toni, A. Sudanese, A. Giunti, A. Pizzoferrato, Microradiographic and histochemical evaluation of mineralization inhibition at the bone-alumina interface. Biomaterials **13**(10), 664–667 (1992)
16. A. Wennerberg, The importance of surface roughness for implant incorporation. Int. J. Mach. Tool Manu. **38**(5–6), 657–662 (1998)
17. A. Piattelli, M. Degidi, M. Paolantonio, C. Mangano, A. Scarano, Residual aluminum oxide on the surface of titanium implants has no effect on osseointegration. Biomaterials **24**(22), 4081–4089 (2003)
18. A. Wennerberg, T. Albrektsson, B. Andersson, J.J. Krol, A histomorghometric study of screw-shaped and removal torque titanium implants with three different surface topographies. Clin. Oral Implants Res. **6**(1), 24–30 (1995)

19. M. Wong, J. Eulenberger, R. Schenk, E. Hunziker, Effect of surface topology on the osseointegration of implant materials in trabecular bone. J. Biomed. Mater. Res. **29**(12), 1567–1575 (1995)
20. L.F. Cooper, Y. Zhou, J. Takebe, J. Guo, A. Abron, A. Holmén, J.E. Ellingsen, Fluoride modification effects on osteoblast behavior and bone formation at TiO_2 grit-blasted c. P. Titanium endosseous implants. Biomaterials **27**(6), 926–936 (2006)
21. B. Yang, M. Uchida, H.-M. Kim, X. Zhang, T. Kokubo, Preparation of bioactive titanium metal via anodic oxidation treatment. Biomaterials **25**(6), 1003–1010 (2004)
22. Y.T. Sul, C. Johansson, A. Wennerberg, L.R. Cho, B.S. Chang, T. Albrektsson, Optimum surface properties of oxidized implants for reinforcement of osseointegration: Surface chemistry, oxide thickness, porosity, roughness, and crystal structure. Int. J. Oral Maxillofac. Implants **20**(3), 349–359 (2005)
23. X. Liu, P.K. Chu, C. Ding, Surface modification of titanium, titanium alloys, and related materials for biomedical applications. Mat. Sci. Eng. R: Rep. **47**(3–4), 49–121 (2004)
24. T.A. Horbett, L.J. Brash, Proteins at interfaces: current issues and future prospects. In: *Proteins at Interfaces, American Chemical Society*, Chapter 1, pp 1–33 (1987)
25. J.E. Sundgren, P. Bodö, I. Lundström, Auger electron spectroscopic studies of the interface between human tissue and implants of titanium and stainless steel. J. Colloid Interface Sci. **110**(1), 9–20 (1986)
26. L.D. Dorr, R. Bloebaum, J. Emmanual, R. Meldrum, Histologic, biochemical, and ion analysis of tissue and fluids retrieved during total hip arthroplasty. Clin. Orthop. Relat. Res. **261**, 82–95 (1990)
27. J.J. Jacobs, A.K. Skipor, L.M. Patterson, N.J. Hallab, W.G. Paprosky, J. Black, J.O. Galante, Metal release in patients who have had a primary total hip arthroplasty. A prospective, controlled, longitudinal study. J. Bone Joint Surg. Am. **80**(10), 1447–1458 (1998)
28. K.G. Nichols, D.A. Puleo, Effect of metal ions on the formation and function of osteoclastic cells in vitro. J. Biomed. Mater. Res. **35**(2), 265–271 (1997)
29. R. Tejero, E. Anitua, G. Orive, Toward the biomimetic implant surface: Biopolymers on titanium-based implants for bone regeneration. Prog. Polym. Sci. **39**(7), 1406–1447 (2014)
30. G. Schmidmaier, B. Wildemann, F. Cromme, F. Kandziora, N.P. Haas, M. Raschke, Bone morphogenetic protein-2 coating of titanium implants increases biomechanical strength and accelerates bone remodeling in fracture treatment: a biomechanical and histological study in rats. Bone **30**(6), 816–822 (2002)
31. M. Yoshinari, Y. Oda, T. Inoue, K. Matsuzaka, M. Shimono, Bone response to calcium phosphate-coated and bisphosphonate-immobilized titanium implants. Biomaterials **23**(14), 2879–2885 (2002)
32. J.G.E. Hendriks, J.R. Van Horn, H.C. Van Der Mei, H.J. Busscher, Backgrounds of antibiotic-loaded bone cement and prosthesis-related infection. Biomaterials **25**(3), 545–556 (2004)
33. J. Parvizi, K.J. Saleh, P.S. Ragland, A.E. Pour, M.A. Mont, Efficacy of antibiotic-impregnated cement in total hip replacement. Acta Orthop. **79**(3), 335–341 (2008)
34. K. Anagnostakos, O. Fürst, J. Kelm, Antibiotic-impregnated PMMA hip spacers: current status. Acta Orthop. **77**(4), 628–637 (2006)
35. M.E. Shirtliff, J.H. Calhoun, J.T. Mader, Experimental osteomyelitis treatment with antibiotic-impregnated hydroxyapatite. Clin. Orthop. Relat. Res. **401**, 239–247 (2002)
36. M. Gabriel, K. Nazmi, E.C. Veerman, A.V. Nieuw Amerongen, A. Zentner, Preparation of LL-37-grafted titanium surfaces with bactericidal activity. Bioconj. Chem. **17**(2), 548–550 (2006)
37. P. Roy, S. Berger, P. Schmuki, TiO_2 nanotubes: synthesis and applications. Angew. Chem. Int. Ed. **50**(13), 2904–2939 (2011)
38. P. Hoyer, Formation of a titanium dioxide nanotube array. Langmuir **12**(6), 1411–1413 (1996)
39. B.B. Lakshmi, P.K. Dorhout, C.R. Martin, Sol−gel template synthesis of semiconductor nanostructures. Chem. Mater. **9**(3), 857–862 (1997)

40. T. Kasuga, M. Hiramatsu, A. Hoson, T. Sekino, K. Niihara, Titania nanotubes prepared by chemical processing. Adv. Mater. **11**(15), 1307–1311 (1999)
41. M. Leskelä, M. Ritala, Atomic layer deposition chemistry: recent developments and future challenges. Angew. Chem. Int. Ed. **42**(45), 5548–5554 (2003)
42. Y.R. Smith, B. Sarma, S.K. Mohanty, M. Misra, Light-assisted anodized TiO_2 nanotube arrays. ACS Appl. Mater. Interfaces **4**(11), 5883–5890 (2012)
43. M.P. Neupane, I.S. Park, T.S. Bae, M.H. Lee, Sonochemical assisted synthesis of nano-structured titanium oxide by anodic oxidation. J. Alloy. Compd. **581**, 418–422 (2013)
44. V. Zwilling, M. Aucouturier, E. Darque-Ceretti, Anodic oxidation of titanium and TA6 V alloy in chromic media. An electrochemical approach. Electrochim. Acta **45**(6), 921–929 (1999)
45. V. Zwilling, E. Darque-Ceretti, A. Boutry-Forveille, D. David, M.Y. Perrin, M. Aucouturier, Structure and physicochemistry of anodic oxide films on titanium and TA6Valloy. Surf. Interface Anal. **27**(7), 629–637 (1999)
46. J.M. Macak, H. Tsuchiya, P. Schmuki, High-aspect-ratio TiO_2 nanotubes by anodization of titanium. Angew. Chem. Int. Ed. **44**(14), 2100–2102 (2005)
47. J.M. Macak, H. Tsuchiya, L. Taveira, S. Aldabergerova, P. Schmuki, Smooth anodic TiO_2 nanotubes. Angew. Chem. Int. Ed. **44**(45), 7463–7465 (2005)
48. J.M. Macak, K. Sirotna, P. Schmuki, Self-organized porous titanium oxide prepared in Na_2SO_4/NaF electrolytes. Electrochim. Acta **50**(18), 3679–3684 (2005)
49. H.E. Prakasam, K. Shankar, M. Paulose, O.K. Varghese, C.A. Grimes, A new benchmark for TiO_2 nanotube array growth by anodization. J. Phys. Chem. C **111**(20), 7235–7241 (2007)
50. M. Paulose, H.E. Prakasam, O.K. Varghese, L. Peng, K.C. Popat, G.K. Mor, T.A. Desai, C. A. Grimes, TiO2 nanotube arrays of 1000 μm length by anodization of titanium foil: Phenol red diffusion. J. Phys. Chem. C **111**(41), 14992–14997 (2007)
51. N.K. Allam, C.A. Grimes, Formation of vertically oriented TiO_2 nanotube arrays using a fluoride free HCl aqueous electrolyte. J. Phys. Chem. C **111**(35), 13028–13032 (2007)
52. S.P. Albu, D. Kim, P. Schmuki, Growth of aligned TiO_2 bamboo-type nanotubes and highly ordered nanolace. Angew. Chem. **120**(10), 1942–1945 (2008)
53. J. Yu, D. Wang, Y. Huang, X. Fan, X. Tang, C. Gao, J. Li, D. Zou, K. Wu, A cylindrical core-shell-like TiO_2 nanotube array anode for flexible fiber-type dye-sensitized solar cells. Nanoscale Res. Lett. **6**(1), 94 (2011)
54. K. Gulati, M.S. Aw, D. Losic, Drug-eluting Ti wires with titania nanotube arrays for bone fixation and reduced bone infection. Nanoscale Res. Lett. **6**(1), 571 (2011)
55. Q.Y. Zeng, M. Xi, W. Xu, X.J. Li, Preparation of titanium dioxide nanotube arrays on titanium mesh by anodization in $(NH_4)_2SO_4$/NH_4F electrolyte. Mater. Corros. **64**(11), 1001–1006 (2013)
56. L. Sun, X. Wang, M. Li, S. Zhang, Q. Wang, Anodic titania nanotubes grown on titanium tubular electrodes. Langmuir **30**(10), 2835–2841 (2014)
57. K. Gulati, M.S. Aw, D. Losic, Nanoengineered drug-releasing Ti wires as an alternative for local delivery of chemotherapeutics in the brain. Int. J. Nanomed. **7**, 2069–2076 (2012)
58. M.S. Aw, K.A. Khalid, K. Gulati, G.J. Atkins, P. Pivonka, D.M. Findlay, D. Losic, Characterization of drug-release kinetics in trabecular bone from titania nanotube implants. Int. J. Nanomed. **7**, 4883–4892 (2012)
59. K. Gulati, G.J. Atkins, D.M. Findlay, D. Losic, Nano-engineered titanium for enhanced bone therapy, Proc SPIE 8812. Biosensing Nanomed. VI, 88120C (September 11, 2013). doi:10.1117/12.2027151
60. M. Long, H.J. Rack, Titanium alloys in total joint replacement—a materials science perspective. Biomaterials **19**(18), 1621–1639 (1998)
61. J.M. Macak, H. Tsuchiya, L. Taveira, A. Ghicov, P. Schmuki, Self-organized nanotubular oxide layers on Ti-6Al-7Nb and Ti-6Al-4V formed by anodization in NH_4F solutions. J. Biomed. Mater. Res. A **75A**(4), 928–933 (2005)

62. X.J. Feng, J.M. Macak, S.P. Albu, P. Schmuki, Electrochemical formation of self-organized anodic nanotube coating on Ti–28ZR–8Nb biomedical alloy surface. Acta Biomater. **4**(2), 318–323 (2008)
63. K. Yasuda, P. Schmuki, Control of morphology and composition of self-organized zirconium titanate nanotubes formed in $(NH_4)_2SO_4/NH_4F$ electrolytes. Electrochim. Acta **52**(12), 4053–4061 (2007)
64. H. Jha, R. Hahn, P. Schmuki, Ultrafast oxide nanotube formation on TiNb, TiZr and TiTa alloys by rapid breakdown anodization. Electrochim. Acta **55**(28), 8883–8887 (2010)
65. Y.Q. Liang, Z.D. Cui, S.L. Zhu, X.J. Yang, Characterization of self-organized TiO_2 nanotubes on Ti–4Zr–22Nb–2Sn alloys and the application in drug delivery system. J. Mater. Sci. Mater. Med. **22**(3), 461–467 (2011)
66. L. Wang, T.T. Zhao, Z. Zhang, G. Li, Fabrication of highly ordered TiO_2 nanotube arrays via anodization of ti-6al-4v alloy sheet. J. Nanosci. Nanotechnol. **10**(12), 8312–8321 (2010)
67. E. Feschet-Chassot, V. Raspal, Y. Sibaud, O.K. Awitor, F. Bonnemoy, J.L. Bonnet, J. Bohatier, Tunable functionality and toxicity studies of titanium dioxide nanotube layers. Thin Solid Films **519**(8), 2564–2568 (2011)
68. B.D. Boyan, T.W. Hummert, D.D. Dean, Z. Schwartz, Role of material surfaces in regulating bone and cartilage cell response. Biomaterials **17**(2), 137–146 (1996)
69. K. Gulati, S. Ramakrishnan, M.S. Aw, G.J. Atkins, D.M. Findlay, D. Losic, Biocompatible polymer coating of titania nanotube arrays for improved drug elution and osteoblast adhesion. Acta Biomater. **8**(1), 449–456 (2012)
70. K.C. Popat, L. Leoni, C.A. Grimes, T.A. Desai, Influence of engineered titania nanotubular surfaces on bone cells. Biomaterials **28**(21), 3188–3197 (2007)
71. K.C. Popat, M. Eltgroth, T.J. Latempa, C.A. Grimes, T.A. Desai, Decreased staphylococcus epidermis adhesion and increased osteoblast functionality on antibiotic-loaded titania nanotubes. Biomaterials **28**(32), 4880–4888 (2007)
72. L. Peng, M.L. Eltgroth, T.J. Latempa, C.A. Grimes, T.A. Desai, The effect of TiO_2 nanotubes on endothelial function and smooth muscle proliferation. Biomaterials **30**(7), 1268–1272 (2009)
73. P. Neacsu, A. Mazare, A. Cimpean, J. Park, M. Costache, P. Schmuki, I. Demetrescu, Reduced inflammatory activity of raw 264.7 macrophages on titania nanotube modified Ti surface. Int. J. Biochem. Cell Biol. **55**, 187–195 (2014)
74. L.M. Bjursten, L. Rasmusson, S. Oh, G.C. Smith, K.S. Brammer, S. Jin, Titanium dioxide nanotubes enhance bone bonding in vivo. J. Biomed. Mater. Res. A. **92A**(3), 1218–1224 (2010)
75. W.C. Schroer, K.R. Berend, A.V. Lombardi, C.L. Barnes, M.P. Bolognesi, M.E. Berend, M. A. Ritter, R.M. Nunley, Why are total knees failing today? Etiology of total knee revision in 2010 and 2011. J. Arthroplasty **28**(8, Supplement), 116–119 (2013)
76. S. Franz, S. Rammelt, D. Scharnweber, J.C. Simon, Immune responses to implants—a review of the implications for the design of immunomodulatory biomaterials. Biomaterials **32**(28), 6692–6709 (2011)
77. B.D. Ratner, The engineering of biomaterials exhibiting recognition and specificity. J. Mol. Recognit. **9**(5–6), 617–625 (1996)
78. C. Rungsiyakull, Q. Li, G. Sun, W. Li, M.V. Swain, Surface morphology optimization for osseointegration of coated implants. Biomaterials **31**(27), 7196–7204 (2010)
79. K.M. Ainslie, S.L. Tao, K.C. Popat, H. Daniels, V. Hardev, C.A. Grimes, T.A. Desai, In vitro inflammatory response of nanostructured titania, silicon oxide, and polycaprolactone. J. Biomed. Mater. Res. A **91A**(3), 647–655 (2009)
80. B.S. Smith, P. Capellato, S. Kelley, M. Gonzalez-Juarrero, K.C. Popat, Reduced in vitro immune response on titania nanotube arrays compared to titanium surface. Biomater. Sci. **1** (3), 322–332 (2013)
81. G.E. Aninwene, C. Yao, T.J. Webster, Enhanced osteoblast adhesion to drug-coated anodized nanotubular titanium surfaces. Int. J. Nanomed. **3**(2), 257–264 (2008)

82. S.S. Mandal, D. Jose, A.J. Bhattacharyya, Role of surface chemistry in modulating drug release kinetics in titania nanotubes. Mater. Chem. Phys. **147**(1–2), 247–253 (2014)
83. T. Shokuhfar, S. Sinha-Ray, C. Sukotjo, A.L. Yarin, Intercalation of anti-inflammatory drug molecules within TiO_2 nanotubes. RSC Adv. **3**(38), 17380–17386 (2013)
84. M. Aw, K. Gulati, D. Losic, Controlling drug release from titania nanotube arrays using polymer nanocarriers and biopolymer coating. Biomater. Nanobiotechnol. **2**, 477–484 (2011)
85. M.S. Aw, M. Kurian, D. Losic, Non-eroding drug-releasing implants with ordered nanoporous and nanotubular structures: concepts for controlling drug release. Biomater. Sci. **2**(1), 10–34 (2014)
86. C.R. Hauck, K. Ohlsen, Sticky connections: Extracellular matrix protein recognition and integrin-mediated cellular invasion by staphylococcus aureus. Curr. Opin. Microbiol. **9**(1), 5–11 (2006)
87. A. Gristina, Biomaterial-centered infection: microbial adhesion versus tissue integration. Science **237**(4822), 1588–1595 (1987)
88. N.J. Hickok, I.M. Shapiro, Immobilized antibiotics to prevent orthopaedic implant infections. Adv Drug Del Rev. **64**(12), 1165–1176 (2012)
89. J.W. Costerton, P.S. Stewart, E.P. Greenberg, Bacterial biofilms: A common cause of persistent infections. Science **284**(5418), 1318–1322 (1999)
90. S.S. Rogers, C. Van Der Walle, T.A. Waigh, Microrheology of bacterial biofilms in vitro: staphylococcus aureus and pseudomonas aeruginosa. Langmuir **24**(23), 13549–13555 (2008)
91. S.D. Puckett, E. Taylor, T. Raimondo, T.J. Webster, The relationship between the nanostructure of titanium surfaces and bacterial attachment. Biomaterials **31**(4), 706–713 (2010)
92. B. Ercan, T. Erik, A. Ece, J.W. Thomas, Diameter of titanium nanotubes influences anti-bacterial efficacy. Nanotechnology **22**(29), 295102 (2011)
93. T. Das, P.K. Sharma, H.J. Busscher, H.C. Van Der Mei, B.P. Krom, Role of extracellular DNA in initial bacterial adhesion and surface aggregation. Appl. Environ. Microbiol. **76**(10), 3405–3408 (2010)
94. H. Zhang, Y. Sun, A. Tian, X.X. Xue, L. Wang, A. Alquhali, X. Bai, Improved antibacterial activity and biocompatibility on vancomycin-loaded TiO_2 nanotubes: in vivo and in vitro studies. Int. J. Nanomed. **8**, 4379–4389 (2013)
95. M. Kazemzadeh-Narbat, J. Kindrachuk, K. Duan, H. Jenssen, R.E.W. Hancock, R. Wang, Antimicrobial peptides on calcium phosphate-coated titanium for the prevention of implant-associated infections. Biomaterials **31**(36), 9519–9526 (2010)
96. M. Ma, M. Kazemzadeh-Narbat, Y. Hui, S. Lu, C. Ding, D.D.Y. Chen, R.E.W. Hancock, R. Wang, Local delivery of antimicrobial peptides using self-organized TiO_2 nanotube arrays for peri-implant infections. J. Biomed. Mater. Res. A **100A**(2), 278–285 (2012)
97. L. Zhao, H. Wang, K. Huo, L. Cui, W. Zhang, H. Ni, Y. Zhang, Z. Wu, P.K. Chu, Antibacterial nano-structured titania coating incorporated with silver nanoparticles. Biomaterials **32**(24), 5706–5716 (2011)
98. K. Huo, X. Zhang, H. Wang, L. Zhao, X. Liu, P.K. Chu, Osteogenic activity and antibacterial effects on titanium surfaces modified with Zn-incorporated nanotube arrays. Biomaterials **34**(13), 3467–3478 (2013)
99. T. Kumeria, H. Mon, M.S. Aw, K. Gulati, H.J. Griesser, D. Losic, Advanced biopolymer-coated drug-releasing titania nanotubes (TNTs) implants with simultaneously enhanced osteoblast adhesion and antibacterial properties (2015) (unpublished)
100. X. Chen, K. Cai, J. Fang, M. Lai, Y. Hou, J. Li, Z. Luo, Y. Hu, L. Tang, Fabrication of selenium-deposited and chitosan-coated titania nanotubes with anticancer and antibacterial properties. Colloids Surf. B Biointerfaces **103**, 149–157 (2013)
101. B. Ercan, K.M. Kummer, K.M. Tarquinio, T.J. Webster, Decreased staphylococcus aureus biofilm growth on anodized nanotubular titanium and the effect of electrical stimulation. Acta Biomater. **7**(7), 3003–3012 (2011)

102. J.L. Del Pozo, M.S. Rouse, J.N. Mandrekar, J.M. Steckelberg, R. Patel, The electricidal effect: Reduction of staphylococcus and pseudomonas biofilms by prolonged exposure to low-intensity electrical current. Antimicrob. Agents Chemother. **53**(1), 41–45 (2009)
103. A. Chug, S. Shukla, L. Mahesh, S. Jadwani, Osseointegration—molecular events at the bone–implant interface: A review. J. Oral Maxillofac. Surg. **25**(1), 1–4 (2013)
104. C. Yao, V. Perla, J.L. Mckenzie, E.B. Slamovich, T.J. Webster, Anodized ti and Ti6Al4 V possessing nanometer surface features enhances osteoblast adhesion. J. Biomed. Nanotech. **1** (1), 68–73 (2005)
105. T.J. Webster, J.U. Ejiofor, Increased osteoblast adhesion on nanophase metals: Ti, Ti6Al4V, and CoCrMo. Biomaterials **25**(19), 4731–4739 (2004)
106. C. Von Wilmowsky, S. Bauer, R. Lutz, M. Meisel, F.W. Neukam, T. Toyoshima, P. Schmuki, E. Nkenke, K.A. Schlegel, In vivo evaluation of anodic TiO_2 nanotubes: an experimental study in the pig. J. Biomed. Mater. Res. B Appl. Biomater. **89B**(1), 165–171 (2009)
107. M.P. Neupane, I.S. Park, T.S. Bae, H.K. Yi, M. Uo, F. Watari, M.H. Lee, Titania nanotubes supported gelatin stabilized gold nanoparticles for medical implants. J. Mater. Chem. **21**(32), 12078–12082 (2011)
108. L. Zhao, H. Wang, K. Huo, X. Zhang, W. Wang, Y. Zhang, Z. Wu, P.K. Chu, The osteogenic activity of strontium loaded titania nanotube arrays on titanium substrates. Biomaterials **34**(1), 19–29 (2013)
109. J. Kunze, L. Müller, J.M. Macak, P. Greil, P. Schmuki, F.A. Müller, Time-dependent growth of biomimetic apatite on anodic TiO_2 nanotubes. Electrochim. Acta **53**(23), 6995–7003 (2008)
110. A. Kar, K.S. Raja, M. Misra, Electrodeposition of hydroxyapatite onto nanotubular TiO_2 for implant applications. Surf. Coat. Technol. **201**(6), 3723–3731 (2006)
111. A. Kodama, S. Bauer, A. Komatsu, H. Asoh, S. Ono, P. Schmuki, Bioactivation of titanium surfaces using coatings of TiO_2 nanotubes rapidly pre-loaded with synthetic hydroxyapatite. Acta Biomater. **5**(6), 2322–2330 (2009)
112. Y.-X. Gu, J. Du, J.-M. Zhao, M.-S. Si, J.-J. Mo, H.-C. Lai, Characterization and preosteoblastic behavior of hydroxyapatite-deposited nanotube surface of titanium prepared by anodization coupled with alternative immersion method. J. Biomed. Mater. Res. B Appl. Biomater. **100B**(8), 2122–2130 (2012)
113. S. Oh, S. Jin, Titanium oxide nanotubes with controlled morphology for enhanced bone growth. Mater. Sci. Eng. C **26**(8), 1301–1306 (2006)
114. T.N. Vo, F.K. Kasper, A.G. Mikos, Strategies for controlled delivery of growth factors and cells for bone regeneration. Adv. Drug Deliv. Rev. **64**(12), 1292–1309 (2012)
115. M. Lai, K. Cai, L. Zhao, X. Chen, Y. Hou, Z. Yang, Surface functionalization of TiO_2 nanotubes with Bone Morphogenetic Protein 2 and its synergistic effect on the differentiation of mesenchymal stem cells. Biomacromolecules **12**(4), 1097–1105 (2011)
116. Y. Hu, K. Cai, Z. Luo, D. Xu, D. Xie, Y. Huang, W. Yang, P. Liu, Tio2 nanotubes as drug nanoreservoirs for the regulation of mobility and differentiation of mesenchymal stem cells. Acta Biomater. **8**(1), 439–448 (2012)
117. T.-H. Koo, J. Borah, Z.C. Xing, S.M. Moon, Y. Jeong, I.K. Kang, Immobilization of pamidronic acids on the nanotube surface of titanium discs and their interaction with bone cells. Nanoscale Res. Lett. **8**(1), 1–9 (2013)
118. S.J. Lee, T.J. Oh, T.S. Bae, M.H. Lee, Y. Soh, B.I. Kim, H.S. Kim, Effect of bisphosphonates on anodized and heat-treated titanium surfaces: an animal experimental study. J. Periodontol. **82**(7), 1035–1042 (2010)
119. H. Wei, S. Wu, Z. Feng, W. Zhou, Y. Dong, G. Wu, S. Bai, Y. Zhao, Increased fibroblast functionality on CNN2-loaded titania nanotubes. Int. J. Nanomed. **7**, 1091–1100 (2012)
120. S. Sun, W. Yu, Y. Zhang, F. Zhang, Increased preosteoblast adhesion and osteogenic gene expression on TiO_2 nanotubes modified with KRSR. J. Mater. Sci. Mater. Med. **24**(4), 1079–1091 (2013)

121. E. Gultepe, D. Nagesha, S. Sridhar, M. Amiji, Nanoporous inorganic membranes or coatings for sustained drug delivery in implantable devices. Adv. Drug Deliv. Rev. **62**(3), 305–315 (2010)
122. L. Peng, A.D. Mendelsohn, T.J. Latempa, S. Yoriya, C.A. Grimes, T.A. Desai, Long-term small molecule and protein elution from TiO_2 nanotubes. Nano Lett. **9**(5), 1932–1936 (2009)
123. C. Yao, T.J. Webster, Prolonged antibiotic delivery from anodized nanotubular titanium using a co-precipitation drug loading method. J. Biomed. Mater. Res. B Appl. Biomater. **91B** (2), 587–595 (2009)
124. I. De Santo, L. Sanguigno, F. Causa, T. Monetta, P.A. Netti, Exploring doxorubicin localization in eluting TiO_2 nanotube arrays through fluorescence correlation spectroscopy analysis. Analyst **137**(21), 5076–5081 (2012)
125. C.M. Han, E.J. Lee, H.E. Kim, Y.H. Koh, J.H. Jang, Porous TiO_2 films on Ti implants for controlled release of tetracycline-hydrochloride (TCH). Thin Solid Films **519**(22), 8074–8076 (2011)
126. M.S. Aw, J. Addai-Mensah, D. Losic, A multi-drug delivery system with sequential release using titania nanotube arrays. Chem. Commun. **48**(27), 3348–3350 (2012)
127. M.S. Aw, J. Addai-Mensah, D. Losic, Magnetic-responsive delivery of drug-carriers using titania nanotube arrays. J. Mater. Chem. **22**(14), 6561–6563 (2012)
128. M.S. Aw, D. Losic, Ultrasound enhanced release of therapeutics from drug-releasing implants based on titania nanotube arrays. Int. J. Pharm. **443**(1–2), 154–162 (2013)
129. Y.Y. Song, F. Schmidt-Stein, S. Bauer, P. Schmuki, Amphiphilic TiO_2 nanotube arrays: an actively controllable drug delivery system. J. Am. Chem. Soc. **131**(12), 4230–4232 (2009)
130. S. Simovic, D. Losic, K. Vasilev, Controlled drug release from porous materials by plasma polymer deposition. Chem. Commun. **46**(8), 1317–1319 (2010)
131. K. Vasilev, Z. Poh, K. Kant, J. Chan, A. Michelmore, D. Losic, Tailoring the surface functionalities of titania nanotube arrays. Biomaterials **31**(3), 532–540 (2010)
132. A.J. Collins, J.A. Cosh, Temperature and biochemical studies of joint inflammation. A preliminary investigation. Ann. Rheum. Dis. **29**(4), 386–392 (1970)
133. K. Cai, F. Jiang, Z. Luo, X. Chen, Temperature-responsive controlled drug delivery system based on titanium nanotubes. Adv. Eng. Mater. **12**(9), B565–B570 (2010)
134. N.K. Shrestha, J.M. Macak, F. Schmidt-Stein, R. Hahn, C.T. Mierke, B. Fabry, P. Schmuki, Magnetically guided titania nanotubes for site-selective photocatalysis and drug release. Angew. Chem. Int. Ed. **48**(5), 969–972 (2009)
135. S. Sirivisoot, R.A. Pareta, T.J. Webster, A conductive nanostructured polymer electrodeposited on titanium as a controllable, local drug delivery platform. J. Biomed. Mater. Res. A **99A**(4), 586–597 (2011)
136. S. Sirivisoot, P. Rajesh, J.W. Thomas, Electrically controlled drug release from nanostructured polypyrrole coated on titanium. Nanotechnology **22**(8), 085101 (2011)
137. M. Bariana, M.S. Aw, E. Moore, N.H. Voelcker, D. Losic, Radiofrequency-triggered release for on-demand delivery of therapeutics from titania nanotube drug-eluting implants. Nanomedicine **9**(8), 1263–1275 (2013)
138. S. Sirivisoot, Y. Chang, X. Xingcheng, W.S. Brian, J.W. Thomas, Greater osteoblast functions on multiwalled carbon nanotubes grown from anodized nanotubular titanium for orthopedic applications. Nanotechnology **18**(36), 365102 (2007)
139. S. Sirivisoot, J.W. Thomas, Multiwalled carbon nanotubes enhance electrochemical properties of titanium to determine in situ bone formation. Nanotechnology. **19**(29), 295101 (2008)
140. D.B. Jones, E. Broeckmann, T. Pohl, E.L. Smith, Development of a mechanical testing and loading system for trabecular bone studies for long term culture. Eur. Cell Mater. **5**, 48–59 (2003)
141. C.M. Davies, D.B. Jones, M.J. Stoddart, K. Koller, E. Smith, C.W. Archer, R.G. Richards, Mechanically loaded ex vivo bone culture system 'zetos': systems and culture preparation. Eur. Cell Mater. **11**, 57–75 (2006)

142. S. Minagar, J. Wang, C.C. Berndt, E.P. Ivanova, C. Wen, Cell response of anodized nanotubes on titanium and titanium alloys. J. Biomed. Mater. Res. A **101A**(9), 2726–2739 (2013)
143. J. Xiao, H. Zhou, L. Zhao, Y. Sun, S. Guan, B. Liu, L. Kong, The effect of hierarchical micro/nanosurface titanium implant on osseointegration in ovariectomized sheep. Osteoporosis Int. **22**(6), 1907–1913 (2011)
144. K. Vandamme, X. Holy, M. Bensidhoum, D. Logeart-Avramoglou, I.E. Naert, J.A. Duyck, H. Petite, In vivo molecular evidence of delayed titanium implant osseointegration in compromised bone. Biomaterials **32**(14), 3547–3554 (2011)
145. N. Harmankaya, J. Karlsson, A. Palmquist, M. Halvarsson, K. Igawa, M. Andersson, P. Tengvall, Raloxifene and alendronate containing thin mesoporous titanium oxide films improve implant fixation to bone. Acta Biomater. **9**, 7064–7073 (2013)
146. J.M. Park, J.Y. Koak, J.H. Jang, C.H. Han, S.K. Kim, S.J. Heo, Osseointegration of anodized titanium implants coated with fibroblast growth factor-fibronectin (FGF-FN) fusion protein. Int. J. Oral Maxillofac. Implants **21**(6), 859–866 (2006)
147. R. Adell, B. Eriksson, U. Lekholm, P.I. Brånemark, T. Jemt, Long-term follow-up study of osseointegrated implants in the treatment of totally edentulous jaws. Int. J. Oral Maxillofac. Implants **5**(4), 347–359 (1990)
148. E.K. Moioli, P.A. Clark, X. Xin, S. Lal, J.J. Mao, Matrices and scaffolds for drug delivery in dental, oral and craniofacial tissue engineering. Adv. Drug Deliv. Rev. **59**(4–5), 308–324 (2007)
149. Q. Ma, S. Mei, K. Ji, Y. Zhang, P.K. Chu, Immobilization of Ag nanoparticles/FGF-2 on a modified titanium implant surface and improved human gingival fibroblasts behavior. J. Biomed. Mater. Res. A **98A**(2), 274–286 (2011)
150. Y.-H. Lee, G. Bhattarai, I.-S. Park, G.-R. Kim, G.-E. Kim, M.-H. Lee, H.-K. Yi, Bone regeneration around n-acetyl cysteine-loaded nanotube titanium dental implant in rat mandible. Biomaterials **34**(38), 10199–10208 (2013)
151. I. Demetrescu, C. Pirvu, V. Mitran, Effect of nano-topographical features of Ti/TiO_2 electrode surface on cell response and electrochemical stability in artificial saliva. Bioelectrochemistry **79**(1), 122–129 (2010)
152. M. Kalbacova, J.M. Macak, F. Schmidt-Stein, C.T. Mierke, P. Schmuki, Tio2 nanotubes: Photocatalyst for cancer cell killing. Phys. Status Solidi Rapid Res. Lett. **2**(4), 194–196 (2008)
153. Q. Li, X. Wang, X. Lu, H. Tian, H. Jiang, G. Lv, D. Guo, C. Wu, B. Chen, The incorporation of daunorubicin in cancer cells through the use of titanium dioxide whiskers. Biomaterials **30** (27), 4708–4715 (2009)
154. P. Mccarthy, K. Otto, M. Rao, Robust penetrating microelectrodes for neural interfaces realized by titanium micromachining. Biomed. Microdevices **13**(3), 503–515 (2011)
155. Y. Wang, J. Wang, X. Deng, J. Wang, H. Wang, M. Wu, Z. Jiao, Y. Liu, Direct imaging of titania nanotubes located in mouse neural stem cell nuclei. Nano Res. **2**(7), 543–552 (2009)
156. World Health Organization (WHO), Medical device regulations. Global overview and guiding principles (2003)
157. J.S. Tsuji, A.D. Maynard, P.C. Howard, J.T. James, C.-W. Lam, D.B. Warheit, A.B. Santamaria, Research strategies for safety evaluation of nanomaterials, part IV: risk assessment of nanoparticles. Toxicol. Sci. **89**(1), 42–50 (2006)
158. Y. Nuevo-Ordóñez, M. Montes-Bayón, E. Blanco-González, J. Paz-Aparicio, J.D. Raimundez, J.M. Tejerina, M.A. Peña, A. Sanz-Medel, Titanium release in serum of patients with different bone fixation implants and its interaction with serum biomolecules at physiological levels. Anal. Bioanal. Chem. **401**(9), 2747–2754 (2011)
159. X. Li, L. Wang, Y. Fan, Q. Feng, F.-Z. Cui, Biocompatibility and toxicity of nanoparticles and nanotubes. J. Nanomat. **2012**, 548389 (2012)
160. C.M. Sayes, R. Wahi, P.A. Kurian, Y. Liu, J.L. West, K.D. Ausman, D.B. Warheit, V.L. Colvin, Correlating nanoscale titania structure with toxicity: A cytotoxicity and inflammatory

response study with human dermal fibroblasts and human lung epithelial cells. Toxicol. Sci. **92**(1), 174–185 (2006)
161. N. Wang, H. Li, W. Lü, J. Li, J. Wang, Z. Zhang, Y. Liu, Effects of TiO_2 nanotubes with different diameters on gene expression and osseointegration of implants in minipigs. Biomaterials **32**(29), 6900–6911 (2011)
162. G.C. Smith, L. Chamberlain, L. Faxius, G.W. Johnston, S. Jin, L.M. Bjursten, Soft tissue response to titanium dioxide nanotube modified implants. Acta Biomater. **7**(8), 3209–3215 (2011)

Index

D. Losic and A. Santos (eds.), *Electrochemically Engineered Nanoporous Materials*, Springer Series in Materials Science 220,
DOI 10.1007/978-3-319-20346-1